F. E. M. Saboya
E. M. Sparrow

Department of Mechanical Engineering,
University of Minnesota,
Minneapolis, Minn.

Local and Average Transfer Coefficients for One-Row Plate Fin and Tube Heat Exchanger Configurations

The analogy between heat and mass transfer has been used to obtain local and average transfer coefficients for a one-row plate fin and tube heat exchanger configuration. The mass transfer experiments were performed using the naphthalene sublimation technique. A heat exchanger passage was modeled using naphthalene plates; spacer disks simulated the tubes. Detailed measurements of the surface elevation of the naphthalene plates were made before and after a data run, and this enabled evaluation of the local transfer coefficients. Average transfer coefficients were determined both by surface integration of the local mass transfer or by weighing the test plate with a precision balance; the two methods gave results that agree within one or two percent. The local measurements revealed high values of the transfer coefficient on the forward part of the fin due to the presence of developing boundary layers. In addition, owing to a natural augmentation effect caused by a vortex system which develops in front of the tube, there are very high fin transfer coefficients in a U-shaped band that rings the tube. The effect of the vortex system is more pronounced at higher Reynolds numbers. Relatively low transfer coefficients are encountered on the portion of the fin that lies downstream of the minimum flow cross section. The coefficients are especially low in the region behind the tube.

Introduction

Heat exchange devices that consist of a set of parallel plates and an array of tubes passing perpendicularly through the plates are commonly employed in engineering applications, for example, air conditioning machines. Such devices are often referred to as plate fin and tube heat exchangers. In addition, these heat exchangers are designated as single row or multi-row depending upon the number of rows of tubes that are encountered by the fluid passing between the plates. The present paper is concerned with the transfer characteristics of single row exchangers.

In view of the wide-spread use of plate fin and tube heat exchangers, it is remarkable that so little information about their heat transfer characteristics is available in the published literature. For single-row exchangers with plane fins, the most extensive set of results is due to Shepherd [1].[1] The heat transfer information presented by Shepherd is in the form of average air-side transfer coefficients and transfer rates. These transfer coefficients were evaluated without account being taken of the role of the fin efficiency (i.e., nonuniform fin temperatures) and, in addition, there are other uncertainties in the data reduction procedure which will be discussed later. The most dense fin arrangement investigated by Shepherd was 11 fins per in. Gebhart [2] has also reported some average heat transfer results for the plane fin case in conjunction with a study of fins having slots, holes, and tabs. Bunge [3] gave results for two single-row plane fin units, arranged one behind the other, with a variable open space between.

Quite apart from the available average transfer coefficients and their possible limitations with respect to parameter ranges and accuracy, it is also relevant to note that local transfer coefficients on the fin surface are altogether unavailable. The absence of such information is understandable in view of the formidable difficulties of measuring local heat transfer rates and temperatures on fin plates that are typically 0.15 mm (0.006 in.) thick and are separated by about 1½ mm (0.060 in.) from adjacent fins.

In the present research, local transfer coefficients on the fins of a one-row fin and tube heat exchanger configuration have been obtained by means of the analogy between heat and mass transfer. Average transfer coefficients were also determined. The mass transfer experiments were performed utilizing the naphthalene

[1] Numbers in brackets designate References at end of paper.

Contributed by the Heat Transfer Division for publication in the JOURNAL OF HEAT TRANSFER. Manuscript received by the Heat Transfer Division, December 19, 1973. Paper No. 74-HT-UU.

sublimation technique. Although this technique has been employed in a variety of research problems, it has not, within the knowledge of the authors, been applied to obtain quantitative data for local transfer coefficients in complex three-dimensional flows of the type encountered here. Due recognition should, however, be accorded to Fukui and Sakamoto [4] who used the technique to get average transfer coefficients and qualitative local information for multi-row fin and tube heat exchanger configurations.[2]

To employ the method, naphthalene plates were cast in a specially designed mold which, together with the casting technique itself, ensured that the plate surfaces would possess a high degree of flatness. A pair of such plates, spaced apart by a row of circular disks, formed the mass transfer test section. The disks play the same role with respect to the flow field between the plates as do the tubes in an actual fin and tube heat exchanger. Painstaking measurements of the surface contour of the naphthalene plates before and after a test run were made with a sensitive dial gage. Corrections were carefully applied to account for natural convection sublimation from the surfaces that occurred during the time required for the contour measurements and for setting up the equipment.

The net change in local elevation of the naphthalene surface resulting from the mass transfer during a test run was determined from the contour measurements and the corrections and, from this, the local mass transfer rates and transfer coefficients were evaluated. In addition, the local changes in elevation were integrated over the surface of the plates in order to yield the overall mass transfer. An alternative and fully independent determination of the overall mass transfer was made by direct weighing with a sensitive balance. The results obtained from the surface-integrated local mass transfer and from the balance measurements were compared and found to agree remarkably well (1 or 2 percent).

The experimentally determined local and average transfer coefficients will be presented in dimensionless form in terms of the Sherwood number, which is the mass transfer analogue of the Nusselt number. As will be discussed later, the Sherwood numbers can be converted to Nusselt numbers by employing the analogy between heat and mass transfer.

It is interesting to preview certain noteworthy aspects of the results by calling attention to an observation which may be made outside the laboratory. During or after a winter snowstorm which has been accompanied by wind, one may observe that the snow has been swept away from an annular region at the base of a tree. The hydrodynamic conditions which are responsible for the sweeping action are expected to be operative as the flow impinges on the tubes in a fin and tube heat exchanger. Consequently, adjacent to a tube, one might expect to find a band of very high fin transfer coefficients. This expectation is verified by the mass transfer results that will be reported later.

A schematic diagram of the physical problem under study is presented in Fig. 1. The upper sketch is a general pictorial view of a one-row plate fin and tube heat exchanger configuration. The lower sketch is a plan view of the configuration that was studied in the present investigation. As seen therein, the tube array was modeled by four full tubes and by two half tubes situated at the two ends of the span. The region enclosed by dashed lines is one of the symmetry zones which repeats across the span of the fins.

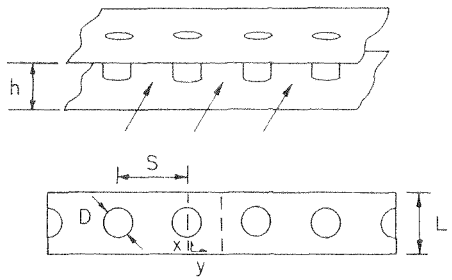

Fig. 1 Schematic of one-row plate fin and tube heat exchanger configuration

Fig. 1 also contains dimensional nomenclature as well as the x,y coordinates that will be used to identify positions on the surface of the fin. Although the actual dimensions h, L, S, and D of the test apparatus will be indicated shortly, it is relevant to note that the results have a much more general applicability when the parameters are expressed in dimensionless terms. The dimensionless parameters which govern the results may be written as

$$\frac{h}{D}, \frac{S}{D}, \frac{L}{D}, \text{Re, Sc or Pr}$$

The dimension ratios for the present test apparatus were $h/D = 0.193$, $S/D = 2.5$, and $L/D = 2.16$. These values are typical of present-day heat exchangers encountered in air conditioning applications. The results presented herein should be applicable to heat exchangers where the dimension ratios are in the same range (but not necessarily identical) to those stated in the foregoing. The actual values of the apparatus dimensions are: $h = 0.165$ cm (0.065 in.), $D = 0.853$ cm (0.336 in.), $S = 2.15$ cm (0.848 in.) and $L = 1.85$ cm (0.727 in.).

The Reynolds number may be defined in various ways and, indeed, numerous definitions appear in the heat exchanger literature. For the Kays and London definition [5] (see Re definition in equation (12)), the range is from about 150 to 1270. Once again, this range is relevant to present-day air-conditioning machines. In terms of the usual channel Reynolds number (hydraulic diameter equal to twice the channel height), the range is very nearly the same as the aforementioned.

The Schmidt number for naphthalene mass transfer to air is 2.5. Since the Schmidt number plays a role analogous to the Prandtl number, the scaling of the results from 2.5 to 0.7 (Prandtl number for air) can be accomplished by a power law representation.

Test Apparatus and Experimental Methods

The description of the experimental apparatus is facilitated by reference to Fig. 2, which is a schematic side view of the test section. As shown therein, air from the laboratory room is drawn

[2] Recognition should also be given to Kruckels [9] who employed a mass transfer method based on photometric measurements. Kruckels' paper contains fragmentary local transfer coefficient information.

Nomenclature

D = tube diameter
D_h = hydraulic diameter, equation (8)
$\mathcal{D}$ = diffusion coefficient
h = spacing between plates
K = local mass transfer coefficient, equation (5)
$\overline{K}$ = average mass transfer coefficient, equation (9)
L = streamwise length of channel
$\dot{m}$ = local rate of mass transfer/area
$\dot{M}$ = surface integrated mass transfer rate
Pr = Prandtl number
Re = Reynolds number, equation (12)
S = distance between tube centers
Sc = Schmidt number
Sh = local Sherwood number, equation (6)
$\overline{\text{Sh}}$ = average Sherwood number, equation (11)
t_0 = duration time of a data run
x,y = surface coordinates, Fig. 1
δ = local sublimation depth
ν = kinematic viscosity
$\rho_{n,b}$ = bulk concentration of naphthalene vapor
$\rho_{n,w}$ = wall concentration of naphthalene vapor
ρ_s = density of solid naphthalene

into the channel formed by the naphthalene plates. Upon traversing the length of the channel, the air exits to a plenum chamber from which it passes successively to a flow meter and a blower, and is finally ducted to an exhaust system which discharges to the atmosphere at the roof of the building.

At the upstream end of the test section, the naphthalene plates rest in a slot cut into a baffle. The upstream edge faces of the plates were carefully aligned with the upstream face of the baffle in order to provide a continuous surface. To ensure against extraneous mass transfer during the course of a data run, all surfaces and edges of the naphthalene plates were covered by a pressure sensitive tape, except for the pair of parallel surfaces which bound the air flow channel. These surfaces were left exposed along an axial length $0 \leq x \leq L$, but were covered downstream of $x = L$. The downstream region ($x > L$) was designed to be available for subsequent multi-row studies.

The placement of the blower downstream of the test section, rather than upstream, was a purposeful decision intended to avoid uncertainties in the results. Had the blower been upstream, preheating of the air prior to its entry into the test section might have occurred, thereby causing a temperature rise. The vapor pressure of the naphthalene (which is the driving force for the mass transfer) is very sensitive to temperature level, with the variation being about 10 percent per deg C at room temperature. Therefore, deviations from temperature uniformity could well have altered the mass transfer results.

To ensure well defined thermal conditions, the naphthalene plates, sealed between glass with a plastic outer wrap, were left in the laboratory room (itself temperature controlled) for a period of 24 hours prior to a test run. Preliminary air flow experiments in which thermocouples were embedded in a naphthalene plate adjacent to the subliming surface indicated that the latent heat requirements of the sublimation process were too small to cause a depression of the surface temperature. Furthermore, the use of the building exhaust system ensured against the presence of naphthalene vapor in the laboratory room, so that the air entering the test section was also naphthalene-free.

The naphthalene plates used in the experiments were cast in a mold that had been painstakingly fabricated to provide castings with surfaces which were very smooth, flat, and parallel. The metallic components of the mold, stainless steel plates, and brass bars, were subjected to a succession of hand polishing and lapping operations which produced a mirror finish. When assembled, the mold had the form of a rectangular cavity whose top was left open for pouring the molten naphthalene. Once poured, the naphthalene was allowed to solidfy under air cooling conditions. Removal of a cast plate was accomplished by hammer blows on strategic positions on the mold.

The resulting naphthalene test surfaces were smooth, flat, and parallel to a degree that no further machining or finishing operations were necessary. Furthermore, lubricants were never used to facilitate the removal of the plates from the mold. Each test plate was cast from fresh (i.e., previously unused) reagent grade naphthalene, and all implements associated with the casting procedure were kept scrupulously clean. The test surface was never touched subsequent to unmolding. In view of these procedures and precautions, it can be assumed with confidence that the test surfaces of the naphthalene plates were free of contamination.

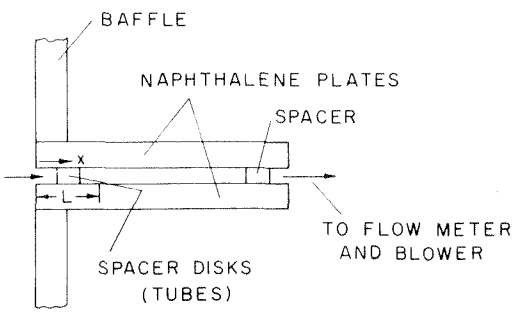

Fig. 2 Schematic side view of the test section

Further details relating to the fabrication of the mold, the casting procedure, and the subsequent handling techniques are available in [6].

The circular disks used to model the tubes were made of delrin, a free-machining plastic. The disks were fitted with pins which mated with holes drilled into the surfaces of the naphthalene plates, thereby ensuring proper positioning. Since the thickness of the disks controlled the channel height h, they were hand finished to a tolerance of 0.0125 mm (0.0005 in.) to ensure channel height uniformity.

Whereas the disks served to establish the proper hydrodynamic conditions found in an actual fin and tube configuration, they did not participate in the mass transfer process. The dimensions D and h of the disks (defined in Fig. 1) have already been stated at the end of the Introduction. From the data given there, one can calculate that the surface area of the disks (i.e., the transfer surface) is only about 6.5 percent of the transfer surface of the fins. It is believed that the nonparticipation of the disks in the mass transfer process does not have an important influence on the fin transfer coefficients.

The contour of the naphthalene surface was measured both before and after a data run by a precision dial gage whose smallest scale division was 0.00005 in. (~0.001 mm). The dial gage was mounted on a fixed strut that overhung a movable coordinate table. The coordinate table enabled the surface to be independently traversed in two directions (i.e., the x and y directions) in the horizontal plane. The traversing was controlled by micrometer heads which could be read to 0.002 mm (~0.0001 in.). During the contour measurements, the naphthalene plates were held firmly against the coordinate table by flat springs.

Surface profile measurements made during preliminary data runs verified the expected spanwise symmetries. Consequently, measurements for all final data runs were confined to the typical section outlined by dashed lines in the lower diagram of Fig. 1. Contour measurements were made at as many as 250 discrete locations.

The overall mass transfer was measured with a Mettler precision balance capable of discriminating to within 0.05 mg for specimens having a mass up to 200 g. Measurements of the flow rate through the test section were made with a calibrated rotameter and, for corroboration, with a gas meter connected in series. Typically, the gas meter reading divided by the duration time of a test run was within 1 or 2 percent of the rotameter reading.

The temperature of the air entering the test section was sensed by a precision-grade laboratory thermometer that could be read to 0.1 deg C. A digital timer was used to measure the duration of a data run as well as the times required for setting up the experiment and for executing the surface contour measurements. The latter times were employed in evaluating natural convection corrections.

Data Reduction Procedure

The local rate of mass transfer at any surface location on the naphthalene plates can be evaluated from the local change of surface elevation in conjunction with the duration time of the respective data run. The change of elevation will be referred to as the sublimation depth δ and, for the present experiments, $\delta = \delta(x,y)$. The surface distribution of δ was determined by differencing the measured surface elevations before and after a data run, and subsequently applying three corrections that will now be discussed.

One of the corrections accounted for the sublimation mass transfer during the period when surface contour measurements were being made on the coordinate table. Auxiliary experiments with the plate positioned on the coordinate table were performed to provide input information for these corrections. The second correction was to account for sublimation during the set-up time for a test run and, also for these corrections, in situ experiments

were carried out to obtain quantitative input data. In making both of the aforementioned corrections, records were kept of the time during which the extraneous mass transfer occurred.

To motivate the third correction, it is relevant to note that the surface-averaged sublimation depth during the course of a data run was only about 0.025 mm (0.001 in.), this limitation being imposed to avoid significant changes in channel dimensions and geometry. Furthermore, in spite of precautions and mechanical aids, it is not possible to position, remove, and then reposition a given plate on the coordinate table to yield precisely identical elevation readings at a given x,y coordinate setting. For example, the force with which the plate is pressed against the table during the positioning process may have a slight influence. Fortunately, any such elevation changes may be accounted for by making use of reference points on the naphthalene plates which do not participate in the mass transfer process. Such reference points include the area covered by the delrin disks and, in addition, the surface area of thin aluminum shims positioned just downstream of the fin trailing edge. Before and after dial gage measurements at the reference points enabled an accurate accounting of elevation differences due to positioning.

The detailed procedures for making the corrections are described in [6]. The accuracy of the corrections is attested to by the consistent 1 to 2 percent closure of the mass balances.

The surface profile measurements, corrected as described in the foregoing paragraphs, yielded the surface distribution of the sublimation depth $\delta(x,y)$. Then, using the density ρ_s of the solid naphthalene (ρ_s = 1.145 [7]) and the measured duration time t_0 of a data run, the local rate of mass transfer $\dot{m}$ per unit area was evaluated from

$$\dot{m}(x, y) = \rho_s \delta(x, y)/t_0 \tag{1}$$

The basic input data for equation (1), δ and t_0, are available in the Appendix of [6] for all test runs.

To define transfer coefficients, it is necessary to employ a concentration difference whose role is analogous to the temperature difference used in the definition of the heat transfer coefficient. Let $\rho_{n,w}$ represent the concentration of naphthalene vapor at the wall and $\rho_{n,bx}$ be the bulk concentration of naphthalene vapor in the airflow passing through the cross section $x = x$. For determining $\rho_{n,w}$, the vapor pressure—temperature relation for naphthalene can be employed. The Sogin [8] vapor pressure correlation, which was used here, is

$$\log_{10} p_{n,w} = 11.884 - (6713/T_w) \tag{2}$$

where $p_{n,w}$ is in lb/ft^2 and T_w is in deg R. With $p_{n,w}$ from equation (2), $\rho_{n,w}$ was evaluated from the perfect gas law (molecular weight of naphthalene vapor = 128.17).

To facilitate the calculation of the bulk concentration $\rho_{n,bx}$, we first evaluate the rate of mass transfer from the fin surface between $x = 0$ and $x = x$. This quantity, denoted by $\dot{M}(x)$, is given by

$$\dot{M}(x) = 2\int_0^x \left[\int_{y=0}^{s/2} \dot{m}(x, y)dy\right]dx \tag{3}$$

The factor 2 multiplying the integral takes account of mass transfer from both of the fins which bound a channel. The y integration extends over the range from 0 to $S/2$, thereby spanning the typical element delineated by the dashed lines in the lower diagram of Fig. 1. For points x,y that lie on the part of the fin that is blocked out by the tube, the integrand $\dot{m}(x,y)$ is set equal to zero.

Then, once $\dot{M}$ is known, $\rho_{n,bx}$ follows as

$$\rho_{n,bx} = \rho_{n,b0} + \dot{M}(x)/\dot{Q} \tag{4}$$

in which $\dot{Q}$ is the volume flow passing through the typical element (Fig. 1). Owing to the minute amounts of naphthalene that are sublimed, $\dot{Q}$ is constant throughout the test section and equal to the volume flow of air. The quantity $\rho_{n,b0}$ is the bulk concentration of naphthalene vapor in the air entering the exchanger. In the present investigation, $\rho_{n,b0} = 0$.

On the basis of the foregoing paragraphs, a local mass transfer coefficient K can be defined as

$$K(x, y) = \frac{\dot{m}(x, y)}{\rho_{n,w} - \rho_{n,bx}} \tag{5}$$

A dimensionless representation can then be made by introducing the local Sherwood number Sh

$$\mathrm{Sh} = KD_h/\mathfrak{D} \tag{6}$$

in which $\mathfrak{D}$ is the diffusion coefficient and D_h is the hydraulic diameter. The diffusion coefficient can be expressed in terms of the Schmidt number Sc as follows

$$\mathrm{Sc} = \nu/\mathfrak{D} \quad \text{or} \quad \mathfrak{D} = \nu/\mathrm{Sc} \tag{7}$$

The Schmidt number is 2.5 [8], and the kinematic viscosity ν can be evaluated as that for pure air.

The hydraulic diameter can be defined in various ways. Here, we use the London and Kays definition and notation [5]

$$D_h = 4A_cL/A \tag{8}$$

where A_c is the minimum flow area, L the streamwise length, and A the transfer surface area. In terms of the present dimensions (Fig. 1), the D_h of equation (8) can be evaluated as

$$D_h = \frac{4(S - D)hL}{2[SL - (\pi D^2/4)] + \pi Dh} \tag{8a}$$

The lateral surface area πDh of the tubes has been included in the denominator of equation (8a) to facilitate direct application of the Sherwood number results to analogous heat transfer situations. The quantity h appearing in (8a) was evaluated as the average of the initial and final channel heights.

An average mass transfer coefficient $\bar{K}$ and average Sherwood number $\overline{\mathrm{Sh}}$ can also be introduced. Let $\dot{M}_{\mathrm{total}}$ be the overall rate of mass transfer[3] and A_f be the corresponding fin surface area. Then,

$$\bar{K} = \frac{(\dot{M}_{\mathrm{total}}/A_f)}{(\Delta\rho_n)_m} \tag{9}$$

in which $(\Delta\rho_n)_m$ is the log-mean concentration difference given by

$$(\Delta\rho_n)_m = \frac{(\rho_{n,w} - \rho_{n,b0}) - (\rho_{n,w} - \rho_{n,bL})}{\ln (\rho_{n,w} - \rho_{n,b0})/(\rho_{n,w} - \rho_{n,bL})} \tag{10}$$

For most of the Reynolds number range of the experiments, the log-mean $\Delta\rho_n$ was very nearly equal to the arithmetic mean $\Delta\rho_n$. The extreme difference between the two was 2¼ percent at the lowest Reynolds number. The average Sherwood number then follows as

$$\overline{\mathrm{Sh}} = \bar{K}D_h/\mathfrak{D} \tag{11}$$

The Sherwood number results will be parameterized by the Reynolds number. The primary Reynolds number definition to be used here is that of London and Kays [5]

$$\mathrm{Re} = D_hG/\nu \tag{12}$$

where G is the mass velocity based on the minimum flow area and D_h is from equation (8a). Different Reynolds number definitions may be preferred by other investigators. The relationship of other Reynolds numbers to the Re of equation (12) is listed in Table 1. The last of the definitions in Table 1 is that for a parallel-plate channel.

Both the local and average Sherwood number results can be

[3] Typically, the overall mass transfer from one plate during a data run was about 50 mg. The duration time of a run varied from about 35 to 80 min, depending on the Reynolds number.

Table 1 Reynolds number relationships

i	Basis for G	D_h	$\mathrm{Re}_i/\mathrm{Re}$
1	minimum area	D	3.87
2	Channel area	D	2.32
3	Channel area	h	0.46
4	Channel area	$2h$	0.91

converted to Nusselt number results by employing the analogy between heat and mass transfer. According to the analogy

$$\mathrm{Sh} = C_1 f_1(\mathrm{Re})\mathrm{Sc}^n \quad \text{and} \quad \mathrm{Nu} = C_1 f_1(\mathrm{Re})\mathrm{Pr}^n \tag{13}$$

$$\overline{\mathrm{Sh}} = C_2 f_2(\mathrm{Re})\mathrm{Sc}^m \quad \text{and} \quad \overline{\mathrm{Nu}} = C_2 f_2(\mathrm{Re})\mathrm{Pr}^m \tag{14}$$

From these, it follows that

$$\mathrm{Nu} = (\mathrm{Pr}/\mathrm{Sc})^n \mathrm{Sh} \tag{15}$$

and

$$\overline{\mathrm{Nu}} = (\mathrm{Pr}/\mathrm{Sc})^m \overline{\mathrm{Sh}} \tag{16}$$

The exponents m and n are either ⅓ or 0.4, depending on the correlation that is used. To convert the present results for application to heat exchangers in which air is the flowing fluid, the Sherwood numbers would be multiplied by the ratio (0.7/2.5) raised either to the ⅓ or 0.4 power.

Before leaving this section, it is relevant to call attention to the boundary conditions of the present experiments. Since the naphthalene surfaces are isothermal, the concentration of naphthalene vapor at the wall is uniform (i.e., $\rho_{n,w}$ is the same at all surface locations). According to the analogy between heat and mass transfer, the vapor concentration at the wall plays the same role in the mass transfer problem as does the wall temperature in the heat transfer problem. Therefore, the present mass transfer experiments correspond to heat transfer from isothermal fins, that is, to heat transfer fins whose efficiency η is equal to one.

This is a fortunate outcome, since it is current practice to correct and standardize heat exchanger results so that they are referred to fins having an efficiency of one. Such corrections need not be applied to the present results inasmuch as they already pertain to $\eta = 1$.

Results and Discussion

A presentation of representative results for the distribution of local transfer coefficients on the fin surface is given in Figs. 3, 4, and 5, respectively, for Reynolds numbers of 1271, 648, and 214 (Re is defined by equation (12)). Similar results for other Reynolds numbers in this range are available in [6]. The local Sherwood numbers presented in these figures can be converted to local Nusselt numbers by employing equation (15). Each of Figs. 3, 4, and 5 is made up of a number of graphs, with each graph corresponding to a given streamwise station characterized by x/L. The graphs are arranged with the smallest x/L results at the lower left and largest x/L results at the upper right. Values of $x/L < 0.269$ denote fin locations upstream of the tube, whereas $x/L > 0.731$ denotes locations downstream of the tube. The station of minimum air flow cross section is $x/L = 0.5$.

The ordinate variable is the local Sherwood number. Each graph has its own ordinate scale as is needed to accommodate the local values of the Sherwood number. The abscissa variable for each graph is the spanwise coordinate y made dimensionless by the half-spacing $S/2$. Thus, each graph portrays the spanwise distribution of the Sherwood number at a given axial station.

Attention will first be turned to Fig. 3, which is for the highest of the Reynolds numbers investigated. The results of Fig. 3 will be discussed by starting at the smallest x/L (lower left) and proceeding downstream to successively larger values of x/L. At the first axial station ($x/L = 0.059$), the flow is in the regime of boundary layer development and the transfer coefficients are, therefore, relatively high. The blockage of the channel resulting from the presence of the tube is seen to have a precursive effect by inducing a spanwise variation of the transfer coefficients. At the next two axial stations, the diminution of the transfer coefficients with streamwise growth of the boundary layers is in evidence.

At the fourth station ($x/L = 0.221$), one encounters a peak in the transfer coefficient distribution. This peak is a manifestation of a vortex pattern which develops in front of the tube and is swept around the side by the flowing fluid. In this connection, it may be noted that inspection of the surface of the naphthalene plate after a data run indicated the presence of U-shaped grooves adjacent to each tube. For the Reynolds number of Fig. 3, there were two grooves, one within the other. Both grooves were wrapped around the tube, with the closed end of the U upstream of the tube and the open end downstream.[4] These grooves were indicative of the high local mass transfer rates associated with the aforementioned vortex pattern. The peak evidenced in Fig. 3 at $x/L = 0.221$ is associated with the outermost of the grooves.

At the $x/L = 0.235$ station, a second peak in the transfer coefficient distribution begins to emerge. The second peak becomes predominant in the distribution curve for $x/L = 0.245$. This axial station is directly upstream of the tube (i.e., the forward stagnation point is at $x/L = 0.269$).

The next distribution curve ($x/L = 0.289$), as well as the six that follow, correspond to axial stations at the side of the tube. These curves do not extend all the way to $y = 0$ owing to the fact that a part of the fin is blocked out by the tube. Both peaks persist with somewhat diminishing magnitude for stations up to $x/L \sim 0.5$ (about half way around the tube), and thereafter only the stronger peak survives. At its highest value, the Sherwood number exhibited by the stronger peak ($\sim$52) is substantially greater than that in the boundary layer region at small x/L.

For stations downstream of the tube ($x/L > 0.731$), the most interesting finding is the very low transfer coefficients behind the tube. The values of Sherwood number in that region range from one to four, which is a small fraction of the Sherwood number values elsewhere on the fin. Clearly, the region behind the tube contributes very little to the performance of the exchanger.

The local transfer coefficients are significantly affected by the Reynolds number, as may be seen from an inspection of Fig. 4 which corresponds to Re = 648. First of all, as expected, the level of the Sherwood number diminishes with decreasing Reynolds number. Even more interesting is the effect on the peaks in the distribution curves. Whereas for the higher Reynolds number case there were two peaks in the distribution curves, now there is only one peak. This finding is corroborated by the visual inspection of the naphthalene test plate, which showed only a single U-shaped groove adjacent to a tube. In addition, the peak does not persist all the way around the tube into the wake region, as was true at the higher Reynolds number. Evidently, the vortex pattern is now damped out by the relatively stronger viscous forces.

The trends with Reynolds number are even more in evidence as one proceeds to lower Re values, as can be seen in Fig. 5 for Re = 214. Here, a relatively small peak appears in a few of the distribution curves upstream of the tube, and it persists for only a short distance around the side of the tube. Evidently, the vortex system which induces the peaks is weak and dissipates quickly. It is also interesting to note that for low Reynolds numbers, the downstream transfer coefficient distributions tend to "fill-in" in the region behind the tube much more than do those for higher Reynolds numbers. The level of the Sherwood numbers for Re = 214 is substantially below that for the Reynolds numbers of the earlier figures.

It is relevant to inquire as to which axial stations on the fin surface transfer greater amounts of mass (or heat) and which

[4] The Kruckels paper [9] contains a photograph of such grooves, but there, the closed end of the U appears to be situated considerably farther upstream of the tube than is indicated by the present data.

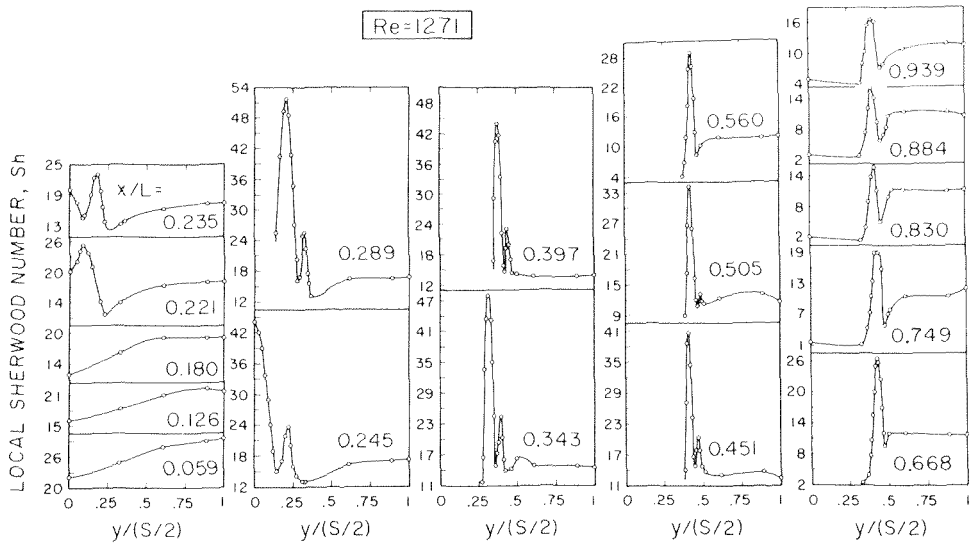

Fig. 3 Distribution of local Sherwood number on the fin surface, Re = 1271 and Sc = 2.5

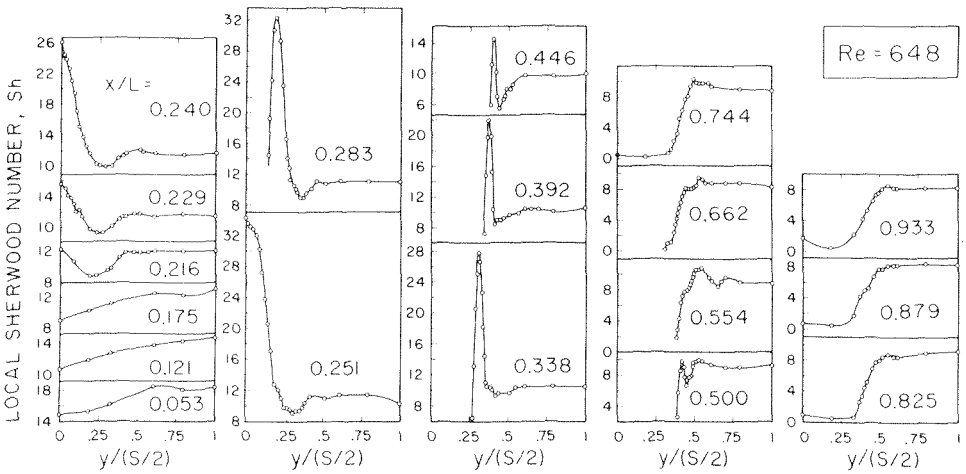

Fig. 4 Distribution of local Sherwood number on the fin surface, Re = 648 and Sc = 2.5

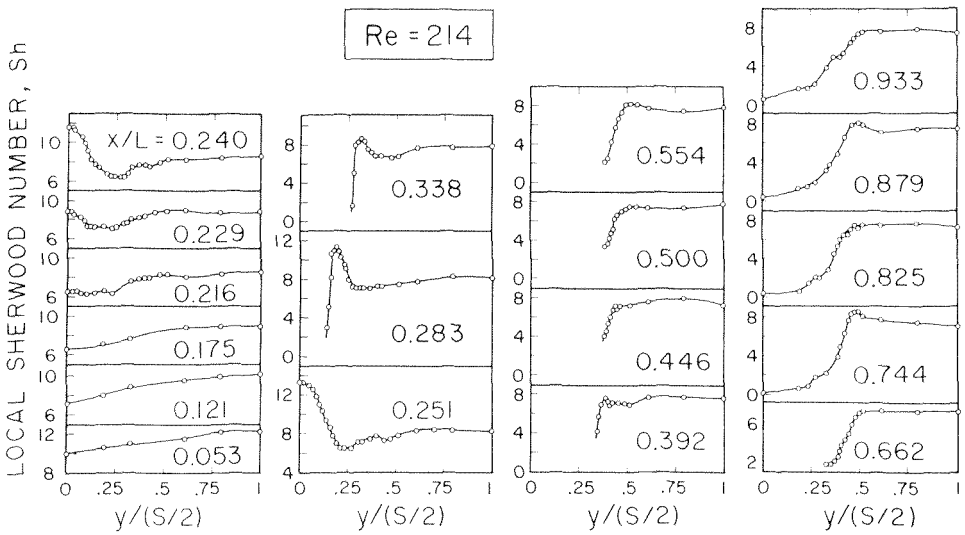

Fig. 5 Distribution of local Sherwood number on the fin surface, Re = 214 and Sc = 2.5

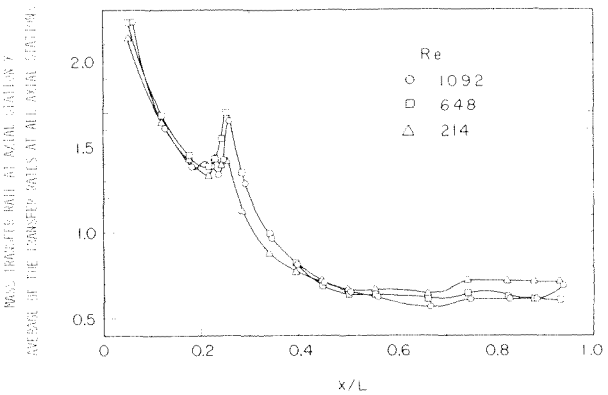

Fig. 6 Transfer rates as a function of axial position

axial stations transfer lesser amounts. To examine this question, we form the ratio

$$\frac{\text{mass transfer rate at axial station } x}{\text{average of the transfer rates at all axial stations}} \tag{17}$$

The numerator of this ratio was evaluated from

$$\int_{y=0}^{S/2} \dot{m}(x, y)dy \tag{18}$$

at each of the axial stations x at which data were collected. It should be noted that at those axial stations where a portion of the fin is blocked out by the tube (i.e., at $0.269 < x/L < 0.731$), the integrand $\dot{m}(x,y)$ was set equal to zero at the y values at which the blockage occurred. Thus, in effect, the integration range at those axial stations was confined to the y values where fin mass transfer took place. The average value indicated by the denominator of equation (17) was obtained by averaging the mass transfer rates at all axial stations, that is

$$\frac{1}{L}\int_{x=0}^{L}\left[\int_{y=0}^{S/2}\dot{m}(x, y)dy\right]dx \tag{19}$$

The results obtained by evaluating the ratio expressed by equation (17) are plotted in Fig. 6 as a function of the axial coordinate x/L. The figure contains data for three Reynolds numbers,[5] 1092, 648, and 214. Inspection of the figure indicates that the transfer rates at axial stations on the forward part of the fin are substantially higher than the average and those on the rear part of the fin are well below the average. At axial stations adjacent to the front of the tube, a local maximum and a general augmentation are in evidence.

The high transfer rates that are encountered on the initial portion of the fin are due to the thin boundary layers. These boundary layers grow with increasing x and cause a corresponding reduction in the transfer rates. The reduction is arrested by the augmentation provided by the vortex system which develops in front of the tube and is carried around the side. At axial stations situated at the side of the tube ($0.269 < x/L < 0.731$), the diminished fin area decreases the transfer rate. However, even as the fin area recovers in the range $0.5 < x/L < 0.731$, the transfer rates do not recover. Downstream of the tube ($x/L > 0.731$), there is a slight increase in the transfer rates, especially at the lowest Reynolds number.

It is interesting to observe that when the results are plotted in a ratio form as in Fig. 6, the axial distributions are relatively insensitive to the Reynolds number. There are some differences in detail in the augmented region adjacent to the front of the tube and in the downstream wake but, in general, the three curves are remarkably close together.

Average mass transfer coefficients, expressed in terms of the average Sherwood number, were evaluated from equation (11) in conjunction with equations (8*a*), (9), and (10). These results are plotted in Fig. 7 as a function of the Reynolds number Re. The data points have been connected by a faired solid line to provide continuity. The data points do not accommodate a straight line correlation, and there is no reason to expect such a correlation to be appropriate. Indeed, if one considers flow field changes with Reynolds number as evidenced by the changing strength of the vortex pattern and by the filling in of the wake, a straight line correlation does not have a rational basis.

As seen in the figure, the average Sherwood number increases slowly with Reynolds number at small Re and then increases more rapidly at larger values of Reynolds number. The augmentation provided by the vortex pattern at larger Reynolds numbers is believed to be responsible, at least in part, for this trend.

It is relevant to compare the present average transfer results with those in the literature. To this end, Shepherd's results [1] were recast into the present variables and plotted as dashed lines in Fig. 7. The specific fin-tube coil selected for comparison from among those investigated by Shepherd was his No. 5, its dimension ratios being rather close to those of the present configuration. Shepherd does not report actual experimental data, but rather presents straight lines on log-log plots which, presumably, represent a smoothing of the data points.

As mentioned in the Introduction, there are some uncertainties in Shepherd's data as well as in the data reduction. The method for determining the air-side heat transfer coefficients was to measure the overall thermal resistance from the water side to the air side (hot water was passed through the tubes) and then to extrapolate to the case of zero water-side resistance. Furthermore, the water circuit was such that the tube wall temperatures were not uniform throughout the exchanger. Finally, the effect of nonuniform fin temperatures was not rationalized, for instance, by use of a fin efficiency. These points about Shepherd's work are being mentioned not to minimize his contribution, but rather to suggest that his results should not necessarily be taken as gospel.

Shepherd's results were recast in the form of $\overline{\text{Nu}}$ versus Re, where $\overline{\text{Nu}}$ is the average Nusselt number based on the hydraulic diameter defined by equation (8). Then, since the $\overline{\text{Nu}}$ values correspond to a Prandtl number of 0.7, it was necessary to scale them to Pr = 2.5, which corresponds to the Schmidt number of the present mass transfer experiments. The scaling can be performed by employing equation (16), which can be rewritten as

$$\overline{\text{Sh}} = (\text{Sc}/\text{Pr})^m\overline{\text{Nu}} = (2.5/0.7)^m\overline{\text{Nu}} \tag{20}$$

The upper and lower dashed lines plotted in Fig. 7 correspond, respectively, to $m = 0.4$ and $m = \frac{1}{3}$.

Examination of Fig. 7 reveals a very satisfactory level of agree-

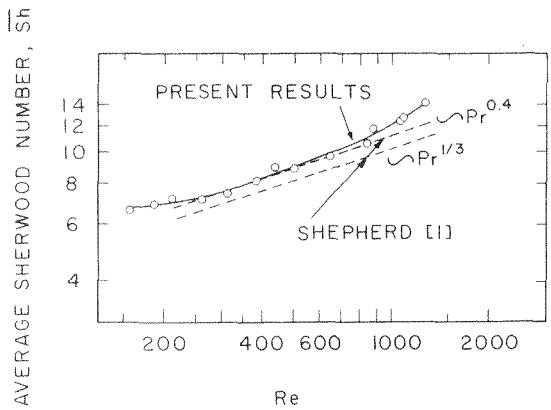

Fig. 7 Average Sherwood numbers as a function of Reynolds number, Sc = 2.5. Average Nusselt numbers can be obtained from equation (16).

[5] A preliminary plot indicated that the x/L positions at which data were available for Re = 1271 did not permit good resolution of the local maximum in the neighborhood of $x/L = 0.25$. Therefore, the data for Re = 1092 are used instead.

ment between the present results and those of Shepherd. The greatest deviations appear at higher Reynolds numbers. These deviations could, perhaps, be due to Shepherd's extrapolation or smoothing of his data (e.g., forcing a straight line representation) or to the neglect of the fin efficiency effect in the reduction of his data. Indeed, if the $m = \frac{1}{3}$ line were to be taken as the representation of Shepherd's results, then its low-side deviation could be rationalized by the fin-efficiency effect. In general, the level of agreement evidenced in Fig. 7 lends support both to the present results and to those of Shepherd.

As was mentioned earlier, the overall mass transfer rates of the present experiments were determined by two independent methods. One approach was to integrate the local measurements of sublimation depth over the surface of the plate, and the second was to determine the overall change in mass directly by a precision balance. For the six data runs for which such dual measurements were made, there was typically 1 to 2 percent agreement. This outcome adds strong support to the measurement technique.

Concluding Remarks

It has been demonstrated that the naphthalene sublimation technique is a viable tool for obtaining both local and average transfer coefficients for heat exchanger configurations of practical interest. The measured Sherwood numbers can be converted to Nusselt numbers by employing equations (15) and (16).

The local measurements revealed high values of the transfer coefficient on the forward part of the fin due to the presence of developing boundary layers. In addition, owing to the natural augmentation afforded by a vortex system, high coefficients are also encountered adjacent to the front of the tube. Relatively low coefficients were found to exist downstream of the minimum flow cross section. It is in this downstream region where artificial augmentation devices would be beneficial.

Before closing, cognizance may be taken of possible differences in fluid flow inlet conditions between the present single-channel model and the multi-channel array found in actual heat exchangers. The inlet conditions that might be affected are the degree of uniformity of the velocity profile and the presence or absence of separation. The local mass transfer measurements did not contain any identifiable characteristics that indicated the presence of separation. Furthermore, the authors do not believe that the transfer coefficients were markedly affected by possible differences between the inlet velocity profiles. This conclusion is based on the results of [10], where mass transfer coefficients in the entrance region of a parallel-plate channel were determined in an apparatus similar to that used here; in particular, the fluid inlet configuration was the same. The transfer coefficients measured in [10] were within 5 percent of analytical predictions based on a flat inlet velocity profile. The inlet velocity profile for a channel in a stacked array should, if anything, be flatter than that for the present inlet configuration. On this basis, it may be expected that the effect of the inlet velocity profile would be minor.

Acknowledgment

Scholarship support extended to F. E. M. Saboya by the Conselho Nacional de Pesquisas and by the Instituto Tecnologico de Aeronautica (both Brazilian institutions) is gratefully appreciated.

References

1 Shepherd, D. G., "Performance of One-Row Tube Coils With Thin-Plate Fins, Low Velocity Forced Convection," *Heating, Piping, and Air Conditioning*, Vol. 28, 1956, pp. 137–144.

2 Gebhart, B., "Flow and Heat Exchange Characteristics of Finned Tube Exchangers," *ASHRAE Transactions*, Vol. 67, 1961, pp. 133–153.

3 Bunge, A. F., "Toetsing van de berekening op theoretische grondslag van lamellen-luchtverwarmers aan experimenteel onderzoek," *De Ingenieur*, Vol. 71, No. 26, 1959, pp. 123–140.

4 Fukui, S., and Sakamoto, M., "Some Experiments on Heat Transfer Characteristics of Air Cooled Heat Exchangers for Air Conditioning Devices," *Bulletin JSME*, Vol. 11, 1968, pp. 303–311.

5 Kays, W. M., and London, A. L., *Compact Heat Exchangers*, Second ed., McGraw-Hill, New York, 1964.

6 Saboya, F. E. M., "Local and Average Transfer Coefficients in a Plate Fin and Tube Exchanger Configuration," PhD thesis, Department of Mechanical Engineering, University of Minnesota, Minneapolis, Minn., 1974.

7 *Handbook of Chemistry and Physics*, 47th ed., Chemical Rubber Publishing Company, Cleveland, Ohio, 1966–1967, p. C-414.

8 Sogin, H. H., "Sublimation From Disks to Air Streams Flowing Normal to Their Surfaces," TRANS. ASME, Vol. 80, 1958, pp. 61–71.

9 Kruckels, W. W., "Determination of Local Heat Transfer Coefficients in Forced Convection Air Flow by Aid of Photometric Measurements," *AIChE Symposium Series*, Vol. 67, No. 118, 1972, pp. 112–118.

10 Lombardi, G., and Sparrow, E. M., "Measurements of Local Transfer Coefficients for Developing Laminar Flow in Flat Rectangular Ducts," *International Journal of Heat and Mass Transfer*, in press.

A. J. Patton
Assist. Professor,
Roger Williams College,
Providence, R. I. Assoc. Mem. ASME

F. L. Test
Professor. Mem. ASME

W. M. Hagist
Assoc. Professor. Mem. ASME

Department of Mechanical Engineering
and Applied Mechanics,
University of Rhode Island,
Kingston, R. I.

An Experimental Investigation of a Heated Two-Dimensional Water Jet Discharge Into a Moving Stream

The experimental results are presented for a study of the behavior of heated and unheated two-dimensional water jets injected from the bottom of a moving water stream. The jet characteristics are described in terms of velocity and temperature profiles, velocity and temperature decay, jet width, jet trajectory, and jet turbulence. The conditions which favor the formation of an upstream thermal wedge are investigated.

Introduction

This paper presents the results of an experimental investigation of a two-dimensional heated water jet discharging into an open water channel. The jet enters through a slot across the channel bottom with the slot oriented perpendicular to the flow direction in the channel. The flow is analogous to that of a heated effluent discharging into a river or estuary when the outfall is a perforated pipe extending across the bottom of the flow channel.

Harleman, et al. [1],[1] conducted an experimental investigation to determine a diffuser design for thermal discharges. They proposed a manifold of diffuser pipes with circular ports, with the pipes located on the river bottom perpendicular to the ambient flow direction. Mahajan and John [2] experimentally investigated a shallow submerged heated slot jet. The depth of the jet below the free surface was varied. Carter [3] conducted a study of the characteristics of a vertical heated slot jet discharging into a transverse current.

Fan [4], Motz and Benedict [5] and Campbell and Schetz [6] investigated the characteristics of buoyant round water jets. The investigators in references [4, 6] used dye injection to determine the jet trajectories. The behavior of round jets, however, cannot be extended directly to slot jets across a river channel as the ambient flow cannot pass around the slot jet. Ramsey and Goldstein [7] experimentally studied a heated subsonic circular air jet in a deflecting air stream. The use of air as the fluid facilitated the measurement of turbulent flow properties.

Apparatus and Experimental Techniques

The experimental program for this study was carried out in a laboratory channel of rectangular cross section. Fig. 1 illustrates the configuration of the jet penetrating into the channel flow for a 90° jet injection angle. Fig. 2 presents the overall layout of the channel and related equipment.

A preliminary study of the channel characteristics revealed that the velocity profile across the width of the channel was flat at distances greater than 6 ft from the channel inlet. It was decided, therefore, to locate the jet inlet 7½ ft from the inlet end of the channel. The channel enables one to model two-dimensional variations in a flowing stream and assumes that channel width effects can be neglected. The jet width was sized to give a ratio of jet flow to main stream flow that would approximate that for a typical condenser outfall discharging into a river. A weigh tank located at the end of the channel allowed both the jet flow and the channel flow to be measured separately.

The temperature of the jet inlet water was measured with a calibrated copper-constantan thermocouple inside the jet box. Cylindrical fiber-film probes were used with a DISA 55D00 universal anemometer system to measure mean and fluctuating values of velocities and temperatures. The unit was operated in a

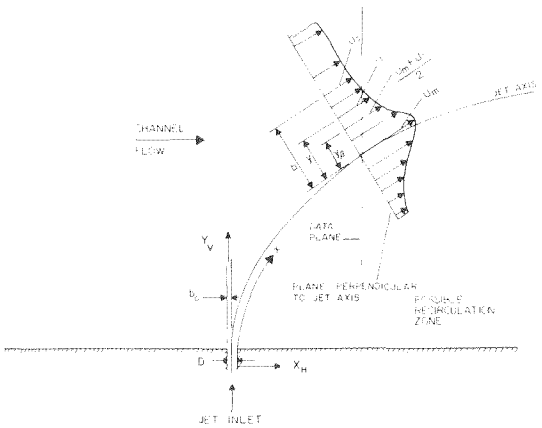

Fig. 1 Jet geometry

[1] Numbers in brackets designate References at end of paper.

Contributed by the Heat Transfer Division for publication in the JOURNAL OF HEAT TRANSFER. Manuscript received by the Heat Transfer Division, March 15, 1973. Paper No. 74-HT-GG.

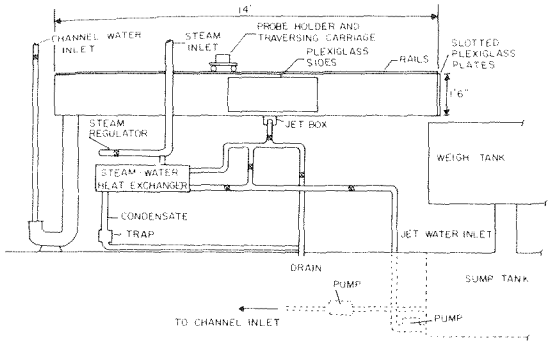

Fig. 2 The laboratory channel

constant temperature mode for velocity measurements and a constant current mode for temperature measurements. When used for temperature measurements the hot film probe was calibrated using the thermocouple in the jet box.

The hot film probe was supported by a carriage that could traverse the length of the channel on tracks. The probe sensor, which is 70 microns in diameter, was located in a horizontal position with its axis perpendicular to the axis of the channel. Mean temperature, temperature fluctuations, mean velocity, and velocity fluctuations in the direction of the mean velocity were measured at discrete locations as the probe was lowered vertically into the channel. The velocity fluctuations, however, could be measured only for those runs in which the temperatures of the jet and ambient flow were the same (isothermal runs). The jet trajectory was determined from the locus of maximum velocity points after vertical traverses were taken at several locations downstream from the jet entrance. The data were taken in a plane perpendicular to the channel bottom and then corrected to values in a plane perpendicular to the jet axis. The jet curvature and jet width were such that this correction was normally negligible. The hot film probe was calibrated for velocity at the beginning and end of each run by placing the probe in a rotating basin of water which was mounted adjacent to the open channel.

Data

The conditions for the runs on which the figures are based are summarized in Tables 1 and 2. Runs which have the same numerical classification but different alphabetical designation are duplicates that were taken several days apart to determine experimental reproducibility. The isothermal runs with a 90° inlet angle carry a graphical symbol which is used to identify them when the results are plotted in Fig. 4.

The jet Reynolds number based on inlet conditions is important in determining whether or not the jet flow is turbulent. Experiments by Andrade [8] indicate that two-dimensional jet flow

Table 1 Channel conditions

Run Number	Mean Channel Velocity (ft/sec)	Channel Depth (ft)	Channel Temperature (°F)	Channel Reynolds Number	Channel Froude Number	Symbol in Figure 4
1A	.25	1.0	66	25,000	.049	○
1B	.28	1.0	66	25,000	.049	●
1C	.28	1.0	66	25,000	.049	▲
2A	.43	1.0	66	37,500	.074	▽
2B	.40	1.0	66	35,500	.070	△
3	.24	1.0	66	25,000	.049	□
4	.43	1.0	66	37,500	.074	●
5	.23	.5	67	10,400	.057	◑
6	.34	.5	67	15,400	.084	■
7	.29	1.0	68	37,300	.043	◪
8	.18	.5	69	8,200	.045	○
9	.26	1.0	70	27,500	.049	
10	.28	1.0	70	27,500	.049	
11	.28	1.0	69	26,200	.049	
12	.43	1.0	70	42,200	.075	
13	.42	1.0	71	41,200	.074	
14	.42	1.0	71	40,400	.074	
15	.03	1.0	71	2,500	.005	
16	.08	1.0	71	8,000	.014	
17	.28	1.0	63	24,400	.048	
18	.42	1.0	63	36,400	.073	
19	.28	1.0	63	24,000	.048	
20	.28	1.0	65	24,800	.049	
21	.05	1.0	66	4,600	.009	

is definitely laminar for Reynolds numbers below 30. Foster and Parker [9] state that jet flow may be somewhat unstable up to Reynolds numbers of about 300 but above this the flow becomes turbulent. The jet flow for the experiments reported in this paper is thus well in the turbulent range.

There were only two jet injection angles used: a 90° injection angle as illustrated in Fig. 1 and a jet angle that was 30° from the horizontal with the jet directed in an upstream direction.

Discussion of Results

A. Isothermal Jets—90° Injection Angle. The behavior of the isothermal jet will be discussed first as that forms a basis for the understanding of the heated jet. Fig. 3 presents mean velocity and turbulence intensity profiles for runs 1A and 4. The probe cannot determine flow direction and the values shown are velocity magnitudes. Visual observations of particles in the flow and dye injection experiments indicated that a region of backflow existed beneath the jet. The profiles were thus plotted showing backflow in this region as the probable condition although the precise direction is unknown.

Fig. 4 is a plot of the generalized velocity profile in a plane perpendicular to the jet axis for an isothermal jet with a 90° injection angle. The coordinates are those normally used in plotting jet profiles as described by Abramovich [10] and Schlichting [11], and the data represent profiles for several axial locations. U_c, which is used in calculating the ordinate, is the channel velocity at the upper edge of the jet (see Fig. 1). The upper edge of the jet

Nomenclature

b = distance normal to jet axis from the jet axis to the upper jet boundary
b_0 = half-width of slot forming jet entrance
D = width of slot forming jet entrance
$F_c = U_a/\sqrt{gH}$ = channel Froude number
$F_d = U_a/\sqrt{gH\Delta\rho/\rho_a}$ = densimetric Froude number
g = gravitational acceleration
H = channel depth
Q_c = channel volume flow rate
Q_j = jet volume flow rate
T_c = channel temperature
T_j = jet temperature at the origin
T_m = jet center-line temperature
T_{mm} = mixed downstream temperature
U = mean velocity at any point in the jet
u' = fluctuating velocity in the jet in the direction of the jet axis
U_a = mean channel velocity upstream from the jet
U_c = mean channel velocity at a particular location downstream from the jet entrance
U_j = jet entrance velocity
U_m = mean jet velocity on the jet axis
x = distance along the jet axis downstream from the jet entrance
x_H = distance measured horizontally from the jet entrance
y = distance normal to the jet axis from the jet axis
y_c = distance measured vertically from the jet entrance
$y_{.5}$ = distance normal to the jet axis from the jet axis to the point where $\frac{U - U_c}{U_m - U_c} = 0.5$
ρ_a = density of water in channel before mixing with jet
$\Delta\rho$ = density difference between channel fluid and fluid at mixed downstream temperature

Table 2 Jet conditions

Run Number	Jet Entrance Velocity (ft/sec)	Jet Entrance Width (ft)	Jet Angle (degrees)	Jet Temperature (°F)	Jet Reynolds Number	Densimetric Froude Number	$\frac{U_j}{U_a}$
1A	1.8	.0104	90	66	1630		6.3
1B	1.8	.0104	90	66	1630		6.3
1C	1.8	.0104	90	66	1630		6.3
2A	1.8	.0104	90	66	1630		4.2
2B	1.8	.0104	90	66	1630		4.5
3	1.3	.0104	90	66	1150		4.5
4	1.3	.0104	90	66	1150		2.9
5	1.3	.0052	90	67	670		6.1
6	1.3	.0052	90	67	620		3.8
7	3.0	.0156	90	64	4200		10.3
8	2.0	.0052	90	64	950		11.1
9	1.8	.0104	90	90	2200	4.0	6.3
10	1.8	.0104	90	111	2600	2.8	6.3
11	1.3	.0104	90	111	1860	3.3	4.5
12	1.8	.0104	90	111	2630	5.3	4.1
13	1.3	.0104	90	90	1590	8.7	3.0
14	1.3	.0104	90	111	1860	6.1	3.0
15	1.0	.0104	90	109	1400	.13	37.3
16	1.0	.0104	90	111	1460	.62	12.1
17	1.8	.0104	30	63	1590		6.4
18	1.8	.0104	30	63	1590		4.2
19	1.3	.0104	30	63	1120		4.5
20	1.3	.0104	30	88	1530	4.5	4.5
21	1.0	.0104	30	105	1390	.34	18.1

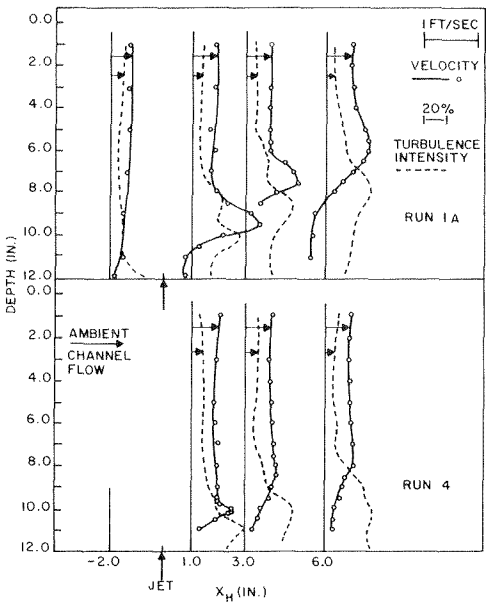

Fig. 3 Velocity and turbulence intensity profiles—90° jet injection angle

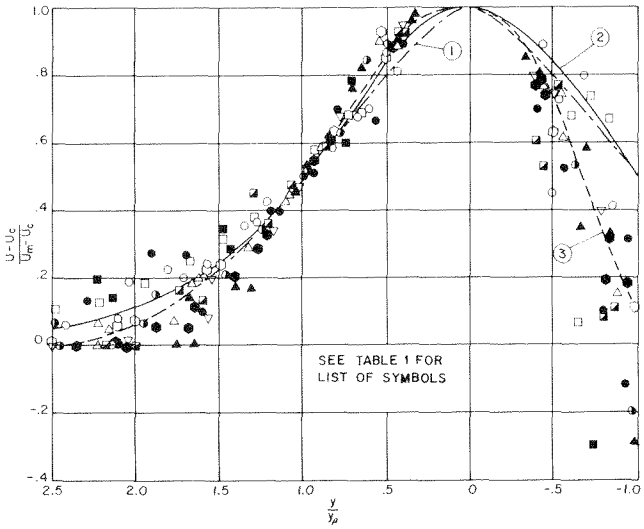

Fig. 4 Generalized velocity profile—90° jet injection angle

is taken to be the point at which dU/dy is zero. A point defined in this manner is difficult to locate experimentally and this is the reason for the amount of scatter at the left-hand side of Fig. 4. As a result $y_{\frac{1}{2}}$ is more satisfactory than b as a characteristic jet dimension.

The plane jet penetrating the boundary layer at the bottom of the channel tends to form a block to the channel flow. As a result the channel flow attempts to ride over the jet and thus accelerates, although this effect is somewhat diminished by entrainment of some of the channel flow into the jet.

Curve 1 in Fig. 4 is a plot of a theoretical symmetrical profile as derived by Tollmien [12] using Prandtl's mixing length hypothesis and Curve 2 is a symmetrical profile by Goertler [13] based on the assumption of constant eddy viscosity across the jet. Curve 3 is a graphical fit of the data points. Above the jet axis (left side of Fig. 4) the experimental profile is very close to the theoretical symmetrical profiles, with the theory according to Goertler giving the best comparison. Below the jet axis (right side of Fig. 4) the experimental profile differs greatly from the theoretical profiles as symmetry is impossible since the jet velocity must go to zero at the channel floor and a recirculation zone usually results in this region.

Fig. 3 shows the turbulence intensity for two typical runs. Near the jet entrance the turbulence intensity has maxima at both the upper boundary and the lower shear layer of the jet but the maximum at the lower shear layer is the greater and tends to become more dominant as the jet moves downstream. The equations that reduce the hot film anemometer data to values of $\sqrt{\overline{u'^2}}$ depend on simplifying assumptions that are questionable if $\sqrt{\overline{u'^2}}/U > 0.2$. This will tend to occur in the region under the jet axis but the trends in turbulence intensity should be correct as shown.

B. Heated Jets—90° Injection Angle. Fig. 5 shows temperature distributions for heated jets with the experimental conditions the same as in runs 1A and 4 except for jet inlet temperature. The fact that recirculation of heated water occurs beneath the jet and mixing with the cold ambient fluid takes place only at the top edge of the jet results in the region beneath the jet being well mixed and of relatively high temperature. This would tend to

cause the maximum temperature location to occur beneath the maximum velocity location.

A comparison of runs 9 and 10 in Fig. 5 indicates that the jet trajectory and jet spread as determined by maximum temperatures are relatively unaffected by jet temperature. In order to investigate this further a limited amount of data was obtained to determine the position of maximum velocity for a heated jet. This involved adjusting the cold resistance of the hot film probe at each data point and calibrating the probe at different ambient temperatures. From the data it was concluded that the jet trajectory, as determined from the location of maximum velocity, does not change with jet temperature, at least for velocity ratios (U_j/U_a) less than 6.5 and jet temperature of up to 40 deg F over the ambient. This leads to the conclusion that the buoyant force has a negligible influence on the jet trajectory for a two-dimensional jet with a low velocity ratio entering a homogeneous receiving fluid. This would not be the case for a round jet where the cold ambient fluid can pass around the jet and exert a buoyant force on the jet.

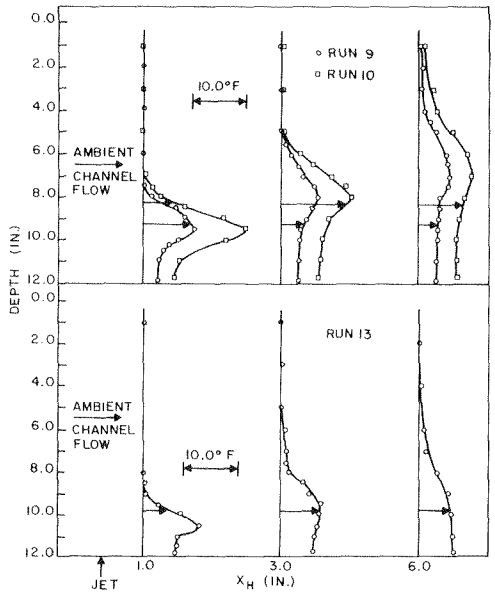

Fig. 5 Temperature profiles—90° jet injection angle

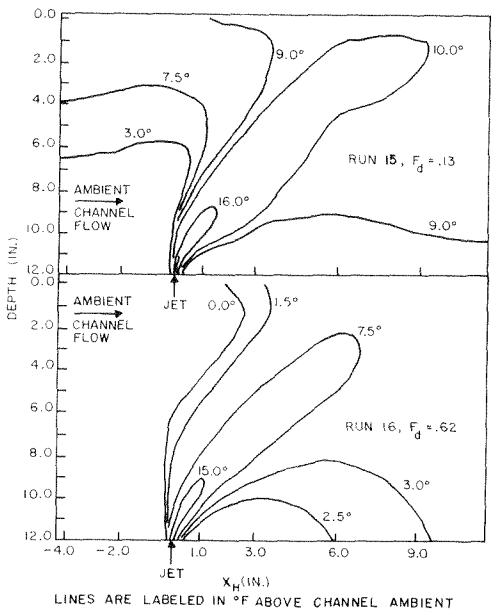

Fig. 6 Isotherms—90° jet injection angle

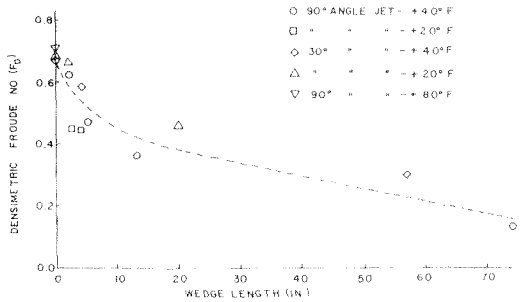

Fig. 7 Thermal wedge length as a function of densimetric Froude number

The phenomenon of a thermal wedge is illustrated by the isotherms plotted in Fig. 6. Runs 15 and 16 are for a 90 deg injection angle and an inlet jet temperature that is 40 deg F above the ambient. Harleman [1] states that the basic modeling parameter for the determination of the thermal wedge is the densimetric Froude number F_d. They conducted an experimental investigation which modeled an actual diffuser configuration consisting of rows of closely spaced holes, and concluded that a thermal wedge will form if $F_d < 1.0$.

Wigh [14] developed an analytic expression for the shape of the steady-state thermal wedge. The solution, however, required an assumption concerning the shear stress at the interface and knowledge of the initial wedge thickness. From his experimental investigation of a slot jet located in the side of a channel, extending from the free surface to the channel bottom, Wigh concluded that a wedge will form if $F_d < 0.75$.

The data of the study presented in this paper indicate that a thermal wedge will not form unless the densimetric Froude number is less than 0.7. This criterion is valid for both jets with a 90 deg and a 30 deg upstream injection angle. The results are shown in Fig. 7 which illustrates that the distance the wedge extends upstream is a function of the densimetric Froude number. The dashed line is simply an approximate mean of the data points for illustrative purposes. The data for some of the runs shown in Fig. 7 are not given in Tables 1 and 2. A complete listing of all the data is given in a thesis by Patton [15].

C. Jets With 30 deg Upstream Injection Angle. The general behavior of jets with a 30 deg upstream injection angle is compared to that with a 90 deg injection angle in Fig. 8. The solid and dashed lines shown in Fig. 8 are plots resulting from an empirical nondimensional curve fitting technique as described by Patton [15]. The jet first flows upstream being continually deflected by the ambient current. The trajectory is initially horseshoe shaped and eventually becomes similar to the 90 deg jet. When the jet is directed upstream with a sufficiently high velocity the momentum of the ambient flow is insufficient to deflect the jet flow up from the channel bottom and the main flow tends to ride over the jet. The upstream penetration distance increases significantly with increasing U_j/U_a ratios.

The decay of maximum velocity for the 30 deg jets is shown in Fig. 9 which clearly illustrates the effect of jet trajectory on the mixing characteristic of the jet and channel flows. Run 17 in which the jet remained close to the channel bottom as a result of a high velocity ratio initially has a much slower decay rate than the runs with a lower velocity ratio. The turbulent mixing between the jet and the ambient flow is greatly reduced when the jet is moving upstream near the bottom of the channel.

The velocity and temperature profiles for a typical 30 deg case are shown in Fig. 10. The temperature profiles are drawn with temperature increases above ambient shown to the left of the vertical line reflecting the fact that the highest temperatures are associated with the upstream flow. There are two maxima in both the velocity and temperature profiles for short distances upstream of the jet entrance. This reflects the upstream flow along the channel bottom and the return flow.

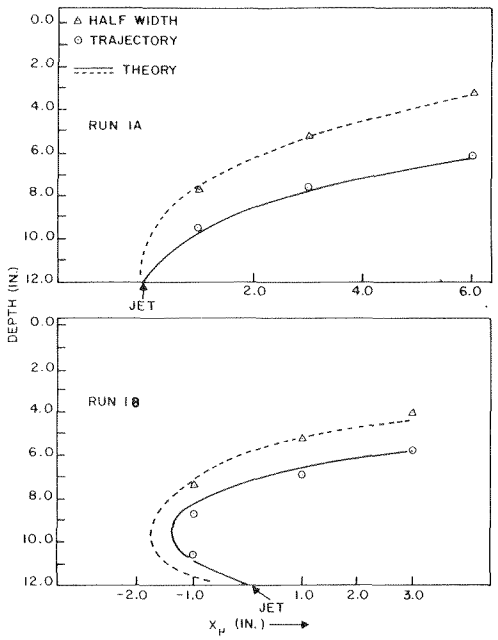

Fig. 8 Comparison of trajectories and half widths—90° and 30° jet injection angles

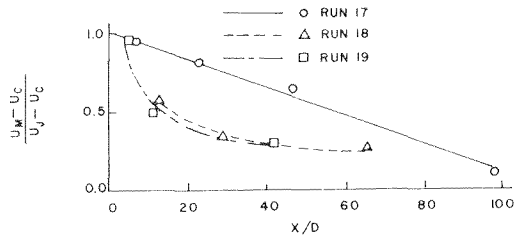

Fig. 9 Maximum velocity decay—30° jet injection angle

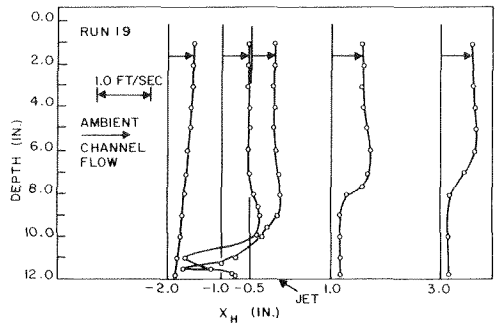

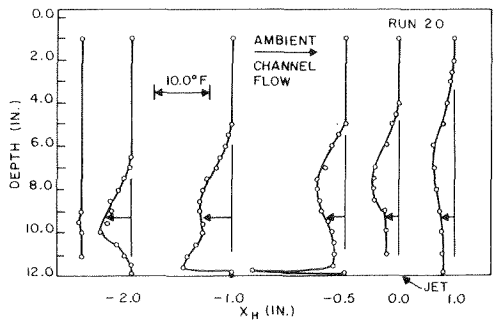

Fig. 10 Velocity and temperature profiles—30° jet injection angle

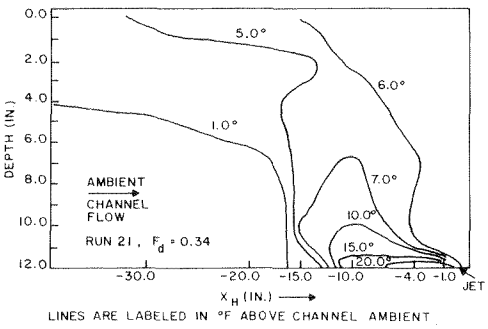

Fig. 11 Isotherms—30° jet injection angle

The criteria ($F_d < 0.7$) for the formation of a thermal wedge for the 30 deg jet is the same as for the 90 deg jet as was seen in Fig. 7. The only difference is that the wedge forms from a point upstream of the jet entrance as shown in Fig. 11. This results from the jet initially tending to move upstream along the bottom of the channel for a considerable distance when the velocity ratios have the high values that usually go with a low densimetric Froude number.

Summary

The experimental study presented in this paper investigates the flow resulting from the discharge of heated water into a moving stream. The particular type of discharge studied results from a slot across the bottom of the flow channel and perpendicular to the flow direction.

The maximum turbulence is generated by the shear layer beneath the jet and its magnitude is about the same as that for symmetrical two-dimensional jets. The jet behavior is influenced by the acceleration of the channel flow which tends to ride up over the jet flow. This blocking action of the jet prevents cool ambient water from getting beneath the jet and exerting a buoyant force on the jet provided the velocity ratio, U_j/U_a, is not too high.

If the velocity ratio is high a low value of densimetric Froude number, F_d, may occur and an upstream wedge of warm surface water can develop. This upstream wedge occurs if $F_d < 0.7$ and the length of the wedge increases as the value of F_d decreases. The wedge behavior appears to be independent of the jet injection angle.

References

1 Harlemann, R. F., Hall, C. L., and Curtis, T. G., "Thermal Diffusion of Condenser Water in a River During Steady and Unsteady Flows," Hydrodynamics Laboratory Report No. 111, Department of Civil Engineering, M.I.T., Cambridge, Mass., 1968.

2 Mahajan, B. M., and John, J. E., "The Mixing of a Shallow Submerged Heated Water Jet With an Ambient Reservoir," A.I.A.A. paper No. 71-71, A.I.A.A. 9th Aerospace Sciences Meeting, Jan., 1971.

3 Carter, H. H., "A Preliminary Report on the Characteristics of a Heated Jet Discharged Horizontally Into a Transverse Current, Part I—Constant Depth," Technical Report 61, Chesapeake Bay Institute, The Johns Hopkins University, Nov. 1969.

4 Fan, L. N., "Turbulent Buoyant Jets Into Stratified or Flowing Ambient Fluids," Report No. KH-R-15, W. M. Keck Laboratory of Hydraulics and Water Resources, California Institute of Technology, Pasadena, Calif. 1967.

5 Motz, L. H., and Benedict, B. A., "Heated Surface Jet Discharged Into a Flowing Ambient Stream," Report No. 4, Department of Environmental and Water Resources Engineering, Vanderbilt University, Nashville, Tenn., 1970.

6 Campbell, J. F., and Schetz, J. A., "Flow Properties of Submerged Heated Effluents in a Waterway," presented at the 10th Aerospace Sciences Meeting, San Diego, Calif., Jan. 1972.

7 Ramsey, J. W., and Goldstein, R. J., "Interaction of Heated Jet With a Deflecting Stream," ASME Paper No. 71-HT-2.

8 Andrade, E. N., "The Velocity Distribution in a Liquid-Into-Liquid Jet. The Plane Jet," *Proceedings Physical Society*, London, Vol. 51, 1939, pp. 784–793.

9 Foster, K., and Parker, G. A., *Fluidics: Components and Circuits*, Wiley, New York, 1970, pp. 95–110.

10 Abramovich, G. N., *The Theory of Turbulent Jets*, The M.I.T Press, Cambridge, Mass., 1963.

11 Schlichting, H., "Free Turbulent Flows, Jets and Wakes," *Boundary Layer Theory*, Sixth ed., McGraw-Hill, New York, 1968, pp. 681–703.
12 Tollimien, W., "Berechnung Turbulenter Ausbreitungsvorgange," *ZAMM*, Vol. 6, 1926, pp. 468–478.
13 Goertler, H., "Berechnung von Aufgaben freien Turbulenz auf Grund eines neuen Naherungsansatzes," *ZAMM*, Vol. 22, pp. 244–254, 1942.
14 Wigh, R. J., "The Effect of Outlet and Intake Design on Cooling Water Recirculation," thesis presented to the Massachusetts Institute of Technology at Cambridge, Mass., Sept., in partial fulfillment of the requirements for the degree of MS, 1967.
15 Patton, A. J., "Turbulent Thermal Diffusion of a Slot Jet Flowing Into a Moving Stream" thesis presented to the University of Rhode Island at Kingston, R. I., in partial fulfillment of the requirements for the degree of Doctor of Philosophy, 1972.

ERRATA

An errata on H. O. Buhr, E. A. Horsten, and A. D. Carr, "The Distortion of Turbulent Velocity and Temperature Profiles on Heating, for Mercury in a Vertical Pipe," published in the May, 1974, issue of the JOURNAL OF HEAT TRANSFER, pp. 152-158.

This is the corrected version of Fig. 3:

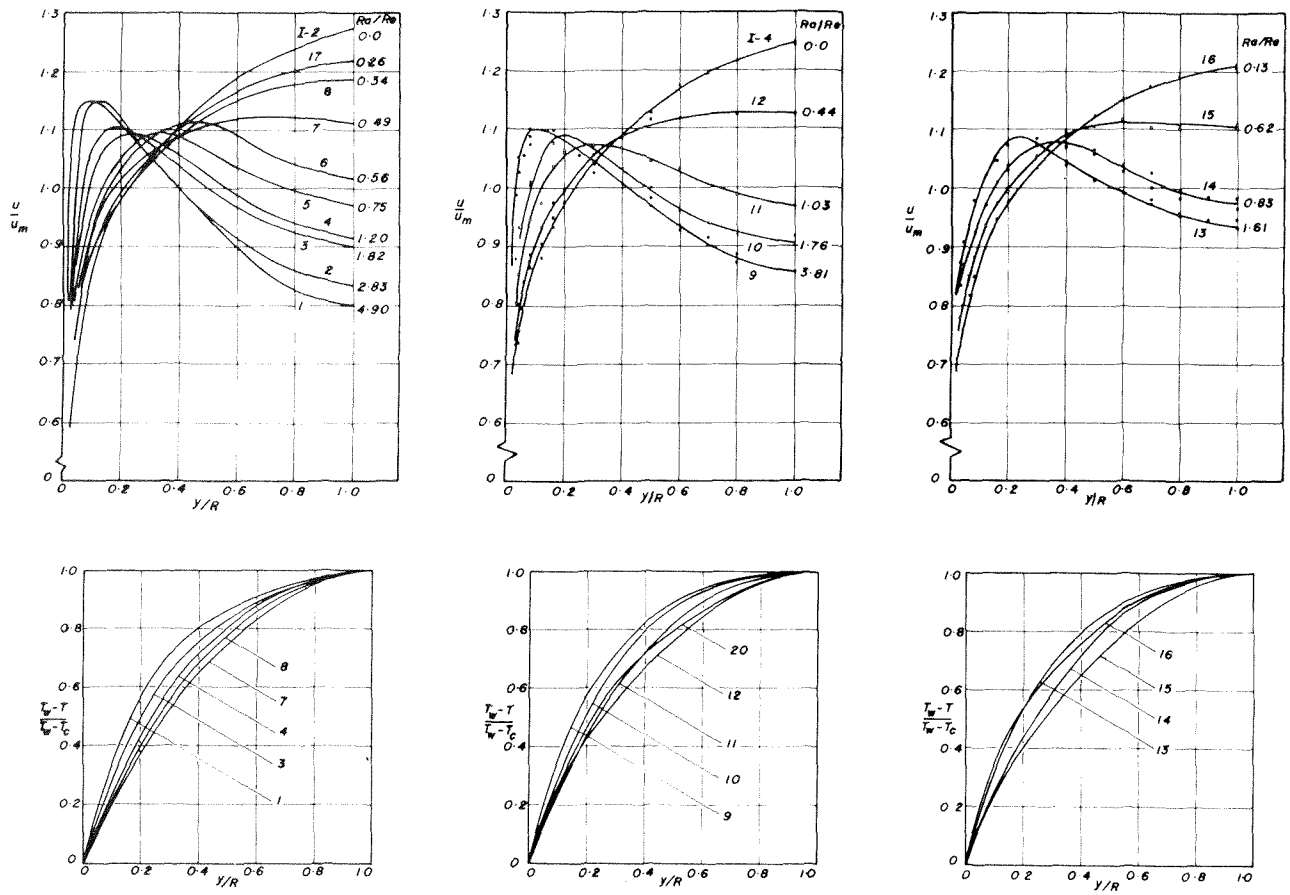

Re ≃ 20,000 Re ≃ 30,000 Re ≃ 60,000

Fig. 3 Effect of heat flux on velocity and temperature distributions in mercury

F. K. Moore
Professor.

T. Hsieh
Research Associate.

School of Mechanical and Aerospace Engineering, Cornell University, Ithaca, N. Y.

Concurrent Reduction of Draft Height and Heat-Exchange Area for Large Dry Cooling Towers

A procedure is outlined to meet simultaneous requirements to reduce overall size of a dry cooling tower for a large power plant, and to reduce the size (surface area) of the associated air-water heat exchanger. First, tower exit dimensions (or fan power) are specified as attainable fractions of their theoretical minima as found from a draft equation. Then a heat-exchanger type is chosen, having as small an air hydraulic diameter as feasible. Appropriate equations and assumptions dealing with air side and water side heat exchange and water pumping power then yield a full description of tower and heat-exchanger characteristics for a given tower duty. A specific example is worked out and compared with the tower at Rugeley, England. We find that a very open heat exchanger, of shallow depth (one in. or less) results from our analysis, and in a proposed configuration of acceptable header loss, gives a 1/3 height reduction and a four-fold reduction of heat-exchanger area.

Introduction

There is growing acceptance of the future necessity for dry cooling systems for large power plants, not only to conserve water and avoid condensing plumes, but to avoid the need to site power plants on water margins, in disadvantageous competition with other uses projected for those special regions.

Typically, dry systems are very large; discouragingly so when sized for gigawatt-class power plants. For example, the natural-draft dry tower in Rugeley, England [1, 2][1] has a height of 340 ft, and about 12 of these would be needed to serve a 1 GWe power plant. Further, the fin-tube heat exchanger devised by Forgo for that and subsequent applications [3] is massive; one may estimate [4] that the air-side heat-exchange area for a single tower is about $8 \cdot 10^6$ ft^2, provided by about $8.4 \cdot 10^5$ lb of aluminum. Thus, we may assume that strong incentives exist for simultaneously reducing draft height (or fan power, commonly estimated at 3 per cent of plant output [5]) and heat-exchange area, which we take to be a suitable measure of heat exchanger size and cost.

In a previous paper [6], we have indicated how a minimum tower size could be approached by improving certain heat-exchange performance parameters, but chiefly by making the heat exchanger more "open" in relation to tower flow area. This means, referring to Fig. 1*(a)*, that the free-flow area A_c should be large compared to A_E. In a subsequent paper [4], it was shown that heat-exchange area A_a could, in principle, simultaneously be minimized by making the free-flow volume $A_c L_a$ small. Thus, if A_c is to be large, then the heat-exchanger depth must be very small, perhaps of the order of 1 in. or less (compared with 6 in. for the Forgo device).

The notion of a very shallow heat exchanger for a very large cooling tower raises a number of further questions: Especially, can water be delivered to such a fine-grained heat exchanger without incurring unacceptable losses of water-side heat transfer effectiveness, water pumping power, or draft, owing to the air drags of water headers and passages? Can air-side fin effectiveness be made acceptable for the small scales of interest?

In this paper we will address the foregoing questions, which are of a more practical character than those issues of minimization treated in [6]. Accordingly, we formulate a particular decision sequence for preliminary design based on the theories of [4, 6], and show how it may be carried through with a heat-exchanger type of documented performance to give a dry cooling tower of specific dimensions and performance. Comparison is then made with the Forgo-Rugeley design as it might be adapted to serve a 1 GWe power plant.

A Practical Minimum For Tower Size

We begin by writing the draft equation derived in [6] on the basis of one-dimensional flow in the tower at very low Mach number and with negligible exit loss. We include, however, a new term (the second) which accounts for the head loss of the air as it experiences contraction and expansion when entering and leaving the heat exchanger; thus, the blockage due to water passages is accounted for.

[1] Numbers in brackets designate References at end of paper.

Contributed by the Heat Transfer Division for publication in the JOURNAL OF HEAT TRANSFER. Manuscript received by the Heat Transfer Division, February 7, 1974. Paper No. 74-HT-00.

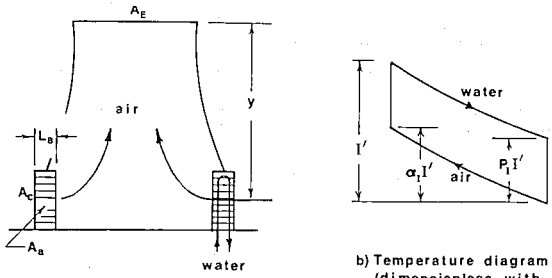

Fig. 1 Sketches illustrating nomenclature

$$I'^3 \frac{YA_E^2}{l^5} = \frac{KE\psi}{F}\left(\frac{A_E}{A_C}\right)^2 + (K_e + K_c)\frac{1}{\alpha_I^3}\left(\frac{A_E}{A_C}\right)^2 + \frac{1}{\alpha_I^3} \quad (1)$$

The left side of this equation expresses size of the tower in dimensionless form (a scale length l is defined in the Nomenclature), and equivalent draft height of any mechanical-draft fan is included in the definition

$$Y \equiv y + \frac{C_{p_0} T_0}{g}\frac{P_f}{Q} \quad (2)$$

Fig. 1 helps to define various symbols appearing in equations (1) and (2). The first term on the right refers to air drag inside the heat exchanger; E is a factor (ideally equal to 1) which specifies fin effectiveness and water-side resistance; that is,

$$E \equiv \frac{1}{\eta_0} + \frac{A_a h_a}{A_w h_w}; \quad \text{also, } Q = F\Delta T_E \frac{A_a h_a}{E} \quad (3)$$

where ΔT_E is the log-mean temperature difference ($= I'T_0/(\alpha_I^2\psi)$). F is the counterflow-equivalence factor, also ideally equal to 1. ψ is a function of α_I and P_I, explained in [6], which has a minimum at about $\alpha_I = 0.83$, for all P_I (see Table 1, to follow). The last term on the right refers essentially to the kinetic energy of the air jet leaving the tower at the exit (A_E).

Now, if we wish to make Y small, we presumably want also to make A_E small, because for a particular tower type, we would probably keep a constant tower "shape," or ratio $Y/\sqrt{A_E}$. Equation (1) thus suggests that A_E and Y can be made small by making A_E/A_c small. However, in [4] it is explained that diminishing returns limit the value of this strategy; there is an asymptotic minimum value of size given by $I'^3 Y A_E^2 = l^5/\alpha_I^3$ which is reached as free-flow area A_c approaches ∞. Because large A_c implies a bulky heat exchanger, and, as we shall see, forces a small exchanger depth L_a, it would seem sensible to specify that A_c be made only large enough for A_E to be some factor ξ above its minimum for a given Y. Thus,

$$A_E = \xi \frac{l^{5/2}}{(\alpha_I I')^{3/2}\sqrt{Y}} \quad (4)$$

and hence, from equation (1), we find that

$$A_c = \sqrt{\frac{K'E}{(\alpha_I I')^2 Y}} \cdot \frac{\alpha_I^2 \psi}{FI'} \frac{\xi}{\sqrt{\xi^2 - 1}} l^{5/2}; \quad K' \equiv K + \frac{F(K_e + K_c)}{E\alpha_I^3 \psi} \quad (5)$$

where the Reynolds'-analogy factor K has been redefined to include entering and leaving losses. If the tower shape $Y/\sqrt{A_E}$ is fixed instead of Y itself, then equations (4) and (5) may both be suitably transformed by multiplying both sides by $A_E^{1/4}$ and then taking the 4/5 root of the results.

In effect, choosing a value of ξ sets a practical minimum for tower size, and also sets the degree of openness (A_c) needed to achieve that size.

Air-Side Heat Exchange Area

Next, we may quickly summarize previous results [4, 6] for air-side heat-exchange area, A_a. Into equation (35) of [6] we may insert the definitions of Reynolds number (equation (32) of [6]) and of the function ψ (equations (29) and (39) of [6]), giving

$$A_c L_a = \frac{EWl r_{h_a}^2}{\mathrm{St}_a \mathrm{Re}_a I' F}\alpha_I^2 \psi \quad (6)$$

We next recall the definition $A_a r_{h_a} \equiv A_c L_a$ which tells us that if

Nomenclature

A_a, A_w = heat-exchange areas on air and water sides, respectively
A_c, A_f = free-flow area and frontal area of heat exchanger, respectively
A_E = exit area of tower
b, c = width of air and water passages, respectively, (Fig. 2)
C_p = specific heat at constant pressure
D_E = diameter of tower exit
D_H = diameter of header (Fig. 3)
E = effectiveness factor (equation (3))
F = counterflow equivalence factor
f = friction factor
H = height of heat-exchange columns
h_a, h_w = heat-transfer coefficients, air and water sides, respectively
I' = ratio of initial temperature difference (ITD) to ambient air temperature (Fig. 1(b))
K = Reynolds'-analogy factor, f_a/St_a
K' = Reynolds'-analogy factor including entering and leaving loss coefficients, K_e and K_c (equation (5))
L_a = heat exchanger depth (Fig. 1(a))
L_w = length of water passages (Fig. 2)
l = characteristic length $[Q/(\sqrt{2g}\rho_0 C_{p0} T)]^{2/5}$
N = number of heat-transfer modules (Fig. 2)
N_c = number of columns in each tower
n = number of water passes
P_I = dimensionless approach (Fig. 1(b))
P_f, P_w = mechanical-draft fan power, and water pumping power, respectively
Q = heat rejected from one tower
r_h = hydraulic radius
Pr, Re, St = Prandtl, Reynolds, and Stanton numbers, respectively
T_0 = ambient air temperature
v = average velocity of fluid
W = dimensionless coefficient $4Q/(C_{p_0} T_0 \mu_0 l)$
Y, y = generalized draft height (equation (2)), and height of tower above heat exchanger, respectively
α_I = ratio of air temperature rise to ITD
β = ratio of air heat-transfer area to volume between plates
μ, ν, ρ = viscosity, kinematic viscosity, and density, respectively
λ = deviation of E from unity; $\lambda \equiv 1 - 1/\eta_0 E$
η_0 = air-side overall fin effectiveness
ξ = ratio of actual A_E to its minimum (equation (4))
ψ = function of α_I and P_I (Tables 1 and 6)

Subscript 0 represents ambient air conditions, w represents quantities for water side, and a represents air side

$r_{h(a)}$ is given, A_a is proportional to the "free-flow volume" A_cL_a. However, we have not chosen $r_{h(a)}$, nor should we do so without knowing its own effect on A_a. Clearly, then, we should use equation (6) to eliminate $r_{h(a)}$. We find

$$A_a = \sqrt{\frac{WlE\alpha_I^2\psi}{\mathrm{St}_a\mathrm{Re}_{a'}F}}\sqrt{A_cL_a} \tag{7}$$

and L_a is the only geometrical dimension of the heat exchanger which, entering as the square root, is needed to find A_a.

We may compare equations (5) and (7), observing that, having made ξ near 1 in order to make Y and A_E small, we have made A_c large. Thus, if A_a is to be small, L_a must be small indeed. Of course, for a given ξ, the size of A_c is minimized if E and F are near 1, K is as small as possible, and ψ is near its minimum. The same provisions are consistent with minimizing A_a as well, with the exception that $\alpha_I^2\psi$ is not a minimum at $\alpha_I = 0.83$. As Table 1 illustrates, $\alpha_I^2\psi$ is a rather slowly-changing monotonic function. Presumably, an α_I somewhat below 0.83 would be the best choice.

Equation (7) shows that $\mathrm{St}_a\mathrm{Re}_a$ should be large for small A_a. This suggests laminar flow, for which $\mathrm{St}_a\mathrm{Re}_a$ has its largest value and is constant, and, happily, this is in fact what we will have if L_a is made very small: Since free-flow velocity is inversely proportional to A_c, Reynolds number is proportional to $r_{h(a)}/A_c = L_a/A_a$ by definition; thus, equation (7) says that Re_a is proportional to $\sqrt{L_a/A_c}$; and if L_a is small and A_c is large, Re_a will be very small and the air flow through the heat exchanger will be laminar.

Finally, we note that equation (6) requires $r_{h(a)}$ to be small if L_a is small; in fact, L_a is proportional to $r_{h(a)}^2$. Thus, we should choose a very "fine-grained" heat exchanger.

The foregoing arguments will become more specific in terms of a particular example to follow. At this point, we observe that E is unknown; to complete our set of equations, we must therefore consider the water side.

Water-Side Requirements

If L_a is to be very small, we must ask whether water can be distributed in such a fine-grained device without incurring unacceptable pumping and heat-transfer effectiveness losses. Probably our heat exchanger should be of the plate-fin type, in order to provide maximum space for water flow, and we are led to consider the configuration shown in Fig. 2. We imagine that there will be N modules with narrow water passages of length L_w and number of passes n ($n = 2$ is illustrated). Each module communicates with a water header.

Obviously, there is a geometrical connection between the free-flow area A_c and the area NL_wb. Adopting the notation of [7], the constant of proportionality β depends on exchanger type:

$$A_c = \beta NL_wbr_{h_a} \tag{8}$$

Entering and Leaving Loss. If L_a is small, b will need to be small for the sake of fin effectiveness, and c will have to be small in comparison to b in order that $K_e + K_c$ (air drag due to blockage) is small. Referring to equation (6), we would like K' to be within 10 percent (say) of K. Typical numerical values ($K = 2.7$, $\psi = 4.75$, $\alpha_I = 0.83$, $E = 1.1$, $F = 0.94$) would then suggest that $K_e + K_c$ should be less than about 0.8. This is easily arranged: Fig. 5-3 of [7] tells us that if $c = {}^1/_2b$, then $K_e + K_c$ would be about 0.5 for laminar flow and 0.4 for a Reynolds number (based on b) of 2000. We expect to be in the middle of that range, and therefore conservatively specify $c = {}^1/_2b$ and $K_e + K_c = 0.45$.

Pumping Power. Water pumping power should be limited to some reasonable fraction, certainly less than 1 percent, of plant output, or ½ percent of Q. We assume for the moment that the important resistance is frictional, and that the flow is turbulent in a Reynolds number range for which the Colburn formulas apply:

Table 1 Size functions ψ and $\alpha_I^2\psi$, for $P_I = 0.5$

α_I	0.4	0.6	0.7	0.829	0.9
ψ	11.40	6.20	5.21	4.75	4.97
$\alpha_I^2\psi$	1.82	2.23	2.55	3.26	4.03

$$\frac{1}{8}f_w = 0.023\ \mathrm{Re}_w^{-1/5} = \mathrm{Pr}^{2/3}\mathrm{St}_w;\ \mathrm{Re}_w \equiv \frac{v_{c_w}4r_{h_w}}{\nu_w} \tag{9}$$

The pumping power is, for each module,

$$\frac{P_w}{N} = \frac{1}{2}\rho_w v_{c_w}{}^3 A_{c_w}{}'\frac{nL_w}{4r_{h_w}}f_w \tag{10}$$

and, for each module,

$$\frac{Q}{N} = \rho_w C_{p_w}\Delta T_w v_{c_w}A_{c_w}{}';\ \Delta T_w \equiv I'T_0(1 - P_I) \tag{11}$$

For the geometry shown in Fig. 2,

$$A_{c_w}{}' = L_ac/n;\ A_w{}' = 2L_w(L_a + nc);\ 4r_{h_w} = 2c/(1 + nc/L_a) \tag{12}$$

Perhaps, for the sake of counterflow equivalence, we would add a partition in each of the passes. In that case,

$$A_w{}' = 2L_w(L_a + 2nc);\ 4r_{h_w} = 2c/(1 + 2nc/L_a) \tag{13}$$

Clearly, in equation (10), we can use equations (9), (11), and (12) or (13) to express P_w/N in terms of Q, N, n, c, L_a, ΔT_w, L_w and the properties of water.

Heat Transfer Effectiveness. To find the remaining unknown E, we return to equation (3). We may eliminate A_ah_a, and use the Stanton number from equation (9) to eliminate h_w. Further noting that $A_w \equiv NA_w'$, we may express E in the same terms as P_w. It is convenient to give E in terms of its deviation from 1: $\lambda \equiv 1 - (\eta_0E)^{-1}$ Thus, by an algebraic process too tedious to describe, the two equations (3) and (10) may finally be put in convenient forms from which L_w has been eliminated by use of equations (6) and (8):

$$NL_a\lambda^{1/2} = \frac{0.2500}{G}\frac{Wl^2}{c}\frac{n}{(\Delta T_w/T_0)(P_w/Q)^{1/2}}\left(\frac{\eta_0}{\eta_w}\right)^{1/2}\left(\frac{\alpha_I^2\psi}{\eta_0FI'}\right)^{1/2} \tag{14}$$

$$\frac{\lambda^{7/5}}{1-\lambda}\left(1 + \frac{nc}{L_a}\right)^{6/5} = \frac{6.242}{J^{4/5}}\frac{\beta bl^{4/5}c^{1/5}}{r_{h_a}}\frac{\mathrm{St}_a\mathrm{Re}_a}{(P_w/Q)^{2/5}}\left(\frac{\eta_0}{\eta_w}\right)^{7/5}\left(\frac{\alpha_I^2\psi}{\eta_0FI'}\right)^{2/5} \tag{15}$$

where G and J are related to a sort of Reynolds number based on l:

$$G \equiv \frac{\rho_w}{\rho_a}\left(\frac{C_{p_w}}{C_{p_a}}\right)^{3/2}\frac{(C_{p_a}T_0)^{1/2}l}{\nu_a\mathrm{Pr}^{1/3}};$$

$$J \equiv \frac{\rho_w}{\rho_a}\left(\frac{C_{p_w}}{C_{p_a}}\right)^{7/4}\left(\frac{\mu_w}{\mu_a}\right)^{1/4}\frac{(C_{p_a}T_0)^{1/2}l}{\nu_a\mathrm{Pr}^{7/6}} \tag{16}$$

Equation (14) says that the number of passes (n) should be small, to keep N or λ small as possible. In equation (15), n is coupled with the small ratio c/L_a, and is not important. However, if n is not at least 2, counterflow equivalence (F) will suffer, and tower size will be large. Probably, $n = 2$ is the best choice. With $n = 2$, the fin effectiveness on the water side (η_w) may confidently set equal to 1.

Our set of basic equations is now complete; equations (8), (14), and (15) yield E, N, and L_w, after a pumping-power level P_w/Q is specified. Pumping losses related to module-header connections and the headers themselves will be mentioned later. We are now

ready to select a heat-exchanger type and a set of operating parameters.

Heat Exchanger Selection

A careful survey was made of the heat-exchanger characteristics collected by Kays and London [7]. We require small values of K and $r_{h(a)}$ and a large value of St_aRe_a, and because we know L_a will have to be small, we limit consideration to the plate-fin category. We should emphasize that our purpose is to illustrate technical possibilities; thus, we are not concerned here with such questions as relative construction costs or fouling and corrosion susceptibility. Neither shall we insist that our choice among the possibilities detailed in [7] is uniquely the best.

The interrupted strip-fin plate-fin device shown in Fig. 10–60 of [7] and the present Fig. 2 seems to be an attractive choice. The following tabulation of properties (at low Reynolds number) serve to define this device.

The values of K and St_aRe_a are conservative because the test results were probably obtained at constant wall temperature, whereas constant temperature difference or heat flux would be more appropriate, and would give slightly higher values of St_a.

From the foregoing data we can calculate the fin effectiveness η_0. From equations (2–3) of [7], $ml = 0.31$, and from Fig. 2–11 and equations (2–3) of [7], we find

$$\eta_f = 0.97\,;\ \eta_0 = 1 - 0.843(1 - \eta_f) = 0.98 \qquad (17)$$

This result is conservative because the effect of the splitter has been neglected. Probably, such a high fin effectiveness is not necessary for the cooling-tower application, and some penalty in overall material utilization is being paid.

Duty Parameters For An Illustrative Example

Temperatures. For purposes of further calculation, we adopt the temperature requirements shown in parentheses on Fig. 2. The condenser temperature is taken to be 134 F, corresponding to condensation at 5.03 in Hg, which is a practical maximum for conventional steam turbines. A minimum temperature difference between condensing steam and cooling water of 7 F is usual; thus, the entering water temperature is 127 F. The ambient air temperature is taken to be 87 F, which, for example, is exceeded only 5 percent of the time at Philadelphia. Thus, ITD is 40 F. We choose a water range of 20 F ($P_I = 0.5$) as typical, but we consider the three illustrated possibilities for air range. 120.2 F corresponds to $\alpha_I = 0.83$, and would give minimum tower size. 111 F and 103 F correspond to $\alpha_I = 0.6$ and 0.4; these presumably give smaller heat exchangers but larger towers. Table 1 gives the corresponding values of ψ and $\alpha_I{}^2\psi$.

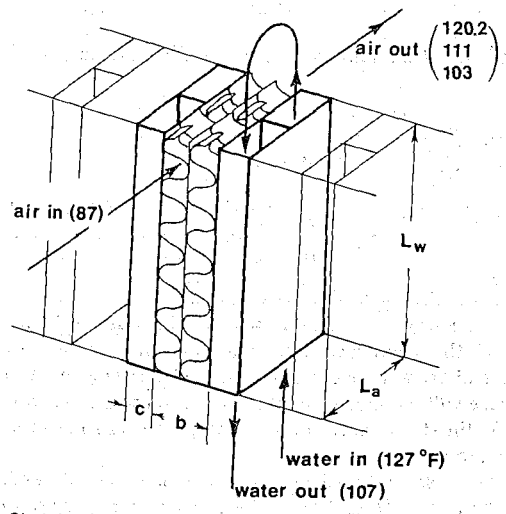

Fig. 2 Sketch of heat-exchanger module. There are N such modules each of width $b + c$. 2 water passes are illustrated. Three "air out" temperatures correspond to $\alpha_I = 0.829$, 0.6, and 0.4.

Counterflow Equivalence. From the temperatures specified in Fig. 2 we may calculate counterflow equivalence. Most heat-transfer books (see [8, Chapter 11]) display the appropriate graphs, but only for a single pass. It is easy and quite accurate to assume the two passes of our problem have equal heat-transfer coefficients, and equal temperature changes. Values of F can then be found for both passes separately, and averaged in proportion to the mean air-water temperature differences for each pass.

For two passes, without partitions, each water pass is "mixed," while the air side is unmixed. Fig. 11–14 of [8] gives F = (0.65, 0.94, 0.98) for the first water pass, when $\alpha_I = 0.829$, 0.6 and 0.4. F = (0.92, 0.95, 0.97) for the second pass. The combined value is then F = (0.81, 0.94, 0.97). The first of these results, 0.81, is perhaps unsatisfactory. If a partition is introduced into each pass, so that the water side is also "unmixed" then Fig. 11–15 of [8] gives the overall result F = (0.91, 0.94, 0.97). These are the counterflow equivalences we will assume for our numerical example. Obviously, it is only when α_I is large (0.829, say) that partitions make a difference; for our example, we will assume partitions for $\alpha_I = 0.829$ but not for 0.6 or 0.4.

If we had assumed $n = 1$, and one partition, we would have found F = (0.74, 0.87, 0.92). With no partition, F = (- - -, 0.76, 0.90). These results suggest that if the lower air-range values are chosen (to emphasize air-side area minimization), then a single-pass arrangement may be acceptable.

Heating and Pumping Power. We choose $Q = 1.6 \cdot 10^5$ Btu/sec = 168 MW, for ease of later comparison with the Rugeley tower [1, 2], and we should keep in mind that for a 1000 MWe power plant of 33 percent thermal efficiency, 12 of our towers will be needed. We take water pumping power to be $5 \cdot 10^{-4}\ Q$, or 94 kW for each tower. If the plant is 33 percent efficient, that is only 0.001 of electric power. This is greater than that for Rugeley, which we estimate to require about $2 \cdot 10^{-4}\ Q$; however, there is no point in insisting on such a very low pumping power level, if a more important advantage should lie with a somewhat higher level. We may note the following quantities calculated from Q, using average air and water temperatures of 100 F and 117 F: l = 21.28 ft; $W = 1.741 \cdot 10^7$ ft; $G = 1.0164 \cdot 10^{12}$; and $J = 1.1018 \cdot 10^{12}$ (see equation (16)).

Draft Height. For natural draft, we adopt the same "shape" as at Rugeley, where the height above the midpoint of the heat-exchange columns is 332 ft and the exit diameter is 220 ft. Thus, $Y = 1.703\sqrt{A_E}$. For mechanical draft, we choose the fan mechanical power to be $5 \cdot 10^{-3}\ Q$, or about 1 percent of typical electric output. This is a very severe requirement; 3 percent is more commonly assumed [5]. In our case, equivalent draft height is constant, according to equation (2): $Y = 522$ ft.

We also specify that $\xi = 1.5$, and values of D_E follow from equation (4) for both types of draft.

Numerical Results and the Rugeley Tower

Numerical Results. For our illustrative example, we now may make appropriate numerical substitutions in equations (4), (5), (6), (7), (8), (14), (15), and solve them to yield the results in Table 3. The quantities in the last three rows will be defined subsequently, as will the entries under the "Rugeley" column. All lengths are in ft. Neglecting the water-passage wall thickness, the frontal area $A_f = (b + c)NL_w$. Dividing by equation (8), we see that A_f/A_c is a constant, = 1.75 under our assumptions.

Scaling Rules and Rugeley Tower Description. Before discussing Table 3, we should introduce certain details of the Rugel-

Table 2 Properties of heat exchanger

$b = 0.201$ in.	fin thickness $\delta = 0.004$ in.
Fin spacing 0.0499 in.	splitter thickness = 0.006 in.
0.125 in. interruptions	$\dfrac{\text{heat transfer area}}{\text{volume}} \equiv \beta = 698\ \text{ft}^{-1}$
$4r_{h_a} = 0.004892$ ft.	$St_aRe_a = 12$; $K = 2.7$

Table 3 Features of illustrative towers

	Natural draft			Mechanical draft			Rug-eley
α_I	0.829	0.6	0.4	0.829	0.6	0.4	0.65
λ	0.0984	0.0936	0.0777	0.1098	0.1010	0.0836	0.242
L_a	0.0634	0.0400	0.0255	0.1017	0.0581	0.0327	0.507
L_w	13.78	10.88	8.67	14.74	11.39	9.05	7.68
$N \cdot 10^{-4}$	20.51	27.12	41.56	12.11	17.99	31.22	...
$A_c \cdot 10^{-4}$	4.04	4.22	5.15	2.55	2.93	4.04	4.39
$A_a \cdot 10^{-4}$	209.6	138.0	107.4	212.3	139.1	108.2	747
$A_f \cdot 10^{-4}$	7.09	7.40	9.04	4.48	5.14	7.09	7.66
$A_E \cdot 10^{-4}$	1.46	2.16	3.51	0.919	1.49	2.74	3.52
D_E	136	166	211	108	138	187	211
Y	206	250	319	522	522	522	319
A_c/A_E	2.76	1.96	1.47	2.78	1.96	1.47	1.25
v_E	19.3	18.1	16.7	30.8	26.2	21.4	10.9
Re_a	190	252	310	301	363	395	615
Re_w	4015	5184	4546	4874	5925	5167	14,400
H	62.2	53.5	51.2	49.6	44.6	45.4	46.1
N_c	82	127	204	61	101	172	216
D_H	0.98	0.81	0.67	1.05	0.85	0.70	...

ey tower, scaled for the temperature parameters assumed for this study. This will provide a basis for comparison, and also suggest a physical arrangement for our tower design.

One may easily derive the scaling laws by which the various calculated quantities would change if only the heat load changed, all other parameters kept the same, and if only ITD changed, all else the same. For example, A_a scales as Q or as $(I')^{-1}$ for both natural and mechanical draft. D_E and Y go as $Q^{2/5}$ or $(I')^{3/5}$ for natural draft; D_E goes as $Q^{1/2}$ or $(I')^{-3/4}$ for mechanical draft. L_a scales as $(I')^{1/5}$ and $(I')^{1/2}$ for natural and mechanical draft, respectively.

The Rugeley tower was designed for an I' of 0.0683, and α_I = 0.65, P_I = 0.47, for which ψ = 5.7. The tower height and exit diameter are 332 ft and 220 ft. The heat exchanger is a finned-tube device with an air hydraulic diameter one may estimate to be about 0.013 ft. Probably, F is about 0.92 and E is about 1.60, with a fin effectiveness of about 0.83. For the Rugeley service, l = 21.5 ft. One may then infer from equation (1) the reasonable value of 4.9 for the overall K'. It is very difficult to speculate about performance parameters of this proprietary heat exchanger, but we may note that an important contribution to K' may have to do with the arrangement of heat exchangers in the tower. In effect, there are 216 vertical columns, 8 ft wide, 6 in. deep, and 48 ft high, arranged in a sawtooth, or delta pattern about a base circle of 325 ft. The vertex angle of the deltas is about 67.5 deg; the ratio of A_f to the entering flow area ($\pi \cdot 48 \cdot 325$) is 1.69. The configuration is sketched in Fig. 3. Table 3 and Fig. 3 show the slightly different values obtained by scaling for our slightly higher I' = 0.0731 (Q is the same, of course). The vertical tubes, in a two-pass system, communicate with headers around the base of the tower. Especially at the inner vertex of each delta one must expect substantial flow separation and consequent loss of effectiveness (see [2]). Referring to equation (1), this loss would appear as a diminution of A_c, entering as the square, equivalent to an increase of K.

A Proposed Arrangement of Heat Exchangers

Returning to the present design suggestion, we address the question of how our fine-grained heat exchanger is to be connected with water headers and arranged in a cooling tower. We may observe in Table 3 that values of L_w are all in the range of 7-15 ft, comparable to the width of the Rugeley columns. Thus, we are led to a suggestion of Pimputkar [9] that the heat exchanger modules be horizontal, and communicate with vertical headers. One version of this scheme is sketched in Fig. 3, with the resulting columns organized about the tower in the same delta arrangement as at Rugeley. Let us suppose the same vertex angle 67.5 deg, and the same proportion of base to exit diameter as at Rugeley; the column height can then be shown to be $H = 0.120\, A_f/D_E$; this formula furnishes results displayed in Table 3.[2] Again, we find column heights comparable to Rugeley's 48 ft. The number N_c of such columns required for the tower is given by bN/H; these are also displayed in Table 3. In summary, for example we have calculated that for natural draft and α_I = 0.829, our tower requires 83 columns 62.2 ft high, 13.8 ft wide, and 0.76 in. deep.

The header diameter should be large large enough that the water velocity is low, to give satisfactorily low losses as water is supplied to the modules. For Fig. 3, Pimputkar's thesis [9] indicates that the most important water pressure loss, in addition to that already accounted for in the heat transfer passages, is the frictional loss within the headers themselves. A simple calculation may be based on equation (10) as applied to the headers, remembering that the water flow (of $130/N_c$ cfs) is double-pass within the single pipe of diameter D_H:

$$P_H = 259{,}600\ H D_H^{-4.8} N_c^{-2.8}\ \text{ft-lb/s}$$

The frictional power in the heat transfer passages is P_c (= $62240/N_c$) ft-lb/sec per column, and thus if we choose P_H/P_c to be 1/10, for example, we find

$$D_H = 2.18\ H^{0.208} N_c^{-0.375} \qquad (18)$$

Equation (18) gives the last row of Table 3, and we see that D_H is about (1/15) L_w in all cases, which would seem to pose no serious

[2] It is noteworthy that our value of A_f/A_c = 1.75 matches that of Rugeley exactly, by accident.

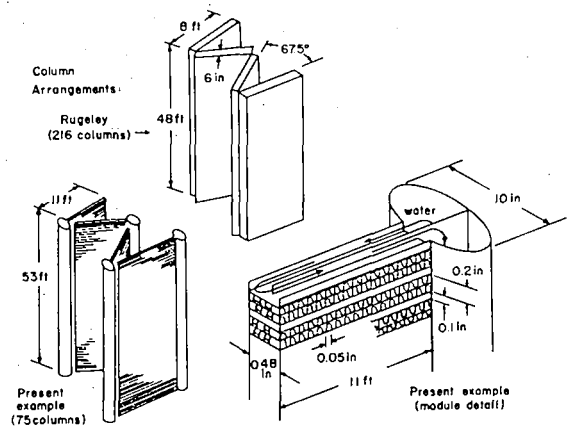

Fig. 3 A heat-exchanger configuration based on Table 1, α_I = 0.600; sketches are distorted in scale

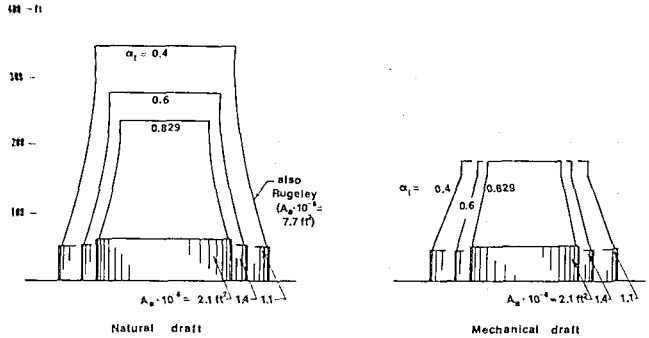

Fig. 4 Sizes of cooling towers for $1.6 \cdot 10^5$ Btu/sec according to Table 1; 12 are needed for a 1000 MWe plant—heights are measured from center of heat-exchanger columns

problem of flow blockage. Further, if we allow P_H/P_c to be 1 (thus, overall water pumping power would be $1 \cdot 10^{-3}$ Q instead of $5 \cdot 10^{-4}$ Q) then all diameters would be smaller by the factor 0.62, and D_H would be only about (1/25) L_w.

Presumably, these headers might be shaped aerodynamically to reduce their drag effect, or might be incorporated in guide vanes designed to turn the flow properly through the deltas. One should realize, in any further studies of this concept, that a low-drag heat exchanger such as we propose may not turn the air flow as efficiently as the higher-drag Forgo device; then, either airfoils must be provided to turn the flow normal to each column face, or the delta configuration must be abandoned as a means of increasing A_c.

Discussion of Results

Returning to Table 3, we may compare our calculated towers with each other and with Rugeley. Fig. 4 sketches external size results for the various values of α_I and tower type. Typically, 12 such towers would be needed to cool a 1000 MWe plant. Of course, size and number may be traded off by use of equation (1); if fan considerations restricted the exit diameter of the mechanical-draft tower (with α_I = 0.829) to 50 ft, then 18 towers would be needed, with the same total A_a.

The sizes illustrated show that natural-draft towers of much less visual impact than Rugeley may be achieved. The smaller sizes are due chiefly to the increased free-flow to exit area ratios; for α_I = 0.829, A_c/A_E = 2.76 as compared with Rugeley's 1.25, and A_c/A_E enters as the square. Secondarily, smaller values of K and E contribute to size reduction. The reason smaller values of α_I lead to larger size is that the minimum A_E (the 1.5 multiple of which is our actual A_E) increases as α_I is made smaller.

The heat-exchanger surface areas are noted on Fig. 4, and show that the heat-exchanger area may reasonably be less than one-quarter that of Rugeley. The basic reason for this reduction is that the present exchanger type is finer; our air hydraulic diameter is $r_{h(a)} \approx 0.005$ ft compared with 0.013 (estimated) for Rugeley. Secondarily, E is smaller; here E = 1.13 for α_I = 0.829, compared with 1.60 (estimated) for Rugeley, and equations (6) and (7) tell us that E enters as the 3/2 power. Parenthetically, the smaller value of E is associated with a larger coefficient of total heat transfer per frontal area; e.g., 728 Btu/(ft² deg F hr) for natural draft and α_I = 0.83, as compared with 578 Btu/(ft² deg F hr) for Rugeley.

Table 3 and Fig. 4 bear out the expectation that a smaller air range α_I leads to a smaller heat exchanger but a larger tower. These trends require a smaller depth L_a; for α_I = 0.4, one finds $L_a \approx 0.3$ in., which is almost absurdly thin.

Typically, the exit velocities from the tower are largest for the smallest towers, especially for mechanical draft because of the greater draft height assumed in those cases. For natural draft, velocity is twice that at Rugeley, while for mechanical draft, it is three times more than at Rugeley. However, because of the smaller air passages, the air Reynolds numbers are substantially lower than Rugeleys, and are firmly in the laminar regime. Water Reynold's numbers are still turbulent, but are about 1/3 of the Rugeley values, again because the passages are small. Correspondingly, the Rugeley water pumping power is less than that chosen here; we feel that pumping power at these very low levels (up to only 1/10 percent) is not a serious problem, and may be rather arbitrary.

The mechanical-draft systems are somewhat more compact than the natural draft. However, it seems to us that natural draft might well be preferred, if the height does not exceed 200 ft for each tower. Even the mechanical draft tower would be very large, and the costs of machinery and maintenance, the development costs of large fans, and the inevitable difficulties about fan noise would seem to place it at a disadvantage compared with the natural-draft type.

Concluding Remarks

We have shown that a strong incentive exists for a fundamental redesign of dry cooling towers, based on an open, very shallow heat exchanger, adopted in order to reduce sizes of both the heat exchanger and the tower shell. The same principles ought also to improve the dry paths of "wet/dry" hybrid systems [10]. We believe that our calculations for a particular example and set of assumptions show that no fundamental obstacles block this approach.

There are, of course, difficulties to be encountered in further development. Three such are: (1) One must expect fouling of a fine heat exchanger with dirt and other matter, and metal corrosion when exposed to outside air for a long time. In view of the reliability required of power-plant components, these problems will require careful study. (2) A fine heat exchanger, arranged in columns such as those sketched in Fig. 3, will require mechanical support; this in turn will introduce unwanted drag increments. (3) The best configuration of heat exchanger for turning the air flow efficiently must be found. This will be a touchier problem than at Rugeley, because our flow resistance is less.

Solution of these and other problems would depend on whether the natural or the mechanical draft tower is thought more attractive. We tend to favor the natural draft principle in this case, for reasons already mentioned.

In conclusion, we should emphasize that certain of our assumptions were rather arbitrary, and merit further study. For example, a single-pass heat exchanger might be acceptable; if so, provision of a practical shallow heat exchanger might be easier. The fin effectiveness of our plate-fin device is much higher than it needs to be; perhaps the water passage (quantity c) should be wider. Finally, we have varied air range (α_I) but not water approach (P_I); this should be done, though α_I is no doubt the more critical parameter.

Acknowledgment

This research has been supported by the National Science Foundation, Division of Advanced Technology Applications (RANN).

References

1 Christopher, P. J., and Forster, V. T., "Rugeley Dry Cooling Tower System," *Proc. Inst. Mech. Engr.*, Vol. 184, Part 1, No. 11, 1969–1970, pp. 197–222.

2 Moore, F. K., "On the Minimum Size of Natural-Draft Dry Cooling Towers for Large Power Plants," ASME Paper No. 72-WA/HT-60.

3 Forgo, L., "ein neuer Wärmeübertrager aus Aluminium," *Allgemeine Warmetechnik*, Bd. 10, H.8, 1961, pp. 149–156.

4 Moore, F. K., "The Minimization of Air Heat-Exchange Surface Areas of Dry Cooling Towers for Large Power Plants," *Dry and Wet/Dry Cooling Towers for Power Plants*, ASME Publication HTD-Vol. 6, R. L. Webb and R. E. Barry, eds. Nov. 1973, pp. 13–23.

5 Larinoff, M. W., "Dry Cooling Tower Power Plant Design Specifications and Performance Characteristics," *Dry and Wet/Dry Cooling Towers for Power Plants*, ASME Publication HTD-Vol. 6, R. L. Webb and R. E. Barry, eds., Nov. 1973, pp. 57–83.

6 Moore, F. K., "On the Minimum Size of Large Dry Cooling Towers With Combined Mechanical and Natural Draft," JOURNAL OF HEAT TRANSFER, TRANS. ASME, Series C, Vol. 95, Aug. 1973, pp. 383–389.

7 Kays, W., and London, A. L., *Compact Heat Exchangers,* 1952, Second ed., McGraw-Hill, New York, 1964.

8 Kreith, F., *Principles of Heat Transfer,* International, Scranton, Pa., 1958.

9 Pimputkar, S. M., "Configuration of Module Heat-Exchangers for Dry Cooling Towers of Large Power Plants," MS thesis, Cornell University, Jan. 1974.

10 Hansen, E. P., "Dry Towers and Wet/Dry Towers for the Indirect Power Plant Cycle," *Dry and Wet/Dry Cooling Towers for Power Plants,* ASME Publication HTD-Vol. 6, R. L. Webb and R. E. Barry, eds., Nov. 1973, pp. 109–117.

R. W. Porter
Assoc. Professor.
Mem. ASME

K. H. Chen
Research Assistant.

Illinois Institute of Technology.
Chicago, Ill.

Heat and Mass Transfer of Spray Canals

A numerical analysis is presented for the heat-exchanger performance of open, direct-contact evaporative spray cooling of large electric power plants. Floating spray modules are placed essentially in series in this large-scale application. The module "unit performance" is formulated in terms of Number of Transfer Units (NTU) as suggested by elementary drop dynamical theory. The overall canal performance is analyzed by a numerical procedure of marching along from pass to pass of spray modules. Hydrodynamic mixing within the canal and air-vapor circulation interference above the canal are incorporated as suggested by theoretical considerations and field experiments. The analysis was applied to a number of field tests of several spray canals and the apparent values of NTU were correlated with wind speed.

Introduction

Upward of 10^6 gpm (4×10^6 liter/min) of cooling water is heated about 25 F (14 C) in the cooling of condensors of multiple 10^3 − MW(e) steam-electric power plants. In order to avoid this enormous concentrated thermal discharge to natural water bodies, increasing attention is being devoted toward supplemental and closed-cycle cooling directly to the atmosphere. Depending on local economic and environmental factors, the spray canal is an attractive alternative to the artificial cooling pond and the evaporative cooling tower. A canal or series placement of sprays is used in order to alleviate the heating and humidification of air that occurs toward the center of large spray ponds.

Heat-and mass-transfer aspects of cooling ponds [1][1] and evaporative cooling towers [2] are relatively well known in terms of heat-exchanger performance. While the fundamental aspects of direct-contact evaporative cooling are reasonably understood, spray-canal analyses were not available in a manner that could be calibrated by field tests [3].

In the present work, the Number of Transfer Units (NTU) concept is applied to the individual spray module and incorporated into the numerical analysis of the entire canal. Both cooling range and evaporative loss are determined. The NTU may be determined by comprehensive drop dynamical theory or by performance tests of individual modules. However, in the present case the NTU are determined from tests of entire canals by matching their observed performance to the theory. This approach provides the calibration necessary for theory, experiment and design.

Some typical floating spray modules are shown in Fig. 1. Spray module "*A*" incorporates manifolded cone-impact spray heads [4] while module "*B*" uses a single slot nozzle integral with its float [5]. Both units spray about 10^4 gpm (4×10^4 liter/min) of approximately ½-in. (1-cm) dia drops and are powered by nominally 75-hp (56-kW) electric motor pumps. Several hundred of these units are needed for closed-cycle cooling of multiple 10^3-MW(e) generating capacity. Moored perhaps 4 rows wide (4 units per pass), a canal 200 ft (61.0 m) wide and several miles (several km) long is required. A depth of 10 ft (3.05 m) and a flow of 10^6 gpm (3.8×10^6 liter/min) results in a canal velocity of about 1 fps (0.3 m/s). The most critical condition occurs in hot humid weather when the electrical demand, thermal load, and wet-bulb temperature (the cooling potential) are all maximum.

Current systems incorporate up to about 100 units and are used mainly for supplemental cooling. Tests of these systems are discussed later. Larger systems under construction are based largely on this experience [6].

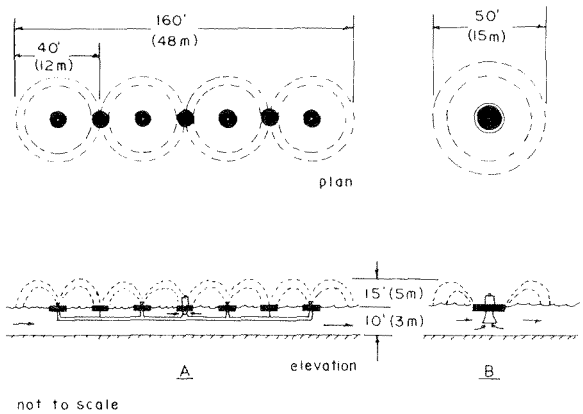

Fig. 1 Schematic diagram of typical spray modules using (*A*) manifolded multiple cone-impact spray heads, (*B*) integral float and slot nozzle

[1] Numbers in brackets designate Reference at end of paper.

Contributed by the Heat Transfer Division for publication in the JOURNAL OF HEAT TRANSFER. Manuscript received by the Heat Transfer Division, December 12, 1973. Paper No. 74-HT-AA.

The canal for closed-cycle application is best laid out over a large loop. This configuration reduces both air-vapor interference and the environmental impact of the concentration of moisture and heat. Drift amounts typically to less than 0.01 percent of spray flow [6] and is insignificant from the thermal point of view. Evaporation, however, typically amounts to several percent and is incorporated into the thermal analysis in terms of both the energy balance and make-up water requirements.

As the plant-discharge water flows down the canal from pass to pass, each spray module cools a small portion of it by direct-contact cooling. This spray water mixes with the bulk flow and there is a gradual approach toward the wet-bulb temperature depending on the number of modules employed.

Major problems with spray canals include: (1) the unit performance of individual spray modules, (2) the pass-to-pass balance of energy along the canal, and (3) the interference of air-vapor circulation among modules. These problems are discussed in the following sections. The analysis is then applied to conditions of canal field tests. The unit performance parameter, NTU, was varied until the observed cooling was reproduced. Results are correlated with wind speed.

Unit Performance

It is possible to study spherical water droplets in a uniform medium and to determine their trajectory, cooling, and evaporation. Empirical [7] or analytical [8] transport coefficients may be employed. Unfortunately, the drops emitted from a spray module are translated through a three-dimensional air-vapor flow field determined by the ambient wind, entrainment and natural convection. Elgawhary [9] defined "air cells" associated with the drops in order to account for air heating and humidification but this ignores the dynamics both as it affects the drop trajectory directly and as it affects diffusion of heat and vapor indirectly.

In addition, the drop size is not known and is subject to a distribution dependent on flow instability phenomena. Here, one would have to rely on empirical data obtained from tests of similar spray generators [10]. Further, drops generated in spray modules, typically ¼ to 1 in. (0.6 to 2.5 cm) in diameter and translating up to about 40 fps (12 m/s), are unstable due to flow-induced stresses overcoming the balance between pressure and surface tension [11]. This leads to an increasing fineness in the direction of flow. Finer drops are also generated in the presence of higher wind speeds, an effect suggested by Wilson [12] leading to greater cooling than otherwise predicted by using a constant drop size.

In summary, drop dynamical theory must incorporate a degree of empiricism. In the present approach this is done so that a single performance factor, Number of Transfer Units (NTU), is involved in a manner analogous to conventional heat exchangers.

The rate-of-change equations for mass and energy of a typical water droplet are

$$-dM/dt = KA(w_g(T) - w_a) \tag{1}$$

$$-d(Mu_\ell(T))/dt = HA(T - T_a) + KAi_g(T)(w_g(T) - w_a) \tag{2}$$

where M is drop mass, K mass transfer coefficient, A drop surface area, w humidity (mass of water vapor per mass of dry air), T temperature, u specific internal energy, H sensible heat transfer coefficient, i specific enthalpy, and where subscript ℓ denotes liquid water, g denotes saturated air and vapor in equilibrium and contact with the liquid, and a denotes the local surrounding air and vapor.

Neglecting the difference between liquid-water internal energy and saturated liquid-water enthalpy and using the ideal caloric equation of state, assumptions justified under atmospheric pressure, equations (1) and (2) combine to

$$-c_w MdT/dt = KA[\epsilon c_s(T - T_a) + i_{fg}(w_g(T) - w_a)] \equiv kA(h(T) - h_a) \tag{3}$$

where c_w is specific heat of liquid water, $\epsilon = H/(c_s K)$ (psychro ratio), c_s is the specific heat at constant pressure of air and vapor (humid heat), i_{fg} is the specific latent heat of vaporization of water and h is the sigma function or total heat, the specific enthalpy of air and vapor (per unit mass of dry air) subtracting the contribution by the amount of moisture present taken as saturated liquid. This shifting datum of h results in its dependence only on the adiabatic-saturation temperature, the (thermodynamic) wet-bulb temperature. Values of $h(T)$ may be calculated or obtained from tables of thermodynamic properties [13]. The factor ϵ has been absorbed in the coefficient k which replaces K. For air and vapor ϵ is approximately unity owing to the analogy of heat and mass transfer, the thermal and vapor diffusivities being nearly equal [14].

Equation (3) can be written

$$-c_w \int_{T_n}^{T_s} \frac{dT}{h(T) - h_a} = \overline{(kA/M)}t \tag{4}$$

where n denotes the initial state in the spray nozzle and s denotes the state at the end of the spray trajectory. The use of an average kA/M over the time of flight t integrates the complex dynamical effect into a single parameter. Equation (4) is known as Merkel's equation and is widely used in cooling-tower analysis where direct-contact evaporative cooling is also involved. In that case, the heating and humidification of air is accounted for by employing an energy balance (for counter flow) $dh_a/dT = c_w L/G$ where L/G is liquid-to-gas mass-flow ratio [2].

Nomenclature

A = drop surface area
B = Bowen ratio of sensible to evaporative heat transfer
c_S = air-vapor specific heat at constant pressure
c_W = liquid-water specific heat
e = ratio of evaporative to initial-canal flow rate
f = dimensionless increment in wet-bulb temperature
h = total heat or sigma function
H = drop convective sensible heat transfer coefficient
i_{fg} = specific latent heat of vaporization at constant pressure of water
i = specific enthalpy of water
k = effective drop convective heat transfer coefficient
K = drop convective mass transfer coefficient
m = number of rows of spray modules across canal
M = drop mass
NTU = number of transfer units of spray module
r = ratio of spray-module to initial-canal flow rates
t = time of flight of drop
T = temperature of liquid water of canal or drop
T_a = air-vapor (dry-bulb) temperature
T_{WB} = wet-bulb temperature
u_ℓ = specific internal energy of liquid water
w = absolute humidity
x_k = distance to kth row
α = fraction of spray-module flow evaporated
ϵ = psychro ratio (Hc_S/K)

Subscripts

a = air-vapor mixture
g = saturated vapor
i = pass along canal
n = initial spray nozzle
s = final spray
WB = wet bulb
0 = canal inlet
∞ = ambient

Superscripts

j = row across canal

In the case of open sprays subject to ambient wind, entrainment and buoyancy, L/G is unknown. Further, the definition of a specific relative flow orientation is uncertain although departure from counter flow could be absorbed in a configuration factor, as in conventional heat exchangers, and absorbed in the RHS of equation (4). It appears preferable to avoid the artificial introduction of L/G instead by taking h_a to be constant over the integration. One may consider that h_a incorporates an average "circulation" allowance above the ambient value.

Chen [15] has shown that for typical spray modules the LHS of equation (4) can be closely approximated by using an average integrand over the integration. Thus, equation (4) is replaced with [6]

$$\frac{c_w(T_n - T_s)}{(h(T_s) + h(T_n))/2 - h(T_{wB_a})} \equiv \text{NTU} \tag{5}$$

where T_{WBa} is the local wet-bulb temperature at which h_a is evaluated. The performance factor NTU is identified as the RHS of equation (4) and could be calculated accordingly from a more detailed drop dynamical theory. The value of NTU might also be determined by measuring T_s, T_n, and T_{WBa}. As noted earlier, in the present approach values of NTU are determined as implied by the observed performance of entire canals. In any case, once NTU is known

$$T_s = T_s(T_n, T_{wB_a}, \text{NTU}) \tag{6}$$

represents the inversion of equation (5). This may be accomplished numerically, for example, by using the well-known Newton-Raphson method of iteration [15].

The fraction of sprayed water evaporated can be found from the ratio of final to initial drop size. This ratio can be determined by combining equation (1) and the first expression of equation (3) and integrating. Thus

$$\alpha = 1 - M_s/M_n = 1 - \exp\{-c_w(T_n - T_s)/(i_{fg}(1 + B))\}$$
$$\approx c_w(T_n - T_s)/(i_{fg}(1 + B)) \tag{7}$$

where B is the so-called Bowen ratio of sensible to evaporative heat transfer, assumed constant over the integration

$$B = \epsilon c_s(T - T_a)/[i_{fg}(w_g(T) - w_a)] \tag{8}$$

The approximation in equation (7) can be made because of the smallness of $c_w/i_{fg} \doteq 9.524 \times 10^{-4}$ F^{-1} (1.7153×10^{-3} C^{-1}). The fraction of sprayed water is thus small, and from the thermal point of view results are weakly dependent on B [15]. Thus, the spray performance effectively depends on the wet-bulb temperature rather than both the dry-bulb temperature and the humidity. The latter parameters can be eliminated conservatively by taking $B = 0$ which corresponds to the maximum possible spray evaporated and lost to the cooling of the bulk canal flow. Further, the upper limit on evaporative make-up water required is computed on this basis.

Canal Performance

Considerations for an energy balance of a typical pass of modules (Fig. 2) include the nature of mixing, possible flow reversal and recirculation into the module intake, and the circulation of air and vapor among modules.

The extent of mixing in a cross section of the canal was investigated at Dresden Station (Illinois) of Commonwealth Edison Company. Units of type A were employed (Fig. 1) one unit per pass in the test canal which was approximately 60 ft (18 m) wide and 10 ft (3 m) deep and flowing at about 3 fps (0.9 m/s). Temperature was sounded by using a portable thermistor probe suspended from shore by cables. Under the test conditions, 10^4 gpm (3.8×10^4 liter/min) of spray was cooled about 20 F (11 C) by each module before falling back into the nominally 10^6-gpm (4×10^6-liter/min) canal. Ten modules preceeded the test section which extended downstream without modules therein. The objective was to determine the length of decay of any stratification. At the edge of the last spray pattern preceeding the unoccupied section, the maximum temperature variation was found to be only 0.6 F (0.33 C) in width and 0.8 F (0.44 C) in depth excluding the visible spray itself. Eighty ft (24.4 m) further downstream (undisturbed), the variation was halved to 0.3 (0.17) and 0.4 F (0.22 C), respectively. Since the modules occupy about 160 ft (48.8 m) of length, one can conclude that the test canal is operating virtually mixed pass to pass.

Because the Dresden canal is not completely typical of anticipated systems of three-times larger width and one-third smaller velocity (same depth), consideration of scaling is necessary. The longitudinal distances for mixing over depth d and width w scale with the characteristic diffusion lengths given by the products of longitudinal (canal) velocity V and the respective characteristic diffusion times, d^2/α_d and w^2/α_w. For open channels, diffusivities α are both proportional to Vd although the former is about three-times larger than the latter [16]. Denoting the test condition as "o," the longitudinal mixing distances are thus $L_d = L_{d\,0}\,d/d_0$ and $L_w = L_{w\,0}\,(w/w_0)^2 d_0/d$ for mixing over depth and width, respectively. We conclude that equal depth canals will be equally mixed over depth—say requiring 80 ft (24.4 m) or ½ pass according to the Dresden data. However, the three-times wider canal will require nine-times the lateral mixing length. Assuming the lateral diffusivity is three-times greater than the vertical, the anticipated mixing distance is 240 (73.2 m) or 1.5 passes. Because a much larger number of passes is generally involved, it is reasonable to consider the canal as being mixed at each cross section from pass to pass.

The effect of downstream recirculation into the module intake can be estimated by considering the ratio of velocity induced by the modules relative to the canal. For four 10^4-gpm (3.8×10^4-liter/min) modules per pass in a 10^6-gpm (3.8×10^6-liter/min) canal, the ratio is 0.04 which is felt too small for large-scale reversal in flow. Accordingly, the module intake, located mid length, might be taken at mid temperature before and after the module. Chen [15] has shown that using the upstream temperature alone leads to less than 1 percent error in canal cooling range under typical conditions. This is due to the small fraction of water being sprayed per pass and the subsequently small temperature drop per pass in the canal. The effect of vertical recirculation of sprayed water would seem to be avoided by the high degree of mixing achieved.

The consideration of air-vapor circulation among modules is deferred until the next section. It is assumed here that the local wet-bulb temperature is known at each module or at least can be determined from quantities known from the computation.

The control volume for a single module of row j and pass i, m_i rows per pass, is shown in Fig. 2. An equal portion of the canal flow, $1/m_i$, is attributed to each row across the width of the canal. The quantities in the square brackets of Fig. 2 denote the flow rates in ratio to the plant-discharge flow rate. The quantity r_i is thus the spray-module flow ratio (a known parameter), e_{i-1} is the evaporation flow (ratio) lost up to pass i and $\alpha_i^{(j)}$ is the

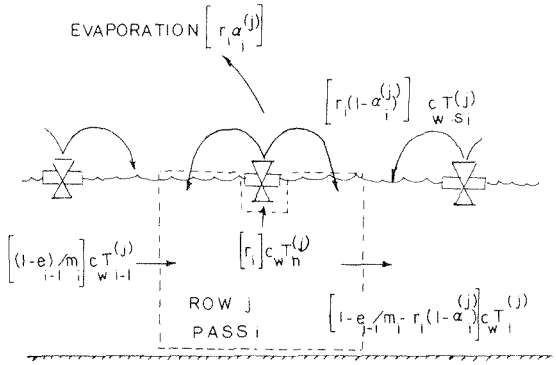

Fig. 2 Energy balance for an element of a spray canal consisting of m units per pass

fraction of sprayed water evaporated so that $r_i\alpha_i^{(j)}$ is the module evaporation flow ratio.

As noted before, the upstream temperature $T_{i-1}^{(j)}$ and the nozzle-intake temperature $T_{n_i i}^{(j)}$ are both taken as the upstream mixed-canal temperature T_{i-1}. Making these representations, balancing the energy flow through the control volume of Fig. 2 and solving for the downstream temperature

$$T_i^{(j)} = \frac{(1 - e_{i-1} - m_i r_i)T_{i-1} + m_i r_i (1 - \alpha_i^{(j)})T_{s_i}^{(j)}}{1 - e_{i-1} - m_i r_i \alpha_i^{(j)}} \quad (9)$$

where it is implied that all variables of subscript i-1 are known from the previous pass. The canal-inlet conditions are $e_0 = 0$ and $T_0 = T_{tl}$, the plant-discharge temperature (a known parameter).

The sprayed-water temperature is given by equation (6)

$$T_{s_i}^{(j)} = T_s(T_{i-1}, T_{wB_{a_i}}^{(j)}, \text{NTU}) \quad (10)$$

In the present case, the numerical approach included linear interpolation of thermodynamic data $h(T)$ tabulated [13] in 1-F (0.5556-C) increments assuming standard atmospheric pressure.

The fraction of sprayed water evaporated is given by equation (7). Using the conservative (and weak) assumption of $B = 0$

$$\alpha_i^{(j)} = (c_w/i_{fg})(T_{i-1} - T_{s_i}^{(j)}) \quad (11)$$

Equations (10), (11), and (9) are solved in that sequence for each row j. Then the average canal temperature after pass i is computed

$$T_i = \frac{1}{m_i} \sum_{j=1}^{m_i} T_i^{(j)} \quad (12)$$

The evaporation flow ratio (to plant-discharge flow) is

$$e_i = e_{i-1} + \sum_{j=1}^{m_i} r_i \alpha_i^{(j)} \quad (13)$$

so that the necessary information is ready for the next pass $i + 1$, etc. It is thus possible to march down the canal for any number of passes, the spray and the canal approaching the wet-bulb temperature.

In the steady state, a pass-to-pass distribution of canal temperature is obtained. In an unsteady state, we can regard the distribution as following a slug of fluid from the plant discharge according to the flow velocity. Knowing the flow time between passes, meteorological conditions can be referred to each pass for the selected slug.

Air-Vapor Circulation Interference

Air and vapor is heated and humidified as it comes in contact with the spray. As noted earlier, for flow within a cooling tower this is accounted for by an energy balance incorporating L/G, the liquid-to-gas mass flow ratio. Recirculation allowances are also recommended to account for partial circulation of the discharge into the intake from the same or an adjacent tower.

In the case of open sprays, L/G is not well defined, and there is no single region for the definition of recirculation intake and its measurement. Accordingly, NTU was based on a "local" wet-bulb temperature assumed constant for a spray module. However, the local wet-bulb temperature is variable due to circulation among modules especially when they are placed several units wide across the canal. Further, circumstances may require a return canal loop in close proximity. The air wet-bulb temperature is driven toward the (local) canal temperature which suggests

$$T_{wB} - T_{wB_\infty} = f(T - T_{wB_\infty}) \quad (14)$$

where $0 \le f \le 1$.

The value of f as a function of distance downwind from the geometric center of individual spray modules was also investigated at Dresden Station. Results are shown in Fig. 3 for two types of modules operating at three flow rates. The canal temperature was again determined by the portable thermistor probe. The wet-bulb temperature was averaged over several minutes using a mercury-in-glass sling psychrometer, and wind speed was determined by a cup-type anemometer. There is little variation in data over the range of 2–8 mph (0.89– 3.6 m/s) and over the three module configurations. The experiments have shown no effect upwind which suggests plume-or wake-type phenomena.

A single $f(x)$ curve is proposed to fit the data on Fig. 3. If we assume superposition as suggested by the diffusion equations neglecting induced flow, the local value of f due to upwind modules at distance x_k would be

$$f_j = \sum_{k=1}^{j-1} f(x_k) \quad (15)$$

Values of f_j for typical 50-ft (15.2-m) spacing are shown in Fig. 3. For a multiple-row system of this spacing, the values of f would be 0, 0.18, 0.26, 0.26, . . . , 0.26 proceeding in the downwind direction. In effect, the influence of a given module does not extend beyond two rows dowmwind. Measurements using electronic psychrometry and series of modules arranged both one and two units per pass suggests good agreement (within gusts of 1 F (0.56 C)) if the distance normal to the rows of modules is used independent of wind angle to the canal, up to a few degrees of being parallel.

In the numerical model, the value of f is specified for each row of modules across the width of the canal. The above estimate of f and superposition is suggested in the interim until more detailed theory and experiment are available.

Systems Experiments

Hoffman [6] has reported performance tests of three spray canals operating under a number of conditions. The data are summarized in Table 1 along with that of a new configuration. In all of these tests, modules of type A [4] were employed. Measurements included upstream and downstream canal temperatures, ambient wet-bulb temperature and wind speed. Also noted in Table 1 is the ratio of module to canal flow rate according to pump specifications.

Canal D1 refers to Commonwealth Edison's Dresden Station in a test configuration where ½ of the modules were in each of two connected canal elements in counter flow about 100 ft (30.5 m) apart on center. This configuration was incorporated into the determination of f. Units were arranged one unit per pass in each canal. A total of 92 modules were operating. Canal C refers to Virginia Electric Power's Chesterfield (Virginia) station where 40 modules are arranged 4 units per pass. Canal F refers to Detroit

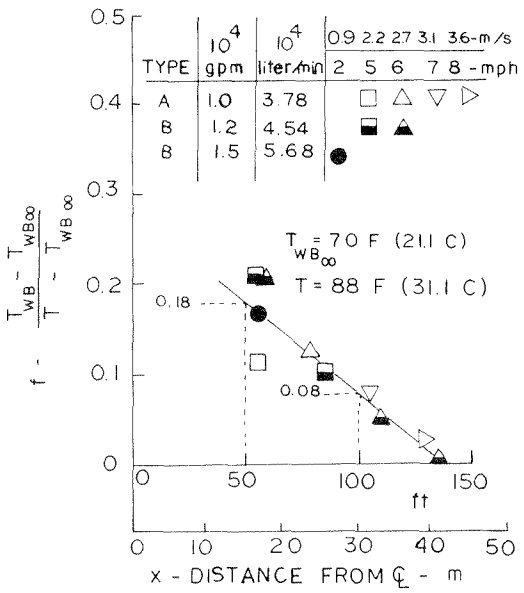

Fig. 3 Experimental data and proposed correlation for the dimensionless air-vapor circulation allowance

Table 1 Systems performance data

Canal	Plant-discharge temp.-F (C)	Wet-bulb temp.-F (C)	Wind speed-mph (m/s)	Canal-discharge temp.-F (C)
*D*1[6]	88.5 (31.39)	55.5 (13.06)	5.0 (2.2)	82.7 (28.17)
"	80.5 (26.94)	49.0 (9.44)	2.5 (1.1)	75.4 (24.11)
"	81.0 (27.22)	60.0 (15.56)	6.0 (2.7)	76.0 (24.44)
"	81.5 (27.50)	56.3 (13.5)	4.5 (2.0)	75.9 (24.39)
"	85.2 (29.56)	62.0 (16.67)	5.0 (2.2)	79.8 (26.56)
"	86.2 (30.11)	58.0 (14.44)	4.0 (1.8)	80.2 (26.78)
"	87.5 (30.83)	58.0 (14.44)	4.0 (1.8)	81.8 (27.67)
C[6]	109.1 (42.83)	81.0 (27.22)	3.0 (1.3)	102.8 (39.33)
"	108.5 (42.50)	81.0 (27.22)	3.0 (1.3)	101.7 (38.72)
F[6]	74.0 (23.33)	60.0 (15.56)	5.0 (2.2)	72.5 (22.5)
*D*2	72.7 (22.61)	31.7 (−0.17)	7.5 (3.4)	69.0 (20.56)

Notes: Canal *D*1: $r = 0.010$ (module flow/canal flow), 1 unit/pass, 92 operating units (1971).
Canal *C*: $r = 0.020$, 4 units/pass, 40 units (1971).
Canal *F*: $r = 0.080$, 1 unit/pass, 5 units (1971–1972).
Canal *D*2: $r = 0.010$, 2 units/pass, 38 units (1973).

Edison's Fermi Station test section using 5 modules arranged 1 unit per pass.

Canal D2 represents a portion of the Dresden canal now arranged 2 units per pass, 40 ft (12.2 me) apart. This case is also of interest because of the lower air wet-bulb temperature and the higher wind speed. In the latter case, gusts are appreciable and must be averaged over the time of flow. Meteorological conditions were obtained from portable mechanical weather stations located on each side of the canal.

The numerical approach was applied to the test cases by using various NTU until the test conditions were duplicated within 0.05 F (0.03 C) of the cooling range which is at most $\frac{1}{10}$ of the probable experimental error. Results are plotted in Fig. 4 versus wind speed which is regarded as the principal variable for a specific module.

An indication of the accuracy of present technique can be obtained by assuming the NTU determined by the solid curve of Fig. 4 applies. The predicted canal discharge temperature can then be compared with the observed value and the error expressed as a percent of observed cooling range for each case. Excluding the "low point" in Fig. 4, the percent errors ranged from −3 to 12 percent with an average absolute error of 5 percent. The latter corresponds to less than 0.5 F (0.28 C) error in temperature for the present systems and is probably within experimental accuracy.

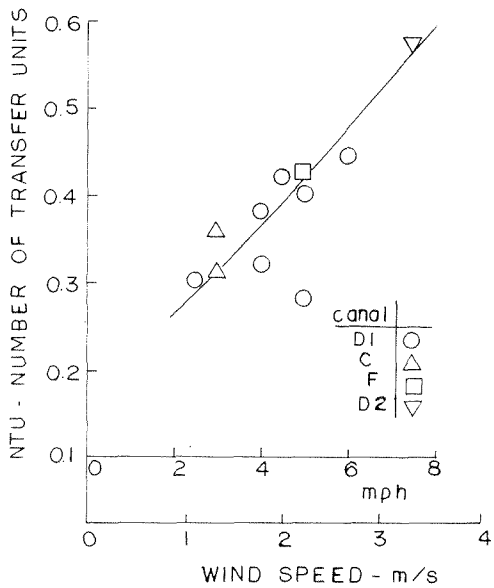

Fig. 4 NTU determined from systems performance tests (Table 1) of several spray canals employing modules of Type *A* [4]

As noted earlier, it is also possible to determine NTU by observing the performance of a single spray module and measuring the temperatures on the LHS of equation (5). Unfortunately, there are difficulties in collecting the large flow rates involved or in sampling the spray spatially. While a manufacturer will pursue this course in his developmental program, the resultant data are considered proprietary. Hoffman [6] describes such a study but the results have not been published.

Conclusions

The performance of a spray-canal cooling system was shown to depend on three principal effects. These include the performance of an individual module, the energy-flow balance marching along the canal pass to pass, and the air-vapor circulation interference. In the present case, the module NTU was determined by matching theory to experimental results for entire canals. The interference allowance, defined in terms of a dimensionless wet-bulb temperature increment, was obtained experimentally. In both cases, the results apply to a specific type of spray modules. Thus, results are useful primarily in substantiation and calibrating existing systems and in extrapolating to new canal designs in terms of present experience.

Additional theory and experiment are especially needed in the case of the air-vapor circulation allowance. This determines, in effect, how the performance of the entire system departs from the sum of its parts. The lack of effect upwind of modules suggests a plume or wake model may be appropriate. The effects of wind speed and direction, spray geometry, row spacing, etc., require further study.

In terms of spray-module performance, individual modules can also be tested in terms of observed temperature drop of sprayed water. While this procedure is considered less accurate because of sampling problems, gusts, and the like, it is necessary when introducing new designs. It is also desirable to develop more detailed drop dynamical theory in order to predict NTU in proposed designs and to evaluate existing ones.

The numerical method incorporating known NTU and interference allowances can be used to determine the required number of spray modules for specified design conditions of plant-discharge flow rate and temperature, wind speed, wet-bulb temperature, and the desired canal-discharge temperature. This approach has been used in the design of several large systems [5, 6]. For off-design conditions, the design number of units can be used to determine the canal-discharge temperature achieved. Such information is necessary in order to fully evaluate the economics of the overall plant performance. It is also necessary for performance acceptance tests since they seldom will be conducted under the exact design condition.

Acknowledgments

The authors would like to thank Michael Groppi of Commonwealth Edison Company for his assistance and support in carrying out field experiments at Dresden Station.

References

1 Ryan, P. J. and Harleman, D. R. F., "An Analytical and Experimental Study of Transient Cooling Pond Behavior," Ralph M. Parsons Laboratory for Water Resources and Hydrodynamics Report No. 161, Massachusetts Institute of Technology, Cambridge, 1973.

2 Frass, A. P. and Ozisik, M. M., *Heat Exchanger Design*, Wiley, New York, Chapter 15, 1965.

3 Ryan, P. J., "Temperature Prediction and Design of Cooling Ponds," *Engineering Aspects of Heat Disposal From Power Generation*, Ralph M. Parsons Laboratory for Water Resources and Hydrodynamics, Massachusetts Institute of Technology, Cambridge, Chapter II, 1972.

4 Frohwerk, P. A., "Spray Modules Cool Plant Discharge Water," *Power*, Sept. 1971, p. 52.

5 Kelley, R. B., "Large-Scale Spray Cooling," *Industrial Water Engineering*, Aug.-Sept. 1971, p. 18.

6 Hoffman, D. P., "Spray Cooling for Power Plants," *Proceedings of the American Power Conference*, Vol. 35, 1973, p. 702.

7 Nottage, H. B., and Boelter, L. M. K., "Dynamic and Thermal Behavior of Water Drops in Evaporative Cooling Processes," ASHVE Report No. 1146, *ASHVE Transactions*, Vol. 46, 1940, p. 41.

8 Chao, B. T., "Transient Heat and Mass Transfer to a Translating Droplet," JOURNAL OF HEAT TRANSFER, TRANS. ASME, Series C, Vol. 91, No. 2, May 1969, p. 273.

9 Elgawhary, A. M., "Spray Pond Mathematical Model for Cooling Fresh Water and Brine," PhD dissertation, Oklahoma State University, Stillwater, Aug. 1969.

10 Berman, L. D., *Evaporative Cooling of Circulating Water*, Pergamon, New York, 1961, p. 111.

11 Levich, G. D., *Physicochemical Hydrodynamics*, Prentice-Hall, Englewood Cliffs, 1961, p. 454.

12 Wilson, D. E., "Thermal Performance of Powered Spray Modules," MS thesis, University of Illinois, Urbana, 1972.

13 Berry, C. H., "Mixtures of Gases and Vapors," *Mechanical Engineers' Handbook*, T. Baumeister, ed., McGraw-Hill, New York, 1958, p. 4-82.

14 McAdams, W. H., *Heat Transmission*, McGraw-Hill, New York, 1954, p. 356.

15 Chen, K. H., "Thermal Analysis of Spray Canal Design," MS thesis, Illinois Institute of Technology, Chicago, May 1973.

16 Fischer, H. B., "Longitudinal Dispersion and Turbulent Mixing in Open-Channel Flow," *Annual Reviews in Fluid Mechanics*, Vol. 5, 1973, p. 59.

H. Q. Oliveira
Assist. Professor,
Escola de Engenharia,
Universidade Federal do Espírito Santo,
Vitoria, Brazil

R. P. Forslund
Engineer,
URCA,
Rio de Janeiro,
Brazil. Assoc. Mem. ASME

The Effect of Thermal Construction Resistance in the Design of Channel-Plate Heat Exchangers

Introduction

The purpose of this paper is to show the behavior of the thermal constriction resistance that occurs in a channel-plate type heat exchanger.

The study was prompted by the evaluation of designs for rejecting heat from submarine hulls, in particular deep submergence hulls of spherical or cylindrical geometry. In these latter cases, the hull walls are thick to counteract the extreme water pressure at great depths. In addition, because of the considerations of stress concentrations it is desirable not to penetrate the hull with piping in order to provide for an external heat exchanger. Thus, the design is limited to using the hull itself as the heat exchanger surface. Channels on the inside of the hull carry the coolant fluid to the hull surface.

A typical arrangement of the channel-hull design is shown in Fig. 1. Here the channels are considered to be made of an elastic material to accommodate the contractions in the hull itself when under pressure. The elastic material is bonded to the hull in the area beyond the channels thus leaving the coolant fluid to be in intimate contact with the inside hull surface. The constriction of the heat flux lines in the plate are shown for one of the channels. The geometry studied here however is a rectangular one as shown in Fig. 2, since it is the most easily presented. The results however may be used to estimate the effect of the constriction resistance on other geometries.

This problem is similar to that of Van Sant [1][1] and Schmitz [2] who studied the problem of a strip heated flat plate. Van Sant was concerned with the variation in temperature on the convectively cooled surface for cases of both uniformly heated strips and uniform temperature strips. In the present study, the former case is employed to obtain a constriction resistance coefficient (C_{UHF}) for uniform heat flux (UHF). Unfortunately, no comparison of the present study can be made with that of Van Sant since in his work he was concerned with temperature variations, whereas in the present study attention is given to thermal resistances. However the same equation for temperatures is employed, although it is expressed in a different coordinate system.

The present study is extended to consider the case of a convective heat flux (CHF) boundary condition at the channel surface. This part of the present study constitutes the more important contribution to this paper, since it gives a feel to the designer as to the importance for taking into account a more complex boundary condition.

Schmitz was concerned with the problem of predicting the heat flux through a flat plate maintained at a constant temperature on one side and heated uniformly by strips on the other side. Here also the work of Schmitz cannot be easily compared with the present study, since in the present study attention was confined to a convective heat flux boundary condition at the outer surface of the hull, which represents a more real condition for the purpose of this study. Limiting conditions, such as an infinite external heat transfer coefficient in this study would provide such a comparison, but was not made.

Analysis

The problem treated here [3] is the evaluation of the constriction resistance, R_C, between the inner channel surface, a, and the entire external surface, b, whose average temperatures are T_a and T_b respectively;

$$R_C = (T_a - T_b)/Q \tag{1}$$

$$T_a = (1/a) \int_0^a T(0, z)dz \tag{2}$$

$$T_b = (1/b) \int_0^b T(t, z)dz$$

and Q is the heat load for half a channel.

This type of presentation is better adapted for the design of heat exchangers where the thermal resistance of the coolant fluids on both sides of the plate are considered in an application. In this case the total resistance is given by

$$R_T = 1/h_I a + R_C + 1/h_o b = Q/(T_I - T_0) \tag{3}$$

The constriction resistance R_C is a function not only of the geometry and conductivity of the plate, but also of the heat transfer coefficients, h_I and h_0. In Van Sant's work the problem was simplified to exclude the effect of h_I by assuming that uniform heat flux occurs over the surface covered by the channel. This ap-

[1] Numbers in brackets designate References at end of paper.

Contributed by the Heat Transfer Division for publication in the JOURNAL OF HEAT TRANSFER. Manuscript received by the Heat Transfer Division, May 29, 1974. Paper No. 74-HT-TT.

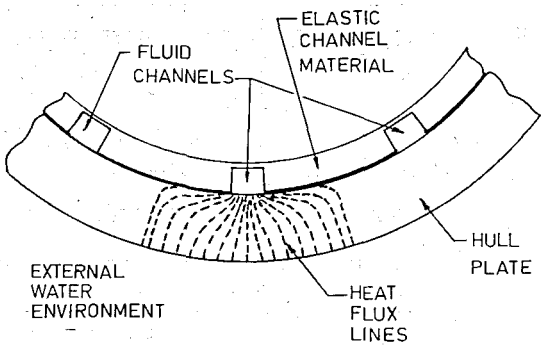

Fig. 1 Configuration of channel-plate heat exchanger

proach is also taken in this study in order to provide a rational for the solution of the more complex problem involving h_I.

Solution

The problem consists in the solution of the Laplace equation $\Delta^2 T = 0$ with the following boundary conditions:

$$\left.\frac{\partial T}{\partial z}\right|_{z=0} = 0 \qquad \text{for} (0 < y < t) \tag{4}$$

$$\left.\frac{\partial T}{\partial z}\right|_{z=b} = 0 \qquad \text{for } (0 < y < t) \tag{5}$$

$$\left.\frac{\partial T}{\partial y}\right|_{y=t} = \phi_0[T_0 - T(t,z)] \qquad \text{for } (0 < z < b) \tag{6}$$

$$\left.\frac{\partial T}{\partial y}\right|_{y=0} = \begin{cases} -\phi_I|T_I - T(0,z)| \text{ for convective heat flux,} \\ \text{or } -Q/ak \text{ for uniform heat flux over} \\ (0 < z < a), \text{ and 0 over } (a < z < b) \end{cases} \tag{7}$$

where $\phi_0 = h_0/k$ and $\phi_I = h_I/k$

When the first three of the boundary conditions are applied, the solution for the temperature of the plate is given by

$$T(y,z) = T_0 + D_0(y/t - 1 - 1/\phi_0 t) + \sum_{j=1}^{\infty} D_j(\xi e^{\lambda_j y} + e^{\lambda_j y}) \cos \lambda_j z \tag{8}$$

where

$$\xi = [(\lambda_j t - \phi_0 t)/(\lambda_j t + \phi_0 t)] \exp(-2\lambda_j t) \tag{9}$$

$$\lambda_j = j\pi/b, j = 1, 2, 3, \ldots \tag{10}$$

and D_0 is the zeroth coefficient which contains the term t.

In both cases, uniform heat flux (UHF) and convective heat flux (CHF), the average surface temperatures T_a and T_b given by equation (2) are the same.

$$T_a = T_0 + D_0(-1 - 1/\phi_0 t) + \sum_{j=1}^{\infty} \Psi_0 D_j (\sin \lambda_j a)/\lambda_j a \tag{11}$$

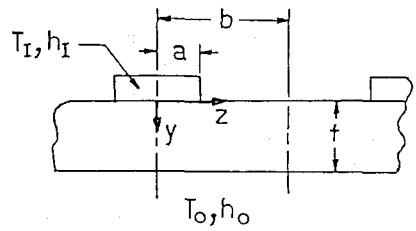

Fig. 2 Rectangular geometry

where

$$\Psi_0 = \xi + 1 \tag{12}$$

$$T_b = T_0 - D_0/\phi_0 t \tag{13}$$

Since for both cases

$$Q = -h_0 b(T_0 - T_b) = -D_0(bk/t) \tag{14}$$

the constriction resistance R_C given by equation (1) for both cases is

$$R_C = (t/bk)[1 - (1/D_0) \sum_{j=1}^{\infty} \Psi_0 D_j (\sin \lambda_j a)/\lambda_j a] \tag{15}$$

Equation (15) can be normalized by dividing by the plate resistance (t/bk) to obtain the constriction coefficient C:

$$C = R_C/(t/bk) = 1 - (1/D_0) \sum_{j=1}^{\infty} \Psi_0 D_j (\sin \lambda_j a)/\lambda_j a \tag{16}$$

In both cases the coefficients D_0 and D_j are determined by applying a Fourier series expansion to their respective fourth boundary conditions (7).

Uniform Heat Flux. In the case of uniform heat flux both D_0 and D_j are explicit functions of the arbitrary heat load Q.

$$D_0 = -QT/bk \tag{17}$$

$$D_j = (-2Q/bk\Psi_0') (\sin \lambda_j a)/\lambda_j a \tag{18}$$

where

$$\Psi_0' = \lambda_j(\xi - 1)$$

Since D_0 is directly proportional to the arbitrary Q, it is expedient to consider D_0 to be the arbitrary quantity in this study. Thus

$$D_j = (2D_0/\Psi_0' t) (\sin \lambda_j a)/\lambda_j a \tag{19}$$

When equation (19) is applied to equation (16), the constriction resistance C_{UHF} for the uniform heat flux case becomes

$$C_{UHF} = 1 - \sum_{j=1}^{\infty} (2\Psi_0/\Psi_0' t) [(\sin \lambda_j a)/\lambda_j a]^2 \tag{20}$$

Equation (20) was found to converge rapidly, usually requiring about 10 to 20 terms to gain convergence to within one percent or less. This is in accord with the work of Van Sant who found that his equation for temperature distribution converged rapidly. The constriction coefficient C_{UHF} is shown in Fig. 3 for the common ranges of design parameters, a/b, t/b, and $h_0 t/k$. For very thick

Nomenclature

A_{ij} = coefficient matrix
a = half channel width
B_{ij} = defined by equations (25) and (26)
b = half distance between tubes
C = constriction coefficient
C_C = correction factor for the convective heat flux case
D_j = Fourier coefficients for temperature
h = heat transfer coefficients
k = thermal conductivity
Q = heat rate for half channel
R_C = thermal constriction resistance of the plate
R_T = total thermal resistance
T = temperature
t = plate thickness
y = coordinate normal to the plate
z = coordinate parallel to plate and normal to channel
V_i = coefficient vector
α_I = defined by equation (24)
ϕ_I = h_I/k
ϕ_0 = h_0/k
ϕ_{I0} = defined by equation (23)
ξ = defined by equation (9)
ψ_0 = defined by equation (12)
ψ_0' = $\lambda_j(\xi - 1)$
λ = eigen values

Subscripts

a = plate surface in contact with channel fluid
b = plate surface in contact with external fluid
I = internal
0 = external
CHF = convective heat flux
UHF = uniform heat flux
i,j = subscripts for matrix or series

walls ($t/b \rightarrow \infty$) the constriction coefficient approaches unity as can be seen upon inspection of equation (20). For very thin walls ($t/b \rightarrow 0$) the wall resistance approaches that of the wall area under the channel (t/ka). However the definition of the constriction coefficient is based on the entire area of the wall (t/bk), hence it goes to infinity when t/b goes to zero.

Convective Heat Flux. In the convective heat flux case, the coefficients D_0 and D_j are dependent upon each other in addition to the arbitrary temperature difference $\Delta T = T_I - T_0$ in a directly proportional fashion.

$$D_0 = \phi_{I0}\left[-\Delta T + \sum_{j=1}^{\infty} \Psi_0(j) D_j (\sin \lambda_j a)/\lambda_j a\right] \quad (21)$$

$$D_i = \alpha_i \left\{\left[-\Delta T + D_0(-1 - 1/\phi_0 t)\right]\left[(\sin \lambda_i a)/\lambda_n a\right] + \sum_{\substack{j=1 \\ j \neq n}}^{\infty} \Psi_0(j) B_{ij} D_j \right\} \quad (22)$$

where

$$\phi_{I0} = (\frac{a}{b}\phi_I t)/[1 - \frac{a}{b}\phi_I t(-1 - 1/\phi_0 t)] \quad (23)$$

$$\alpha_i = (2\frac{a}{b}\phi_I t)/[\Psi_0'(i)t - (2\frac{a}{b}\phi_I t)\Psi_0(i) B_{ii}] \quad (24)$$

$$B_{ij} = \frac{\sin(\lambda_j - \lambda_i)a}{2(\lambda_j - \lambda_i)a} + \frac{\sin(\lambda_j + \lambda_i)a}{2(\lambda_j + \lambda_i)a} \quad (25)$$

and

$$B_{ii} = 0.5 + (\sin 2\lambda_i a)/4\lambda_i a \quad (26)$$

ΔT is eliminated by combining equations (21) and (22). As in the UHF case, D_0 is taken to be the arbitrary variable, whose value is conveniently set to minus unity. Equation (22) can be solved by either an iterative technique similar to the Gauss-Seidel iteration, or by rearranging the equation in matrix form for reduction by either Gauss or Gauss-Jordan reduction. In the latter cases the representation is given by

$$|A_{ij}| \cdot |D_j| = |V_i| \quad (27)$$

where

$$A_{ij}\big|_{i \neq j} = \Psi_0(i)[B_{ij} - (\sin\lambda_i a/\lambda_i a)(\sin \lambda_j a/\lambda_j a)] \quad (28)$$

$$A_{ii} = -1/\alpha_i - \Psi_0(i)(\sin \lambda_i a/\lambda_i a)^2 \quad (29)$$

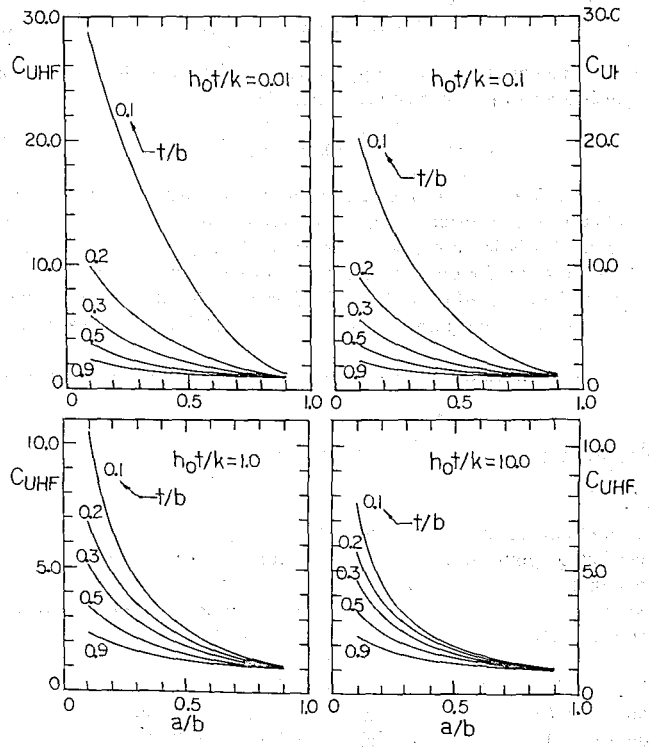

Fig. 3 Constriction coefficient C_{UHF} for uniform heat flux

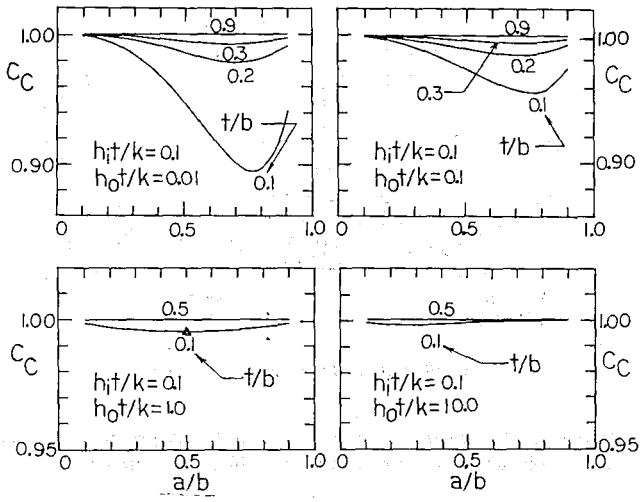

Fig. 4 Correction factor C_C for convective heat flux for $h_I t/k = 0.1$

$$V_i = -(a/b)(h_I t/k)(\sin \lambda_i a/\lambda_i a) \quad (30)$$

After D_j is determined it is introduced into equation (16) to obtain the constriction coefficient for the convective heat flux case. The values for C_{CHF} in terms of the ratio

$$C_C = C_{CHF}/C_{UHF} \quad (31)$$

are shown in Figs. 4, 5, and 6 for common ranges of the parameters a/b, t/b, $h_0 t/k$, and $h_I t/k$. The curves in the figures were obtained using the iterative method. Because of what seemed to be abnormal behavior of some of the data, both the Gauss and the Gauss-Jordan reductions were used to verify the results. The verifications are shown by symbols (circles for Gauss and triangles for Gauss-Jordan). In only a few cases was it found that the iterative technique gave poor results, differing at worst by 1 percent from the results of the matrix reductions. The dashed curves represent those points that were in error. It is suspected that cumulative roundoff error in generating as many as 200 terms during the iteration was the reason for the difference.

Characteristics of the Matrix

For all the check points considered it was found that the matrix A was a well behaved one, where the largest elements grouped themselves on and near the diagonal. These terms generally increased by no more than an order of magnitude along the diagonal.

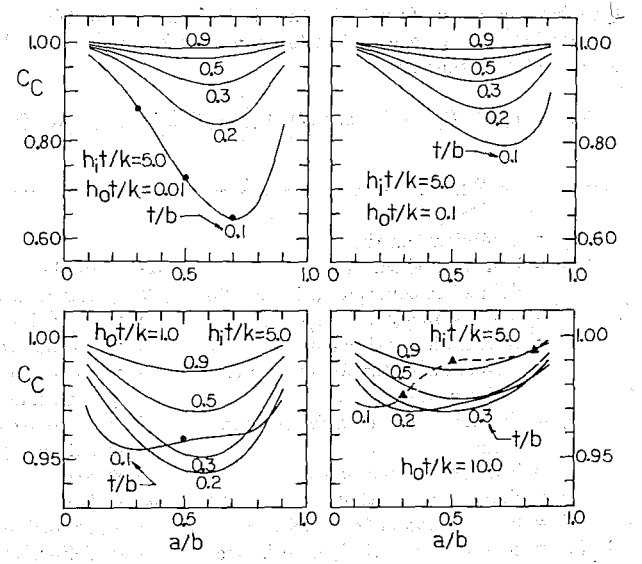

Fig. 5 Correction factor C_C for convective heat flux for $h_I t/k = 5.0$

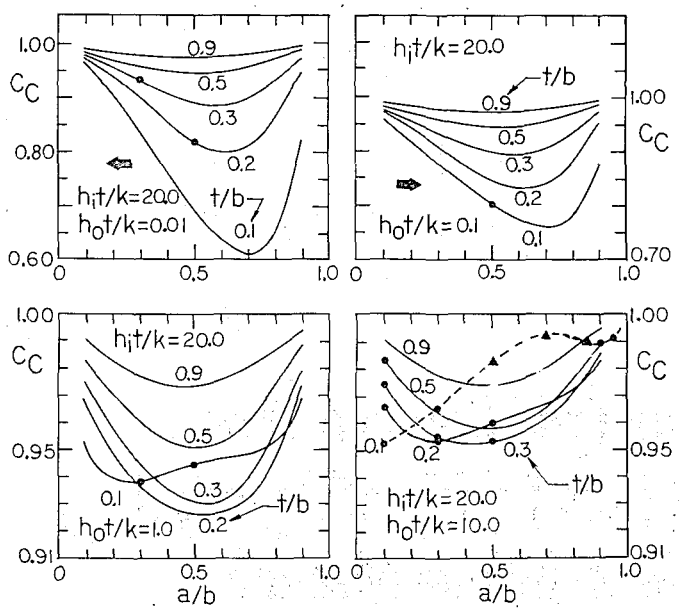

Fig. 6 Correction factor C_C for convective heat flux for $h_I t/k = 20.0$

In the reduction of the matrix using the simple Gauss method, it was found that it was not necessary to interchange rows, since no division by very small numbers occurred that would produce roundoff error. In reducing the matrix using the Gauss-Jordan technique with double pivoting, it was found that only the first 3 rows and columns needed to be exchanged. But the effect of the exchange was very small. Because of this characteristic, it was deemed unnecessary to extend the study by pivoting on the largest element in the matrix. Pivoting on the largest element would essentially give a reduction in reverse fashion, but along the diagonal elements whose magnitudes are the same.

As a check on roundoff errors that occur in the matrix reductions, the original matrix A_{ij} was multiplied by the calculated vector D_j to obtain a new vector V_i' that was compared with the original vector V_i. It was found that the worst difference between the two occurred beyond the twelfth place, thus indicating that roundoff error was indeed very small.

As a check on the convergence when using the matrix reductions, various numbers of terms were used, from 20 up to as many as 230 in some cases. For most cases 40 and 100 terms were used to indicate convergence. An example of the convergence behavior of one the "abnormal" points is given in Fig. 7 for various matrix sizes. It appears to have converged within $\frac{1}{10}$th of a percent in 100 terms.

Range of Parameters

The range of the parameters a/b, t/b, $h_0 t/k$, and $h_I t/k$ have been chosen as being reasonable for design purposes. For improved heat transfer, according to Fig. 3, a/b must be made as large as possible, thus $a/b = 0.1$ appears to be a reasonable lower limit. Likewise, from Fig. 3, t/b should be made as large as possible, thus $t/b = 0.1$ also appears to be a reasonable lower limit. It should be remembered that in the design of a submersible hull heat exchanger, the thickness of the hull is usually prescribed; the designer can only vary b in the ratio t/b. It is wise for the designer to avoid low values of a/b and t/b, for if design does fall in this lower range, the designer should opt for a smaller heat exchanger instead. One should be careful not to use only the C_C data of Figs. 4, 5, and 6 to make comparisons of the behavior of t/b since it is the product of C_C and C_{UHF} which is important (C_{UHF} varies more than C_C).

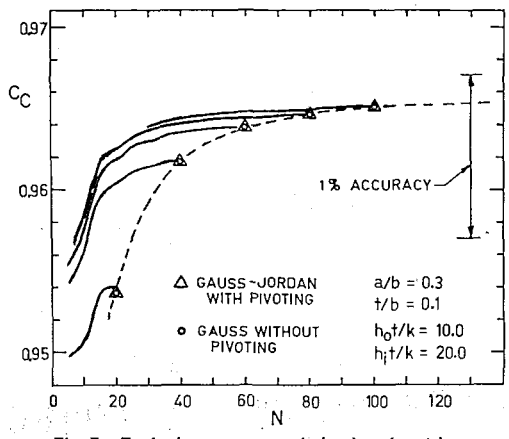

Fig. 7 Typical convergence behavior of matrices

The range of $h_0 t/k$ and $h_I t/k$ generally encompass thickness up to several inches, and the conductivities of aluminum, steel, and titanium, which are the candidate materials for deep submersible hulls. The internal and external heat transfer coefficients range between approximately 50 to 1000 and 20 to 150 Btu/hr/ft^2/F, respectively.

Conclusion

The principal objective of this study was to determine the behavior of the constriction resistance under the more realistic convective heat flux boundary condition. The results show that for the range of parameters considered, the constriction resistance is lower for the CHF case than that for the UHF case. This is to be expected since in the CHF case the heat flux at the channel surface increases in the direction of a, thus spreading the heat flux lines more evenly out over the plate. This is due to the fact that the temperature difference $(T_I - T(0,z))$ along the channel surface increases in the direction of a.

That C_C in Figs. 4, 5, and 6 goes to unity at the end points of the curves is due to the fact that at $a/b = 1$, UHF must occur, and at $a/b = 0$, the heat flux must be infinite over an infinitessimal area, hence a UHF condition.

The physical reason for the abnormality of some of the data was never determined, however the results are mathematically correct. The designer need not be concerned by this abnormality since it occurs in a region where C_{CHF} differs from C_{UHF} by less than 10 percent; other resistances in equation (3) are perhaps known with less accuracy.

Furthermore one can conclude that the designer need not pay much attention to the CHF condition if he is striving for a conservative design, since all the C_C data is less than unity.

Acknowledgments

The electronic computation was performed at Rio Data Centro of PUC, Rio de Janeiro. The authors are grateful to Drs. Kesavan Nair and Sidney Stuckenbruck for their suggestions on computation, and to Ms.'s Nair Alves and Rosely Marins for their careful preparation of this paper.

References

1 Van Sant, J. H., JOURNAL OF HEAT TRANSFER, TRANS. ASME, Series C, Vol. 89, 1967, p. 372.

2 Schmitz, R. A., JOURNAL OF HEAT TRANSFER, TRANS. ASME, Series C, Vol. 92, 1970, p. 201.

3 Oliveira, H. Q., "Resistência Térmica em Trocadores do Tipo Tubo-Placa com Estrangulamento do Fluxo de Calor," MS thesis, Pontifícia Universidade Católica, Rio de Janeiro, 1973.

T. A. Balasubramaniam
Graduate Student

H. F. Bowman
Assoc. Professor,
Department of Mechanical Engineering,
Northeastern University,
Boston, Mass.

Temperature Field Due to a Time Dependent Heat Source of Spherical Geometry in an Infinite Medium

A solution is given for the heat conduction problem in which a sphere generating heat, at a rate which is proportional to time raised to the minus one-half power, is embedded in an infinite medium. The solution is of use in the thermistor probe technique for the determination of both the thermal conductivity and diffusivity of media which wet the surface of the thermistor. The thermistor bead is treated as a spherical distributed thermal mass and the coupled thermal response of the bead and the medium are presented. Typical temperature profiles both in the sphere and in the surrounding medium are presented.

Introduction

The thermistor probe technique utilizes a thermistor bead as both a temperature sensor and a heat source. When the bead is immersed in the medium of interest, the power dissipated in the electrically resistive probe to maintain a constant mean temperature step above the medium, is dependent upon the thermal properties of the medium. The heat generation function required to maintain the constant mean temperature rise of the probe has been found experimentally and has been included in the analysis.

The thermistor probe technique was first employed by Chato [1].[1] He assumed the thermistor bead to be a spherical lumped thermal mass and solved the diffusion equation in the surrounding medium. The solution suggested the possibility of extracting thermal conductivity and thermal inertia, $\sqrt{k\rho c}$, from experimental measurement of the power versus time. In actual practice the physical situation is such that the solution is only applicable for media with thermal conductivities very much smaller than the thermal conductivity of the thermistor bead. To compensate for this limitation Chato's method requires the use of calibration materials of essentially the same thermal properties in the determination of effective bead radii.

The current approach of treating the thermistor bead as a distributed thermal mass and solving for the coupled thermal response of both the bead and the medium acknowledges the presence of a temperature gradient within the bead. The heat generation term, $\Gamma + \beta t^{-1/2}$, is determined experimentally and has been shown to provide a very fast rise in the mean temperature of the thermistor bead. The magnitude of the applied temperature step is predetermined and is achieved with an electronic power controller.

The solution is of value in any situation where a sphere, embedded in an infinite medium generates heat in accordance with the $\Gamma + \beta t^{-1/2}$ form. The nondimensional transient temperature distribution at the center of the sphere is presented separately for the Γ and $\beta t^{-1/2}$ terms of the heat generation function. Also, the spatial temperature distribution in the thermistor bead and surrounding medium is presented for actual experimental situations, in the application of the thermistor probe technique.

Analysis

The thermistor bead is treated as a sphere of radius "a" embedded in a homogeneous medium with no surface contact thermal resistance. Heat is generated in the bead for time $t > 0$ at a rate of $\Gamma + \beta t^{-1/2}$ per unit volume of the bead. Both the bead and the surrounding medium are initially at zero temperature. The governing heat diffusion equations are:

$$\left.\begin{aligned} \frac{1}{r^2}\frac{\partial}{\partial r}\left(r^2\frac{\partial V_b}{\partial r}\right) + \frac{\beta t^{-1/2}}{k_b} + \frac{\Gamma}{k_b} &= \frac{1}{\alpha_b}\frac{\partial V_b}{\partial t} \qquad 0 \le r \le a \\ \frac{1}{r^2}\frac{\partial}{\partial r}\left(r^2\frac{\partial V_m}{\partial r}\right) &= \frac{1}{\alpha_m}\frac{\partial V_m}{\partial t} \qquad r \ge a \end{aligned}\right\} \quad t > 0 \qquad (1), (2)$$

The heat generation function in the spherical region is represented as $\Gamma + \beta t^{-1/2}$ where Γ and $\beta t^{-1/2}$ are on a unit volume basis.

The governing differential equations are subject to the following initial and boundary conditions.

$$V_b = V_m = 0 \qquad at = 0 \qquad (3)$$

V_b and V_m are finite when $r \to 0$ and $r \to \infty$, respectively (4)

$$V_b = V_m \qquad ar = a \qquad (5)$$

$$k_b\frac{\partial V_b}{\partial r} = k_m\frac{\partial V_m}{\partial r} \quad ar = a, t > 0 \qquad (6)$$

Introducing the Laplace transform of V, defined by

$$L[V(t)] = \overline{V} = \int_0^\infty e^{-pt}V(t)dt$$

then the subsidiary equations are

[1] Numbers in brackets designate References at end of paper.

Contributed by the Heat Transfer Division for publication in the JOURNAL OF HEAT TRANSFER. Manuscript received by the Heat Transfer Division, August 7, 1973. Paper No. 74-HT-CC.

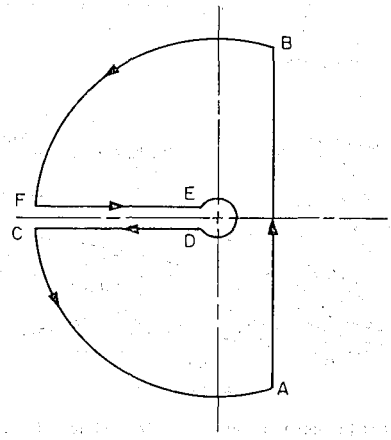

Fig. 1 Contour of integration

$$\frac{1}{r^2}\frac{d}{dr}\left(r^2\frac{d\bar{V}_b}{dr}\right)+\frac{\beta}{k_b}L(t^{-1/2})+\frac{\Gamma}{k_b}L(1)=\frac{1}{\alpha_b}[p\bar{V}_b-V_b(r,0)] \tag{7}$$

$$\frac{1}{r^2}\frac{d}{dr}\left(r^2\frac{d\bar{V}_m}{dr}\right)=\frac{1}{\alpha_m}[p\bar{V}_m-V_m(r,0)] \tag{8}$$

which reduce to

$$\frac{d^2}{dr^2}[r\bar{V}_b]-q_b^2(r\bar{V}_b)=-\frac{\beta}{k_b}\sqrt{\frac{\pi}{p}}r-\frac{\Gamma}{k_b p}r \quad 0\le r\le a \tag{9}$$

$$\frac{d^2}{dr^2}[r\bar{V}_m]-q_m^2(r\bar{V}_m)=0 \qquad r\ge a \tag{10}$$

where

$$q_b^2=\frac{p}{\alpha_b} \text{ and } q_m^2=\frac{p}{\alpha_m}$$

The solutions of the foregoing equations are

$$r\bar{V}_b=Ae^{q_b r}+Be^{-q_b r}+\frac{r}{k_b}\left[\beta\sqrt{\frac{\pi}{p}}+\frac{\Gamma}{p}\right]\frac{1}{q_b^2} \tag{11}$$

$$r\bar{V}_m=Ce^{q_m r}+De^{-q_m r} \tag{12}$$

where A, B, C, and D are constants to be evaluated by the previously stated boundary conditions.

The foregoing solutions subject to the first boundary condition, equation (4) are

$$\bar{V}_b=\frac{A}{r}\sinh q_b r+\frac{1}{k_b q_b^2}\left[\beta\sqrt{\frac{\pi}{p}}+\frac{\Gamma}{p}\right] \tag{13}$$

$$\bar{V}_m=\frac{1}{r}De^{-q_m r} \tag{14}$$

The constants A and D are evaluated with the boundary conditions, equations (5) and (6):

$$\bar{V}_b=\frac{\alpha_b}{k_b p^2}[\beta\sqrt{\pi p}+\Gamma]\left\{1+\frac{\frac{k_m}{k_b}a\sinh q_b r}{r\mathfrak{D}(p)}\right\} \tag{15}$$

$$\bar{V}_m=\frac{a}{r}\frac{\alpha_b}{k_b p^2}[\beta\sqrt{\pi p}+\Gamma]\left\{\frac{\sinh q_b a-aq_b\cosh q_b a}{(1+aq_m)\mathfrak{D}(p)}\right\}e^{q_m(a-r)} \tag{16}$$

where

$$\mathfrak{D}(p)=\left[\frac{\sinh q_b a-aq_b\cosh q_b a}{aq_m+1}-\frac{k_m}{k_b}\sinh q_b a\right]$$

Separating the steady and transient heat generation terms gives

$$\bar{V}_b=\frac{\Gamma\alpha_b}{k_b}\left[\frac{1}{p^2}+\frac{\frac{k_m}{k_b}a\sinh q_b r}{rp^2\mathfrak{D}(p)}\right]+\frac{\alpha_b}{k_b}\beta\sqrt{\pi}\left[\frac{1}{p^{3/2}}+\frac{\frac{k_m}{k_b}a\sinh q_b r}{p^{3/2}r\mathfrak{D}(p)}\right] \tag{17}$$

$$\bar{V}_m=\frac{\Gamma\alpha_b}{k_b}\frac{a}{r}\left[\frac{\sinh q_b a-aq_b\cosh q_b a}{p^2(1+aq_m)\mathfrak{D}(p)}\right]e^{q_m(a-r)}+\beta\sqrt{\pi}\frac{\alpha_b}{k_b}\frac{a}{r}\left[\frac{\sinh q_b a-aq_b\cosh q_b a}{p^{3/2}(1+aq_m)\mathfrak{D}(p)}\right]e^{q_m(a-r)} \tag{18}$$

Such that

$$\bar{V}_b=\bar{V}_{b_I}+\bar{V}_{b_{II}} \tag{19}$$

and

$$\bar{V}_m=\bar{V}_{m_I}+\bar{V}_{m_{II}} \tag{20}$$

The inversions for $\bar{V}_{b(I)}$ and $\bar{V}_{m(I)}$ have been given by Goldenberg and Tranter [3] as

$$V_{b_I}(r,t)=\frac{a^2\Gamma}{k_b}\left\{\frac{1}{3}\frac{k_b}{k_m}+\frac{1}{6}\left(1-\frac{r^2}{a^2}\right)-\frac{2ab}{\pi r}\int_0^\infty\frac{\exp(-y^2t/\gamma_b)(\sin y-y\cos y)\sin\left(\frac{ry}{a}\right)dy}{y^2[(c\sin y-y\cos y)^2+b^2y^2\sin^2 y]}\right\} \tag{21}$$

$$V_{m_I}(r,t)=\frac{a^3\Gamma}{rk_b}\left\{\frac{1}{3}\frac{k_b}{k_m}-\frac{2}{\pi}\int_0^\infty\frac{\exp(-y^2t/\gamma_b)(\sin y-y\cos y)[by\sin y\cos\sigma y-(c\sin y-y\cos y)\sin\sigma y]dy}{y^3[(c\sin y-y\cos y)^2+b^2y^2\sin^2 y]}\right\} \tag{22}$$

where $b=\frac{k_m}{k_b}\sqrt{\frac{\alpha_b}{\alpha_m}}$, $c=1-\frac{k_m}{k_b}$,

$$\gamma_b=\frac{a^2}{\alpha_b}, \text{ and } \sigma=\left(\frac{r}{a}-1\right)\sqrt{\frac{\alpha_b}{\alpha_m}}$$

To invert $\bar{V}_{b(II)}$ and $\bar{V}_{m(II)}$ we use the following theorem.

If $L[\phi(t)]=\Phi(p)$, then $L[\lambda\phi(\lambda t)]=\Phi(p/\lambda)$ where λ is real and positive.

$$V_{b_{II}}=\beta\frac{\alpha_b}{k_b}\sqrt{\pi}f_{b_{II}}(t) \tag{23}$$

where

$$\frac{1}{(\gamma_b)^{1/2}}f_{b_{II}}(\gamma_b t)=L^{-1}\left\{\frac{1}{p^{3/2}}+\frac{\frac{a}{r}\frac{k_m}{k_b}\left[1+\sqrt{\frac{\alpha_b p}{\alpha_m}}\right]\sinh\left(\sqrt{p}\frac{r}{a}\right)}{p^{3/2}F(p)}\right\} \tag{24}$$

and

$$F(p)\equiv(c-b\sqrt{p})\sinh\sqrt{p}-\sqrt{p}\cosh\sqrt{p} \tag{25}$$

By the inversion theorem for Laplace transformation

$$\frac{1}{(\gamma_b)^{1/2}}f_{b_{II}}(\gamma_b t)=\frac{1}{2\pi i}\int_{s-i\infty}^{s+i\infty}e^{pt}\left\{\frac{1}{p^{3/2}}+\frac{\frac{a}{r}\frac{k_m}{k_b}\left[1+\sqrt{\frac{\alpha_b p}{\alpha_m}}\right]\sinh\left(\sqrt{p}\frac{r}{a}\right)}{p^{3/2}F(p)}\right\}dp \tag{26}$$

where s is sufficiently large to include all singularities of the integrand to the left of the line $(s-i\infty, s+i\infty)$. To evaluate this integral the contour as shown in the Fig. 1 was chosen to avoid the branch point at the origin. It can be shown that for physically

Nomenclature

a = surface radius of the sphere
r = radius
b = $(k_m/k_b)\sqrt{\alpha_b/\alpha_m}$
c = $1-k_m/k_b$
k = thermal conductivity
c' = specific heat
p = variable of Laplace transform
Q = heat generation per unit time and volume
t = time
V = temperature
$\bar{V}$ = Laplace transform of temperature
y = variable of integration
α = thermal diffusivity
β = slope of Q versus $t^{-1/2}$ straight line
Γ = steady-state heat generation per unit time and volume
γ = a^2/α
σ = $(\frac{r}{a}-1)\sqrt{\alpha_b/\alpha_m}$

Subscripts

m = medium
b = bead

possible values of b and c there are no poles inside or on the contour. It can also be shown that the integrals over the arcs BF and CA tend to zero as the radius of these circular arcs tend to infinity. The only contribution for this integral around the closed contour is from FE, DC, and small circle ED. A combined integral may be derived from those along FE and DC to yield

$$\frac{4}{2\pi}\int_0^\infty \frac{\exp(-y^2t)}{y^2}\left\{-1 + \frac{\frac{a}{r}\frac{k_m}{k_b}[y\cos y - c\sin y + by^2\sqrt{\frac{\alpha_b}{\alpha_m}}\sin y]\sin(\frac{ry}{a})}{b^2y^2\sin^2 y + (y\cos y - c\sin y)^2}\right\}dy$$

The integral over the small circle ED can be evaluated by expanding the integrand in ascending powers of p. The coefficients of p^{-2}, $p^{-3/2}$, p^{-1} all equal zero.

$$f_{b_{II}}(t) = (\gamma_b)^{1/2}\frac{2}{\pi}\int_0^\infty \frac{\exp(-y^2t/\gamma_b)}{y^2}\left\{-1 + \frac{\frac{a}{r}\frac{k_m}{k_b}[y\cos y - c\sin y + by^2\sqrt{\frac{\alpha_b}{\alpha_m}}\sin y]\sin(\frac{ry}{a})}{b^2y^2\sin^2 y + (y\cos y - c\sin y)^2}\right\}dy \tag{27}$$

$$V_{b_{II}}(r,t) = \frac{2\beta a}{k_b}\sqrt{\frac{\alpha_b}{\pi}}\int_0^\infty \frac{\exp(-y^2t/\gamma_b)}{y^2}\left\{-1 + \frac{\frac{a}{r}\frac{k_m}{k_b}[y\cos y - c\sin y + by^2\sqrt{\frac{\alpha_b}{\alpha_m}}\sin y]\sin(\frac{ry}{a})}{(c\sin y - y\cos y)^2 + b^2y^2\sin^2 y}\right\}dy \tag{28}$$

Proceeding on the same lines, the temperature of the medium due to the transient heat generation term, can be shown to be

$$V_{m_{II}}(r,t) = -\frac{2\beta a^2}{k_b r}\sqrt{\frac{\alpha_b}{\pi}}\int_0^\infty \frac{\exp(-y^2t/\gamma_b)}{y^2}\cdot \frac{(\sin y - y\cos y)[by\sin y\sin\sigma y + (c\sin y - y\cos y)\cos\sigma y]}{(c\sin y - y\cos y)^2 + b^2y^2\sin^2 y}dy \tag{29}$$

Finally, combining the solutions we get

$$V_b(r,t) = \frac{a^2\Gamma}{k_b}\left\{\frac{1}{3}\frac{k_b}{k_m} + \frac{1}{6}(1-\frac{r^2}{a^2}) - \frac{2ab}{\pi r}\int_0^\infty \frac{\exp(-y^2t/\gamma_b)(\sin y - y\cos y)\sin(\frac{ry}{a})}{y^2[(c\sin y - y\cos y)^2 + b^2y^2\sin^2 y]}dy\right\} + \frac{2\beta a}{k_b}\sqrt{\frac{\alpha_b}{\pi}}\int_0^\infty \frac{\exp(-y^2t/\gamma_b)}{y^2}\left\{-1 + \frac{\frac{a}{r}\frac{k_m}{k_b}[y\cos y - c\sin y + by^2\sqrt{\frac{\alpha_b}{\alpha_m}}\sin y]\sin(\frac{ry}{a})}{(c\sin y - y\cos y)^2 + b^2y^2\sin^2 y}\right\}dy \tag{30}$$

$$V_m(r,t) = \frac{a^3\Gamma}{rk_b}\left\{\frac{1}{3}\frac{k_b}{k_m} - \frac{2}{\pi}\int_0^\infty \frac{\exp(-y^2t/\gamma_b)(\sin y - y\cos y)[by\sin y\cos\sigma y - (c\sin y - y\cos y)\sin\sigma y]}{y^3[(c\sin y - y\cos y)^2 + b^2y^2\sin^2 y]}dy\right\} - \frac{2\beta a}{k_b r}\sqrt{\frac{\alpha_b}{\pi}}\int_0^\infty \frac{\exp(-y^2t/\gamma_b)(\sin y - y\cos y)[by\sin y\sin\sigma y + (c\sin y - y\cos y)\cos\sigma y]}{y^2[(c\sin y - y\cos y)^2 + b^2y^2\sin^2 y]}dy \tag{31}$$

Discussion

The transient temperature at the center of the sphere, for a range of k_m/k_b values with the diffusivities of the sphere and the medium equal in each case, has been computed from equation (30) by numerical integration using standard library programs. The integrals converge faster at larger values of time due to the presence of the $\exp(-y^2t/\gamma_b)$ term. Fig. 2 shows the resulting contributions in nondimensional form. The transient contribution

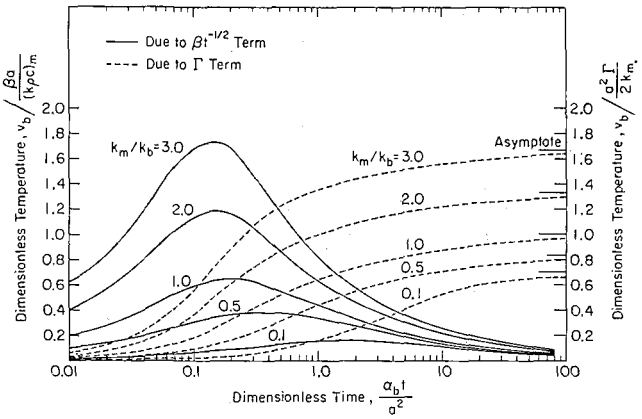

Fig. 2 Transient temperature at the center of the sphere due to the β and Γ terms

due to the $\beta t^{-1/2}$ term is shown in solid lines, whereas the transient contribution due to the Γ term is shown in broken lines. We see that for any particular k_m/k_b value the temperature due to the $\beta t^{-1/2}$ term rises rapidly compared to that due to the Γ term. As k_m/k_b increases the rate of rise in temperature due to the $\beta t^{-1/2}$ term is increasingly fast and approximates a step rise in temperature.

To demonstrate the analytically determined temperature distribution in the sphere and in the medium due to the combined effect of both the Γ and the $\beta t^{-1/2}$ heat generation terms, water and ethylene glycol were used as typical experimental test media. The power versus $t^{-1/2}$ relation was experimentally obtained by establishing and maintaining the resistance of the thermistor bead at a constant predetermined value by using an electronic controller. The heat generation functions thus found are plotted versus $t^{-1/2}$ in Fig. 3. For low viscosity liquids such as water a free convection effect can take place as time progresses, depending on the temperature step imposed on the bead. If a sufficient number of data points are obtained in the power measurement before free convection sets in then the straight line graph can be extrapolated to give the Γ value as if the heat flow through the medium was diffusion controlled at all times. This is demonstrated in Fig. 3 where for the case of water the heat generation deviates somewhat from the straight line after about 5 sec. For a smaller temperature step the value of time for free convection to set in is greater.

Fig. 4 shows the developing temperature profile both in the bead and in the medium for the case of water as calculated from equations (30) and (31) wherein the experimentally determined β and Γ values from Fig. 3 have been used. The temperature distri-

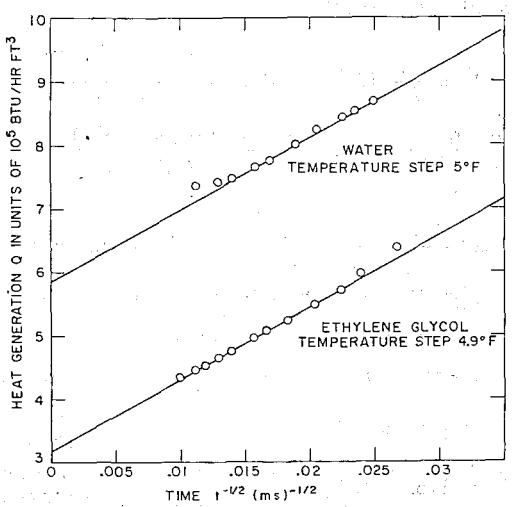

Fig. 3 Volumetric heat generation rate versus time raised to the minus one-half power

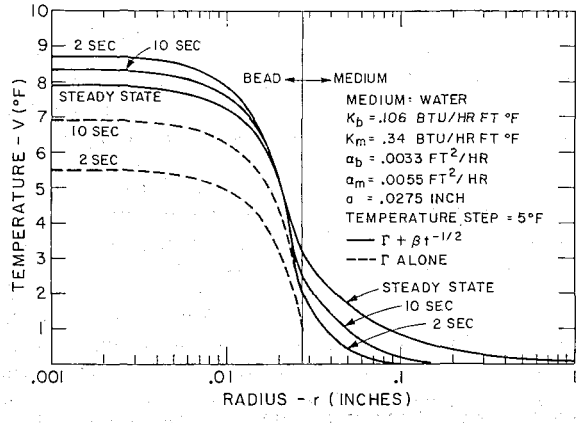

Fig. 4 Temperature field development in thermistor bead and water medium for both $\Gamma + \beta t^{-1/2}$ and Γ alone

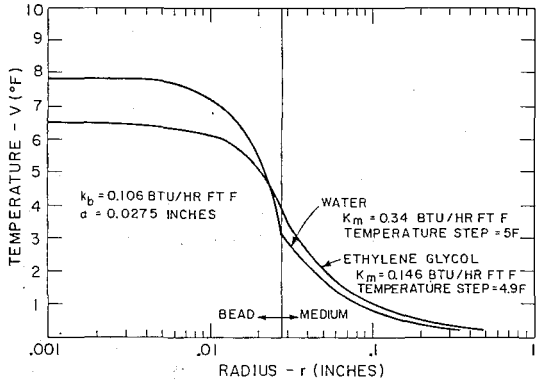

Fig. 5 Steady-state temperature distributions for water and ethylene glycol

butions in the bead are shown to cross one another as the local temperature relaxes toward the steady-state level. This confirms that the spatial average temperature within the bead is constant with time in accordance with the design criteria of the electronic controller. For comparison the developing temperature profile in the bead for the case of constant heat generation (Γ term only) is shown in the same figure. Thus, the $\beta t^{-1/2}$ term of the heat generation function accelerates the development of the temperature field within the bead. The early development of a constant spatially averaged temperature in the bead is essential for the determination of the thermal diffusivity of the medium.

Fig. 5 clearly shows that as the conductivity of the medium increases for a given bead conductivity the interfacial temperature is lowered. This is so even when the same average temperature step is applied to the bead. Thus, when the thermistor probe technique is used in the evaluation of thermal conductivity of unknown media, the temperature profile within the bead must be known unless a truly lumped situation pertains, i.e., the bead thermal resistance is negligible in comparison to that of the medium.

Application of the Solution. Equation (30) shows that the steady-state temperature distribution in the bead is given by the relation

$$V_b(r) = \frac{a^2\Gamma}{k_b}\left\{\frac{1}{3}\frac{k_b}{k_m} + \frac{1}{6}\left(1 - \frac{r^2}{a^2}\right)\right\} \tag{32}$$

and is seen to be a function of the radius of the bead and of the thermal conductivity of the bead and the surrounding medium. To correlate the experimentally applied temperature step with the analytical expression for temperature in the steady state, one has to average the temperature distribution over the whole bead volume. This gives

$$V_{b_{\text{ave}}}(ss) = \frac{\Gamma}{3}\frac{a^2}{k_b}\left[\frac{k_b}{k_m} + 0.2\right] \tag{33}$$

Equating this analytically determined average temperature of the bead to the applied temperature step for the bead, knowing "a" and k_b, and measuring Γ the thermal conductivity of various media can be determined.

The same averaging technique applied to the transient temperature profile over the whole bead at any instant of time was used to determine the diffusivity of the media. The bead diffusivity was determined as $\alpha = k_b/\rho_{bcb}$' where k_b was independently measured. This averaging technique is possible after 10 msec as the controller error signal goes to zero implying constant average probe resistance (temperature). A detailed discussion of the application of this technique and initial data can be found in reference [2].

Conclusion

The analytical basis for the determination of both thermal conductivity and diffusivity values with significantly improved accuracy, by experimentally determining the heat rate required to maintain constant average probe resistance (temperature) and incorporating that heat rate into the solution to the general heat diffusion equation, is given. A temperature gradient exists within the bead which must be accounted for. The average bead temperature reaches a constant value much sooner than the actual steady-state condition is reached due to the $\beta t^{-1/2}$ term. The solution for the temperature distribution in the medium also provides the minimum sample size required for thermal conductivity and diffusivity measurements. Careful acquisition of experimental data on short time interval provides steady-state information without actually waiting for it. For low viscosity liquids, the effect of natural convection can be avoided by taking sufficient data before the effect sets in.

Acknowledgments

This research was supported by the National Heart and Lung Institute Grant No. HL14322-01 to the Harvard-MIT Program in Health Science and Technology. The authors wish to acknowledge the helpful discussions with Professor John W. Cipolla, Jr.

References

1 Chato, J. C., "A Method for the Measurement of Thermal Properties of Biological Materials," ASME Symposium on Thermal Problems in Biotechnology, LCNO 68-58741, 1968.

2 Bowman, H. F., and Balasubramaniam, T. A., "A New Technique Utilizing Thermistor Probes for the Measurement of Thermal Properties of Biomaterials," accepted for publication in Cryobiology, 1974.

3 Goldenberg, H., and Tranter, C. J., "Heat Flow in an Infinite Medium Heated by a Sphere," *British Journal of Applied Physics*, Sept. 1952, pp. 296–298.

J. A. Copley
Naval Weapons Laboratory,
Dahlgren, Va.

W. C. Thomas
Mechanical Engineering Department,
Virginia Polytechnic Institute and
State University,
Blacksburg, Va.

Two-Dimensional Transient Temperature Distribution in Cylindrical Bodies With Pulsating Time and Space-Dependent Boundary Conditions

The two-dimensional conduction equation is solved for a hollow cylinder subjected to a series of heat flux pulses on the inner boundary. The periodic heat flux is represented by an exponentially decreasing pulse with a spatial distribution of peak magnitude. The analytical techniques and representation of the boundary conditions apply to different situations involving pulsating boundary conditions. An application to the gun barrel heating problem is given. Calculated bore surface and internal temperature histories are in good agreement with experimental data. During the actual firing time in rapidly-firing guns, results show that external cooling is generally ineffective for controlling barrel bore surface temperature.

Introduction

The internal temperature distribution resulting from repeated heat flux pulses on a surface of a body is important in many practical situations. This situation is encountered, for example, during the warm-up of a reciprocating engine, in the "on-off" type of heating associated with certain automatic control systems, and in the heating of gun barrels during rapid firings. In general, the boundary heat flux is a function of position and time and may be cyclic. An analytical solution is presented for the temperature distribution in a body subjected to pulsating boundary heat flux. An application to the gun barrel heating problem is given. Solutions based on numerical methods are also used in analyzing gun barrel heating and both methods have a place in gun barrel design work. The analytical solution is useful for parametric studies (particularly if a one-dimensional representation is satisfactory), evaluating truncation error in numerical solutions and may give accuracy well within the error resulting from the uncertainties introduced in modeling the boundary conditions. The specific pulsating bore surface heat flux boundary condition used is compatible with experimental findings. The analysis of the boundary conditions and methods of solution are general and can be applied directly to determine the transient temperatures in many similar problems.

Gun Barrel Heating. Whenever a gun is fired, a portion of the propellant energy, in the form of heat, is transferred to the barrel bore surface. Although the details of the heat transfer mechanism have not been conclusively established, it is generally attributed to convection from the high-velocity, high-temperature propellant gases [1].[1] Other modes, including radiation between the gases and the bore surface and friction between the projectile and the surface, have been considered and are believed to be lesser contributors [2].

The barrel heating problem is customarily divided into two main parts: first, that of determining the energy transfer from the propellant gases to the bore surface and, second, that of determining the barrel temperature distribution resulting from this heat transfer. Separating the problem in this manner permits the heat transfer analysis to be carried out without a detailed knowledge of local projectile velocity and propellant gas properties. This separation is necessary for a practical approach to an extremely complex problem.

A number of investigations of the heat transfer and temperature distributions in gun barrels have been reported [3-7]. All analyses reported have been limited to the one-dimensional case while the present analysis has been extended to apply also to two-dimensional cases. Also, a more accurate representation of the bore heat flux function, which is supported by recent experi-

Contributed by the Heat Transfer Division for publication in the JOURNAL OF HEAT TRANSFER. Manuscript received by the Heat Transfer Division, December 12, 1973. Paper No. 74-HT-SS.

[1] Numbers in brackets designate References at end of paper.

mental findings, has been incorporated into the present analysis. These improvements in the analysis lead to closer agreement between results predicted in the present solution and the experimental data currently available.

Anthony [3, 4] obtained solutions for three different pulsating boundary conditions applied at the inner surface of a cylinder. The conditions used were a constant amplitude and a time-decreasing amplitude rectangular pulse representation of heat flux and a rectangular pulse heat transfer coefficient. An insulated outer boundary was considered in all cases. For these boundary conditions, Anthony was able to calculate peak bore surface temperatures to within 80 C to 170 C of experimentally measured values for a single-round firing. The analytical solutions indicated temperatures as much as 170 C lower after the peak occurred than those observed. Hendry and Bendersky [5] concluded that neglecting heat transfer at the exterior surface prevented these solutions from being adequate for calculating the temperature distribution from multiple-round firings and that complete bore surface temperature histories predicted by any one of the solutions was inadequate when compared with experimental data. A detailed discussion on the limitations of rectangular pulses to approximate the heat transfer in a gun barrel is included in their paper. Pascual, et al. [6], while investigating thermal stresses in gun tubes, solved the one-dimensional cylindrical problem with a convective outer boundary for a prescribed internal surface temperature history. The solution, however, applies only to a single-round-firing temperature calculation. More recently, Chu and Benzkofer [7] presented a solution to the one-dimensional problem by assuming a convective boundary condition at both the inner and outer surfaces. They obtained a solution in the form of an integral equation which allowed for an arbitrary initial internal temperature distribution. For multiple firings, the final temperature distribution must be obtained by successive integrations of the temperature distributions which result from each preceding round fired. No comparisons between the previous two solutions and experimental data were presented.

Several extensive experimental studies have been conducted in an effort to measure bore surface temperatures and heat flux in guns [8-13]. Although the transient bore surface heat flux has not been directly measured in a gun barrel, a method has been presented by Giedt [13] by which it may be extrapolated from experimental bore surface temperature curves. Giedt used a solution for the temperature distribution in a semi-infinite solid with an arbitrarily imposed time-dependent surface temperature. From this solution, he obtained an equation for the instantaneous heat flux in terms of the slope of the bore surface temperature-time curve and, by graphically differentiating the experimental curve, plotted the bore surface heat flux as a function of time. A heat flux plot from [13], along with a corresponding temperature curve for one axial location in a 40-mm gun barrel, is shown in Fig. 1. While the accuracy of graphically differentiating the temperature-time curve to obtain the heat flux history may be subject to question by some, the characteristic shape of the curve provides a basis for an improved functional representation of the bore surface heat flux.

Interior Boundary Condition: Bore Surface Heat Flux. Assuming that the shape of the curve in Fig. 1 is characteristic of the heat flux for conventional type guns, a function of the form of an exponential decreasing with time is selected for representing the pulsating heat flux at the bore surface. To account for the variation in heat transfer along the bore surface, this exponential function is multiplied by an amplitude function, $f(z)$, dependent on the axial coordinate only. This functional representation assumes that all axial locations experience a distribution $f(z)$ of peak heat flux simultaneously rather than progressively as is the case for a rapidly-moving projectile. The simplification is supported by the relatively short time from firing initiation until the projectile clears the muzzle. Finally, the effect of multiple-round firings is accounted for by incorporating Heaviside's unit step function into the boundary condition. The resulting expression for the bore surface heat flux is

$$-k\frac{\partial T}{\partial r}(a,z,t) = f(z)\sum_{n=0}^{N}[\delta(t-n\tau) - \delta(t-(n+1)\tau)]e^{-c(t-n\tau)} \quad (1)$$

where the unit step function is defined by

$$\delta(t-\tau) = 0 \;;\; t < \tau$$
$$\delta(t-\tau) = 1 \;;\; t \geq \tau \quad (2)$$

The constant c and function $f(z)$ are to be determined from experimental observations. A representative plot of equation (1), at a fixed axial location, is depicted in Fig. 2.

Governing Equations and Method of Solution. The differential form of the conduction equation which applies is

$$\frac{\partial^2 T}{\partial r^2} + \frac{1}{r}\frac{\partial T}{\partial r} + \frac{\partial^2 T}{\partial z^2} = \frac{1}{\alpha}\frac{\partial T}{\partial t} \quad (3)$$

where angular symmetry and constant thermal properties have been assumed. The remaining boundary conditions and initial

$$-k\frac{\partial T}{\partial r}(b,z,t) = h[T(b,z,t) - T_a] \quad (4)$$

$$\frac{\partial T}{\partial z}(r,z,t) = 0 \;;\; z = 0, L \quad (5)$$

Nomenclature

A_0 = amplitude of the heat flux pulse, equation (25), cal/sq cm-s
A_z = integral defined by equation (23)
a = inside radius, cm
B_z = integral defined by equation (24)
b = outside radius, cm
C_n = function defined by equation (22)
c = exponential decay coefficient, equation (1), s^{-1}
D_m = function defined by equation (15)
D_0 = function defined by equation (14)
$F(t)$ = arbitrary function, equation (18)
F_n = function defined by equation (20)
$f(z)$ = amplitude function, equation (1)
G_n = function defined by equation (21)
h = heat transfer coefficient, cal/sq cm-s-C
k = thermal conductivity cal/cm-s-C
L = length of gun barrel, cm
l = summation index defining the number of the round being fired
m = summation index defined in equation (13)
N = final round fired
n = summation index defining the roots of equation (16)
Q = heat transfer per unit area, cal/sq cm
q = $\lambda s/\alpha$
r = radial coordinate, cm
s = complex Laplace transform variable
T = temperature, C
T_a = ambient temperature, C
T_0 = initial temperature of the gun barrel, C
t = time, s
u = $\lambda c/\alpha$
z = axial coordinate, cm
α = thermal diffusivity, sq cm/s
β_n = roots of equation (16)
δ = unit step function, equation (2)
θ = temperature difference, $T - T_0$, C
$\bar{\theta}$ = Laplace transform of θ
λ_m = separation constant defined by equation (13)
τ = time between firing pulses, s

$$T(r, z, 0) = T_0 \tag{6}$$

The periodic bore surface boundary condition suggests a solution by the method of Laplace transforms. Introducing $\theta(r,z,t) = T(r,z,t) - T_0$ for convenience and transforming equations (1), (3), (4), and (5), respectively, gives

$$-k\frac{\partial\bar{\theta}}{\partial r}(a,z) = \frac{f(z)}{c+s}[1 + (1-e^{-c\tau})(e^{-s\tau} + e^{-2s\tau} + e^{-3s\tau} + \ldots)] \tag{7}$$

$$\frac{\partial^2\bar{\theta}}{\partial r^2} + \frac{1}{r}\frac{\partial\bar{\theta}}{\partial r} + \frac{\partial^2\bar{\theta}}{\partial z^2} = \frac{s}{\alpha}\bar{\theta} \tag{8}$$

$$\frac{\partial\bar{\theta}}{\partial r}(b,z) = -\frac{h}{k}\bar{\theta}(b,z) + \frac{h}{sk}[T_a - T_0] \tag{9}$$

$$\frac{\partial\bar{\theta}}{\partial z}(r,z) = 0 \; ; \; z = 0, L \tag{10}$$

The constant c, which governs the time rate of decay of the heat flux pulse is later shown to be of the order of 10^3 s^{-1} while the time between firings τ is 60 ms or more for even the faster firing guns. The maximum value of $\exp(-c\tau)$ is then of the order of 10^{-27}, or less, and can be neglected. The significance of this assumption and the error introduced for other values of $c\tau$ is noted in the Appendix. With this simplification, equation (7) becomes

$$-k\frac{\partial\bar{\theta}}{\partial r}(a,z) = \frac{f(z)}{c+s}[1 + e^{-s\tau} + e^{-2s\tau} + e^{-3s\tau} + \ldots]$$

or

$$-k\frac{\partial\bar{\theta}}{\partial r}(a,z) = \frac{f(z)}{(c+s)(1-e^{-s\tau})} \tag{11}$$

Equation (8) is solved with the transformed boundary conditions by the method of separation of variables to give

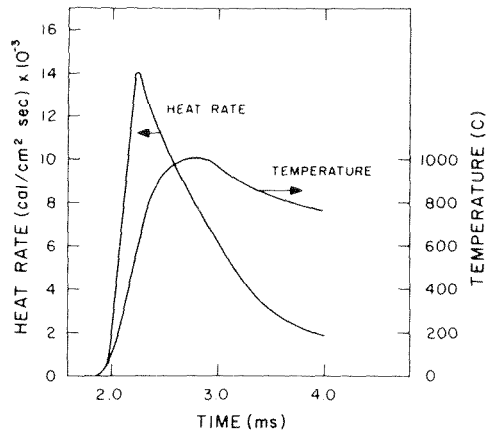

Fig. 1 Bore surface heat flux and temperature at a fixed axial location in a 40-mm gun barrel

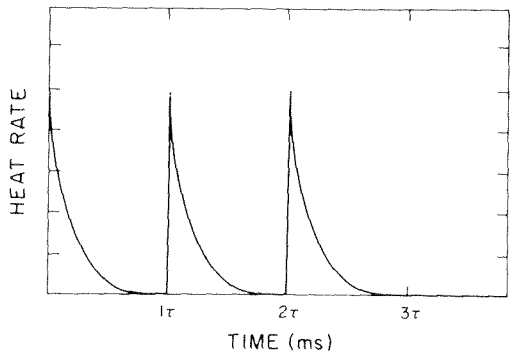

Fig. 2 Heat flux function representation for multiple firings

$$\bar{\theta}(r,z) = \frac{-h[T_a - T_0]\,[I_0(qr)K_1(qa) + K_0(qr)I_1(qa)]}{ks\,D_0}$$

$$-\frac{\frac{1}{Lk}\int_0^L f(z)dz\,\{[qK_1(qb) - \frac{h}{k}K_0(qb)]I_0(qr) + [qI_1(qb) + \frac{h}{k}I_0(qb)]K_0(qr)\}}{[s+c][1-e^{-s\tau}]\,qD_0}$$

$$-\sum_{m=1}^{\infty}\cos\left(\frac{m\pi}{L}z\right)\frac{\{[\lambda_m K_1(\lambda_m b) - \frac{h}{k}K_0(\lambda_m b)]I_0(\lambda_m r) + [\lambda_m I_1(\lambda_m b) + \frac{h}{k}I_0(\lambda_m b)]K_0(\lambda_m r)\}\,\{\frac{2}{Lk}\int_0^L f(z)\cos(m\pi z/L)dz\}}{[s+c][1-e^{-s\tau}]\lambda_m D_m} \tag{12}$$

where

$$\lambda_m = \sqrt{\left(\frac{m\pi}{L}\right)^2 + q^2} \; ; \; m = 0, 1, 2, 3, \ldots \tag{13}$$

$$D_0 = I_1(qa)[qK_1(qb) - \frac{h}{k}K_0(qb)] - K_1(qa)[qI_1(qb) + \frac{h}{k}I_0(qb)] \tag{14}$$

$$D_m = I_1(\lambda_m a)[\lambda_m K_1(\lambda_m b) - \frac{h}{k}K_0(\lambda_m b)] - K_1(\lambda_m a)[\lambda_m I_1(\lambda_m b) + \frac{h}{k}I_0(\lambda_m b)] \tag{15}$$

The temperature distribution is determined using the inversion theorem [14] by evaluating and summing the residues of equation (12) at its poles. The poles of the first, second, and third terms on the right side of equation (12) are at $s = 0$ and $s = -\alpha\beta_n^2$ where $\pm\beta_n$ are the roots of

$$\beta_n[J_1(\beta_n a)Y_1(\beta_n b) - J_1(\beta_n b)Y_1(\beta_n a)] + \frac{h}{k}[J_0(\beta_n b)Y_1(\beta_n a) - J_1(\beta_n a)Y_0(\beta_n b)] = 0 \tag{16}$$

The mathematical details of evaluating the residues of each term at its poles are quite lengthy (see reference [15]) and have been omitted from this paper. The mathematical procedure for evaluating the residues of the first term presents no new problems. The general techniques for inverting the second and third terms of equation (12) will be noted, however, as these apply generally to this type of boundary condition. Each of these terms may be put into the form

$$\bar{\theta} = \frac{\bar{F}(s)}{(1-e^{-s\tau})} \tag{17}$$

Expanding the denominator into an exponential series and applying the Laplace transform shifting theorem [14], the inversion of equation (17) is then reduced to inverting $F(s)$ times the unit step function where the arguments are shifted in time as determined by the exponent of each accompanying exponential term. Using this technique and denoting the inverse transform of $F(s)$ by $F(t)$, the inversion of equation (17) is

$$\theta = \delta(t)F(t) + \delta(t-\tau)F(t-\tau) + \delta(t-2\tau)F(t-2\tau) + \dots$$

$$\theta = \sum_{n=0}^{N} \delta(t-n\tau)F(t-n\tau) \tag{18}$$

Therefore, to invert the last two terms of equation (12), the exponential series expansion is removed and the inversion problem is reduced to that of evaluating the residue of the transform of a single-pulse solution and multiplying this by the unit step function.

The solution of equation (3) with boundary and initial conditions given by equations (1), (4), (5), and (6) is

$$T(r,z,t) = T_0 + [T_a - T_0]\left[1 + \pi \sum_{n=1}^{\infty} \frac{he^{-\alpha\beta_n^2 t}J_1(\beta_n a)F_n(\beta_n b)G_n(\beta_n r, a)}{kC_n(\beta_n, a, b)}\right]$$

$$- \sum_{l=0}^{N-1} \delta(t-l\tau)\left\{\frac{e^{-c[t-l\tau]}A_z\left[\left[uJ_1(ub) - \frac{h}{k}J_0(ub)\right]Y_0(ur) - \left[uY_1(ub) - \frac{h}{k}Y_0(ub)\right]J_0(ur)\right]}{u\left[\left[uJ_1(ub) - \frac{h}{k}J_0(ub)\right]Y_1(ua) - \left[uY_1(ub) - \frac{h}{k}Y_0(ub)\right]J_1(ua)\right]}\right.$$

$$+ \pi \sum_{n=1}^{\infty} \frac{\alpha\beta_n e^{-\alpha\beta_n^2[t-l\tau]}A_z[F_n(\beta_n b)]^2 G_n(\beta_n r, a)}{[c - \alpha\beta_n^2]C_n(\beta_n, a, b)} + \pi \sum_{n=1}^{\infty}\sum_{m=1}^{\infty} \frac{\alpha\beta_n e^{-\alpha[\beta_n^2 + (\frac{m\pi}{L})^2][t-l\tau]}B_z G_n(\beta_n r, a)[F_n(\beta_n b)]^2 \cos\frac{m\pi}{L}z}{\left[c - \alpha\left[\beta_n^2 + \left(\frac{m\pi}{L}\right)^2\right]\right]C_n(\beta_n, a, b)}$$

$$\left. - \sum_{m=1}^{\infty} \frac{e^{-c[t-l\tau]}B_z\left[\left[\lambda_m Y_1(\lambda_m b) - \frac{h}{k}Y_0(\lambda_m b)\right]J_0(\lambda_m r) - \left[\lambda_m J_1(\lambda_m b) - \frac{h}{k}J_0(\lambda_m b)\right]Y_0(\lambda_m r)\right]\cos\frac{m\pi}{L}z}{\lambda_m\left[\left[\lambda_m Y_1(\lambda_m b) - \frac{h}{k}Y_0(\lambda_m b)\right]J_1(\lambda_m a) - \left[\lambda_m J_1(\lambda_m b) - \frac{h}{k}J_0(\lambda_m b)\right]Y_1(\lambda_m a)\right]}\right\} \tag{19}$$

where λ_m is taken as $\sqrt{c/\alpha - (m\pi/L)^2}$ and the following notation has been used for convenience.

$$F_n(\beta_n b) = \beta_n J_1(\beta_n b) - \frac{h}{k}J_0(\beta_n b) \tag{20}$$

$$G_n(\beta_n, r, a) = J_0(\beta_n r)Y_1(\beta_n a) - J_1(\beta_n a)Y_0(\beta_n r) \tag{21}$$

$$C_n(\beta_n, a, b) = \left[\beta_n^2 + \left(\frac{h}{k}\right)^2\right][J_1(\beta_n a)]^2 - [F_n(\beta_n b)]^2 \tag{22}$$

$$A_z = \frac{1}{Lk}\int_0^L f(z)\,dz \tag{23}$$

$$B_z = \frac{2}{Lk}\int_0^L f(z)\cos\frac{m\pi}{L}\,dz \tag{24}$$

For values of $c/\alpha < (m\pi/L)^2$, the last term of equation (19) is replaced by

$$- \sum_{m=1}^{\infty} \frac{[\cos\frac{m\pi}{L}z]e^{-ct}B_z\left[\left[\lambda_m K_1(\lambda_m b) - \frac{h}{k}K_0(\lambda_m b)\right]I_0(\lambda_m r) + \left[\lambda_m I_1(\lambda_m b) + \frac{h}{k}I_0(\lambda_m b)\right]K_0(\lambda_m r)\right]}{\lambda_m\left[\left[\lambda_m K_1(\lambda_m b) - \frac{h}{k}K_0(\lambda_m b)\right]I_1(\lambda_m a) - \left[\lambda_m I_1(\lambda_m b) + \frac{h}{k}I_0(\lambda_m b)\right]K_1(\lambda_m a)\right]}$$

to correspond to the real values of λ_m.

Since an algebraic expression has been obtained for the temperature distribution, the mathematical accuracy depends only on the number of terms used for each series and on calculation round-off error. However, the accuracy in representing the temperature distribution in the physical system depends on the applicability of the boundary heat flux model and on the simplifying assumptions incorporated in the analysis. Equation (19) has been evaluated with the aid of a digital computer for a range of gun barrel applications and the results are compared with experimental data.

Results

The solution accounts for convective cooling on the outer surface and a series of exponentially decreasing heat flux pulses on the inner boundary. The solution depends on $f(z)$ which describes the variation of the peak value of heat flux in the z direction and c which describes the time rate of decay of each pulse. In this section, $f(z)$ and c are selected to represent the heat transfer into the bore surface of a gun barrel. The selection is based on a fit to experimental temperature-time curves obtained for the bore surface during a single-round firing. The calculated temperature distributions for single- and multiple-round firings are then compared with available experimental data.

One-Dimensional Case, Bore Surface Temperature, Single-Round Firing. As a first approximation, the temperature gradient in the z direction is neglected during the relatively short heating time associated with a single-round firing. The heating time is of the order of that required for a round to clear the muzzle. Consequently, heat diffuses in the r direction for only a few thousandths of a centimeter, and the radial gradient is much larger than the axial gradient. With an A_0 corresponding to a given location, one takes

$$f(z) = A_0 \tag{25}$$

$$A_z = A_0/k \tag{26}$$

$$B_z = 0 \tag{27}$$

and equation (19) reduces to

$$T(r,z,t) = T_0 + [T_a - T_0]\left[1 + \pi \sum_{n=1}^{\infty} \frac{he^{-\alpha\beta_n^2 t}J_1(\beta_n a)F_n(\beta_n b)G_n(\beta_n r, a)}{kC_n(\beta_n, a, b,)}\right]$$

$$- \sum_{l=0}^{N-1} \delta(t-l\tau)\left[\frac{e^{-c[t-l\tau]}A_0\left[\left[uJ_1(ub) - \frac{h}{k}J_0(ub)\right]Y_0(ur) - \left[uY_1(ub) - \frac{h}{k}Y_0(ub)\right]J_0(ur)\right]}{ku\left[\left[uJ_1(ub) - \frac{h}{k}J_0(ub)\right]Y_1(ua) - \left[uY_1(ub) - \frac{h}{k}Y_0(ub)\right]J_1(ua)\right]}\right.$$

$$\left. + \pi \sum_{n=1}^{\infty} \frac{\alpha\beta_n e^{-\alpha\beta_n^2[t-l\tau]}A_0[F_n(\beta_n b)]^2 G_n(\beta_n r, a)}{k[c - \alpha\beta_n^2]C_n(\beta_n, a, b)}\right] \tag{28}$$

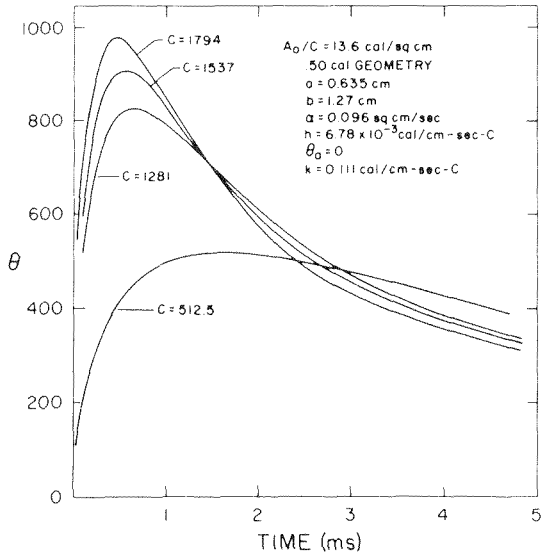

Fig. 3 Bore surface temperature calculated from equation (19)

The total heat transfer per unit area to the bore surface is:

$$Q = \int_0^\infty -k \frac{\partial T}{\partial r}(a, t)dt = A_0/c \tag{29}$$

A_0 and c may be selected so that the calculated bore surface temperature history corresponds to the characteristic shape noted experimentally subject to the constraint that A_0/c is the total heat transfer. Fig. 3 shows the sensitivity of the bore surface temperature to variations in A_0 and c for a constant barrel heat transfer. Note that the bore surface temperature history (Fig. 3) can be adjusted to conform closely to the characteristic shape suggested by experiment (Fig. 1).

In an alternate approach, Fig. 4 shows the result of directly adjusting A_0 and c to fit an experimental bore surface temperature-time curve for a single-round firing in a 0.60 caliber barrel [5]. The previously reported analytical results [4], also shown, are based on rectangular pulse representations of the bore heat flux and heat transfer coefficient, respectively. The duration of each of the constant amplitude pulses is fixed by the time from firing initiation until the peak bore temperature was observed experimentally for a single-round firing. The amplitude was selected to correspond to an overall average total heat transfer of 9.77 cal/sq cm obtained from calorimetric measurements after an automatic firing burst. Alternately, the amplitude could be selected to match the peak observed temperature but, for increasing time, the analytical solution would still be considerably below the measured temperatures. The values of A_0 and c used for the present exponentially decaying pulse were 13,400 cal/sq cm-s and 900 s^{-1}, respectively, corresponding to a heat transfer of 14.9 cal/sq cm. The present solution is in better overall agreement with the experimental temperature distribution.

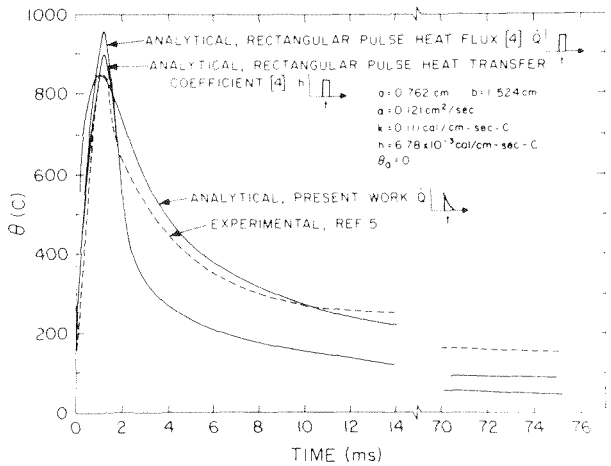

Fig. 4 Comparison of analytical and experimental bore surface temperature for a 0.60 caliber barrel

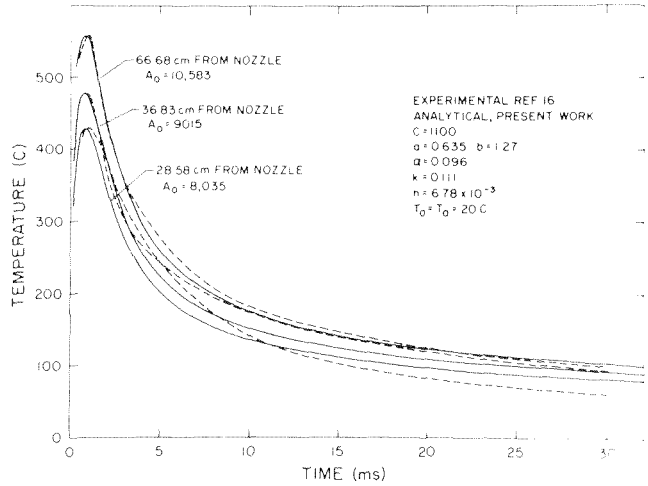

Fig. 5 Comparisons of analytical and experimental bore surface temperature for a 0.50 caliber barrel

In Figs. 5 and 6, A_0 and c have been selected to fit experimentally observed bore surface temperature-time curves at different axial locations in a 0.50 caliber barrel [16] and a 40-mm barrel [13]. It should be noted that c shows negligible dependence on the axial location within a given barrel although it does differ for the various barrels considered. The validity of the assumptions that c is independent of z and is of the order of 10^3 s^{-1} is thus established within the limitations of available experimental data.

Two-Dimensional Case, Interior Temperature, Multiple-Round Firing. Extending the results from the one-dimensional analysis, $f(z)$ may be approximated by a polynominal fit of the A_0 values at different axial locations for a given barrel. With this polynominal, equations (23) and (24) may be integrated and equation (19) then gives the two-dimensional transient temperature

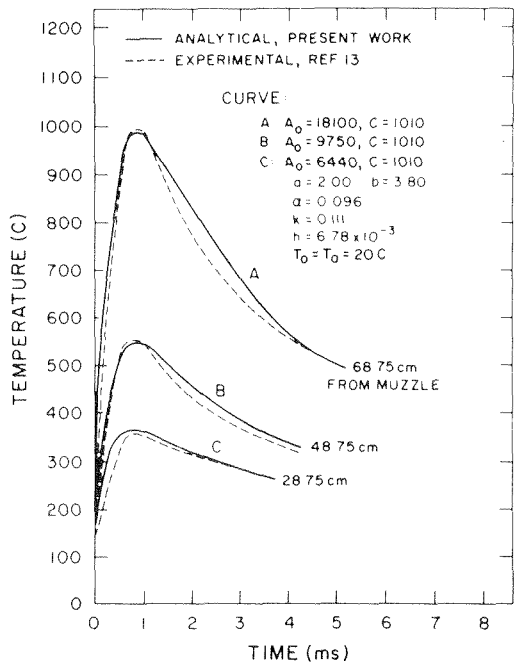

Fig. 6 Comparisons of analytical and experimental bore surface temperatures at different axial locations in a 40-mm barrel

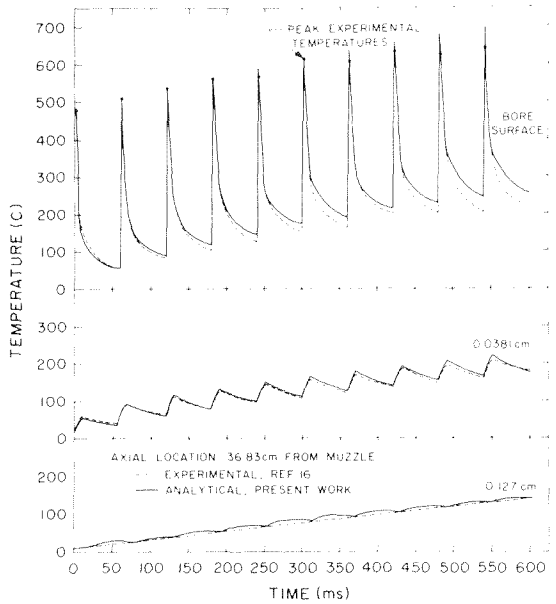

Fig. 7 Comparisons of analytical and experimental bore surface and internal temperatures during a ten-round firing burst

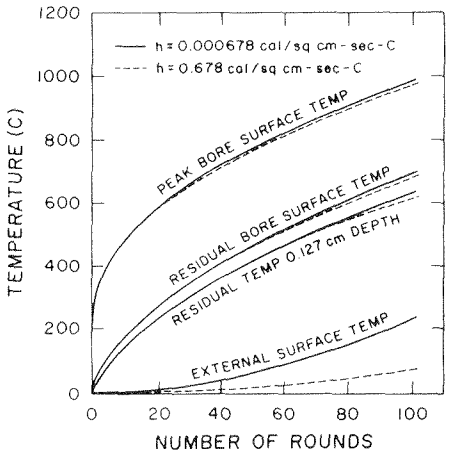

Fig. 8 Effect of external cooling on calculated temperatures during a 100-round firing burst

distribution. Using the three values of A_0 as shown in Fig. 5 gives for the 0.50 caliber barrel

$$f(z) = 2809.5 + 232.5\,z^2 - 1.74\,z^2 \text{ cal/sq cm-s} \quad (30)$$

where z is the distance in centimeters from the muzzle. Fig. 7 compares the analytical results thus obtained with experimental temperature-time data [16] at the bore surface and two internal locations during a ten-round firing burst. The experimental bore surface temperatures do not increase by equal amounts from round to round in successive peak values nor in successive residual temperatures at the end of each firing cycle. Two factors contribute to this difference between the experimental and analytical results. First, the interior boundary condition does not account for the decreased heat transfer as the bore surface temperature increases with successive rounds. The analysis is based on specifying the bore heat flux independent of round sequence rather than by deducing the flux from appropriate convective considerations. Second, a residue may be deposited on the bore surface during multiple-round firings, as noted in reference [6], resulting in lower surface temperatures. However, the analytical results are generally in good agreement with the data for 10 rounds and the agreement is closer at the interior locations.

Comparing the peak bore temperatures at 36.83 cm calculated in Figs. 5 and 7 indicates that for these conditions the effect of axial conduction is not important. Solving the two-dimensional case, however, presents no new problems and the solution is included for completeness.

Effect of External Cooling. Equation (19) accounts for convective heat transfer at the outer surface of the barrel. The effect of external cooling on temperatures at different radial locations for the 0.50 caliber barrel is shown in Fig. 8. The two heat transfer coefficients for which results are shown correspond approximately to free convection in air and to boiling water. The results indicate that, although the outside cooling rate is varied by three orders of magnitude, there is an insignificant effect on bore surface temperature. Temperatures at other radial locations are affected somewhat more with a maximum difference of 160 C at the outer surface after 100 rounds. Fig. 8 shows clearly the ineffectiveness of external cooling for controlling bore surface temperatures during a rapid-firing burst. However, external cooling is important in reducing the average barrel temperature as well as the time required for cooling the barrel between successive bursts.

Conclusions

The two-dimensional transient heat conduction equation with a pulsating time and spatially dependent boundary condition has been solved analytically. Laplace transform techniques were shown to provide a tractable method for handling periodic exponentially-decaying pulses characterized by rapid time-rates of decay.

As an application of this solution, the temperature distribution in a gun barrel was determined. A series of exponentially-decaying pulses was used to represent the bore-surface heat flux during multiple-round firing. The resulting solution agreed more closely with experimental bore-surface temperature-time curves than previous solutions which represented bore surface heat transfer by rectangular pulse functions. Using information from a single-round firing to characterize the heat transfer to the barrel, a solution applicable to multiple-round firing was obtained which agreed closely with the experimental data for a ten-round burst. Calculated interior barrel temperatures during the burst nearly coincide with the corresponding data. The bore surface temperatures predicted during the same firing burst were somewhat higher than experimental values. The results of the analysis indicated that external cooling methods are ineffective for bore surface temperature control of rapidly-firing guns during the actual firing times.

References

1 Nordheim, L. W., Soodak, H., and Nordheim, G., "Thermal Effects of Propellant Gases in Erosion Vents and in Guns," National Defense Research Committee, *Armor and Ordnance Report No. A-262*, OSRD No. 3447, 1944.

2 Adams, L. H., Kracek, F. G., and Benedict, W. S., "Hypervelocity Guns and the Control of Erosion," Summary Technical Report of the National Defense Research Committee, Washington, D.C., 1946.

3 Anthony, M. L., "*Feasibility Study for a 60-mm Anti-Aircraft Gun*, T157, and Feed System," Final Report, Contract No. DA-11-022-ORD-314, Armor Research Foundation, Dec. 17, 1951.

4 Anthony, M. L., "Temperature Distribution in Gun Barrels, an Analytical Study in Connection with Projects 90-813K, 90-829K, 90-870K, 90-990K, 90-1026L, and 2349QQK," *Armour Research Foundation*, May, 1952.

5 Hendry, W. B., and Bendersky, D., "Survey of Bore-Surface Temperature Investigations Conducted at Armour Research Foundation, Purdue University and Midwest Research Institute," Midwest Research Engineering Division *Phase Report No. 9*, Nov. 1952.

6 Pascual, M. J., Zweig, J. E., Sutherland, C. D., and Loatman, P. J., "Transient Thermal Stress in Gun Tubes—Part II," Watervliet Arsenal Technical Report No. WVT-RR-6280, May 1962.

7 Chu, S. C., and Benzkofer, P. D., "An Analytical Solution of the Heat Flow in a Gun Tube," U. S. Army Weapons Command, Rock Island Arsenal Report No. RE-70-160, Nov. 1970.

8 Kafadar, A. D., et al., "Surface Temperature Measurements," Memorandum Reports Nos. 1, 2, 3, 4, and 5, Project No. 122-772D, Armour Research Foundation, Apr. 7, 1950, to Aug. 8, 1952.

9 Hawkins, G. A., et al., "*A Preliminary Report on a Method for Bore Temperature Measurements in Machine Gun Barrels*," Report No. 262,

Purdue University, Mar. 27, 1951.
10 Bendersky, D., "A Thermocouple for Accurate Measurements of Steady or Rapidly Varying Surface Temperatures," Memorandum Report No. 1, Midwest Research Institute, 1952.
11 Hackman, P., "A Method for Measuring Rapidly Changing Surface Temperatures and Its Application to Gun Barrels," British Technical Information Bureau Translation No. GDC 10/1230T, Jan. 1941.
12 Nanigian, J., "A Thermocouple to Record Transient Temperatures at the Bore Surface of Guns," Naval Proving Ground Report No. 1130, July 15, 1953.
13 Giedt, W. H., "The Determination of Transient Temperatures and Heat Transfer at a Gas-Metal Interface Applied to a 40-mm Gun Barrel," Jet Propulsion, Apr. 1955, pp. 158–162.
14 Carslaw, H. S., and Jaeger, J. C., *Operational Methods in Applied Mathematics*, Oxford University Press, London, 1941.
15 Copley, J. A., "An Analytical Solution of the Two-Dimensional Transient Heat Conduction Equation With a Pulsating Time and Space Dependent Boundary Condition," PhD Thesis, Virginia Polytechnic Institute and State University, May, 1971; (available from University Microfilms).
16 Bergdolt, V. E., "Three-Dimensional Temperatures," Purdue University Engineering Experiment Station Report No. 300, June 30, 1954.

APPENDIX

The physical significance of neglecting $\exp(-\tau c)$ in equation (7) is that the bore surface heat flux representation, equation (11), does not completely zero a pulse prior to the start of the next round. The simplification is necessary to obtain terms in equation (12) of the form illustrated by equation (17) that can be inverted by using the inversion theorem. The error introduced by this simplification is negligible even for a large number of rounds when a fast time-rate of decay is associated with the heat flux pulse. The bore surface heat flux representation for nonterminated pulses is given by

$$-k\frac{\partial T}{\partial r}(a,t) = A_0 \sum_{n=0}^{\infty} \exp(-c[t-n\tau])\,\delta(t-n\tau) \qquad (31)$$

The transform of equation (31) is equation (11). The error introduced for successive rounds ($n = 2, 3, 4 \ldots i \ldots$) is then equation (31) minus equation (1) and for the nth round is

$$A_0[\exp(-nc\tau) + \exp(-[n-1]c\tau) + \exp(-[n-2]c\tau) + \ldots \exp(-c\tau)]$$

In the limit as the number of rounds increases ($n \to \infty$) the series is summable and the maximum error, resulting from the simplification is at most

$$A_0\left[\frac{\exp(-c\tau)}{1-e^{-c\tau}}\right]$$

The term inside the brackets is <0.01 for $c\tau \geq 5$ and for the 0.50 caliber gun shown in Fig. 7, the term is of the order 10^{-25}.

M. J. Reiser
Technical Systems Manager,
Procter and Gamble Manufacturing Co.,
Dallas, Texas

F. J. Appl
Professor,
School of Aerospace, Mechanical
and Nuclear Engineering,
University of Oklahoma,
Norman, Oklahoma. Mem. ASME

A Numerical Method for Heat Conduction Problems

A singular integral method of numerical analysis for two-dimensional steady-state heat conduction problems with any combination of temperature, gradient, or convection boundary conditions is presented. Excellent agreement with the exact solution is illustrated for an example problem. The method is used to determine the solution for a fin bank with convection.

Introduction

The determination of temperatures and gradients on, and within, the boundary of two-dimensional members in steady-state heat conduction has been a problem of long standing interest. Most exact solutions have been for members of relatively simple geometric shape. The classical method usually used is to solve the governing differential equations by separation of variables and satisfy the boundary conditions. These classical methods give solutions which are exact relationships or are at least exact in the limit of a summation of successive terms. The solutions obtained for a particular problem are valid only for that problem. Exact solutions for temperature expressed in series form are often slowly convergent and can result in poor gradient predictions. Holman [1],[1] Chapman [2], Carslaw and Jaeger [3], and Carslaw [4] are representative of the many sources giving general presentations of the classical method of solution by separation of variables.

Many problems are not readily solved by exact means and approximate solutions must be determined. Two general classes of approximate solution techniques can be categorized as those requiring nodal or element descriptions on, and within, the boundary of the domain of interest and those requiring descriptions only on the boundary of the domain.

Finite difference and finite element methods fall into the first class as they require writing and solution of simultaneous nodal equations at each point of interest on, and within, the boundary of the domain. References [1, 2, 5] are representative of the many sources giving general discussions of various methods of treating finite difference approaches. Zienkiewicz [6] describes the finite element method and solutions.

The second classification includes those methods generally described as boundary collocation methods and includes many different techniques. "Point-matching" and singular integral techniques are forms of the boundary collocation approach.

The first known paper to appear in the literature using point-matching was presented by Slater [7] in 1934 and dealt with electronic energy bonds in metals. Barta [8] was the first to apply the method to a plate bending problem in 1937. Fend, et al. [9] employed the technique in the solution of a temperature distribution problem in 1950. In 1960 a paper by Conway [10] lead to widespread use of the technique. Ojalvo and Linzer [11] summarized the method and offered suggestions for improving the method. In this form of point-matching, a series solution, each term of which satisfies the governing differential equation, is truncated with N terms. Boundary conditions are specified at N locations around the boundary. A solution is determined by solving the N resulting simultaneous equations. The solution satisfies the boundary conditions at each of the N specified boundary points but can fluctuate widely at other points on the boundary.

If M boundary conditions are specified and N terms retained in the truncated series, where $M > N$, then the resulting set of equations is overdetermined and the resulting solution will be a least-squares best-fit solution. In this variation of the point-matching method, the resulting solution will not satisfy the boundary conditions exactly anywhere, but will be a least-squares best-fit solution of all of the M boundary conditions. This procedure limits the fluctuations at locations between the prescribed boundary points encountered in the method previously discussed. Representative references of this general type of approach are [12–15], each of which has its own variations.

Point-matching approaches to problems involving domains that are relatively long and slender can result in ill-conditioned equations and/or matrices where the largest elements are not on the principal diagonal which makes accurate solutions difficult or impossible. Solutions to problems involving abrupt changes in geometry and/or boundary conditions determined by point matching usually blur over the change points, which are often the regions of interest.

Singular-integral boundary collocation approaches to approximate solutions of boundary value problems are of two general forms: those that use a surface density approach as presented for example in [16 and 17] and those that use a potential function approach as presented for example in [18 and 19]. The singular-integral method for two-dimensional steady-state heat-conduction problems using the potential function approach is presented in [19]. While this form of the singular-integral approach is in gener-

[1] Numbers in brackets designate References at end of paper.

Contributed by the Heat Transfer Division for publication in the JOURNAL OF HEAT TRANSFER. Manuscript received by the Heat Transfer Division, October 9, 1973. Paper No. 74-HT-JJ.

al excellent, certain restrictions on determining temperatures and gradients near the boundary and the possibility of ill-conditioned equations were found.

Lo, et al. [16] used one singular integral term in conjunction with the point-matching method to determine an improved solution to a problem of heat conduction in a plate with a combination of gradient and temperature boundary conditions. However, the singular integral term was used only to improve the point-matching solution in the vicinity of a very abrupt change in boundary condition in their consideration of steady-state heat conduction. Reference [16] presents a complete development with applications of the singular integral method for torsion, membrane, and plate bending problems and suggests that a similar method could be developed for steady-state two-dimensional heat conduction, and for plane elasticity. A complete development with application of the singular integral method to plane elasticity is presented in [17].

The singular integral method for two-dimensional steady-state heat conduction problems using the surface density approach is presented herein. The method is applicable to two-dimensional steady-state heat conduction problems involving any geometrical shape and any combination of temperature, gradient, or convective boundary conditions. The method requires only that the domain boundary and the boundary conditions be specified in order to obtain solutions for temperatures and gradients at any point interior to or on the boundary of the region.

This method requires the use of a computer with sufficient core storage. The coefficient matrices generated during the solution are dense, as is also typical of matrices in point matching methods, whereas the matrices from finite element methods are banded. However, a relatively small number of equations is necessary to obtain an accurate solution, since the singular integral method is a boundary collocation method. If an accurate solution is determined using N equations obtained from satisfying the boundary conditions at N locations, then a similar solution using relaxation, finite difference or finite element methods in which the boundary and the interior nodes are as adequately described would result in approximately N^2 equations. Further the singular integral method results in coefficient matrices in which the largest elements are on the principal diagonal and hence the matrices are well-conditioned and accurate solutions of the simultaneous equations are obtained easily.

Perhaps, the greatest advantages of the singular integral method are the ease of use and the versatility of application. The main body of the method need be programmed only once and thereafter only a subroutine describing the boundary contour and the boundary conditions need be changed for application to different problems. The authors' experiences with finite element methods has been that the preparation of input data and the selection of node locations is very time consuming and each change of geometry necessitates a completely new set of input data. The CPU time for finite element solutions of some problems may be somewhat less due to the banded nature of the matrices. If, however, total effort of man and machine is considered, the authors have found the singular integral method superior to the finite element method. In certain problems involving smooth boundaries and boundary conditions easily specified in analytical form, the point matching methods of [14, 15] may also require less CPU time than a singular integral solution. However, these approaches can also require significant prior analysis and integration for each specific problem.

Theoretical Analysis

The singular integral method presented herein is based on the use of steady-state sources and sinks of variable strength. For a line source in the Z or thickness direction acting in an infinite isotropic, homogeneous solid, the solution of the Fourier heat conduction equation for steady-state conditions:

$$\nabla^2 T = 0 \tag{1}$$

is of the form:

$$T = \frac{q}{2\pi k} \ln r + \text{constant} \tag{2}$$

as shown in [3].

For use in formulating the singular integral method, equation (2) can be expressed as:

$$T = \frac{1}{1 + \ln c}\left[-T_0 \ln \frac{r}{c} + \text{constant}\right], \quad r < c \tag{3}$$

where T is the temperature at a point i due to a source at location j, r is the distance between the two points, and c is an arbitrary constant greater than r. This form of the singularity function shows that T decreases as the distance from the source increases and that the temperature at point i is always positive when temperatures are based on an absolute scale. It can be shown that T_0, which is termed a fictitious temperature, is related to q, the rate of heat flow from the source, as:

$$T_0 = \frac{q(1 + \ln c)}{2\pi k} \tag{4}$$

and is proportional to the magnitude of the strength of the source.

The effect at a point due to a line segment in the X-Y directions with a step density function (a constant fictitious temperature) along its length is determined. The effect of a line segment may be treated as the summation of the effects of all the sources along it or as the integral of increments dt, each with a concentrated density function at its center. The temperature at point i, T_{ij}, due to a line segment j of length S_j is:

$$T_{ij} = \frac{1}{1 + \ln c}\left[-\frac{T_{0j}}{S_j}\int_{-S_j/2}^{S_j/2} \ln \frac{r}{c} dl + T_{0j} \ln \frac{S_j}{2}\right], \quad r < c \tag{5}$$

where T_{0j} is the step density function of the jth segment. Equation (5) also satisfies the requirement that $T_{ij} = T_{0j}$ for the limiting case of $R_j = 0$, i.e., a point "looking at" itself.

To determine the effect at point i of an entire boundary, it is then necessary to divide the boundary into segments, each with a step density function. The effect at i is then seen to be the summation of effects of each of the segments.

$$T_i = \sum_{j=1}^{N} T_{ij} \tag{6}$$

where N is the number of segments on the boundary.

The boundary condition at the center of segment i on the boundary is then set equal to T_i, i.e., equal to the sum of the effects of all the boundary segments, each with a step density function, T_{0j}. This is done for all N segments around the boundary to generate N equations with N unknowns, where the values of T_{0j} are the unknowns. The values of the T_{0j} are determined by matrix solution of the simultaneous equations.

A similar procedure is followed if gradient boundary conditions are specified. When solving problems with mixed boundary conditions, some of the N equations will be set up using temperature boundary conditions and some gradient boundary conditions, but all are expressed in terms of the same fictitious T_{0j} and will solve for a specific T_{0j} for each segment.

Fig. 1 depicts the coordinate system used to determine the effect at a point due to a line segment with step density function. From Fig. 1:

$$r = [(t - R_j SN)^2 + R_j^2 CN^2]^{1/2} \tag{7}$$

where $SN = \sin(\theta_j - \psi_j)$ and $CN = -\cos(\theta_j - \psi_j)$.

Using equation (7), equation (5) is integrated by parts to obtain the effect at point i due to line segment j in general form for $R_j \neq 0$ and $CN \neq 0$:

$$T_{ij} = -\frac{T_{0j}}{1 + \ln c}\left\{\left(\frac{0.5S_j + R_j SN}{2S_j}\right) \ln\left[\left(\frac{S_j}{2} + R_j SN\right)^2 + R_j^2 CN^2\right] + \left(\frac{0.5S_j - R_j SN}{2S_j}\right) \ln\left[\left(\frac{S_j}{2} - R_j SN\right)^2 + R_j^2 CN^2\right] + \frac{R_j CN}{S_j}\left[\tan^{-1}\left(\frac{0.5S_j - R_j SN}{R_j CN}\right) + \tan^{-1}\left(\frac{0.5S_j + R_j SN}{R_j CN}\right)\right] - 1 - \ln c - \ln \frac{S_j}{2}\right\} \tag{8}$$

For $R_j = 0$, equation (8) reduces to

$$T_{ij} = T_{0j} \tag{9}$$

For $CN = 0$ and $R_j \neq 0$, equation (8) becomes

$$T_{ij} = -\frac{T_{0j}}{1 + \ln c}\left[\left(\frac{0.5S_j + R_jSN}{2S_j}\right) \ln \left(\frac{S_j}{2} + R_jSN\right)^2 + \left(\frac{0.5S_j - R_jSN}{2S_j}\right) \ln \left(\frac{S_j}{2} - R_jSN\right)^2 - 1 - \ln c - \ln \frac{S_j}{2}\right] \tag{10}$$

Since the ratio T_{ij}/T_{0j} must always be positive, it can be shown from equation (5) that an additional constraint on the value of c is:

$$c^2 > 1 + 4\,\frac{(R_j^2)_{\max}}{(S_j^2)_{\min}} \tag{11}$$

The gradient in any direction n is:

$$\frac{\partial T}{\partial n} = \cos(\eta)\,\frac{\partial T}{\partial X} + \sin(\eta)\,\frac{\partial T}{\partial Y} \tag{12}$$

where η is the angle between the X axis and the direction of the desired gradient as shown in Fig. 1.

The partial derivatives of temperature with respect to the X and Y directions obtained from equation (5) for the general case of $R_j \neq 0$ and $CN \neq 0$ are:

$$\frac{\partial T_{ij}}{\partial X} = \frac{T_{0j}}{S_j(1 + \ln c)}\left\{\cos \psi_j\left[\tan^{-1}\left(\frac{0.5S_j - R_jSN}{R_jCN}\right) + \tan^{-1}\left(\frac{0.5S_j + R_jSN}{R_jCN}\right)\right] + \frac{\sin \psi_j}{2}\left[\ln\left(R_j^2 + R_jS_jSN + \frac{S_j^2}{4}\right) - \ln\left(R_j^2 - R_jS_jSN + \frac{S_j^2}{4}\right)\right]\right\} \tag{13}$$

and

$$\frac{\partial T_{ij}}{\partial Y} = \frac{T_{0j}}{S_j(1 + \ln c)}\left\{\sin \psi_j\left[\tan^{-1}\left(\frac{0.5S_j - R_jSN}{R_jCN}\right) + \tan^{-1}\left(\frac{0.5S_j + R_jSN}{R_jCN}\right)\right] - \frac{\cos \psi_j}{2}\left[\ln\left(R_j^2 + R_jS_jSN + \frac{S_j^2}{4}\right) - \ln\left(R_j^2 - R_jS_jSN + \frac{S_j^2}{4}\right)\right]\right\} \tag{14}$$

For $R_j = 0$, equations (13) and (14) reduce to

$$\frac{\partial T_{ij}}{\partial X} = 0 \tag{15}$$

and

$$\frac{\partial T_{ij}}{\partial Y} = 0 \tag{16}$$

For $CN = 0$ and $R_j \neq 0$, equations (13) and (14) become

$$\frac{\partial T_{ij}}{\partial X} = -\frac{T_{0j} \sin \psi_j}{S_j(1 + \ln c)} \ln \frac{R_jSN - 0.5S_j}{R_jSN + 0.5S_j} \tag{17}$$

and

$$\frac{\partial T_{ij}}{\partial Y} = \frac{T_{0j} \cos \psi_j}{S_j(1 + \ln c)} \ln \frac{R_jSN - 0.5S_j}{R_jSN + 0.5S_j} \tag{18}$$

for $R_j > S_j/2$.

The condition of $R_j = S_j/2$, a segment looking at its end points, produces values which are undefined. Therefore, singularities occur at the end points of the segments and these points cannot be considered. All other points are well behaved. Since, when dealing with a boundary segment, only the midpoint of the segment is considered, cases of $R_j < S_j/2$ reduce to the special case of $R_j = 0$.

Equations (8) to (10) and (13) to (18) are the relationships used to determine the values of the fictitious step density functions and, from them, the values of temperature or gradient at any point within the boundary or at the midpoints of the boundary segments.

When solving for gradients on the boundary or when considering members with any gradient boundary conditions, numerical difficulties occur due to the contributions from equations (15) and (16). This difficulty is eliminated by circumscribing a closed boundary around the boundary of the member in question. The fictitious solutions are placed on the circumscribed boundary

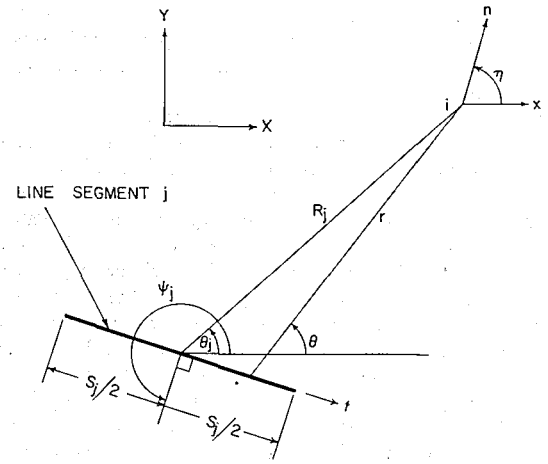

Fig. 1 Definition of coordinate system for determining the effect of line segments

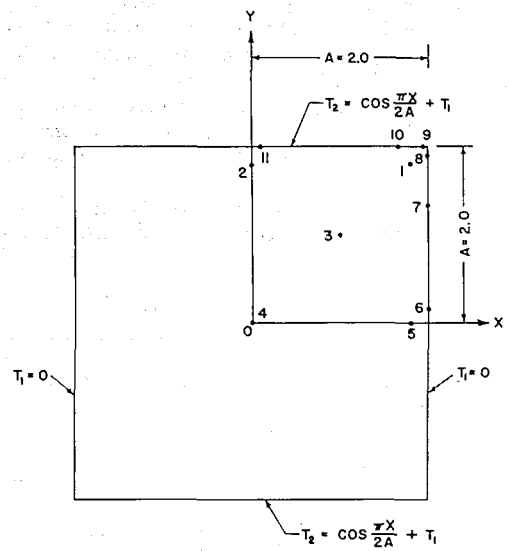

Fig. 2 Representation of example problem

which means that the member boundary is treated as being internal to the larger boundary and numerical problems incurred when using the condition $R_j = 0$ for gradient solutions are eliminated. *In effect, equations (15) and (16) are never used when using a circumscribed boundary.*

Application of Method

The accuracy of the method presented herein is illustrated by comparison of the results of this method to an exact solution. The problem selected as an example is a square flat plate in steady-state heat conduction. Fig. 2 gives a representation of the problem, which is doubly symmetric with respect to both geometry and boundary conditions. The exact temperature solution to this problem is given in [1, 2]. Gradients in the X and Y directions were obtained by differentiation of the exact solution.

A computer program was written for the exact solution and its derivatives to give the temperature and gradients in the X and Y directions a 54 points on the boundary of the first quadrant and 100 internal points in the same quadrant of the plate. Using the numerical method, the temperature and gradient in the X and Y directions at the same 54 boundary points and 100 internal points were computed. The results at these points were compared.

Table 1 presents the results of three numerical solutions using different boundary conditions. Results are shown for the eleven points indicated in Fig. 2. Point 1 is a critical point since it is closest to the corner where an accurate solution is difficult to ob-

tain by any method. The comparison of these eleven points is representative of the comparison at all 154 points and no worse agreement was found among any other points than among the eleven presented.

Using temperature boundary conditions and fictitious step density functions on the plate boundary, accurate results were obtained for temperatures and gradients at the internal points and for temperatures on the boundary. Results for gradients on the boundary, however, were incorrect, as shown in col. 6 of Table 1. Incorrect results for all quantities were also obtained when gradient boundary conditions were specified in whole or in part when the step density functions were applied on the actual plate boundary as discussed previously. A circumscribed boundary around the plate was defined and the fictitious step density functions placed on that boundary. Segments were placed on the enclosing boundary in the same manner as on the plate boundary as shown in Fig. 3. Table 1 reflects the accuracy obtained using the circumscribed boundary. The results are for the case of mixed boundary conditions, and show accuracy to at least three decimal places for all quantities both on the boundary and internally.

For problems having only gradient boundary conditions, temperatures can only be determined within a constant. Table 1 illustrates the accuracy of the solution of this problem with gradient boundary conditions. The correct constant was obtained by comparing the temperature solutions to the exact solutions. After the constant was determined, the temperature solutions were adjusted accordingly to enable a better comparison of accuracy to

Table 1 Results of numerical method for various boundary conditions compared with exact solution

1	2	3	4	5	6	7	8
					Numerical Method		
						Circumscribed Solution	
	Point	X	Y	Exact Solution	Temp. B.C.	Mixed B.C.	Grad. B.C.
	1	1.800	1.800	.135740	.13571	.13595	.136
	2	0.000	1.800	.867703	.86765	.86796	.868
	3	1.000	1.000	.373286	.37326	.37347	.373
	4	0.000	0.000	.398537	.39850	.39878	.398
	5	1.800	0.000	.062346	.06227	.06250	.062
	6	2.000	0.176	.000000	-.00002	.00022	.000
TEMP							
	7	2.000	1.352	.000000	-.00003	.00021	.000
	8	2.000	1.883	.000000	-.00003	.00026	.000
	9	1.944	2.000	.043970	.04394	.04418	.044
	10	1.642	2.000	.277484	.27746	.27766	.277
	11	0.097	2.000	.997099	.99707	.99738	.997
	1	1.800	1.800	-.673102	-.67315	-.67307	-.67311
	2	0.000	1.800	.000000	.00000	.00000	.00000
	3	1.000	1.000	-.293178	-.29317	-.29318	-.29318
	4	0.000	0.000	.000000	.00000	.00000	.00000
	5	1.800	0.000	-.309157	-.30943	-.30917	-.30914
	6	2.000	0.176	-.316005	-.11365	-.31600	-.31600
GRAD X							
	7	2.000	1.352	-.506693	-.18064	-.50669	-.50669
	8	2.000	1.883	-.722431	-.14511	-.72243	-.72243
	9	1.944	2.000	-.784638	---	---	---
	10	1.642	2.000	-.754555	---	---	---
	11	0.097	2.000	-.059775	---	---	---

Table 1 (Cont'd)

1	2	3	4	5	6	7	8
					Numerical Method		
						Circumscribed Solution	
	Point	X	Y	Exact Solution	Temp. B.C.	Mixed B.C.	Grad. B.C.
	1	1.800	1.800	.094699	.09465	.09469	.09470
	2	0.000	1.800	.605356	.60524	.60529	.60536
	3	1.000	1.000	.192264	.19226	.19226	.19226
	4	0.000	0.000	.000000	.00000	.00000	.00000
	5	1.800	0.000	.000000	.00000	.00000	.00000
	6.	2.000	0.176	.000000	---	---	---
GRAD Y							
	7	2.000	1.352	.000000	---	---	---
	8	2.000	1.883	.000000	---	---	---
	9	1.944	2.000	.031673	.53485	.03162	.03167
	10	1.642	2.000	.199880	.19460	.19991	.19988
	11	0.097	2.000	.718241	.04648	.71800	.71824

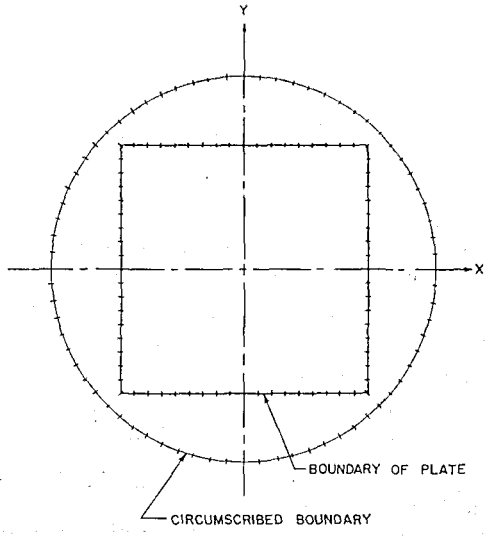

Fig. 3 Circumscribed boundary and placement of segments

be made. Table 1, col. 8, clearly shows that accuracy to three places was obtained for the temperature solutions both internally and on the boundary, and the gradient solutions exhibited five place accuracy both internally and on the boundary.

The number and distribution of boundary segments for which boundary conditions are specified will affect the accuracy of the solutions. The effect of various distributions and number of segments was investigated for the example problem. In general, best overall results were obtained using a uniform distribution of segments. Even in the vicinity of the corner, which is subject to corner effects [17], the uniform distribution gave results for all quantities accurate to three places. When comparing results for the various distributions, it was necessary to go to the fourth or fifth place to discern any differences. Since it made so little difference in accuracy, it is concluded that a uniform distribution is sufficient and is most convenient to describe.

More accurate results were obtained as the number of boundary segments increased, as was expected. However, three place accuracy for all quantities was obtained at all points using only 30 boundary segments. To discern better accuracy with greater numbers of boundary segments, it was necessary to compare in the fourth and fifth places. It was found that once convergence was attained, a further increase in number of boundary segments gave little or no improvement in the accuracy of results.

For the IBM 360-50 system used, run time in seconds was approximately equal to twenty-four times the number of boundary segments in the first quadrant raised to the 0.85 power. Since it is necessary to compare the fourth and fifth places to discern differences in accuracy obtained with 30, 60, and 75 segments, it would be more economical and sufficiently accurate to use the 30 boundary segment solution for this particular problem.

Convection Boundary Conditions

Although heat transfer by convection is actually accomplished by conduction to a fluid layer at the wall, the effects of the flow field must be considered. The overall effect of convection is expressed by Newton's law of cooling [1]:

$$q = hA(T_w - T_\infty) \tag{19}$$

or by an energy balance of conduction to convection

$$-k \left.\frac{\partial T}{\partial n}\right|_w = h(T_w - T_\infty) \tag{20}$$

where T_w is the interface temperature and T_∞ is the ambient temperature.

The validity of using the numerical method of this work in obtaining solutions for temperatures and gradients by means of summation of the products of the calculated values of T_{0j} and a

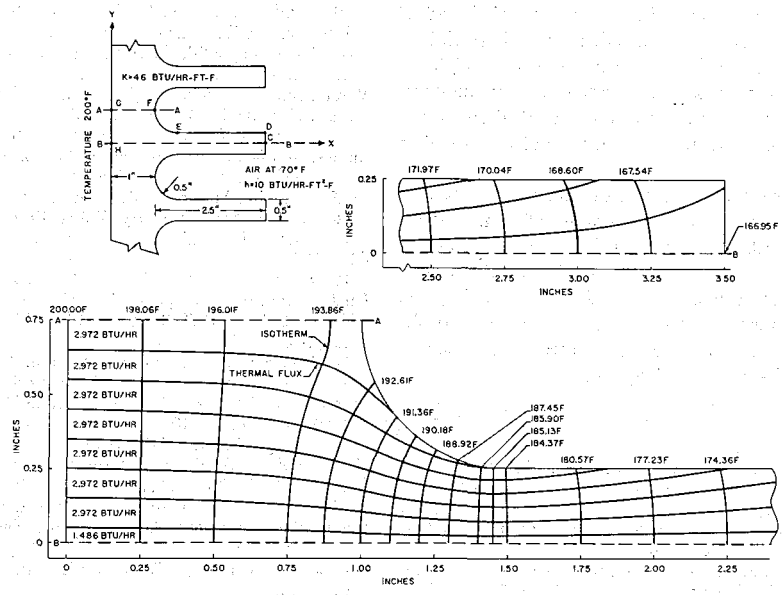

Fig. 4 Steady-state solution for a fin bank with convection

coefficient determined from the temperature or gradient relationships developed herein has been shown. This same numerical method may be applied to conduction-convection systems by virtue of equation (20).

At a point, the gradient term of equation (20) in the foregoing may be expressed as the sum of the products of the step density functions T_{0j} and coefficients (coef G) determined from the gradient relationships, equations (13) to (18). At the same point, the temperature term may be expressed as the sum of the products of T_{0j} and coefficients (coef T) determined from the temperature relationships, equations (8) to (10). Using this approach, equation (20) can be expressed as:

$$\sum_j [h(\text{coef } T) + k(\text{coef } G)]T_{0j} = hT_\infty \qquad (21)$$

For convection boundary conditions, the proper values of the T_{0j} are determined in the same manner as presented previously by using the product hT_∞ as the boundary condition and the sum $[h(\text{coef } T) + k(\text{coef } G)]$ as the relationship of the effect of a line segment upon a point with a convection boundary condition. After the T_{0j} are determined, the values of temperature and gradient at any point may be found in the same manner as described previously.

The following solution is presented as an example of the versatility, accuracy and applicability of the method. The problem selected is a bank of fins, which is assumed to be very long in the Z direction and has dimensions in the X–Y directions as shown in Fig. 4. The temperature at the base of the wall was assumed as an isotherm of 200 deg F. The surrounding medium was assumed to be air at 70 deg F with a convective coefficient h of 10 Btu/hr-ft^2-F. The fin material conduction coefficient k was taken as 46 Btu/h-ft-F.

This fin problem was analyzed by considering one complete fin as the region of interest. The fin then is singly symmetric about the X axis.

This is a problem with mixed boundary conditions which were expressed as follows for one half of the fin: a constant temperature of 200 deg F along G-H, zero gradient in the y direction along *F-G,* and convection along the remainder of the boundary *(C-D-E-F)* which is exposed to air.

The solution shown in Fig. 4 was determined using 75 boundary segments to describe one half of the fin. The segments were distributed as follows: 6 segments uniformly spaced along *C-D,* 24 segments uniformly spaced along *D-E,* 15 segments uniformly spaced along the fillet *E-F,* 15 segments uniformly spaced along *F-G,* and 15 segments uniformly spaced along *G-H.*

Since some of the boundary conditions are gradient conditions, a circumscribed boundary was used, as discussed previously. The circumscribed boundary was separated from the fin boundary by 0.2 in. and the distribution of segments was the same as on the fin boundary.

Temperatures and gradients in the X and Y directions were computed at the midpoints of each of the 75 boundary segments around one half of the fin boundary and at 207 points inside the fin between section lines *A-A* and *B-B.*

The energy entering one fin at the 200 deg F wall as determined from gradient data along *G-H* was 44.58 Btu/hr per ft of dimension in the Z direction. The energy leaving the fin by convection was found from temperature data along the fin boundary *(C-D-E-F)* and was within one percent of the energy entering the fin. Gradients in the Y direction calculated at various points along *F-G* were all less than 0.0002 and along *B-B* were less than 0.002. The calculated temperature at the midpoints of the boundary segments along *G-H* ranged from 199.997 to 200.004 deg F. These checks on the conservation of energy, the satisfaction of temperature and gradient boundary conditions, and the gradient conditions at the line of symmetry *B-B* all demonstrate that a highly accurate solution has been obtained.

By interpolation of gradient data at 207 interior points and 75 boundary points, thermal flux lines were determined as shown in Fig. 4. The energy conducted through each of the 15 flux tubes is 2.972 Btu/hr *per ft of dimension in the Z direction.* By interpolation of temperature data at the 207 interior points and 75 boundary points, isotherms were determined as shown in Fig. 4. The isotherms and flux lines intersect at right angles and the isotherms intersect lines *F-G* and *B-B* at right angles.

The same fin problem was solved using a convective coefficient of zero, and the solution showed a uniform temperature distribution with all temperatures between 199.999 and 200.000 deg F and all gradients less than 0.002.

Conclusions

The method presented herein gives solutions for both temperature and gradient at interior and boundary points for two-dimensional, steady-state heat conduction problems having temperature, gradient, convection or mixed boundary conditions and any shape of closed boundary. A completely new analysis is not necessary for each different problem. Only the geometry and boundary conditions of each new problem must be described. The problem need not be doubly nor even singly symmetric, although economies of core storage and computing time can be effected in problems with symmetry.

If only temperature boundary conditions are specified and if gradient solutions on the boundary are not desired, it is sufficient to describe only the boundary of the member in question. If, however, the boundary conditions consist of gradients in whole or in part, or if gradient solutions on the boundary are desired, a circumscribed boundary around the actual boundary of the member must be used.

The checks and comparisons presented demonstrate that this numerical method gives highly accurate values of temperature and gradients at points both interior to and on the boundary of the member. Consistently accurate results can be obtained with uniformly distributed boundary segments. After increasing the number of boundary segments to the minimum necessary to obtain satisfactory convergence, little or no improvement occurs with a further increase in the number of segments.

References

1 Holman, J. P., *Heat Transfer*, McGraw-Hill, New York, 1968.

2 Chapman, A. J., *Heat Transfer*, Second ed., Macmillan, Collier-Macmillan Limited, London, 1969.

3 Carslaw, H. S., and Jaeger, J. C., *Conduction of Heat in Solids*, Second ed., Oxford University Press, Glasgow, 1959.

4 Carslaw, H. S., *Introduction to the Mathematical Theory of the Conduction of Heat in Solids*, Second ed., revised, Dover Publications, New York, 1945.

5 Eckert, E. R. G., and Drake, R. M., Jr., *Heat and Mass Transfer*, McGraw-Hill, New York, 1959.

6 Zienkiewicz, O. C., *The Finite Element Method in Engineering Science*, McGraw-Hill, New York, Chapter 15, 1971.

7 Slater, J. C., "Electron Energy Bands in Metals," *Physical Review*, Vol. 45, 1934, pp. 794-801.

8 Barta, J., "On the Numerical Solution of a Two-Dimensional Elasticity Problem," (in German), *ZAMM*, Vol. 7, No. 3, 1937, pp. 184-185.

9 Fend, F. A., Baroody, E. M., and Bell, J. C., "An Approximate Calculation of the Temperature Distribution Surrounding Coolant Holes in a Heat Generating Solid," Battelle Memorial Institute Report T-42, 1950.

10 Conway, H. D., "The Approximate Analysis of Certain Boundary-Value Problems," *Journal of Applied Mechanics*, Vol. 27, TRANS. ASME, Series E, Vol. 82, No. 2, 1960, pp. 275-277.

11 Ojalvo, I. U., and Linzer, F. D., "Improved Point-Matching Techniques," *J. Mech. and Appl. Math*, Vol. 18, 1965, pp. 41-56.

12 Niedenfuhr, F. W., Leissa, A. W., and Lo, C. C., "A Study of the Point-Matching Method as Applied to Thermally and Transversely Loaded Plates and Other Boundary Value Problems," AFFDL-TR-64-159, Air Force Flight Dynamics Laboratory, Wright-Patterson Air Force Base, Ohio, 1964.

13 Sparrow, E. M. and Haji-Sheikh, A., "Flow and Heat Transfer in Ducts of Arbitrary Shape With Arbitrary Thermal Boundary Conditions," JOURNAL OF HEAT TRANSFER, TRANS. ASME, Series C., Vol. 88, 1966, pp. 351-358.

14 Sparrow, E. M., and Haji-Sheikh, A., "Transient and Steady Heat Conduction in Arbitrary Bodies With Arbitrary Boundary and Initial Conditions," JOURNAL OF HEAT TRANSFER, TRANS. ASME, Series C, Vol. 90, 1968, pp. 103-108.

15 France, D. M., "Analytical Solution to Steady-State Heat-Conduction Problems With Irregularly Shaped Boundaries," JOURNAL OF HEAT TRANSFER, TRANS. ASME, Series C., Vol. 93, 1971, pp. 449-454.

16 Lo, C. C., Niedenfuhr, F. W., and Leissa, A. W., "Further Studies in the Application of the Point-Matching Technique to Plate Bending and Other Harmonic and Biharmonic Boundary Value Problems," AFFDL-TR-65-114, Air Force Flight Dynamics Laboratory, Wright-Patterson Air Force Base, Ohio, 1966.

17 Appl, F. J., and Koerner, D. R., "Numerical Analysis of Plane Elasticity Problems," *Jl. Engr. Mech. Div., Proc. ASCE*, Vol. 94, No. EM3, 1968, pp. 743-752.

18 Rizzo, F. J., "An Integral Equation Approach to Boundary Value Problems of Classical Elastostatics," *Quarterly of Applied Mathematics*, Vol. 25, No. 1, 1967, pp. 83-95.

19 Rizzo, F. J., and Shippy, D. J., "A Method of Solution for Certain Problems of Transient Heat Conduction," *AIAA Journal*, Vol. 8, No. 11, 1970, pp. 2004-2009.

J. Padovan
Assoc. Professor,
University of Akron,
Akron, Ohio

Steady Conduction of Heat in Linear and Nonlinear Fully Anisotropic Media by Finite Elements

Using a constrained variational procedure, a finite element approximation is developed which can treat steady heat conduction in anisotropic media whose thermal material properties may be spatially, as well as, temperature dependent. Based on the element approximation, the numerical results of several linear and nonlinear steady conduction problems are presented. These reveal the important effects of thermal material anisotropy.

Introduction

Compared with the problem of conduction of heat in isotropic media, few investigations are available which deal with the more general fully anisotropic problem. In light of the increased structural usage of inherently anisotropic composite media, further investigation is needed in this area. With the exception of brief discussions given in Carslaw and Jaeger [1][1] and Ozisik [2], the few recent investigations that are available in the fully anisotropic category have been reported by Padovan [3–7] and Chang, et al. [8, 9]. These studies have centered on (i) developing solution capabilities and (ii) obtaining a clearer understanding of the possible effects of thermally anisotropic material properties on conduction heat transfer. Besides the quasi-analytical development of Padovan [6], several other finite element procedures have been successfully developed [10–14]. These have generally been implemented for isotropic problems with constant conductivities. Furthermore, with the exception of the related developments of Volker [15], Ahmed and Suneda [16], and Winslow [17] on nonlinear flows in porous media and magnetic fields, there are no investigations which have dealt strictly with nonlinear anisotropic heat conduction problems to any degree of generality.

In this context, the present paper will develop a steady-state finite element procedure which can treat the problem of conduction of heat in anisotropic media whose fully populated conductivity tensor may be spatially, as well as, temperature dependent. The governing 3-D element equations are developed from the constrained variational [18, 19] point of view. To add to the versatility of the results derived herein, the elements are developed for bodies described in cartesian as well as cylindrical[2] coordinates. Since the resulting element equations are nonlinear for temperature dependent conductivities, Newton's procedure is used for their solution.

In the sections to follow, brief discussions are given on:

(i) The governing differential and constrained functional formulations of the conduction equations;

(ii) Presentation of finite element developed numerical results juxtaposed with available "exact solutions" for several linear and nonlinear anisotropic conductivity problems;

(iii) Presentation of several effects of thermal material anisotropy.

2 Differential and Functional Representation of Conduction Equations

In cartesian coordinates (x_1, x_2, x_3), for a fully anisotropic medium, the thermal constitutive relation is given by[3]

$$q_i = \kappa_{ij} T_{,j}; \quad i,j = 1,2,3 \tag{1}$$

such that the conductivity tensor is positive definite [1, 20] and due to Onsager's reciprocity relation, $\kappa_{ij} = \kappa_{ji}$ [21]. For the present development, since composite material constructions are also being considered, κ_{ij} are spacially, as well as, temperature dependent, that is,

$$\kappa_{ij} = \kappa_{ij}(x_1, x_2, x_3, T) \tag{2}$$

In terms of equations (1) and (2), the governing 3-D conduction equation takes the form

$$(\kappa_{ij}(x_1, x_2, x_3, T)T_{,j})_{,i} + Q = 0 \text{ in } R \tag{3}$$

The boundary condition associated with equation (3) is given by

$$n_i \kappa_{ij}(x_1, x_2, x_3, T)T_{,j} + \alpha T + q = 0 \text{ on } \partial R \tag{4}$$

where with the appropriate choice of α and q, either Dirichlet, Neumann or Cauchy type boundary conditions can be developed

[1] Numbers in brackets designate References at end of paper.

[2] Used for axisymmetric bodies [6].

Contributed by the Heat Transfer Division for publication in the JOURNAL OF HEAT TRANSFER. Manuscript received by the Heat Transfer Division, December 17, 1973. Paper No. 74-HT-LL.

[3] Cartesian tensor notation is used throughout. The index variables i and j range over $i, j = 1, 2, 3$.

from equation (4).

Considering that the differential equations denoted by equations (3) and (4) represent minimizing Euler conditions, with the aid of the calculus of variations, it can be immediately verified that an equivalent formulation is the requirement that a certain functional representation be minimized. For the present paper, since $\kappa_{ij}(x_1, x_2, x_3, T)$ is temperature dependent, a constrained variational procedure [18, 19] must be used to develop the proper functional representation. In cartesian coordinates, this formulation takes the form

$$\int_R ((1/2)\kappa_{ij}(x_1, x_2, x_3, \bar{T})T_{,i}T_{,j} - QT)dV + \int_{\partial R} (qT + (1/2)\alpha T^2)ds = I(T) \quad (5)$$

where $I(T)$ is subject to the auxiliary condition [18]

$$\bar{T} = T \quad (6)$$

such that $\bar{T}$ is the constrained variable.

Since axisymmetric geometries are also being considered, in cylindrical coordinates (r, θ, x), equation (5) reduces to [5, 6]

$$\int_0^{2\pi} \left(\int_A ((1/2)(r\kappa_{rr}(r, \theta, z, \bar{T})(T_{,r})^2 + (1/r)\kappa_{\theta\theta}(r, \theta, z, \bar{T})(T_{,\theta})^2 + r\kappa_{zz}(r, \theta, z, \bar{T}) \times (T_{,z})^2 + 2\kappa_{r\theta}(r, \theta, z, \bar{T})T_{,r}T_{,\theta} + 2\kappa_{\theta z}(r, \theta, z, \bar{T})T_{,\theta}T_{,z} + 2r\kappa_{rz}(r, \theta, z, \bar{T})T_{,r}T_{,z}) - rQT)drdz + \int_{\partial A} (qT + (1/2)\alpha T^2)dc \right) d\theta = I(T) \quad (7)$$

where here again, $I(T)$ is subject to the auxiliary condition denoted by equation (6).

3 Finite Element Development

To develop the governing finite element approximation for the stated problem, the constrained functional representation depicted by equations (5) and (7) subject to (6) will be used to develop the requisite finite element equations for both the cartesian and axisymmetric problems.

For the cartesian formulation, taking the first variation of equation (5) subject to the constraint, equation (6), yields the following necessary minimizing criterion

$$\int_R (\kappa_{ij}(x_1, x_2, x_3, T)T_{,i}\delta T_{,j} - Q\delta T)dV + \int_{\partial R} (q\delta T + \alpha T\delta T)ds = 0 \quad (8)$$

Specializing equation (8) to the eth element yields

$$\int_{R_e} (\kappa_{eij}(x_1, x_2, x_3, T_e)T_{e,i}\delta T_{e,j} - Q_e\delta T_e)dV + \int_{\partial R_e} (q_e\delta T_e + \alpha_e T_e\delta T_e)ds = 0 \quad (9)$$

Following the traditional finite element development [6, 12], for the eth element, T is taken as

$$T_e = [N_e]\{\tau_e\} \quad (10)$$

where the shape function $[N_e]$ and the nodal temperatures $\{\tau_e\}$ have the form [12]

$$[N_e] = [N_{ek}, N_{el}, N_{em}, N_{en}, \ldots] \quad (11)$$

$$\{\tau_e\}^T = \{\tau_{ek}, \tau_{el}, \tau_{em}, \tau_{en}, \ldots\} \quad (12)$$

such that N_{ek} refer's to the kth node of the eth element. In terms of equation (10), δT_e and $T_{e,i}$ take the form

$$\delta T_e = [N_e]\delta\{\tau_e\} \quad (13)$$

$$T_{e,i} = [N_{e,i}]\{\tau_e\} \quad (14)$$

such that

$$\delta\{\tau_e\}^T = \{\delta\tau_{ek}, \delta\tau_{el}, \delta\tau_{em}, \delta\tau_{en}, \ldots\} \quad (15)$$

$$[N_{e,i}] = [N_{ek,i}, N_{el,i}, N_{em,i}, N_{en,i}, \ldots] \quad (16)$$

Using equations (13) to (16), equation (9) reduces to

$$\int_{R_e} (\kappa_{eij}(x_1, x_2, x_3, [N_e]\{\tau_e\})[N_{e,i}]\{\tau_e\}[N_{e,j}] \times \delta\{\tau_e\} - Q_e[N_e]\delta\{\tau_e\})dV + \int_{\partial R_e} (q_e[N_e]\delta\{\tau_e\}$$

Nomenclature

A = θ facial area of axisymmetric body
$\{F\}$ = inhomogeneity of equation (26)
$\{F_e\}$ = eth element counterpart of $\{F\}$, equation (19)
i = cartesian tensor index variable, ranges over 1, 2, 3
$I(t)$ = functional representation of conduction equation
j = same as i
$[J]$ = Jacobian operator
k = node number
$[K]$ = coefficient matrix of equation (26), independent of b.c.
$[K^*]$ = coefficient matrix of equation (26), function of b.c.
$[K_e]$, $[K_e^*]$ = eth element counterparts of $[K]$, $[K^*]$, see equation (19)
l,m,n = node numbers
n_i = components of normal to ∂R
$[N_e]$ = eth element shape function
$N_{ek}, N_{el}, \ldots$ = elements of $[N_e]$
q = surface flux input
q_e = surface flux input of eth element, defined on ∂R only
q_i = components of heat flux vector
Q = global heat generation
Q_e = eth element heat generation
r = radial coordinates (cylindrical)
R = region occupied by entire structure
R_e = region occupied by eth element
T = temperature
T_e = eth element temperature
$\bar{T}$ = constrained temperature
V = volume
x_1, x_2, x_3 = cartesian coordinates
z = axial coordinate (cylindrical)
α = boundary constant, defined on ∂R
α_e = boundary constant of eth element, defined on ∂R only
ΔT = change in temperature
δT, δT_e, $\delta\{\tau_e\}$ = variations of T, T_e, and $\{\tau_e\}$
θ = circumferential coordinate (cylindrical)
κ = conductivity tensor
κ_{ij} = component of conductivity tensor
κ_{eij} = component of conductivity tensor of eth element
$\kappa_{rr}, \kappa_{\theta\theta}, \ldots$ = component of conductivity tensor in cylindrical coordinates
$\{\tau\}$ = global column matrix denoting nodal temperatures
$\{\tau_e\}$ = eth element column matrix denoting nodal temperatures
τ_{ek}, τ_{el} = temperatures of kth and lth nodes
$\partial R, \partial R_e$ = surface areas of R and R_e
$(\ )_{,i}$ = partial differentiation
$[\ ]^{-1}$ = matrix inversion
$\{\ \}$ = column vector
$[\ ]$ = matrix
$[\ ]^T$ = transposed matrix

$$+ \alpha_e [N_e]\{\tau_e\}[N_e]\{\delta\tau_e\})ds = 0 \quad (17)$$

Since $\delta\tau_{ep}$; $p = k, l, m, n, \ldots$ are arbitrary variations, equations (17) reduces to

$$\int_{R_e} (\kappa_{eij}(x_1, x_2, x_3, [N_e]\{\tau_e\})N_{ep,j}[N_{e,i}]\{\tau_e\} - Q_e N_{ep})dV + \int_{\partial R_e} (q_e N_{ep} + \alpha_e N_{ep}[N_e]\{\tau_e\})ds = 0 \quad (18)$$

where $p = k, l, m, n, \ldots$

In matrix form, equation (18) may be rewritten as follows

$$[[K_e(\{\tau_e\})] + [K_e{}^*]]\{\tau_e\} = \{F_e\} \quad (19)$$

where the various elements of the matrices $[K_e(\{\tau_e\})]$, $[K_e{}^*]$ and $\{F_e\}$ have the form

$$K_{ekl}(\{\tau_e\}) = \int_{R_e} \kappa_{eij}(x_1, x_2, x_3, [N_e]\{\tau_e\})N_{ek,j}N_{el,i}dV \quad (20)$$

$$K_{ekl}{}^* = \int_{\partial R_e} \alpha_e N_{ek}N_{el}ds \quad (21)$$

$$F_{ek} = \int_{R_e} Q_e N_{ek}dV - \int_{\partial R_e} q_e N_{ek}ds \quad (22)$$

If the same procedure had been applied to equation (7) subject to equation (6), then the various elements of the matrices $[K_e(\{\tau_e\})]$, $[K_e{}^*]$ and $\{F_e\}$ would reduce to

$$\begin{aligned} K_{ekl}(\{\tau_e\}) = \int_{R_e} (& r\kappa_{err}(r,\theta,z,[N_e]\{\tau_e\})N_{ek,r}N_{el,r} \\ &+ (1/r)\kappa_{e\theta\theta}(r,\theta,z,[N_e]\{\tau_e\})N_{ek,\theta}N_{el,\theta} \\ &+ r\kappa_{ezz}(r,\theta,z,[N_e]\{\tau_e\})N_{ek,z}N_{el,z} \\ &+ \kappa_{er\theta}(r,\theta,z,[N_e]\{\tau_e\})N_{ek,r}N_{el,\theta} \\ &+ \kappa_{er\theta}(r,\theta,z,[N_e]\{\tau_e\})N_{ek,\theta}N_{el,r} \\ &+ \kappa_{e\theta z}(r,\theta,z,[N_e]\{\tau_e\})N_{ek,\theta}N_{el,z} \\ &+ \kappa_{e\theta z}(r,\theta,z,[N_e]\{\tau_e\})N_{ek,z}N_{el,\theta} \\ &+ r\kappa_{erz}(r,\theta,z,[N_e]\{\tau_e\})N_{ek,r}N_{el,z} \\ &+ r\kappa_{erz}(r,\theta,z,[N_e]\{\tau_e\})N_{ek,z}N_{el,r})drdzd\theta \end{aligned} \quad (23)$$

$$K_{ek}{}^* = \int_{\partial R_e} \alpha_e N_{ek}N_{el}ds \quad (24)$$

$$F_{ek} = \int_{R_e} Q_e N_{ek} r dr d\theta dz - \int_{\partial R_e} q_e N_{ek}ds \quad (25)$$

such that the basic matrix form of equation (19) remains unchanged.

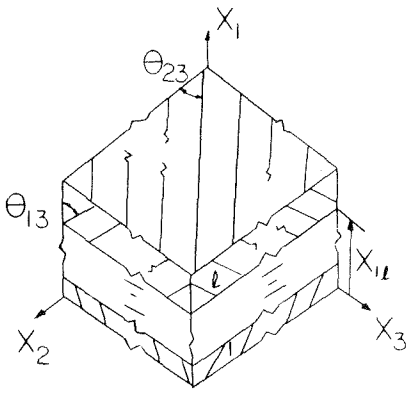

$$K_{11}^{(\ell)} = K_{22}^{(\ell)}$$

$$K_{11}^{(\ell)}/K_{33}^{(\ell)} = .1526$$

Fig. 1 Slab geometry

For the overall structure, the assembly of the local element equations, (19), yields the following global set

$$[[K(\{\tau\})] + [K^*]]\{\tau\} = \{F\} \quad (26)$$

where $[K(\{\tau\})]$, $[K^*]$, $\{\tau\}$ and $\{F\}$ represent the global counterparts of the local set.

Considering structures for which τ_{ij} (x_1, x_2, x_3, T) is only weakly dependent on T, for conduction problems for which ΔT is small, the cartesian and cylindrical forms of equations (19), (20), (23), and (26) reduce to

$$[K_e(\{\tau_e\})] \to [K_e] \quad (27)$$

$$K_{ekl} \to \int_{R_e} K_{eij}(x_1, x_2, x_3)N_{ek,j}N_{el,i}dV \quad (28)$$

$$\begin{aligned} K_{ekl} \to \int_{R_e} (& r\kappa_{err}(r,\theta,z)N_{ek,r}N_{el,r} \\ &+ (1/r)\kappa_{e\theta\theta}(r,\theta,z)N_{ek,\theta}N_{el,\theta} + r\kappa_{ezz}(r,\theta,z)N_{ek,z}N_{el,z} \\ &+ \kappa_{er\theta}(r,\theta,z)N_{ek,r}N_{el,\theta} + \kappa_{er\theta}(r,\theta,z)N_{ek,\theta}N_{el,r} \\ &+ \kappa_{e\theta z}(r,\theta,z)N_{ek,\theta}N_{el,z} + \kappa_{e\theta z}(r,\theta,z)N_{ek,z}N_{el,\theta} \\ &+ r\kappa_{erz}(r,\theta,z)N_{ek,r}N_{el,z} + r\kappa_{erz}(r,\theta,z)N_{ek,z}N_{el,r})drdzd\theta \end{aligned} \quad (29)$$

$$[K(\{\tau\})] \to [K] \quad (30)$$

Due to the essentially quadratic nature of the constrained functional representation depicted by equations (5) and (6), equivalent results, equations (26) to (30), would have been obtained through the use of Galerkin's procedure [12].

4 Nonlinear Algorithm

Considering constructions for which κ_{ij} (x_1, x_2, x_3, T) is temperature dependent, the global matrix equation given by equation (26) is nonlinear since $[K_e(\{\tau\})]$ and thus $[K(\{\tau\})]$ are dependent on the nodal temperatures. For the present paper these equations are solved using the general and modified forms of Newton's method [12]. The algorithms used take the following forms:

(i) general algorithm;

$$\{\tau_r\} = \{\tau_{r-1}\} - [J(\{\tau_{r-1}\})]^{-1}\{G(\{\tau_{r-1}\})\} \quad (31)$$

(ii) modified algorithm;

$$\{\tau_r\} = \{\tau_{r-1}\} - [J(\{\tau_s\})]^{-1}\{G(\{\tau_{r-1}\})\} \quad (32)$$

$$r - 1 > s$$

where $\{G(\{\tau_{r-1}\})\}$ and the Jacobian operators $[J(\{\tau_{r-1}\})]$ and $\{J(\{\tau_s\})\}$ are given by

$$[J(\{\tau_{r-1}\})] = [J([[K(\{\tau_{r-1}\})] + [K^*]]\{\tau_{r-1}\})] \quad (33)$$

$$[G(\{\tau_{r-1}\})] = [[K(\{\tau_{r-1}\})] + [K^*]]\{\tau_0\} - \{F\} \quad (34)$$

and

$$[J(\{\tau_s\})] = [J([[K(\{\tau_s\})] + [K^*]]\{\tau_s\})] \quad (35)$$

respectively.

5 Discussion

To verify the numerical capabilities of the finite element approximations derived herein, several computer programs have been written. In developing these programs, the solution to the linearized version of equation (26) is obtained using the usual Gaussian elimination procedure. For the nonlinear version of equation (26), the general and modified Newton's algorithms given by equations (31) and (32) are used. For the sake of simplicity, triangular and brick elements are used for the numerical examples given herein.

The examples that are presented are intended to demonstrate the procedure juxtaposed with exact solutions [3, 6, 7] and to present several of the more important effects inherent to material

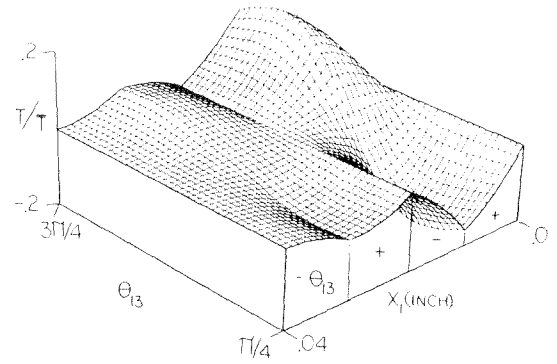

Fig. 2 Effects of θ_{13} on the $T(x_1, 0, L_2/2)$ field of an x_2 monoclinic four layered alternately plied slab

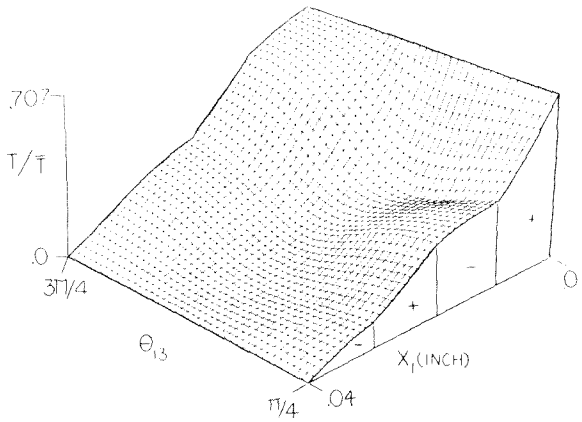

Fig. 3 Effects of θ_{13} on the $T(x_1, 0, L_2/4)$ field of an x_2 monoclinic four layered alternately plied slab

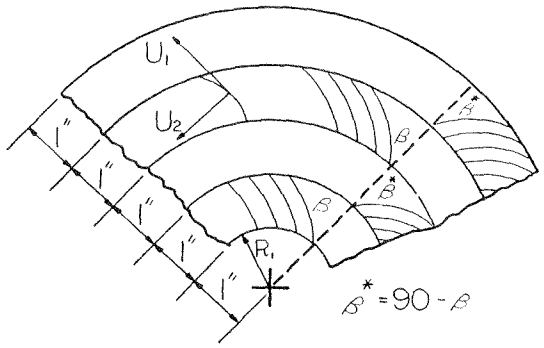

MATERIAL PROPERTIES

LAYER	$K^{(i)}_{U11}$	$K^{(i)}_{U22}$	$K^{(i)}_{U12}$
1	$10\frac{BTU}{HR°F-FT}$	$1\frac{BTU}{HR°F-FT}$	0
2	"	"	"
3	"	"	"
4	"	"	"

Fig. 4 Geometry of layered cylinder

anisotropy. For a generally anisotropic medium, since the principal coordinates usually do not line up with those used to describe the governing thermal equations, for the present paper, the usual second order tensor transformation law will be used to obtain the required conductivities.

5a Laminated Slab. Fig. 1 illustrates the geometry of a four layered slab with alternating plies composed of linear thermally anisotropic material whose principal orientation is described by

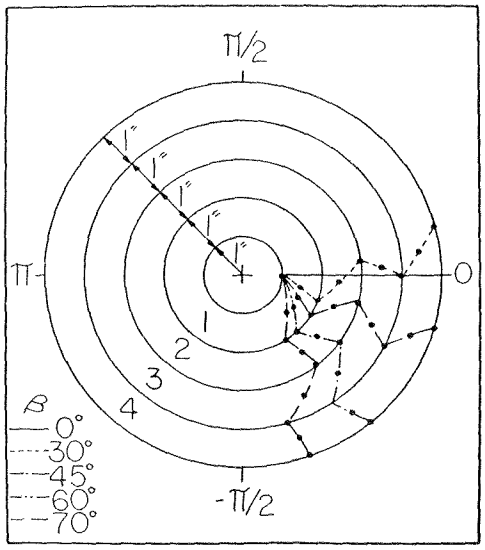

Fig. 5 Loci of maximum temperature

the angle θ. Considering that the slabs boundary conditions are given by

$$\text{at} \quad x_1 = x_{11}, \; T = \bar{T} \cos(\pi x_2/L_2) \cos(\pi x_3/L_3)$$

$$\text{at} \quad x_1 = x_{15}, \; T = 0; \quad L_2 = L_3 = 1 \tag{36}$$

Figs. 2 and 3 present the temperature profile obtained using the element procedure developed herein. These results compare favorably with the exact solution recently obtained by Padovan [7]. As can be seen from Figs. 2 and 3, significant topological redistributions may occur in the temperature field as the principal orientations of the various plies are altered.

5b Laminated Cylinder. Fig. 4 illustrates the geometry of a four layered cylinder with alternating plies composed of linear thermally anisotropic material whose principal orientation is described by the angle β. The thermal boundary conditions are given by

$$\text{at} \quad r = R_1, \; T = \bar{T} \cos\theta$$

$$\text{at} \quad r = R_5, \; T = 0 \tag{37}$$

Fig. 5 juxtaposes the loci of maximum temperature obtained using the element procedure derived herein and the known exact results [7]. The same loci were also obtained using a recently developed semi-analytical finite element procedure [6]. Here again, excellent agreement is found. As with the slab configuration, the effects of material anisotropy, $\beta \in (0, \pi/2)$, is typified by significant topological redistributions in the temperature field. Similar redistributions also occur in the flux field.

5c Cylinder With Eccentric Hole. To illustrate the capabilities of the element procedure with regard to nonlinear conductivity problems, the following comparison with a known exact solution is made. Fig. 6 shows the geometry of a long cylinder with an eccentric hole and whose inner and outer surfaces are maintained at 100 deg and 0 deg, respectively. The conductivity tensor of the cylinder is considered isotropic and proportional to $(1 + \epsilon T)$. Fig. 7 illustrates various aspects of the temperature field along with a comparison of the exact and the numerically generated solutions for several values of ϵ. As might be expected, to achieve the correct local temperature profiles, as ϵ increased, the numerical solution required an increasing number of iterations in order for the Newton's algorithm to converge to within the preselected accuracy. Importantly, although the number of required iterations increases, adequate convergence is obtained even for the exaggerated nonlinearity described in Fig. 7.

5d Anisotropic Cylinder. As a further illustration of the nonlinear capabilities of the element procedure, the following

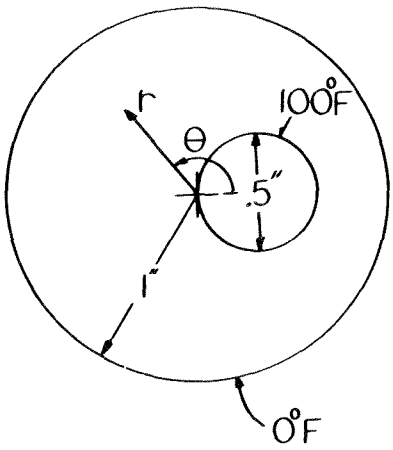

Fig. 6 Geometry of cylinder with eccentric hole

problem is considered. Fig. 8 illustrates the geometry of an anisotropic cylinder whose conductivity tensor has the form $(1 + \epsilon T)$ κ_{ij} and whose boundary conditions are defined by

$$r = R_i,\ R_0,\ q_r = 0$$
$$z = 0,\ T = 100 \cos 2\theta \tag{38}$$
$$z = L,\ T = 0$$

In terms of the principal conductivities defined in Fig. 8, Figs. 9 and 10 illustrate the midplane temperature field at $\theta = 0$ and $\pi/2$ for variations of the principal orientation β (see Fig. 8) in the interval $[0, \pi/2]$. The element generated results compare favorably with the "exact" solution obtained using Kirchhoff's transformation in conjunction with the recent developments given by [3, 6]. As can be seen from Figs. 9 and 10, the apparent material anisotropies caused by the β variations can create significant redistributions in the temperature field. Similar redistributions have also been reported recently by Padovan for linear materials [3, 6].

References

1 Carslaw, H. S., and Jaeger, J. C., *Conduction of Heat in Solids*, Second ed., Oxford Press, London, 1959.

2 Ozisik, M. N., *Boundary Value Problems of Heat Conduction*, International Textbook Co., Scranton, Pa., 1968.

3 Padovan, J., "Temperature Distributions in Anisotropic Shells of Revolution," *AIAA Journal*, Vol. 10, No. 1, Jan. 1972, p. 60.

4 Padovan, J., "Transient Temperature Distributions of an Anisotropic Half Space," *AIAA Journal*, Vol. 11, No. 4, Apr. 1973, p. 565.

5 Padovan, J., "Analysis of Heat Conduction in Anisotropic Axisymmetric Solids," presented at the Ninth Southeastern Seminar on Thermal Sciences, Old Dominion University, July, 1973, p. 17.

6 Padovan, J., "Quasi-Analytical Finite Element Procedure for Conduction in Anisotropic Axisymmetric Solids," *International Journal for Numerical Methods in Engineering*, Vol. 8, No. 2, 1974, p. 295.

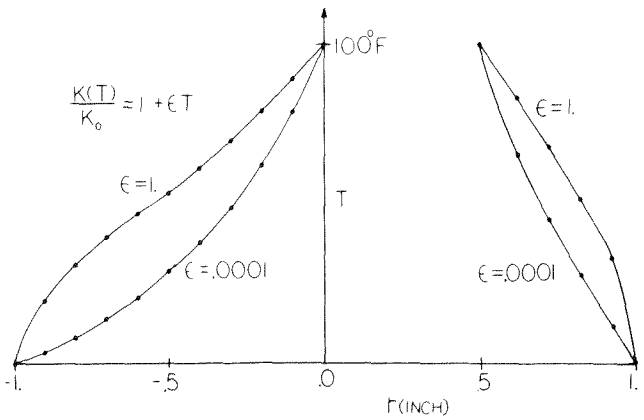

Fig. 7 Effects of ϵ on temperature profile

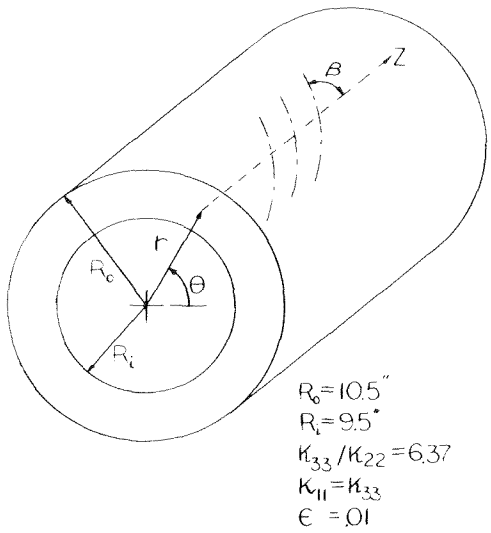

Fig. 8 Anisotropic cylinder geometry

7 Padovan, J., "Conduction in Anisotropic Composite Slabs and Cylinder," to be presented at the Fifth International Conference of Heat Transfer, Tokyo, Sept. 1974.

8 Chang, Y. P., Kang, C. S., and Chen, D. J., "The Use of Fundamental Green's Functions for the Solution of Problems of Heat Conduction in Anisotropic Media," *International Journal of Heat and Mass Transfer*, Vol. 16, 1973, p. 1905.

9 Tsou, C. H., and Chang, Y. P., "Moving Heat Sources in Anisotropic Solids," to appear in *Appl. Sci. Res.*

10 Visser, W., "A Finite Element Method for the Determination of Non-Stationary Temperature Distribution and Thermal Deformations," *Proc. Conf. on Matrix Methods in Structural Mechanics*, Air Force of Technology, Wright Patterson A. F. Base, Ohio, 1965.

11 Wilson, L. E., and Nickell, R. E., "Application of Finite Element Method to Heat Conduction Analysis," *Nuclear Engineering and Design*, Vol. 4, 1966, p. 1.

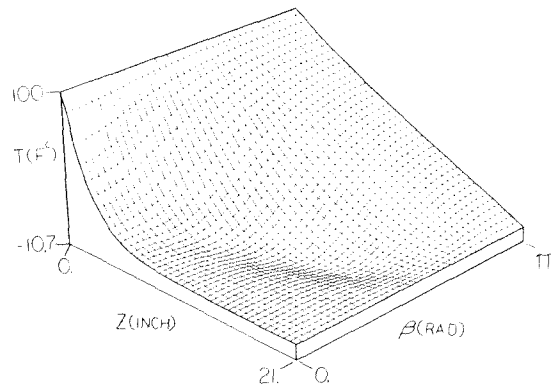

Fig. 9 Effects of fiber orientation on midplane temperature field for $\theta = 0$ deg

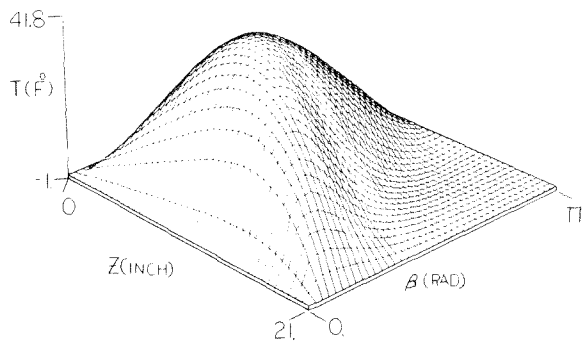

Fig. 10 Effects of fiber orientation on midplane temperature field for $\theta = \pi/4$

12 Zienkiewicz, O. C., *The Finite Element Method in Engineering Science*, McGraw-Hill, London, 1971.

13 Yalamanchili, R. V. S., and Chu, S. C., "Stability and Oscillation Characteristics of Finite-Element, Finite Difference, and Weighted-Residuals Methods for Transient Two-Dimensional Heat Conduction in Solids," JOURNAL OF HEAT TRANSFER, TRANS. ASME, Series C, Vol. 95, No. 2, May, 1973, p. 235.

14 Emery, A. F., "The Use of Singularity Programming in Finite Difference and Finite Element Computations of Temperature," JOURNAL OF HEAT TRANSFER, TRANS. ASME, Series C, Vol. 95, No. 3, Aug. 1973, p. 344.

15 Volker, R. W., "Nonlinear Flow in Porous Media by Finite Elements," *Proc. Am. Soc. Civ. Eng.*, Vol. 95, HY, 1969, p. 2093.

16 Ahmed, N. and Suneda, D. K., "Nonlinear Flow in Porous Media," *Proc. Am. Soc. Civ. Eng.*, Vol. 95, HY6, 1969, p. 1847.

17 Winslow, A. M., "Numerical Solution of the Quasi-Linear Poisson's Equation in a Nonuniform Triangle Mesh," *Journal of Computational Physics*, 1967, p. 149.

18 Courant, R., and Hilbert, D., *Methods of Mathematical Physics*, Interscience Publishes, New York, 1953.

19 Schechter, R. S., *The Variational Method in Engineering*, McGraw Hill, New York, 1967.

20 Eringen, A. C., *Mechanics of Continua*, Wiley, New York, 1967.

21 Onsager, L., "Reciprocal Relations in Irreversible Processes," *Physics Review* parts I and II, Vol. 37, 1931, p. 405 and Vol. 38, pp. 2265.

M. D. Burghardt
Engineering Department,
U. S. Merchant Marine Academy,
Kings Point, N. Y.

W. W. Bowley
Mechanical Engineering Department,
University of Connecticut,
Storrs, Conn.

Sublimation in a Porous Continuum Developed From Nonequilibrium Thermodynamics

The case of sublimation dehydration of a porous continuum is analyzed from the viewpoint of nonequilibrium thermodynamics. The general energy and mass transport equations are shown and the application of sublimation is illustrated.

A generalized approach to energy and mass transfer equations in a porous continuum has been developed [1].[1] The equations' development, as per reference [1], is briefly explained in the following section, and then the final equations for energy and mass transfer are applied to the case of sublimation.

General Development

Nonequilibrium thermodynamic analysis of a porous continuum affords insight into all factors affecting transfer within the continuum. By starting with the general equations of mass, momentum, and total energy for a continuous system and by using the boundary conditions of a porous continuum, the transfer equations evolve by the inspection of the entropy production of the system. The entropy production term will illustrate which forces and fluxes are involved in the transfer process,

$$\sigma = \sum_i \mathbf{J}_i \cdot \mathbf{X}_i \qquad (a)$$

where $\mathbf{J}_i$ are the fluxes and $\mathbf{X}_i$ are the forces. The fluxes are assumed to be a linear summations of the forces.

$$\mathbf{J}_i = \sum_j L_{ij} \mathbf{X}_j \qquad (b)$$

where L_{ij} are phenomenological coefficients which are determined experimentally. The entropy production may now be expressed in terms of the forces

$$\sigma = \sum_{i,j} L_{ij} \mathbf{X}_j \cdot \mathbf{X}_i \qquad (c)$$

The Onsager reciprocal relationships,

$$L_{ij} = L_{ji} \qquad (d)$$

will be used to simplify the number of unknown phenomenological coefficients.

The theoretical model which will be used is a macroscopic model, which considers the porous continuum and the fluid as two continua, and the properties are volume averaged to eliminate microscopic quantities, leaving macroscopic quantities to be analyzed. This model will be based on the fundamentals of nonequilibrium thermodynamics as presented by De Groot and Mazur [2]. The model is limited by the Onsager reciprocal relationships and the linear coupling of forces and fluxes. A paper by Luikov [3] illustrates conditions for which this linear coupling is invalid; however, the conditions must be extreme and the case of sublimation is not.

The conservation of mass for a fixed control volume may be written as

$$\frac{d\rho}{d\tau} = -\rho_k \operatorname{div} \mathbf{v} - \operatorname{div} \mathbf{J}_k \qquad (1)$$

where $\mathbf{v}$ is the barycentric velocity, $\mathbf{v} = \Sigma_{k=1}^{n} \rho_k \mathbf{v}_k / \rho$ and $\mathbf{J}_k$ is the barycentric flux of specie k, $\mathbf{J}_k = \rho_k(\mathbf{v}_k - \mathbf{v})$. If the mass fraction, $c_k = \rho_k/\rho$, is used, equation (1) becomes

$$\rho \frac{dc_k}{d\tau} = -\operatorname{div} \mathbf{J}_k \qquad (2)$$

The equation of motion may be written as

$$\frac{\partial(\rho \mathbf{v})}{\partial \tau} = -\operatorname{Div}(\rho \mathbf{v}\mathbf{v} + \underset{\approx}{P}) + \sum_{k=1}^{n} \rho_k \mathbf{F}_k \qquad (3)$$

where $\underset{\approx}{P}$ is the total pressure tensor and $\mathbf{F}_k$ is the force per unit mass exerted on component k. Equation (3) may be physically interpreted as a conservation for the momentum density, $\rho\mathbf{v}$, where $\rho\mathbf{v}\mathbf{v}$ is the convective part of the momentum flow $\rho\mathbf{v}\mathbf{v} + \underset{\approx}{P}$, and $\Sigma_{k=1}^{n} \rho_k \mathbf{F}_k$ is the source of momentum. The force per unit mass is not a function of time and may be expressed as the gradient of a scalar potential

$$\mathbf{F}_k = -\operatorname{grad} \psi_k \qquad (4)$$

The total pressure tensor, $\underset{\approx}{P}$, is to be considered a fluid pressure tensor, it may be separated into a scalar part, p, and a tensor part, $\underset{\approx}{\pi}$

$$\underset{\approx}{P} = \underset{\approx}{U} p + \underset{\approx}{\pi} \qquad (5)$$

p is the thermodynamic pressure, and $\underset{\approx}{\pi}$ is the viscous pressure tensor.

The change of kinetic energy with respect to time is

$$\frac{\partial(1/2\rho v^2)}{\partial \tau} = -\operatorname{div}(\frac{1}{2}\rho v^2 \mathbf{v} + \underset{\approx}{P} \cdot \mathbf{v}) + \underset{\approx}{P} : \operatorname{Grad}\mathbf{v} + \sum_{k=1}^{n} \rho_k \mathbf{F}_k \cdot \mathbf{v} \qquad (6)$$

and the change of potential energy density is

[1] Numbers in brackets designate References at end of paper.

Contributed by the Heat Transfer Division for publication in the JOURNAL OF HEAT TRANSFER. Manuscript received by the Heat Transfer Division, August 24, 1973. Paper No. 74-HT-DD.

$$\frac{\partial(\rho\psi)}{\partial\tau} = -\operatorname{div}\left(\sum_{k=1}^{n}\psi_k\mathbf{J}_k + \rho\psi\mathbf{v}\right) - \sum_{k=1}^{n}\mathbf{J}_k\cdot\mathbf{F}_k - \sum_{k=1}^{n}\rho\mathbf{F}_k\cdot\mathbf{v} \quad (7)$$

The total specific energy, e, is defined as

$$e = u + \psi + \frac{1}{2}v^2 \quad (8)$$

The total energy flux, $\mathbf{J}_e$ is defined as

$$\mathbf{J}_e = \rho e\mathbf{v} + \underset{\approx}{P}\cdot\mathbf{v} + \sum_{k=1}^{n}\psi_k\mathbf{J}_k + \mathbf{J}_q \quad (9)$$

where ρev is the convective energy flux; $P\cdot\mathbf{v}$ is the work of the surface forces; $\Sigma_{k=1}^{n}\psi_k\mathbf{J}_k$ is the transport of potential energy by diffusion; and $\mathbf{J}_q$ is the heat flux. By making an energy balance over the control volume one is able to develop an expression for the internal energy

$$\rho\frac{du}{d\tau} = \operatorname{div}\mathbf{J}_q - p\ \operatorname{div}\mathbf{v} - \underset{\approx}{\pi}:\operatorname{Grad}\mathbf{v} + \sum_{k=1}^{n}\mathbf{F}_k\cdot\mathbf{J}_k \quad (10)$$

The time rate of change of entropy within the control volume may be developed in terms of the entropy flux and entropy production and this is related to the equation expressing the dependence of entropy on internal energy, specific volume, and the mass fractions.

$$s = s(u, v, c_k) \quad (11)$$

$$ds = \frac{1}{T}du + \frac{P}{T}dv - \sum_{k=1}^{n}\frac{\mu_k}{T}dc_k \quad (12)$$

Since there is local equilibrium

$$\frac{Tds}{d\tau} = \frac{du}{d\tau} + P\frac{dv}{d\tau} - \sum_{k=1}^{n}\mu_k\frac{dc_k}{d\tau} \quad (13)$$

It is this step which brings an equilibrium equation to a nonequilibrium equation. The reason this step is allowed, is that the time necessary to establish local thermodynamic equilibrium is very much longer than the time between molecular collisions. The time between molecular collisions is a measure of the departure of the process from local thermodynamic equilibrium.

When equation (13) is compared to the equation derived for the time rate of change of entropy in a control volume, the expression for the entropy production may be deduced.

$$\sigma = -\frac{\mathbf{J}_q'}{T^2}\cdot\operatorname{grad}T - \frac{\mathbf{J}_i}{T}\cdot\sum_{k=1}^{n-1}\left(\frac{\mu_{kk}{}^c}{c_n}\operatorname{grad}c_k + (v_k - v_n)\operatorname{grad}p + \mathbf{F}_k - \mathbf{F}_n\right) + \frac{\underset{\approx}{\pi}}{T}:\operatorname{Grad}\mathbf{v} \quad (14)$$

By using the Curie principle that only fluxes and forces of even tensor order may couple, the entropy production may be written as the sum of two parts: the first part for the first-order fluxes and forces, and the second part for the second-order fluxes and forces.

$$\sigma = \sigma_1 + \sigma_2 \quad (15)$$

The equations of energy and mass transfer in a porous medium involve only first-order fluxes and forces, hence

$$\sigma_1 = -\frac{\mathbf{J}_q'}{T^2}\cdot\operatorname{grad}T - \frac{\mathbf{J}_i}{T}\cdot\sum_{k=1}^{n-1}\left(\frac{\mu_{kk}{}^c}{c_n}\operatorname{grad}c_k + (v_k - v_n)\operatorname{grad}p + \mathbf{F}_k - \mathbf{F}_n\right) \quad (16)$$

Volume averaging of microscopic parameters, such as density over an infinitesimal volume element, brings the microscopic continua to macroscopic continua. The volume element has been explicitly calculated by Whitaker [4]. An edge of the volume element must be at least ten times the characteristic length of the macroscopic continuum and must be much greater than ten times the characteristic length of the microscopic porous continuum. Since the microscopic model permits a characteristic length of 10^{-8} cm, a wide range of porosities is allowed. The properties of a porous continuum do not degenerate to a point, but only to a region defined by the characteristic length of the porous structure.

The volume averaging of any property, x, on the microscope level, to x' on the macroscopic level, is accomplished by integrating the property over an infinitesimal volume element:

$$x' = \lim_{v\to\delta v}\frac{\int_v x\,dv}{\int_v dv} \quad (17)$$

Equation (16) becomes

$$\langle\sigma_1\rangle = -\frac{\mathbf{J}_1''}{T^2}\cdot\operatorname{grad}T - \frac{\mathbf{J}_i'}{T}\cdot\sum_{k=1}^{n-1}\left(\frac{\mu_{kk}{}^x}{x_n}\operatorname{grad}x_k + (v_k - v_n)\operatorname{grad}p' + (\mathbf{F}_k' - \mathbf{F}_n')\right) \quad (18)$$

The body force on the solid specie is the only term which remains to be evaluated. This is the force which holds the solid particles in place under a pressure gradient. This is calculated by using the equation of motion with the condition of negligible acceleration, yielding a relationship between the body force and the fluid pressure tensor.

$$0 = -\operatorname{Div}\underset{\approx}{P} + \rho_2\mathbf{F}_2 \quad (19)$$

Nomenclature

V = volume
A = surface area
τ = time
ρ_k = specie density
$\mathbf{v}_k$ = specie velocity
ρ = total density
$\mathbf{v}$ = barycentric velocity
$\mathbf{J}_k$ = flux of specie relative to the center of gravity
c_k = mass fraction of specie k
v = specific volume
$\mathbf{P}$ = total pressure tensor
$\mathbf{F}_k$ = external force exerted on specie k
ψ_k = potential energy of component k
e = total specific energy
u = specific internal energy
$\mathbf{J}_e$ = total energy flux
$\mathbf{J}_q$ = heat flux
p = thermodynamic pressure
$\underset{\approx}{\pi}$ = viscous pressure tensor
T = absolute temperature
s = entropy per unit mass
σ = entropy production
$\mu_{ii}{}^c = (\partial\mu_i/\partial c_i)_{T,p,c_j}$
μ_k = chemical potential of specie k
$\mathbf{J}_q'$ = reduced heat flux
L_{ik} = phenomenological coefficients
σ_1 = first order entropy production
σ_2 = second order entropy production
$\langle\sigma_1\rangle$ = volume averaged first order entropy production
t = volume averaged temperature
x_i = volume averaged mass fraction of specie i
γ_i = volume averaged density of specie i
ν_i = volume averaged specific volume of specie i
$\mathbf{w}_k$ = volume averaged velocity of specie k
$\mathbf{J}_q''$ = volume averaged reduced heat flux
$\mathbf{J}_i'$ = volume averaged barycentric mass flux of specie i
p' = volume averaged pressure
$\mu_{ii}{}^x$ = volume averaged $\mu_{ii}{}^c$
$\mathbf{F}_i'$ = volume averaged external force on specie i
$\mathbf{P}'$ = volume averaged pressure tensor
$\underset{\approx}{\pi}'$ = volume averaged viscous pressure tensor
μ = viscosity
μ_T = Joule-Thompson coefficient
κ = permeability
λ = coefficient of thermal conductivity
D = diffusion coefficient
D' = thermal diffusion coefficient
D'' = Dufour diffusion coefficient
R = ideal gas constant
a = interface position
c = unknown constant
c_p = specific heat
γ_m = ratio of ice density to vapor density at the subliming interface
α = thermal diffusivity
β = porosity
γ_s = density of ice
η = dimensionless coordinate
x = coordinate direction
t^* = dimensionless temperature
torr = one mm Hg

Equation (19) may be simplified to yield for the condition of incompressibility and with volume averaging.

$$\gamma_2 \mathbf{F}_2' = \text{grad}\, p' - 2\mu \,\text{Div Grad}\, \mathbf{w} \tag{20}$$

The velocity is a function of the gradient of the pressure, the second term on the right-hand side of equation (20) is two orders of magnitude less than the first term. If the body force is then assumed to be just a function of the gradient of the pressure, the entropy production becomes for $n = 2$

$$\langle \sigma_1 \rangle = -\frac{\mathbf{J}_q''}{l^2} \cdot \text{grad}\, l - \frac{\mathbf{J}_1'}{l} \cdot \left(\frac{\mu_{11}{}^x}{x_2} \text{grad} x_1 + \nu_1 \,\text{grad} p' \right) \tag{21}$$

Thus, using the Onsager relationships, and the linear coupling of forces:

$$\mathbf{J}_q'' = -\frac{L_{qq}}{l^2} \text{grad}\, l - \frac{L_q'}{l} \left(\frac{\mu_{11}{}^x}{x_2} \text{grad} x_1 + \nu_1 \text{grad} p' \right) \tag{22}$$

$$\mathbf{J}_1' = -\frac{L_{1q}}{l^2} \text{grad}\, l - \frac{L_{11}}{l} \left(\frac{\mu_{11}{}^x}{x_2} \text{grad} x_1 + \nu_1 \text{grad} p' \right) \tag{23}$$

Recalling equations (2) and (9) on the volume averaged basis

$$\frac{dx_1}{d\tau} = -\frac{1}{\gamma} \,\text{div}\, \mathbf{J}_1' \tag{24}$$

$$\gamma \frac{dH}{d\tau} = -\text{div}\, \mathbf{J}_q'' - \underset{\approx}{\pi}'' \cdot \text{Grad}\, \mathbf{w} - \mathbf{w} \cdot \text{grad} p' \tag{25}$$

If Darcy's law is used for the velocity distribution, $\mathbf{w} = x/\mu \cdot \text{grad}\, p'$, the equations for energy and mass transfer become

$$\gamma \frac{dH}{d\tau} = \text{div}[\lambda \,\text{grad}\, l + D'' \gamma l (x_1 \mu_{11}{}^x \,\text{grad} x_1 + x_1 x_2 \nu_1 \text{grad}\, p')] + \frac{x^2}{2\mu} \left(\frac{\partial^2 p'}{\partial x^i \partial x^j} \right) + \frac{x}{\mu} (\text{grad} p')^2 \quad i \neq j \quad i, j = 1,2,3 \tag{26}$$

and

$$\frac{dx_1}{d\tau} = \text{div}[D' x_1 x_2 \text{grad}\, l + D\gamma \,\text{grad} x_1 + \frac{\gamma x_2 \nu_1}{\mu_{11}{}^x} D \,\text{grad} p'] \tag{27}$$

Application to Sublimation

In the freeze-drying process, the product is frozen quickly at a low temperature. The ice crystals formed by low temperature freezing do not expand and rupture the material structure of the product as would happen if the freezing were done slowly. After the product is frozen, it is placed in a vacuum chamber where the absolute pressure is less than the absolute pressure at the triple point of water (less than 4.58 torr). The water in the product will slowly sublime in order to achieve thermodynamic equilibrium. This natural subliming process under a partial pressure gradient is a very slow process. The subliming rate may be increased by using a radiant heater to raise the temperature of the product's surface. Thus, there is a coupled process of energy and mass transfer in a porous medium.

The general equations in the development may be written in terms of the volume averaged temperature and mass fraction by noting that $du = c_v\, dt$, equations (26) and (27) become

$$\gamma c_v \frac{dt}{d\tau} = \text{div}[\lambda \,\text{grad}\, l + D'' \gamma l (x_1 \mu_{11}{}^x \text{grad} x_1 + x_1 x_2 \nu_1 \text{grad} p')] + \frac{x^2}{2\mu} \left(\frac{\partial^2 p'}{\partial x^i \partial x^j} \right) + \frac{x}{\mu} (\text{grad} p')^2 \quad i \neq j \quad i, j = 1,2,3 \tag{28}$$

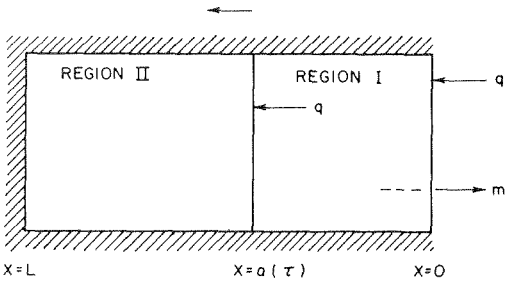

Fig. 1 Schematic diagram of porous material with heat and mass flows

and

$$\frac{dx_1}{d\tau} = \text{div}[D' x_1 x_2 \,\text{grad}\, l + D\gamma \,\text{grad} x_1 + \frac{\gamma x_2 \nu_1}{\mu_{11}{}^x} D \text{grad} p'] \tag{29}$$

In this case the "2" species is the solid stationary species and the "1" species is the subliming water vapor.

If the equation of state of an ideal gas is used

$$p' = \gamma x_1 R l \tag{30}$$

equations (28) and (29) become

$$\gamma c_v \frac{dt}{d\tau} = \text{div}[\lambda \,\text{grad}\, l + D'' \gamma l (x_1 \mu_{11}{}^x - x_1 R l + R l) \text{grad} x_1] + \frac{\gamma R l x^2}{2\mu} \left(\frac{\partial^2 x_1}{\partial x^i \partial x^j} \right) + \frac{x \gamma R l}{\mu} (\text{grad} x_1)^2 \quad i \neq j \quad i, j = 1,2,3 \tag{31}$$

and

$$\frac{dx_1}{d\tau} = \text{div}[D' x_1 x_2 \,\text{grad}\, l + D\left(1 + \frac{Rl}{\mu_{11}{}^x x_1} - \frac{Rl}{\mu_{11}{}^x}\right) \text{grad} x_1] \tag{32}$$

where the identity $x_1 + x_2 = 1$ has been used.

For constant pressure the diffusion coefficients are essentially constant and not a function of distance. However, the diffusion coefficients are strongly dependent on pressure, and would in general, not be constant for flow with a pressure gradient. The flow regime for the vapor is in the transitional region where there is both bulk and diffusional flow. An analogy may be made between the diffusion coefficients and wall shearing stress in a fluid. The equivalent wall shearing stress may be computed for a constant pressure gradient and will be constant for this gradient. An analogous method may be applied to diffusion coefficients for a given pressure gradient. Dyer and Sunderland [5] have suggested a method for doing this. This fact should be borne in mind when evaluating the diffusion coefficients. Both effects contribute to the flow and both effects should be accounted for, and an effective diffusion coefficient is developed in reference [5]. Fox and Thomson [6] also note that two flow regimes may exist and an effective diffusion coefficient may be used to describe this motion. Since this model is macroscopic, the use of effective values is necessary; if the continuum were left on the microscopic level such would not be the case. The value of the effective diffusion coefficient may be found from reference [5]. The use of effective diffusion coefficients determined from experimental results increases the accuracy of the model. The diffusion coefficients were measured in a situation where air was present in the porous structure, thus the effective values include the effect air had on the diffusion process, without inclusion of another specie flux in the analysis. The subliming interface is assumed to move as time to the one-half. Dyer and Sunderland [7] have noted this to be an accurate approximation.

The position of interface is then

$$\alpha(\tau) = c\tau^{1/2} \tag{33}$$

where $\alpha(\tau)$ is the interface position and c is a constant to be determined by an energy balance of the dried porous region, region I in Figs. 1 and 2.

The energy balance of the dried porous region is

The energy into the porous region = The energy into the ice region + The latent heat of sublimation + The energy in the dry porous region (34)

$$-\lambda_1 \left. \frac{\partial t}{\partial x} \right|_{x=0} = -\lambda_2 \left. \frac{\partial t}{\partial x} \right|_{x=\alpha(\tau)} + \gamma_{si} \beta \Delta H c \alpha^{1/2} + c_v \gamma_{si} \beta c \alpha^{1/2} (t_{avg} - t_a) \tag{35}$$

where γ_s is the density of the ice and β is the porosity. The average temperature must be used in evaluating the energy stored above the datum in region 1. For constant temperature in region II, the solid frozen region, and using the transform, $\eta = x/2\sqrt{\alpha\tau}$, the boundary conditions become

$$-\lambda_1 \left. \frac{dt}{d\eta} \right|_{\eta=0} = -\gamma_{si} \beta \Delta H c \alpha^{1/2} + c_v \gamma_{si} \beta c \alpha^{1/2} (t_{avg} - t_a) \tag{36}$$

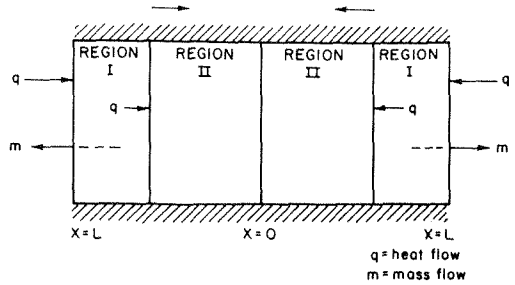

Fig. 2 Complete one-dimensional model of porous material with heat and mass flows

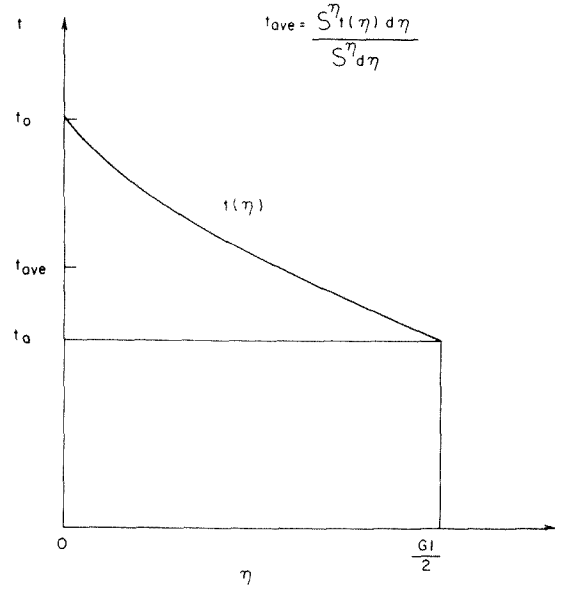

Fig. 3 Diagram of the average temperature in region I

The other two boundary conditions are

$$\eta = 0 \qquad \begin{matrix} t = t_0 \\ x_1 = x_1{}^0 \end{matrix} \tag{37}$$

$$\eta = \frac{c}{2\alpha^{1/2}} \qquad \begin{matrix} t = t_a \\ x_1 = x_1{}^a \end{matrix} \tag{38}$$

The boundary conditions and the equations for energy and mass transfer are not in their optimum form; the following dimensionless coefficients will be used

$$\begin{aligned} t^* &= t/t_0 & Bb &= \mu_{11}{}^x/c_v t_0 & Sd &= \frac{c_v \gamma_s \alpha (t_{arc} - t_a)}{\lambda_1 t_0} \\ Lu &= D/\alpha & \eta &= \eta & \beta &= \beta \\ \mathrm{St} &= D' t_0/D = D'' t_0/D & x_1 &= x_1 & Rc &= R/c_v \\ GI &= c/\alpha^{1/2} & Pa &= \Delta H \gamma_s \alpha/\lambda_1 t_0 & Db &= \frac{x\gamma R t_0}{\mu\alpha} \\ & & Rb &= R t_0/\mu_{11}{}^x \end{aligned} \tag{39}$$

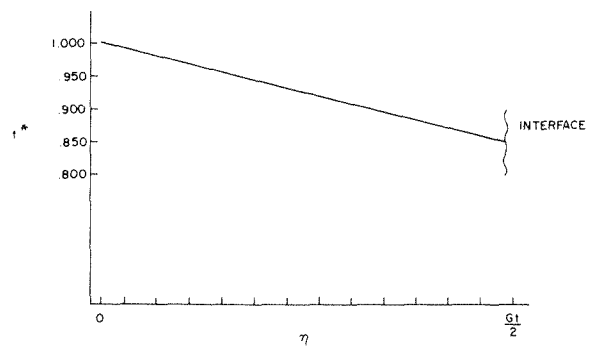

Fig. 4 The dimensionless temperature distribution in region I for the coupled equations with a total pressure gradient

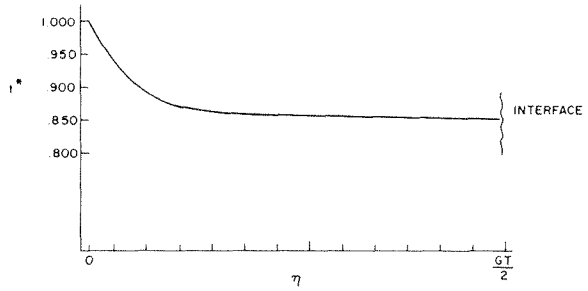

Fig. 5 Dimensionless temperature distribution with porous medium for the uncoupled case

The boundary conditions become

$$\eta = 0 \qquad \begin{matrix} t^* = 1 \\ x_1 = \dfrac{\gamma_1}{\gamma_1 + \gamma_2} \end{matrix} \tag{40}$$

$$\eta = \frac{GI}{2} \qquad \begin{matrix} t^* = t_a/t_0 \\ x_1 = \dfrac{\gamma_1}{\gamma_1 + \gamma_2} \end{matrix} \tag{41}$$

$$GI = -\left.\frac{dt^*}{d\eta}\right|_{\eta=0} / \beta(Sd - Pa) \tag{42}$$

and equations (27) and (28) become

$$\begin{aligned} &\frac{d^2t^*}{d\eta^2} + Lu\,\mathrm{St}\,Bbt^* x_1 \frac{d^2x_1}{d\eta^2} + Lu\,\mathrm{St}\,Bbt^* \left(\frac{dx_1}{d\eta}\right)^2 \\ &\quad + Lu\,\mathrm{St}\,Bbx_1 \frac{dt^*}{d\eta}\frac{dx_1}{d\eta} - Lu\,\mathrm{St}\,Rcx_1 (t^*)^2 \frac{d^2x_1}{d\eta^2} \\ &\quad - 2Lu\,\mathrm{St}\,Rcx_1 t^* \frac{dt^*}{d\eta}\frac{dx_1}{d\eta} - Lu\,\mathrm{St}\,Rct^* \left(\frac{dx_1}{d\eta}\right)^2 \\ &+ Lu\,\mathrm{St}\,Rc(t^*)^2 \frac{d^2x_1}{d\eta^2} + 2Lu\,\mathrm{St}\,Rct^* \frac{dt^*}{d\eta}\frac{dx_1}{d\eta} + DbRc(t^*)^2 \left(\frac{dx_1}{d\eta}\right)^2 \\ &\quad + Dbt^* \frac{dx_1}{d\eta} + 2\eta \frac{dt^*}{d\eta} = 0 \end{aligned} \tag{43}$$

$$\begin{aligned} &\mathrm{St}\,x_1 \frac{d^2t^*}{d\eta^2} + \mathrm{St}\,\frac{dx_1}{d\eta}\frac{dt^*}{d\eta} - \mathrm{St}(x_1)^2 \frac{d^2t^*}{d\eta^2} - 2\,\mathrm{St}\,x_1 \frac{dx_1}{d\eta}\frac{dt^*}{d\eta} + \frac{d^2x_1}{d\eta^2} \\ &\quad + \frac{Rbt^*}{x_1}\frac{d^2x_1}{d\eta^2} + \frac{Rb}{x_1}\frac{dt^*}{d\eta}\frac{dx_1}{d\eta} - \frac{Rb}{(x_1)^2}\left(\frac{dx_1}{d\eta}\right)^2 - Rbt^* \frac{d^2x_1}{d\eta^2} \\ &\quad - Rb\frac{dt^*}{d\eta}\frac{dx_1}{d\eta} + \frac{Dbt^*}{Lu}\left(\frac{dx_1}{d\eta}\right)^2 + \frac{2\eta}{Lu}\left(\frac{dx_1}{d\eta}\right) = 0 \end{aligned} \tag{44}$$

Equations (43) and (44) have been programmed on an IBM 360 using a modified Newton-Rapson inversion technique [8]. From the computer solutions the effect each dimensionless coefficient had on the interface position was obtained. Also, the temperature distribution was obtained for the coupled equations with a total pressure gradient. Because of the marked increase in the number of terms when the entire equation for energy transfer is used, it is difficult to assess the physical meaning to the difference between the dimensionless temperature distribution for the coupled equations, Fig. 4, and that for the uncoupled heat equation, Fig. 5.

The effect the thermal diffusivity and porsity have on the subliming interface position is illustrated in Fig. 6. If the porosity increases, the rate of the interface movement decreases as there is more ice per unit volume which has to sublime. Also, the void space in the dried section increases and the effective thermal conductivity of the section decreases, lowering the heat transfer to the interface.

In Fig. 7, the plot of the minimum and maximum interface position versus time is plotted. This illustrates the degree of variance which can be expected. To obtain the minimum and maximum plots, the dimensionless coefficients were varied about by a factor of ten. The effect the dimensionless coefficients have on the interface position was then determined.

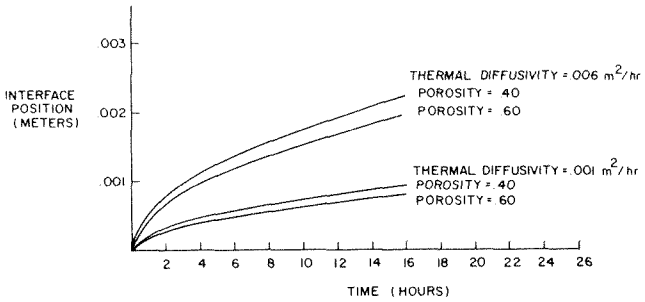

Fig. 6 A comparison of the interface position for the uncoupled case at two different porosities and thermal diffusivities

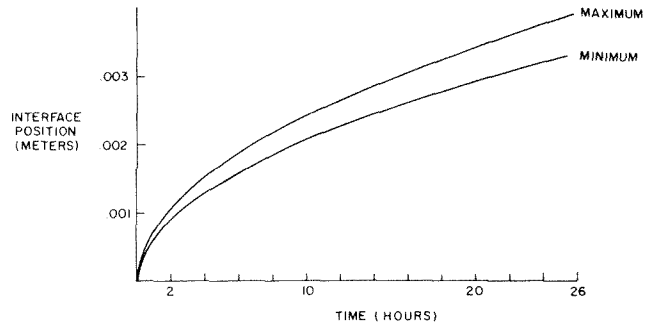

Fig. 7 A comparison of the maximum and minimum interface position for the coupled equations with a total pressure gradient

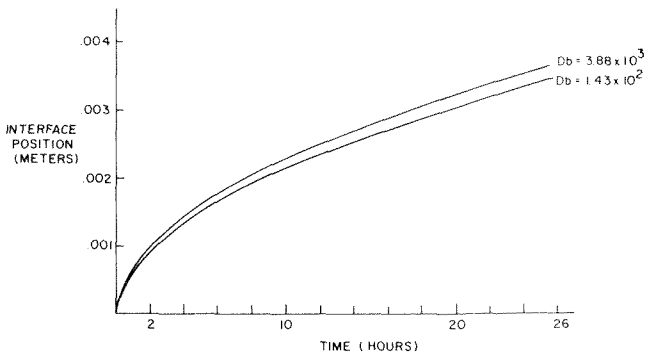

Fig. 8 A comparison of the interface position at different values of *Db*

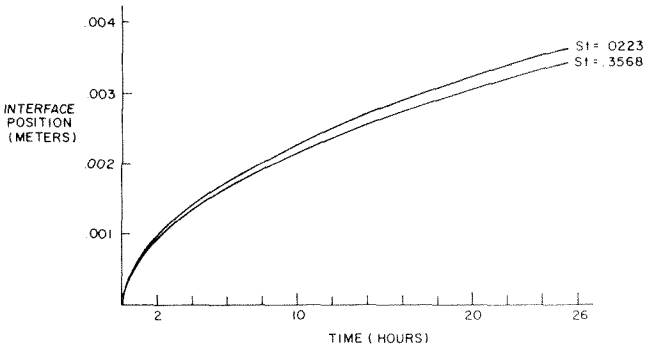

Fig. 9 The interface position at different values of St

For example, the dimensionless number, *Db*, increases and the interface movement increases; this is because *Db* indicates the ease with which the fluid flows through the porous material. The easier it can flow through, the greater the sublimation. The effect of St on the interface position is because of the relative change in the thermal diffusion coefficient, *D*.

The heat flux has a primary driving force, the thermal diffusivity times the gradient of the temperature and a secondary force, the thermal diffusion coefficient times the gradient of the mass fraction. In this case the mass fraction gradient is opposite to the temperature gradient, so an increase in the thermal diffusion coefficient acts to reduce the heat flux and hence the interface movement. The other dimensionless numbers act in a similarly predictable manner.

The application of the generalized equations of energy and mass transfer to the problem of sublimation illustrates interesting effects: one, the number of terms which must be included in coupled equations dramatically shows the simplifications involved when the uncoupled heat transfer equation is used; two, the effect the secondary terms have on the sublimation is calculable. Additionally, since the secondary terms are calculable, it should be possible to determine an optimum sublimation condition if another gas is diffusing in the direction of their temperature gradient against the vapor flow. Such a procedure has been experimentally accomplished by Kan and deWinter [9]. However, the values of the diffusion coefficients, thermal, mutual, and self will probably be extremely difficult to determine.

An important advantage in choosing a "thermodynamic" model is that it incorporates all the transport phenomena and their cross effects. At times, the cross-effects are not predominant and may be neglected. This is what the simplified analysis have done without proven justification. An example, which was illustrated, is the Soret and Dufour effect. Under a concentration gradient, a heat flux will result even with isothermal initial conditions. This is because the heat flux is a function, in part, of the concentration as well as the temperature. The primary cause of a heat flux is a temperature gradient, but at times the other cross-effects should be included in the formulation. It is known that the effect of concentration on a heat flux is quite small, usually not more than 5 percent of the total flux. However, as the main driving force decreases, the cross-effects become important. Similarly, at very high transfer rates, the cross phenomena could again contribute significantly to the transfer process. The magnitude of these effects has been illustrated for the case of sublimation in a porous continuum.

References

1 Burghardt, M., David, and Bowley, Wallace W., "A Non-Equilibrium Thermodynamic Development of Energy and Mass Transfer in a Porous Medium," *Powder Technology*, Vol. 6, 1972.

2 DeGroot, S. R., and Mazur, P., *Non-Equilibrium Thermodynamics*, North-Holland, Amsterdam, 1963.

3 Luikov, A. V., "Application of Irreversible Thermodynamic Methods to Investigation of Heat and Mass Transfer," *International Journal of Heat and Mass Transfer*, Vol. 7, 1966, pp. 139–152.

4 Whitaker, S., "The Equation of Motion in Porous Media," *Chem. Eng. Sci.*, 21 (1966) 291–300.

5 Dyer, D. F., and Sunderland, J. E., "Bulk and Diffusional Transport in the Region Between the Molecular and Viscous Flow," *International Journal of Heat and Mass Transfer*, Vol. 8, 1966, pp. 519–526.

6 Fox, E. C., and Thomson, W. J., "Coupled Heat and Mass Transport in Unsteady Sublimation Drying," *AIChE Journal*, Vol. 18, 1972, pp. 792–797.

7 Dyer, D. F., and Sunderland, J. E., "The Transient Temperature Distribution During Sublimation Dehydration," JOURNAL OF HEAT TRANSFER, TRANS. ASME, Series C, Vol. 89, 1967.

8 Burghardt, M. David, "A Non-Equilibrium Thermodynamic Analysis of Sublimation in a Porous Medium," PhD thesis, University of Connecticut, 1971.

9 Kan, B., and deWinter, F., "Accelerating Freeze-Drying Through Improved Heat Transfer," *Food Technology*, Vol. 22, 1968.

J. C. Y. Koh
Aerospace Group,
The Boeing Co.,
Seattle, Wash.

R. Colony
Boeing Computer Service, Inc.,
Seattle, Wash.

Analysis of Cooling Effectiveness for Porous Material in a Coolant Passage

An analytical investigation of the performance of a heat exchanger containing a conductive porous media was made. The partial differential equations governing the steady-state temperature distributions for both the porous media and the coolant fluid are given. A method for obtaining an approximate solution of the governing equations is shown. A computer program was written in FORTRAN IV and the results are provided for determining the cooling effectiveness.

Introduction

In a high temperature environment, the structural integrity of a body may be maintained by proper cooling such as convection cooling or mass transfer cooling. The latter cooling scheme includes ablation, transpiration, and film cooling. Mass transfer cooling is suitable for the thermal protection of a structure exposed to an extremely high heat flux environment such as that of a re-entry vehicle. Convection cooling is suitable for a relatively low heat flux environment such as that of a conventional rocket nozzle. The limitation of convection cooling to the low heat flux environment is due to the slow heat transfer rate from the wall to a coolant. Thus, if convective cooling is attempted for a high heat flux environment, the heat transfer from the environment to the wall, at maximum allowable wall temperature, would be significantly higher than the heat removed from the wall by the coolant, resulting in thermal damage to the structure. This limitation may be partially overcome by inserting a high conductivity porous material in the coolant passage (Fig. 1). This will significantly increase the heat transfer area and, therefore, increase the heat transfer from the wall to the coolant. Also, the temperature difference between the wall and the coolant would be significantly reduced. In view of the high heat transfer area between the porous material and the coolant per unit volume, this arrangement may be considered as a super compact heat exchanger. The purpose of this report is to present an analysis of the temperature distribution in this super heat exchanger. From the temperature distribution, the enhancement of cooling effectiveness due to the presence of the porous material will be determined.

Analysis

Physical Model. The physical model is sketched in Fig. 1. A two-dimensional channel is exposed to the external heat flux $q_0(x)$ on one wall and $q_1(x)$ on the other wall. The heat flux is removed by passing a coolant at a flow rate of $\dot{m}$ through the porous material in the channel. In the case of convective cooling for the thermal protection of a rocket nozzle, $q_1(x)$ would be zero and $q_0(x)$ would be the heat transfer from the combustion gas to the nozzle wall. In the case of a heat exchanger, either q_0 or q_1 or both could be the heat transfer from the hot stream to the channel wall. For this analysis, it will be assumed that both $q_0(x)$ and $q_1(x)$ are prescribed. Our purpose then is to calculate the temperature distribution in the porous material and the coolant.

Governing Equations. It will be assumed that the flow is steady and the channel width δ is small in comparison with the length such that the coolant flux is independent of location. In addition, it will be assumed that the gas conduction is negligibly small in comparison with the porous material conduction. Furthermore, property values will be taken as constant. Thus, the temperature distributions are governed by the following energy equations:

$$\dot{m}c_p \frac{\partial T_g}{\partial X} = h'(T_m - T_g) \tag{1}$$

$$k \frac{\partial^2 T_m}{\partial X^2} + k \frac{\partial^2 T_m}{\partial Y^2} = h'(T_m - T_g) \tag{2}$$

The boundary conditions are:

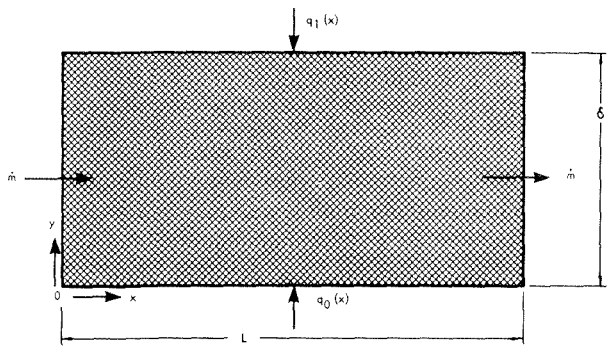

Fig. 1 Physical model

Contributed by the Heat Transfer Division for publication in the JOURNAL OF HEAT TRANSFER. Manuscript received by the Heat Transfer Division, October 30, 1973. Paper No. 74-HT-KK.

At $x = 0$

$$k \frac{\partial T_m}{\partial x} = 0, \; T_g = T_g^0, \tag{3a,b}$$

At $x = 0$

$$-k \frac{\partial T_m}{\partial y} = q_0(x) \tag{3c}$$

At $y = \delta$

$$k \frac{\partial T_m}{\partial y} = q_1(x) \tag{3d}$$

At $x = L$

$$k \frac{\partial T_m}{\partial x} = 0 \tag{3e}$$

Equations (1), (2), and (3) are rewritten in the following dimensionless forms:

$$\frac{\partial \theta_g}{\partial \xi} = A^*(\theta_m - \theta_g) \tag{4}$$

$$\frac{\partial^2 \theta_m}{\partial \xi^2} + \frac{\partial^2 \theta_m}{\partial \eta^2} = B^*(\theta_m - \theta_g) \tag{5}$$

At $\xi = 0$

$$\frac{\partial \theta_m}{\partial \xi} = 0, \; \theta_g = 0 \tag{6a,b}$$

at $\eta = 0$

$$-\frac{\partial \theta_m}{\partial \eta} = q_0^*(\xi) = q_0(\delta\xi)\left[\frac{\delta}{KT^*}\right] \tag{6c}$$

at $\eta = 1$

$$\frac{\partial \theta_m}{\partial \eta} = q_1^*(\xi) = q_1(\delta\xi)\left[\frac{\delta}{KT^*}\right] \tag{6d}$$

at $\xi = \xi_L$

$$\frac{\partial \theta_m}{\partial \xi} = 0 \tag{6e}$$

where

$$A^* = \frac{h'\delta}{\dot{m}C_p}, \quad B^* = \frac{h'\delta^2}{k},$$

$$\xi = \frac{x}{\delta}, \quad \eta = \frac{y}{\delta},$$

$$\theta_g = \frac{T_g - T_g^0}{T^*}, \quad \theta_m = \frac{T_m - T_g^0}{T^*}.$$

Method of Solution. The technique for obtaining an approximate solution of equations (4) and (5) will parallel the classical Fourier transform methods. Rather than an integral transform of a continuous variable, a finite (discrete) Fourier transform of a discrete mesh function will accomplish the elimination of one of the independent variables. The finite Fourier transform approach has been successfully applied to finite difference equations in a number of problems [5, 6].[1]

The approximate solution of the differential equations will be given in terms of a sum of products involving $\cos(\pi\alpha\eta)$ for α an integer. At $\eta = 0$ and $\eta = 1$ the normal derivative will be zero. To accommodate this a new pair of dependent variables is introduced.

$$u = u(\xi,\eta) = \theta_m - R(\xi,\eta) \tag{7a}$$

$$v = v(\xi,\eta) = \theta_g \tag{7b}$$

where

$$R = R(\xi,\eta) = q_2^*(\xi)\eta^2/2 + q_1^*(\xi)\eta(1 - \eta/2).$$

The differential equations are now

$$\frac{\partial v}{\partial \xi} = A^*(u - v) + A^*R \tag{8a}$$

$$\nabla^2 u = B^*(u - v) + B^*R - \nabla^2 R \tag{8b}$$

with the new boundary conditions

[1] Numbers in brackets designate References at end of paper.

Nomenclature

A, B, C, D = matrices defining the block tridiagonal matrix which determines $[F]_i$ and $[G]_i$

$A^* = \frac{h'\delta}{\dot{m}c_p}$

$B^* = \frac{h'\delta^2}{k}$

C_p = specific heat at constant pressure

E, F = matrices defining the factorization of the tridiagonal matrix

$[F]_i$ = vector $\{F_{i,0}, F_{i,1}, \ldots F_{i,\alpha}, \ldots F_{i,m}\}$

$F_{i,\alpha}$ = the αth coefficient of the cosine transform of $[U]_i$

$[G]_i$ = vector $\{G_{i,0}, G_{i,1}, \ldots G_{i,\alpha}, \ldots, G_{i,m}\}$

$G_{i,\alpha}$ = αth coefficient of the cosine transform of $[V]_i$

h' = heat transfer coefficient per unit volume

k = thermal conductivity of porous material

L = channel length

M = number of subdivisions for η on $[0, 1]$

N = number of subdivisions for ξ on $[0, \xi_L]$

q = heat flux

$Q_{1,2} = \frac{\partial u}{\partial \xi}$ at $\xi = 0$ and $\xi = \xi_L$

R = function of the boundary condition used to change the dependent variable θ_m to the dependent variable u

$[R]_i$ = vector $\{R_{i,0}, R_{i,1}, \ldots R_{i,\alpha}, \ldots R_{i,m}\}$

$R_{ij} = R(i\Delta x, j\Delta y)$

$[\tilde{R}]_i$ = vector $\{\tilde{R}_{i,0}, \tilde{R}_{i,1}, \ldots \tilde{R}_{i,\alpha}, \ldots \tilde{R}_{i,m}\}$

$\tilde{R}_{i,\alpha}$ = the αth coefficient of the cosine transform of $[\tilde{R}]_i$

T = temperature

u = dependent variable having $\frac{\partial u}{\partial \eta} = 0, \eta = 0, \eta = 1$

$[U]_i$ = vector $\{U_{i,0}, U_{i,1}, \ldots U_{i,j}, \ldots U_{i,m}\}$

U_{ij} = approximation of $u(i\Delta x, j\Delta y)$

v = dependent variable, θ_g

$[V]_i$ = vector $\{V_{i,0}, V_{i,1}, \ldots V_{i,j}, \ldots V_{i,m}\}$

V_{ij} = approximation of $V(i\Delta x, j\Delta y)$

x = distance along flow direction

ΔX = mesh size in ξ direction

y = distance normal to flow direction

Δy = mesh size in η direction

$\theta_g = \frac{T_g - T_g^0}{T^*}$

$\theta_m = \frac{T_m - T_g^0}{T^*}$

δ = channel width

$\xi = \frac{x}{\delta}$

$\eta = \frac{y}{\delta}$

Subscripts

g = gas

i = denoting evaluation at $i\Delta x$

j = denoting evaluation of $j\Delta y$

L = at $X = L$

m = material

1 = at $y = \delta$

0 = at $y = 0$

α = denoting the αth term of a discrete cosine transform

Superscripts

0 = at $X = 0$

* = reference

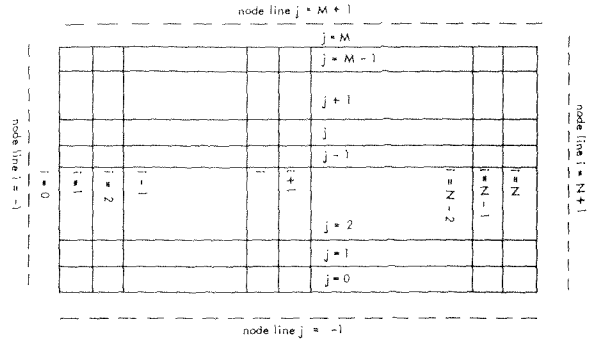

Fig. 2 Node lines

$$\text{at} \quad \xi = 0; \quad \frac{\partial u}{\partial \xi} = Q_1(\eta), \quad t = 0, \tag{9}$$

$$\text{at} \quad \xi = \xi_L; \quad \frac{\partial u}{\partial \xi} = Q_2(\eta)$$

$$\text{at} \quad \eta = 0 \text{ and } \eta = 1; \quad \frac{\partial u}{\partial \eta} = 0$$

where

$$Q_1(\eta) = -\frac{\partial q_2^*(0)}{\partial \xi}\left[\frac{\eta^2}{2}\right] - \frac{\partial q_1^*(0)}{\partial \xi}[\eta(1 - \eta/2)],$$

$$Q_2(\eta) = -\frac{\partial q_2^*(\xi_L)}{\partial \xi}\left[\frac{\eta^2}{2}\right] - \frac{\partial q_1^*(\xi_L)}{\partial \xi}[\eta(1 - \eta/2)].$$

A popular method for obtaining approximations to the solutions of partial differential equations are the finite difference equations. For the aforementioned problem, the rectangle $0 \le \eta \le 1, 0 \le \xi \le \xi_L$ is partitioned by the set of node lines (Fig. 2).

$$\xi_i = i\Delta x, \quad \xi_L = N\Delta x, \quad i = 0,1,2,\ldots,N,$$

$$\eta_j = j\Delta y, \quad 1 = M\Delta y, \quad j = 0,1,2,\ldots,M.$$

Let $U_{i,j}$ be some approximation to $u(\xi_i,\eta_j)$ and $V_{i,j}$ be some approximation to $v(\xi_i,\eta_j)$. The $U_{i,j}$ and $V_{i,j}$ are to satisfy the following difference equations.

Equation (8*a*) is approximated as

$$V_{i,j} - V_{i-1,j} = \Delta x A^*[U_{i,j} + U_{i-1,j} - V_{i,j} - V_{i-1,j}]/2 + \Delta x A^*[R_{i,j} + R_{i-1,j}]/2 \tag{10a}$$

$$\text{for } i = 1,2,\ldots,N, \quad j = 0,1,2,\ldots,M$$

$$R_{i,j} = R(\xi_i,\eta_j).$$

The boundary condition gives

$$V_{0,j} = 0, \quad j = 0,1,\ldots,M. \tag{10b}$$

Equation (8*b*) is approximated as

$$\sigma[U_{i-1,j} - 2U_{i,j} + U_{i+1,j}] + [U_{i,j-1} - 2U_{i,j} + U_{i,j+1}] = \Delta y^2 B^*[U_{i,j} - V_{i,j}] + \Delta y^2 S_{i,j} \tag{11a}$$

where

$$\sigma = \Delta y^2/\Delta x^2$$

$$S_{i,j} = B^* R_{i,j} - \nabla^2 R(\xi_i,\eta_j)$$

$$\text{for} \quad i = 0,1,2,\ldots,N, \quad j = 0,1,2,\ldots,M.$$

In addition the boundary conditions are approximated as

$$U_{1,j} - U_{-1,j} = 2\Delta x\, Q_1(\eta_j), \tag{11b}$$

$$U_{N+1,j} - U_{N-1,j} = 2\Delta x\, Q_2(\eta_j), \tag{11c}$$

$$\text{for} \quad j = 0,1,2,\ldots,M,$$

and

$$U_{i,-1} = U_{i,1}, \quad U_{i,M-1} = U_{i,M+1},$$

$$\text{for} \quad i = 0,1,2,\ldots,N.$$

The use of the "fictitious" dependent variables having indices of $i = -1$ or $N + 1$ and $j = -1$ or $M + 1$ allows a higher order approximation to be made.

Consider any mesh function $\phi_j, j = 0,1,2,\ldots,M$. It can be shown [7]

$$\phi_j = \frac{\tilde{\phi}_0}{2} + \sum_{\alpha=1}^{M-1} \tilde{\phi}_\alpha \cos(\pi\alpha j/M) + (-1)^j \frac{\tilde{\phi}_M}{2}$$

where

$$\tilde{\phi}_\alpha = \frac{2}{M}\left[\frac{\phi_0}{2} + \sum_{j=1}^{M-1} \phi_j \cos(\pi\alpha j/M) + (-1)^\alpha \frac{\phi_M}{2}\right].$$

In addition, the set of functions 1, $\cos(\pi x/M)$ $\cos(2\pi x/M)$ ..., $\cos([M - 1]\pi x/M)$, and $\cos(\pi x)$ are orthogonal under summation. Furthermore,

$$\phi_{-1} = \phi_1 \text{ and } \phi_{M-1} = \phi_{M+1}.$$

The orthogonality conditions and the foregoing boundary conditions will be used to advantage.

If a solution $U_{i,j}, V_{i,j}$ exists, then it can be written as

$$U_{i,j} = \frac{F_{i,0}}{2} + \sum_{\alpha=1}^{M-1} F_{i,\alpha} \cos(\pi\alpha j/M) + \frac{(-1)^j}{2} F_{i,M} \tag{12a}$$

$$V_{i,j} = \frac{G_{i,0}}{2} + \sum_{\alpha=1}^{M-1} G_{i,\alpha} \cos(\pi\alpha j/M) + \frac{(-1)^j}{2} G_{i,M} \tag{12b}$$

The mesh function $R_{i,j}$ can be written as

$$R_{i,j} = \frac{\tilde{R}_{j,0}}{2} + \sum_{\alpha=1}^{M-1} \tilde{R}_{i,\alpha} \cos(\pi\alpha j/M) + \frac{(-1)^j}{2} R_{i,M} \tag{13}$$

At this point let us define the following mesh functions of η_j

$$s_j^{(1)} = \eta_j^2/2$$

$$s_j^{(2)} = \eta_j(1 - \eta_j/2)$$

$$s_j^{(3)} = 1$$

and their finite cosine transforms

$$\tilde{s}_\alpha^{(k)} = \frac{2}{M}\left[\frac{s_0^{(k)}}{2} + \sum_{j=1}^{M-1} s_j^{(k)} \cos(\pi\alpha j/M) + \frac{(-1)^\alpha}{2} s_M^{(k)}\right]$$

Now the transform $\tilde{R}_{i,\alpha}$ of $R_{i,j}$ can be written as

$$\tilde{R}_{i,\alpha} = q_2^*(\xi_i)\tilde{s}_\alpha^{(1)} + q_1^*(\xi_i)\tilde{s}_\alpha^{(2)}$$

Substituting equations (12) and (13) into equation (10*a*) and noting that the orthogonal expansion of the zero function is zero, the result is

$$G_{i,\alpha} - G_{i-1,\alpha} = \frac{\Delta x A^*}{2}[F_{i,\alpha} + F_{i-1,\alpha} - G_{i,\alpha} - G_{i-1,\alpha}] + \frac{\Delta x A^*}{2}[\tilde{R}_{i,\alpha} + \tilde{R}_{i-1,\alpha}] \tag{14a}$$

for $\alpha = 0,1,2,\ldots,M$, $i = 1,2,\ldots,N$, from the condition $V_{0,j} = 0$, $G_{0,\alpha} = 0$. (14b)

Similarly $S_{i,j}$ is written as

$$S_{i,j} = \frac{\tilde{S}_{i,0}}{2} + \sum_{\alpha=1}^{M-1} \tilde{S}_{i,\alpha} \cos(\pi\alpha j/M) + \frac{(-1)^j}{2} \tilde{S}_{i,M}$$

where

$$\tilde{S}_{i,\alpha} = [B^* q_2^*(\xi_i) - \frac{\partial^2 q_2^*}{\partial \xi^2}(\xi_i)]\tilde{s}_\alpha^{(1)} + [B^* q_1^*(\xi_i) - \frac{\partial^2 q_2^*}{\partial \xi^2}(\xi_i)]\tilde{s}_\alpha^{(2)} + [q_1^*(\xi_i) - q_2^*(\xi_i)]\tilde{s}_\alpha^{(3)}$$

Equation (11*a*) is rewritten as

$$\sigma[F_{i-1,\alpha} - 2F_{i,\alpha} + F_{i+1,\alpha}] + \lambda_\alpha F_{i,\alpha} = \Delta y^2 B^*[F_{i,\alpha} - G_{i,\alpha}] + \Delta y^2 \tilde{S}_{i,\alpha} \tag{15a}$$

$$\lambda_\alpha = [-2 + 2\cos(\pi\alpha/M)]$$

for $\alpha = 0,1,2,\ldots,M$, $i = 0,1,2,\ldots,N$. The transformed boundary conditions, equations (11*b*,*c*) are

$$F_{1,\alpha} - F_{-1,\alpha} = 2\Delta x \tilde{Q}_\alpha^{(1)} \tag{15b}$$

$$F_{N+1,\alpha} - F_{N-1,\alpha} = 2\Delta x \widetilde{Q}_\alpha^{(2)} \tag{15c}$$

where

$$\widetilde{Q}_\alpha^{(1)} = \frac{\partial q_2^*(0)}{\partial \xi}[\widetilde{S}_\alpha^{(1)}] + \frac{\partial q_1^*(0)}{\partial \xi}[\widetilde{S}_\alpha^{(2)}]$$

$$Q_\alpha^{(2)} = \frac{\partial q_2^*(\xi_L)}{\partial \xi}[\widetilde{S}_\alpha^{(1)}] + \frac{\partial q_1^*(\xi_L)}{\partial \xi}[\widetilde{S}_\alpha^{(2)}]$$

It is important to note that equations (14) and (15) are uncoupled for each α. Whereas before, equations (10) and (11) (excluding "ficticious" nodes) numbered $2(M+1)(N+1)$ simultaneous linear difference equations, now equations (14) and (15) have $(M+1)$ sets of $2(N+1)$ simultaneous linear equations. Because of the sparceness and structure of the linear equations, a special algorithm may be used.

Equations (14) and (15) are now written in block tridiagonal form for each α as

$$\begin{bmatrix} B_0 & C_0 & 0 & 0 & & & \\ A & B & C & 0 & & & \\ & & \ddots & & & & \\ & & A & B & C & 0 & \\ & & 0 & A & B & C & \\ & & 0 & 0 & A_N & B_N \end{bmatrix} \begin{bmatrix} \phi_0 \\ \phi_1 \\ \phi_2 \\ \vdots \\ \phi_{N-2} \\ \phi_{N-2} \\ \phi_N \end{bmatrix} = \begin{bmatrix} D_0 \\ D_1 \\ D_2 \\ \vdots \\ D_{N-2} \\ D_{N-1} \\ D_N \end{bmatrix}$$

where

$$\phi_i = \begin{bmatrix} F_{i,\alpha} \\ G_{i,\alpha} \end{bmatrix}, \quad D_i = \begin{bmatrix} d_1^{(i)} \\ d_2^{(i)} \end{bmatrix}$$

and

$$A = \{a_{m,n}\},\ B = \{b_{m,n}\},\ C = \{c_{m,n}\}.$$

The elements are

$$a_{11} = \sigma, \quad a_{12} = 0$$

$$a_{21} = -\frac{\Delta x A^*}{2}, \quad a_{22} = -1 + \frac{\Delta x A^*}{2}$$

$$b_{11} = \lambda_\alpha - 2\sigma - \Delta y^2 B^*, \quad b_{12} = \Delta y^2 B^*$$

$$b_{21} = -\frac{\Delta x A^*}{2}, \quad b_{22} = 1 - \frac{\Delta x A^*}{2}$$

$$c_{11} = \sigma, \quad c_{12} = 0$$

$$c_{21} = c_{22} = 0$$

$$d_1^{(i)} = \Delta y^2 \widetilde{S}_{i,\alpha}, \quad d_2^{(i)} = \frac{\Delta x A^*}{2}[\widetilde{R}_{i,\alpha} + \widetilde{R}_{i-1,\alpha}]$$

The ficticious boundary quantities are eliminated and the boundary matrices become

$$B_0 = \begin{bmatrix} b_{11} & b_{12} \\ 0 & 1 \end{bmatrix}, \quad C_0 = \begin{bmatrix} 2c_{11} & c_{12} \\ 0 & 0 \end{bmatrix}, \quad D_0 = \begin{bmatrix} d_1^{(0)} \\ 0 \end{bmatrix}$$

$$d_1^{(0)} = \Delta y^2 \widetilde{S}_{0,\alpha} + 2\Delta x \sigma \widetilde{Q}_\alpha^{(1)}$$

$$A_N = \begin{bmatrix} 2a_{11} & a_{12} \\ a_{21} & a_{22} \end{bmatrix}, \quad B_N = B, \quad D_N = \begin{bmatrix} d_1^{(N)} \\ d_2^{(N)} \end{bmatrix}$$

$$d_1^{(N)} = \Delta y^2 \widetilde{S}_{N,\alpha} - 2\Delta x \sigma \widetilde{Q}_\alpha^{(2)}$$

$$d_2^{(N)} = \Delta x A^*/2\,[\widetilde{R}_{N,\alpha} + \widetilde{R}_{N-1,\alpha}]$$

The efficient determination of ϕ from equation (16) is well known [8]. For completeness it is given here.

$$E_0 = B_0^{-1} C_0, \quad E_i = (B_i - A_i E_{i-1})^{-1} C_i$$

$$F_0 = B_0^{-1} D_0, \quad F_i = (B_i - A_i E_{i-1})^{-1}(D_i - A_i E_{i-1})$$

$$i = 1, 2, \ldots, N-1$$

Then

$$\phi_N = (B_N - A_N E_{N-1})^{-1}(D_N - A_N E_{N-1})$$

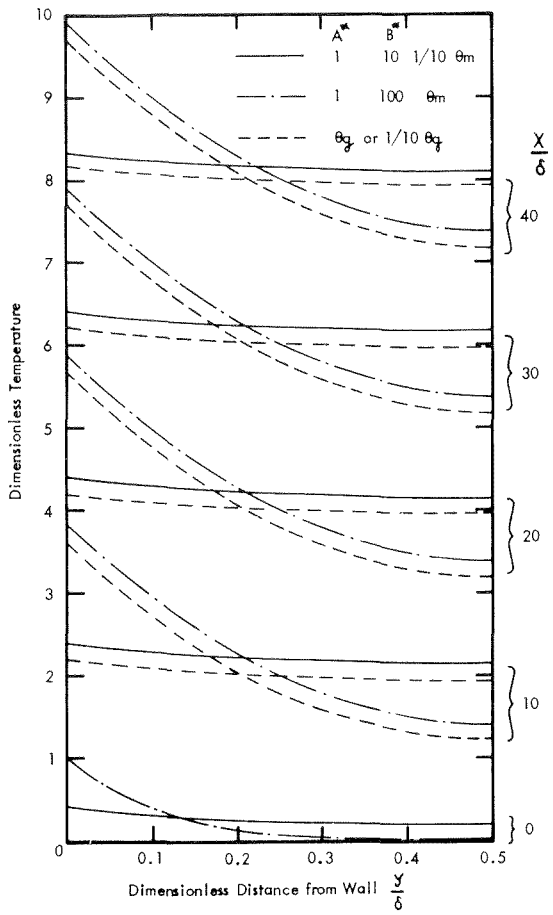

Fig. 3 Dimensionless temperature distribution ($|\theta_m'(0)| = |\theta_m'(1)| = 10$)

$$\phi_i = F_i - E_i \phi_{i+1}$$

$$i = N-1, N-2, \ldots, 1, 0.$$

The matrices F_i here are not to be confused with the $F_{i\alpha}$ used in previous notation.

Once the finite Fourier coefficients $F_{i\alpha}$, $G_{i,\alpha}$ are determined, the mesh functions $U_{i,j}$ and $V_{i,j}$ can be constructed from equation (12). Finally, θ_g and θ_m are approximated from equation (7).

Results and Discussions

The governing differential equations and boundary conditions presented in the foregoing section have been solved numerically for several combinations of the parameters $A^*, B^*, \theta_m'(0), L/\delta$. The results are shown in Figs. 3 to 9, and are discussed in the following.

Fig. 3 shows the dimensionless temperature profiles for $A^* = 1$, $B^* = 10$, 100 and $|\theta_m'(0)| = |\theta_m'(1)| = 10$. Since the temperature profiles are symmetric with respect to $y/\delta = 0.5$, only half of the profiles are shown in the figure. With the exception of the coolant entrance where the dimensionless gas temperature θ_g is zero, the dimensionless gas temperature profile is approximately parallel to the dimensionless porous material temperature. Also, the temperature profiles are quite flat for low value of B^*/A^* but relatively steep for high value of B^*/A^*. Since $B^*/A^* = \dot{m} C_p \delta/k$, represents the ratio of the heat sink to the heat conduction, a low value of B^*/A^* would imply a high degree of readiness of the local element to conduct the energy away and therefore the temperature gradient would be small. On the other hand, a high value of B^*/A^* would imply a relatively poor ability for the local element to conduct the energy away and therefore the temperature gradient would be great. For the consideration of cooling effectiveness, it is important to have a low value of B^*/A^* so that the temperature variation across the channel will be small.

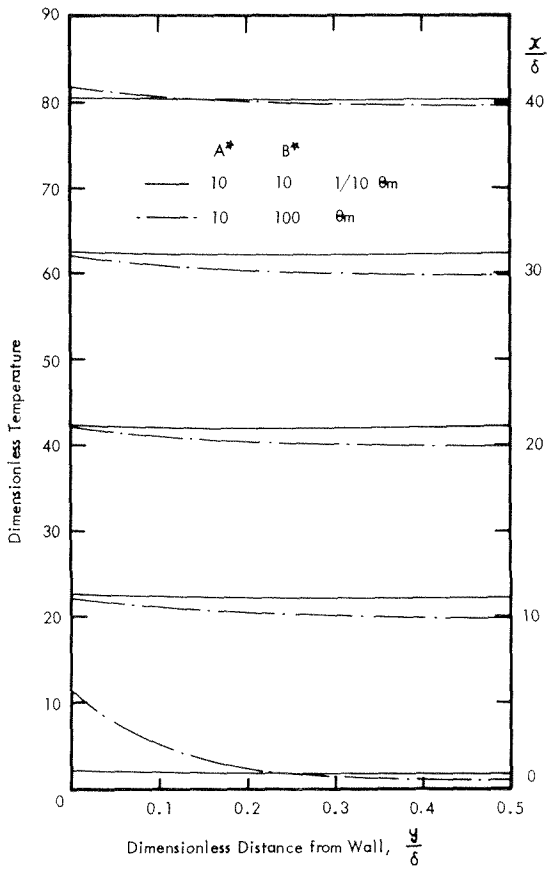

Fig. 4 Dimensionless temperature distribution ($|\theta_m'(0)| = |\theta_m'(1)| = 10$)

Fig. 4 shows the dimensionless temperature profiles for $A^* = 10$, $B^* = 10$, 100 and $|\theta_m'(0)| = |\theta_m'(1)| = 10$. With the exception of the entrance region, the coolant temperature is very close to and almost indistinguishable from the porous material temperature shown in Fig. 4. Notice that the parameter A^* in Fig. 4 is 10 and that in Fig. 3 is 1. Thus, the parameter A^* has a significant effect on the temperature difference between the porous material and the coolant. From the cooling effectiveness point of view, it is desirable to have a high value of A^*.

Fig. 5 shows the effect of heat transfer on the temperature profile. The symmetric curves are for the case of uniform heating on both walls, while the unsymmetric ones are for the case of uniform heating on one wall and insulation on the other wall. The total heating is the same in both cases. As expected, the temperature near the heating side is significantly higher and the temperature near the insulated wall is significantly lower than the case of uniformly heating on both sides. Again, with the exception of the entrance region, the dimensionless coolant temperature is below and approximately parallel to the dimensionless porous material temperature.

Fig. 6 shows the effects of parameters A^* and B^* or B^*/A^* on the dimensionless temperature along the wall. A high value of B^*/A^* is equivalent to a low conductivity material and, therefore, a high wall temperature if the heat flux is fixed. Also, the temperature increases as the distance from the entrance increases.

Fig. 7 shows the effect of the parameter B^* on the dimensionless temperature along the wall. For the same reason as pointed out in the foregoing paragraph, the wall temperature increases as the parameter B^* increases. A comparison between Figs. 6 and 7 shows that the temperature difference between the porous material and the coolant increases as the parameter A^* decreases. This is because a high value of A^* is equivalent to a high value of heat transfer per unit volume, h', and, therefore, a low value of temperature difference between the material and the coolant.

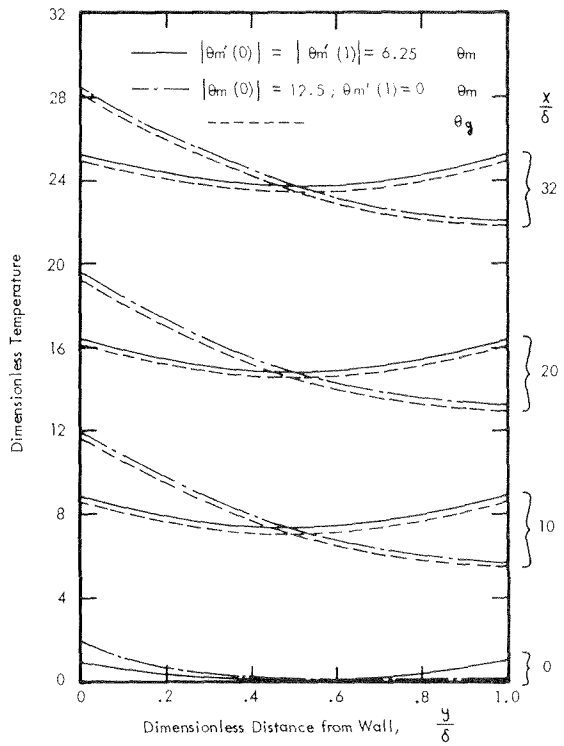

Fig. 5 Dimensionless temperature distribution ($A^* = 3$ $B^* = 50$

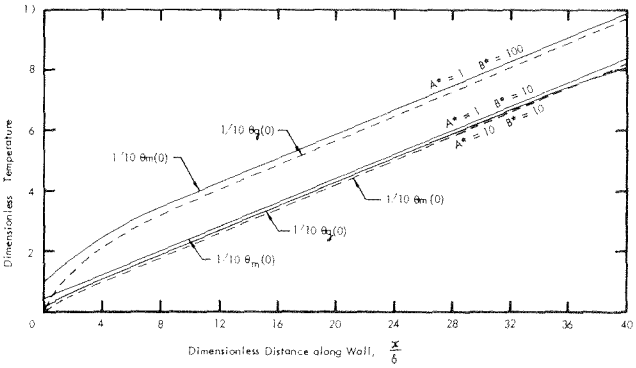

Fig. 6 Effects of A^* and B^* on dimensionless temperature along wall ($|\theta_m'(0)| = |\theta_m'(1)| = 10$)

Cooling Effectiveness

The cooling effectiveness of a channel with porous materials in comparison with that of a channel without porous materials may be determined by the ratio of allowable maximum wall heat flux for the two cases with the constraint that the wall material temperature be limited to a certain preselected value. For example, the maximum wall temperature may not exceed 2000 deg F if the wall material is superalloy. This maximum temperature together with the channel dimensions (width and length L) and the coolant flow rate will determine the heat flux at the channel wall for both with and without porous materials in the coolant passages. Algebraic equations used for this comparison are presented in the following.

Channels Without Porous Materials. It will be assumed that the heat transfer coefficient between the channel wall and the coolant is given by the following fully developed flow equations:

$$h = \frac{k_g}{2\delta} \mathrm{Nu}$$

$$\mathrm{Nu} = 8.2 \quad \text{(laminar flow)}$$

$$\mathrm{Nu}_t = 0.0243\ (\mathrm{Re})^{0.8}(\mathrm{Pr})^{0.4} \quad \text{(turbulent flow)}$$

The bulk coolant temperature as a function of distance x from the

entrance is given by the following energy balance equation

$$T_g = T_g^0 + \frac{2q}{\dot{m}\delta C_p} x$$

The wall temperature as a function of x is given by the definition of the heat transfer coefficient

$$T_w = T_g + \frac{q}{h}$$

The maximum wall temperature as found by substituting $x = L$ in the foregoing two equations is given by

$$(T_W)_{\max} = T_g^0 + q\left(\frac{2L}{\dot{m}C_p\delta} + \frac{1}{h}\right)$$

Thus, for given channel dimensions L and δ, coolant, coolant flux $\dot{m}$ and $(T_W)_{\max}$ the heat flux can be computed by the above equation. From the foregoing equation it maybe noted that for a prescribed heat flux q, the maximum wall temperature depends only on the local heat transfer coefficient at the end of the channel. Therefore, the high heat transfer coefficient at the entrance of a channel only reduces the local wall surface temperature at the entrance but does not reduce the maximum wall surface temperature at the end of the channel.

Channel With Porous Materials. To determine the heat flux corresponding to a maximum allowable wall material temperature, the parameters A^*, B^*, and $\theta_m'(0)$ must be estimated. Corresponding to these A^*, B^*, and $\theta_m'(0)$, the dimensionless temperature for the coolant and the porous materials can be found from the solutions of the governing equations (Figs. 3 to 7). This will determine the reference temperature T^* to be used in the definition of dimensionless temperature.

$$T^* = \frac{(T_W)_{\max} - T_g^0}{(\theta_m)_{\max}}$$

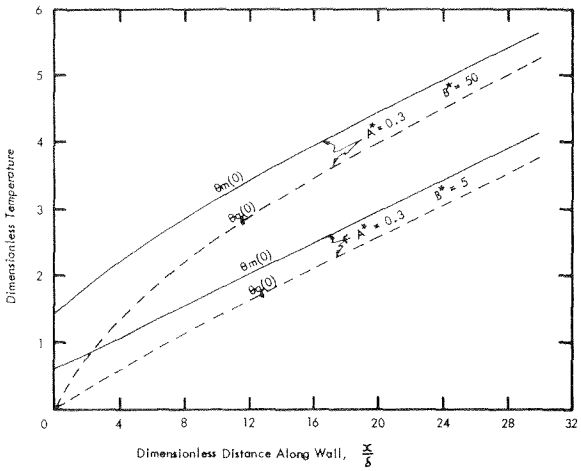

Fig. 7 Effects of A^* and B^* on dimensionless temperature along wall ($|\theta_m'(0)| = |\theta_m'(1)| = 10$)

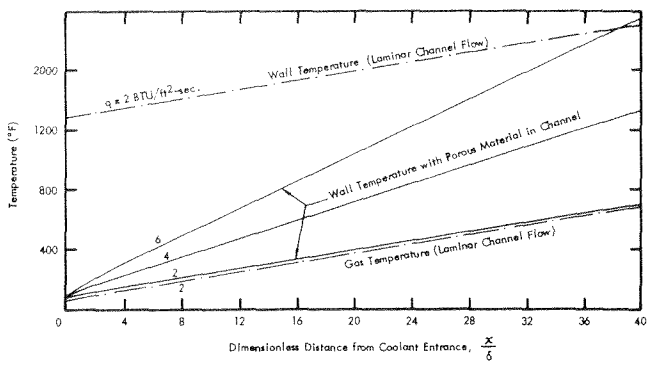

Fig. 8 Effects of porous materials in channel on cooling effectiveness ($A^* = 10$, $B^* = 100$, $\dot{m} = 1$ lb/ft^2-s)

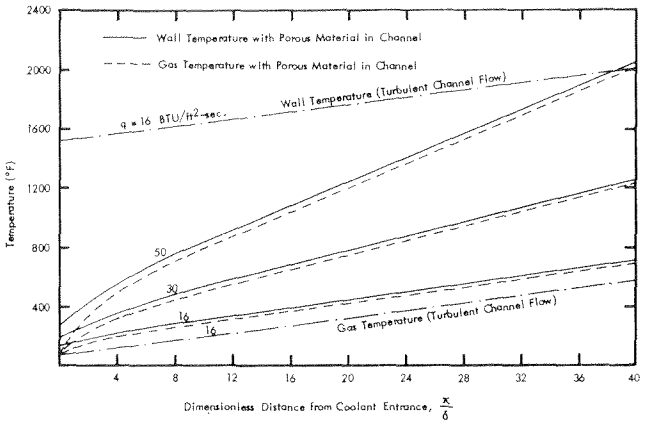

Fig. 9 Effects of porous materials in channel on cooling effectiveness ($A^* = 1$, $B^* = 100$, $\dot{m} = 10$ lb/ft^2-s

Finally, the heat flux can be calculated from the energy balance equation given by

$$q = \dot{m}C_p(\theta_g)_{x=L}\left(\frac{T^*\delta}{2L}\right)$$

If the selection of A^*, B^* and $\theta_m'(0)$ is correct, the heat flux so computed should agree with that found by the following equation

$$q = kT^* \frac{\theta_m'(0)}{\delta}$$

For example, if $A^* = 1$, $B^* = 100$, $\theta_m'(0) = 10$ and $L/\delta = 40$ the maximum dimensionless porous material temperature at the end of the channel as given by Fig. 3 is 9.85. If we limit the wall temperature to around 2000 deg F and the coolant temperature at entrance is taken as 70 deg, the reference temperature T^* would be

$$T^* = \frac{2000 - 70}{9.85} \simeq 200$$

If air is used as coolant at a flow rate of 10 lb/ft^2-s, the heat flux would be

$$q = \dot{m}C_p(\theta_g)_{x=L}T^*\frac{\delta}{2L} = 10(0.25)\cdot(8)\cdot\frac{200}{2\cdot 40} = 50 \text{ Btu/ft}^2\text{-s}$$

If the channel width δ is ¼ in. and the conductivity of the porous material k is 1.9 Btu/ft hr deg F, the heat flux computed by $kT^*\theta_m'(0)/\delta$ is also Btu/ft^2 s.

Heat Transfer Coefficient per Unit Volume. The heat transfer coefficient per unit volume h' is a function of mass flux and microstructures of the porous material. For packed bed of spherical particles and Rigimesh, data shown in reference [4] yield the following values of heat transfer coefficient per unit volume:

Heat transfer coefficient per unit volume h' at 40 percent porosity

$\dot{m}$(lb/ft^2-s)	Particle sizes of packed bed 0.01 in.	0.05 in.	0.1 in.	Rigimesh (hydraulic dia = 0.011 in.)
1	301	32	12	112
5	810	87	33	365
10	1240	134	51	682

Calculations. Calculations have been performed for $A^* = 10$, $B^* = 100$, $\dot{m} = 1$ and $A^* = 1$, $B^* = 100$ and $\dot{m} = 10$. Temperature distribution along the channel wall for these two cases are shown in Figs. 8 and 9, respectively. The temperature distribution and heat flux corresponding to the conventional channel flow is also shown in the figures.

For $A^* = 10$, $B^* = 100$, $\dot{m} = 1$ the flow in a ¼ in. width channel would be laminar and therefore the laminar heat transfer equation must be used. If the maximum wall temperature is limited to 2000 deg F, the maximum heat flux at the wall would be 2 Btu/ft^2 s as shown in Fig. 8. However, if the channel is packed with porous materials, the maximum heat flux could be 6 Btu/ft^2

s. Also, if the channel is packed with porous material and the heat flux is 2 Btu/ft² s the maximum wall temperature would be reducted to about 600 deg F. Thus, for a fixed heat flux, the effect of the porous material in the channel is to reduce the wall temperature. While for a fixed maximum wall temperature the effect of the porous material is to increase the heat flux at the wall.

For $A^* = 1$, $B^* = 100$, $\dot{m} = 10$, Fig. 9 shows that the cooling capability is increased from 16 Btu/ft² s without porous material to 50 Btu/ft² s with porous material. If the heat flux is maintained at 16 Btu/ft² s, the wall temperature at the end of the channel ($L/\delta = 40$) is decreased from 2000 deg F without porous material to about 700 deg F with porous material.

Calculation was also performed using hydrogen as coolant and it was found that the heat flux shown in Fig. 9 can be increased by four times. That is, the maximum wall heat flux with and without porous materials would be about 200 and 64 Btu/ft² s, respectively. By proper selections of porous materials and dimensions, this maximum heat flux could be increased significantly. In all cases computed, the cooling effectiveness is increased by over three times by use of porous material in the channel. This suggests the use of the scheme to augment the regenerative cooling in rocket nozzle where the convective cooling has reached its limit.

Conclusions

Temperature distribution in a channel packed with porous materials is analyzed. Numerical solutions to the governing equations are performed for a range of parameters. It was found that for fixed allowable wall temperature, the heat flux at the channel wall can be increased by over three times by use of porous material in the channel. For fixed heat flux at the channel wall, the effect of porous material in the channel is to decrease significantly the wall temperature. Thus, the scheme can be used to augment the regenerative cooling in rocket nozzle where the convective cooling of nozzle wall has reached its limit.

References

1 Siegel, R., and Goldstein, M. E., "Theory of Heat Transfer in a Two-Dimensional Porous Cooled Medium and Application to an Eccentric Annular Region," JOURNAL OF HEAT TRANSFER, TRANS. ASME, Series C, Vol. 94, Nov. 1972, pp 425–431.

2 Koh, J. C. Y., and del Casal, E., "Heat and Mass Flow Through Porous Matrices for Transpiration Cooling," *Proceedings of 1965 Heat Transfer and Fluid Mechanics Institute*. Stanford University Press, 1965.

3 Jacob, M., *Heat Transfer*. Vol. II, Wiley, New York, 1957, pp. 329ff, 394ff, 530ff.

4 Koh, J. C. Y., Dutton, J. L., and Benson, B. A., "Fundamental Study of Transpiration Cooling," NASA CR-134523, 1973.

5 Buzbee, B. L., Golub, G. H., Nielson, C. W., "The Method of Odd-Even Reduction and Factorization With Application to Poisson's Equation," Stanford University Computer Science Department, Tech. Report No. CS128, 1969.

6 Hockney, R. W., "The Potential Calculation and Some Applications," in *Methods in Computation Physics*. Vol. 9, 1970.

7 Hamming, R. W., *Numerical Methods for Scientists and Engineers*, McGraw-Hill, New York, 1962.

8 Forsythe, G. E., and Wasow, W. R., Finite-Difference Methods for Partial Differential Equations, Wiley, New York, 1960.

A. Abhat
Research Assistant[1]

R. A. Seban
Professor,
University of California at Berkeley,
Berkeley, Calif.

Boiling and Evaporation From Heat Pipe Wicks With Water and Acetone

Heat transfer for pool boiling with fluxes in the range of 5×10^2 to 5×10^4 Btu/(ft^2 hr) and the associated excess of wall over saturation temperatures are presented, primarily for atmospheric pressure, for vertical tubes in water, ethanol, and acetone, bare or wrapped with screen or felt metal. For the wrapped tubes, this performance is given also for evaporation into surrounding saturated vapor with the liquid being supplied by the wick; this is the significant mode in respect to heat pipe applications. For this mode maximum evaporation rates are also indicated and it is shown that this maximum can be rationalized either in terms of a partially full wick with conduction transfer to the evaporation surface or in terms of a full wick with vapor holes originating at nucleation sites on the tube surface.

Introduction

The two important aspects of evaporation from wicks that are related to heat pipe design are the relation between the excess of wall over saturation temperature as a function of the evaporation rate, and the maximum evaporation attainable within the capillary pumping limits of the wick. Because of the possible relation between evaporation from a wick bounded by the vapor of the evaporating liquid and boiling under conditions of submergence in saturated liquid, it is appropriate also to examine the wicks under the latter condition, and to determine as well the boiling performance of the tube upon which the wick is wound.

Results of this type for stainless steel wicks wound on copper tubes have been given by Seban and Abhat [1][2] and the continuation of that work has led to a more comprehensive specification by Abhat [2]. It is the purpose of this paper to summarize these latter results, which involve screen and felt metal wicks; to demonstrate the boiling performance of the bare tubes, and of the wicks submerged, and the evaporation performance of the wick surrounded by saturated vapor, including the maximum evaporation rate attained under the latter conditions. The fluids used were distilled water and commercially pure methanol and acetone.

Apparatus

The apparatus, shown in Fig. 1, consists of a glass enclosure holding a pool of liquid, the liquid temperature being maintained by immersion heaters in the bottom of the pool. A hollow vertical tube, 0.67 in. in diameter, with 0.09 in. wall thickness, extends downward from the top of the container, and this tube is subdivided into a top, stainless steel section, a 1.25 in. long copper section, and a long lower stainless steel tube. The copper section, the evaporator, is fitted with an internal heater of Kanthal wire wound on ceramic, and three thermocouples (located at 0.187, 0.625, and 1.062 in. below the top of the copper) are fitted into its wall. The heater is inserted into this test section through the hollow top stainless steel section, the walls of which are grooved at 90 deg intervals to carry the leads of the three thermocouples from the copper tube, and one additional thermocouple is fixed in this stainless tube near its joint with the copper tube.

Fig. 1 indicates also the other apparatus associated with the system, the operation of which involved initial heating of the pool fluid, degassing by reducing the system pressure, reattainment of saturated conditions, and energization of the evaporator heater in the tube. When operated for evaporation to surrounding vapor, the tube was first completely immersed and then the pool was lowered to the desired level.

The essential data were obtained from the electrical input and the response of the three tube thermocouples, compared to that of thermocouples in the liquid and vapor regions. The average of the three thermocouples, T_W, was used as the temperature of the copper evaporation section and the input to the heater was charged directly to the evaporation, thus ignoring the losses to the top stainless steel tube and to conduction in the heater connecting wires. These losses, estimated to be about 6 per cent of the input, were subtracted from the heat rates given in reference [1], but are included in them here.

Wicks

Table 1 contains dimensional data on the stainless steel and phosphor bronze screen and nickel felt metal wicks for which results are reported herein, and all of these were held onto the tube by stainless steel wire ties spaced at 0.25 in. on the heater section and 0.37 in. on the lower (adiabatic) tube. The top of the wick was even with the top of the copper section of the tube and the first tie was 0.03 in. below that point.

[1] Presently at Institute fur Kernenergetic, Stuttgart, West Germany.
[2] Numbers in brackets designate References at end of paper.

Contributed by the Heat Transfer Division for publication in the JOURNAL OF HEAT TRANSFER. Manuscript received by the Heat Transfer Division, November 14, 1973. Paper No. 74-HT-II.

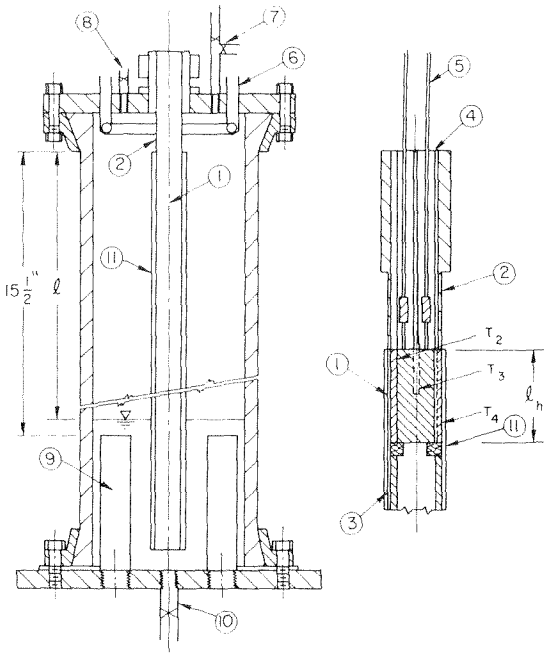

Fig. 1 Tube, wick, and test enclosure: 1 = heater and evaporator section; 2 = upper section, *SS* tube; 3 = lower section *SS* tube; 4 = thermocouple wire grooves; 5 = heater electrical leads, 6 = water cooled condenser; 7 = manometer and aspirator connections; 8 = vent; 9 = pool heaters; 10 = connection to reservoir; 11 = Wick; T_2, T_3, T_4 = thermocouples in copper evaporator section

Wicks were cleaned by repeated washing with water and acetone in an ultrasonic cleaner prior to installation on the tube, and cleaned by rinsing after being wound on the tube.

Operation with water over a long period produced a fine white deposit on the wick in the area near the top of the copper tube, which deposit became apparent upon removal of the wick from the tube. This occurrence was noted in reference [1] and while its severity subsequentially was reduced, its existence was not eliminated by revisions which minimized the use of soft solder in the assembly of the tube and by changes which eliminated soft solder in the remainder of the system. In a related adjustment, the copper evaporator section of one of the tubes contained a sputtered film of stainless steel on its copper surface, so that the entire tube surface was then stainless. But even with this tube a slight sedimentation occurred. The sedimentation, however, never produced any discernible effect on the data; this could be because the wicks were discarded upon suspicion of this occurrence.

Capillarity and Permeability

The wicks that were used, or similar wicks, were tested for capillary rise, l_s, by immersing the end of the wick into a pool, and for fall, by complete immersion followed by withdrawal and observation of the resulting equilibrium height, l_F, attained thereafter. Observations were made at room temperature, in circumstances which minimized evaporation, by touching the outside of the wick with litmus paper to detect locations wet with slightly acidified fluid. These observed heights are contained in Table 1.

Some attempts were made to deduce the permeability from temporal observation of the dynamic rise of the liquid in the wick but these led partly anomalous results, probably due to the dependence of wetting angle on the rise velocity.

Boiling From the Tube Submerged in Water

Operation at atmospheric pressure with a bare tube, with pool water level at the top of the heater section, provided the results that are shown in Fig. 2. The results that are shown for the lowest fluxes indicate values of the difference between average wall and saturation temperature, T_W-T_S, much below those (curve $F1$) associated with free convection from a vertical cylinder having the height of the evaporator section. This difference is at least partly attributable to the circulation induced by boiling from the pool heaters, which created a substantial velocity, and hence forced convection, over the heated section of the tube.

The first appearance of bubbles evolving from the heated tube is indicated by shaded points on Fig. 2. As the number of nucleation sites increased, the conductance did also, and for $q > 1.6 \times 10^4$ Btu/ft^2 hr (5.05×10^4 w/m^2) all the data are indicated by line $N1$, in proximity to the Rohsenow prediction, $R1$ ($C = 0.013$), even though one of the tubes, designated as SS, had a sputtered stainless steel rather than a copper surface.

At a pressure of 6 in. Hg the performance begins nearer to the expected free convection behavior given by curve $F2$, because at the lower operating temperature the heat input, and thus the general circulation due to the pool heaters, was much reduced. After nucleation begins, the performance approaches curve $N2$, which however is substantially above the Rohsenow prediction, $R2$, for the lower pressure.

The point of first bubbles for the lower pressure is predictable from the similar point at one atmosphere in terms of the increased surface tension and the equilibrium bubble model.

Boiling From the Tube Submerged in Acetone

The data for the boiling of acetone at atmospheric pressure, shown in Fig. 3, also began far above the prediction for free convection, $F3$. This is anomalous compared to the results for water, because at the lower temperature prevailing for alcohol the input to the pool heaters was low, and the expectation would be for the kind of correspondence achieved with water at 6 in. Hg, for which the saturation temperature was 141 deg F. Nucleation first occurs at the shaded points, and thereafter the performance is given by curve $N3$. It is close to the result given by Kutadeladze [3],[3] indicated by curve $K3$. This is considerably above the prediction, $R3$, of Rohsenow with $C = 0.003$.

Despite the reduction in surface tension, nucleation with acetone begins at an excess temperature substantially above, rather than below, that found for water.

At a pressure of 8 in. Hg, the performance is closer to, but still in excess of that associated with free convection—curve $F4$. Nucleation begins at a larger temperature difference than it does at one atmosphere, and this excess is predictable in terms of the increase in surface tension. As the nucleation increases the perfor-

[3] p. 361.

Nomenclature

d = outside diameter of tube (inside diameter of wick)
g = gravity acceleration
k = thermal conductivity
K = wick permeability
l = vertical height from pool surface to top of heater; l_H, heater length; l_S, l_F, capillary rise and holdup height
N = nucleation sites per unit area; N_T sites on the entire heater surface
Q = heat release by heater, Q_N estimated release per nucleation site
q = heat flux, heat release divided by outside area of the heater section
r = radius; r_e equivalent radius of a wick pore, r_0 equivalent radius of a vapor hole
T = temperature, T_w average wall temperature; T_s saturation temperature
V = liquid velocity in the wick
δ = wick thickness
θ = wetting angle
λ = latent heat of vaporization
μ = viscosity; μ_L, liquid; μ_V, vapor
ρ = density; ρ_L, liquid; ρ_V, vapor
σ = surface tension

Table 1 Wick geometry and capillary performance

Wick Metal	Wick Mesh	Turns	Cloth Thickness (mils)	Wire dia. (mils)	Wick Thickness (mils)	WATER Rise λ_S in	WATER Hold Up λ_F in	ACETONE Rise λ_S in	ACETONE Hold Up λ_F in	WATER k_A Btu/(fthr°F)	WATER k_S Btu/(fthr°F)	ACETONE k_A Btu/(fthr°F)	ACETONE k_S Btu/(fthr°F)
SS	150	4	5.2	3.0	17	3.7	8.6		5.2	.65	.76	.47	.20
SSS	325	4	3.1	1.4	12	4			--	.76	.57	.30	.15
SS	325	11	3.1	1.4	35	3.5	19.5	3.5	--	1.20	.57	1.34	.15
PB	325	4	3.1	1.4	11			3.5	--	1.03	.57	0.21	.15
Ni	Felt Metal	1	(80% porosity)		29			4	>12	1.35	.45	0.75	.13

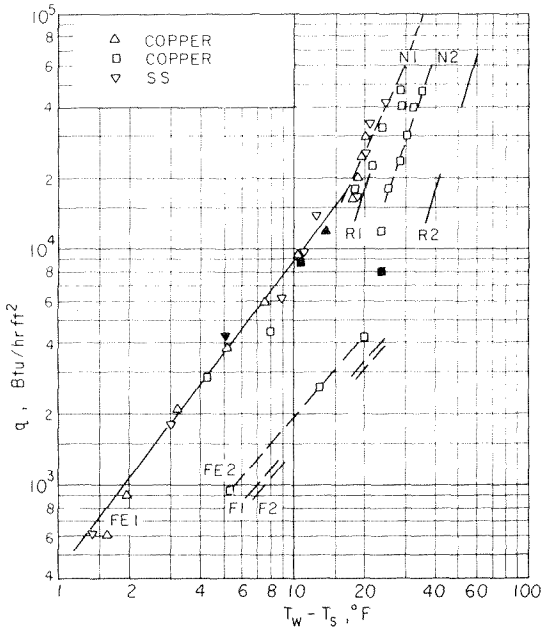

Fig. 2 Water boiling on the evaporator tube. Results are shown for three different tubes at atmospheric pressure. For one of the tubes results are shown for a pressure of 6 in. of mercury, these points beginning on line $F2$ and ending on line N_2. Ordinate values multiplied by 3.16 give the flux in w/(m)^2. Shaded points indicate first visible nucleation.

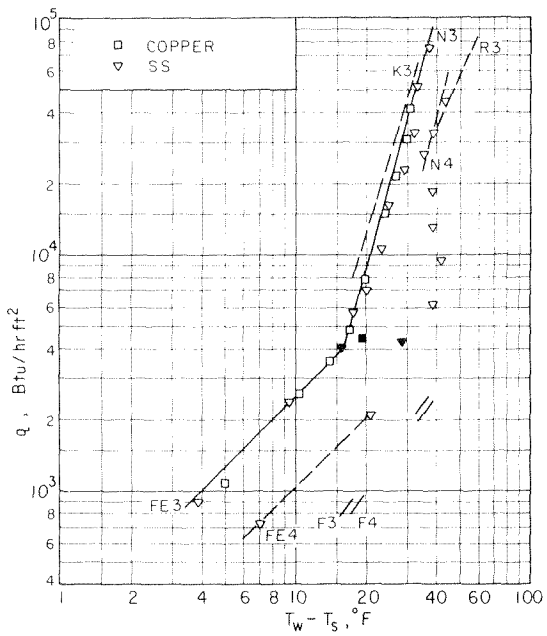

Fig. 3 Acetone boiling on the evaporator tube

mance tends to curve $N4$.

The performance shown in Fig. 3 was found to be the same with ethanol, as expected because of the similarity of the pertinent physical properties for the two fluids.

Boiling From Wicks Submerged in Water

Fig. 4 shows the results for the boiling from a number of wicks submerged in water at atmospheric pressure. The performance at a low heat input is close to the curve $FE1$ established by the bare tube results. Nucleation, indicated by the shaded points, occurs at much smaller temperature differences and makes the points rise above curve $FE1$. At the large fluxes, the points tend toward line $N1$, though for the SS-350 mesh wick, and for some other tested, there is a tendency to fall below curve $N1$ at fluxes above 2×10^4 Btu/(ft^2 hr). Curve B1 is established by the results that are shown on this figure and by similar results for other wicks. Except for the results that are shown for the PB 325-4 mesh wick, this curve correlates the other results within ±20 percent. At $q = 4.8 \times 10^4$, the wall temperatures for the SS 325-11 wick showed a gradual increase, which progressed to 100 deg F, the limit of safe heater operation. With this thicker wick, either the radial inflow of water or the discharge of vapor could no longer be accommodated by the available capillary forces.

One set of results, for a 150 mesh wick, is shown for the lower pressure of 6 in. Hg. At low fluxes these are in general correspondence with the similar bare tube performance that is specified by curve $FE2$ from Fig. 2, and at high fluxes these results exceed curve $N2$ of Fig. 2 in the way some of the atmospheric pressure data exceeds curve $N1$.

Observations of the number of bubble sites, N_T, over the whole heated section were made for some of the wicks, and Table 2 contains these numbers as a function of the heat flux. Such observations were not made repeatedly, but general observations indicated their qualitative reproducibility. If a wick conductance is estimated from the data for the lowest heat rates, then the excess of the flux indicated on Fig. 4 over that for pure conduction through the wick (which would be approximated by a 45 deg line drawn through the points at the lowest flux) is attributable to nucleation occurring on the surface of the tube. This difference, divided by the number of sites, is denoted by Q_N in Table 2. It is of the order of 1 w per site.

Boiling From Wicks Submerged in Acetone and Ethanol

Contrary to the experience with water, these wicks when submerged in ethanol and in acetone produced results, shown on Fig. 5, that are substantially different from those found for the bare tube as shown on Fig. 3 where they were characterized by the curves $FE3$ and $N3$.

Fig. 5 shows by the shaded point that nucleation occurred at the lowest heat input for the 150 mesh screen, and all of the results, up to $q = 1.5 \times 10^4$, can be approximated by the curve $B3$ established by this figure. At higher fluxes, the results for this screen are below this curve and the curve $N3$ that indicates the bare pipe performance at high fluxes.

The felt metal wick begins similarly, gives the highest heat transfer coefficient, and at the highest flux that was measured gives a performance typical of curve $N3$.

The other wicks initiated their performance near curve $F3$ and did not attain substantial nucleation until a flux of about 3000. At higher fluxes, the 325 mesh phosphor bronze wick gave a performance typified by curve $B3$. The 325 mesh four layer stainless

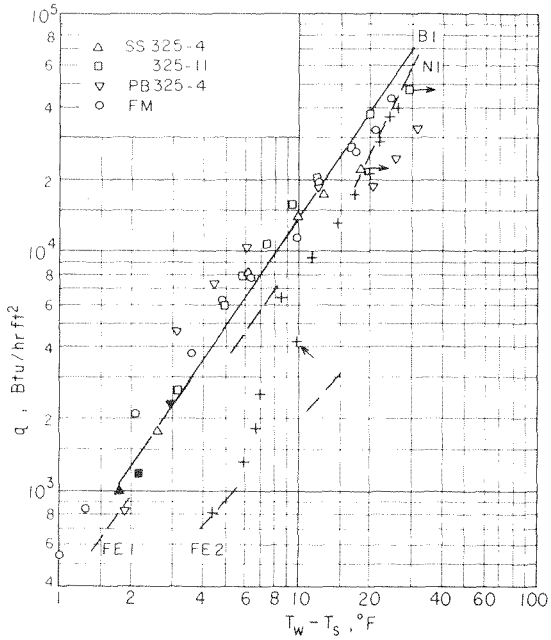

Fig. 4 Water boiling on the tube covered with a wick. The figure establishes Line *B*1. Other lines from Fig. 2. The "plus" points originating at *FE*2 are for the *SS* 150-4 wick at 6 in. mercury pressure, all other data at atmospheric pressure. Shaded points indicate first nucleation; an arrow is used for the plus points. Arrows at high fluxes indicate a progressive rise in temperature after the indicated point.

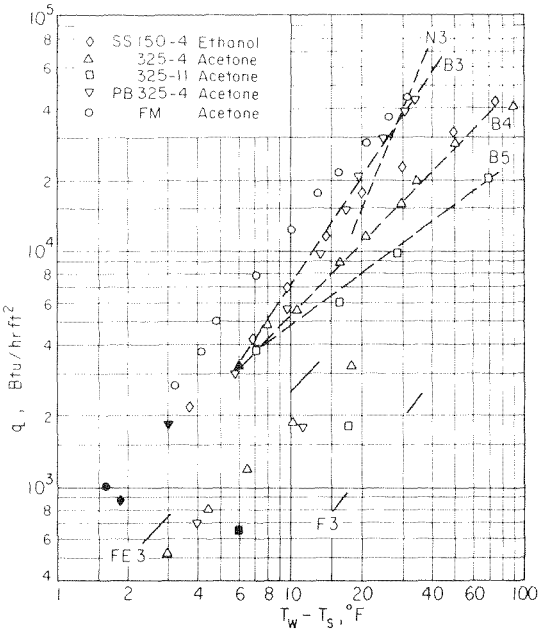

Fig. 5 Ethanol and acetone boiling on the tube covered with a wick. All results are for atmospheric pressure.

steel wick gave the diminished performance indicated by curve *B*4, and the similar eleven layer wick produced the further diminished performance indicated by curve *B*5. Thus, all the stainless wicks exhibited a diminished performance, the 325 mesh wicks in proportion to their thickness.

Observations of nucleation were made for some of the wicks, and for three of those shown on Fig. 5 the nucleation results evaluated as already mentioned for water are given on Table 2. Beyond the highest heat rates that are shown there the number of bubble sites was so large as to be uncountable. Comparison with the results for water that are contained in Table 2 shows the presence of a greater number of sites at a given rate; at $q \simeq 10^4$, for the *SS*-325-11 wick, there were 40 with water and more than 130 with acetone.

Evaporation From Wicks Into Water Vapor

With the liquid level below the bottom of the evaporation section, vaporization takes place from the liquid in the wick to the saturated vapor surrounding it, with the liquid being supplied from the pool by the capillary suction produced by the wick. This is the mode of operation characteristic of the heat pipe. It is terminated by the heat rate corresponding to the limiting liquid supply rate, and this maximum heat rate is discussed in a following section, while this one considers rates below this maximum. With this mode of operation, of course, nucleation could no longer be observed. All that could be seen, with the 150 mesh wick and with the felt metal wick, was a mist of liquid issuing from the wick surface at high heat rates ($q > 2 \times 10^4$). This was not seen with the 325 mesh wick.

Fig. 6 shows the performance of a number of wicks at various pool depths in comparison to the curve *B*1 established by the submerged performance that is shown on Fig. 4, to indicate that the behavior with evaporation into vapor tends to be of the same order as it is when the wick is submerged.

The results for the lowest heat rates are used to establish an apparent conductivity, k_A, shown in Table 1, on the assumption that at this input the wick is completely full of liquid, with evaporation taking place only from the surface. Table 1 also contains the apparent conductivity, k_s, which would be realized from a series arrangement of the water within and the metal of the wick. The observed values are closer to k_s than to an apparent coefficient for a parallel arrangement, but the apparent values are themselves questionable because it is not certain that there was absolutely no nucleation even at the lowest heat inputs, where perforce the accuracy of measurement was also poor.

A continuation to higher heat rates of such conduction through the entire wick thickness would produce on Fig. 6 a 45 deg line beyond the first operating point. This is far below actuality, so that either the liquid must retreat into the wick or nucleation must take place locally within the wick, with evolution of vapor streams through the otherwise full wick. The latter view is in closer correspondence with the performance that established curve *B*1, for when submerged, the wick should have been full and most of the transfer that then occurred was probably due to nucleation that occurred at the tube surface, with evolution of the vapor through "holes" in the liquid-metal matrix of the wick.

Table 2 Number of nucleation sites on evaporation

SS 325-4 (2)				SS 325-11				Felt Metal			
ℓ_{SH} = 17.7		K = 3.7 x 10^{-10}(μ^2)		ℓ_{SH} = 17.7		K = 3.7 x 10^{-10}		ℓ_{SH} = 11.9		K = 4.1 x 10^{-3}	
ℓ(in)	Q(watts)	$\frac{\delta}{\delta_w}$	r_o (mil)	ℓ	Q	$\frac{\delta}{\delta_w}$	r_o	ℓ	Q	$\frac{\delta}{\delta_w}$	r_o
3.2	128	.26	5.8	3.2	208	0.10	7.0	3.2	220		
4.0	105	.26		5.3	141	0.10		4.5	4.4	.18	11
5.2	82	.34		6.5	117	0.11	9.0	6.5	3.4	.23	
6.0	71	.34	9.2					7.5	2.2	.31	16

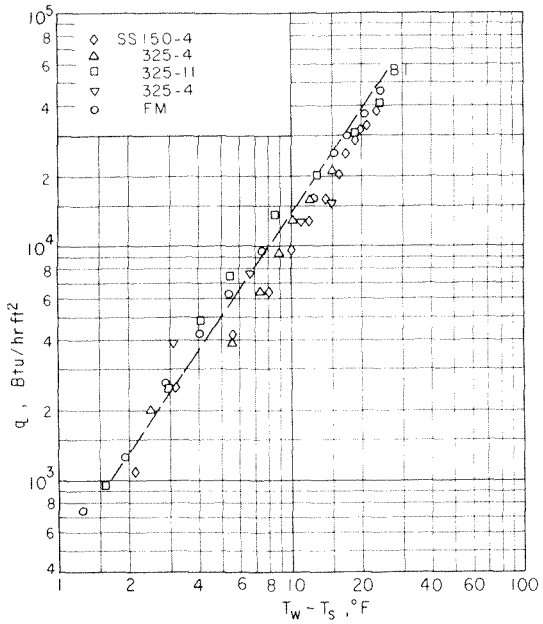

Fig. 6 Evaporation of water in the wick to its vapor. All data are for atmospheric pressure. Values of *l* vary from 1.5 to 4 in.

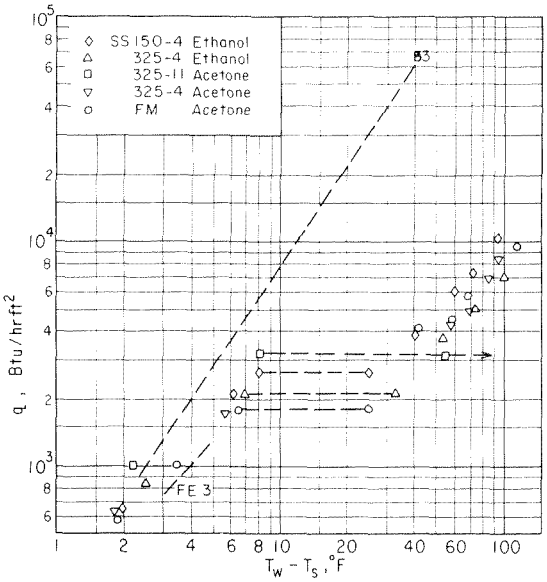

Fig. 7 Evaporation of ethanol and of acetone in the wick to the vapor. All data are for atmospheric pressure. The value of *l* was 1.5 in.

Evaporation From Wicks Into Ethanol and Acetone Vapor

When operated with ethanol or acetone, the correspondence between submerged and "evaporation" performance that was exhibited for water essentially was eliminated, and any similarity was lost completely for heat fluxes over 2000 to 3000 Btu/ft² hr.

Fig. 7 shows by results for a pool depth of 1.5 in. (0.25 in. below the heater), that at the lowest fluxes the results are in some correspondence with curve *B*3 and they are not far from curve *FE*3, the conductances at the lowest fluxes being slightly higher than they were when the wick was immersed. Apparent thermal conductivities obtained from these results on the assumption of a full wick are contained in Table 1. These are greater than implied by a series model but they are substantially less than would be indicated for a parallel arrangement.

An increase of the heat input to a still low value of approximately 10 watts produced results near curve *F*3 but at this point instability developed, with a slow increase in the temperature difference, until stable operation was again achieved at a temperature difference of about 30 deg F. Higher heat inputs yielded further stable operation at conductances about $\frac{1}{25}$ of those indicated by curve *B*3, up to the 100 deg F temperature difference which was the safe operating limit of the apparatus. There is evidence from the behavior of the three temperatures measured on the surface of the evaporator section that the slow rise in temperature at an input of about 10 w was due to a gradual fall of the level of the liquid in the wick, and that the stable conditions found at the larger temperature differences involved an almost completely dry wick, with most of the heater input being conducted downward into the stainless steel portion of the tube, where the heat transfer from the liquid in the wick then occurred from the short length of exposed wick on the adiabatic section or within the pool itself.

Maximum Evaporation Rate With Water

At a certain heat input, for every pool depth, there occurs a departure from the performance illustrated for water on Fig. 6, the departures involving a slow increase of the evaporator temperature, particularly at the top of the evaporator. If this increase was less than 1 deg F/hr, the performance was assessed as steady and that performance was included on Fig. 6, but if the increase was greater than this the maximum evaporation rate was considered to have been achieved. Clearly this slow variation, appraised against other slow temperature changes which occurred in the system, made difficult the evaluation of the maximum evaporation rate, and the quoted values thereof should be reduced substantially for a guarantee of indefinite steady operation of the system.

Fig. 8 contains these maximum evaporation rates, as found for various wicks, as a function of the distance, *l*, from the top of the wick to the surface of the pool.

This maximum rate is a hydrodynamic limitation, resulting from a balance between the capillary forces and those involved with the elevation of the fluid above the pool and the pressure drops associated with the fluid flow. Because of the general concern with the prediction of the maximum evaporation rate, the analysis has been repeated often, essentially as outlined below, but with variations on the assumptions, particularly in respect to

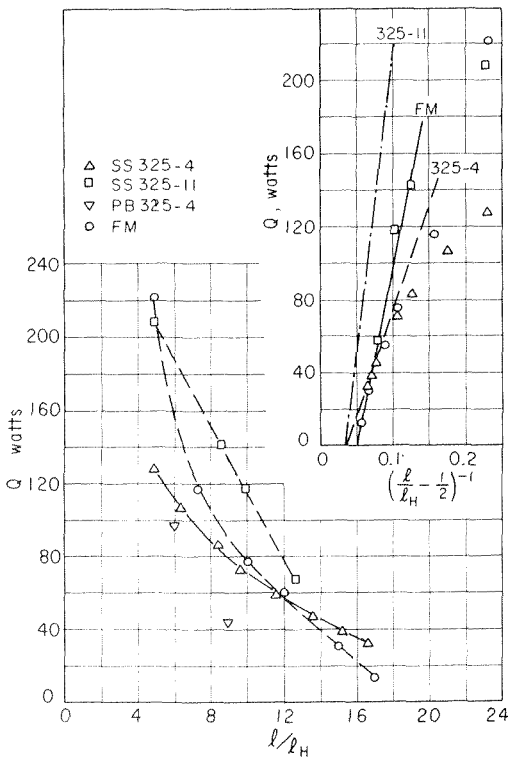

Fig. 8 Maximum evaporation rates for water

Table 3 Maximum evaporation rates and deductions

SS-(SS325-11 water			SS-325-11 acetone			SS-325-4 ethanol			P8 325-4 acetone			SS 150-4 ethanol		
$q \times 10^{-3}$	N_T	Q_N watts	$q \times 10^{-3}$	N_T	Q_N watts	$q \times 10^{-3}$	N_T	Q_N	$q \times 10^{-3}$	N_T	Q_N	$q \times 10^{-3}$	N_T	Q_N
1.15	1	--	.67	4	--	2.90	20	.55	.83	16	--	.87	3	0.10
2.56	5	.76	1.73	10	--	4.91	40	.42	1.73	24	.25	2.2	25	0.32
6.02	15	.86	3.86	45	.33	7.80	90	.33	3.59	60	.22	4.1	45	0.36
8.35	25	.81	5.4	85	.26	12.40	UC					6.8	60	0.42
11.1	40	.73	9.7	130	.26							11.0	UC	
15.3	55	.81	2×10^4	UC										
20.6	70	.90												
27.4	85	1.00												
38.4	120	1.14												

the fluid flow in the evaporation section.

The capillary suction that is produced is $(2\sigma\cos\theta)/r_e$, when θ is the wetting angle and r_e is the equivalent radius of the wetted aperture in the wick. Taking $(2\sigma\cos\theta)/r_e = \rho g l_{SH}$, where l_{SH} is the effective suction height, as associated with l_s or l_F of Table 1; this suction balances:

(a) the pressure due to elevation of the liquid above the pool, $\rho g l$.

(b) The frictional pressure drop in the adiabatic section, presumed to be full, with a uniform velocity distribution.

$$\frac{\mu_L}{K}\frac{Q}{(\pi d\delta_W)(\lambda\rho_L)}(l - l_H)$$

(c) The friction resistance in the wick

$$\frac{\mu_L}{K}\frac{1}{\delta}\int_0^{l_H}\int_0^{l} V dx dy$$

Here K is the permeability of the wick, λ is the latent heat of vaporization and δ is the thickness of the liquid layer in the wick. For a fully saturated wick $\delta = \delta_W$, and for constant heat flow and unidimensional fluid flow, term ("c") then becomes $(\mu_L/K)(Q/\rho\lambda)(1/\pi d\delta_W)(l_H/2)$, but it was found in early investigations of the maximum evaporation rate that the balance made with this form of term *(c)* overpredicted the maximum evaporation rate. Chun [4] showed that $\delta < \delta_W$ yielded an improved prediction for screen wicks, with δ equal to one or two layer thicknesses. Goluba [5] did this too, but also postulated a velocity nonuniform in y, and found for felt metal that δ/δ_W of the order of 1/6 rationalized his data. Roberts [6] also took $\delta < \delta_W$, but nonuniform in x. Considering all these variations, the contribution of term *(c)* can be made to cover a considerable range of pressure drops for the same flow rate.

In addition to the foregoing pressure drops, there may be an additional pressure drop due to vapor flow in the wick. For an unsaturated wick with a homogeneous liquid layer of the thickness, δ, the vapor pressure drop for flow through the distance $(\delta_W - \delta)$ is negligibly small compared to terms *a*, *b*, and, *c* in the foregoing, but if there are vapor holes through the liquid layer due to nucleation at rate Q_N at the surface of the evaporator tube then the vapor pressure drop through such a hole, of radius r_0, would be the possibly significant amount:

$$(d)\ \left(\frac{\mu_v}{K}\right)(1/\pi r_0^2)$$

$Q_N/(\rho_v\lambda)\delta$ where subscript v denotes vapor properties.

Taking all these pressure drops into account, and adjusting the velocity in term *(c)* by the factor $(1 - N\pi r_0^2)^{-1}$ to account for the presence of N such holes per unit area, gives the balance

$$\rho_L g l_{SH} = \rho_L g l + \frac{\mu_L}{K}\frac{Q}{\pi d\delta_W(\lambda\rho_L)}\left\{l - \frac{l_H}{2} + l_H\left(\frac{\delta_W}{\delta}\frac{1}{(1 - N\pi r_0^2)} - 1\right)\right\} + \frac{\mu_v}{K}\frac{1}{\pi r_0^2}\left(\frac{Q_N}{(\rho_v\lambda)}\right)\delta \qquad (1)$$

Here the vapor pressure drop is taken for a hole right at the top of the wick, the pressure drop for holes at lower levels would be accommodated by the greater liquid pressures at those locations.

If in equation (1), $\delta = \delta_W$ and $N = 0$ then there is obtained the most elementary result,

$$\rho_L g l_{SH} = \rho_L g l + \frac{\mu_L}{K}\frac{Q}{\pi d\delta_W(\rho_L\lambda)}(l - \frac{l_H}{2}) \qquad (2)$$

which may still apply at $l \gg (l_H/2)$ even if $\delta \neq \delta_W$ and $N \neq 0$ because then the pressure drop in the adiabatic section may dominate that in the evaporation section of the wick. Equation (2) can be rearranged to

$$Q = \frac{K\pi d\delta_W\lambda\rho_L}{\rho_L g}\left\{\frac{l_{SH} - \frac{l_H}{2}}{l - \frac{l_H}{2}} - 1\right\} \qquad (3)$$

so that a plot of Q as a function of $(l - l_H/2)^{-1}$ should be linear and l_{SH} and K could be deduced from the slope and intercept. The inset of Fig. 8 shows this representation and indicates that for the 325-4 wick there is reasonable correspondence with linear variation at large l. Table 3 contains l_{SH} and K deduced in this way and the magnitude of l_{SH} is of the order of the hold up heights indicated in Table 1. This was the only 325 mesh wick for which sufficient points were obtained a large l, so this K and l_{SH} were used for all of the 325 mesh wicks. The values of l_{SH} and K for the 150 mesh wicks, indicated in Table 3 were obtained from a similar plot.

For the major region in which Q is not given by equation (3) the values of K and l_{SH} deduced from it for large values of l could, in principle, be used in equation (1) to determine the remaining terms. But the data are not accurate enough to enable the determination of δ/δ_W, N, Q_N, and r_0 from the simultaneous solution of equation (1) for four different values of l, so that only the aggregate of the terms $l_H/2\,[(\delta_W/\delta)(1/(1-N\pi r_0^2))-1] + (\mu_r/K)(1/\pi r_0^2)(Q_N/(\rho_L\lambda))\delta$ can be evaluated. Then a value of δ/δ_W can be evaluated for $Q_N = 0$ or with $\delta = \delta_W$ a value of r_0 can be deduced from the values of Q_N given in Table 2.

For the first assumption, $N = 0$, the resulting values of δ/δ_W that are indicated in Table 3 are much less than unity, like those of other investigators, but the values are erratic because of experimental uncertainty in the determination of Q. For the *SS*-325-4 wick δ/δ_W is 1/3 or less, and for the *SS*-325-11 wick about 1/10, so that in both cases the effective liquid layer thickness is about one screen layer. This in turn raises serious questions about the use of the permeability, K, which was deduced for conditions of a dominant pressure drop in the presumably full adiabatic section. The felt metal wick gives δ/δ_W as small as 1/5, similar to the 1/6 used by Goluba [5] for a stainless steel felt metal wick. In a contradictory result, Corman and Walmet [7] indicate agreement with $N = 0$, $\delta_W = \delta$, using a higher permeability (7.1×10^{-10}), for wicks just like the felt metal wick with thicknesses up to 40 mils, though for higher δ_W than this those results indicate $\delta < \delta_W$.

Conversely, it can be assumed that $\delta = \delta_W$, with $N\pi r_0^2 \ll 1$; Q_N can be taken as about 1 w, and the value of r_0 evaluated. The consequence, shown on Table 3, is of the order of $r_0 = 6$ mils (or about 2 mesh widths). With $N = 75$ sites on the screen this gives $N\pi r_0^2 = 4 \times 10^{-3}$, small enough to be neglected. This shows that the vapor holes, even if of appreciable diameter, can produce a vapor pressure drop like that needed to produce the observed maximum evaporation even if $\delta = \delta_W$.

Possibility of a Maximum Rate With Alcohol and Acetone

The results for acetone and alcohol are not amenable to the foregoing analysis because the limitation shown on Fig. 7 near $q = 2 \times 10^3$ Btu/(ft² hr) was observed also with pool depths greater than 1.5 in. If, despite this, equation (3) is applied for this depth

for a heat input of about 10 w, and if l_{SH} is taken as the rise height of 4 in. rather than a larger hold up height, than the values of δ/δ_W indicated for $N = 0$ are 0.18 for the four layer 325 mesh wick and 0.08 for the 11 layer wick. These values are of the order indicated in Table 3 for water, but their specification in terms of the rise height implies that some failure of capillarity may be the true cause of the limited maximum rate.

If the wick is taken to be full, $\delta = \delta_W$, with holes through the liquid, the retention of the value $\delta_{SH} = 4$ in. and the choice of Q_N to be of the order of 1 w (indicated by the difference between the points below and above curve *FE*3 on Fig. 5 and the nucleation site counts on Table 2) yields from equation (1) for the 325-4 wick a value of r_0 about the same magnitude as indicated for water. Thus, as for water, the hole concept could account for the limitation on evaporation as well as does the one of reduced liquid layer thickness in the wick.

Summary

With water, up to heat fluxes of 5×10^4 Btu/ft^2 hr, the magnitude of the heat transfer coefficient, $q/(T_w - T_s)$, is of the same magnitude for the screen or felt metal wrapped tube as for the bare tube. Thus the nucleation that occurs with the wrapped tube must originate at or near the tube surface. The performance with evaporation from the wick to surrounding vapor is also similar to that in the submerged condition, so that it can be implied that the same kind of nucleation persists, though in this mode of operation the performance could also be rationalized by the assumption of a retreat of the liquid surface into the wick. Both views can also partially rationalize the observed maximum evaporation rates in terms of an increased flow resistance in the evaporation section of the wick, one by an increased liquid flow resistance due to a liquid layer thinner than the wick and the other by vapor flow resistance in holes connecting the nucleation sites at the tube surface with the exterior of the wick.

With alcohol and ethanol, the presence of the wick does make a difference in the submerged performance. Thicker screen wicks give poorer performance while the thick felt metal gives about the same performance as does the bare tube. But with evaporation into surrounding vapor the performance is similar to that when immersed only at the lowest heat rates. This performance terminates at a low input and the conductance at higher inputs is very much lower. This failure in wick performance can be associated weakly with a maximum evaporation rate if the capillary suction is appraised from the observed values of static rise but its true nature remains indecisive; it may be as much due to a failure of capillary suction as to the fluid friction in the wick.

References

1 Seban, R. A., and Abhat, A., "Steady and Maximum Evaporation From Screen Wicks," ASME Paper No 71-WA/HT-12.

2 Abhat, A., "Evaporation and Nucleate Boiling From Heat Pipe Wicks," PhD dissertation, 1972, University of California at Berkeley.

3 Kutadeladze, S. S., *Fundamentals of Heat Transfer*, Academic Press, New York, 1963.

4 Chun, K. R., "Some Experiments on Screen Wick Dry Out Limits," JOURNAL OF HEAT TRANSFER, Trans. ASME, Series C, Vol. 94, 1972, pp. 46–51.

5 Goluba, R., and Van Sant, J., "Evaporation From a Capillary-Wetted Surface," ASME Paper No. 72-WA/HT-12.

6 Roberts, C., and Feldman, K., "Predicting Performance of Heat Pipes With Partially Saturated Wicks," ASME Paper No. 72-WA/HT-38.

7 Corman, J., and Walmet, G., "Vaporization From Capillary Wick Structures," ASME Paper No. 71-HT-35.

A. Brosh
Y. Winograd

Faculty of Mechanical Engineering,
Technion-Israel Institute of Technology,
Haifa, Israel

Experimental Study of Turbulent Flow in a Tube With Wall Suction

The effect of wall suction on the turbulent flow of air in a porous tube has been studied. Measurements of the radial distribution of the turbulent velocity fluctuations were obtained over a range of Reynolds numbers from 10^4 to 2×10^5. Various suction rates were employed, for both local suction over a short length of tube and continuous suction over various lengths. The results obtained for local suction (step reduction in Reynolds number) show that approximately 40 dia are required for the turbulent velocity fluctuations to reach flow equilibrium at the lower downstream value of the Reynolds number. The results for the case of continuous suction show that after a short suction length, there is an apparent increase in the turbulence level compared with that found at the same Reynolds number with no suction. This appears to be due to the greater turbulence level which exists at the higher (presuction) Reynolds number. Longer suction lengths, above 40 dia, always result in a decrease in the turbulence level compared with turbulent flow with no suction at the same Reynolds number. The present results suggest that simple mixing-length models, incorporating local flow parameters, may be inadequate to describe the turbulent momentum transport in a tube with surface suction. Certainly, the existing mixing-length models should be re-examined in the light of this new experimental data.

Introduction

It is known that the withdrawal of fluid through the flow boundary (surface suction) had a marked effect on the turbulent transport of heat, mass, and momentum. For external flows, this effect has been studied thoroughly, both analytically and experimentally [1-4],[1] and it is well established that the suction has a laminarizing effect. Less work has been done for tube flow, and contradicting results are reported in the literature. Kinney and Sparrow [5] approached the problem analytically and developed a model for the prediction of the flow field from basic equations. In their analysis, they used the usual mixing length relation with a Van Driest damping factor [6] modified for wall suction, and the model predicts that the turbulence level (i.e., mixing length), at a fixed distance from the wall, should increase with suction. A similar analytical model, but with different modification of the Van Driest damping factor, was presented by Merkine, Solan, and Winograd [7]. Similar mean axial velocity profiles and pressure drops are predicted by the two models. However, in contradiction to the model of Kinney and Sparrow, the model of Merkine, et al., predicts a decrease of the turbulence level (i.e., mixing length) with suction. Both analytical approaches assume local similarity in the velocity profiles.

The results of the few experiments that are reported in the literature are also in contradiction. Weissberg and Berman [8, 9] measured the velocity field and pressure drop in tube flow with suction, and observed that the turbulence levels over the entire cross section are lowered by suction. The suction length varied in their experiments from 25 to 70 dia. Aurille [10] measured velocity profiles and pressure drops in turbulent pipe flow subjected to uniform suction and also concluded that the turbulence level is lowered by suction. Recently, Aggarwal, et al. [11] measured pressure gradients, temporal mean axial velocity profiles, and the turbulent velocity fluctuations over a wide range of Reynolds numbers and ratios of the transverse ("suction") velocity to mean axial velocity. Unlike the experimental results of the previous investigators, it is reported in [11] that the turbulence level was found to increase with suction. The maximum suction length in those experiments was less than 10 dia.

While the contradiction between the predictions of [5, 7] results from the different modifications of the Van Driest damping factor introduced in the models, the disagreement between the experimental results is obviously due to some difference in the experimental conditions. Therefore, the present work was undertaken in order to better understand the reasons for the contradiction between the reported experimental results and to find sound experimental evidence in support of one of the analytical models.

The Experimental System

The experimental setup, shown schematically in Fig. 1, was constructed so that the suction length could be varied from 0 to 90 dia. In this way, the flow conditions of both [8, 11] could be reproduced. Air from the main blower was delivered through fine mesh screens and a calming chamber into a 0.060m dia and 5.4m

[1] Numbers in brackets designate References at end of paper.

Contributed by the Heat Transfer Division for publication in the JOURNAL OF HEAT TRANSFER. Manuscript received by the Heat Transfer Division, August 24, 1973. Paper No. 74-HT-BB.

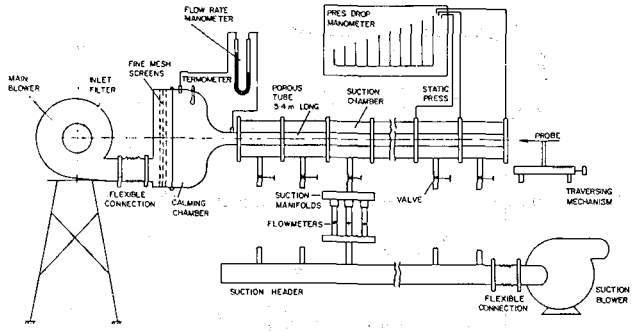

Fig. 1 Diagram of flow apparatus

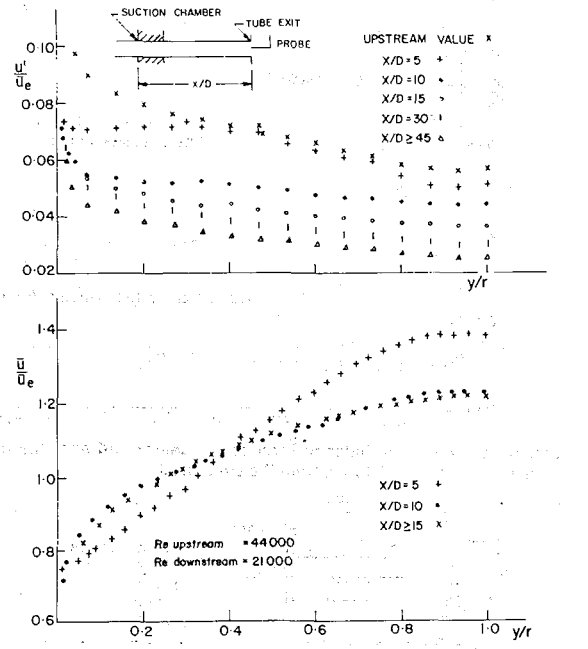

Fig. 2 Effect of downstream tube-length on the mean velocity and turbulent-velocity-fluctuations following local suction: low Reynolds number case

long porous tube. The porous tube was composed of six polyethylene sections, each 0.9m long, supplied by Bel Art, Inc., New Jersey. The pore size of the tube's wall was 60μ, and its relative roughness, ϵ/D, was 0.0115. The permeability of the tube was checked in the azimuthal and longitudinal directions and was found to be uniform. The ends of each section were machined in order to reduce the discontinuity in the joints to less than the roughness size. The test section was leveled with the aid of a theodolite and its alignment was checked by means of a laser beam.

Eighteen static pressure taps, at equal distances, were provided along the tube. The inlet Reynolds number could be varied between 10^4 to 2×10^5 and suction rates, α (the ratio of the transverse velocity at the wall, v_w, to the temporal mean axial velocity averaged over the cross section, $\bar{u}_m$) between 0 to 0.02. The suction was provided by an auxiliary suction blower through a suction header which was connected through flow meters and gate valves to eighteen suction chambers which surround the porous tube (see Fig. 1). Each suction chamber was isolated from the others so that the flow rate through each, and correspondingly the average suction velocity through the 0.30m long porous tube section which it surrounds, could be controlled and measured independently by means of the gate valve and flow meter connecting it to the suction header.

Measurements of the mean axial velocity and the turbulent velocity fluctuations were taken with a DISA 55D01 constant temperature anemometer with 5 percent accuracy. A hot wire probe, DISA type 55A22, was used for axial velocity-fluctuation measurements, and an X-probe made on special order by Thermo-Systems Inc., was used for the transverse velocity fluctuations. The probes were calibrated before and checked after each run in a TSI 1125C calibrator. A micrometric stage with 0.01mm accuracy allowed for radial traverse of the exit plane of the porous tube.

In order to test the equipment, two sets of preliminary experiments were carried out. The first set was performed in a smooth (nonporous) tube and the results of the measurements were compared and found to be in agreement with those of Laufer [12]. The second set of experiments was carried out in the porous tube but with no suction applied. This set was a basis for comparison to the data of the experiments with suction.

Experimental Results

Results With Local Suction. In the first set of experiments, the flow was subjected to local suction by withdrawing fluid through one chamer only (5 dia in length). Measurements were always made at the outlet of the complete setup (that is at the open end of the test section). The downstream mean axial velocity profile and radial distribution of the turbulent velocity-fluctuations were measured for varying upstream locations of the suction site. This varied from $x/D = 5$ (the last chamber) to $x/D = 60$ (corresponding to suction from the first chamber). In this way the length required for the flow to readjust from the higher upstream (presuction) Reynolds number to the lower downstream Reynolds number could be determined.

Typical results are shown in Figs. 2 and 3. The radial distribution of the mean axial velocity shows that the effect of the local suction is to flatten the velocity profile over the central portion of the flow. The adjustment is made within 10 to 15 dia from the beginning of the suction site. For longer distances, the profile is indistinguishable from the fully developed velocity profile at the same (downstream) Reynolds number. However, it is clear from the radial distribution of the axial turbulent-velocity-fluctuations, that the effect of the local suction extends much further downstream than 15 dia. Only after 45 dia is the turbulence profile the same as that for a turbulent flow with no suction but at the same exit Reynolds number. The radial distribution at the upstream Reynolds number is also shown in Figs. 2 and 3, and it should be noted that at no point in the cross section is the relative turbulence increased by the suction.

The results of Fig. 2 are examined further in Fig. 4. Here, the

Nomenclature

D = inside diameter of the porous tube
$P(u'/\sqrt{u'^2})$ = probability density of $(u'/\sqrt{u'^2})$
Re = Reynolds number [$= \rho \bar{u}_m D/\mu$]
r = radius of the porous tube [$= D/2$]
u_m = temporal mean axial velocity
$\bar{u}_m$ = temporal mean axial velocity averaged over the cross section
$\bar{u}_e$ = temporal mean axial velocity averaged over the exit cross section
u' = axial turbulent velocity fluctuation
$\sqrt{u'^2}$ = RMS value of u'
v_w = radial velocity at the wall
v' = radial turbulent velocity fluctuation
x = axial distance measured from the beginning of the suction site
y = radial distance, measured from the wall
α = suction ratio [$= v_w/\bar{u}_m$]
ϵ = wall roughness size

turbulence level in the center of the tube ($y/r = 1$) and near the wall ($y/r = 0.08$) is plotted as a function of the distance from the upstream end of the suction site. In the center of the tube, the turbulence decays monotonously like $(x/D)^{-1/2}$ from the high Reynolds number level to the low Reynolds number level, much like the decay of isotropic turbulence behind a grid. Near the wall there is a sharp decrease in the turbulence followed by a slow adjustment to the far downstream level. Similar results were obtained for the transverse turbulent-velocity-fluctuations.

Results With Continuous Suction. When wall suction is applied to a tube flow, the Reynolds number decreases continuously along the tube length. This is unlike the situation in tube flow without suction in which the Reynolds number is a constant. With sufficiently large suction rates, flow conditions that might be called "fully developed" (to which the analytical models of [5, 7] apply) would never be realized because all the fluid is removed through the wall before local flow equilibrium is established. In the present set of experiments, entrance flows and suction rates were selected such that the effect of the varying length of the continuous suction could be observed at the exit of the tube for a fixed exit Reynolds number (based on the temporal mean axial velocity) which is maintained there. Approximately uniform suction ratios, α, were achieved by adjusting downward the flow rate through each suction chamber (and thus v_w) in proportion to the change in the average axial velocity resulting from the suction. Measurements were taken for varying exit Reynolds number ($10^4 < \mathrm{Re} < 7 \times 10^4$) and suction ratios ($0.001 < \alpha < 0.018$).

Typical results, for $\mathrm{Re} = 2.1 \times 10^4$ and suction ratios of $\alpha = 4 \times 10^{-3}$ and $\alpha = 2.69 \times 10^{-3}$, are shown in Fig. 5 and 6, respectively. From these figures, it is clearly seen that after suction has been applied along a sufficient length, a fully developed flow is established in the sense that the normalized velocity distribution is independent of the suction length required to achieve a given exit Reynolds number. Just as for the results obtained with local suction, the fully developed distribution of the temporal-mean velocity is reached after about 10 dia. Also, it takes over 40 dia for the distribution of the turbulent velocity-fluctuations to be

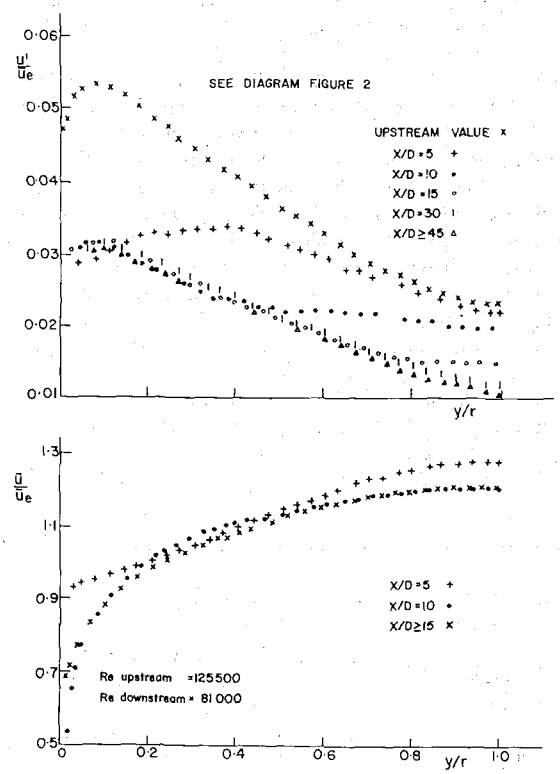

Fig. 3 Effect of downstream tube-length on the mean velocity and turbulent-velocity-fluctuations following local suction: high Reynolds number case

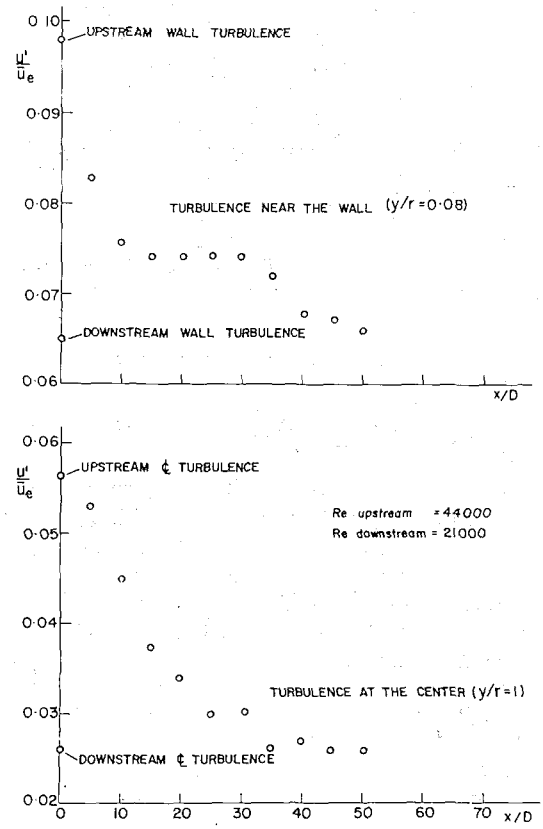

Fig. 4 Change in turbulence level at the center and near the tube wall as a function of the distance from the suction site

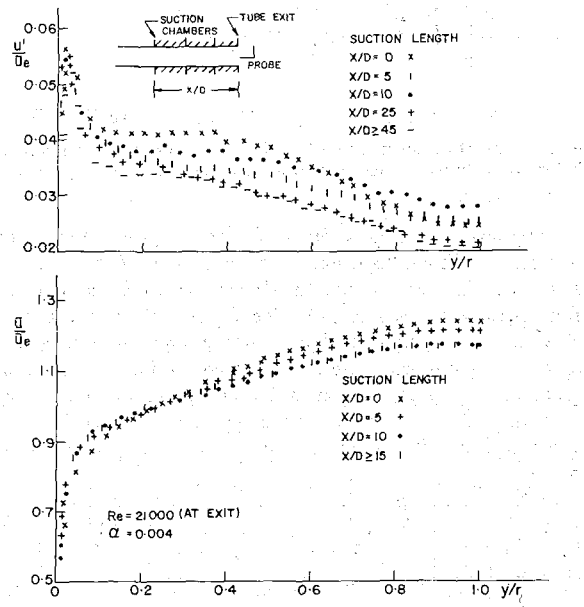

Fig. 5 Effect of continuous suction length on profiles of the mean velocity and turbulent-velocity-fluctuations: high suction ratio

fully established. After suction has been applied over a short length only ($x/D < 10$), the turbulence level in the center of the tube is above that of the same Reynolds number but with no suction. This is in accord with the findings reported by Aggarwal, et al. [11]. However, as the suction length increases ($x/D > 25$), the turbulence level decreases. This is in agreement with the observation of Weissberg and Berman [8, 9] that turbulence level is lowered by suction.

The results of Fig. 6 are replotted in Fig. 7, in the form of turbulence level at the center of the tube and near the wall as a

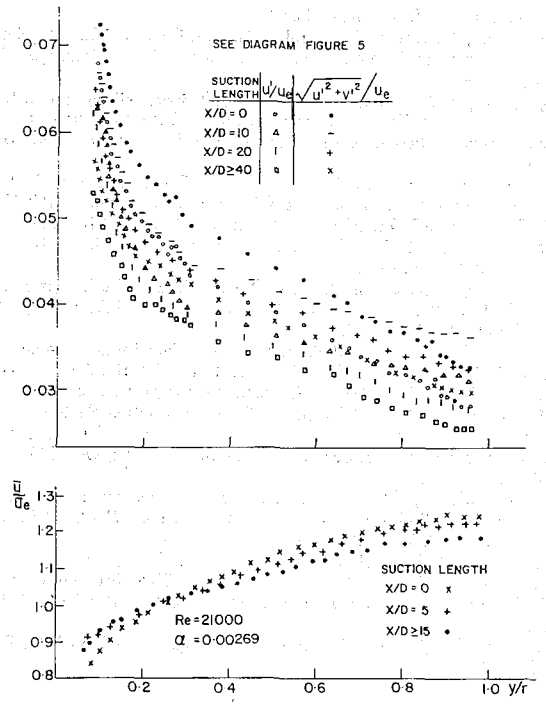

Fig. 6 Effect of continuous suction length on profiles of the mean velocity and turbulent-velocity-fluctuations: low suction ratio

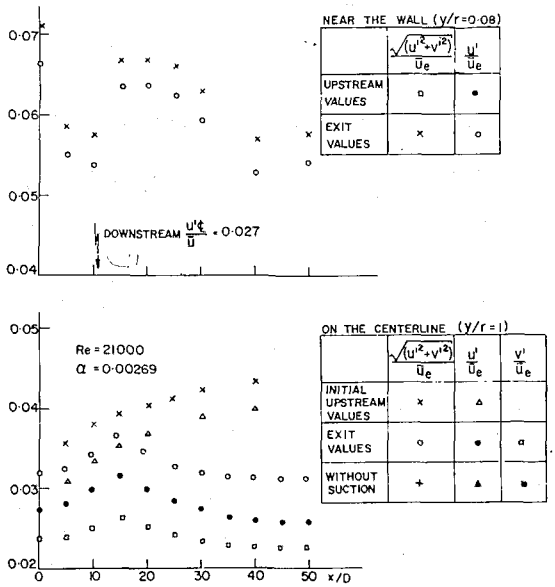

Fig. 7 Turbulence level at the center and near the wall of the tube as a function of suction length

function of the suction length. The turbulence level at the upstream point (prior to where suction has been started) and at the exit plane for the same Reynolds number but with no suction, are also indicated in Fig. 7. The upstream turbulence (lower portion of the figure) varies with x/D because the longer the suction length, the higher the upstream Reynolds number must be in order to maintain the same exit plane Reynolds number.

In the center of the tube, the turbulence level first increases to a maximum and then decreases to a level below the turbulence at the same Reynolds number but with no suction. At no point, however, is the turbulence higher than its upstream value.

Near the wall, the turbulence decreases sharply immediately after the suction has started. It then rises, never exceeding the upstream level, and with continued suction it drops slowly to its fully developed level.

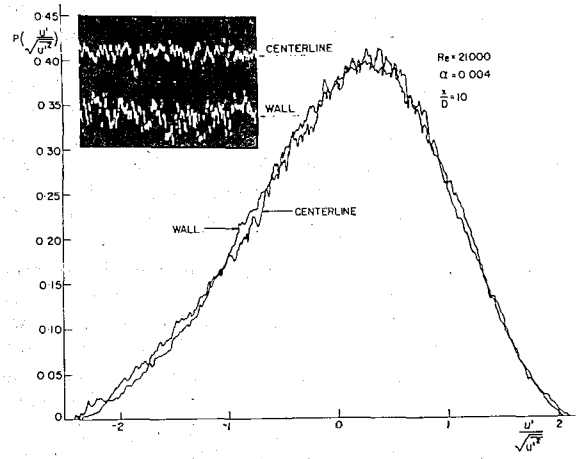

Fig. 8 Amplitude probability density of u' fluctuations at the center and near the wall of the tube with suction

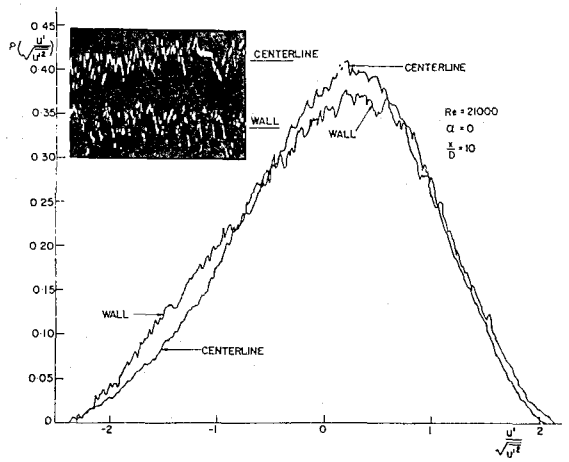

Fig. 9 Amplitude probability density of u' fluctuations at the center and near the wall of the tube with no suction

Discussion and Conclusions

In varying the suction length continuously from 5 dia to 90 dia the apparently contradicting results of Weissberg and Berman [8, 9], and Aggarwal, et al. [11] were found to be reproducible. Recall that the results obtained for local suction show that the decay of the turbulence level after a step reduction in the Reynolds number occurred over a length on the order of 40 dia. The length required for the establishment of a fully developed turbulent flow with a continuous suction was found to be of the same order. This suggests that the apparent increase in the turbulence level in the center of the tube, which is observed after suction has been applied over a short length, results directly from the fact that the turbulence there was generated at a higher upstream Reynolds number.

The dependence of the turbulence in the center of the tube on the suction length, which shows an increase to a maximum and then decreases to the fully developed level, results from the combined effects of the axial convection of turbulence generated at higher upstream Reynolds number, together with the decay of the turbulence as a result of the suction. The turbulence near the wall exhibits a more complicated behavior which points to the existence of a third effect, the radial convection of turbulence from the center (where it is lower) to the wall, a mechanism which contributes to the sharp decrease in the turbulence near the wall immediately after the start of suction.

To gain a better picture of the foregoing lateral transport mechanism, amplitude probability density measurements were taken at the center of the tube and near the wall, with and without suction. The results, shown in Figs. 8 and 9, support the assumption

that as a result of the suction, radial convection of turbulence from the center to the wall contributes to the turbulence near the wall. For flow with short suction (i.e., in the transition zone), the amplitude probability density distribution near the wall is almost the same as that in the center (Fig. 8), which is the same as the distribution in the center of the tube with no suction. This is unlike the well-known situation which is found when no suction is applied (Fig. 9). In this latter instance, there is a distinct difference between the amplitude probability density distribution in the center and near the wall.

In conclusion, the turbulence level in fully developed turbulent flow with suction, to which the analytical models of [5, 7] apply, seems to be lower than in the corresponding turbulent flow with no suction. From the phenomenological point of view, this result is in favour of the analytical model proposed by Merkin, et al. [7], but basically the flow seems to be much more complex than originally thought, and the simple mixing length models fall way short of describing the effect of suction on turbulent pipe flow. Much more experimental work especially in the transition zone, is clearly indicated.

References

1 Schlichting, H., *Boundary Layer Theory,* McGraw Hill., New York, Sixth ed., 1968, p. 483.

2 Kays, W. M., Moffat, R. T., and Thielbahr, W. H., "Heat Transfer to the Highly Accelerated Turbulent Boundary Layer With and Without Mass Addition," ASME Paper No. 69-HT-53.

3 Favre, A., Dumas, R., Verollet, E., and Coantic, M., "Couche limite turbulente sur paroi poreuse avec aspiration," *J. de Mecanique,* Vol. 5, 1966, pp. 3-28.

4 Rotta, J. C., "Über die Geschwindigkeitsverteilung bei turbulenter Stroemung in der Naehe poroeser Waende," *Deutsche Luft- and Raumfahrt, Forschungsbericht 66-45, Aerodynamische Versuchsanstalt Goettingen,* 1966.

5 Kinney, R. B., and Sparrow, E. M., "Turbulent Flow, Heat Transfer, and Mass Transfer in a Tube With Surface Suction," JOURNAL OF HEAT TRANSFER, TRANS. ASME, Series C, Vol. 92, 1970, p. 117.

6 Van Driest, E. R., "On Turbulent Flow Near Wall," *J. Aeronautical Sci.,* Vol. 23, 1956, p. 1007.

7 Merkine, L., Solan, A., and Winograd, Y., "Turbulent Flow in a Tube With Wall Suction," JOURNAL OF HEAT TRANSFER, TRANS. ASME, Vol. 93, 1971, p. 242.

8 Weissberg, H. L., and Berman, A. S., "Velocity and Pressure Distributions in Turbulent Pipe Flow With Uniform Wall Suction," *Proceedings Heat Transfer and Fluid Mechanics Institute,* XIV/1-30, 1955.

9 Weissberg, H. L., "Velocity Profiles and Friction Factors for Turbulent Pipe Flow With Uniform Wall Suction," Report K-1264, Union Carbide Nuclear Co., Oak Ridge Gaseous Diffusion Plant, Oak Ridge, Tenn., 1966.

10 Aureille, A., "Contribution a l'etude de l'ecoulement turbulent dans une conduite cylindrique poreuse avec aspiration," *Publs. Scient. Tech. Minist. Air,* No. 433, 1967.

11 Aggarwal, J. K., Hollingsworth, H. A., and Mayhew, Y. R., "Experimental Friction Factors for Turbulent Flow With Suction in a Porous Tube," *International Journal of Heat and Mass Transfer,* Vol. 15, 1972, p. 1585.

12 Laufer, J., "The Structure of Turbulent Pipe Flow," T. R. 1174, NACA, 1954.

G. Walker
R. M. Terrill

Department of Applied Mathematics
and Theoretical Physics,
University of Liverpool,
Liverpool, England

Mass Transfer Cooling of Laminar Flow Between Parallel Porous Plates

The limiting temperature and mass concentration profiles and the limiting wall Nusselt number are obtained for the laminar nonisothermal flow in a two-dimensional porous channel. Results are reported for a uniform rate of injection at the wall of a foreign component of higher thermal capacity than the fluid in the channel. An exact solution of the diffusion equation is found while numerical and analytic solutions of the energy equation are discussed for small injection rates. It is shown that the enthalpy transport resulting from the diffusion process has an effect equivalent to increasing the Prandtl number. It is also found that, for a given injection velocity at the wall, the limiting Nusselt number is significantly reduced by the injection of a foreign component of high thermal capacity.

1 Introduction

In recent years a great deal of attention has been focussed upon the use of transpiration cooling as a means of maintaining tolerable surface temperatures within the flow of a hot fluid. This method appears to have first been used to protect airfoil surfaces in hypersonic flight. As a result, many authors have considered the problem of mass transfer in laminar boundary layer flow over a porous flat plate, and a comprehensive survey has been given by Hartnett and Eckert [1].[1] It was also thought that these boundary layer solutions might be applicable to transpiration cooling problems associated with combustion chambers, rocket motors, gas turbine blades, and nuclear reactor cooling systems. However, since analytic and numerical solutions to the full Navier-Stokes equations for the flow through a porous pipe and through porous parallel plates have now been developed, it is possible to attempt solutions to the corresponding mass transfer problems. In particular, the validity of results for flow through porous channels and pipes based on the boundary layer assumptions can be tested.

The first attempt to solve the latter class of problems was made by Yuan and Finkelstein [2] who investigated nonisothermal laminar flow through a porous pipe. They assumed that the suction or injection at the wall was small and obtained the heat transfer coefficient when the flow experienced a discontinuous change in wall temperature. More recently, Kinney [3] extended Yuan and Finkelstein's results to discuss the fully developed skin friction and heat transfer coefficients and Libby, Lui, and Williams [4] have given a detailed discussion of the pressure and frictional characteristics in the entry length of a porous pipe with isothermal mass transfer. Variable property solutions of the heat and mass transfer problem in a circular pipe have been given by Yuan and Peng [5, 6].

Solutions to the heat and mass transfer problems for flow through porous parallel plates have been given by Terrill [7] and Terrill and Walker [8]. They considered a flow which experienced a discontinuous change in wall temperature corresponding to the solutions of Prins, Mulder, and Schenk [9] and Hatton and Turton [10] for impermeable plates. Raithby [11, 12] discusses the thermal entrance and thermally developed regions for both the porous circular pipe and porous parallel plate geometries. He considers a wide range of wall suction Reynolds numbers and gives solutions for both the constant wall temperature and constant heat flux boundary conditions. All these results show that the heat transfer coefficient at the wall decreases with increasing injection and increases with increasing suction.

A variable property heat transfer solution for porous parallel plates has been reported by Doughty and Perkins [13] who show that the principal effect of property variation is to slightly increase the Nusselt number above its constant property value. The previous papers were all concerned with the injection of a like fluid through the wall whereas the present paper determines, for a fixed rate of injection, the effect upon the heat transfer coefficient when a foreign component of higher thermal capacity is injected at the wall. The injection of a foreign component through the wall gives rise to an additional equation, the diffusion equation, which must be solved together with the Navier-Stokes, continuity and energy equations. It also introduces an extra term into the energy equation corresponding to the net transport of enthalpy within the system. Hartnett and Eckert [1] neglected this term by assuming that the specific heats of the individual components were not too different. The enthalpy transport term was also neglected by Sparrow and Yu [14] in their consideration of the fully developed temperature and mass fraction profiles for the injection of a foreign component through the walls of a porous parallel plate channel when the velocities of injection at the walls are unequal. Papers in which the enthalpy transport term has been included have usually been primarily concerned with variable property solutions. For example, the paper by Yuan and Peng [6] on pipe flow, the paper by Sparrow, Minkowycz, Eckert, and Ibele [15] on the effects of diffusion thermo and thermal dif-

[1] Numbers in brackets designate References at end of paper.

Contributed by the Heat Transfer Division for publication in the JOURNAL OF HEAT TRANSFER. Manuscript received by the Heat Transfer Division, July 23, 1973. Paper No. 74-HT-FF.

fusion in the variable property boundary layer and also the paper by Hurley [16] which dealt with the effects of injecting various different fluids into a mainstream boundary layer flow. In the present constant property analysis the enthalpy transport term will be retained and it will be seen to be significant.

2 The Equations of Motion

A fluid, with constant properties, flows between two porous parallel plates. Take x and y to be the distances measured parallel and perpendicular to the channel walls, respectively, and u and v to be the velocity components in the directions of x and y increasing, respectively. Choose a nondimensional distance $\eta = y/h$ such that $\eta = 0$ is the center of the channel and $\eta = \pm 1$ at the walls. Berman [17] has shown that the equation of continuity can be satisfied by

$$u = \left(\frac{hU - Vx}{h}\right) f'(\eta); \quad v = Vf(\eta), \tag{1}$$

where V is the constant velocity of suction at the wall and U is the velocity of the fluid in the x direction at $x = 0$. The Navier-Stokes equations reduce to

$$f^{iv} + R(f'f'' - ff''') = 0 \tag{2}$$

with boundary conditions

$$\begin{aligned} f(0) &= 0 & f''(0) &= 0 \\ f(1) &= 1 & f'(1) &= 0, \end{aligned} \tag{3}$$

where $R = Vh/\nu$ is the suction Reynolds number. For small R, the solution of (2) and (3) is given in [18], namely,

$$f(\eta) = \left(\frac{3}{2}\eta - \frac{1}{2}\eta^3\right) + R/280(-\eta^7 + 3\eta^3 - 2\eta) + 0(R^2). \tag{4}$$

It is worth noting that solution (4) is accurate for $-7 \leq R \leq 7$.

3 The Mass Transfer Problem

The injection of a foreign component into the fully developed flow of the primary component begins at $x = 0$. Conservation of mass gives rise to the diffusion equation

$$u\frac{\partial \omega}{\partial x} + v\frac{\partial \omega}{\partial y} = D_{12}\left(\frac{\partial^2 \omega}{\partial x^2} + \frac{\partial^2 \omega}{\partial y^2}\right), \tag{5}$$

where ω is the mass fraction of the diffusing component, and where D_{12}, the coefficient of diffusion, is constant. Write $W = 1 - \omega$ and neglect the longitudinal diffusion compared to the lateral mass diffusion; then equation (5) becomes, after substitution of the velocity components from (1),

$$(1 - \mathrm{RSc}\xi)f'(\eta)\frac{\partial W}{\partial \xi} + (\mathrm{RSc})f(\eta)\frac{\partial W}{\partial \eta} = \frac{\partial^2 W}{\partial \eta^2} \tag{6}$$

where $\xi = x/h\mathrm{R}^*\mathrm{Sc}$, $\eta = y/h$, $\mathrm{Sc} = \nu/D_{12}$ is the Schmidt number and $\mathrm{R}^* = Uh/\nu$ is the channel Reynolds number. The boundary conditions on W are

$$\left.\begin{aligned} &W = 1 \quad \text{at} \quad \xi = 0, && -1 < \eta < 1; \\ &\text{by symmetry,} \ \frac{\partial W}{\partial \eta} = 0 \quad \text{at } \eta = 0, && \xi > 0; \\ &\text{and} \qquad \mathrm{RSc}\,W = \frac{\partial W}{\partial \eta} \ \text{at } \eta = \pm 1, && \xi > 0. \end{aligned}\right\} \tag{7}$$

The final boundary condition on W was obtained from the condition that the net mass flux of the primary component at the wall is zero. It is clear from (6) that the parameter of major importance in the solution for W, and hence ω, is the product RSc. This result is not surprising since the analogous heat transfer problem is strongly dependent upon the product RPr. The deviation from total dependence upon these products is brought about by the $f(\eta)$, which, from (4), is weakly dependent upon R.

A solution of (6) can be found by writing $W(\xi, \eta) = N(\xi)M(\eta)$; it follows that

$$N(\xi) = (1 - \mathrm{RSc}\xi)^{\gamma^2/\mathrm{RSc}} \tag{8}$$

and

$$M''(\eta) - \mathrm{RSc}f(\eta)M'(\eta) + \gamma^2 f'(\eta)M(\eta) = 0, \tag{9}$$

where γ is a constant. Thus the solution of the diffusion equation is

$$1 - \omega = W(\xi, \eta) = \sum_j E_j(1 - \mathrm{RSc}\xi)^{\gamma_j^2/\mathrm{RSc}} M_j(\eta); \tag{10}$$

The E_j are constants to be determined from the boundary condition at $\xi = 0$, and the $M_j(\eta)$ are those eigenfunctions, corresponding to eigenvalues γ_j, for which solutions of (9) satisfy the boundary conditions

$$\begin{aligned} M_j(0) &= 1 & M_j'(0) &= 0 \\ \mathrm{RSc}M_j(\eta) &= M_j'(\eta) \ \text{ for } \eta = \pm 1. \end{aligned} \tag{11}$$

It can be shown that the eigenfunctions $M_j(\eta)$ ($j = 1,2,3, \ldots,$) obey the usual orthogonality relationships and that the constants E_j are given by

$$E_j = -2/\gamma_j\left\{\frac{\partial M_j}{\partial \gamma_j} - \frac{1}{\mathrm{RSc}}\frac{\partial^2 M_j}{\partial \gamma_j \partial \eta}\right\}_{\eta=1} \tag{12}$$

Numerical solutions of equation (9), subject to (11), were obtained by means of a Runge-Kutta procedure on the computer. Only the first, and most important, eigensolution will be discussed here as it alone affects the heat transfer problem under consideration and, sufficiently far downstream, the fully developed concentration profile is given by this eigensolution. Further

Nomenclature

$B_n(\eta)$ = eigenfunctions
$B_0^{(0)}(\eta)$ = first eigenfunction for no injection
$B_0^{(m)}(\eta)$ = corrections to eigenfunctions for small injection
Cp = specific heat at constant pressure
D_{12} = coefficient of diffusion
D = constant defined by equation (27)
E_j = eigenconstants given by equation (12)
$f(\eta)$ = function defined in equation (1)
$2h$ = channel width
k = thermal conductivity
K_0 = eigenconstant defined in Section 4
$M_j(\eta)$ = eigenfunctions
Nu* = limiting Nusselt number
Pr = $\mu Cp/k$ = Prandtl number
R = Vh/ν = suction Reynolds number
R* = Uh/ν = channel Reynolds number
Sc = ν/D_{12} = Schmidt number
T = temperature
U = velocity of fluid at $x = 0$
V = constant velocity of fluid at the wall
x, y = distances measured parallel and perpendicular to the channel walls, respectively
$Y = \frac{\partial M_0}{\partial \gamma_0}$ = derivative of eigenfunction with respect to eigenvalue
β_0^2 = eigenvalue
γ_j^2 = eigenvalues
$\eta = y/h$ = nondimensional distance perpendicular to the channel walls
ν = kinematic viscosity
$\xi = x/(h\mathrm{R}^*Sc)$ = nondimensional distance along the channel
ρ = density
$\theta = \frac{T - T_w}{T_0 - T_w}$ = nondimensional temperature
ω = mass fraction of the foreign component

Subscripts

1 = foreign component
2 = primary component
w = wall
CL = center line $y = 0$

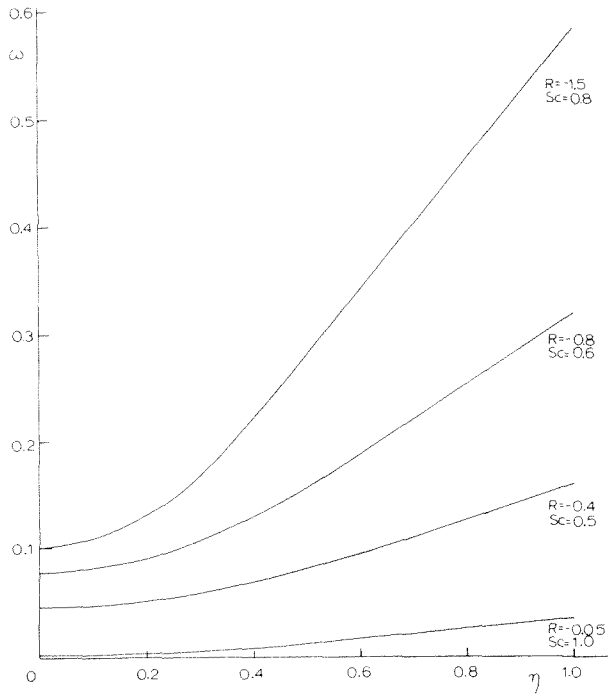

Fig. 1 Mass concentration profiles

eigensolutions can be obtained from the authors. Profiles, for several values of R and Sc, evaluated at the cross section given by $x/h = R^*/5$, are shown in Fig. 1.

An analytical expression for the first eigensolution will now be attempted. The equation for $M_0(\eta)$ is

$$M_0''(\eta) - \mathrm{RSc} f(\eta) M_0'(\eta) + \gamma_0^2 f'(\eta) M_0(\eta) = 0 \qquad (13)$$

with boundary conditions

$$M_0(0) = 1,\ M_0'(0) = 0,\ \mathrm{RSc} M_0(1) = M_0'(1). \qquad (14)$$

When the injection Reynolds number is small, it can be shown, after considerable mathematical work, that

$$\gamma_0^2 = -\mathrm{RSc}. \qquad (15)$$

For this value of γ_0^2 equation (13), subject to boundary conditions (14), can be integrated exactly, viz.

$$M_0(\eta) = \exp\{\mathrm{RSc} \int_0^\eta f(\eta) d\eta\}\ . \qquad (16)$$

The solution (16) is remarkable since it is an *exact* solution of the diffusion equation. (In fact (15) and (16) are the solution of (13) for all values of R; for large R the appropriate $f(\eta)$ is given in [18].) There is perfect agreement between this exact solution and numerical results. It is worth noting that the variation of the $\int_0^\eta f(\eta) d\eta$ with R is very small, so that, $M_0(\eta)$ depends almost entirely on the value of the product RSc.

To complete the first eigensolution, E_0, given by (12), must be found. Write $Y(\eta) = \partial M_0/\partial \gamma_0$; then differentiating (13) with respect to γ_0 gives

$$Y''(\eta) - \mathrm{RSc} f(\eta) Y'(\eta) + \gamma_0^2 f'(\eta) Y(\eta) = -2\gamma_0 f'(\eta) M_0(\eta)\ , \qquad (17)$$

while the boundary conditions are

$$Y(0) = 0,\ \ Y'(0) = 0\,. \qquad (18)$$

By integrating (17), subject to (18), it can be shown that

$$E_0 = [\int_0^1 f'(\eta) M_0(\eta) d\eta]^{-1}. \qquad (19)$$

Substitution for $f(\eta)$ from (4) and $M_0(\eta)$ from (16) yields

$$E_0 = 1 - \mathrm{RSc}(0.13929 + 0.00034\mathrm{R} + 0.00003\mathrm{R}^2) + \mathrm{R}^2\mathrm{Sc}^2(-0.00048 + 0.00002\mathrm{R}) + \mathrm{R}^3\mathrm{Sc}^3(0.00044) + 0(\mathrm{R}^4\mathrm{Sc},\ \mathrm{R}^4\mathrm{Sc}^2,\ \mathrm{R}^4\mathrm{Sc}^3), \qquad (20)$$

after the exponential has been expanded for R small. The values of E_0 obtained from (21) agree to within an error of at most 10^{-4} with numerical results for the range of values of R and Sc used in Fig. 1. It follows that when particular values of R and Sc are specified, accurate results for $M_0(\eta)$, γ_0 and E_0 can be obtained from (15), (16), and (20) thus rendering numerical solutions for $M_0(\eta)$ unnecessary.

4 The Heat Transfer Problem

The effects of a discontinuous change of wall temperature at $x = 0$ can now be studied. Suppose that the constant temperature of the walls and fluid is $T = T_0$ for $x < 0$ while for $x > 0$ the constant temperature of the walls is $T = T_W$. For constant fluid properties the equation of energy may be written as

$$\rho Cp(u\frac{\partial T}{\partial x} + v\frac{\partial T}{\partial y}) = k(\frac{\partial^2 T}{\partial x^2} + \frac{\partial^2 T}{\partial y^2}) + \rho D_{12}(Cp_1 - Cp_2)(\frac{\partial T}{\partial x}\frac{\partial \omega}{\partial x} + \frac{\partial T}{\partial y}\frac{\partial \omega}{\partial y}) \qquad (21)$$

where Cp and Cp_i are the specific heats at constant pressure of the mixture and species i, respectively, and k is the thermal conductivity. The work due to the pressure gradient and viscous dissipation have been neglected in deriving (21) while the final term in the equation accounts for the net transport of enthalpy within the system. Introducing a nondimensional temperature

$$\theta = \frac{T - T_w}{T_0 - T_w}$$

and neglecting the longitudinal heat conduction and enthalpy transport, equation (21) may be rewritten as

$$\frac{\mathrm{Pr}}{\mathrm{Sc}}(1 - \mathrm{RSc}\xi) f'(\eta)\frac{\partial \theta}{\partial \xi} + \mathrm{RPr} f(\eta)\frac{\partial \theta}{\partial \eta} = \frac{\partial^2 \theta}{\partial \eta^2} + (\frac{Cp_1 - Cp_2}{Cp})\frac{\mathrm{Pr}}{\mathrm{Sc}}\frac{\partial \theta}{\partial \eta}\frac{\partial \omega}{\partial \eta}\,, \qquad (22)$$

where $\mathrm{Pr} = \mu Cp/k$ is the Prandtl number. The boundary conditions on θ are

$$\left.\begin{aligned} \theta &= 1 \quad \text{at } \xi = 0, \quad -1 < \eta < 1 \\ \theta &= 0 \quad \text{for } \xi > 0, \quad \eta = \pm 1 \\ \frac{\partial \theta}{\partial \eta} &= 0 \quad \text{for } \xi > 0, \quad \eta = 0 \end{aligned}\right\} \qquad (23)$$

the last condition arising from symmetry.

To make further progress with the solution of (22) it is usually assumed that the enthalpy transport term is zero. Here the term $(\partial \omega/\partial \eta)$ will be taken to vary slowly with ξ so that the resulting solution will be almost asymptotic. Hence from (10),

$$(\frac{\partial \omega}{\partial \eta})_{\xi = \xi_0} = -E_0(1 - \mathrm{RSc}\xi_0)^{-1} M_0'(\eta), \qquad (24)$$

which is evaluated at a particular value ξ_0 of ξ and which is taken to be almost constant.

The asymptotic solution of (22) is obtained by writing

$$\theta(\xi, \eta) = A(\xi) B(\eta)$$

which yields

$$\theta = K_0(1 - \mathrm{RSc}\xi)^{\beta_0^2/\mathrm{RPr}} B_0(\eta)$$

where

$$K_0 = -2/\beta_0[\frac{\partial B_0}{\partial \beta_0}]_{\eta = 1}$$

The first eigenfunction $B_0(\eta)$, corresponding to the first eigenvalue β_0, satisfies

$$B_0''(\eta) + \{\frac{\mathrm{Pr}}{\mathrm{Sc}}(\frac{Cp_1 - Cp_2}{Cp})(\frac{\partial \omega}{\partial \eta})_{\xi = \xi_0} - \mathrm{RPr} f(\eta)\} B_0'(\eta) + \beta_0^2 f'(\eta) B_0(\eta) = 0, \qquad (25)$$

and

$$B_0(0) = 1, \quad B_0'(0) = 0, \quad B_0(1) = 0. \qquad (26)$$

Numerical solutions of (25) were obtained about the cross section

$x_0/h = R^*/5$ at first, by using the first three eigenfunctions in $(\partial\omega/\partial\eta)$ and then by using just the form (24); the difference between the numerical results obtained was negligible. The resulting solutions were used to compute the nondimensional temperature profiles shown in Fig. 2 for various values of R, Pr, Sc, and D where

$$D = \left(\frac{Cp_1 - Cp_2}{Cp}\right)E_0(1 - \mathrm{RSc}\xi_0)^{-1}. \tag{27}$$

A simplified analytic solution exhibiting the effects of the various parameters on the temperature will now be developed. For small R, equation (25) reduces to

$$B_0''(\eta) - \mathrm{RPr}[1 + D]f(\eta)B_0'(\eta) + \beta_0^2 f'(\eta)B_0(\eta) = 0.$$

Following [8], the solution of this equation gives

$$\theta = \{1.2008 - 0.0568\ \mathrm{RPr}(D + 1) + 0.0264\mathrm{R}^2\mathrm{Pr}^2(D + 1)^2 + 0.0008\mathrm{R}\} \times (1 - \mathrm{RSc}\xi)^{\beta_0^2/\mathrm{RPr}}\{B_0^{(0)}(\eta) + \mathrm{RPr}(D + 1)B_0^{(i)}(\eta) + \mathrm{R}^2\mathrm{Pr}^2(D + 1)^2B_0^{(ii)}(\eta) + \mathrm{RB}_0^{(iv)}(\eta)\},$$

where $\beta_0^2 = 2/3\{2.828 - 0.75\mathrm{RPr}(D + 1) + 0.065\mathrm{R}^2\mathrm{Pr}^2(D + 1)^2 + 0.008\mathrm{R}\}$

and the functions $B_0^{(m)}(\eta)$ are tabulated in [8]. Profiles of the nondimensional temperature θ calculated from this analytic solution were in excellent agreement with the numerical results shown in Fig. 2. A limiting Nusselt number Nu* can also be obtained by following the analysis of [8], and thus

$$\mathrm{Nu}^* = 3.770 + \mathrm{RPr}(D + 1) + 0.086\mathrm{R}^2\mathrm{Pr}^2(D + 1)^2. \tag{28}$$

Values of Nu* obtained from (28) are in excellent agreement with the numerical results shown in Fig. 3.

6 Discussion

The assumption that the fluid properties remain constant means that the governing equations may be solved independently.

In Section 3 an exact analytic solution for the first eigenfunction of the diffusion equation is found, which is valid for all R. It is seen that the mass concentration ω is almost totally dependent upon the product RSc. For example, the difference between the solutions for ω when R = −1.0, Sc = 0.1 and when R = −0.1, Sc = 1.0 is negligibly small. Some profiles of the limiting mass concentration ω, evaluated at the cross section $x/h = R^*/5$, are shown in Fig. 1 for a range of values of RSc. The figure shows that the mass concentration increases with increasing |RSc| and that, for a fixed value of RSc, the mass concentration gradient is positive and increases to a maximum value at the wall.

In Section 4, we see that when the enthalpy transport term is included in the energy equation, eigensolutions of this equation can be found if it is assumed that $\partial\omega/\partial\eta$ varies slowly with ξ. In this case the energy equation separates to yield a solution which shows that the major effect of injecting a fluid of higher thermal capacity than the primary component is to increase the Prandtl number by a factor $(D + 1)$. The mass transfer Peclet number RPr is also increased by this factor and, as in Terrill and Walker [8], it is found that as the magnitude of the modified Peclet number increases the magnitude of the temperature gradient at the wall decreases. This result is exhibited in Fig. 2 which shows limiting nondimensional temperature profiles for various R, Pr, Sc, and D. The limiting Nusselt number Nu* also decreases as the magnitude of the Peclet number increases. Fig. 3 shows that Nu* decreases almost linearly with increasing |RPr$(D + 1)$| over the range of values of RPr$(D + 1)$ which were considered. This conclusion is verified by the analytical expression for Nu* given by (28).

It is worth examining how, for a fixed rate of injection, the temperature gradient and hence the limiting Nusselt number, may be most effectively reduced. For fixed R, RPr$(D + 1)$ may be increased by increasing either Pr or D. For most gas mixtures the Prandtl numbers are about unity so the choice of diffusing component has little effect upon Pr. D, however, may be increased most effectively by increasing $(Cp_1 - Cp_2)/Cp$. Thus, for example, the injection of hydrogen into a primary flow of air would be more effective in reducing the temperature gradient at the wall than would the injection of carbon dioxide. Hurley [16] found this to be the case in variable property boundary layer flow. It is also important to note that the value of Sc has little or no effect on the value of D and thus the limiting temperature distribution and Nusselt number are independent of Sc.

It is clear from the analysis that the inclusion of the enthalpy transport term leads to an effective increase in the fluid Prandtl number. The enthalpy transport term is thus a significant term in the energy equation and should be included.

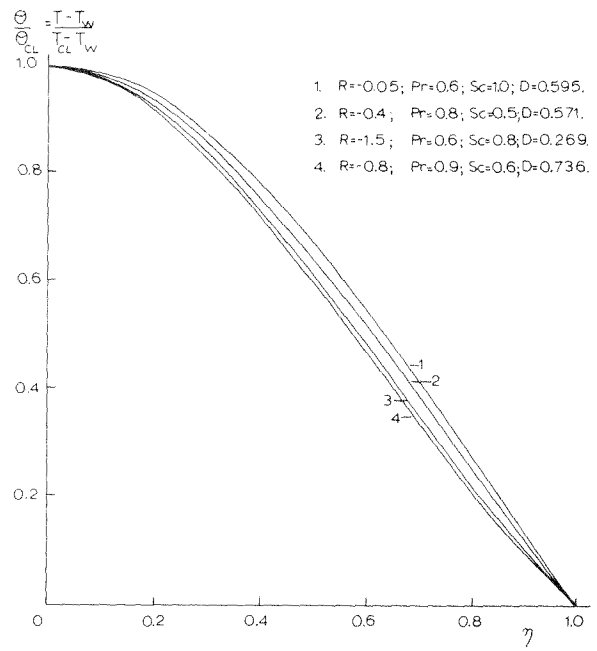

Fig. 2 Temperature difference ratio

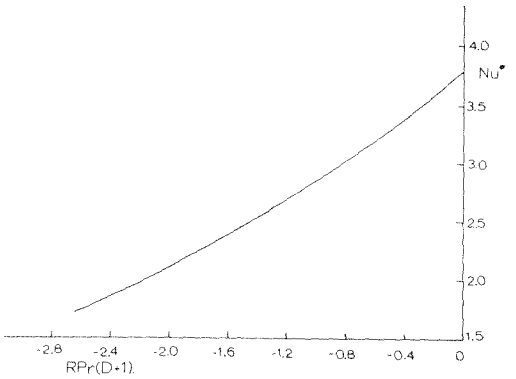

Fig. 3 Limiting Nusselt number

References

1 Hartnett, J. P., and Eckert, E. R. G., "Mass Transfer Cooling in a Laminar Boundary Layer With Constant Fluid Properties," Trans. ASME, Vol. 79, 1957, p. 247.

2 Yuan, S. W., and Finkelstein, A. B., "Heat Transfer in Laminar Pipe Flow With Uniform Coolant Injection," *Jet Propulsion*, Vol. 28, No. 3, 1958, p. 178.

3 Kinney, R. B., "Fully Developed Frictional and Heat Transfer Characteristics of Laminar Flow in Porous Tubes," *International Journal of Heat and Mass Transfer*, Vol. 11, 1968, p. 1393.

4 Libby, P. A., Liu, T. M., and Williams, F. A., "Flow Development in a Tube With Injection of a Light or Heavy Gas," *International Journal of*

Heat and Mass Transfer, Vol. 12, No. 10, 1969, p. 1267.

5 Yuan, S. W., and Peng, Y., "Laminar Non-Isothermal Pipe Flow With Coolant Injection at the Wall," *International Developments in Heat Transfer*, Vol. 4, 1961, p. 717.

6 Yuan, S. W., and Peng, Y., "Laminar Pipe Flow With Mass Transfer Cooling," JOURNAL OF HEAT TRANSFER, TRANS. ASME, Series C, Vol. 87, 1965, p. 252.

7 Terrill, R. M., "Heat Transfer in Laminar Flow Between Parallel Porous Plates," *International Journal of Heat and Mass Transfer*, Vol. 8, 1965, p. 1491.

8 Terrill, R. M., and Walker, G., "Heat and Mass Transfer in Laminar Flow Between Parallel Porous Plates," *Applied Scientific Research*, Vol. 18, 1967, p. 2611.

9 Prins, J. A., Mulder, J., and Schenk, J., "Heat Transfer in Laminary Flow of Fluid Between Parallel Plates," *Applied Scientific Research A2*, 1950, p. 431.

10 Hatton, A. P., and Turton, J. S., "Heat transfer in the Thermal Entry Length With Laminar Flow Between Parallel Walls at Unequal Temperatures," *International Journal of Heat and Mass Transfer*, Vol. 5, 1962, p. 673.

11 Raithby, G., "Laminar Heat Transfer in the Thermal Entrance Region of Circular Tubes and Two Dimensional Rectangular Ducts With Wall Suction and Injection," *International Journal of Heat and Mass Transfer*, Vol. 14, 1971, p. 223.

12 Raithby, G., "Heat Transfer in Tubes and Ducts With Wall Mass Transfer," *The Canadian Journal of Chemical Engineering*, Vol. 50, 1972, p. 456.

13 Doughty, J. R., and Perkins, H. C., "Variable Properties Laminar Gas Flow Heat Transfer in the Entry Region of Parallel Porous Plates," *International Journal of Heat and Mass Transfer*, Vol. 16, 1973, p. 663.

14 Sparrow, E. M., and Yu, H. S., "Heat and Mass Transfer in a Channel With Surface Mass Addition: Application to Phase Change Processes," *Journal of the American Institute of Chemical Engineers*, Vol. 16, No. 4, 1970, p. 588.

15 Sparrow, E. M., Minkowycz, W. J., Eckert, E. R. G., and Ibele, W. E., "The Effect of Diffusion Thermo and Thermal Diffusion for Helium Injection Into Plane and Axisymmetric Stagnation Flow of Air," JOURNAL OF HEAT TRANSFER, Series C, Vol. 86, No. 3, 1964, p. 311.

16 Hurley, D. G., "Mass Transfer Cooling in a Boundary Layer," *Aeronautical Quarterly* Vol. 12, 1961, p. 165.

17 Berman, A. S., "Laminar Flow in Channels with Porous Walls," *Journal of Applied Physics*, Vol. 24, 1953, p. 1232.

18 Terrill, R. M., "Laminar Flow in a Uniformly Porous Channel," *Aeronautical Quarterly*, Vol. 15, 1964, p. 299.

L. C. Thomas
Mechanical Engineering Department,
The University of Akron,
Akron, Ohio

Adaptation of the Surface Renewal Approach to Momentum and Heat Transfer for Turbulent Pulsatile Flow

This paper presents a surface renewal based formulation for convective heat transfer for hydrodynamically and thermally fully developed turbulent flow in a tube. Based on the modeling concept presented in this paper, turbulent pulsatile flow is categorized according to the hydrodynamically unsteady mean residence time, $\tau(t)$.

Introduction

Although the effects of flow pulsation on time average heat transfer characteristics for turbulent tube flow have been investigated as early as 1943 [1],[1] few theoretical analyses appear in the literature for this complex problem. In this connection, the use of the classical eddy diffusivity technique has been greatly hindered by a lack of knowledge concerning the effects of pulsation on ϵ_m and ϵ_H [2]. Because relationships for the time dependent eddy diffusivities are not available in the literature, previous analyses of this type have utilized steady flow information. A general turbulent transport model of another kind has been recently developed, however, for hydrodynamically unsteady operation [3] which provides a foundation for the analysis of this problem. This model is based on the principle of surface renewal which has strong experimental support and which has been adapted to a broad range of turbulent hydrodynamic steady flow convection processes [4, 5, 6, 7 and others], including thermally unsteady processes [8, 9].

In this paper, the surface renewal and penetration model will be adapted to convective heat transfer for hydrodynamically and thermally fully developed turbulent pulsatile flow in a tube.

Mathematical Model

The adaptation of the elementary surface renewal and penetration model to turbulent momentum and heat (mass) transfer involves a consideration of *(a)* the instantaneous molecular transport to individual fluid elements in residence at the surface, and *(b)* the local spatial average transport which is the resultant of the contribution of the numerous eddies which reside in any given vicinity. Because the flow is hydrodynamically unsteady, the analysis of the momentum transport proves to be the key to the successful modeling of this turbulent convection process.

Instantaneous Transport Properties. The development of relationships for the instantaneous momentum transport properties for individual elements of fluid at the surface for values of Re(t) well above the transition region involves a system of equations of the form

$$\frac{\partial u}{\partial \theta} = \nu \frac{\partial^2 u}{\partial y^2} \tag{1}$$

$$u = U_i(t - \xi) \quad \text{at } \theta = 0 \tag{2}$$

$$u = 0 \quad \text{at } y = 0 \tag{3}$$

$$u = U_i(t - \xi) \quad \text{as } y \to \infty \tag{4}$$

where θ is the instantaneous contact time, ξ is the length of time the fluid element has been in contact with the surface, t is the process time, and $U_i(t)$ is the eddy velocity at the first instant of renewal for a hydrodynamically unsteady process. Although the pressure term is assumed to be negligible in the present analysis, this term has been found to become quite important for values of the Reynolds number much less than 10^4 for steady tube or channel flow [7]. Therefore, this analysis is restricted to conditions for which Re$(t) \gtrsim 10^4$.

During the brief residency of an individual fluid element at the surface, molecular penetration is assumed to be shallow such that the driving potential, $U_i(t - \xi)$, can be assumed to be constant with respect to the contact time, θ. Based on this physical constraint, a relationship can be written for the instantaneous velocity profile, $u(\theta,t)$, and wall shear stress, $\sigma_0(\theta,t)$, of the forms (for constant properties)

$$u(\theta,t) = U_i(t - \theta) \operatorname{erf} \frac{y}{2\sqrt{\nu\theta}} \tag{5}$$

and

$$\sigma_0(\theta,t) = \rho U_i(t - \theta) \sqrt{\frac{\nu}{\pi\theta}} \tag{6}$$

Similarly, expressions can be written for the instantaneous temperature profile, $T(\theta,t)$, and heat transfer, $q_0(\theta,t)$, for an assumed uniform wall temperature as [4]

$$T(\theta,t) - T_0 = [T_i(t - \theta) - T_0] \operatorname{erf} \frac{y}{2\sqrt{\alpha\theta}} \tag{7}$$

[1] Numbers in brackets designate References at end of paper.

Contributed by the Heat Transfer Division for publication in the JOURNAL OF HEAT TRANSFER. Manuscript received by the Heat Transfer Division, September 6, 1973. Paper No. 74-HT-MM.

$$q_0(\theta,t) = [T_0 - T_i(t-\theta)]\sqrt{\frac{\rho c k}{\pi\theta}} \tag{8}$$

Spatial Mean Transport Properties. The development of relationships for the local spatial mean momentum and heat transport properties requires the utilization of the contact time distribution, $\phi(\theta,t)$, which is defined such that the product $\phi(\theta,t)d\theta$ represents the fraction of the surface, for any t, with instantaneous contact time between θ and $\theta + d\theta$. Expressions can therefore be written for the local spatial average velocity profile, $u(t)$, wall shear stress, $\sigma_0(t)$, temperature profile, $T(t)$, and heat transfer $q_0(t)$, of the form

$$\psi(t) = \int_0^{C(t)} \psi[\theta,(t-\theta)]\phi(\theta,t)d\theta \tag{9}$$

where ψ represents the specific transport property of interest, and

$$\int_0^{C(t)} \phi(\theta,t)d\theta = 1 \tag{10}$$

The term $\psi[\theta,(t-\theta)]$ represents the contributions to the spatial mean transport property at time t of fluid elements that arrived at the surface prior to t. This point will be expanded momentarily.

With $u(\theta,t)$, $\sigma_0(\theta,t)$, $T(\theta,t)$ and $q_0(\theta,t)$ given by equations (5) to (8), the use of equation (9) in predicting the local spatial average transport properties for pulsatile flow requires the development of a meaningful relationship for $\phi(\theta,t)$ and the associated mean residence time, $\tau(t)$. These important aspects of the analysis are now presented.

Contact Time Distribution for Periodic Flow Conditions. In the context of the surface renewal and penetration model, the hydrodynamic conditions are reflected in the mean residence time, as well as in the contact time distribution. Hence, for hydrodynamic unsteady operation the mean residence time becomes a function of time, $\tau(t)$. For the case in which the flow rate is a periodic function, such as for pulsatile flow, $\tau(t)$ too must be periodic. For this situation, a relationship can be written for $\phi(\theta,t)$ on the basis of a previous general formulation for a hydrodynamically unsteady uniform contact time distribution [3]. This unsteady distribution associated with a periodic $\tau(t)$ can be written as

$$\phi(\theta,t) = \frac{1}{\tau(t-\theta)} \qquad 0 \le \theta < C(t) \tag{11a}$$

$$\phi(\theta,t) = 0 \qquad C(t) < \theta \tag{11b}$$

where $C(t)$ is defined such that

$$\int_0^{C(t)} \frac{1}{\tau(t-\theta)}d\theta = 1 \tag{11c}$$

Formulation for $\tau(t)$. In the analysis of hydrodynamically steady turbulent flow, predictions for the mean residence time have been obtained in terms of the mean wall shear stress through the direct application of the surface renewal and penetration model to momentum transfer [4–13]. This type of analysis has resulted in an expression for τ of the form (based on a uniform contact time distribution)

$$U^*\sqrt{\frac{\tau}{\nu}} = \frac{2}{\sqrt{\pi}}\frac{U_i}{U^*} \tag{12}$$

where U^* is the friction velocity. With U_i set equal to the bulk stream velocity, V, this expression has been found to be in quite good agreement with experimental data for τ [12, 13].

A similar approach is now proposed in the evaluation of $\tau(t)$ for hydrodynamically fully developed pulsatile flow. With equations (6) and (11) substituted into equation (9), an expression can be written for $\sigma_0(t)$ of the form

$$\sigma_0(t) = \rho\sqrt{\frac{\nu}{\pi}}\int_0^{C(t)} \frac{U_i(t-\theta)}{\sqrt{\theta}}\frac{1}{\tau(t-\theta)}d\theta \tag{13}$$

where $U_i(t-\theta)$ will be set equal to $V(t-\theta)$ as in the steady flow analysis. It should be noted that at any given instant t, eddies reside at the surface with values of U_i which range from U_i $[t - C(t)]$ to $U_i(t)$. Hence, the inclusion of the velocity term $U_i(t-\theta)$ in equation (13) accounts for the contribution of all the eddies which arrive at the surface during the time interval $t - C(t)$ to t.

Equation (13) provides a relationship between $\tau(t)$ and the turbulent momentum transport properties $\sigma_0(t)$ and $V(t)$. Specific predictions for $\tau(t)$ therefore require the evaluation of $\sigma_0(t)$ and $V(t)$.

Evaluation of $\sigma_0(t)$. An expression can be obtained for $\sigma_0(t)$ for hydrodynamically fully developed pulsatile tube flow by the mere application of the momentum principle to a radially lumped differential element. This expression takes the form

$$\sigma_0(t) = -\frac{D}{4}\left[\rho\frac{dV(t)}{dt} + \frac{dP(t)}{dx}\right] \tag{14}$$

Hence, $\sigma_0(t)$ could be specified if adequate experimental data for $V(t)$ and $dP(t)/dx$ were available.

In this connection, a very elementary but useful quasi-steady analysis for momentum transfer associated with turbulent pulsatile flow has been proposed which utilizes equation (14) [14–17 and others]. This technique involves the approximation of $\sigma_0(t)$ by $\rho V^2(t)f_s/2$, where f_s is taken from the standard empirical steady-state friction factor information for values of the Reynolds number, $\mathrm{Re}(t)$, equal to $DV(t)/\nu$. This analysis has given rise to reasonable predictions for $dP(t)/dx$ for moderate to low frequencies and amplitude ratios [14, 15]. An expression for the transition between quasi-steady and nonquasi-steady behavior has been proposed of the form [16, 18]

$$\frac{\omega D^2}{\nu} \simeq 0.1\,\overline{\mathrm{Re}} \tag{15}$$

Because of its simplicity, the quasi-steady model will be used to approximate $\sigma_0(t)$ in the present formulation.

With an assumed time variation in bulk stream velocity of the form

Nomenclature

$C(t)$ = defined by equation (10)
D = tube dimension
f = quasi-steady friction factor
h = coefficient of heat transfer
k = thermal conductivity
Nu = Nusselt number
P = pressure
Pr = Prandtl number
Re = Reynolds number
t = process time
T = temperature
q_0 = heat transfer flux
u, U = velocity
V = bulk velocity
x = axial coordinate
y = distance from wall
β = phase angle defined by equation (22)
ω = pulsation frequency
ψ = general transport property which represents u, T, σ_0, q_0
σ_0 = wall shear stress
ν = kinematic viscosity
θ = instantaneous contact time
τ = mean residence time
ρ = density
ϕ = contact time distribution

Subscripts

0 = wall condition
i = condition at first instant of renewal
s = quasi-steady

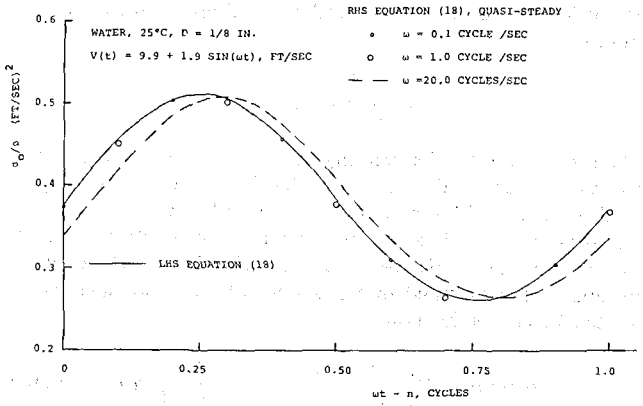

Fig. 1 Comparison of LHS and RHS of equation (18) for quasi-steady assumption for $\tau(t)$

$$V(t) = V_1 + V_2 \sin \omega t \tag{16}$$

the quasi-steady assumption leads to a relationship for $\sigma_0(t)$ of the form

$$\sigma_0(t) = 0.0395\rho\left(\frac{\nu}{D}\right)^{0.25}(V_1 + V_2 \sin \omega t)^{1.75} \tag{17}$$

Predictions for $\tau(t)$. Based on equations (16) and (17), equation (13) takes the form

$$0.0395\rho\left(\frac{\nu}{D}\right)^{0.25}(V_1 + V_2 \sin \omega t)^{1.75} = \rho\sqrt{\frac{\nu}{\pi}}\int_0^{C(t)}\left[\frac{V_1 + V_2 \sin \omega(t-\theta)}{\sqrt{\theta}}\right]\frac{1}{\tau(t-\theta)}d\theta \tag{18}$$

Hence, equations (11c) and (18) provide a basis for the prediction of $\tau(t)$. However, these integral equations are of such a form that numerical solution techniques are required, except for the limiting case for which $\tau(t)$ is very small such that $\tau(t-\theta)$ and $V(t-\theta)$ change very little as θ ranges from 0 to $\tau(t)$. Consideration will first be given to the limiting solution, after which a preliminary approximate solution will be presented for the case in which variations of $\tau(t-\theta)$ and $V(t-\theta)$ within the integral become significant. For convenience, consideration will be limited to $D = \frac{1}{8}$ in. and $\nu = 0.917 \times 10^{-5}$ ft²/s (water, 25 deg C).

For $\tau(t) \ll 1/\omega$, equation (18) reduces to

$$\sigma_0(t) = 2\rho\sqrt{\frac{\nu}{\pi}}\frac{V(t)}{\tau(t)}\sqrt{C(t)} \tag{19}$$

and equation (11c) gives $C(t) = \tau(t)$. Hence, a relationship can be written for $\tau(t)$ for this limiting case of the form

$$U^*(t)\sqrt{\frac{\tau(t)}{\nu}} = \frac{2}{\sqrt{\pi}}\frac{V(t)}{U^*(t)} \tag{20}$$

This quasi-steady expression is of the form of equation (12), but each time dependent parameter is evaluated on the basis of steady state conditions at the corresponding instantaneous velocity.

In order to determine the region of applicability of the foregoing quasi-steady approximation for $\tau(t)$, equations (11c) and (18) have been numerically integrated for $V_1 = 9.9$ ft/sec and $V_2 = 1.9$ ft/sec and with $\tau(t)$ given by equation (20). The error introduced by the quasi-steady approximation is reflected by Fig. 1 in which the LHS of equation (18) is compared with the RHS for several values of ω. For $\omega \gg 1$, very obvious discrepancies in both amplitude and phase occur between the LHS and RHS. As $\omega \to 1$, the phase shift error becomes negligible and the amplitude error falls below 1 percent. Hence, this quasi-steady relationship can be utilized for $\omega \lesssim 1$ [for $D = \frac{1}{8}$ in., $\mathrm{Re}(t) \gtrsim 10^4$, water].

Table 1

Re	V_1 ft/sec	V_2 ft/sec	T sec	ω cycle/sec	τ_1 sec	τ_2 sec	β cycle	Ω %
11,200	9.9	1.9	0.0081					
				0.1	0.00807	0.0296	~0	
				1.0	0.00807	0.0296	~0	
				5.0	0.00807	0.0286	0.010	1.6
				10.0	0.00807	0.0296	0.025	0.5
				20.0	0.00807	0.0286	0.050	1.2
				30.0	0.00807	0.0286	0.070	2.9
				50.0	0.00807	0.0286	0.110	9.5
11,200	9.9	3.9	0.0081					
				1.0			~0	2.0
				10.0			0.025	1.1

Conditions: Tube 1.0 = 118 in., water at 25°
Ω = (LHS - RHS)/LHS of Equation (18)

For ω very much greater than unity, the solution of equation (18) can only be obtained with $\tau(t-\theta)$ and $V(t-\theta)$ retained within integrand of the RHS. In order to obtain an approximate solution of equations (11c) and (18) for $\tau(t)$, a first order Fourier expansion of $1/\tau(t)$ is assumed of the form

$$\frac{1}{\tau(t)} = a + b \sin \omega t + c \cos \omega t \tag{21}$$

or more conveniently,

$$\frac{1}{\tau(t)} = \frac{1}{\tau_1} + \frac{1}{\tau_2}\sin(\omega t + \beta) \tag{22}$$

with $a = 1/\tau_1$, $b = (\cos \beta)/\tau_2$, and $c = (\sin \beta)/\tau_2$. The Fourier coefficients were evaluated by a trial and error procedure that involved *(a)* the numerical integration of the RHS of equation (18) with assumed values for τ_1, τ_2, and β; *(b)* the adjustment of these coefficients based on a comparison between the LHS and RHS of equation (18); *(c)* the repetition of the first step based on the modified coefficients, and so on. The necessary adjustments in τ_1, τ_2, and β can be guided by the fact that these coefficients essentially determine *(a)* the relative mean value; *(b)* the relative amplitude; and *(c)* the relative angular location, respectively, of $\sigma_0(t)$ calculated on the basis of the RHS of equation (18).

This approximate solution procedure was carried out for several frequencies and amplitude ratios. The values of τ_1, τ_2, and β obtained on the basis of this analysis are presented in Table 1. Fig. 2 compares the LHS of equation (18), which represents the approximate measured values for $\sigma_0(t)$, to the RHS, which represents predictions for $\sigma_0(t)$ obtained on the basis of the surface renewal and penetration model. The maximum percent deviation between the LHS and RHS of equation (18) is also given in Table 1 for each set of conditions. For $\omega = 1$ cycle/s, β was found to

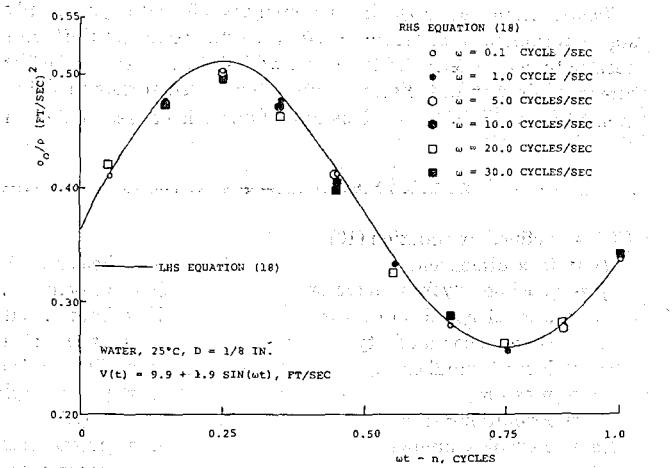

Fig. 2 Comparison of LHS and RHS of equation (18) with $\tau(t)$ approximated by equation (22)

be essentially equal to zero, such that $1/\tau(t)$ is implied to be in phase with $V(t)$. However, for the case in which ω ranged between 1 and 30 cycle/s, β was found to increase as ω was increased, with τ_1 and τ_2 remaining essentially unchanged. Whereas the maximum error is less than 3 percent for $\omega \leq 30$ cycles/s, the error becomes large for $\omega = 50$ cycles/s such that the first order Fourier approximation for $1/\tau(t)$ given by equation (22) becomes inadequate.

Predictions for $\tau(t)$ obtained on the basis of this analysis are shown in Fig. 3 in terms of ωt for several values of ω. Calculations for $\tau(t)$ given by the quasi-steady relationship, equation (20), are also shown in this figure. The quasi-steady based predictions are seen to be in quite good agreement with the results of the direct analysis for $\omega = 1$ cycle/s. However, as ω increases above 1 cycle/s, predictions for $\tau(t)$ based on the approximate solution lead the quasi-steady calculations by β.

Calculations for $C(t)$ are also shown in Fig. 3. In addition, calculations for $\tau(t)$ with $\omega = 0$, τ, are presented in Table 1. This value is seen to be approximately equal to τ_1. This result is consistent with equation (22) which directly gives $\lim/\omega \to 0\ \tau(t) = \tau_1$, since $\beta \to 0$ as $\omega \to 0$.

Predictions for $u(t)$ and $T(t)$. The substitution of equations (5) and (7) into equation (9), with $\phi(\theta,t)$ given by equation (11), leads to expressions for the mean velocity and temperature profiles of the forms

$$u(t) = \int_0^{C(t)} U_i(t-\theta)\,\mathrm{erf}\left(\frac{y}{2\sqrt{\nu\theta}}\right)\frac{1}{\tau(t-\theta)}d\theta \tag{23}$$

and

$$T(t) - T_0 = \int_0^{C(t)} [T_i(t-\theta) - T_0]\,\mathrm{erf}\left(\frac{y\sqrt{\mathrm{Pr}}}{2\sqrt{\nu\theta}}\right)\frac{1}{\tau(t-\theta)}d\theta \tag{24}$$

where $U_i(t)$ and $T_i(t)$ can be set equal to the bulk stream conditions, except for low Prandtl number fluids, for which case $T_i(t) \neq T_b(t)$ (4). Whereas $V(t)$ is specified in this problem, $T_b(t)$ is not known a priori. However, for small values of ω and for $\mathrm{Re}(t)$ well above the transitional value, the quasi-steady assumption $T_b(t-\theta) \simeq T_b(t)$ becomes appropriate. With this simplification, equation (24) becomes

$$\frac{T(t) - T_0}{T_b(t) - T_0} = \int_0^{C(t)} \mathrm{erf}\left(\frac{y\sqrt{\mathrm{Pr}}}{2\sqrt{\nu\theta}}\right)\frac{1}{\tau(t-\theta)}d\theta \tag{25}$$

Predictions for $u(t)$ and $T(t)$ versus ωt are shown in Fig. 4 at one point within the wall region ($y/D = 0.005$) for $\omega = 1$ and 20 cycle/s. The foregoing quasi-steady approximation for $T_b(t)$ can be assumed to introduce some error in the predictions for $T(t)$ for $\omega > 1$ cycle/s.

Predictions for $h(t)$. Equations (8), (9), and (11) lead to an expression for the local spatial average heat transfer of the form

$$q(t) \equiv h(t)[T_0 - T_b(t)] = \sqrt{\frac{\rho ck}{\pi}}\int_0^{C(t)} \frac{[T_0 - T_i(t-\theta)]}{\sqrt{\theta}}\frac{1}{\tau(t-\theta)}d\theta \tag{26}$$

For the small values of ω for which the quasi-steady assumptions for $\tau(t)$ and $T_b(t)$ are appropriate, equation (26) reduces to a quasi-steady relationship for $h(t)$ of the form

$$h(t) = 2\sqrt{\frac{\rho ck}{\pi\tau(t)}} \tag{27}$$

With $\tau(t)$ given by equation (12), equation (27) gives rise to a quasi-steady approximation for the Nusselt number of the form

$$\mathrm{Nu}\ (t) = \frac{f_s}{2}\,\mathrm{Re}(t)\,\sqrt{\mathrm{Pr}} \tag{28}$$

As $\omega \to 0$, equation (26) and (27) reduce to

$$h = 2\sqrt{\frac{\rho ck}{\pi\tau}} \tag{29}$$

and equation (28) becomes

$$\mathrm{Nu} = \frac{f}{2}\,\mathrm{Re}\,\sqrt{\mathrm{Pr}} \tag{30}$$

These relationships have been previously developed for steady operating conditions [11, 12].

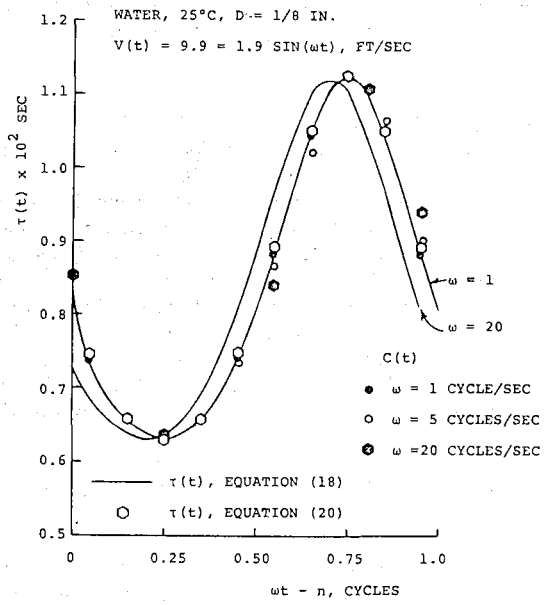

Fig. 3 Predictions for $\tau(t)$

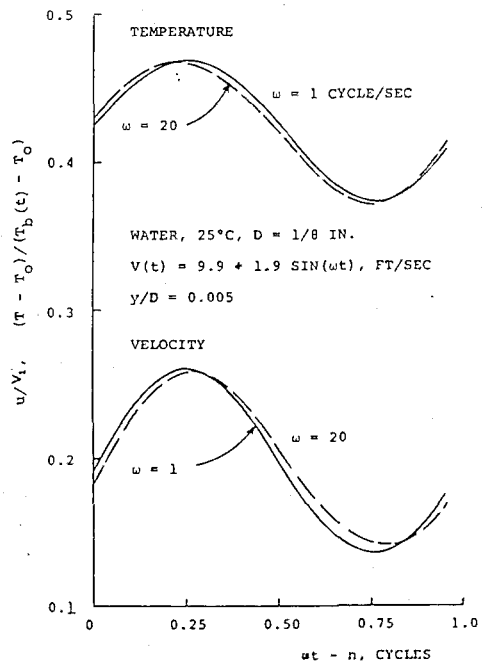

Fig. 4 Predictions for $u(t)$ and $T(t)$ at $Y/D = 0.005$

Strictly speaking, the use of equations (18), (22), and (26) to predict $h(t)$ for $\omega > 1$ cycle/s requires that the parameter $T_b(t - \theta)$ be retained within the integral. However, a rough indication of the effects of ω on $h(t)$ for $\omega > 1$ can be obtained by again utilizing the quasi-steady approximation $T_b(t - \theta) \simeq T_b(t)$. This approach leads to an approximate relationship for $h(t)$ of the form

$$h(t) = \sqrt{\frac{\rho ck}{\pi}} \int_0^{C(t)} \frac{1}{\sqrt{\theta}} \left[\frac{1}{\tau_1} + \frac{1}{\tau_2} \sin\left(\omega[t - \theta] + \beta\right)\right] d\theta \quad (31)$$

Values of τ_1, τ_2, and β are given in Table 1 for the conditions considered in the previous section. Equation (31) gives rise to predictions for Nu(t) as shown in Fig. 5. Calculations based on equation (28) are also shown. For $\omega < 1$ cycle/s, predictions for $h(t)$ based on equations (28) and (31) are congruent. However, the effect of the renewal process history is seen to become important for $\omega = 20$ and 30 cycles/s.

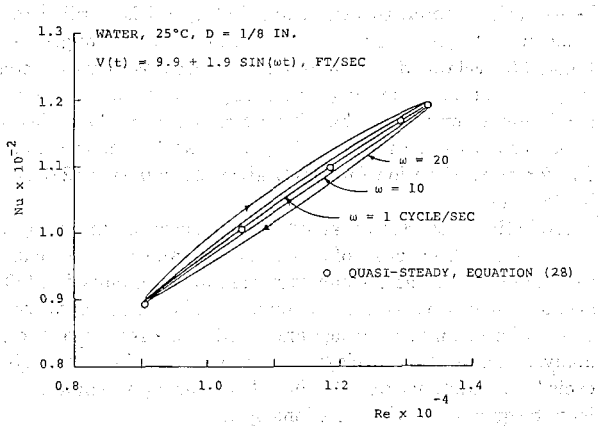

Fig. 5 Predictions for Nu(t)

Summary and Conclusion

In this analysis, a comprehensive form of the surface renewal and penetration model has been adapted to convective heat transfer for turbulent pulsatile flow. This analysis accounts for the contribution to $\sigma_0(t)$ and $q(t)$ at any given time, t, of all fluid elements which arrived at the surface prior to t. Similar to previous formulations of the surface renewal and penetration model for steady flow, a relationship has been developed between $\tau(t)$ and $\sigma_0(t)$. Because $\sigma_0(t)$ has been represented by the well known quasi-steady approximation, predictions obtained for $\tau(t)$ from equation (18) are limited to situations for which $\omega D^2/\nu \lesssim 0.1\ \overline{\mathrm{Re}}$. The use of exact experimental data for $\sigma_0(t)$ in terms of $V(t)$ and $dP(t)/dx$ (see equation (14)) would be expected to produce small changes in the calculations for $\tau(t)$. However, the use of the quasi-steady approximation for $\sigma_0(t)$ facilitates the presentation of the key aspects of the proposed analysis and should provide reasonable results for $\tau(t)$.

Based on the modeling concept presented herein, turbulent pulsatile flow can be categorized according to the behavior of $\tau(t)$. For low values of ω (i.e., $\omega < 1$ cycle/s for water at 25 deg C and $D = \frac{1}{8}$ in.), $\tau(t)$ is essentially independent of ω and can be expressed in terms of the quasi-steady expression given by equation (20). In this domain, the velocity and temperature profiles, as well as the Nusselt number, are in phase with $\sigma_0(t)$ and are expressed by simple quasi-steady relationships of the form

$$\psi(t) = \frac{1}{\tau(t)} \int_0^{C(t)} \psi(\theta) d\theta \quad (32)$$

Such an expression is given for Nu(t) by equation (28).

For large values of ω, the more general relationship for $\psi(t)$ given by equation (9) must be utilized. For the simple sinusoidal wave form considered here, the present preliminary analysis reflects the effect of ω on $\psi(t)$ for $1 < \omega < 30$ cycles/s. For these values of ω, the frequency of renewal, $1/\tau(t)$, leads $\sigma_0(t)$ by β. The consequence of the renewal process history is also seen in the predictions for $u(t)$, $T(t)$ and Nu(t).

In regard to previous experimental data, conflicting results have often been reported. For example, the study by Martinelli, et al. [1] showed no effect of pulsation on the time average heat transfer. Parenthetically, these workers intuitively reasoned that the instantaneous heat transfer at any value of t is approximately equal to the steady flow value corresponding to a flow rate equal to the instantaneous flow rate. This conclusion is synonymous to the predictions based on the present model for quasi-steady $\tau(t)$ conditions. In contrast, other experimental studies of this problem have shown increases in mean heat transfer with pulsation [19,20].

To add to the confusion, no satisfactory theoretical analysis of this problem has been available. As mentioned earlier, the standard eddy diffusivity approach has been hampered due to the lack of knowledge concerning the effects of pulsation on ϵ_m and ϵ_H. For the limited flow conditions considered in this study, the time average heat flux was not predicted to be noticeably affected by the pulsations. However, flow conditions outside the range studied here may possibly give rise to attenuated or enhanced mean heat transfer rates.

Although the approximate solution technique used in this paper provides an indication of the effect of pulsation on the mean transport properties, certain improvements will be required to fully develop the potential strength of the present model for handling flow conditions for which ω is large, and for more complicated pulse forms. In particular, a more rigorous and accurate solution technique is needed for the evaluation of $\tau(t)$ based on equation (18). Further, a better estimate is needed for $T_b(t - \theta)$. Similar to other formulations for turbulent heat transfer which are based on the elementary surface renewal and penetration model, the present results must be restricted to moderate values of the Prandtl number ($0.5 \lesssim \mathrm{Pr} \lesssim 5.0$). For values of $\mathrm{Pr} \gg 5.0$ the effect of the unreplenished layer of fluid at the surface becomes important [21], and for $\mathrm{Pr} < 0.5$ the molecular transport to eddies in flight [4] and finite penetration depth [22] must be considered. In addition, for values of Re and V_2/V_1 such that the minimum instantaneous Reynolds number is much less than 10^4, the effects of axial pressure gradient and curvature must be considered.

Finally, near the conclusion of the present study the author's attention was brought [23] to a recently proposed modeling concept [16] in which the surface renewal and penetration model was adapted to turbulent pulsating tube flow in an effort to predict $\tau(t)$. In contrast to the stochastic approach utilized in the present study, this analysis was formulated on the basis of a consideration of the time variation in $\tau(t)$ at a single renewal site. The computational procedure involves the analysis of the effect of the sequence of renewals that occurs at a given point on the surface during a pulse cycle. Although this analysis requires some refinement, the concept may prove to be useful for small values of ω.

Acknowledgment

This investigation was supported by Research Grants GK 35883 and HL 1258803 from the National Science Foundation and the National Heart and Lung Institute, respectively. The very helpful assistance of Mr. M. L. Wood in the computations involved in this study is also acknowledged.

References

1 Martinelli, R. C., Boelter, L. M. K., Weinberg, E. B., and Yakahi, S., "Heat Transfer to a Fluid Flowing Periodically at Low Frequencies in a Vertical Tube," TRANS. ASME, Vol. 65, 1943, p. 789.

2 Barnett, D. O., and Vachon, R. I., "An Analysis of Convective Heat Transfer for Pulsating Flow in a Tube," *4th International Heat Transfer Conference*, Paris, France, III, 1970, p. FC 9.1.

3 Thomas, L. C., "A Surface Renewal Based Analysis for Hydrodynamic Unsteady Convection Heat Transfer," *Can. J. Chem. Eng.*, in press, 1974.

4 Thomas, L. C., "Temperature Profiles for Liquid Metals and Moder-

ate-Prandtl-Number Fluids," JOURNAL OF HEAT TRANSFER, TRANS. ASME, Series C, Vol. 92, 1970, p. 565.

5 Thomas, L. C., and Chung, B. T. F., "A Theoretical Analysis of the Recovery Factor for High-Speed Turbulent Flow," JOURNAL OF HEAT TRANSFER, TRANS. ASME, Series C, Vol. 95, 1973, p. 272.

6 Thomas, L. C., Rajagopal, R., and Chung, B. T. F., "An Analysis of Heat Transfer in Turbulent Pipe Flow With Variable Properties," ASME Paper No. 72-HT-59, presented at National Heat Transfer Conference, Denver, Col., JOURNAL OF HEAT TRANSFER, TRANS. ASME, Series C, Vol. 96, 1974, p. 107.

7 Gross, R. J., and Thomas, L. C., "Significance of the Pressure Gradient on Fully Developed Turbulent Flow in a Pipe," JOURNAL OF HEAT TRANSFER, TRANS. ASME, Series C, Vol. 94, 1972, p. 494.

8 Chung, B. T. F., and Thomas, L. C., "Unsteady Heat Transfer for Turbulent Flow," *Can. J. Chem. Eng.*, Vol. 49, 1971, p. 879.

9 Thomas, L. C., and Chung, B. T. F., "Unsteady Heat Transfer for Turbulent Flow With Time Dependent Wall Temperature," JOURNAL OF HEAT TRANSFER, TRANS. ASME, Series C, Vol. 96, 1974, p. 117.

10 Einstein, H. A., and Li, H., "The Viscous Sublayer Along a Smooth Boundary," *ASCE, Eng. Mech. Div. J.*, Vol. 82, 1956, p. 1.

11 Hanratty, T. J., "Turbulent Exchange of Mass and Momentum With a Boundary," *AIChE Journal*, Vol. 2, 1956, p. 395.

12 Meek, R. L., and Baer, A. O., "The Periodic Viscous Sublayer in Turbulent Flow," *AIChE Journal*, Vol. 16, 1970, p. 841.

13 Thomas, L. C., and Greene, H. L., "An Experimental and Theoretical Study of the Viscous Sublayer for Turbulent Tube Flow," 3rd Symposium on Turbulence in Liquids, University of Missouri-Rolla, 1973.

14 Baird, M. H. I., Round, E. F., and Cardenas, J. N., "Friction Factors in Pulsed Turbulent Flow," *Can. J. Chem. Eng.*, Vol. 49, 1971, p. 220.

15 Combs, G. D., and Gilbreck, D. A., "Pulsating Flow Research," Res. Rept. Series No. 4., University of Arkansas, 1964.

16 Lu, S., "Pulsating Turbulent Water Flow in A Tube," PhD thesis, Clarkson College of Technology, 1972.

17 Streeter, V. L., Wylie, E. G., "Hydraulic Transients Caused by Reciprocating Pumps," *Journal of Engineering for Power*, TRANS. ASME, Series A, Vol. 89, 1967, p. 615.

18 Brown, F. T., Margolis, R. L., and Shah, R. P., "Small-Amplitude Frequency Behavior of Fluid Lines With Turbulent Flow," *Journal of Basic Engineering*, TRANS. ASME, Vol. 910, 1969, p. 678.

19 West, F. B., and Taylor, A. T., "The Effect of Pulsations on Heat Transfer," *Chem Eng. Prog.*, Vol. 48, 1952, p. 39.

20 Bogdanoff, D. N., "A Study of the Mechanisms of Heat Transfer in Oscillating Flow," Princeton Univ., Dept. of Aerospace and Mechanical Sciences Report. No. 483-f, 1967.

21 Thomas, L. C., Chung, B. T. F., and Mahalder, S. K., "Temperature Profiles for Turbulent Flow of High Prandtl Number Fluids," *International Journal of Heat and Mass Transfer* Vol. 14, 1971, p. 1465.

22 Kakarala, C. R., PhD thesis, The University of Akron, in progress, 1973.

23 Nunge, R. J., Private Communication, 1973.

H. J. Hickman

Center for the Studies of the Physical Environment,
University of Minnesota,
Minneapolis, Minn.

An Asymptotic Study of the Nusselt-Graetz Problem

Part I: Large x Behavior

A method is given for determining the large x behavior of the Nusselt number for a variety of Nusselt-Graetz problems. Exploitation of properties of the Laplace transform of the temperature yields analytic expressions for Nu as explicit functions of the other parameters of the problem. Accurate results (<1 percent error) are deduced for problems involving the laminar flow of a Newtonian flow between parallel plates and in a circular pipe (valid for all values of the wall Nusselt number).

The Nusselt-Graetz problem (the computation of the rate of diffusive convection of heat or mass) models a large number of practical devices. Most of the available solutions to this problem (Kays [4][1]) apply to the limiting cases of constant wall temperate (or concentration) or constant wall heat (or mass) flux, situations which are seldom encountered in practice (in a precise sense). A boundary condition that allows for a finite wall resistance (Van der Does De Bye and Schenk [6]) rectifies this deficiency but at the cost of a nontrivial increase in the computational difficulty. The classical approach to this problem requires the construction of a large number of functions of high precision (of little ultimate interest) in some indirect fashion with subsequent numerical evaluation. In problems containing parameters (e.g., wall Nusselt numbers to account for finite wall resistance) the classical procedure becomes cumbersome since a complete set of eigenvalues must be determined numerically for each set of parameters and the results reported in graphical or tabular form. In problems with two or more parameters (e.g., convective heat transfer in an annulus with conductive walls) the difficulty of extracting useful results increases enormously.

In this work we report efficient procedures which yield, explicitly, the dependence of the Nusselt number on the system's parameters. The procedures do not require machine computation and can be easily applied to multi parameter problems.

Part I of this work is restricted to the large x behavior of axisymmetric problems.

The method involves Laplace transforming the governing equation with respect to the axial coordinate; the resulting ordinary differential equation is then solved by means of an ordinary perturbation expansion in the transform variable. The asymptotic value of the Nusselt number follows directly from this expansion upon exploiting certain of its properties. The method is applied to two duct configurations, circular pipes and parallel plates.

Conclusions and Significance

The goal of this study has been achieved; an analytic procedure has been developed and tested which yields the asymptotic dependence of the Nusselt number on the system parameters. The first approximation yields values of the log-mean Nusselt numbers with ~0.5 percent error for the parallel plate problem and ~2 percent error for the circular pipe case. The second approximation reduces the error tenfold. The results are useful for $x > 0.02$, thus it is reasonable to expect the approximations deduced here to share a common domain with small x approximations.

The Problem

Here we consider the steady, laminar, fully developed flow of a Newtonian fluid of constant physical properties in a duct. Upstream of the plane $x = 0$ the duct is insulated, downstream of this plane the duct walls have a finite conductivity.

For the symmetric problem the equation to be solved is

$$v\theta_x = \nabla^2\theta \tag{1}$$

subject to

$$\theta(y,0) = 1 \tag{2}$$

$$\theta_y(0, x) = 0 \tag{3}$$

$$\theta_y(1/2, x) = -\mathrm{Nu}_w\theta(1/2, x) \tag{4}$$

The wall Nusselt number Nu_w, introduced by Van der Does de Bye and Schenk [6], accounts for the thermal resistance of the duct wall and any other resistances in series with it on its exterior. The problem as posed has been shown by Colton, et al. [3] to include the cases of constant wall temperature ($\mathrm{Nu}_w \to \infty$) and constant wall heat flux ($\mathrm{Nu}_w \to 0$) as limiting cases.

The quantities of interest are the local overall and fluid side Nusselt numbers

[1] Numbers in brackets designate References at end of paper.

Contributed by the Heat Transfer Division for publication in the JOURNAL OF HEAT TRANSFER. Manuscript received by the Heat Transfer Division, January 11, 1974. Paper No. 74-HT-QQ.

$$\mathrm{Nu}_0 \equiv -\theta_y(1/2, x)/\bar{\theta}(x) \tag{5}$$

$$= -\bar{\theta}_x(x)/2\bar{\theta}(x) \equiv -\tfrac{1}{2}\frac{d \ln \bar{\theta}(x)}{dx} \tag{6}$$

$$\mathrm{Nu}_f \equiv -\theta_y(1/2, x)/[\bar{\theta}(x) - \theta(1/2, x)] \tag{7}$$

i.e.,

$$1/\mathrm{Nu}_0 \equiv 1/\mathrm{Nu}_f + 1/\mathrm{Nu}_w \tag{8}$$

where the bulk temperature is defined by

$$\bar{\theta}(x) \equiv \int_{A_c} v\theta dA \Big/ \int_{A_c} v dA \tag{9}$$

Equation (6) follows upon integrating equation (1) over y. The log-mean overall and fluid side Nusselt numbers are defined in the standard fashion,

$$\overline{\mathrm{Nu}}_0 \equiv \int_{x=0}^{x=L} \mathrm{Nu}_0(x)dx/L = -\ln(\bar{\theta}(L))/2L \tag{10}$$

$$1/\overline{\mathrm{Nu}}_f \equiv 1/\overline{\mathrm{Nu}}_0 - 1/\mathrm{Nu}_w \tag{11}$$

Parallel Plates (Symmetric Case). For this case equation (1) becomes

$$(3/2)[1 - 4y^2]\theta_x = \theta_{yy} \tag{12}$$

Laplace transforming equation (12) and its boundary conditions yields

$$(3/2)[1 - 4y^2]s\phi = \phi_{yy} \tag{13}$$

$$\phi_y(0, s) = 0 \tag{14}$$

$$\phi_y(1/2, s) = -\mathrm{Nu}_w[1/s + \phi(1/2, s)] \tag{15}$$

where

$$\phi(y, s) \equiv v\theta(y, x) - 1/s \tag{16}$$

Equation (13) defines one form of the Parabolic Cylinder function (Abramowitz and Stegen [1]). The standard power series representation of the two independent solutions to equation (13) suffice to generate all of the results reported here. Rather than exploiting these series we report a procedure of broader utility. Expanding equation (13) in a power series in s we obtain the two general solutions

$$G = G^{(0)} + sG^{(1)} + s^2G^{(2)} + \ldots \tag{17}$$

and

$$\xi = \xi^{(0)} + s\xi^{(1)} + s^2\xi^{(2)} + \ldots \tag{18}$$

(G even in y, ξ odd)

$$\begin{aligned}
G^{(0)} &= 1 \\
G^{(1)} &= 3y^2/4 - y^4/2 \\
G^{(2)} &= 3[y^4/4 - 7y^6/15 + y^8/7]/8 \\
G^{(3)} &= 3[y^6/40 - 11y^8/140 + 211y^{10}/3150 - y^{12}/77]/16 \\
G^{(4)} &= 9[y^8/160 - y^{10}/36 + 1201y^{12}/29700 \\
&\vdots \\
&\quad - 4867y^{14}/225225 + y^{16}/330]/448
\end{aligned} \tag{19}$$

$$\begin{aligned}
\xi^{(0)} &= y \\
\xi^{(1)} &= 3[y^3/6 - y^5/5]/2 \\
\xi^{(2)} &= 3[y^5/4 - 13y^7/21 + y^9/3]/40 \\
&\vdots \qquad\qquad \vdots
\end{aligned} \tag{20}$$

The value of the Wronskian $W[G, \xi]$ is seen to be unity. We wish to emphasize that these functions are independent of the boundary and initial conditions.

Of particular interest are the values of these functions and their derivatives at $y = 1/2$

$$\dot{G} \equiv G(1/2,s) = 1 + \alpha_1 s + \alpha_2 s^2 + \ldots \tag{21}$$

$$\dot{G}_y \equiv G_y(1/2,s) = s[1/2 + \beta_1 s + \beta_2 s^2 + \ldots] \tag{22}$$

$$\begin{aligned}
\alpha_1 &= 5/32 & \beta_1 &= 39/(70)(32) \\
\alpha_2 &= 239/(70)(32)^2 & \beta_2 &= 179/(942)(32)^2 \\
\alpha_3 &= 10357/(165)(70)(32)^3 & \beta_3 &= 297/(130)(70)(32)^3 \\
&\vdots & &\vdots
\end{aligned} \tag{23}$$

$$\dot{\xi} \equiv \xi(1/2,s) = 1/2 + \epsilon_1 s + \epsilon_2 s^2 + \ldots \tag{24}$$

$$\dot{\xi}_y \equiv \xi_y(1/2,s) = 1 + \delta_1 s + \delta_2 s^2 + \ldots \tag{25}$$

Nomenclature

A_i = constants (equation (33))
a_i, b_i, c_i, d_i = constants
G = even solution to equation (13)
h = local heat transfer coefficient
$\bar{h}$ = log mean h
h_w = wall heat transfer coefficient
k = thermal conductivity of the fluid
L = dimensionless axial distance
$\mathfrak{L}$ = Laplace transform operator
Nu = local Nusselt number, hW/k
$\overline{\mathrm{Nu}}$ = log mean Nusselt number, $\bar{h}W/k$
Nu_w = wall Nusselt number, h_wW/k
$\mathrm{N}^+, \mathrm{N}^-$ = wall Nusselt numbers for plates at $y = 1/2$, $y = -1/2$
r = dimensionless radial coordinate, $\bar{r}/W$
$\bar{r}$ = radial coordinate
s = Laplace transform variable
s_i = eigenvalues (equation (34))
t = transverse coordinate
T = temperature
v = axial velocity
$\bar{v}$ = average axial velocity
W = characteristic transverse dimension (diameter or channel width)
x = dimensionless axial coordinate, $z\alpha/\bar{v}W^2$
y = dimensionless transverse coordinate, t/W
z = axial coordinate
α = thermal diffusivity
α_i = constants (equation (21))
β_i = constants (equation (22))
γ_i = constants (equation (74))
δ_i = constants (equation (25))
ϵ_i = constants (equation (24))
ξ = odd solution to equation (13)
η_i = constants (equation (74))
θ = dimensionless temperature $= (T - T_0)/(T_i - T_0)$
$\bar{\theta}$ = dimensionless bulk mean temperature (equation (9))
ϕ = modified Laplace transform of θ
Φ = even solution to equation (70)

Superscripts

(i) = ith term in perturbation expansion, ith approximation
$\cdot$ = value at wall
$\sim$ = Laplace transformed quantity
$+$ = value at $y = 1/2$
$-$ = value at $\bar{y} = -1/2$
$-$ = average value or approximate value

Subscripts

f = fluid side
i = initial, serial index
0 = overall, outside wall
w = wall
∞ = value at $L = \infty$

$$\epsilon_1 = 7/(10)(32) \qquad \delta_1 = 3/32$$
$$\epsilon_2 = 17/(10)(32)^2 \qquad \delta_2 = 39/(140)(32)^2 \tag{26}$$
$$\vdots \qquad\qquad \vdots$$

The solution to equation (13) subject to equations (14) and (15) is obtained directly

$$\phi = -G/[s(\dot{G} + \dot{G}_y/\mathrm{Nu}_w)] \tag{27}$$

The quantity of major interest, $\tilde{\bar{\theta}}$, follows

$$\tilde{\bar{\theta}} = [1 + 2\phi_y(1/2, s)]/s \tag{28}$$
$$= [\dot{G} + \dot{G}_y(1/\mathrm{Nu}_w - 2/s)]/[s(\dot{G} + \dot{G}_y/\mathrm{Nu}_w)]$$

Substituting series (21) and (22) into equation (28) we obtain an explicit expression for $\tilde{\bar{\theta}}$ valid for small s

$$\tilde{\bar{\theta}} = [a_0 + a_1 s + a_2 s^2 + \ldots]/[1 + b_1 s + b_2 s^2 + \ldots] \tag{29}$$

where

$$a_0 = \alpha_1 - 2\beta_1 + 1/2\ \mathrm{Nu}_w \qquad b_1 = \alpha_1 + 1/2\ \mathrm{Nu}_w$$
$$a_1 = \alpha_2 - 2\beta_2 + \beta_1/\mathrm{Nu}_w \qquad b_2 = \alpha_2 + \beta_1/\mathrm{Nu}_w$$
$$\vdots \qquad\qquad \vdots$$
$$a_i = a_{i+1} - 2\beta_{i+1} + \beta_i/\mathrm{Nu}_w \qquad b_i = \alpha_i + \beta_{i-1}/\mathrm{Nu}_w \tag{30}$$

Expanding equation (29) for small s leads to

$$\tilde{\bar{\theta}} = \sum_{i=0}^{\infty} c_{i+1}(-s)^i \tag{31}$$

where

$$c_1 = a_0$$
$$c_2 = a_0 b_1 - a_1 \tag{32}$$
$$c_3 = a_2 - a_0 b_2 + b_1 c_2$$
$$\vdots \qquad\qquad \vdots$$

We now explore the relationship of these results with the classical eigen function solution which may be written as

$$\bar{\theta}_E = \sum_{i=1}^{\infty} A_i \exp(-s_i x) \tag{33}$$

Thus we have

$$\tilde{\bar{\theta}}_E = \sum_{i=1}^{\infty} A_i/[s_i + s] \tag{34}$$

where A_i and s_i are real and positive, $s_i < s_{i+1}$ and, $A_i > A_{i+1}$. These conditions hold for the problem under consideration (Colton, et al. [3]). Clearly, $\tilde{\bar{\theta}}_E$ as defined by equation (34), is an analytic function whose Taylor series development in the vicinity of $s = 0$ possesses a radius of convergence equal to s_1 (Titchmarsh [5]). Thus

$$\tilde{\bar{\theta}}_E = \Sigma A_i/s_i - s\Sigma A_i/s_i^2 + s^2\Sigma A_i/s_i^3 - \ldots \tag{35}$$

Identifying $\tilde{\bar{\theta}}$ with $\tilde{\bar{\theta}}_E$ leads to the values

$$\Sigma A_i/s_i^n = c_n > 0 : n = 0, 1, 2\ldots \tag{36}$$

where the c_n are given by equation (32) ($c_0 = 1$ follows from equations (2) and (33)).

An efficient procedure for estimating s_1 follows upon noting that $1/\tilde{\bar{\theta}}_E$ is analytic near $s = 0$ with a zero at $s = -s_1$ and a simple pole between $-s_1$ and $-s_2$. Accordingly, the Taylor series development in a small vicinity of $s = -s_1$ lies within the circle of convergence. Hence,

$$1/\tilde{\bar{\theta}}_E = \{1 + [(\Sigma A_i/s_i^2)/(\Sigma A_i/s_i)]s + [(\Sigma A_i/s_i^2)^2/(\Sigma A_i/s_i^2) - (\Sigma A_i/s_i^3)/(\Sigma A_i/s_i)]s^2 + \ldots\}/\Sigma A_i/s_i \tag{37}$$

leads to

$$0 = 1 - (c_2/c_1)s_1 + (c_2^2/c_1^2 - c_3/c_1)s_1^2 + \ldots \tag{38}$$

The first-order approximation leads to the value

$$s_1^{(1)} = c_1/c_2 \tag{39}$$

the second-order approximation is

$$s_1^{(2)} = s_1^{(1)}[1 - (1 - 4\epsilon)^{1/2}]/2\epsilon \tag{40}$$

where

$$\epsilon = 1 - c_3 c_1/c_2^2 < 0 \tag{41}$$

For the case of small ϵ equation (40) may be expanded to give

$$s_1^{(2)} = s_1^{(1)}[1 + \epsilon + 2\epsilon^2 + 5\epsilon^3 + \ldots] \tag{42}$$

Thus $s_1^{(2)} < s_1^{(1)}$ as required. The second and higher-order terms will be dropped from equation (42) since they represent contributions to higher-order approximations. To see this we need only include higher-order terms in equation (38) and invert the series (Abramowitz and Stegun [1]). Equation (42) results with additional terms in ϵ_4, etc. appearing after the linear term.

Since the coefficients of all terms in series (38) (up to and including that of s_1^3) are negative it follows that the first three partial sums possess one and only one positive zero and further, this sequence converges monotonically to s_1.

The values of A_i follow from Heaviside's theorem (Churchill [2])

$$\bar{\theta} = \mathfrak{L}^{-1}[r(s)/p(s)] = \sum_i [r(-s_i)/p'(-s_i)] \tag{43}$$

upon setting $r(s) = 1$ and identifying $p(s)$ with series (37). Thus

$$A^{(1)} = c_1^2/c_2 \tag{44}$$

$$A_1^{(2)} = A_1^{(1)}[1 - 2\epsilon(1 + \epsilon)]^{-1} \tag{45}$$
$$\vdots \qquad\qquad \vdots$$

The asymptotic behavior of $\overline{\mathrm{Nu}}_0$ follows directly from its definition and the foregoing

$$\overline{\mathrm{Nu}}_0 \equiv -\ln[\bar{\theta}]/2L = s_1/2 - \ln[A_1]/2L - \ln[1 + 0(e^{-L})]/2L \tag{46}$$

Accordingly,

$$1/\overline{\mathrm{Nu}}_{f,\infty} = 2/s_1 - 1/\mathrm{Nu}_w \simeq 2/s_1^{(1)} - 1/\mathrm{Nu}_w \tag{47}$$

with

$$s_1^{(1)} = c_1/c_2 = 1/[b_1 - a_1/a_0] \tag{48}$$
$$= 1/[\alpha_1 + 1/2\mathrm{Nu}_w - (\alpha_2 - 2\beta_2 + \beta_1/\mathrm{Nu}_w)/(\alpha_0 - 2\beta_1 + 1/2\mathrm{Nu}_w)]$$

and the numerical values given by equation (23), we obtain

$$\overline{\mathrm{Nu}}_{f,\infty}^{(1)} = [1 + 70/17\ \mathrm{Nu}_w]/[148/561 + 1/\mathrm{Nu}_w] \tag{49}$$

which is the first major result. Comparing this result with the numerical values of Colton, et al. [3] we observe that equation (49) is exact of $\mathrm{Nu}_w = 0$ (constant heat flux) and overestimates the exact value (3.770) for $\mathrm{Nu}_w = \infty$ (constant wall temperature) by about 0.5 percent

$$\overline{\mathrm{Nu}}_{f,\infty}^{(1)}(\mathrm{Nu}_w = \infty) = 561/148 = 3.790 \tag{50}$$

The accuracy of equation (49) at intermediate values of Nu_w is greater than 0.5 percent. The second approximation follows from the truncated form of series (42)

$$s_1^{(2)} = s_1^{(1)}[1 + \epsilon] \tag{51}$$

and the value

$$\epsilon = [(823/78210)^2 - (4657/23823800)(1$$

$$+ 70/17\ \mathrm{Nu}_w)]/[74/561 + 1/\mathrm{Nu}_w + 35/17\ \mathrm{Nu}_w^2]^2 \quad (52)$$

computed from equations (41), (36), (32), (30), and (23). The second approximation to $\overline{\mathrm{Nu}}_{f,\infty}$ is thus

$$\overline{\mathrm{Nu}}_{f,\infty}^{(2)} = [1 + \epsilon]/[1/\overline{\mathrm{Nu}}_{f,\infty}^{(1)} - \epsilon/\mathrm{Nu}_w] \quad (53)$$

In the limit $\mathrm{Nu}_w \to 0$ equation (53) gives the exact result and overestimates the exact value at $\mathrm{Nu}_w = \infty$ by about 0.04 percent

$$\overline{\mathrm{Nu}}_{f,\infty}^{(2)}(\mathrm{Nu}_w = \infty) = 3.772 \quad (54)$$

The values of $\overline{\mathrm{Nu}}_f$ and $\overline{\mathrm{Nu}}_0$ for finite L follow from equations (44), (45), and (46).

$$\overline{\mathrm{Nu}}_0^{(1)} = \overline{\mathrm{Nu}}_{0,\infty}^{(1)} - \ln[A_1^{(1)}]/2L \quad (55)$$

where

$$A_1^{(1)} = [1 + 17\,\mathrm{Nu}_w/35 + 389\,\mathrm{Nu}_w^2/4900]/[1 + 17\,\mathrm{Nu}_w/35 + 74\,\mathrm{Nu}_w^2/1158] \quad (56)$$

This expression yields values indistinguishable from those of Colton, et al. [3] for $\mathrm{Nu}_w = \infty$ and $L \gtrsim 0.02$.

The second order result is

$$\overline{\mathrm{Nu}}_0^{(2)} = \overline{\mathrm{Nu}}_{0,\infty}^{(2)} - \ln[A_1^{(2)}]/2L \quad (57)$$

where $A_1^{(2)}$ is given by equation (45). In the limit $\mathrm{Nu}_w \to 0$ equations (55) and (57) both reduce to

$$\overline{\mathrm{Nu}}_f^{(1)}(\mathrm{Nu}_w = 0) = 70/[17(1 - 823/78540\ L)] \quad (58)$$

The local values of Nu_0 and Nu_f may be obtained upon evaluation of A_2 and s_2. Truncation of the first four equations of set (36) leads to

$$s_{1,2}^{(1)} = s_1^{(1)}[B \pm (B^2 - 4A\epsilon)^{1/2}]/2\epsilon \quad (59)$$

with

$$B = 1 - c_3c_0/c_1c_2$$
$$A = 1 - c_2c_0/c_1^2 \quad (60)$$

It can be shown the two values given by equation (59) are real and positive and represent an overestimate for s_1 and an underestimate for s_2.

Parallel Plates (Unsymmetric Case). We cite here a few (first order) results for the case wherein the wall Nusselt number for the plate located at $y = \frac{1}{2}$ (N^+) differs from the value associated with the plate located at $y = -\frac{1}{2}$ (N^-).

If we replace boundary conditions (3) and (4) by

$$\theta_y^+ = -\mathrm{N}^+\theta^+ \qquad \theta_y^- = \mathrm{N}^-\theta^- \quad (61)$$

and define Nu_0, Nu_0^+, and Nu_0^- by

$$\theta_y^+ \equiv -\mathrm{Nu}_0^+\bar{\theta} \qquad \theta_y^- \equiv \mathrm{Nu}_0^-\bar{\theta} \quad (62)$$

$$2\mathrm{Nu}_0 \equiv \mathrm{Nu}_0^+ + \mathrm{Nu}_0^- = -\frac{d\ \ln\ \bar{\theta}(x)}{dx} \quad (63)$$

we obtain

$$1/\overline{\mathrm{Nu}}_{0,\infty}^{(1)} = [2\,\mathrm{N}^+\mathrm{N}^-/5 + \mathrm{N}^+ + \mathrm{N}^- + 2]/[\mathrm{N}^+\mathrm{N}^- + \mathrm{N}^+ + \mathrm{N}^-] - [382\,\mathrm{N}^+\mathrm{N}^-/165 + 314(\mathrm{N}^+ + \mathrm{N}^-)/33 + 36]/[17\,\mathrm{N}^+\mathrm{N}^- + 52(\mathrm{N}^+ + \mathrm{N}^-) + 140] \quad (64)$$

Equation (64) leads to the value given by equation (49) when $\mathrm{N}^+ = \mathrm{N}^-$. For the case $\mathrm{N}^- \to \infty$ (the lower plate held at a constant temperature) equation (64) reduces to

$$1/\overline{\mathrm{Nu}}_{0,\infty}^{(1)}(\mathrm{N}^- = \infty) = [2\mathrm{N}^+/5 + 1]/[\mathrm{N}^+ + 1] - [382\,\mathrm{N}^+/5 + 314]/[33(17\,\mathrm{N}^+ + 52)] \quad (65)$$

If also $\mathrm{N}^+ = 0$ (the upper plate insulated) we find

$$\overline{\mathrm{Nu}}_{0,\infty}^{-(1)} = 2\overline{\mathrm{Nu}}_{0,\infty}^{(1)} = 2.445 \quad (66)$$

A value about 0.4 percent larger than the exact value cited by Kays [4], 2.43.

The case $\mathrm{N}^- = 0$, N^+ finite (the lower plate insulated) also follows from equation (65)

$$1/\overline{\mathrm{Nu}}_{0,\infty}^{(1)}(\mathrm{N}^- = 0) = 1 + 2/\mathrm{N}^+ - [157\mathrm{N}^+/33 + 18]/[26\mathrm{N}^+ + 70] \quad (67)$$

The value of $\overline{\mathrm{Nu}}_0^{(1)}$ for large L also follows for these various cases upon noting the value

$$A_1^{(1)} = 2\,\overline{\mathrm{Nu}}_{0,\infty}(1)[17\,\mathrm{N}^+\mathrm{N}^-/140 + 13(\mathrm{N}^+ + \mathrm{N}^-)/35 + 1]/[\mathrm{N}^+\mathrm{N}^- + \mathrm{N}^+ + \mathrm{N}^-] \quad (68)$$

We close this section by remarking that a variety of problems, e.g., the cases of nonuniform entrance temperature, one plate moving in a down-stream direction, each plate subject to bathing fluids at different temperatures, and variable wall temperatures and heat fluxes (which are asymptotically stable) may be solved by the present method.

Pipe Flow. For this case equation (1) becomes

$$4[1 - 4r^2]\theta_x = \frac{1}{r}[r\theta_r]_r \quad (69)$$

Laplace transforming equation (69) and its boundary conditions yields

$$4[1 - 4r^2]s\phi = \frac{1}{r}[r\phi_r]_r \quad (70)$$

and equations (14) to (16). Constructing a solution of the form

$$\Phi = \Phi^{(0)} + s\Phi^{(1)} + s^2\Phi^{(2)} + \ldots \quad (71)$$

gives

$$\Phi^{(0)} = 1$$
$$\Phi^{(1)} = r^2 - r^4$$
$$\Phi^{(2)} = r^4/4 - 5r^6/9 - r^8/4$$
$$\Phi^{(3)} = [r^6 - 7r^8/2 + 89r^{10}/25 - r^{12}]/36 \quad (72)$$
$$\vdots \qquad\qquad \vdots$$

The values

$$\Phi' \equiv \Phi(1/2,s) = 1 + \eta_1 s + \eta_2 s^2 + \ldots$$
$$\Phi_y' \equiv \phi_y(1/2,s) = s[1/2 + \gamma_1 s + \gamma_2 s^2 + \ldots] \quad (73)$$

$$\eta_1 = 3/16 \qquad \gamma_1 = 7/192$$
$$\eta_2 = 73/36(16)^2 \qquad \gamma_2 = 83/360(16)^2 \quad (74)$$
$$\vdots \qquad\qquad \vdots$$

follow from equations (72).

Since the algebra for this problem is identical with that of the parallel plate problem we simply report the results.

First Approximation.

$$s_1^{(1)} = 2[1/\mathrm{Nu}_w + (59/220 + 1/\mathrm{Nu}_w)/(1 + 48/11\ \mathrm{Nu}_w)]^{-1} \quad (75)$$

$$A_1^{(1)} = [11/96 + \mathrm{Nu}_w/2]s_1^{(1)} = [1 + 11\,\mathrm{Nu}_w/24 + 121\,\mathrm{Nu}_w^2/2304]/[1 + 11\,\mathrm{Nu}_w/24 + 59\,\mathrm{Nu}_w^2/960] \quad (76)$$

$$\overline{\mathrm{Nu}}_{f,\infty}^{(1)} = [1 + 48/11\ \mathrm{Nu}_w]/[59/220 + 1/\mathrm{Nu}_w] \quad (77)$$

Equation (77) is exact when $\mathrm{Nu}_w = 0$ and overestimates the exact result of 3.658 (Kays [4]) by 1.93 percent when $\mathrm{Nu}_w = \infty$. For finite L we obtain

$$\overline{\mathrm{Nu}}_0^{(1)} = \overline{\mathrm{N}}_{0,\infty}^{(1)} - \ln\,(A_1^{(1)})/2L : \mathrm{Nu}_w > 0 \quad (78)$$

$$\overline{\mathrm{Nu}}_f^{(1)} = 48/[11(1 - 103/23040\ L)]\colon \mathrm{Nu}_w = 0 \qquad (79)$$

A second approximation may be constructed as before which reduces the maximum error by a factor of 10.

Nonuniform symmetric initial temperature profiles and varying wall temperatures and heat fluxes (which are asymptotically stable) may easily be incorporated into the foregoing computational scheme.

Discussion

The procedures developed here should be applicable to a broad class of problems—those whose Laplace transform with respect to the axial coordinate is easily obtained. Members of this class include other Graetz type problems with axial symmetry (viz., flow between concentric cylinders). More complicated Graetz analogs suggest themselves, e.g., the flow of a (dilute) multicomponent reacting solution in an axisymmetric duct. The conservation of energy and species equations may be coupled but of course must be linear.

We recognized that the second approximation discussed here has little value in direct applications; it is cited to illustrate the rapid convergence of the method itself. This agreeable property serves to lend credence to the method, indeed it may have practical value in supporting computations whose results are not known a priori.

There is a measure of arbitrariness in our choices of estimating s_1 and A_1. Other methods of estimating these values are of course possible, e.g., the boundary conditions could be imposed on each member of the perturbation series, alternately the denominator of equation (28) alone could be used to estimate the zeros of $1/\theta$. Neither of these procedures yield results superior to those given here.

The asymptotic values of the Nusselt numbers offered here have little utility for $L \lesssim .02$; part II of this series reports new procedures of utility in this regime.

References

1 Abramowitz, M., and Stegun, I. A., *Handbook of Mathematical Functions*, p. 16, 692, Dover, New York 1965, pp. 16,692.

2 Churchill, R. A., *Modern Operational Mathematics in Engineering*, McGraw-Hill, New York, 1944, p. 170.

3 Colton, C. K., Smith, K. A., Strove, P., and Merrill, E. W., "Laminar Flow Mass Transfer In a Flat Duct With Permeable Walls," *AIChE J.*, 17, 1971, p. 773.

4 Kays, W. M., "Convective Heat and Mass Transfer," McGraw-Hill, New York, 1969, pp. 110, 117.

5 Titschmarsh, E. C., "The Theory of Functions," Oxford University Press, London, 1960, p. 214.

6 Van der Does De Bye, J. A. W., and Schenk, J., *Appl. Sci. Res., Sect. A.*, Vol. 3, 1952, p. 308.

D. M. France
R. D. Carlson
R. R. Rohde
G. T. Charmoli

Argonne National Laboratory, Argonne, Ill.

Experimental Determination of Sodium Superheat Employing LMFBR Simulation Parameters[1]

Sodium superheat experiments were performed in a forced convection facility employing system parameters in the range of interest for application to loop and pot-type liquid metal cooled fast breeder reactors. The test section was representative of a single reactor fuel element with sodium flowing vertically upward in an annulus heated indirectly from the inside wall only. Steady-state operating parameters prior to a flow coast down approach to boiling included: velocity, 17 fps; heat flux, 7×10^5 Btu/hr-ft^2; test section inlet, 600 deg F; test section outlet to plenum, 900 deg F; plenum, 15 psia at 900 deg F and 700 deg F. Other important system variables controlled included sodium inert gas content and system pressure-temperature history. The axial location of boiling initiation in the test section was measured. Five test series encompassing 33 test runs were performed. Applicable superheat results were compared to predictions of the pressure-temperature history model including inert gas effects.

Introduction

One phase of the development program of the liquid metal fast breeder reactor (LMFBR) for application to commercial electric power plants is presently involved in investigations concerned with the nature of coolant boiling subsequent to an abnormal incident. A consequence of the formation of voids in the reactor core may be positive reactivity insertion; fuel-coolant interaction may also occur. The rate of formation of the voids and the physical nature of the phenomenon are important considerations. In the initial stages of voiding the phenomenon is most heavily influenced by the magnitude of the liquid superheat in the system at the inception of boiling. Thus, investigations into the incipient boiling (IB) superheat in liquid metals have been in progress for the past decade. Understanding of the related physical phenomena and prediction of IB superheat in liquid metals has evolved through considerable effort extended by many investigators. A review of the existing experimental results and a discussion of the parameters observed to influence IB superheat were given by Fauske [1][2] in 1968. At that time the parameters considered to have important influence on IB superheat in convective systems essentially included liquid velocity, heat flux, heating surface condition, liquid metal purity, method of heating, system pressure, and system operational time. The data were widely scattered, and in the cases of heat flux and system operational time (aging) conflicting parametric trends were reported by various investigators. It was in this general period of time that the importance of three additional conditions affecting IB superheat was presented. The addition of these conditions supplied a physical explanation for some of the observed inconsistencies in the experimental data. Holtz [2] first presented the pressure-temperature (P-T) history effect on IB superheat and based on this effect developed a predictive model. The Holtz model was subsequently extended [3–6] to include the effect of inert gas in the wall cavity nucleation sites. Control of these two parameters, P-T history and inert gas, during experimentation requires adherence to special conditions and procedures in the entire experimental facility (not only the test section) prior to, during, and in the time period between test runs. It has been postulated that some of the experimentally observed parametric effects were in fact the result of the dominance of these two parameters either or both of which were not controlled. For example, the experiments of Holtz and Singer reported in reference [5] indicated that an inert gas effect on IB superheat could be misinterpreted as a heat flux effect if the inert gas parameter was neglected during experimentation.

The third condition of importance which received recent attention was the experimental determination of the location of boiling inception in the test section. In 1965, Grass, et al. [7] reported the successful implementation of an experimental technique for measuring this location, however, the majority of available experimental superheat data (with notable exceptions) were accumulated without measuring this location, and it was assumed that nucleation always occurred first at the highest superheat in the system. Fauske [8] hypothesized that this measurement omission could account for some of the observed heat flux and velocity ef-

[1] This work was performed under the auspices of the U. S. Atomic Energy Commission.

[2] Numbers in brackets designate References at end of paper.

Contributed by the Heat Transfer Division for publication in the JOURNAL OF HEAT TRANSFER. Manuscript received by the Heat Transfer Division, January 7, 1974. Paper No. 74-HT-PP.

fects on IB superheat. Chen's data [9] were used as an example of alternate possible interpretations depending upon the location of boiling inception. Later experiments in which this measurement was made still exhibited conflicting results [10, 11], but the necessity of the measurement was demonstrated.

The conditions discussed add to the list of parameters postulated as having important influence on IB superheat in liquid metals, the P-T history and the dissolved inert gas. Presently, there remains unresolved questions and conflicting data concerning which parametric effects are dominant and which effects are only apparent. In order to determine the parameters that are indeed important, it is necessary to obtain experimental data while controlling all of the parameters. Early experiments generally did not control or report the P-T history and inert gas parameters and did not measure the location of boiling inception. At least, no single experiment included all the conditions. More recent experiments [9–18] included more of the parametric effects as they became evident. However, several conditions of parametric dominance of IB superheat in liquid metal systems have not as yet been resolved through experimentation. (It is of interest to note that in reference [18], the parameter of temperature rise was added to the list of variables postulated to influence IB superheat.)

The unresolved questions concerning liquid metal IB superheat are pertinent to the prediction of superheat in an arbitrary system where nucleation occurs from wall cavities. However, in the special case of a realistic loop type LMFBR system operating for a period of time sufficient to attain inert gas equilibrium, it has been postulated [1, 19] that IB superheat will always be near zero independent of other system parameters. Boiling initiation under the condition of zero superheat is most desirable in a LMFBR because it minimizes the potential for high voiding rates. It was, therefore, the primary objective of this investigation to test the hypothesis of zero IB superheat by experimental determination in a facility resembling a loop type reactor system. All of the parameters previously mentioned were controlled, and the location of boiling inception was measured. The effect of each variable on IB superheat was not systematically studied. Rather, it was desired to verify whether the IB superheat is indeed near zero in a simulated loop type reactor environment employing values of the system variables in the appropriate range for LMFBR application.

The first tests were performed in a forced convection, sodium, LMFBR simulation loop operating in a mode typifying a loop type reactor. The operation of the experimental facility from the time of filling with sodium to the conclusion of testing was an integral part of the test. This procedural method of operation allowed for the control and observation of the effect of inert gas in the liquid, in the test section wall cavities, and in the form of bubbles in the bulk liquid.

Further experiments were performed simulating pot-type reactor operation. In these tests the IB superheat was not predicted to be consistently near zero independent of other system variables. These superheat data were compared with predictions from the P-T history model including the effects of inert gas in the wall cavities. Parametric values in the LMFBR range of interest were again employed.

Experimental Test Facility

The LMFBR Heat Transfer Simulation Loop in which sodium superheat tests were conducted is shown schematically in Fig. 1.

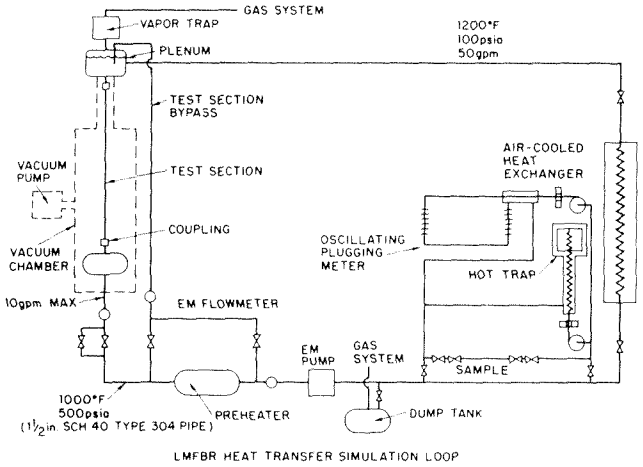

Fig. 1 Experimental facility

The maximum system operating parameters are indicated. During operation the hot trap was not employed and the dump tank served as a cold trap. This arrangement produced a consistent sodium oxide level of ≈15 ppm as indicated by the oscillating plugging meter. Sodium flowed vertically upward through the test section directly into the plenum equipped with an argon cover gas. The entire test section was enclosed in a vacuum chamber which provided thermal insulation and safety protection.

The test section was designed to simulate a single LMFBR fuel element. It consisted of a 0.23 in. OD 45 kW Watlow heater with a 3 ft heated length surrounded by a 0.37 in. ID stainless steel tube. Sodium flowed vertically upward in the annulus in which a spacer wire was employed having a diameter of 0.062 in. and a pitch of 12 in. A 10 in. unheated region existed between the top of the 3 ft heated section and the plenum. The axial distance, Z, is measured positive upward (downstream) from the top end of this heated region. In the spatial region of interest for IB superheat tests, $-6 \leq Z \leq 10$ in., 22 chromel-alumel thermocouples were welded to the outer tube wall. Sixteen void sensor probes (voltage taps) were also welded to the tube wall in this region. Resolution was better than one in. These sensors did not distinguish between argon gas and sodium vapor, thus a recorded void was only known to be nonliquid. The technique employed in measurement of the location of initial test section voiding was an improvement upon the method originally presented by Grass [7]. Using a 60 Hz a-c potential (less than 1 V) axially across the test section to replace the d-c potential previously employed [7] it was possible to place grounded thermbcouples on the test section wall. This arrangement provided the relatively fast thermocouple response desirable for the transient superheat tests. The scheme was facilitated by using an integrating digital voltmeter (to reject the 60 Hz a-c voltage) with a computerized data acquisition system. The details of this technique are given in reference [20].

Measurements during a test were recorded via a Hewlett Packard 2116 B high speed computerized data acquisition system. A complete set of thermocouple and flow meter data was taken every 2.3 s. Prior to boiling, the 16 voltage signals were monitored at 0.016 s intervals. The computer was programmed to detect initial nucleation, record its axial location, allow the system to boil

Nomenclature

G = mass velocity, $lb_m/hr\text{-}ft^2$
P = pressure, psia
R, R' = radius of curvature of surface cavity interface, ft
T = temperature, deg F
V = sodium velocity, ft/s
Z = axial location, ft
σ = surface tension, lb/ft

Subscripts

b = bulk liquid
g = inert gas
I = initial steady-state operating condition
IN = test section inlet
L = bulk liquid
OUT = test section outlet to plenum
P = plenum
SAT = saturation
v = sodium vapor
w = heated wall

for a prescribed time interval, and finally terminate test section power. The last task lengthened the test section lifetime.

Test Procedure

The system operation procedures were an integral part of the superheat tests and were used to control the inert gas content in the system. The experimental facility was filled under vacuum with sodium contained in the system dump tank at 400 deg F and a pressure slightly above atmospheric. The system was brought to the following conditions prior to test series A: test section—inlet 600 deg F, outlet 900 deg F, velocity 17 fps, heat flux 7×10^5 Btu/hr-ft^2, by pass closed; plenum—900 deg F, 15 psia.

All tests reported were performed with a plenum gas pressure of 15 psia and a sodium oxide level of $\approx$15 ppm. Prior to the first boiling test it was desired to have the sodium in the plenum saturated with argon gas simulating steady-state reactor operation. The loop operation time required to achieve this inert gas equilibrium was estimated at 20–30 hr. Thus, the loop was operated for 30.5 hr under the reactor simulation conditions specified above prior to the first test. This operation also served to establish the system P-T history.

In all tests, boiling was approached in a manner indicative of a flow coast down situation, perhaps one of the most credible forms of abnormal reactor operation. The test section velocity was reduced linearly as a function of time. The deceleration was 0.2 ft/s^2 in all tests. This approach to boiling corresponded to a temperature ramp at $Z = 0$ that increased from 200 deg F/min to 2000 deg F/min during the transient. During the flow coast down the test section inlet temperature, plenum temperature and pressure, and test section heat flux remained constant. The test section temperatures and flow were recorded during the flow coast down prior to boiling while the void sensor outputs were monitored. The computer was programmed to define initial voiding via a predetermined deviation in potential between adjacent voltage taps. The coast down duration was approximately 1 min from commencement to boiling inception which occurred at a velocity of approximately 4.5 fps. Subsequent to boiling detection and recording of the axial location of initial nucleation the flow coast down continued, and test section temperatures and flow continued to be recorded. Test section power was terminated 2.7 s after boiling inception; the velocity was then manually held at a constant value. Finally the system was returned to steady-state operation with parameters set to the original values as previously delineated.

Table 1 Pretest history and superheat data

RUN NUMBER	T_p (°F)	TIME FROM LOOP FILL (HRS)	MAXIMUM TEST SECTION BULK SUPERHEAT (°F)	INCIPIENT BOILING BULK SUPERHEAT (°F)
A.1	900	30.5	0	0
A.2	↑	34.8	↑	↑
A.3		45.8		
A.4		54.3		
A.5		58.3		
A.6		78.7		
A.7		79.7		
A.8		79.8		
A.9		79.9		
A.10		80.0		
A.11		80.1		
A.12		80.2		
A.13		80.3		
A.14		80.4		
A.15		86.0		
A.16		86.1		
A.17		86.2		
A.18		93.7		
A.19		104.2		
A.20		104.4		
A.21		104.5		
A.22		106.8		
A.23		106.9		
A.24		107.4		
A.25		108.4		
A.26	900	108.5	0	0
B.1	900	0.8	120	0
B.2	900	1.5	150	60
C.1	700	34.0	40	20
C.2	700	42.0	100	0
D.1	900	20.0	0	0
D.2	900	20.1	0	0
E.1	700	24.0	30	30

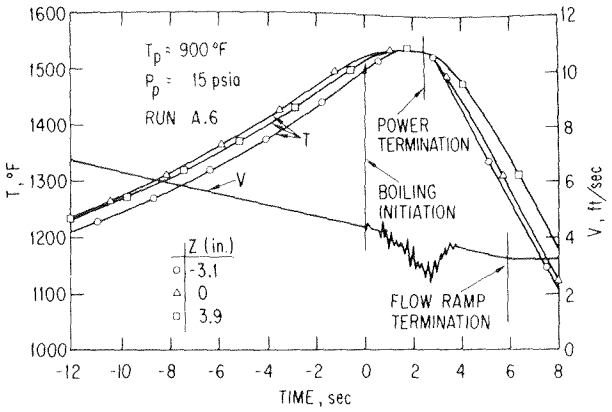

Fig. 2 Zero superheat test data

Subsequent to the first test, the system was again operated in the steady-state mode for a prescribed length of time before the second test was performed. This procedure was followed to allow the inert gas concentration in the wall cavities to return to equilibrium and to re-establish the P-T history imposed by steady-state operation. The second test was performed in a manner identical to the first test. Since the time period between tests necessary to obtain inert gas equilibrium in the wall cavities was not known the steady-state operating time between tests was varied. Twenty-six tests were performed in this series, test series A. The system was run continuously from initial sodium fill to completion of the test series.

Experimental Results and Discussion

The sodium superheats measured in all tests of series A were identical and equal to zero. After the initial operational period of 30.5 hr, the duration of operation between tests varied from 20.4 to 0.1 hr as given in Table 1. Typical transient measurements and results are shown in Fig. 2 where the time scale is relative to the inception of boiling. In the test represented in Fig. 2, boiling was first detected 3.9 in. above the top of the heater, $Z = 3.9$ in. Thereafter, all test section temperatures in the instrumented region approached a relatively constant value indicative of bulk boiling. The velocity shown was recorded on an analog system; the electromagnetic (EM) flow meter was located at the test section inlet. After a short delay subsequent to boiling detection, the velocity decreased more sharply as voids were formed. In general, this result is consistent with the results presented in references [21, 22] for a single test empolying a flow coast down rate faster by approximately a factor of three. After power termination, the velocity returned to the original linear decline until the coast down was terminated. The same temperature data were replotted in Fig. 3 at several times relative to boiling inception. The temperatures shown in Figs. 2 and 3 recorded on the outer, insulated, test section wall differ from the bulk sodium temperature. This condition is a result of test section heat loss. However, using the recorded test section temperature profile after the establishment of bulk boiling as the saturation temperature distribution at boiling inception minimized the error incurred in the calculation of the bulk superheat. For example, the sodium bulk superheat was calculated in test run A.6 as the difference in measured temperatures at times 0 and 1.3 s, as shown in Fig. 3. The IB superheat at $Z = 3.9$ in. is seen to be near zero (slightly subcooled). The maximum superheat in the test section at the time of IB, occurred at $Z \approx 0.5$ in. and was also approximately zero. A distinction between these two superheats is made in Table 1.

The data for all 26 test runs of series A were similar to the data of Figs. 2 and 3. The location of initial nucleation varied while the superheat remained near zero. Nucleation occurred over the axial range in the test section from $Z = -1$ in. to $Z = 5$ in. indicating that no preferential nucleation site existed in the test section. As

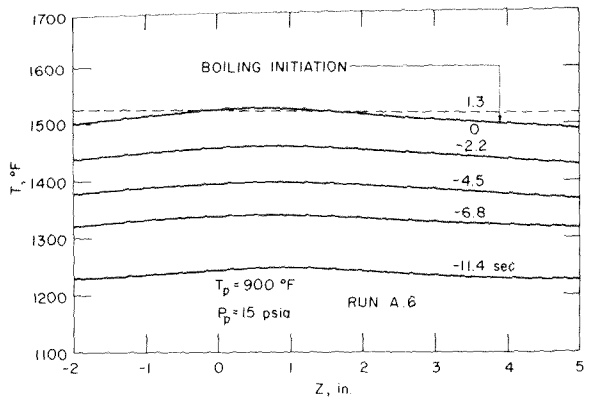

Fig. 3 Zero superheat test results

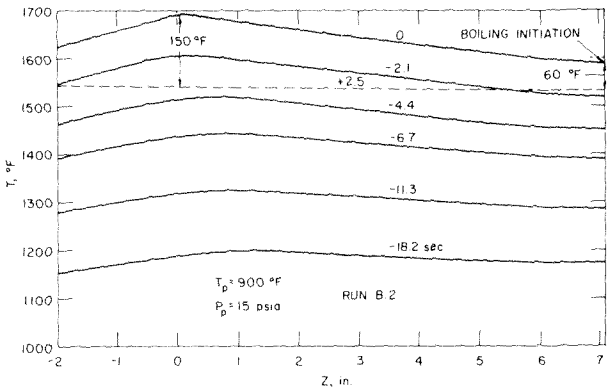

Fig. 4 High superheat test results

seen in Fig. 3, sodium in this portion of the test section reached saturation conditions approximately concurrently.

The results of test series A showing consistently zero superheat might at the outset be attributed to any of several parameters. For example, boiling was obtained at a velocity of approximately 4.5 fps. The results of references [11, 17], although obtained under different parametric conditions, imply that zero bulk superheat would be expected at a velocity greater than about 4 fps. However, this as well as most other parametric considerations that might account for the zero superheat test results are not independent of the manner in which tests are conducted. Test runs A.19–A.26 were performed in relatively close succession as shown in Table 1. Some tests were separated by only 0.1 hr. As mentioned in reference [14], repeated boiling runs of this type have generally been observed to occur at increasingly higher superheats. This result has been attributed to deactivation of wall nucleation sites and to loss of inert gas from the wall sites. The results of test series A did not exhibit this trend. Based on this finding and the occasional observation of relatively large inert gas bubbles in the test section, nucleation was suspected to have occurred from gas bubbles in the bulk liquid. The presence of these nucleation sites, although too small to be effectively measured via the voltage tap instrumentation, would account for the repeated zero superheat results of test series A. Although no measurement was made of which nucleation sites were active (gas bubbles or wall cavities) the results of test series B indicated that the zero superheat observed in series A was a direct consequence of inert gas in the system.

Test series B was performed with the primary objective of obtaining a high test section superheat at boiling incipience. These tests served as a system control showing that zero superheat was not peculiar to the test facility. In addition, this test series supported the contention that the zero superheat of series A was not due to any system parameter other than the inert gas. Test series B was conducted with all parameters identical to those of test series A. There was only one procedural difference. Test B.1 was performed after 0.8 hr of steady-state loop operation subsequent to sodium fill in contrast to 30.5 hr prior to test A.1. This procedure affected the inert gas content of the sodium; test series B was performed with far less argon dissolved in the sodium than in series A. It was unlikely that inert gas bubbles would be present in the test section as in series A, and none was observed in series B. Nucleation in test series B was believed to have occurred from test section wall cavities with a low inert gas pressure. The maximum test section superheat measured in test B.1 was 120 deg F; 150 deg F superheat was obtained in test B.2 0.7 hr later.

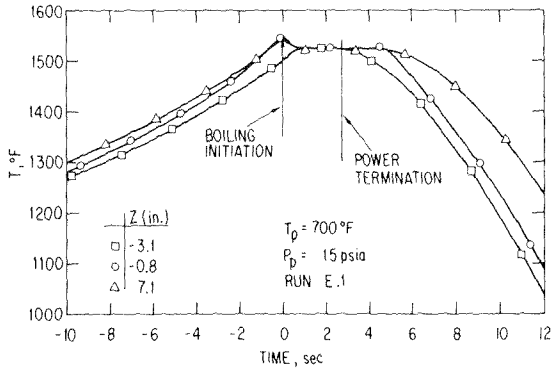

Fig. 5 Superheat test data from pot type operation

The results of test B.2 are presented in Fig. 4. The IB superheat was 60 deg F at $Z = 7.1$ in. while the maximum test section superheat was 150 deg F at $Z \approx 0$ in. This later superheat is of relatively high magnitude and as discussed in the foregoing was obtained under conditions similar to test series A. The important parameter, varied between the two test series, was the inert gas content in the sodium.

A pot-type LMFBR having a sodium-argon interface several hundred deg F lower than the maximum system temperature is not expected to display consistently zero superheat at boiling inception independent of other system parameters. Thus, test series C was performed utilizing a low plenum temperature. This condition was obtained by test facility operation with the test section by-pass open, maintaining the plenum temperature at 700 deg F. The scheme was representative of pot type reactor operational conditions. The test procedure was identical to series A, and the steady-state parameters were as given previously with two exceptions. The steady-state pretest velocity was 13 fps corresponding to a test section heat flux of 5.5×10^5 Btu/hr-ft^2. (The test section inlet and outlet temperatures were 600 deg F and 900 deg F, respectively, and the plenum temperature was 700 deg F.) The duration of the flow coast down transient was approximately 45 s from commencement to boiling inception; the same deceleration of 0.2 ft/s^2 was employed as in previous tests.

The system was filled and operated at steady-state for 34 hr prior to test C.1 wherein moderate superheat was obtained as given in Table 1. A second test, C.2, was made 8 hr later. As a control, the system was dumped, refilled several days later, and test series D was performed. Series D was similar to series A in all respects; the superheats were zero. The loop was then dumped, refilled after several days, and test series E was performed similar in all respects to series C.

The superheat results of tests C.1 and E.1 were similar; the results of E.1 are shown in Fig. 5. Boiling initiated at $Z = -0.8$ in. in both tests and the maximum test section superheat at boiling inception was 30 deg F–40 deg F. Insufficient data were available to determine the cause of the different superheat obtained in test C.2.

It was desired to compare the superheat data to the prediction of the P-T history model as presented in references [6, 23]. However, none of the data from test series A and B was applicable. The suspicion of nucleation from gas bubbles instead of wall cavities in series A and the nonequilibrium plenum inert gas concen-

tration in series B precluded the use of these data. Test series C and E were performed with a low, but equilibrium, inert gas concentration in the sodium. Although the data are limited, the results of tests C.1 and E.1 were compared to the P-T history model for predicting IB superheat.

Theory

Boiling was assumed to occur when the forces due to vapor pressure and inert gas inside a cavity in the surface of the test section heater became larger than the opposing forces due to liquid sodium pressure and surface tension. Such prediction of nucleation from wall cavities requires knowledge of the radius of curvature of the liquid-vapor interface in the cavity at IB as well as the partial pressure of argon gas in the cavity. The P-T history theory provides a method for calculating the radius of curvature, and various models have been used to account for the inert gas pressure [3, 4, 6, 23]. For application to test series C and E, the inert gas models discussed in references [6, 23] which utilize the inert gas equilibrium condition prior to testing were employed. Operating at steady-state the radius of curvature of the liquid vapor interface in the nonwetted cavity was calculated from

$$R'(Z) = \frac{2\sigma(T_I(Z))}{P_{L_I}(Z) - P_v(T_I(Z)) - P_g(T_I(Z))} \quad (1)$$

where T_I is the initial heater wall temperature under steady-state conditions. Assuming that the plenum sodium was saturated with argon gas, the mass fraction of argon was calculated from Henry's law. Then under the assumption that the mass fraction of argon was constant throughout the experimental loop, the partial pressures of argon in the cavities were also calculated from Henry's law.

$$P_g(T_I(Z)) = P_p K(T_p)/K(T_I(Z)) \quad (2)$$

where K is the Henry's law constant. Combining equations (1) and (2), $R'(Z)$ was computed from the steady-state distributions, $T_I(Z)$ and $P_I(Z)$. The result of this calculation for tests series A is shown in Fig. 6 using idealized temperature distributions that were linear across the 3 ft heated length and constant at 900 deg F in the 10 in. unheated region. Boiling is assumed to initiate during the flow coast down test when the following relation was first satisfied in the wetted cavity.

$$P_v(T(Z)) + P_g(T(Z)) = P_L(Z) + \frac{2\sigma(T(Z))}{R(Z)} \quad (3)$$

The heater wall temperature (cavity temperature), $T(Z)$, corresponds to a time during the transient when the liquid pressure is $P_L(Z)$. The radius of curvature, $R(Z)$, in the wetted cavity at boiling incipience was assumed to be related to the nonwetted radius, R', by a relation of the form

$$R/R' = \text{constant} \quad (4)$$

It remains to model the inert gas in the cavity during the transient to complete the superheat prediction via equation (3). Two models were employed representing extreme conditions.

Model 1. It was assumed that the inert gas in the cavity was in constant mass equilibrium during the transient and that the partial pressure, P_g, could be calculated via Henry's law. The result was

$$P_g(T(Z)) = P_p K(T_p)/K(T(Z)) \quad (5)$$

Model 2. It was assumed that the transient was relatively fast such that the mass of inert gas in the cavity was unaltered from its steady-state value. Using the perfect gas law yielded

$$P_g(T(Z)) = P_g(T_I(Z))T(Z)/T_I(Z) \quad (6)$$

Since the time constant for diffusion of inert gas from the cavities is large compared to the rate of the transient, gas model 2 is likely to be more representative of the experiments than model 1. Results from model 1 are similar to predictions made by neglecting inert gas in the surface cavities.

Values of the radius ratio, R/R', in the range of 0.342 to 1.0 have been presented [4, 5, 6, 23] for use with sodium, and superheat predictions employing a value of $R/R' = 1.0$ appear to represent the data most consistently. Two values of this ratio were used in the present calculations, $R/R' = 0.342$ and 1.0. Four predictions of the superheat required for nucleation were obtained from equation (3) using the two gas models, equations (5) and (6), and the two values of R/R'. The results applied to test series A are shown in Fig. 6 at a time during the flow coast down when the mass velocity was reduced to 9.2×10^5 $lb_M/hr\text{-}ft^2$ from its initial steady-state value of $G_I = 3.07 \times 10^6$ $lb_M/hr\text{-}ft^2$. The idealized bulk (T_b) and heated wall (T_w) temperature profiles are shown. The wall temperature was calculated from a heat balance employing a constant empirical heat transfer coefficient in the test section. The temperatures required for nucleation calculated from gas model 2 fell below the saturation temperature. This result implies that inert gas bubbles will nucleate from the cavities prior to reaching saturation conditions, and boiling will occur at zero superheat. Boiling is predicted to occur at the time when the wall temperature first equals the required nucleation temperature at some location in the test section, i.e., when equation (3) is first satisfied by some $T(Z)$ at time, t, and axial location Z. The wall temperature at the time corresponding to Fig. 6 is seen to equal the saturation temperature at $Z = 0$. The prediction of gas model 2 is that boiling would occur at $Z = 0$ at this time.

Employing gas model 1, the intersection of T_w and the required temperature for nucleation occurred at $Z = 0$ at a time later in the transient than represented in Fig. 6 with a superheat greater than zero. This condition may be inferred from Fig. 6. However, the wall temperature distribution employed in the calculation was an idealized estimate of the system transient temperature profile. The temperature measurements shown in Figs. 3 and 4 indicate that the axial wall temperature distribution in the test section was similar to the predicted nucleation temperature curves (shown in Fig. 6) in the region near $Z = 0$.

Under this condition it is equally probable that nucleation will occur anywhere in the superheated region of the test section. Equation (3) would be satisfied in this entire region at approximately the same time, and the experimental results are consistent with this observation. Due to the uncertainty in the prediction of the location of boiling inception, the wall superheats were calculated (using the idealized temperature profiles) at two locations, $Z = 0$ and $Z = 10$ in. and are given in Table 2. These superheat predictions are wall superheats. Bulk superheats were experimentally measured and predicted values are given in Table 2 at conditions of interest.

As previously discussed, nucleation in test series A was sus-

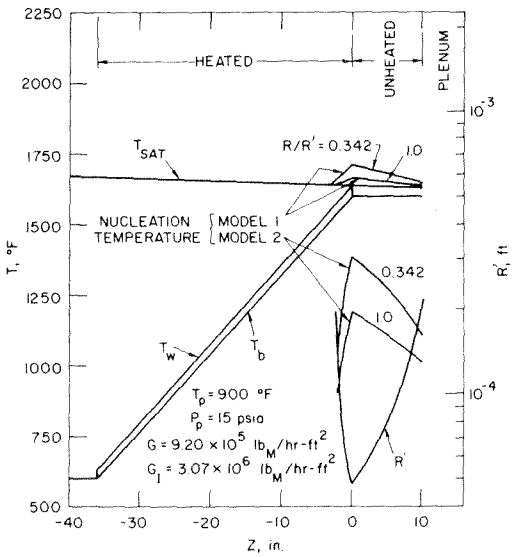

Fig. 6 Superheat prediction

Table 2 Predicted superheat

AXIAL LOCATION	T_P (°F)	GAS MODEL	R/R'	WALL SUPERHEAT (°F)	BULK SUPERHEAT (°F)
TEST SECTION EXIT TO PLENUM (Z = 10 IN.)	900	1	0.342	16	
	900	1	1.0	5	
	900	2	0.342	0	
	900	2	1.0	0	0
	700	1	0.342	220	
	700	1	1.0	100	
	700	2	0.342	210	
	700	2	1.0	80	80
TOP OF HEATER (Z = 0)	900	1	0.342	70	
	900	1	1.0	26	
	900	2	0.342	0	
	900	2	1.0	0	0
	700	1	0.342	240	
	700	1	1.0	110	
	700	2	0.342	220	
	700	2	1.0	90	56

pected to have occurred from gas bubbles rather than wall cavities. However, it is of interest to note that assuming nucleation from wall cavities, zero superheat was predicted using gas model 2. This result was also obtained in reference [19].

Equation (3) was applied to the conditions of test series C and E. In this case, both gas models 1 and 2 predicted superheats greater than zero at boiling inception. The same uncertainty in predicted location of incipient boiling was encountered in test series C and E as was found in series A. Thus the predicted values of superheat are given in Table 2 for two axial locations, $Z = 0$, and $Z = 10$ in. The maximum IB bulk superheat predicted at $Z = 0$ using gas model 2 and $R/R' = 1.0$ was 56 deg F for test series C and E. The corresponding measured values were 30–40 deg F.

As presented in Table 2, the superheat predictions were sensitive to the gas model and the radius ratio employed. Gas model 2 with $R/R' = 1.0$ gave results closest to the data.

Conclusions

It was demonstrated that in a LMFBR loop type system operating at steady-state for a period of time long enough to establish mass equilibrium of inert gas the superheat at boiling inception following a system transient was zero. Based on experimental results and consistent with previous predictions [1, 19] the zero superheat result was attributed to inert gas in the system. These tests were conducted with system parameters of heat flux, velocity, pressure, geometry, liquid purity, surface condition, pressure-temperature history, inert gas content, temperature ramp, and approach to boiling set at single prescribed values in the range of interest for nuclear fast reactor application. Extension of the experiments to include variations in system parameters, remaining in the range of interest to LMFBRs, would be expected to yield the same zero superheat result due to the inert gas. However, this condition remains to be demonstrated.

Sodium superheats from zero to 150 deg F were obtained by altering the system preboiling steady-state operating time thereby influencing the inert gas content of the sodium. These results were obtained at velocities above 4 fps which have been reported [17] to consistently produce near zero superheat in another experimental program.

Superheat data obtained under pot type LMFBR operating conditions were compared to predictions including the effect of inert gas in the wall cavity nucleation sites. The sensitivity of superheat predictions to parameters of gas model, radius, R', and radius ratio, R/R', was demonstrated. However, using reasonable conditions of gas model 2, R' determined from the system P-T history, and $R/R' = 1.0$, the theory compared well with the limited data obtained under pot-type operation.

Acknowledgment

The fine efforts of W. Brewer, J. Killelea, A. Mele, and J. Reed are gratefully acknowledged. Their contributions during design and fabrication of the experimental facility as well as during testing were invaluable.

References

1 Fauske, Hans K., "Superheating of Liquid Metals in Relation to Fast Reactor Safety," Reactor and Fuel-Processing Technology, Vol. 11, No. 2, 1968, pp. 84–88.

(2) Holtz, Robert E., "The Effect of the Pressure-Temperature History Upon Incipient-Boiling Superheats in Liquid Metals," ANL-7184, 1966.

3 Chen, J. C., "Incipient Boiling Superheats in Liquid Metals," JOURNAL OF HEAT TRANSFER, TRANS. ASME, Series C, Vol. 90, No. 3, 1968, pp. 303–312.

4 Dwyer, O. E., "On Incipient-Boiling Wall Superheats in Liquid Metals," *International Journal of Heat Mass Transfer*, Vol. 12, 1969, pp. 1403–1419.

5 Holtz, Robert E., and Singer, Ralph M., "A Study of the Incipient Boiling of Sodium," ANL-7608, 1969.

6 Singer, Ralph M., and Holtz, Robert E., "On the Role of Inert Gas in Incipient Boiling Liquid Metal Experiments," *International Journal of Heat Mass Transfer*, Vol. 12, No. 9, 1969, pp. 1045–1060.

7 Grass, G., Kollowski, H., Milliot, B., "Study of Liquid Metal Boiling Under Forced Convection," ANL-TRANS-257, 1965.

8 Fauske, Hans K., "Transient Liquid Metal Boiling and Two-Phase Flow," presented at the Third Meeting of the Liquid Metal Boiling Working Group, Ispra, Italy, Apr. 1971.

9 Chen, J. C., "An Experimental Investigation of Incipient Vaporization of Potassium in Convection Flow," *Liquid Metal Heat Transfer and Fluid Dynamics*, ASME Symposium, Nov. 1970, pp. 129–134.

10 Henry, R. E., et al., "Reactor Development Progress Report," ANL-7833, June, 1971, pp. 8.1–8.2.

11 Dwyer, O. E., Strickland, G., Kalish, S., Hlovac, P. J., and Schoener, G. A., "Incipient-Boiling Superheat for Sodium in Turbulent Channel Flow: Effects of Heat Flux and Flow Rate," *International Journal of Heat Mass Transfer*, Vol. 16, 1973, pp. 971–984.

12 Schleisiek, Karl, "Heat Transfer and Boiling During Forced Convection of Sodium in an Induction-Heated Tube," *Nucl. Eng. and Design*, Vol. 14, 1970, pp. 60–68.

13 Schultheiss, G. F., "Experimental Investigation of Incipient Boiling Superheat in Wall Cavities," *Liquid Metal Heat Transfer and Fluid Dynamics*, ASME Symposium, Nov. 1972, pp. 100–105.

14 Peppler, W., and Schlechtendahl, E. G., "Experimental and Analytical Investigations of Sodium Boiling Events in Narrow Channels," *Liquid Metal Heat Transfer and Fluid Dynamics*, ASME Symposium, Nov. 1970, pp. 162–171.

15 Kottowski, H., and Grass, G., "Influence on Superheating by Suppression of Nucleation Cavities and Effect of Surface Microstructure on Nucleation Sites," *Liquid Metal Heat Transfer and Fluid Dynamics*, ASME Symposium, Nov. 1970, pp. 108–115.

16 Logan, D., Baroczy, C. J., Landoni, J. A., and Morewitz, H. A., "Studies of Boiling Initiation for Sodium Flowing in a Heated Channel," AI-AEC-12767, 1969.

17 Logan, D., Baroczy, C. J., Landoni, J. A., and Morewitz, H. A., "Effects of Velocity, Oxide Level, and Flow Transients on Boiling Initiation in Sodium," *Liquid Metal Heat Transfer and Fluid Dynamics*, ASME Symposium, Nov. 1970, pp. 116–128.

18 Dwyer, O. E., Strickland, G., Kalish, S., Hlavac, P. J., and Schoener, G. A., "Incipient-Boiling Superheats for Sodium in Turbulent, Channel Flow: Effect of Rate of Temperature Rise," JOURNAL OF HEAT TRANSFER, TRANS. ASME, Series C, Vol. 95, May, 1973, pp. 159–165.

19 Holtz, Robert E., Fauske, Hans K., and Eggen, Donald T., "The Prediction of Incipient Boiling Superheats in Liquid Metal Cooled Reactor Systems," *Nucl. Eng. and Design*, Vol. 16, 1971, pp. 253–265.

20 Carlson, R. C., and Charmoli, G. T., "Sodium Void Detection Using a Digital Computer," to be published.

21 Henry, R. E., et al., "Reactor Development Progress Report," ANL-RDP-14, Feb. 1973, pp. 9.1–9.2.

22 Henry, R. E., Singer, R. M., Quinn, D. J., Spleha, E. A., Erickson, E. G., and Jeans, W. C., "Single-Pin Expulsion and Reentry Test," *Transactions Am. Nucl. Soc.*, Vol. 16, June, 1973, pp. 180–181.

23 Holtz, Robert E., "On the Incipient Boiling of Sodium and Its Application to Reactor Systems," ANL-7884, Nov. 1971.

M. Cumo
G. E. Farello
G. Ferrari
G. Palazzi

Laboratorio Tecnologie Reattori, COMITATO NAZIONALE per l' ENERGIA NUCLEARE, Centro di Studi Nucleari della Casaccia, Italy

The Influence of Twisted Tapes in Subcritical, Once-Through Vapor Generators in Counter flow

The swirl flow of Freon 12 in a tubular heat exchanger, indirectly heated by forced convection of water in an annular gap, is studied. Two identical situations are compared, with and without a twisted tape, to deduce the influence of the swirl flow in the particularly interesting boundary condition of indirect heating by another fluid (and not simply of uniform Joule heating). The heat transfer is greatly increased by the swirl flow, up to a factor of two at the burnout or dryout point.

Introduction

The need to increase power densities in heat exchangers has led to the use of twisted tapes as swirl flow promoters; this is particularly attractive in once-through boilers. Previous research efforts, some conducted by the present authors and performed mostly with electrically heated test sections with part of the power dissipated by the inserted tape itself, have clearly indicated that the insertion of twisted tapes generally increases the burnout quality. The temperature jump at the burnout or dryout point is decreased, and the wall temperature oscillations near the burnout point are reduced.

The uniform Joule heating of the test sections may indeed be a rough approximation of the indirect heating by a secondary fluid (like in sodium steam generators for fast reactor plants) [1].[1] Electric heating does present many experimental advantages of simplicity [2–5], but it may lead to some errors, especially with those fluids which have a small heat of vaporization and a tendency toward thermodynamic nonequilibrium (Freons for example).

The present experiments were performed with a vertical, straight test section with Freon 12 flowing upward in once-through flow, heated by water in forced convection downward flow in an external annular gap (Fig. 1). In this test section it is possible to insert a twisted tape in the inner tube, so to have two reference situations, i.e., one with twisted tape and one other without, with all other parameters being kept constant.

Freon enters as subcooled liquid and exits as saturated or super-heated vapour. Forced flow of pressurized water in the external annular gap has been selected for its high heat transfer coefficient. This selection provides a certain similarity with sodium heated steam generators for fast reactor plants, where the sodium (shell side) corresponds to the water (annular gap) and the vaporizing water (tube side) corresponds to the Freon 12 (tube side).

Experimental Apparatus and Procedure

The experimental apparatus shown in Fig. 1 consists of two coupled stainless steel loops. The first loop (left side) is the Freon loop in which vaporization of the fluid takes place within the test section. A water cooled condenser, a piston pump, and a preheater are the other main components. The water loop, which includes a centrifugal pump and a heater as the main components, is operated at 30 atm. The inlet temperature of the water in the test section is fixed during a given test by adjusting the power to the heater. A detailed description of the loop is available in [6] to which the reader is referred for further description.

The test section was made of stainless steel. The inner tube had an inner diameter of 0.756 cm and a wall thickness of 0.02 cm; the outer tube had an inner diameter of 1.576 cm. The outer tube was externally insulated to minimize heat losses. Along the external wall of the outer tube were fixed 20 wall thermocouples, axially 10 cm apart, with the bead penetrating within the wall as shown in Fig. 2. The heat transfer length of the test section was 200 cm. Fig. 2 shows the dimensions of the cross section, together with the dimensions of the twisted tape (thickness = 0.02 cm). The twist ratio $y = 4.4$ (180° twist length/inner diameter) of the tape is typical of that used in studies of single-phase and two-phase swirl flow [7].

All the signals from the loops (temperature, pressures, flowrates) are periodically scanned and printed by a data logging system, with a period of about 20 sc.

Consider now the two reference situations, with and without a twisted tape, for the same specific mass flowrate and pressure of the Freon at a constant specific mass flowrate of water, but with gradually varying water inlet temperature. First of all, it is important to remark that the two coupled loops had to be operated

[1] Numbers in brackets designate References at end of paper.

Contributed by the Heat Transfer Division for publication in the JOURNAL OF HEAT TRANSFER. Manuscript received by the Heat Transfer Division, June 20, 1974. Paper No. 74-HT-XX.

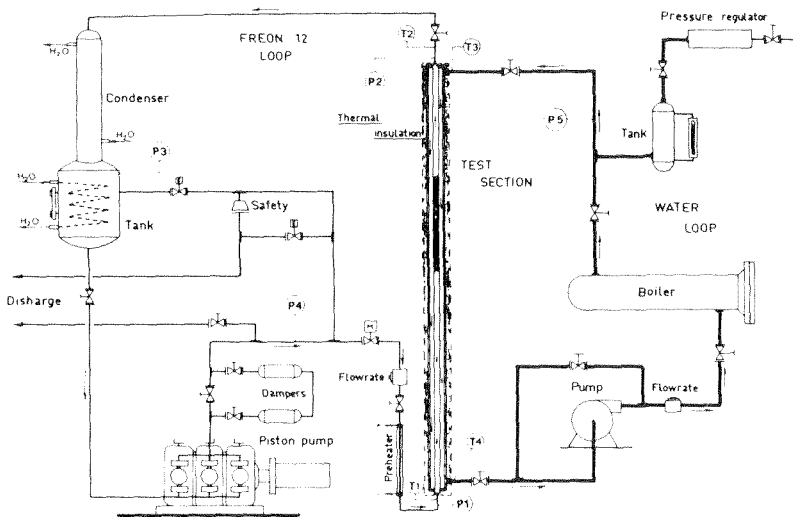

Fig. 1 Flow diagram of loop CF-1

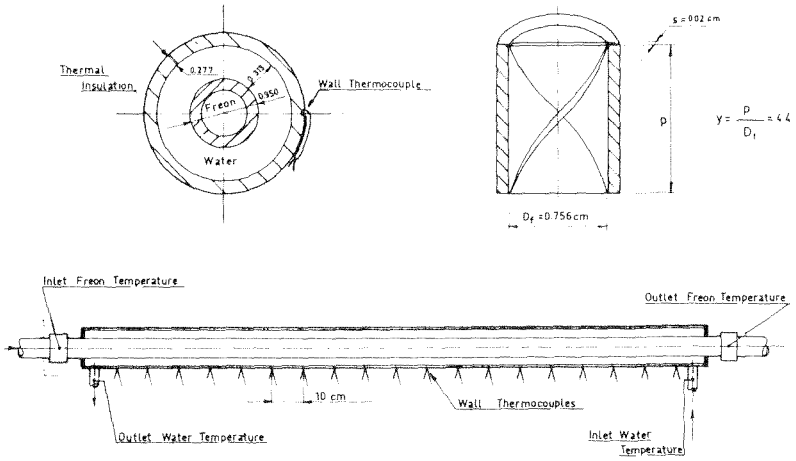

Fig. 2 Sketch of the characteristic dimensions of the Freon-water test section

very slowly, through quasi-stationary equilibrium states, to avoid unstable conditions.

A typical experimental diagram is shown in Fig. 3, in which two typical situations are compared. It can be seen the insertion of twisted tapes has increased the heat exchanged, so that in the swirl flow case at the outlet there is superheated Freon vapor, whereas for the same conditions, in the straight flow case, the outlet Freon temperature remains at the saturation value.

From the wall temperature profile of the water side, even accounting for the external heat losses, it is not possible to deduce the axial heat flux profile from the various local heat balances. This is due to a certain scatter in the experimental points. This scatter could be reduced by reducing the water flowrate, thereby increasing the overall water temperature difference. However, it was impossible to do this without affecting the heat transfer to the Freon. This drawback of the present work is very difficult to overcome. If the heat flux profiles could be obtained, much information about the burnout power, the post burnout heat transfer, etc. would be available. In the absence of this information, other trends, rather general in character, have been inferred from the experimental sets of data.

Experimental Results

A representative set of the experimental results is shown in Figs. 4 and 5 for some typical situations with and without the

Nomenclature

D = diameter
D_h = equivalent hydraulic diameter
G = freon specific mass flowrate
h = heat transfer coefficient (wall-to-Freon)
H = enthalpy
L = length, heated length
p = pressure
Re = Reynolds number
T = temperature
W = thermal power exchanged between water and Freon
X = qualtiy
y = tape twist ratio (180° twist length/inner diameter)
α = swirl flow geometric parameter
φ = heat flux to Freon (through inner surface of Freon tube)
Γ = total mass flowrate
λ = latent heat of vaporization
μ = dynamic viscosity
$\pi = p/p_{cr}$ = reduced pressure

Subscripts

B.O. = burnout (or dryout)
cr = critical
in = inlet
Jh = Joule heating
out = outlet
sat = saturation
tt = twisted tape, swirl flow

twisted tape insert. On the left side of each graph the Freon outlet temperatures are plotted versus the total heat transfer between water and Freon; on the right side the heat transfer is plotted versus the inlet temperature of the water.

Each diagram refers to the same Freon reduced pressure (π) and to the same specific mass flowrates of Freon and water (G). The right-hand curves are roughly similar to the classical Nukiyama boiling curves, except that in this case the heating medium temperature is the independent variable.

In some of the diagrams, on the right side, the ratio of the heat transfer for the water side to that for the Freon side is presented. This ratio is very close to unity, and the dispersion of the representative points gives an idea of the experimental accuracy.

Some observations may be made relative to the water side curves in Figs. 4 and 5:

— The curves (with and without tape) have an initial, almost overlapping portion which generally corresponds (see Freon outlet temperature curve) to different boiling regimes. The initial change of slope corresponds presumably to the transition from forced convection to nucleate boiling. It may be concluded that there is no significant influence of the swirl flow in subcooled and low quality boiling. This is in agreement with the results given recently in [11].

— The two curves have a similar trend: the heat transfer increases with increasing T_{in} of water, up to a maximum, which may be called more or less properly, $W_{\text{B.O.}}$ (burnout, or dryout

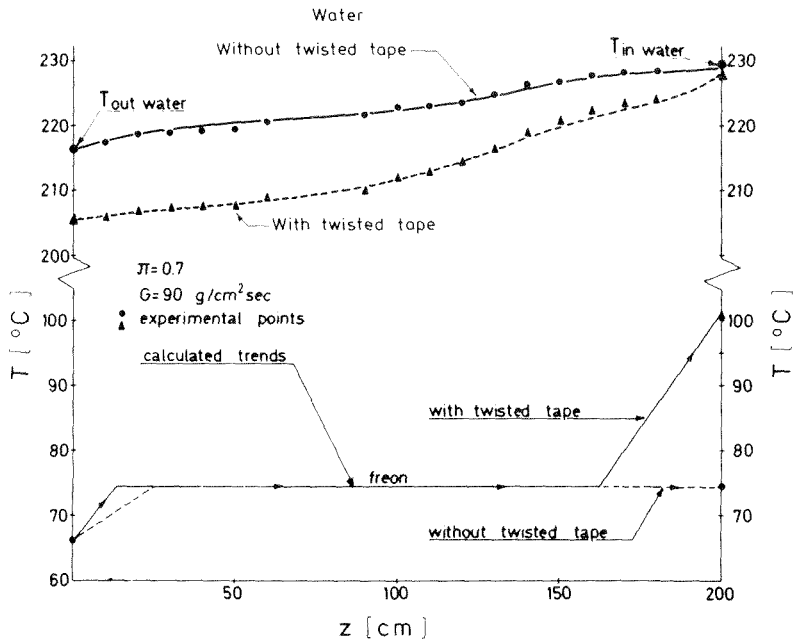

Fig. 3 Typical experimental diagram which shows for the same experimental conditions the increase in heat transfer to Freon achievable with the insertion of the twisted tape

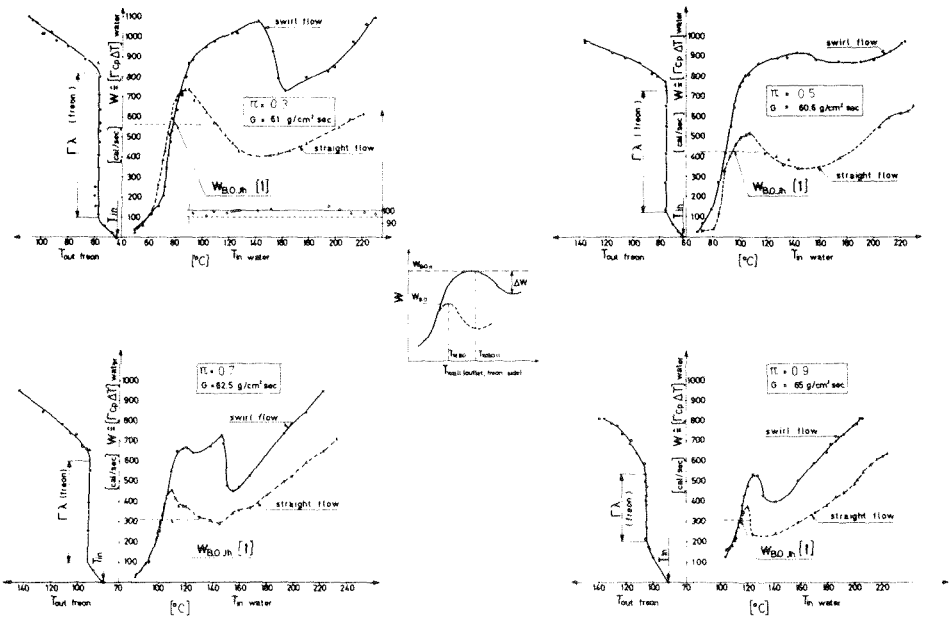

Fig. 4 Heat transfer power (W) with and without twisted tapes as a function of the water inlet temperature ($T_{\text{in water}}$, right) and the Freon outlet temperature ($T_{\text{out freon}}$, left)

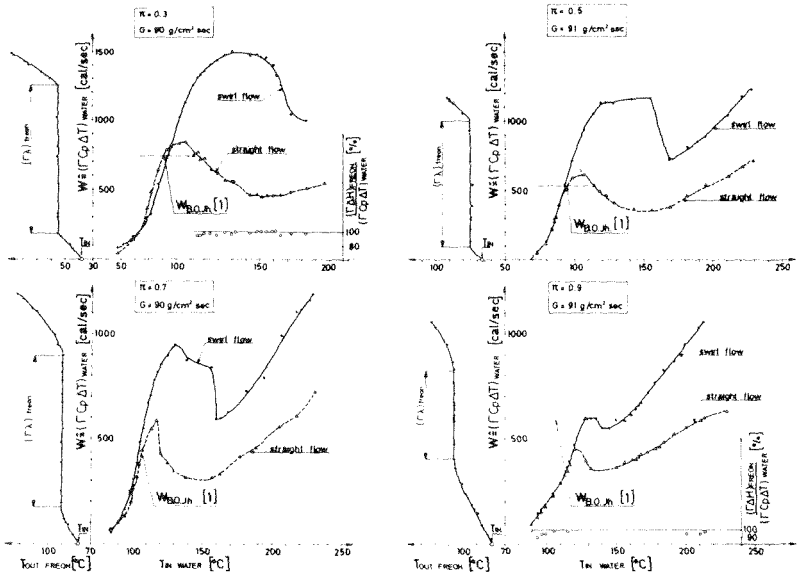

Fig. 5 Exchanged thermal power (W) with and without twisted tapes as a function of the water inlet temperature ($T_{\text{IN water}}$, right) and the freon outlet temperature ($T_{\text{out freon}}$, left)

are terms used as synonyms), then decreases to a minimum, to increase again at higher water temperatures. For both straight and swirl flow, this may be regarded as a kind of burnout which propagates upward and reduces the heat transfer.

A low heat transfer film boiling may be envisioned which originates initially at the outlet (Freon side) of the test section and propagates upward, increasing the water temperatures, up to a minimum value of heat transfer. The increased water-Freon temperature difference then enhances the total heat transfer through different transfer mechanisms.

— The two maxima, $W_{\text{B.O.tt}}$ and $W_{\text{B.O.}}$ differ greatly, with $W_{\text{B.O.tt}}$ always $> W_{\text{B.O.}}$. Also, the corresponding wall temperatures (Freon side, at the outlet, deduced from the water inlet temperatures), $T_{w\text{-B.O.tt}}$ and $T_{w\text{-B.O.}}$ are different, with $T_{w\text{-B.O.tt}} \geq T_{w\text{-B.O.}}$. In addition, the "straight flow" curve has often a narrower peak, showing a stronger dependence of the relative film boiling regime on the wall temperature.

— The "swirl flow" maximum $W_{\text{B.O.tt}}$ frequently corresponds to a Freon outlet equilibrium quality $X \geq 1$ as is apparent from the Freon outlet temperature curve.

— The "straight flow" maximum $W_{\text{B.O.}}$ corresponds to a Freon outlet quality $X < 1$.

— The decreases ΔW of W after the "burnout" points (see Fig. 4) are such that:

$$\left(\frac{\Delta W}{W}\right)_{\text{B.O.tt}} < \left(\frac{\Delta W}{W}\right)_{\text{B.O.}}$$

— Finally, the swirl flow curves are all situated well above the straight flow curves, clearly indicating a better overall heat transfer with the turbulators in all flow regimes.

Fig. 6 shows the ratios of the exchanged thermal powers for a particular situation, ranging from 120 percent to ~170 percent and approaching higher values in the temperature interval between the two burnout points.

The maximum heat transfer for the two reference situations is presented as a function of reduced pressure in Fig. 7. The overall "gain" of 30 to 80 percent obviously looks very interesting.

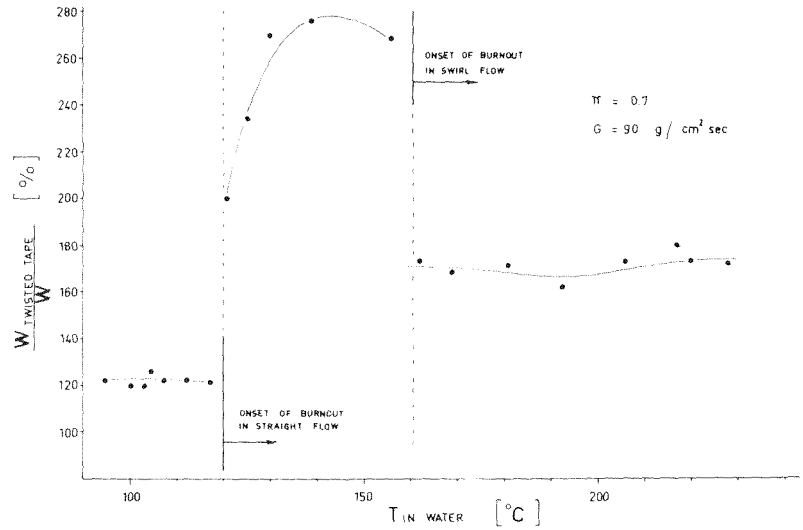

Fig. 6 Ratio of the total heat in swirl and straight flow at different water inlet temperatures

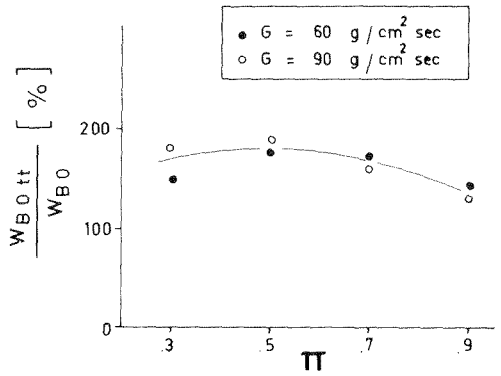

Fig. 7 Increase of the maximum thermal powers exchanged with and without twisted tape as a function of pressure

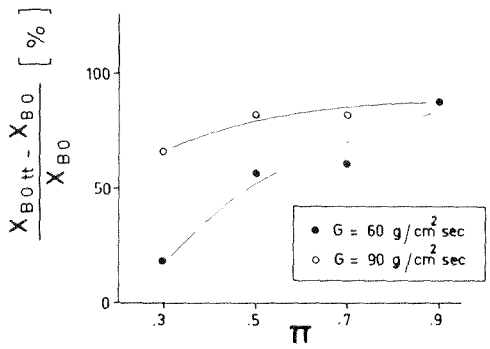

Fig. 8 Increase of burnout quality in swirl flow

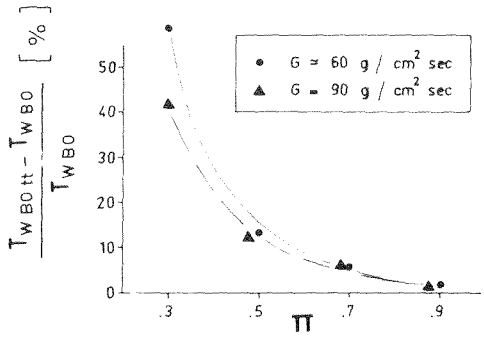

Fig. 9 The decrease of the relative difference of the "burnout" temperatures with pressure

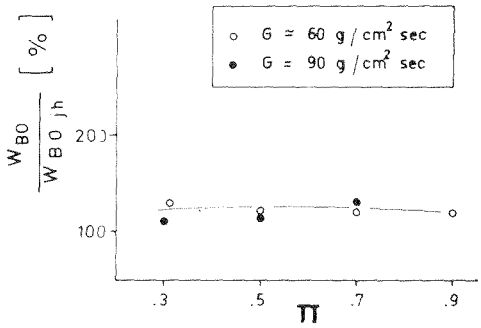

Fig. 10 Increase of burn-out power with indirect heating with respect to the burnout power with uniform Joule heating

The improvement in burnout qualities with the twisted tape is given in Fig. 8. The relative gain in the burnout quality ranges from 55 to 90 percent. This gain might be easily translated to a reduction of heat exchanger length in commercial steam generators.

The wall temperature of the Freon tube at which W_{tt} for increasing inlet temperature of water first begins to decrease has been designated as a burnout wall temperature $T_{w\,B.O.tt}$. This is not strictly correct as $T_{w\,B.O.tt}$ refers to the Freon outlet section (corresponding often to Freon superheats), while the burnout or dryout point may be substantially upstream. Nevertheless, $T_{w\,B.O.tt}$, the wall temperature corresponding to $W_{B.O.tt}$, has an indirect physical significance and is shown in Fig. 9. Fig. 9 synthesizes how the difference in the burnout temperatures which is significant ($\sim$50 percent of $T_{w\,B.O.}$) at low pressure decreases monotonically until it disappears at higher pressures.

It is interesting to compare the burnout powers in straight and swirl flow for this experimental system with the burnout powers predictable by the available correlations for Joule heating. A recent paper by the present authors [8] suggests the following correlation to predict Freon 12 burnout in straight, vertical ducts uniformly heated by the Joule effect over the entire range of pressure.

$$W_{B.O.Jh} = \frac{a - X_{in}}{\frac{b}{L} + 1} \lambda \Gamma \left[1 - \frac{1/4 - \bar{\pi}}{(9/4 - \bar{\pi}^2)}\right] \qquad (1)$$

$$\text{with:} \quad a = \frac{1 - \bar{\pi}}{\left(\frac{G}{100}\right)^{1.75}} \quad b = 0.6\left(\frac{1}{\bar{\pi}} - 1\right) \quad G^{0.4} D^{1.4}$$

(G in g/cm² s; D in cm).

The indexes Jh which have been added to $W_{B.O.}$ mean "Joule heating."

A comparison between the suggested correlation and indirect heating by another fluid is shown in Fig. 10 for straight flow. There is a positive difference, $W_{B.O.}$ being higher than $W_{B.O.Jh}$ by 10 to 30 percent. This difference may be due to a more gradual heat transfer which takes place in the indirect heating which thus allows a higher burnout power.

Consider briefly, now, the other typical heat transfer regimes, besides bulk boiling. As is well known, in a subcritical, once-through flow the following main heat transfer regions may be distinguished:

— the inlet, forced convection regions of subcooled liquid up to the incipient subcooled boiling;

— the bulk boiling region with net vapor generation from the point $X = 0$ to the dry-out point;

— the outlet, forced convection region of superheated vapor from the point $X \simeq 1$ to the outlet section.

In this subdivision the post burnout region from the burnout point to the point $X \simeq 1$, in which droplets of liquid are entrained in the vapor phase, has been neglected. Obviously the relative importance of this region decreases as the burnout quality approaches unity, which happens (Fig. 10) more with indirect heating than with Joule heating, and more (Fig. 8) with swirl flow than with straight flow.

The measurements of the heat transfer coefficients in both the liquid phase and in the vapor phase have been performed keeping, respectively, the liquid all subcooled and the vapor all superheated through the whole test section, from inlet to outlet.

The influence of the twisted tapes in the forced convection region of subcooled liquid is shown in Fig. 11. In the case of swirl flow the Reynolds number is computed as

$$\mathrm{Re} = \mathrm{Re}_{tt} = \frac{\alpha G D_h}{\mu}$$

where α, which takes into account the increase of velocity due to the swirl flow, at the same G, is defined as

$$\alpha = \frac{(4Y^2 + \bar{\pi}^2)^{1/2}}{2Y}$$

The increase of the forced convection heat transfer in swirl flow is evident and approaches, in the investigated Reynolds number range, 100 percent.

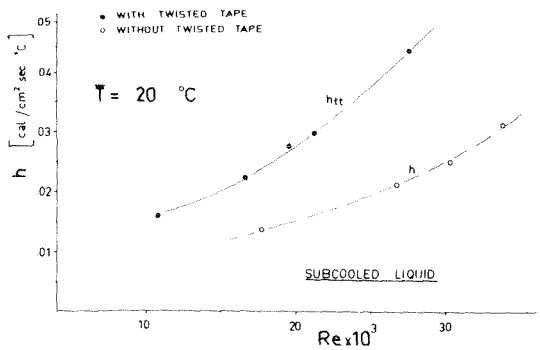

Fig. 11 Heat transfer coefficient for swirl flow and straight flow in forced convection of subcooled liquid

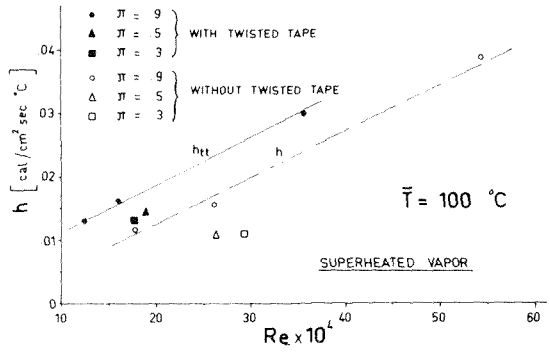

Fig. 12 Heat transfer coefficient for swirl flow and straight flow in forced convection of superheated vapor

Considering the forced convection region of superheated vapor, and comparing the heat transfer coefficients at the same Reynolds numbers (Fig. 12), the advantage of swirl flow is evident but there is only about a 40 percent increase. In the diagram a few data points have been plotted at different pressures, which are not sufficient to delineate a trend, but only to denote a systematic increase of h_{tt} with respect to h.

Conclusions

In the study of swirl flow in subcritical, once-through vapor generators, the axially uniform Joule heating is only a rough approximation of the real boundary condition of heating with another fluid, in which the heat flux profile may not be uniform. Using a counter-current experimental device with a Freon loop and a water loop, coupled in a two-fluid test section, the following general observations may be drawn:

— In the forced convection region of subcooled liquid, the insertion of a twisted tape results in a doubling of the heat coefficient.

— The increase of the burnout power in the boiling region in swirl flow with respect to straight flow is very high (~200 percent) and rather independent of the pressure (up to the critical pressure)

— Burnout powers in straight flow are somewhat higher (10–30 percent) than those predicted with equation (1) obtained employing uniform Joule heating of test sections (Fig. 10)

— The relative increase of burnout qualities in swirl flow with respect to straight flow ranges from 20 to 90 percent (Fig. 8)

— The burnout wall temperatures at burnout in swirl flow increase by 50 to 200 percent, with a weak pressure dependence

— In swirl flow, on increasing the wall temperature, the upstream propagation of the film boiling regime is much more gradual

— In the forced convection region of superheated vapor swirl flow increases the heat transfer coefficient, but to a much smaller extent than with subcooled liquid

In conclusion, it may be said that a swirl flow in subcritical, once-through vapor generators seems a very promising means to increase the heat transfer and the power densities, thus reducing the capital costs. The present experimental work covering a very wide pressure range up to the critical value, strengthens this opinion.

References

1 "Sodium-Cooled Fast Reactor engineering," *Proceedings of a Symposium*, Monaco, Mar. 1970, pp 23–27.

2 Bergles, A. E., Fuller, W. D. Hynek, S. J. "Dispersed Flow Film Boiling of Nitrogen With Swirl Flow", *International Journal of Heat and Mass Transfer*, 1971, pp. 1343–1354

3 Rouvillois, MM. X., Doore, H., Beghin A., "Etude experimentale en ecoulement droit et giratoire du transfert de chaleur en Bouilleur "Once-Through" Utilisant du Freon 12,", European Two-Phase Flow Group Meeting, Karlsruhe, 1969.

4 Bahr, A., Herkenrath, H., Mork-Mörkenstein, P., "The Development of the Heat Transfer Crisis in Tubes With and Without Swirl Generators," EUR/C-IS/785/68e, Ispra, Italy.

5 Brevi, R., Cumo, M., Palmieri, A., Pitimada, D., "Forced Convection Heat Transfer and Burn-Out Measurements With Twisted Tape," XXV Congresso Nazionale ATI, Trieste, Sept. 1970 and A.N.S., Nuclear Science and Engineering, May 1971.

6 Farello, G. E., "Rapporto di sicurezza CF-1," CNEN-RTI/TR(68) 4, STAV 11, 1968.

7 Lopina, R. F., Bergles A. E., "Heat Transfer and Pressure Drop in Tape Generated Swirl Flow," M.I.T. Dep. of Mechanical Engineering, Report No. D.S.C. 70281-47, June 1967, and JOURNAL OF HEAT TRANSFER, TRANS. ASME, Series C, Vol. 91, 1969, pp. 43–442.

8 Cumo, M., Ferrari, G., Urbani, G., "Prediction of Burn-Out Power With Freon 12 up to the Critical Pressure," European Two-Phase Flow Group Meeting, CNEN, CSN Casaccia, June 6–8, 1972, Rome.

9 Gambill, W. R., "Subcooled Swirl-Flow Boiling and Burn-Out With Electrically Heated Twisted Tapes and Zero Wall Flux," JOURNAL OF HEAT TRANSFER, TRANS. ASME, Series C, Aug. 1965, p. 342.

10 Schöneberg, R., "Dynamic Behaviour of a Boiling Channel With Twisted Tapes," 1968 European Two-Phase Flow Group Meeting, Oslo, June 18–20, 1968.

11 Lopina, R. F., and Bergles, A. E., "Subcooled Boiling of Water in Tape-Generated Swirl Flow," JOURNAL OF HEAT TRANSFER, TRANS. ASME, Series C, Vol. 95, 1973, pp. 281–283.

R. Clift
J. R. Grace
V. Sollazzo

Department of Chemical Engineering,
McGill University,
Montreal, Canada

Continuous Slug Flow in Vertical Tubes

A method of simulating the behavior of continuously slugging vertical columns is presented. Slugs are introduced at regular time intervals at some reference level near the bottom of a column and their subsequent motion and coalescence is simulated numerically. Experiments on coalescing slug pairs are used to supply information on slug interactions, while the relationship between slug length and volume is obtained from experiments on single slugs. The numerical predictions are in reasonable agreement with experimental results for continuously slugging liquids.

Introduction

Although considerable attention has been devoted to noninteracting gas slugs rising in confined liquids, there has been little work on interactions between slugs. There are no methods currently available for predicting slug properties for two-phase systems in the slug flow regime, a regime of considerable importance for fluidized beds and in two-phase heat transfer applications.

In the present paper, a method is given for predicting the distribution of gas slugs in a liquid in a column about 1 in. in diameter or larger such that surface tension forces play a negligible role [1].[1] The model is conceptually similar to a model used to predict the motion and coalescence of vertical chains of bubbles in fluidized beds [2]. Contrary to the earlier case, the effect of one slug on the following slug must be found empirically, while forward interactions and second order interactions may be neglected for slugs but not for unconfined bubbles. In addition, the change of slug shape with slug volume must be taken into account.

Coalescence Of Slug Pairs

Moissis and Griffith [3] found that when two slugs rise simultaneously through a vertical tube, the rear slug accelerates and eventually reaches and coalesces with the leading slug. Theoretical analysis of this phenomenon is complex, and a simple account of slug interaction like that for bubbles in fluidized beds [4, 5] is not presently available. A more empirical approach has therefore been adopted, in which the relative velocity between two slugs has been measured as a function of separation, column diameter, and liquid properties.

Moissis and Griffith report similar experiments for slugs in water. In their experiments, two slugs were injected into a tube and the leading slug was held stationary by downward liquid flow while the motion of the second slug was recorded by cinephotography. The velocity of slug 2 relative to slug 1 was found to be given by:

$$U_R/U_{SI} = 8 \exp(-1.06\ x/D) \tag{1}$$

where U_{SI} is the rise velocity of a single slug and x the distance between the nose of slug 2 and the tail of slug 1 (see Fig. 1).

The validity of equation (1) for slugs in free rise is so far uninvestigated. Moreover, equation (1) is unlikely to apply for other systems. We have therefore performed experiments on slug pairs in transparent acrylic tubes of 2.5 and 5 cm dia, using sucrose solutions to cover the liquid viscosity range from 1 cP to 15 poise. In each case, two air slugs were introduced in rapid succession at the base of a stagnant liquid column, and their subsequent motion was recorded by cinephotography. Either a telephoto lens was used and the camera "panned" to follow the slugs, or the camera was mounted on a moveable platform and raised at approximately the velocity of slug 1. Frame-by-frame analysis of the films gave x as a function of time.

Equation (1) may be written in general form

$$\frac{dx}{dt} = -U_R = -aU_{SI}\, e^{-x/b} \tag{2}$$

It is convenient to introduce the dimensionless variables

$$S = x/D \tag{3}$$

$$T = t(g/D)^{1/2} \tag{4}$$

$$A = \frac{aU_{SI}}{b}\left(\frac{D}{g}\right)^{1/2} \tag{5}$$

and

$$B = b/D \tag{6}$$

Equation (2) then becomes

$$\frac{dS}{dT} = -ABe^{-S/B} \tag{7}$$

$T = 0$ is taken as the instant when $S = 0$, i.e., when slug 2 touches slug 1. Equation (7) then yields

$$S = B \ln (1 - AT) \tag{8}$$

Values of A and B were determined by fitting equation (8) using least-squares regression [6]. Two to seven coalescing pairs were used for each solution. Fig. 2 shows the fitted curve and the results of two experimental sequences for one solution in the 5 cm pipe. Equation (8) gives a reasonable representation for all the solutions examined. No effect of the following slug on the velocity of the leading slug nor of slug length on U_R could be detected.

Fig. 3 shows the curves obtained for the solutions tested. The curves form a sequence in order of increasing $C = \rho D(gD)^{1/2}/\mu$, a

[1] Numbers in brackets designate References at end of paper.

Contributed by the Heat Transfer Division for publication in the JOURNAL OF HEAT TRANSFER. Manuscript received by the Heat Transfer Division, January 15, 1974. Paper No. 74-HT-EE.

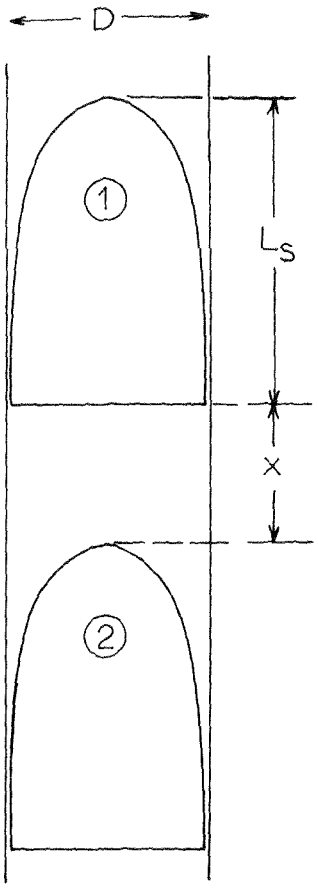

Fig. 1 Two interacting slugs (schematic)

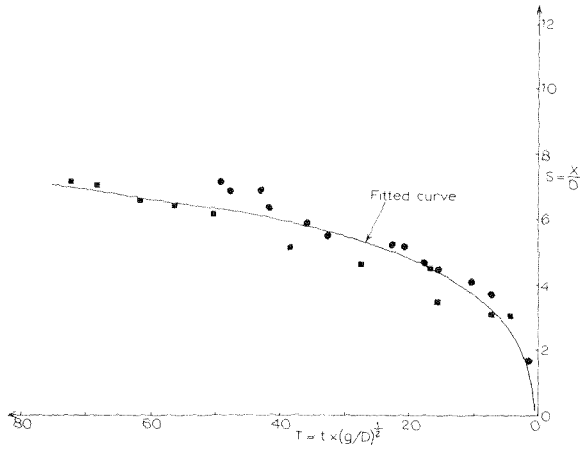

Fig. 2 Relative spacing of interacting slug pairs as a function of time: D = 5.1 cm, μ = 0.135 poise, ρ = 1.24 gm/cc., $C = 3.3 \times 10^{3}$

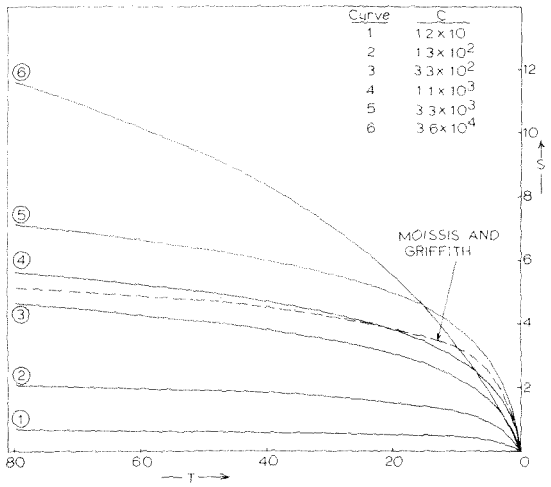

Fig 3 Regression curves for interaction of slugs in various liquids

sort of Reynolds number, since the velocity of an isolated slug is proportional to $(gD)^{1/2}$ [7, 8]. The dimensionless interaction parameters, A and B, are shown as functions of C in Fig. 4. Fig. 4 also shows a, the dimensionless relative velocity of slug 2 at the instant when it reaches slug 1. Fig. 4 can be used to characterize the relative velocity of slugs in systems for which C is known and surface tension is unimportant.

The curve obtained by Moissis and Griffith is also shown in Fig. 3; it differs widely from those obtained in the present work. Although an attempt was made to reproduce the earlier determinations using downflow of water to stabilize the leading slug, the first slug tended to wobble and shed small satellite bubbles, while the second slug approached more slowly and erratically than when two slugs were rising through stagnant liquid. It is therefore concluded that the results of Moissis and Griffith are not applicable to freely rising slugs. Evidently the different conditions in the fluid at the wall near fixed and freely-rising slugs cause different velocity profiles in the wake, and hence different behavior of interacting slugs.

Nomenclature

a = dimensionless interaction parameter, equation (2)
A = dimensionless parameter defined by equation (5)
A = cross-sectional area of column
b = interaction parameter, equation (2)
B = dimensionless parameter defined by equation (6)
c = velocity coefficient defined by equation (13)
C = dimensionless property group, $\rho D(gD)^{1/2}/\mu$
D = column diameter
f = fraction of column occupied by slug excluding the nose region of the slug
F = slug frequency
g = acceleration of gravity
G = shape constant defined by equation (9)
h = height above base of column
k_t = Nicklin constant, equation (14)
L_E = length of empty column whose volume is equal to slug volume
L_n = length of nose portion of slug
L_s = slug length
S = dimensionless spacing, x/d
t = time
t_e = time between entry of successive slugs
T = dimensionless time, $t(g/D)^{1/2}$
u = velocity of a following slug relative to the slug ahead due to interaction between the slugs
U = absolute slug velocity
U_t = superficial gas velocity
U_{sl} = velocity of a slug in the absence of interaction as defined by equation (14)
V_s = slug volume
x = distance between nose of a slug and the tail of the preceding slug
ρ = liquid density
μ = liquid viscosity

Subscripts

e = at entry
$k, 1, 2$ = pertaining to the kth slug, 1st slug, 2nd slug, etc.
0 = surface of liquid in the column
o = beginning of time interval of interest

Some authors [9, 10, 11] have suggested that there is a stable spacing beyond which slugs do not coalesce. The present results give no indication of such a critical spacing. The relative velocity does become small at large separations, particularly for low C. A succession of slugs would therefore rise without coalescence in a column of finite height so that there might well appear to be a stable spacing.

Slug Shape

Simulation of a continuously slugging column requires a relationship between the volume and length of gas slugs. Prediction of slug shape from first principles is complex [12, 13] so a simplified approach has been adopted. A slug is considered to be composed of two portions:

1 A "nose region," of length L_n, in which the fraction of the tube cross section occupied by gas varies with distance below the slug nose. The shape of the nose region is assumed to be independent of slug length, L_s, provided that $L_s > L_n$.

2 The "slug body," in which the slug occupies a fixed fraction, f, of the column area.

This simple model leads immediately to

$$L_e = fL_s - G \tag{9}$$

where

$$L_e = 4V_s/\pi D^2 \tag{10}$$

and G is a constant for given system properties.

Single slugs were photographed as they approached and broke through the stagnant liquid surface for various liquids in 2.5 and 5.1 cm columns. By this means, the slug length, L_s, could be measured directly while L_e was obtained from the difference between

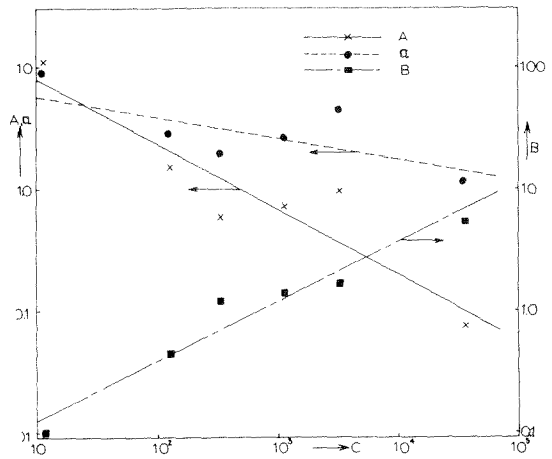

Fig. 4 Interaction parameters as functions of liquid property group

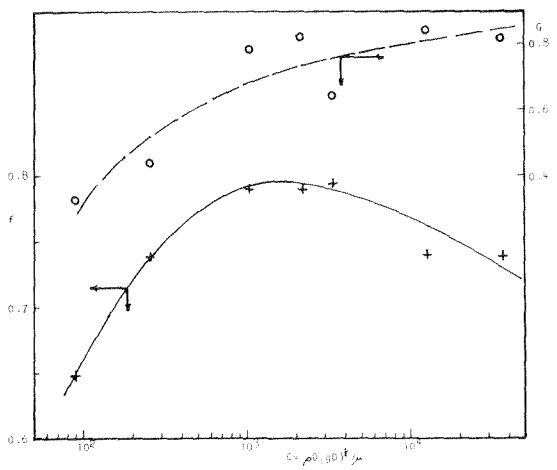

Fig. 5 Slug shape parameters

Table 1 Slug shape parameters

Tube diameter (cm)	Liquid properties: Viscosity (poise)	Density (g/cc)	$C = \frac{\rho g D^{3/2}}{\mu}$	Experimental shape parameters: G	f	Theoretical value of f
5.1	5.62	1.37	87.9	0.327	0.649	0.55
	1.89	1.35	258	0.436	0.738	0.66
	0.457	1.30	1030	0.784	0.790	0.77
	0.135	1.24	3310	0.645	0.794	0.84
	0.01	1.00	36100	0.809	0.738	0.92
2.5	0.07	1.18	2140	0.820	0.790	0.82
	0.01	1.00	12700	0.840	0.740	0.90

the surface levels before and after slug eruption. Equation (9) was found to be an adequate approximation for slug lengths of practical interest. The values of f and G, obtained by a least-squares fit to the measurements, are shown in Fig. 5. For comparison, Table 1 also gives values of f predicted for a liquid film of equilibrium thickness in viscous flow [12, 14]. Fig. 5 may be used to estimate slug shape in systems where surface tension effects are negligible.

An alternative method [15] was also tested [6], but agreement was no better than with the simpler equation. Although use of equation (9) for the simulation of continuous slug flow ignores the effect of slug velocity on equilibrium film thickness as well as any distortion which accompanies slug interactions, the overall effect of this approximation appears slight.

Simulation Of Continuous Slug Flow

In order to simulate a continuously slugging vertical column (Fig. 6), we make the following assumptions:

(i) Gas enters the column at a steady flow rate of $U_{Ge}A$ where U_{Ge} is the superficial velocity at the point of entry. Slugs enter the column with constant frequency and with volume

$$V_{se} = U_{Ge} t_e A \tag{11}$$

where t_e is the time between successive slugs. At break-away, each slug nose is at height $(h_e + L_{se})$ above the entry point where L_{se} is the slug length corresponding to V_{se} and h_e is the reference level.

(ii) The instantaneous velocity of the kth slug is the sum of two components,

$$\frac{dh}{dt} = U_k = U_{SI} + u_k \tag{12}$$

where

$$u_k = aU_{k-1}e^{-x_k/b} \tag{13}$$

is the relative velocity due to slug interactions as derived above while

$$U_{SI} = c(gD)^{1/2} + k_G U_G \tag{14}$$

is the velocity which the slug would have if it were not interacting with other slugs. Values of c and k_G have been measured independently for each system [6]. The term $k_G U_G$ arises from continuity considerations [16] while a graphical correlation for c has been presented by White and Beardmore [1]. No allowance is made for "unhappy slugs," slugs which cling to one wall of the column and have their velocities increased by up to 40 percent [17]. There is no net liquid flow in the column.

(iii) Slug length and slug volume are related by equation (9) with f and G as determined for single slugs.

(iv) Two slugs coalesce instantaneously when the nose of the trailing slug touches the tail of the slug in front, i.e., when some $x_k \leq 0$. The nose of the combined slug coincides with the nose of the original leading slug at this instant. The volumes of coalescing slugs are additive.

(v) The column contains a fixed amount of liquid. The level of the bed surface therefore rises, i.e.,

$$\frac{dh_a}{dt} = U_G \tag{15}$$

during the approach of each slug. When the slug nose reaches the

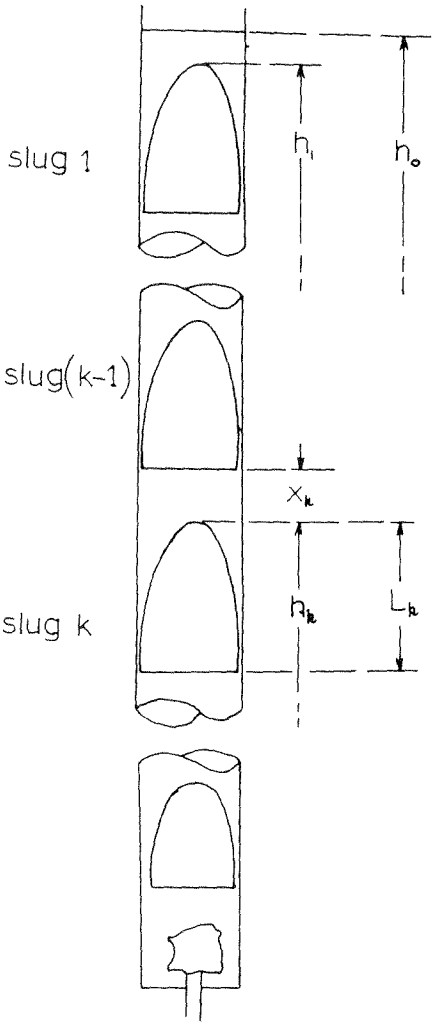

Fig. 6 Continuous slug flow: schematic

surface, the surface falls back instantaneously by a distance V_{s1}/A.

With these assumptions, the velocity of each slug can be calculated beginning with the top slug whose velocity is

$$\frac{dh_1}{dt} = U_{s1} \tag{16}$$

Analytical solutions may be found to the resulting differential equations, but, except for the top slugs, these are too cumbersome for ready use. The equations were therefore integrated numerically using the 4th-order Runge-Kutta-Merson process up to each coalescence, slug exit or slug entry. When one of these events reoccurred, the indices of the slugs in the bed were adjusted. Details of the integration procedure may be obtained from the authors.

Table 2 Conditions for numerical simulation

Fluid: dilute sugar solution (μ = 0.12 poise, ρ = 1.23 g/cc)
Column diameter: 5.1 cm
Initial height of liquid: 500 cm
Interaction parameters: a = 4.59; b = 8.28 cm
Slug shape: V_s/A = 0.794 L_s − 0.645
k_G = 2.11; c = 0.348
(The above values correspond to experimental measurements for one run).

(*a*) To test different boundary conditions (see Fig. 7):

U_G = 12.0 cm/s

Boundary condition:	(i)	(ii)	(iii)
h_e(cm)	28.0	117	10.2
f_e(s^{-1})	18.5	2.4	3.65
L_{se}(cm)	1.63	7.1	5.1

(*b*) To test the effect of flow rate (see Figs. 8 and 9):

h_e = 10.2 cm, L_{se} = 5.1 cm

U_G(cm/s)	6.0	12.0	18.0	24.0
f_e(s^{-1})	1.78	3.56	5.32	7.10

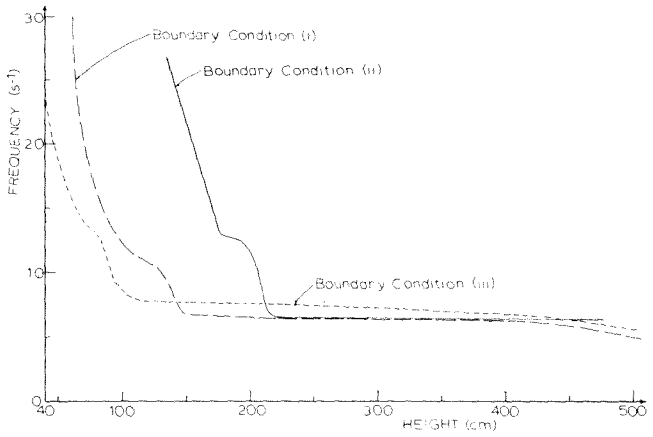

Fig. 7 Dependence of slug frequency on inlet condition; conditions are given in Table 2

Numerical Predictions

Three types of boundary conditions were tried:

(i) Slugs were assumed to form at a nozzle with volumes given by bubble formation studies [10]. The entry length was based on the measurements of Grace, et al. [19].

(ii) Slug frequencies were measured at some level high enough that the slugs were fully developed (i.e., the sphere equivalent bubble diameter was at least as large as the column diameter). The measured frequency and level were used to provide the boundary condition.

(iii) It was assumed that a distance of $h_e = 2D$ is required for small bubbles to coalesce sufficiently to give full slugs ($L_{se} = D$). This is the height required to establish slugging in gas fluidized beds which operate in the slug flow regime [20].

To test these boundary conditions, simulations were carried out for the conditions given in Table 2. The frequencies used with condition (ii) were obtained experimentally. In experiments and simulations alike, at least four slugs were allowed to pass the level of interest before counting commenced, in order to allow for start-up effects. The predicted slug frequencies, F, are plotted in Fig. 7. A slug is counted whenever its nose passes the level in question.

It is clear from Fig. 7 that the choice of boundary condition plays a major role in determining slug behavior over a considerable distance, though there is little effect by the top of the column for the conditions in Table 2. For type (i) boundary conditions the initial bubble volume is too small, even at the highest flow rates, to correspond to fully developed slugs. Hence, the interaction parameters are not accurate at the bottom of the column. For boundary conditions of type (ii), slugs are assumed to pass the lowest level of measurement at perfectly regular intervals whereas, in practice, the intervals between slugs are already highly irregular by this point. Boundary conditions of type (iii) give a reasonable compromise between the first two types of boundary condition.

The effect of gas flow rate on slug frequency is shown in Fig. 8 for conditions given in Table 2. The theory predicts regions of rapid coalescence, where the slug frequency falls off sharply, interspersed with regions where there is little coalescence. Similar regions have also been noted for vertical bubble chains in fluidized beds [2]. For all four flow rates, little coalescence is predicted above a height of about 300 cm so that an observer might well postulate that slugs have achieved a stable spacing. Mean slug lengths, obtained from equations (9) and (10) using a mean slug volume, $U_G A/F$, are plotted in Fig. 9. Slug length generally in-

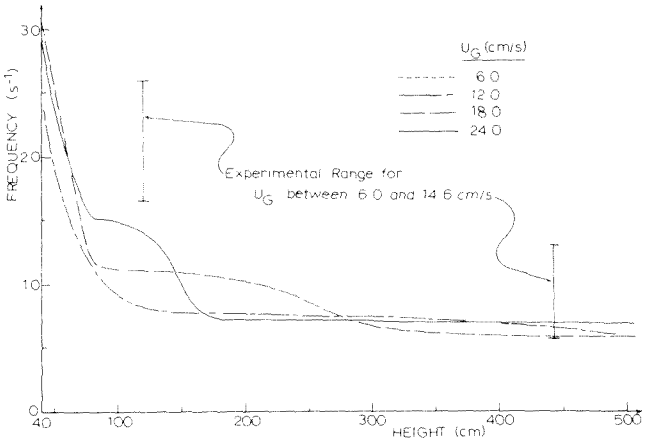

Fig. 8 Predicted variation of slug frequency with height for conditions in Table 2

creases with gas flow rate and height, whereas slug frequency is relatively insensitive to gas flow rate as shown in Fig. 8. The distribution of slug lengths passing a given level was also predicted to become wider with increasing flow rate and height.

Comparison of Predictions With Experiments

Qualitative features of the predictions, for example the insensitivity of slug frequency to gas flow rate, are in good agreement with experiment. Quantitative measurements of slug frequencies and lengths were taken in the 2.5 cm and 5.1 cm columns described earlier, by filming sections of the column and counting the number of slug noses passing given levels (see Table 3). For relatively viscous sugar solutions, little or no slug coalescence is predicted and little or none was obtained. When a boundary condition of the third type was employed, however, the predicted frequencies tended to be too high. This implies either that this boundary condition is inappropriate or that coalescence takes place more rapidly than for slug pairs. For the liquids of lower viscosity (1 and 12 cp), observed slug frequencies tend to be higher than predicted by the model. Acceleration and growth of slugs

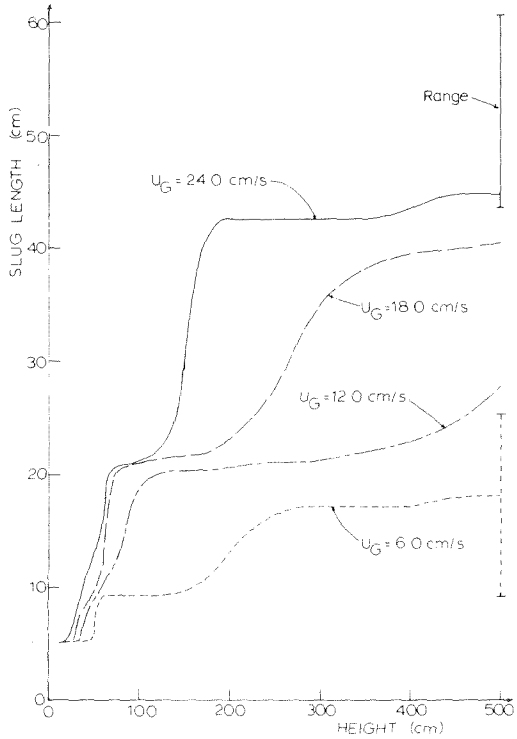

Fig. 9 Predicted variation of slug length with height for conditions in Table 2

due to hydrostatic pressure variation was allowed for by modifying the computer simulation program, but the effect of this expansion was too small to account for the discrepancy observed. Some slug splitting occurred in these low viscosity fluids and this, no doubt, contributed to the discrepancy between experiment and the model (where splitting was neglected). Another contributing factor may have been that slugs did not form cleanly near the base of the column. Instead, many small satellite bubbles formed

Table 3 Comparison of experimental slug frequencies with model predictions

D (cm)	ρ (g/cm³)	μ (poise)	U_{Ge} (cm/s)	h (cm)	Slug frequency, $f(s^{-1})$ Experimental	Model with boundary condition (ii)	Model with boundary condition (iii)
5.1	1.30	0.51	5.9	117	1.2	1.2	1.8
				256	0.86	1.2	1.8
				442	0.98	1.2	1.8
			9.2	117	1.2	1.2	2.8
				256	1.0	1.2	1.7
				442	1.2	1.2	1.3
			15	117	1.45	1.45	2.3
				256	1.6	1.45	2.3
2.5	1.32	0.50	9.9	40	1.1	1.1	1.8
				134	1.3	1.1	1.5
				194	1.2	1.1	1.4
			17	40	1.2	1.2	2.8
				134	1.2	1.2	1.4
				194	1.1	1.2	1.3
5.1	1.23	0.12	6.0	117	1.65	1.65	0.89
				442	0.71	0.53	0.65
			9.2	117	2.2	2.2	0.68
				442	1.3	0.56	0.65
			15	117	2.6	2.6	0.93
				442	1.3	0.65	0.58
5.1	1.0	0.01	4.9	117	1.6	1.6	1.4
				256	1.3	1.6	1.2
				442	1.2	0.62	0.42
			8.1	117	1.9	1.9	2.4
				256	1.5	1.8	1.1
				442	1.5	0.60	0.43

clusters leading eventually to bubbles that were big enough to be counted as slugs. Thus, the occurrence or lack of coalescence is correctly predicted by the model, while differences between predicted and observed slug frequencies probably result from phenomena which are outside the scope of the model.

Unfortunately, there are no experimental results in the literature which permit a more extensive test of the model. Some data on slug lengths and frequencies are given by Hovmand, et al. [21] for fluidized beds. However, their column was of square cross section and, more serious, it is by no means clear what value of C should be assigned to a fluidized bed. Some indirect support for the model is provided by the good agreement (see Table 4) between predicted maximum heights achieved by a liquid column with heights measured by Grace, et al. [19] for water in a 2.5 cm column.

Conclusions

The frequency and lengths of slugs passing any level in a continuously slugging column are predicted using a numerical simulation procedure which takes account of slug interactions. The relative velocity between slugs and slug shapes are characterized using simple empirical relationships. The model correctly predicts the occurrence of coalescence in continuously slugging systems. Quantitative agreement between the model and experiment is reasonable in view of the complexity of two-phase slug flow.

Acknowledgment

The authors are grateful to the National Research Council of Canada for financial assistance.

Table 4 Comparison of maximum expanded column heights (excluding first maximum) predicted by model and observed by Grace et al. [19]

System: Air/water in 2.5 cm dia column
Static ungassed column height: 100 cm

U_G cm/s	H_{max} predicted cm	H_{max} observed cm
5.6	129.2	127.1
8.9	142.4	141.7
11.8	153.7	154.3
18.0	183.8	191.0

References

1 White, E. T., and Beardmore, R. H., "The Velocity of Rise of Single Cylindrical Air Bubbles Through Liquids Contained in Vertical Tubes," *Chem. Eng. Sci.*, Vol. 17, 1962, pp. 351–361.

2 Clift, R., and Grace, J. R., "Coalescence of Bubble Chains in Fluidized Beds," *Trans. Instn. Chem. Engrs.*, Vol. 50, 1972, pp. 364–371.

3 Moissis, R., and Griffith, P., "Entrance Effects in Two Phase Slug Flow," JOURNAL OF HEAT TRANSFER, TRANS. ASME, Series C, Vol. 84, 1962, pp. 29–39.

4 Clift, R., and Grace, J. R., "Bubble Interaction in Fluidized Beds," *Chem. Engng. Progr. Symposium Series*, Vol. 66, No. 105, 1970, pp. 14–27.

5 Clift, R. and Grace, J. R., "Coalescence of Bubbles in Fluidized Beds," *Chem. Engng. Progr. Symposium Series*, Vol. 67, No. 116, 1971, pp. 23–33.

6 Sollazzo, V., "Continuous Rise and Coalescence of Slugs in Liquids," M. Eng. thesis, McGill University, 1974.

7 Dumitrescu, D. T., "Stomung an einer Luftblase im senkrechten Rohr," *Z. Ang. Math. Mech.*, Vol. 23, 1943, pp. 139–149.

8 Griffith, P., and Wallis, G. B., "Two-Phase Slug Flow," JOURNAL OF HEAT TRANSFER, TRANS. ASME, Series C, Series C, Vol. 83, 1961, pp. 307–320.

9 Akagawa, K., and Sakaguchi, T., "Fluctuation of Void Ratio in Two-Phase Flow," *Bulletin of J.S.M.E.*, Vol. 9, 1966, pp. 104–110.

10 Matsen, J. M., Hovmand, S., and Davidson, J. F., "Expansion of Fluidized Beds in Slug Flow," *Chem. Eng. Sci.*, Vol. 24, 1969, pp. 1743–1753.

11 Kehoe, P. W. K., and Davidson, J. F., "Continuously Slugging Fluidized Beds," Chemeca '70 Conference, Butterworths, Melbourne, 1970, pp. 97–105.

12 Brown, R. A. S., "The Mechanics of Large Bubbles in Tubes," *Can. Jl. Chem. Eng.*, Vol. 43, 1965, pp. 217–223.

13 Street, J. R., and Tek, M., "Dynamics of Bullet Shaped Bubbles Encountered in Vertical Gas Liquid Slug Flow," *AIChE Journal*, Vol. 11, 1965, pp. 644–650.

14 Goldsmith, H. L., and Mason, S. G., "The Movement of Single Large Bubbles in Closed Vertical Tubes," *Journal of Fluid Mech.*, Vol. 14, 1962, pp. 42–58.

15 Nicklin, D. J., Wilkes, J. O., and Davidson, J. F., "Two-Phase Flow in Vertical Tubes," *Trans. Instn. Chem. Engrs.*, Vol. 40, 1962, pp. 61–68.

16 Nicklin, D. J., "Two Phase Bubble Flow," *Chem. Eng. Sci.*, Vol. 17, 1962, pp. 693–699.

17 Stewart, P. S. B., and Davidson, J. F., "Slug Flow in Fluidized Beds," *Powder Tech.*, Vol. 1, 1967, pp. 61–80.

18 Davidson, J. F., and Schuler, B. O. G., "Bubble Formation at an Orifice in an Inviscid Liquid," *Trans. Instn. Chem. Engrs.*, Vol. 38, 1960, pp. 335–342.

19 Grace, J. R., Krochmalnek, L., Clift, R., and Farkas, E. J., "Expansion of Liquids and Fluidized Beds in Slug Flow," *Chem. Eng. Sci.*, Vol. 26, 1971, pp. 617–628.

20 Matsen, J. M., *Discussion in Proceedings of International Symposium on Fluidization*, A. A. H. Drinkenburg, ed., Amsterdam, Netherlands University Press, 1967, p. 302.

21 Hovmand, S., Freedman, W., and Davidson, J. F., "Chemical Reaction in a Pilot Scale Fluidized Bed," *Trans. Instn. Chem. Engrs.*, Vol. 49, 1971, pp. 149–162.

F. M. Chiesa
R. I. L. Guthrie

Department of Mining and Metallurgical Engineering, McGill University, Montreal, Quebec, Canada

Natural Convective Heat Transfer Rates During the Solidification and Melting of Metals and Alloy Systems

Analysis of experiments involving a cylindrical column of lead in the process of freezing downward or alternatively, of melting upward from the base of the container, showed that heat transfer rates associated with Bénard convection are less under transient conditions than at steady-state. Analysis of experiments involving the freezing of lead-tin alloys (0.2 – 1.6 wt. percent Sn) showed that the same heat transfer correlation for Bénard convection could be applied, provided the upper bounding "interface" was located on the solidus isotherm for planar and cellular alloy growth, and on the liquidus, for cellular-dendritic alloy growth.

Introduction

In a recent paper, the authors [1][1] presented an experimental study of steady-state Bénard type convection in columns of pure liquid mercury and lead contained in a vertical cylindrical vessel. Despite the inherently high thermal conductivity of liquid metals, turbulent convection was found to prevail under most practical conditions, and the Nusselt number was correlated to the Rayleigh number by the relation:

$$\mathrm{Nu}_0 = 0.078\ (0.68)^{L/D}\ \mathrm{Ra}^{1/3} \qquad (1)$$

The factor $(0.68)^{L/D}$ took into account reduced convecting heat fluxes resulting from wall effects and, as seen, depended on the height to diameter ratio, L/D, of the enclosure.[2]

Since natural convection phenomena invariably accompany many metallurgical processing operatings involving solidification or melting, the work was extended to study the effect of moving interfaces on these steady-state heat fluxes (equation (1)). This particular paper is partly concerned with the effect of upper interfacial movement on Bénard type convection and is of relevance, for example, to freezing ingots or to crust formation on exposed metal/slag surfaces.

Also, since many metallurgical systems involve the solidification of alloys rather than pure metals, heat transfer correlations such as equation (1) are of limited value unless one can develop a procedure which recognizes the most freezing interfaces are of a markedly nonplanar but dendritic character. Thus the present work also considered the effect of interface morphology on heat transfer rates so as to determine how the heat transfer relationship (1) could be extended to alloy systems similar to those studied here.

Previous Work

1 Natural Convective Heat Transfer in Pure Metal Systems. A review of the literature shows that solidification rates have seldom been measured under accurately known heat transfer conditions. Only recently have experimental techniques been developed that enabled this to be done [2, 3].

Natural convective heat transfer under unsteady-state conditions has been studied by a number of authors. Thus Szekely and Chhabra [4] considered the effect of laminar natural convection on the controlled solidification of lead. In this case, the metal was subjected to a horizontal temperature gradient, a case complementary to Bénard convection since, in practical instances, natural convection can often be considered as a combination of the two ideal cases of horizontal and vertical temperature gradients (e.g., solidification processes in molds, ingots, etc.). Transient runs were conducted in which the progression of the interface was predicted using a numerical solution to Fourier's second law of conduction and the appropriate heat transfer relationship (Eckert's correlation) for the solid-liquid interface. Since predicted and experimental results correlated well over the range of freezing rates studied ($R < 10^{-3}$ cm/s), their work verified the applicability of Eckert's heat transfer correlation to the case of a moving interface.

Boger and Westwater [5] studied the unidirectional solidification of a column of water submitted to Bénard convection. Thus their work was very similar to the first part of the present study, but was complicated by the density inversion of water at 4 deg C. Although a net freezing process was induced, localized melting

[1] Numbers in brackets designate References at end of paper.

[2] It should be noted that these results were obtained for enclosure heights varying between 1 and 8 cms and widths between 5 and 8 cms and would not necessarily be applicable to geometrically similar, but much larger or smaller enclosures.

Contributed by the Heat Transfer Division for publication in the JOURNAL OF HEAT TRANSFER. Manuscript received by the Heat Transfer Division, June 8, 1973. Paper No. 74-HT-RR.

was observed and this was attributed to erratic fluid motion inside the convecting liquid. It was found that steady-state relationships could describe natural convective heat transfer under these transient conditions.

Various other studies have been made in which the influence of moving boundaries along with the effect of blowing and suction on surface heat transfer coefficients have been analyzed [6, 7]. For example, Brian and Hales [7] computed the likely influence of interfacial motion on convective heat transfer coefficients for laminar flow around spherical objects. They showed that enhanced heat transfer rates should sometimes be expected for the case of expanding interfaces and phase changes involving contraction (e.g., freezing), while decreased heat transfer rates should be anticipated for shirnking interfaces and phase changes involving expansion (e.g., melting).

2. Solidification of a Binary Alloy—Cellular and Cellular Dendritic Interfaces. Although no work has been previously attempted on a direct determination of the effect of interface morphology on convective heat fluxes to freezing alloy surfaces, the structural phenomena (i.e., alloy microstructures) resulting from alloy solidification processes have been extensively researched by physical metallurgists, and it is appropriate to briefly review the basic elements of the subject. Thus, at a given temperature, the equilibrium solute concentration in a freezing alloy is usually less in the solid than in the liquid. This results in solute being rejected ahead of a growing planar interface. After the freezing process has reached a dynamic equilibrium, the solute concentrations at the interface in the solid and liquid are C_0 and C_0/k_0, respectively, and the temperature at the interface is equal to θ_s, the solidus temperature of the alloy of concentration C_0.

Since this solidification process gives rise to a solute rich layer ahead of the interface, this may result in a portion of melt being supercooled[3] even though the temperature in the liquid is everywhere above that of the interface. If supercooling does exist, the planar interface tends to break down and a transverse periodicity appears, giving rise to the development of cells [9]. The conditions of stability of a planar interface are given by:

$$G/R > \frac{mC_0}{D}\frac{1 - k_0}{k_0}$$

where G is the temperature gradient at the interface, D the diffusion coefficient, m the slope of the liquidus line on the phase diagram, and R the rate of freezing.

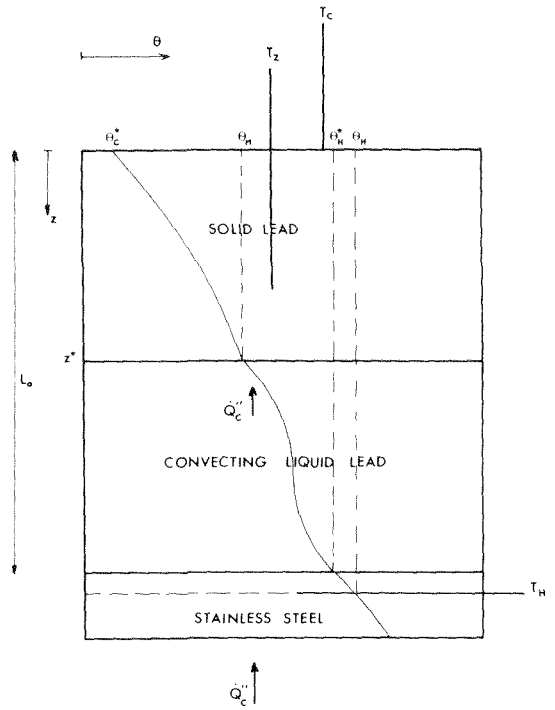

Fig. 1 Schematic representation of system used to study freezing (or melting) rates of pure lead subjected to Bénard natural convection, together with a typical temperature distribution across the system

As the temperature gradient at the interface in the liquid is successively reduced (or R increased), the zone of constitutional supercooling widens and the cells change in character to such an extent that they acquire some of the characteristics of dendrites. The experimentally determined criterion for the stability of the resulting cellular dendritic interface is based on the value of $C_0R^{1/2}/G$ as compared to a critical value $(C_0R^{1/2}/G)_{crit}$ below which the cellular interface is stable. This critical value varies somewhat from one system to another and depends on the orientations of the crystals with respect to the direction of growth. Thus, for a polycrystalline lead-tin system, the total range of crit-

[3] This type of supercooling is usually referred to as constitutional supercooling.

Nomenclature

C_0 = average solute content of the alloy
C_f = reduced heat transfer coefficient ratio for transient conditions involving Bénard convection, $\frac{\mathrm{Nu}}{\mathrm{Nu}_0}$
D = internal diameter of container
G = temperature gradient in the liquid at the freezing interface
k = thermal conductivity (subscripts: "s" solid lead or alloy—"l" liquid lead or alloy)
k_0 = partition coefficient of the alloy considered
L = height of the convecting body of liquid
L_0 = height of sample (i.e., lead or lead-tin alloy
L_F = latent heat of fusion
$\dot{Q}_c''$ = convective heat flux across liquid lead
R = rate of freezing (or melting)
t_c = time at which conduction regime begins
z = vertical distance from uppon bounding plane of lead sample
z^* = vertical distance of freezing interface from upper bounding plate (thickness of solid part of the sample
N_R = dimensionless grouping for transient heat transfer $\frac{LR}{\alpha \mathrm{Nu}}$
Nu = Nusselt number $\left(\frac{\dot{Q}_c'' L}{k\,\Delta\theta}\right)$
Nu_0 = computed Nusselt number for steady-state systems
Ra = Rayleigh number $\frac{g\beta L^3 \Delta\theta}{\alpha\nu}$
α = thermal diffusivity
β = volumetric coefficient of expansion
$\Delta\theta$ = temperature drop across convecting body of liquid; $\Delta\theta = \theta_H^* - \theta_c^*$, $t < 0$; $\theta_H^* - \theta_l^*$, $t \geq 0$
θ_c^* = (cold) temperature at top interface of lead sample
θ_H = temperature in the stainless steel bottom plate as recorded by T_H
θ_H^* = (hot) temperature at bottom interface of lead sample
θ_l^* = temperature of the flat solid-liquid interface (real or fictive) for alloy freezing
θ_M = melting point temperature of pure lead
θ_z = temperature in solid at z, (in present experiments, θ_z measured at $z = L_0/3$)
ν = kinematic viscosity
ρ = density

Superscript
* = interface

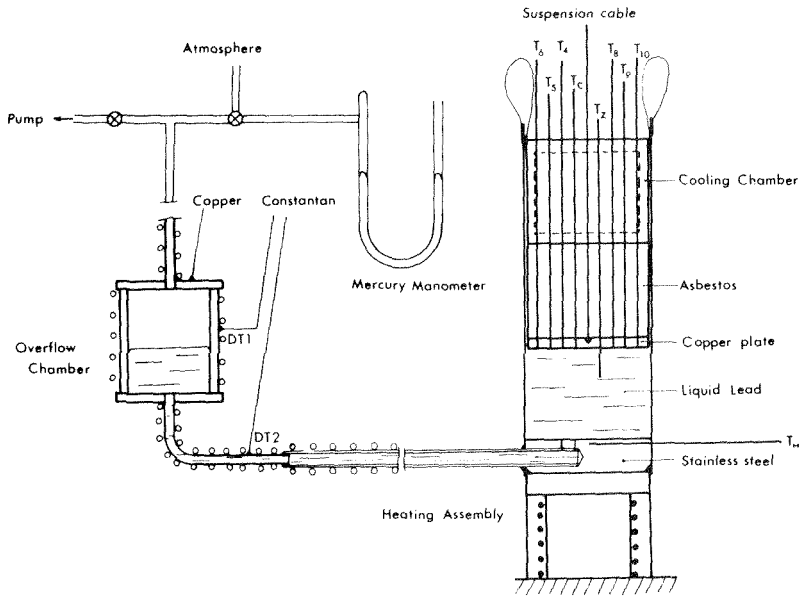

Fig. 2 Diagram of apparatus used for study of freezing (or melting) rates of pure lead subjected to Benard natural convection (thermal lagging not shown in diagram)

ical values lies between the slopes of the two lines shown in Fig. 3. These results were obtained by Tiller and Rutter [10].

Procedure

In order to check the applicability of the steady-state heat transfer relationship previously obtained for steady state turbulent Bénard type convection (i.e., equation (1)) to transient systems, unidirectional freezing and melting of a column of pure lead was investigated in the work now described. Fig. 1 shows the system chosen for investigation, while Fig. 2 shows the experimental apparatus involved. Referring to Fig. 1, a typical temperature profile across the convecting liquid and solidified lead is shown schematically, halfway through the course of a freezing experiment. At the solid/liquid lead interface, $z = z^*$, the temperature is θ_M, the melting point of lead, while at the top surface of the enclosure it is $\theta_c{}^*$, and at the bottom surface $\theta_H{}^*$. Thermocouple T_c monitored the colder upper boundary temperature, being located on the copper plate/lead interface itself, while thermocouple T_H monitored the temperature, θ_H, 0.125 cm below the hotter, lower lead/stainless steel boundary.

Radial temperature distributions across the upper and lower boundaries were confirmed to be flat [8] using thermocouples T_4 to T_{10} at the top boundary and using horizontal traverses by T_H at the lower boundary. Similarly the flatness of the freezing interface (within ± 2mm) during the course of typical freezing experiments was verified, using vertical traverses by thermocouples T_4 – T_{10}. Thus, since the enclosure side walls were well insulated all the heat was transferred vertically upwards in the system.

The system may be mathematically described as follows:

$$0 < z < z^*,\ 0 \leq t \leq T$$

$$\frac{\partial \theta}{\partial t} = \alpha_s \frac{\partial^2 \theta}{\partial z^2} \qquad (2)$$

B.C.1 $z = 0,\ 0 \leq t \leq T,\ \theta = \theta_c{}^* = f_1(t)$

B.C.2 $z = z^*, 0 \leq t \leq T,\ \theta = \theta_M$

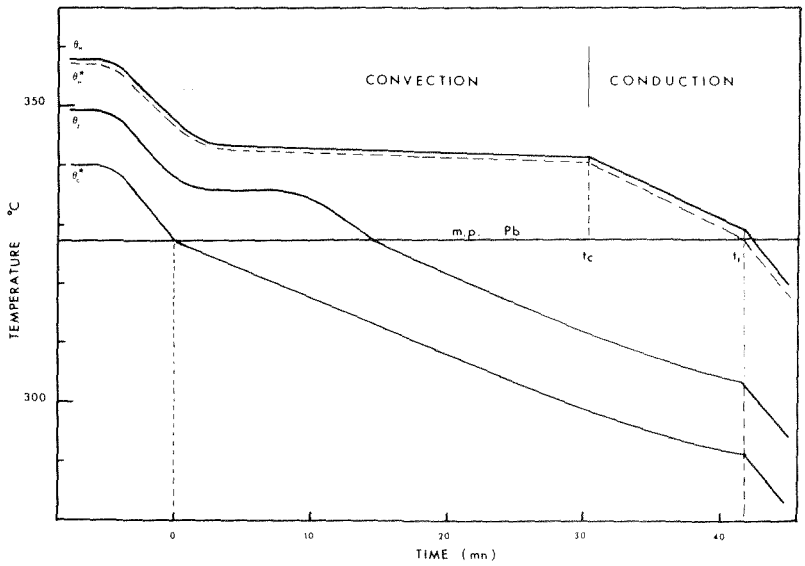

Fig. 3 Typical temperature-time curves recorded by thermocouples located at the bottom (θ_H), top ($\theta_c{}^*$), and one third way down (θ_Z) the cylindrical column of lead during the course of a freezing experiment.

$$\text{B.C.3 } z = z^*,\ 0 \le t \le T,\ k_s \frac{\partial \theta}{\partial z} = \rho L_F \frac{dz^*}{dt} + \dot{Q}_c'' \tag{3}$$

$$\text{where } \dot{Q}_c'' = k_l \frac{\theta_H^* - \theta_M}{L_0 - z^*} \cdot \text{Nu} \qquad (\text{Nu} \not< 1)$$

$$\text{B.C.4 } z = L_0,\ 0 \le t \le T,\ \theta = \theta_H^* = f_2(t)$$

Thus equation (2) is the appropriate statement of Fourier's second law for unidirectional transient heat flow through the solid lead, while equation (3) describes convective heat flow across the liquid lead.

Provided the convective heat flow under transient freezing or melting experiments is the same as for steady-state Bénard convection, Nu may be replaced by Nu_0 (equation (1)) and the system of equations solved numerically without any difficulty by providing experimental data on the way θ_H and θ_c^* vary with time during the course of a freezing (or melting) experiment. Thus, the numerical solution can be used to predict:

(a) freezing rates and interface location

(b) batch cooling curves at any location in the solid

(c) temperature profiles in the solid

(d) transition times, t_c, when the pure conduction regime is entered and Nu = 1.

By comparing any one or more of these against actual experiment recordings it becomes possible to decide whether the steady-state heat transfer relationship is adequate, this being the only variable in doubt in the set of equations and boundary conditions listed in the foregoing.

In the present investigation, experimental recordings of *(b)* and *(d)* were used to determine whether any mismatches arose on account of altered convection rates through the liquid. In some cases significant mismatches did arise, and the value of the Nusselt number, Nu, was then adjusted by a multiplicative factor C_F ($Nu = C_F\ Nu_0$) in the program so as to bring experimental and computed values into line.

The batch cooling curve was recorded by thermocouple T_z, located one-third way down the enclosure while transition times, t_c, were obtained from the sudden slope changes in the temperature-time curves of thermocouple T_H.

The choice of *(b)* and *(d)* over *(a)* in making these comparisons was based on expediency since, for the system studied, it proved impractical to directly measure the location of the freezing interface either by a vertically moving probe (sealing problems associated with liquid metals), or by using ultrasonic means (attenuation of signal and the high temperature environment).

Finally, it should be noted that the experimental system was specifically designed so that only a small controlled vertical heat leak occurred through the system by using an asbestos cylinder (low thermal conductivity) located between the top of the enclosure and the cooling water chamber (Fig. 2). This design resulted in:

1 a slowly moving freezing interface which advanced at a practically constant velocity, and

2 practically constant convective heat fluxes during the major part of an experimental run [8].

Similar procedures were adopted for studying the solidification in the alloy system. However, in order to be able to define a heat transfer relationship, under all alloy freezing conditions a fictive upper planar interface was considered in the work presently described. The solidus temperature isotherm was chosen (i.e., $\theta_l^* = \theta_S$), as defining the location of this fictive interface since for planar growth, this "interface" is identical to the actual interface. However, when cellular dendritic growth took place, this interface was located inside the mushy zone where both liquid and solid phases coexisted.

Apparatus and Experimental Technique

Basically, the experimental setup used in the present work was that designed for the study of steady-state natural convection in lead and mercury and has been described in detail in a previous paper [1]. As shown in Fig. 2, the lead or lead-tin sample (99.99 percent purity) was contained in a 3 in. OD stainless steel tube, heated from the bottom and cooled from the top.

The heating assembly consisted of two 250W semi-cylindrical heaters encasing a plug of stainless steel on top of which a ½ in. thick copper plate was screwed. The cooling assembly consisted of a copper chamber in which thermostated water circulated, and a copper plate in contact with the sample between which asbestos plugs of variable thickness were inserted.

The addition of an overflow chamber to the main container (see Fig. 2) prevented the formation of a shrinkage cavity during freezing. The chamber consisted of a 2 in. ID copper tube, 2.5 in. high closed at both ends. A 10 in. long stainless steel pipe (¼ in. ID, 1/16 in. wall thickness) was screwed into the stainless steel bottom of the main container where a ¼ in. dia orifice allowed communication between the overflow chamber and the container. The overflow assembly was maintained at the desired temperature (monitored by thermocouples DT1 and DT2) using a heating tape wrapped around it. The heat leak along the feed pipe was minimized by adjusting the power input into the heating tape so as to equalize the readings of thermocouples DT2 and T_H. The pressure in the overflow chamber could be adjusted using a suction pump and bleed valve, and monitored using the mercury manometer shown in Fig. 2. The whole overflow assembly was encased in a mild steel shell screwed on the outer casing of the furnace and well insulated with Fiberfax (expanded mica).

Runs were conducted on lead samples approximately 5 cm high. The initial height of liquid lead in the main container being 5 cm or so, the pressure in the overflow chamber was dropped so as to lower the level of lead in the main container by about 1 cm. The cooling assembly was then accurately positioned at the required height above the bottom plate and the liquid lead raised to meet it by bringing the overflow chamber pressure back up to 1 atmosphere.

For any particular run, the amount of heat transported across the column was predetermined by the thickness of the asbestos plug used. Similarly, under these prescribed conditions, freezing rates could be adjusted as desired by appropriate decreases in power input to the heating assembly. As previously noted, the major thermal resistance to heat transfer lay in the asbestos plug, so that an essentially constant heat leak was provided at the top of the column. Finally, thermocouple probes $T_4 - T_{10}$, T_c, and T_z were inserted with a capability for vertical, rather than horizontal traverses, thereby avoiding sealing problems with liquid lead. The design was legitimate since the "fin effect" associated with fluids having low thermal conductivities and heat capacities is not an important factor in the measurement of liquid metal temperatures. This is demonstrated, in solidification studies involving lamellar eutectics in which thermocouple probes used under similar temperature gradients, showed no resultant distortion of the microstructure [18].

The role of the interface morphology was studied on lead-tin alloy samples 5 cms high for tin contents of 0.2 and 0.4 weight percent and on samples 8 cms high for tin contents of 0.8 and 1.6 weight percent.

Table 1 gives the relevant physical properties used in the present analysis for the lead and lead-tin systems.

Results and Discussions

***(a)* Pure Metals Systems.** A typical recording of the temperatures θ_H, θ_Z, θ_c^*, as indicated by thermocouples T_H, T_Z, and T_c, is shown in Fig. 3 and may be explained as follows.

Before the heat input to the bottom was cut down, the column of lead underwent steady-state natural convection. Following the power input reduction, a "dynamic" equilibrium was established in which the top and bottom plate temperatures dropped at a similar rate, the temperature drop, $\Delta\theta$, between them (and hence $\dot{Q}_c''$, the heat transported across the liquid) remaining fairly constant. At time $t = 0$ corresponding to the initiation of freezing, the dynamic equilibrium was drastically alerted in two different ways:

1 The temperature of the upper bounding surface of the liquid

Table 1 Physical and thermal properties of lead and lead-tin alloys used in analyses

Solid (327 deg C)	C.G.S.	S.I.
	Lead	
Density, ρ	11.34 g/cm^3	11,340 kg/m^3
Heat capacity, C_p	0.030 cals/g deg C	0.125 kJ/kg deg C
Thermal conductivity, k	0.083 cals/cm deg C s	34.6 W/m deg C
Thermal diffusivity, α	0.243 cm^2/s	24.3 mm^2/s
Melting point temperature, θ_M	327.3 deg C	327.3 deg C
Latent heat of fusion, L_F	5.60 cals/g	23.34 kJ/kg
Liquid (335 deg C)		
Density	10.56 g/cm^3	10,560 kg/m^3
Heat capacity	0.0387 cals/g deg C	0.161 kJ/kg deg C
Thermal conductivity	0.039 cals/cm deg C s	16.3 W/m deg C
Thermal diffusivity	0.095 cm^2/s	9.5 mm^2/s
Viscosity	1.41 cP	0.00241 Ns/m^2
Volumetric coefficient of expansion	1.14 $\times$ 10^{-4}/deg C	1.14 $\times$ 10^{+4}/deg C
Prandtl number	0.0239	0.0239
Lead-Tin Alloys		
	C.G.S.	S.I.
Thermal conductivity of solid alloys[a]	= 0.083 cals/cm deg C	34.6 W/m^2 deg C
Thermal conductivity of liquid alloys[a]	= 0.039 cals/cm deg C	16.3 W/m^2 deg C
Slope of liquidus temperature versus percent tin content	= -3.0 deg C/wt percent Sn	-3.0 deg C/wt percent Sn
Partition coefficient, k_0 (solidus/liquidus conc.)	= 0.72	0.72
Latent heat of fusion, L_F[b]	= 5.54 cals/gm	23.2 kJ/kg

All other relevant physical properties (ρ, C_p, μ, β) were taken as being equal to those of pure lead.

[a] Since dilute amounts of high conductivity solutes (e.g., Sn in Pb) do not alter thermal conductivity values significantly [15] (experimental data [16] shows that for 20 percent Sn-Pb alloy, $k \not> 1.05k$ Pb) values for pure lead were again taken.

[b] Since the variation in ΔH_F [17] is so small (1149 cal/mole to 1142 cal/mole between 0.2 and 1.6 wt percent Sn, a mean value 0f 1145 cal/mole (or 5.54 cal/g) was taken.

suddenly stopped dropping to remain at 327.3 deg C, the melting temperature of lead.

2 A new heat source (latent heat) initiated at the solid-liquid upper interface.

As a result, the system tended toward a new dynamic equilibrium in which the rate of heat extraction away from the interface was very close to the amount of heat transferred through the liquid, $\dot{Q}_c''$, plus the amount of latent heat evolved.[4] The temperature of the bottom plate thus settled to a plateau value resulting in an approximately constant new value of $\Delta\theta$, or approximately constant $\dot{Q}_c''$. This temperature drop $\Delta\theta$ was, of course, less than that established prior to the initiation of freezing. During the major proportion of the experiment ($0 \leq t \leq t_c$), the liquid was subjected to natural convective heat transfer so that the thinning of the liquid slab did not affect the amount of heat transferred across it. However, when the critical Rayleigh number was reached ($t = t_c$), the conduction regime became stable and $\dot{Q}_c'' \approx k(\theta_H - \theta_M)/l$, l being the thickness of remaining liquid ($L_0 - z^*$). One immediately sees that as $l \to 0$, $\dot{Q}_c'' \to \infty$, if $\theta_H{}^*$ had remained constant. Thus the remaining liquid tended to call for an increasing amount of heat from the metal block as it thinned. ($\dot{Q}_c'' \propto l/L$), and this was only partially satisfied by $\theta_H{}^*$ dropping off so as to increase temperature gradients in the lower metal block and allow more heat to be conducted through it and into the liquid. Thus, referring to Fig. 3, a sharp change in the slope of curve θ_H versus time was observed at the transition between the convection and conduction regimes.

As described in the procedure, the recorded temperature-time relationships for the top and bottom plates, together with the steady-state heat transfer relationship and appropriate thermal properties of solid and liquid lead were sufficient to predict the rate of freezing in the system as well as temperature-time profiles in the solidified metal at any given location. Analysis of similar temperature-time curves, θ_z, to that appearing in Fig. 3 showed that the agreement between predicted and experimental temperatures was satisfactory for experiments conducted at low rates of freezing ($R < 10^{-3}$ cm/s).

However, a substantial discrepancy existed for high rates of freezing as indicated in Fig. 4, where the predicted and experimental temperature curves are shown for low and high freezing rate experiments respectively. It was found that a multiplicative factor, C_F, had to be applied to the steady-state heat transfer relationship (i.e., $C_F = \mathrm{Nu}/\mathrm{Nu}_0$) and, for each experiment, a value of C_F was determined (by a trial and error method) to give a good fit between predicted and experimental values.

By conducting experiments over a wide range of Nusselt numbers (Nu = 1 to Nu = 7), it was found that for equivalent rates of freezing the departure of the heat transfer rate from that given by the steady-state heat transfer relationship was less (and C_F closer

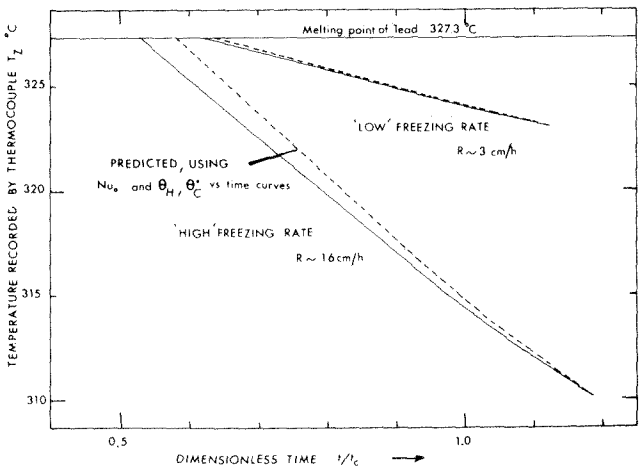

Fig. 4 Temperature of solidified lead one third way down column (θ_Z), versus the dimensionless time ratio, t/t_c, for high and low freezing rates; - - - - - predicted ——— experimental

[4] Temperature profiles in the solidified portion were almost linear, so that transient effects in the solid were small. Similarly, the amount of superheat given up by the liquid during freezing was always less than 3 percent of $\dot{Q}_c''$ and was maximum for high freezing rates.

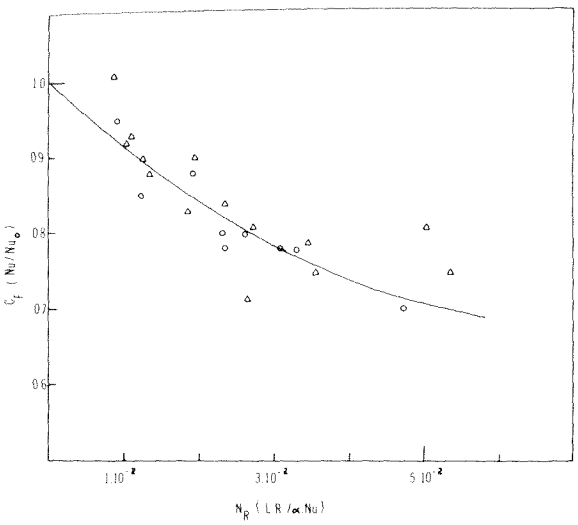

Fig. 5 Plot of reduced heat transfer coefficient ratio C_F, required to bring predicted convective heat fluxes based on equation (1) into line with experimentally recorded heat fluxes in systems involving a moving interface (freezing and melting) versus the dimensionless grouping, N_R (LR/αNu): Δ freezing experiments; ^{0} melting experiments

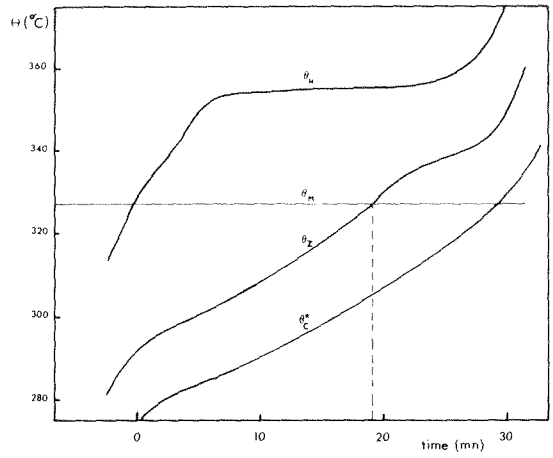

Fig. 6 Typical temperature-time curves recorded by thermocouples located at the bottom (θ_H), top (θ_c^*), and one third way down (θ_Z) the cylindrical column of lead during the course of a melting experiment

to 1) for high intensities of convection.

Consequently, C_F was correlated to a dimensionless group, N_R [8], which includes both the rate of freezing and the intensity of convection

$$C_F = F(N_R) = F\left(\frac{LR}{\alpha \mathrm{Nu}}\right)$$

It is interesting to note that Brian and Hales [7] for instance, use an equivalent grouping in their study of the effects of interface motion on Nusselt numbers.

The graph of Fig. 5 shows the values of C_F obtained as a function of LR/αNu for freezing experiments (triangles).

Similar runs were conducted on melting the lead column and a typical recording of the various thermocouples is shown in Fig. 6. As seen, the plateau exhibited by curve θ_H in the freezing experiment is still clearly apparent.

When the data obtained for melting experiments were treated in a similar fashion to that corresponding to freezing (R becoming the rate of melting) the points (circles) shown on Fig. 5 were obtained.

Since the results were practically identical for both melting and freezing processes, both sets of data were combined so as to determine the best one-parameter curve fit through the points. An exponential function of the form

$$C_F = \exp - (7.8\,\frac{LR}{\alpha \mathrm{Nu}}) \qquad (4)$$

gave the best curve fit, where R represents either the rate of melting or rate of freezing. The average scatter about this line is ±4 percent.

(b) **Alloy Systems.** In order to relate the adequacy of the heat transfer relationships (1) and (4) to the nature of the interface, the ratios of the experimental to computed Nusselt numbers were related to the domains of stability of the cellular and dendritic interfaces as experimentally determined by Tiller and Rutter [10]. These domains are shown in Fig. 7 as a function of the tin content of the alloy, the interfacial temperature gradient G and the freezing rate R. In the present set of experiments the temperature gradient in the liquid at the interface G, was given by:

$$G = \frac{\dot{Q}_c''}{k_l}$$

so that the value of $G/R^{1/2}$ for each experiment could be determined. Thus each point shown in Fig. 7 represents one freezing experiment while each adjoining number indicates the ratio of the experimental to computed Nusselt numbers (i.e., $\mathrm{Nu}/C_F\mathrm{Nu}_0$). As indicated in the previous section, the solidus temperature of the alloy was used as that of the upper bounding plane of the convecting liquid. The circled points appearing correspond to experimental conditions of G, R, and C_0 for which the planar interface was stable (see relation (3)), while the triangles and solid circles represent "low" and "high" Nusselt values (High arbitrarily defined as Nu > 3.0), respectively.

As seen, the ratio of the experimental to computed Nusselt numbers are close to unity for those experiments corresponding to planar and cellular interfaces. One may therefore conclude that relations (1) and (4) used in conjunction with the solidus temperature adequately describes convective heat transfer for planar and cellular interfaces. However, striking discrepancies appear for those experimental conditions for which dendritic interface predominated and this is discussed in the next section.

General Discussion

***(a)* Effect of Departure from Steady-State on the Heat Transfer Rates.** The present experimental study has shown that the heat transferred across a convecting body of liquid lead was always less under unsteady-state conditions. This feature was unexpected, particularly for the freezing experiments for which one would intuitively anticipate that any lag in the system should favour enhanced heat transfer rates. However, an extension of an analysis by Brian and Hales on the effect of moving boundaries and suction due to shrinkage indicated that the effect of motion of the interface and the effect of suction or expansion accompanying the phase change were negligible under the present experimental conditions. Thus, neither the freezing nor melting process were in themselves responsible for any change in heat transfer rates.

The analysis of the temperature profile[5] in the upper "cold" layer of fluid showed that the resistance to heat flow of that layer was increased as conditions departed more and more from steady state whereas the resistance of the lower "hot" layer was unaffected by the transient process [8]. Thus, the decrease in the present heat transfer rates must be attributed to the alteration of the fluid velocity and temperature fields in the layer of liquid adjacent to the interface, and, more specifically, to their departures from the steady state configuration. This interpretation is plausible in view of the work by Wilkes and Churchill [11] who showed that the time lag for convection generated between two vertical walls at a distance "d" from each other is of the order of $0.1\,d^2/\nu$;

[5] Bénard convection is characterized by a temperature profile where the temperature drop is concentrated near the upper and lower bounding planes, the core fluid being at a constant temperature.

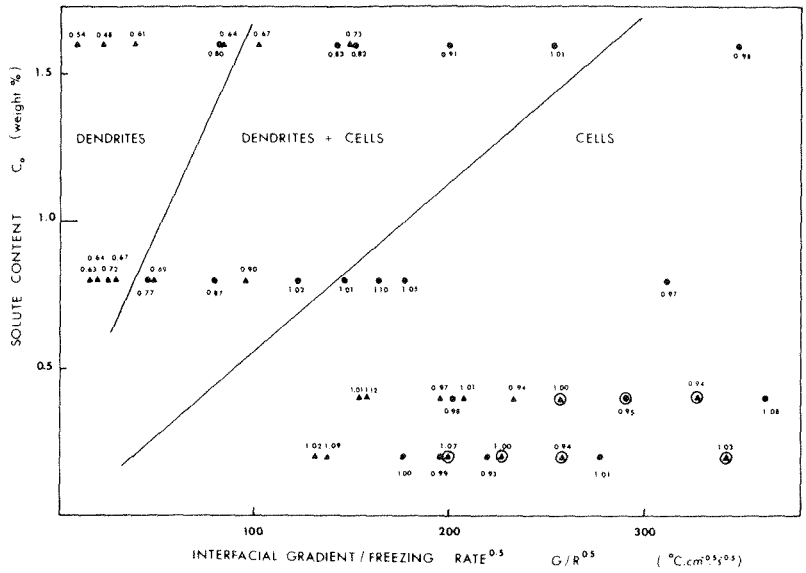

Fig. 7 Diagram [C_0 (wt percent Sn), versus $G/R^{1/2}$ (deg C $cm^{-1/2}s^{1/2}$)] defining the domains of stability of dendritic and cellular interfaces [2]. Data points show relevant experimental conditions (i.e., C_0 and $G/R^{1/2}$) while adjoining members indicate ratios of Nusselt (experimental) to Nusselt (i.e., equation (1) using the solidus temperature to define upper bounding plane of convecting liquid). ○ High Nusselt (>3); ▲ Low Nusselt numbers (<3) 0 planar interface conditions.

it is likely that the time lag for Bénard convection will be much greater in view of its highly unstable nature. Thus, for the present system, the time lag should be of the order of one hour, which implies that in most of the current runs, the departure from the steady-state was substantial.

(b) **Role of Interface Morphology on Heat Transfer Rates.** The lowered transfer rates noted in Fig. 7 and corresponding to dendritic growth can be explained by referring to a simplified representation of a dendritic interface as shown in Fig. 8. Thus, accepting that the solute buildup responsible for supercooling has been eliminated at the dendrite tips (plane P_L), the equilibrium temperature of these tips will be the liquidus temperature, θ_L, of the alloy. It also follows that the fictive "flat" interface defined as the solidus temperature isotherm, will be located inside the mushy zone (i.e., plane P_S).

The use of θ_S as the temperature of the upper bounding plane in calculating the heat transfer relationship implicity assumes that, as far as heat transfer is concerned, the situation is identical to that involving a planar interface at a temperature θ_S. The validity of such an assumption obviously depends on the state of convection in the mushy zone. In between dendrite arms, two driving forces for natural convection exist:

1 a downward temperature gradient (Bénard convection);

2 a transverse density gradient resulting from changes in concentration.

The possibility of either factors causing convection currents have been considered [8] using previous works by Ostrach and Pnueli [12] and Szekely and Chhabra [4]. Both analyses strongly suggest the absence of any convection whatsoever between dendrite arms for these particular experiments with Pb-Sn alloys. Thus, when cellular dendritic growth takes place it is more realistic to consider that natural convection is generated between the lower bounding plane P_B and the plane containing the liquidus temperature isotherm P_L (rather than that containing the fictive interface P_S).

Consequently the Nusselt number was computed using the liquidus temperature as that of the upper bounding plane of the convecting liquid, for those experiments involving dendritic interfaces.

For the 15 experiments involved, the agreement between computed and experimental Nusselt number was then found to be much better, although computed Nusselt number were still generally 10 to 15 percent less than experimental Nusselt Numbers [8].

This slight discrepancy indicates that the temperature at the dendrite tips is probably less than the liquidus temperature of the alloy. The following phenomena may account for this:

1 A slight solute concentration buildup will still exist at the tip of the dendrites after all supercooling has been used up and this will obviously lower the equilibrium temperature.

2 The equilibrium temperature at the tips of a dendrite may also be lowered as a result of sharp curvature (of the order of 1 μ.)

Summary and Conclusions

The analysis of experiments involving freezing and melting of lead columns has shown that, for a prescribed temperature drop, the heat flux transferred across a layer of liquid is maximum under steady state conditions. This experimental result supports Malkus' theoretical hypothesis of the "maximizing flow" which

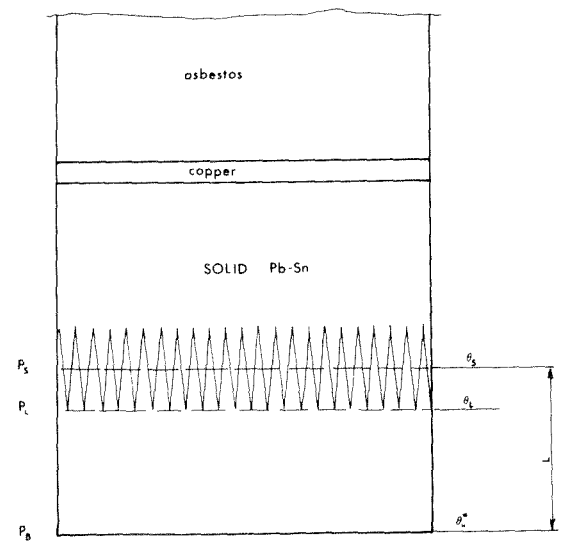

Fig. 8 Simplified representation of a dendritic interface showing location of solidus (θ_S) and liquidus (θ_L) isotherms in relation to the mushy zone of solidification

has successfully explained several aspects of turbulent Bénard convection.

The multiplicative factor, C_F, that should be applied to the steady state Nusselt number is a function of the freezing (or melting) rate, R, and of the intensity of convection. It is given by the relation:

$$C_F = \exp -(7.2 \frac{L R}{\alpha \mathrm{Nu}})$$

Freezing experiments on lead-tin alloys have shown that the heat transfer relationships derived for pure metals can normally be applied to alloy systems undergoing Bénard convection in the following manner:

—When planar or cellular growth takes place, the liquid should be considered as convecting between the bottom plate and an upper plane P_S containing the solidus temperature isotherm.

—when cellular dendritic growth predominates, the liquid alloy should be considered as convecting between the bottom plate and an upper plane P_L containing the liquidus temperature isotherm. (In this case, however, the computed heat flux is slightly underestimated.)

APPENDIX

Since the results presently reported were unexpected, particularly those regarding freezing, possible sources of error in the experimental procedures and treatment of results were analyzed.

1 The apparatus was designed so that radial heat losses from the convecting body of fluid should be minimal. Precautions included the use of a 3 in. thick layer of fibrofax insulating material (expanded mica) which separated the cylindrical lead container from an outer cylindrical steel shall [1]. Heating tapes wound around this steel shell allowed its vertical temperature profile to be matched with that of the lead container. By this means any radial heat losses were negligible in comparison with vertical heat transfer through the convecting column of liquid lead. This was experimentally verified by showing that, at steady-state, the power input to the bottom heater (as measured by a wattmeter) agreed with the amount of heat transferred to the circulating cooling water at the top of the column, within estimated experimental errors of ±3 percent.

Similarly, it was readily shown that the amount of heat conducted up through the walls of the stainless steel container (1 mm thick) never exceeded 3 percent and was generally ~1 percent.

2 In order to avoid any relative temperature corrections being necessary for the curves θ_H, θ_C, and θ_Z shown in Fig. 3, three thermocouples T_H, T_C, and T_Z were selected which registered identical e.m.f. (i.e., ±6 μV or ±0.1 deg C) at the freezing temperature of lead.

3 The validity of choosing a multiplicative factor C_F, to take into account decreased heat transfer rates throughout the freezing process might be questioned. However, when the correction factor obtained by matching the experimental and computed value of t_C was used, the agreement between predicted and experimental temperature-time curves one-third way down the column was very good. This showed that the multiplicative factor, C_F, adequately described convecting heat transfer rates in the liquid, throughout the course of an experiment.

4 In the light of the present experimental results, the possibility of a contact thermal resistance being set up at the upper copper-lead interface was also considered. However, any such resistance would lead to an overestimate in $\dot{Q}_c''$ and a corresponding increase in C_F (i.e., $C_F > 1$).

5 Finally, it should be noted that any experiment involving freezing will result in the liberation of a certain amount of superheat from the liquid (except when $\theta_H^* = \theta_M$). This phenomenon leads to an added contribution to the heat flux at the freezing interface (i.e., $C_F > 1$.) as shown by Heertjes, et al. [14]. In the present experiments, however, this contribution was very small (<3 percent of $\dot{Q}_c''$) and could be discounted in interpreting the results.

Acknowledgments

The authors acknowledge the financial support of the National Research Council of Canada, as well as the Canada Council for providing a Fellowship to F. M. Chiesa.

Finally, the authors acknowledge the many stimulating discussions by Prof. J. E. Gruzleski on alloy systems.

References

1 Chiesa, F., and Guthrie, R.: "An Experimental Study of Natural Convection and Wall Effect in Liquid Metals Contained in Vertical Cylinders," Metallurgical Transactions, vol. 2, 1971, pp. 2833–2838.

2 Hills, A. W. D., and Moore, M. R.: "The Solidification of Pure Metals under Unidirectional Heat Flow Conditions. I—Solidification with Zero Superheat," Trans. AIME Vol. 245, 1969, pp. 1481–1492.

3 Prates, M., Fissolo, J., and Biloni, H.: "Heat Flow Parameters Affecting the Unidirectional Solidification of Pure Metals," Metallurgical Transactions, Vol. 3, 1972, pp. 1419–1425.

4 Szekely, J., and Chhabra, P. S.: "The Effect of Natural Convection on the Shape and Movement of the Melt-Solid Interface in the Controlled Solidification of Lead," Metallurgical Transactions, Vol. 1, 1970, pp 1195–1208.

5 Boger, D. V., and Westwater, J. W.,: "Effect of Buoyancy on the Melting and Freezing Process," Journal of Heat Transfer, Trans. ASME, Vol. 89, 1967, pp. 81–89.

6 Sparrow, E. M. and Cess, R.,: "Free Convection with blowing or Suction," Journal of Heat Transfer, Trans. ASME, Vol. 83, 1961, pp. 387–390.

7 Brian, P. L. T., and Hales, H. B.: "Effect of Transpiration and Changing Diameter on Heat and Mass Transfer to Spheres," A.I. Ch. E. Journal, Vol. 15, 3, 1969, pp. 419–425.

8 Chiesa, F.: "Natural Convection in Liquid Metals and Alloys," Ph.D. Thesis, McGill University, Montreal, Quebec, 1973.

9 Walton, D., Tiller, W. A., Rutter, J. W., and Winegard, W.: "Instability of a Smooth Solid-Liquid interface during Solidification," Trans. AIME, Vol. 203, 1955, pp. 1023–1026.

10 Tiller, W. A., Rutter, J. W.,: "The Effect of Growth Conditions upon the Solidification of a Binary Alloy," Canadian J. of Physics, Vol. 34, Pt. 1, 1956, pp. 96–121.

11 Wilkes, J. O., and Churchill, S. W.,: "The Finite-Differences Computation of Natural Convection in a Rectangular Enclosure," A.I. Ch. E. Journal, Vol. 12, 1966, pp. 161–166.

12 Ostrach, S., and Pnueli, D.,: "The Thermal Instability of Completely Confined Fluids inside some Particular Configurations," J. of Heat Transfer, Trans. AIME, Vol. 85, 1963, pp. 346–354.

13 Szekely, J., and Stanek, V.: "Natural Convection Transients and their Effects in Unidirectional Solidification," Metallurgical Trans., Vol. 1, 1970, pp. 2243–2251.

14 Heertjes, P. M., Jongenelen, F. C. H., and de Leew den Bouter, J. W.: "The Effect of a Moving Boundary on Heat Transfer by Free Convection," Chemical Engineering Science, Vol. 15, 1970, pp. 1881–1890.

15 Calvert, F. G., and Johnson, R.: "On the Relative Power of Metals and their Alloys to Conduct Heat," Proceedings Royal Soc. of London, Vol. 9, 1858, pp. 169–171.

16 "Thermal Conductivity of Metallic Elements," Thermophysical Properties of Matter, Vol. 1, Plenum Press, 1970.

17 Hultgren, R., Orr, R., Anderson, R., and Kelley, K.: "Selected Values of Thermodynamic Properties of Metals and Alloys," John Wiley and Sons, New York 1963.

18 Gruzleski, J. E.: "The Development and Morphology of the Cellular Structure in the Tin-Cadmium Eutectic," Ph.D. Thesis, University of Toronto, 1967, pp. 34–40.

G. A. Domoto
Assoc. Professor. Assoc. Mem. ASME

W. C. Wang[1]
Graduate Student. Assoc. Mem. ASME

Department of Mechanical Engineering,
Columbia University,
New York, N. Y.

Radiative Transfer in Homogeneous Nongray Gases With Nonisotropic Particle Scattering

A perturbation technique is presented to treat the problem of radiative transfer in homogeneous, plane parallel, nongray gases with nonisotropic particle scattering. The technique allows use of nongray narrow-band or wide-band models as well as Mie and Rayleigh scattering coefficients and asymmetry factors. Results are obtained in the form of monochromatic transmittance, reflectance, and absorptance of water clouds typical of those in the earth's atmosphere.

Introduction

The effect of clouds is of major importance in atmospheric radiative transfer. Recent efforts have been made to obtain more accurate values of cloud reflectance, transmittance, and emittance. Van de Hulst [1],[2] Yamamoto, et al. [2], and Hansen [3] have performed extensive numerical calculations considering only the scattering and absorption properties of the water or ice particles. Yamamoto, et al. [4, 5], and Zdunkowski and Crandall [6] have accounted for the effect of both scattering and nongray gases. All calculations have been performed by the foregoing with various size-distribution of scatterers and various nongray gas models. Yamamoto, et al., used finite sums of exponentials to describe the nongray nature of water vapor absorption and carried out solutions of the equation of transfer for homogeneous cloud layers using both Chandrasekhar's principles of invariance [4] (with expansion in single scattering albedo) as well as the discrete ordinate technique [5] (both techniques requiring extensive numerical calculations). Zdunkowski and Crandall [6] used the Elsasser model for nongray gases and solved the equation of transfer using iterative numerical techniques. The purpose of this work is to present a technique for relatively simple solution of the anisotropic scattering problem with nongray gas in a homogeneous layer. The relative simplicity results from use of a modified two flux approximation, expansion of the solution in terms of a backscattering parameter and asymptotic matching of the resulting solution to exact two flux results. The method has the advantage that it can be used to treat nonhomogeneous layers and makes use of relatively simple nongray gas model.

Analysis

The equation of transfer for a homogeneous cloud layer can be written in monochromatic form as

$$\mu \frac{dI}{d\tau} = -I + (1-a)I_b + \frac{a}{2}\int_{-1}^{1} I(\tau_1 \mu')p(\mu_1 \mu')d\mu' \qquad (1)$$

where: τ is the optical depth, a is the single scattering albedo (ratio of scattering to extinction coefficient), $p(\mu, \mu')$ is the scattering phase function and I_b is the monochromatic blackbody intensity at the cloud temperature. The boundary conditions to be applied in the infrared are isotropic incidence at the base, zero incidence at the top, i.e.,

$$\begin{aligned} I(0, \mu) &= I_B \quad \mu > 0 \\ I(\tau_0, \mu) &= 0 \quad \mu < 0 \end{aligned} \qquad (2)$$

Following Chandrasekhar, the phase function is expanded in Legendre polynomials $P_m(\mu)$ as

$$p(\mu_1 \mu') = \sum_m \tilde{\omega}_m P_m(\mu) P_m(\mu') \qquad (3)$$

where the coefficients are obtained from

$$\int_{-1}^{1} p(\mu)\mu^n d\mu = \int_{-1}^{1} \sum_m \tilde{\omega}_m P_m(\mu)\mu^n d\mu$$

Using (3), the zeroth and first moments of the equation of transfer (1) are taken and the resulting integrals are written in Gaussian quadrature form as

$$\frac{d}{d\tau}\left[\sum_i C_i \mu_i I(\tau, \mu_i)\right] = -\sum_i C_i I(\tau, \mu_i) + 2(1-a)I_b + a\tilde{\omega}_0 \sum_i C_i I(\tau, \mu_i) \qquad (4)$$

$$\frac{d}{d\tau}\left[\sum_i C_i \mu_i^2 I(\tau, \mu_i)\right] = -\sum_i C_i \mu_i I(\tau, \mu_i) + \frac{a\tilde{\omega}_1}{3}\sum_i C_i \mu_i I(\tau_1 \mu_i)$$

[1] Presently NAS-NRC Resident Research Associate at Goddard Institute for Space Studies, NASA, New York, N. Y.

[2] Numbers in brackets designate References at end of paper.

Contributed by the Heat Transfer Division of THE AMERICAN SOCIETY OF MECHANICAL ENGINEERS and presented at the ASME-AIChE Heat Transfer Conference, Atlanta, Ga., August 5-8, 1973. Revised manuscript received by the Heat Transfer Division, October 15, 1973. Paper No. 73-HT-9.

For the first approximation, $i = \pm 1$, $c_{\pm 1} = 1$, $\mu_{\pm 1} = \pm 1/\sqrt{3}$, the two equations (4) can be combined to yield;

$$\frac{1}{\sqrt{3}}\frac{dI^+}{d\tau} = -I^+ + (1-a)I_b + a(1-b)I^- + abI^-$$

$$-\frac{1}{\sqrt{3}}\frac{dI^-}{d\tau} = -I^- + (1-a)I_b + a(1-b)I^- + abI^+ \quad (5)$$

where

$$I^+ = I(\tau, 1/\sqrt{3}),\ I^- = I(\tau, -1/\sqrt{3}),\ \tilde{\omega}_0 = 1$$

$$b = \frac{1}{2}\left(1 - \frac{\tilde{\omega}_1}{3}\right) = \frac{1}{2}\left(1 - \frac{1}{2}\int_{-1}^{1} p(\mu)\mu d\mu\right)$$

The equations (5) derived in the foregoing correspond to the modified two flux equations of Sagan and Pollack [7], who obtained the same equations (without emission) through inference from the exact solution of Piotrowski [8]. Sagan and Pollack [7] as well as Irvine [9] have compared the solution of equations (5) with exact solutions. Sagan and Pollack [7] report that for strongly forward scattering ($b = 0.15$) and $8 \leq \tau_0 \leq 32$ the results for reflectance are good to better than 5 percent for conservative scattering.

It is to be noted that although equations (5) can be easily solved for the monochromatic or gray cases, the inclusion of nongray gas absorption causes difficulty in frequency integration. The nongray gas absorption coefficient appears in both the optical thickness and in the denominator of the single scattering albedo, a. In order to make use of nongray gas band models, the absorption coefficient must appear in the solution in the form of transmittance or in a form obtainable from the transmittance. This form can be obtained by noting that for clouds in the infrared the parameter b is quite small and by obtaining a perturbation solution in b.

For small b, the intensities can be expanded as

$$I^+(\tau;b) = I_0^+(\tau) + bI_1^+(\tau) + \ldots$$

$$I^-(\tau;b) = I_0^-(\tau) + bI_1^-(\tau) + \ldots \quad (6)$$

Substitution into (5) yields the following sets of equations

$$\frac{1}{\sqrt{3}}\frac{dI_0^+}{d\tau} = -(1-a)I_0^+ + (1-a)I_b$$

$$-\frac{1}{\sqrt{3}}\frac{dI_0^-}{d\tau} = -(1-a)I_0^- + (1-a)I_b$$

$$\pm\frac{1}{\sqrt{3}}\frac{dI_i^\pm}{d\tau} = -(1-a)I_i^\pm - a(I_{i-1}^\pm - I_{i-1}^\pm);\ i = 1,\ldots,n. \quad (7)$$

The boundary conditions (2) become

$$I_0^+(0) = I_B,\ I_i^+(0) = 0;\ i = 1,\ldots,n.$$

$$I_i^-(\tau_0),\ i = 0,\ldots,n \quad (8)$$

These equations (7) are not necessary in the case of homogeneous layers since the exact solution (5) can be expanded for small b. However, for the nonhomogeneous case, where exact solutions may be impossible, equation (7) can yield relatively simple solution. The solutions of (7) and (8) in the form of zeroth and first order net flux are obtained as follows:

$$F = \frac{2\pi}{\sqrt{3}}(I^+ - I^-) = F_0 + bF_1$$

$$F_0 = \frac{2\pi}{\sqrt{3}}\left[I_B e^{-\sqrt{3}K_a z} + I_b\left(e^{-\sqrt{3}K_a(z_0 - z)} - e^{-\sqrt{3}K_a z}\right)\right]$$

$$F_1 = \frac{2\pi}{\sqrt{3}}\left\{\sqrt{3}\gamma I_b\left[z e^{-\sqrt{3}K_a z} - (z_0 - z)e^{-\sqrt{3}K_a(z_0 - z)}\right] - \sqrt{3}\gamma z I_B e^{-\sqrt{3}K_a z}\right.$$

$$+\frac{1}{2}\frac{\gamma}{K_a} I_b\left[e^{-\sqrt{3}K_a(z_0+z)} - e^{-\sqrt{3}K_a(z_0 - z)} + e^{-\sqrt{3}K_a z} - e^{-\sqrt{3}K_a(2z_0 - z)}\right]$$

$$\left. -\frac{1}{2}\frac{\gamma}{K_a} I_B\left[e^{-\sqrt{3}K_a z} - e^{-\sqrt{3}K_a(2z_0 - z)}\right]\right\} \quad (9)$$

where γ = scattering coefficient, $K_a = K_p + K_g$, K_p = absorption coefficient of particles, K_g = absorption coefficient of gas, z = distance from cloud base.

Due to the Gaussian quadrature approximation used here the transmittance and reflectance must be defined as the ratios of net transmitted and reflected fluxes to flux transmitted through a nonparticipating medium ($\gamma = K_a = 0$).

$$T = e^{-\sqrt{3}K_a z_0} - b(\sqrt{3}\gamma z_0 e^{-\sqrt{3}K_a z_0})$$

$$R = b\frac{1}{2}\frac{\gamma}{K_a}(1 - e^{-2\sqrt{3}K_a z_0}) \quad (10)$$

The emittance is defined as the ratio of the emitted flux to that emitted if ($K_a \to \infty$), i.e.,

$$E = 1 - e^{-\sqrt{3}K_a z_0} - b\left[\frac{1}{2}\frac{\gamma}{K_a}(1 - e^{-2\sqrt{3}K_a z_0}) - \sqrt{3}\gamma z_0 e^{-\sqrt{3}K_a z_0}\right] \quad (11)$$

Clearly, these definitions satisfy conservation of energy and Kirchoff's law at least to order b. Problems associated with the perturbation solution arise for the conservative case with large optical thickness, i.e., $K_a \to 0$,

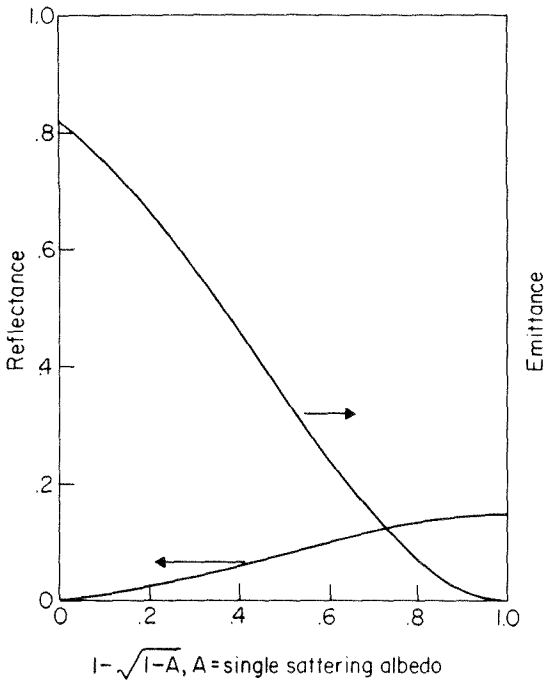

Fig. 1(a) Comparison of modified two flux(0) and present method (+) for asymmetry factor = 0.8, Tauo = 1.00, A = single scattering albedo

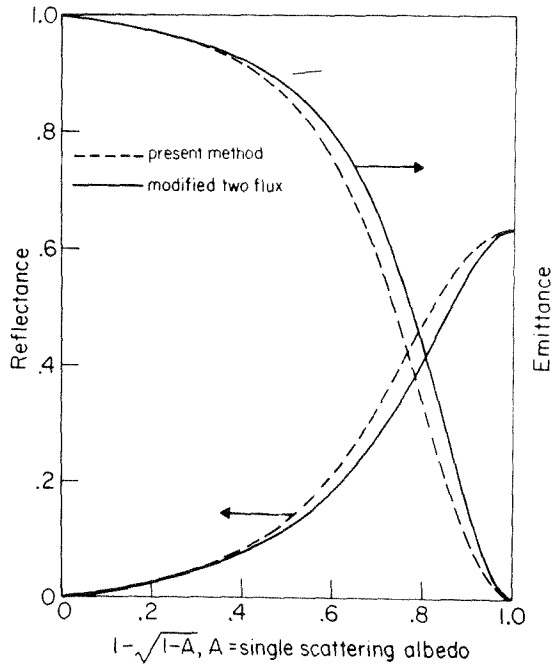

Fig. 1(b) Comparison of modified two flux (0) and present method (+) for asymmetry factor = 0.8, Tauo = 10.0, A = single scattering albedo

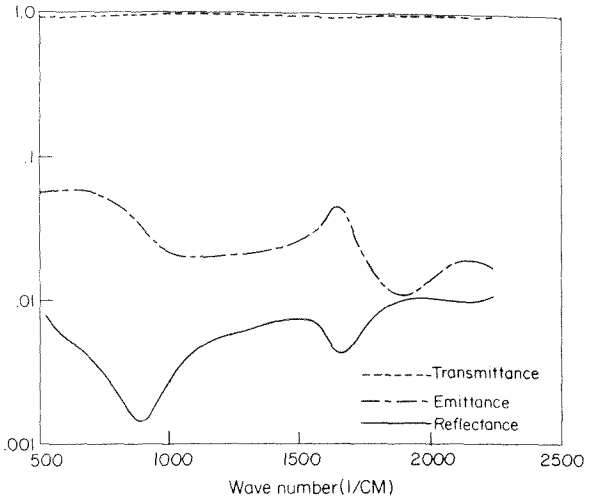

Fig. 2*(a)* Emissivity *(E)*, transmissivity *(T)*, and reflectivity *(R)* for high water cloud. $T = -15c$, $p = 550MB$, vapor density = 0.0GM/M + 3 cloud thickness = 2M, effective radius = 5, effective variance = 0.15. .

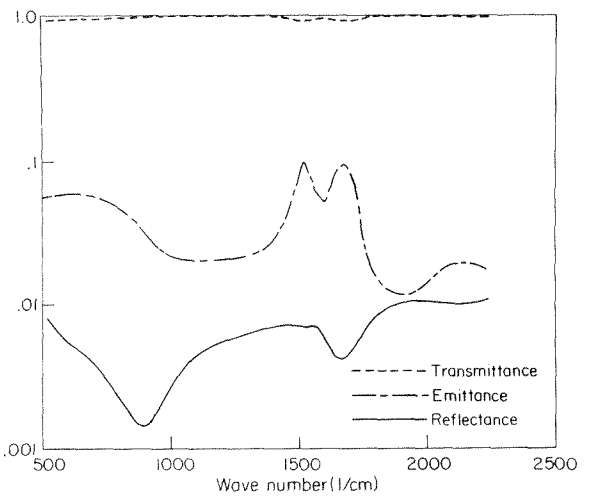

Fig. 2*(b)* Emissivity *(E)*, transmissivity *(T)*, and reflectivity *(R)* for high water cloud. $T = -15c$, $p = 550MB$, vapor density = 1.1605GM/M^3, cloud thickness = 2M, effective radius = 5, effective variance = 0.15.

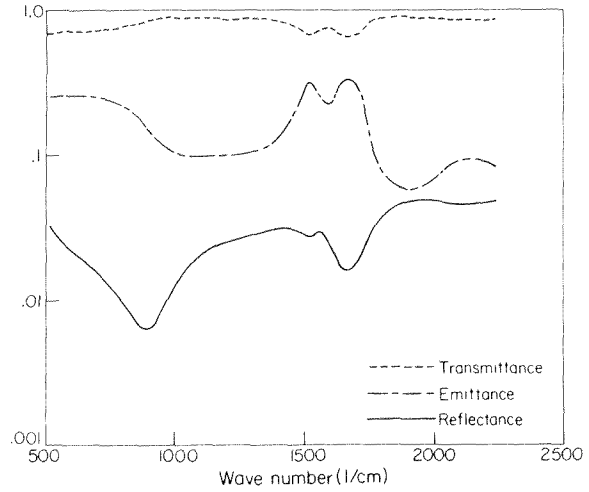

Fig. 2*(c)* Emissivity *(E)*, transmissivity *(T)*, and reflectivity *(R)* for high water cloud. $T = -15c$, $P = 550MB$, vapor density = 1.605GM/M + 3, cloud thickness = 10M, effective radius = 5, effective variance = 0.15.

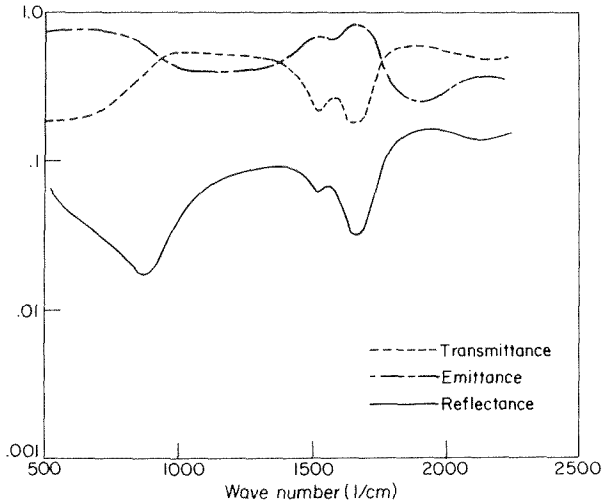

Fig. 2*(d)* Emissivity *(E)*, transmissivity *(T)*, and reflectivity (R) for high water cloud. $T = -15c$, $p = 550MB$, vapor density = 1.605GM/M + 3, cloud thickness = 50M, effective variance = 0.15.

$$T = 1 - b\sqrt{3}\gamma z_0$$

where the solution diverges. However, this problem can be avoided by noting that the exact solution of (5) for transmittance in the conservative case is

$$T = \frac{1}{1 + \sqrt{3}b\gamma z_0} \tag{12}$$

An approximation using the first two terms of the perturbation solution which yields (12) in the conservative case is

$$F = \frac{F_0}{1 - b\dfrac{F_1}{F_0}} \tag{13}$$

For the case ($a \to 1$) expansion of both the exact solution of equation (5) and the approximation, equation (13), in $(1 - a)$ yields agreement through terms of order τ_0. The approximation is thus strictly valid for $\tau_0 < 1$, all values of a, and $b < 1$, but may be applied for $\tau_0 \approx 10$ with reasonable results as will be shown.

It is seen that the absorption coefficient appears in the perturbation solution (9) in the form of gas transmittance or transmittance divided by absorption coefficient. The frequency integration of both these forms are obtainable from band models for nongray gases, assuming I_B, I_b and the scattering and absorption coefficients of the cloud drops do not vary within the frequency interval.

Using an upper bar to denote integration over a small frequency internal (13) may be written in terms of frequency integrals of equations (9) as

$$\bar{F} = \frac{\bar{F}_0}{1 - b\dfrac{\bar{F}_1}{\bar{F}_0}} \tag{14}$$

This approximation of the frequency integration of flux is valid under the same conditions as those for equation (13). The band emittance, reflectance and transmittance can now be calculated using narrow band models [10] or wide band models [11] for nongray gas absorptance.

Since the scattering coefficient and the absorption coefficient of the scatterers are slowly varying functions of frequency when averaged over size distribution, the only frequency integrals required are for transmittance and forms involving transmittance and reciprocals of absorption coefficient. These can be obtained in closed form by using the narrow band model of Malkmus [10] for nongray gases:

$$\frac{1}{\Delta\nu}\int_{\Delta\nu} e^{-K_g y}d\nu = e^{-2\frac{b}{d}\left[\sqrt{1+\frac{s}{b}y}-1\right]} \tag{15}$$

where K_g is the gas absorption coefficient, and s, b, d are the average line intensity, half width, spacing respectively. Equation (15) yields the same form as Goody's random model for large and

small optical thickness. The other frequency integration which arises when (9) is used in (14) is

$$\frac{1}{\Delta\nu}\int_{\Delta\nu}\frac{1-e^{-(K_p+K_\ell)y}}{K_p+K_y}\,d\nu = \frac{1}{K_p}[1-e^{-K_p y}e^{-A(y)}] + \frac{\sqrt{\pi}}{K_p}Be^{c^2}[\mathrm{erf}(c)-\mathrm{erf}(D)]$$

$$A(y) = 2\frac{b}{d}\left[\sqrt{1+\frac{s}{b}y}-1\right],\quad B = \frac{\sqrt{s\,b}}{\bar{d}\,\bar{d}\sqrt{K_p}},\quad C = \left[1+\frac{K_p}{s/d}\right]B$$

$$D = C + \frac{A(y)}{B} \tag{16}$$

Results and Discussions

In order to assess the accuracy of the present method, comparisons were made between equation (13) and the exact solution of the modified two flux equations (5). These comparisons are shown in Figs. 1*(a)* and 1*(b)*. Emittance and reflectance are plotted as a function of $1-\sqrt{1-a}$, where a is the single scattering albedo, for optical thickness of 1.00 (Fig. 1*(a)*) and 10.0 (Fig. 1*(b)*) and an assymetry factor of 0.8 ($b = 0.10$). For an optical thickness of 1.00, it is seen that the present method is in excellent agreement with the exact modified two flux throughout the range of albedo. For optical thickness of 10.0, it is seen that the present method, while having the correct shapes, underestimates the emittance by 30 percent for small values of emittance. However, for single scattering albedo less than about 0.75 or approaching 1.0, the agreement is excellent. For both cases, Kirchoff's law and conservation of energy were satisfied nearly exactly by the present method.

The approximate method presented here has been used to calculate the radiation properties of supercooled water clouds including the nongray effects of water vapor absorption. The results have been obtained for various cloud thicknesses and effective droplet radii of 5 and 10 microns. All of the droplet properties, scattering and absorption coefficient and asymmetry factor, were calculated using a Mie scattering program furnished by Dr. J. E. Hansen and described in reference [3]. The droplet size distribution was taken to be

$$N(R) = \text{constant}\ R^{(1-3B)/B}e^{-R/AB} \tag{17}$$

where A is the mean effective radius and B is the effective variance as defined in [3]. This size distribution is a good fit to observation [12]. The water vapor absorption data were obtained from Elsasser and Culbertson [13].

Figs. 2*(a)*, 2*(b)*, 2*(c)*, and 2*(d)* show the emissivity, reflectivity, and transmissivity for various cloud thicknesses with a droplet number density of 300 cm^{-3}, mean effective radius of 5 microns

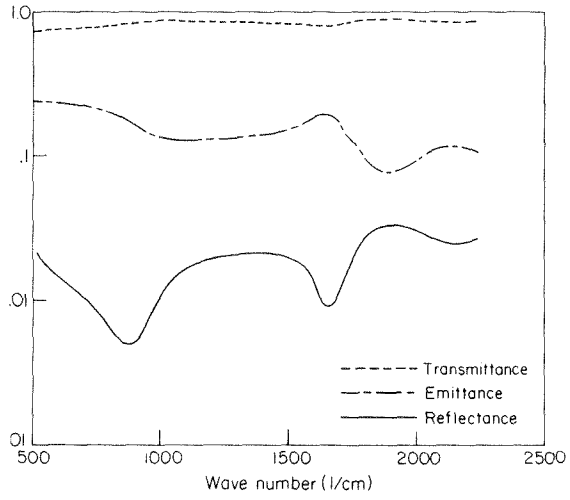

Fig. 3*(a)* Emissivity *(E)*, transmissivity *(T)*, and reflectivity *(R)* for high water cloud. $T = -15c$, $p = 550MB$, vapor density = 0.0GM/M + 3, cloud thickness = 2M, effective radius = 10, effective variance = 0.15.

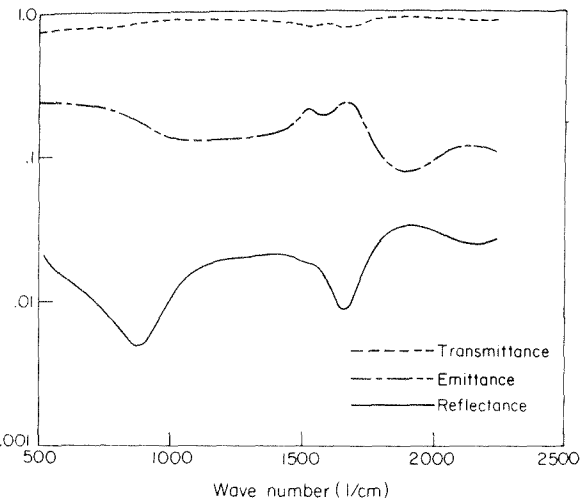

Fig. 3*(b)* Emissivity *(E)*, transmissivity *(T)*, and reflectivity *(R)* for high water cloud. $T = -15c$, $p = 550MB$, vapor density = 1.605GM/M + 3, cloud thickness = 2M, effective radius = 10, effective variance = 0.15.

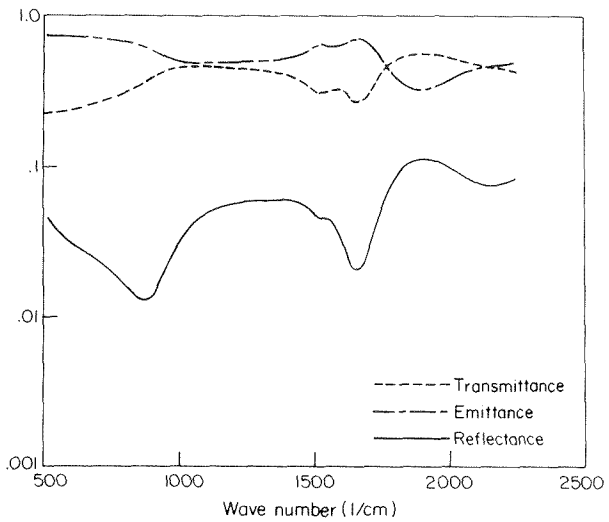

Fig. 3*(c)* Emissivity *(E)*, transmissivity *(T)*, and reflectivity *(R)* for high water cloud. $T = -15c$, $p = 550MB$, vapor density = 1.605GM/M + 3, cloud thickness = 10, effective variance = 0.15.

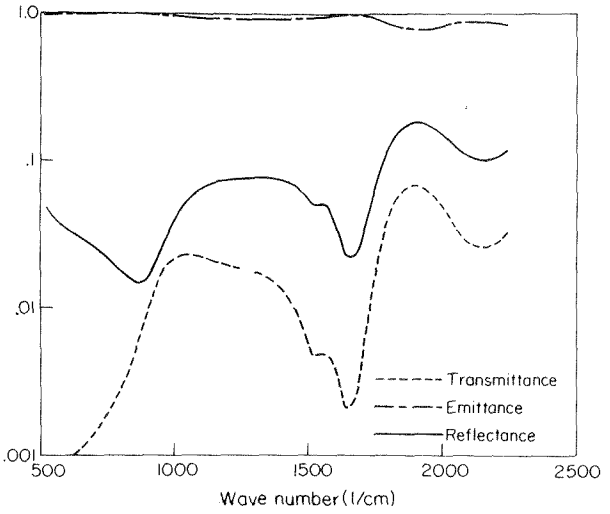

Fig. 3*(d)* Emissivity *(E)*, transmissivity *(T)*, and reflectivity *(R)* for high water cloud. $T = -15c$, $p = 550MB$, vapor density = 1.605GM/M + 3, cloud thickness = 50M, effective radius = 10, effective variance = 0.15.

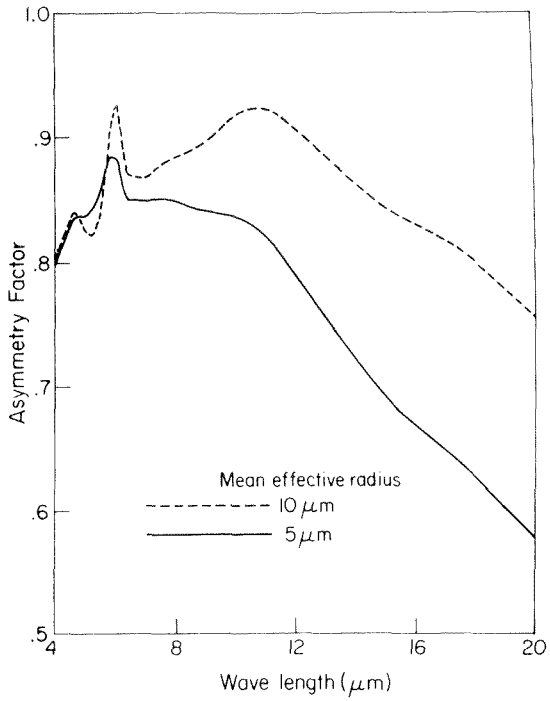

Fig. 4(a) Asymmetry factor for high water clouds. Lower curve for mean effective radius of 5 microns, upper curve for mean effective radius of 10 microns.

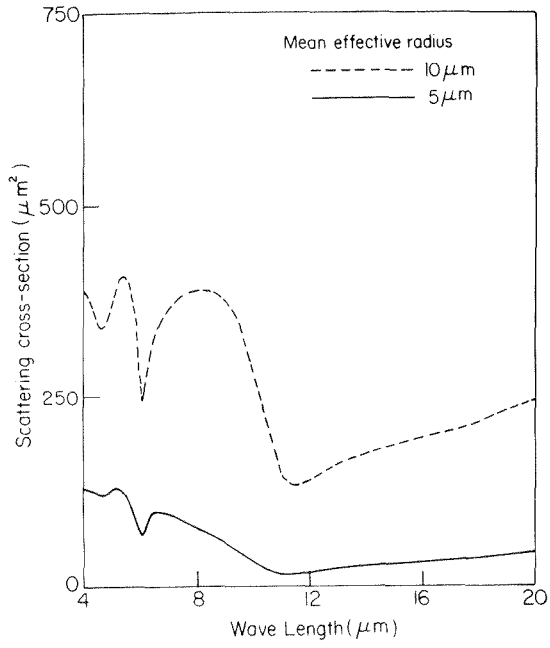

Fig. 4(b) Scattering cross section in (microns) 2 for high water clouds. Lower curve mean effective radius 5 microns, upper curve mean effective radius of 10 microns.

and an effective variance of 0.15. Fig. 2(a) is for a cloud of 2 m thickness with no water vapor present. Fig. 2(b) is the same thickness but with water vapor density taken at the saturation value. The effect of the 6.3 micron (1595 cm^{-1}) water vapor absorption band is quite pronounced resulting in an increased emissivity and decreased transmissivity and reflectivity. As the cloud becomes thicker to 10 m (Fig. 2(c)) and to 50 m (Fig. 2(d)), the emissivity and reflectivity increase while the transmissivity decreases. The effect of the nongray gas on reflectivity and emissivity becomes greater as the thickness increases. All curves show good qualitative agreement with Yamamoto, et al. [4].

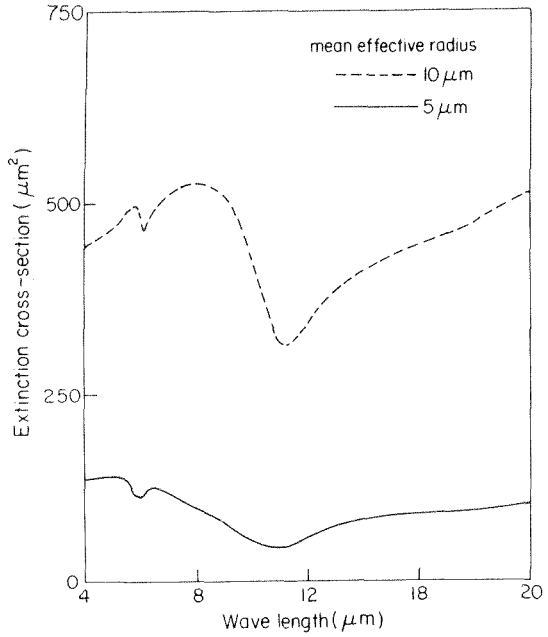

Fig. 4(c) Extinction cross section in (microns) 2 for high water clouds. Lower curve mean effective radius 5 microns, upper curve mean effective radius of 10 microns.

Figs. 3(a), 3(b), 3(c), and 3(d) show the radiation properties of a typical high altitude cloud with drops of mean effective radius of 10 microns and an effective variance of 0.15. The number density was held fixed at 300 cm^{-3}. Comparison of Fig. 3(a) (without water vapor absorption) with Fig. 3(b) (with water vapor) shows the effect of water vapor absorption is much smaller for this case than for the case of mean effective radius of 5 microns. This is to be expected since for the 10 micron mean radius case, the droplet scattering and absorption should be more important. For the most part, the 10 micron mean effective radius case yielded larger values of emissivity and reflectivity than the 5 micron radius case for any given cloud thickness. Again the present results agree qualitatively with those obtained by Yamamoto, et al. [4].

As in the gray case of Figs. 1(a) and 1(b), both Kirchoff's law and conservation of energy were very closely satisfied throughout the range of frequencies. This would imply that the present method is a good approximations which is simple enough to use in calculations of atmospheric heat transfer problems. The authors are presently extending the calculations to the case of ice clouds and into the near infrared and visible portion of the spectrum.

Figs. 4(a), 4(b), and 4(c) show the asymmetry factor, scattering cross section and extinction cross section of the drops as a function of wave length. The lower curves are for the 5 micron mean effective radius case; the upper curves are for the 10 micron mean effective radius case. The back-scattering parameter b can be obtained as a function of wave length from the asymmetry factor by $b = 1/2$ (1-asymmetry factor).

In order to check the accuracy of the approximation in the nongray case, the absorption coefficient distribution function method [14] or the inverse transmission function method [15] was employed to carry out the narrow band frequency integration. Using this method, the exact solution of the modified two flux equations can be integrated over frequency using the absorption coefficient as the variable of integration together with an appropriate kernel function. The kernel for the Malkmus model was obtained in [15] using the inverse Laplace transform of the transmission function. The frequency integration can be written in the following form:

$$\frac{1}{\Delta\nu}\int_{\Delta\nu} A(K_g(\nu))d\nu = \int_0^\infty A(K_g)\,f(K_g)\,dK_g \qquad (18)$$

where $A(K_g(\nu))$ is the transmittance, reflectance or emittance obtained from the exact solution of equations (5). The kernel $f(K_g)$

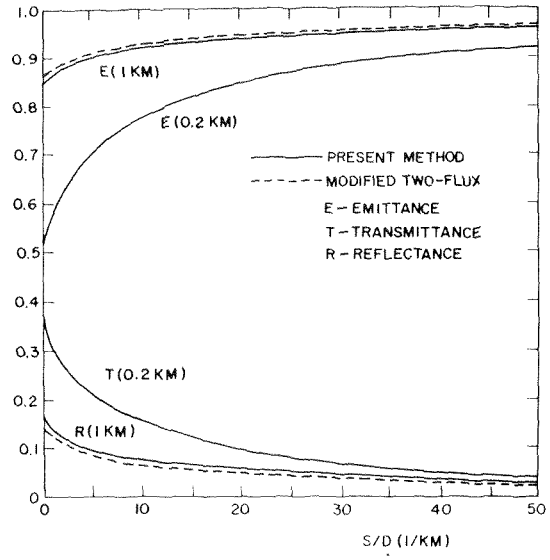

Fig. 5 Emittance, reflectance and transmittance from exact solution of modified two flux equations and present approximation; back scattering parameter b = 0.10, particle scattering = 8 km^{-1}, particle absorption k_p = 2 Km^{-1}, average line half width to spacing ratio = 0.10 cloud thickness of 0.2 km and 1 km.

is given by

$$f(K_g) = \sqrt{\frac{sb}{4d}}^2 \frac{1}{K^{3/2}} e^{\pi/4\, b/d(2-(K/s/d)-(s/d/K))} \qquad (19)$$

The results of the application of equation (18) are shown in Fig. 5 together with the results from the present approximation. The emittance, reflectance and transmittance are plotted for 1 km and 0.2 km thicknesses as functions of s/d, the average line intensity to spacing ratio. The line half-width to spacing ratio was set at 0.10, the particle scattering and absorption coefficients were set at 8 km^{-1} an 2 km^{-1}. These values of the fixed parameters correspond approximately to those used in the cloud calculations. Excellent agreement between the two methods is seen to exist.

Acknowledgments

The authors would like to thank Dr. J. E. Hansen for his interest and help in the Mie Scattering Calculations. The authors would also like to acknowledge the support of NASA grant NGL 33-008-012.

References

1 Van de Hulst, H. C., "Multiple Scattering in Planetary Atmospheres," *J. of Quant. Spectrosc. Radiat. Transfer*, Vol. 11, 1971, pp. 785–795.

2 Yamamoto, G., Tanaka, M., and Kamitani, K., "Radiative Transfer in Water Clouds in the 10-Micron Window Region," *J. of the Atmospheric Sciences*, Vol. 23, 1966, pp. 305–313.

3 Hansen, J. E., "Multiple Scattering of Polarized Light in Planetary Atmosphere. Part II. Sunlight Reflected by Terrestrial Water Clouds," *Journal of Atmospheric Sciences*, Vol. 28, 1971, pp. 1400–1426.

4 Yamamoto, G., Tanaka, M., and Asano, S., "Radiative Transfer in Water Clouds in the Infrared Region," *Journal of the Atmospheric Sciences*, Vol. 27, 1970, pp. 282–292.

5 Yamamoto, G., Tanaka, M., and Asano, S., "Radiative Heat Transfer in Water Clouds by Infrared Radiation," *Journal of Quant. Spectrosc. Radiat. Transfer*, Vol. 11, 1971, pp. 697–708.

6 Zdunkowski, W. G., and Crandall, W. K., "Radiative Transfer of Infrared Radiation in Model Clouds," *Tellus*, Vol. 23, 1971, pp. 517–527.

7 Sagan, C., and Pollack, J. B., "Anistropic Nonconservative Scattering and the Clouds of Venus," *Journal of Geophysical Research*, Vol. 72, 1967, pp. 469–477.

8 Piotrowski, S., "Asympotic Case of the Diffusion of Light Through an Optically Thick Scattering Layer," *Acta Astron.*, Vol. 6, 1956, pp. 61–73.

9 Irvine, W. M., and Pollack, J. B., "Infrared Optical Properties of Water and Ice Spheres," *ICARUS*, Vol. 8, 1968, pp. 324–360.

10 Malkmus, W., "Random Lorentz Band Model With Expotential—Tailed S^{-1} Line Intensity Distribution Function," *Journal of the Optical Society of America*," Vol. 57, No. 3, pp. 323–329.

11 Tien, C. L., "Thermal Radiation Properties of Gases," *Advances in Heat Transfer*, Vol. 5, Academic Press, New York, 1968.

12 Diem, M., "Messungen der Grösse von Wolkenelementen II," *Meteor. Rund.*, Vol. 1, 1948, pp. 261–273.

13 Elsasser, W. M., and Culbertson, M. F., "Atmospheric Radiation Tables," *Meteor. Monographs*, Am. Meteor. Soc., Vol. 4, No. 23, 1960, pp. 1–43.

14 Arking, A., and Grossman, K., "The Influence of Line Shape and Band Structure on Temperatures in Planetary Atmospheres," *Journal of the Atmospheric Sciences*, Vol. 29, 1972, p. 937.

15 Domoto, G. A., "Frequency Integration for Radiative Transfer Problems Involving Homogeneous Non-Gray Gases—The Inverse Transmission Function," Submitted for publication to *Journal of Quantitative Spectroscopy and Radiative Transfer*.

R. E. Chupp
Detroit Diesel Allison,
Division of General Motors Corp.,
Indianapolis, Ind.

R. Viskanta
School of Mechanical Engineering,
Purdue University,
Lafayette, Ind.
Mem. ASME

Development and Evaluation of a Remote Sensing Technique for Determining the Temperature Distribution in Semitransparent Solids

A technique is presented for recovering the temperature profile in semitransparent solids from remotely sensed spectral emission data. The temperature distribution is determined by iteratively solving the equation governing the emerging spectral emission to recover the profile to best match the emission data. The technique is evaluated using both analytical and experimental emission data. Analytical results show the effect of data error, number of data points, method of representing the temperature profile, and optical thickness range. The method is verified experimentally using Corning Code 7940 fused quartz by comparing recovered temperature profiles with those predicted by a combined conduction-radiation heat-transfer analysis.

Introduction

Many applications are encountered in applied physics and engineering where it is necessary to measure the temperature distribution within a semitransparent material at high temperature. Examples of such materials are combustion products in a combustion chamber or afterburner, glass when solid or molten, crystals, plasmas, etc. It is difficult to measure the temperature distribution in such materials. Probes cannot be readily used because they distort and disturb the temperature and radiation fields, and can produce erroneous results. Also, probes must be specially designed for high temperature applications to keep them from melting; e.g., pulsating thermocouples for combustion applications. An alternate approach is to remotely measure the radiation field emerging from the medium and recover the temperature distribution from these data. This is possible because the emerging radiation field from a semitransparent medium is a function of the temperature distribution. For the limiting case of opaque materials, the remote sensing approach reduces to conventional pyrometry and only a surface temperature is recovered.

Thermal remote sensing specifically involves using a spectral sensor (spectrometer or monochrometer with detector, radiometer with filters, etc.) to measure the natural emission of semitransparent media and then employing an inversion technique to recover the temperature profile. This approach is referred to as thermal remote sensing, inversion, spectral scanning, etc. It is attractive because: (1) the measurement technique is nondestructive since probes are not introduced, (2) distortion of the measurement field by a detector is absent, (3) the medium is not exposed to a field of external electromagnetic radiation, i.e., measurement is passive type, and (4) measurements need not be made in the immediate vicinity of the medium providing the effect of the intervening media is included. Limitations of the method are detector sensitivity, spectral resolution and noise level. Also, inversion is inherently unstable and measurement errors can be amplified.

During the last fifteen years, an extensive effort has been devoted to developing remote sensing techniques. This work has been primarily for gaseous radiation sources such as planetary and stellar atmospheres, plasmas, exhaust plumes, etc. Wang [1][1] has reviewed this work. Until recently, only two attempts [2, 3] had been reported where remote sensing techniques have been applied to solids. For this reason, an inversion procedure was developed and evaluated which is applicable primarily to condensed phases. The method is as general as possible with options to include *a priori* information about the temperature profile if desired. The development and analytical evaluation of the procedurg has been reported previously [4]. The technique has also been evaluated experimentally using Corning Code 7940 fused

Contributed by the Heat Transfer Division for publication in the JOURNAL OF HEAT TRANSFER. Manuscript received by the Heat Transfer Division, January 22, 1974.

[1] Numbers in brackets designate References at end of paper.

quartz glass samples. Recovered temperature profiles for the samples were compared with those predicted using a combined conduction-radiation heat transfer analysis to verify the technique. A brief description of the technique, numerical results, experiment, and verification results is given in this paper. A detailed discussion is given elsewhere [5].

Inversion Analysis

Physical Model and Assumptions. The physical situation in an inversion problem is so involved that it is difficult to discuss the technique without applying it to a real system using some of the physical laws and geometry of the system. To illustrate the method, a plane layer of semitransparent solid is considered with one side bounded by an opaque material. Fig. 1 shows a schematic diagram of the physical model and coordinate system. The solid is assumed to be isotropic and homogeneous and to emit but not scatter thermal radiation. Coherence effects are neglected which implies that the thickness L of the material is much greater than the wavelength of radiation. Refraction of radiation within the solid due to variations of refractive index with temperature is neglected. The solid is taken to be in local thermodynamic equilibrium. Hence, Kirchhoff's and Planck's laws appropriately describe emission of radiation from the solid. These assumptions are valid for solid materials such as glass.

The spectral intensity of radiation $I_\nu^-(0, \mu')$ emerging from the layer as shown in Fig. 1 can be evaluated if the intensity just inside the material at the back face $I_\nu^-(L, \mu)$ is known. If the refractive index n of the material is much different from the surrounding material, the effect of reflection and refraction at each interface must be accounted for in $I_\nu^-(L, \mu)$. Accordingly, it is assumed that all interfaces are optically smooth and reflect specularly. Thus, Fresnel's equations of classical electromagnetic theory appropriately describe transmission and reflection of radiation at the interfaces and the radiation field is axially symmetric. The opaque material which bounds the solid is assumed to be a good conductor having a complex index refraction $\tilde{n}_{2\nu} = n_\nu + ik_\nu$. The conductor serves to define the boundary while minimizing emission from the back face.

Formulation of Problem. For a one-dimensional, nonscattering plane layer having axial symmetry, the spectral intensity $I_\nu(y, \mu)$ defining the radiation field is governed by the equation of transfer

$$\mu \frac{dI_\nu}{dy} = \kappa_\nu[I_{b\nu}(y) - I_\nu(y, \mu)] \tag{1}$$

The solution for equation (1) in the forward and backward directions is

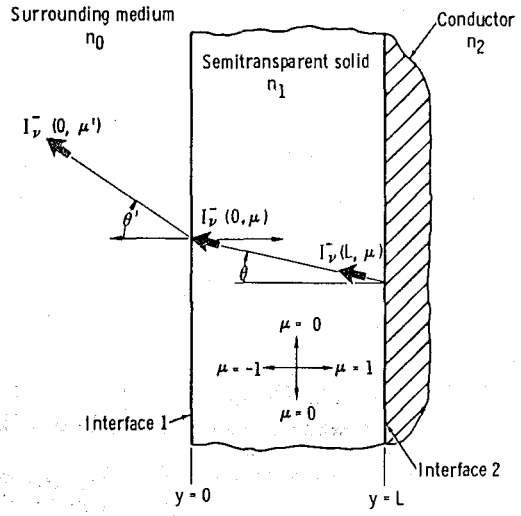

Fig. 1 Physical model and coordinate system

$$I_\nu^+(y, \mu) = I_\nu^+(0, \mu) \exp(-\tau_\nu/\mu) + \int_0^y \kappa_\nu(t) I_{b\nu}(t) \exp\{-[\tau_\nu(y) - \tau_\nu(t)]/\mu\} dt/\mu, \quad 0 < \mu \leq 1 \tag{2}$$

$$I_\nu^-(y, \mu) = I_\nu^-(L, \mu) \exp[(\tau_{0\nu} - \tau_\nu)/\mu] - \int_y^L \kappa_\nu(t) I_{b\nu}(t) \exp\{-[\tau_\nu(y) - \tau_\nu(t)]/\mu\} dt/\mu, \quad -1 \leq \mu < 0 \tag{3}$$

The physical depth y is used in these equations instead of optical depth τ_ν since the temperature varies uniquely with y. The boundary conditions appropriate to equations (2) and (3) are:

$$I_\nu^+(0, \mu) = I_{0\nu}^+(\mu) + \rho_{1\nu}(\mu) I_\nu^-(0, -\mu), \qquad 0 < \mu \leq 1 \tag{4}$$

$$I_\nu^-(L, \mu) = [1 - \rho_{2\nu}(\mu)] I_{b\nu}(T_2) + \rho_{2\nu}(\mu) I_\nu^+(L, -\mu), \qquad -1 \leq \mu < 0 \tag{5}$$

The second term of the right-hand side of these equations represents the specularly reflected radiation from the opposite direction. The first term in equation (5) is the emitted intensity from the conductor and $I_{0\nu}^+$ in equation (4) accounts for external ra-

Nomenclature

C_j = expansion constant in equation (8)
E_n = exponential integral function
F = local radiative flux defined by equation (10)
G_n = function defined in equation (13) which equals E_n for β_ν, $\rho_{1\nu}$, and $\rho_{2\nu} \neq f(\mu)$
I_ν = spectral intensity of radiation
$I_{b\nu}$ = Planck's function
k = thermal conductivity or imaginary part of complex index of refraction
L = thickness of the layer
n = real part of complex index of refraction
$\tilde{n}$ = complex index of refraction, $\tilde{n} = n + ik$
q = heat flux
T = temperature
t = dummy integration variable
y = depth
β_ν = interreflection function defined as $1/\{[1 - \rho_{1\nu}(\mu)\rho_{2\nu}(\mu)\exp(-2\tau_{0\nu}/|\mu|)]\}$
η_ν = function defined as $I_{b\nu}(T)/I_{b\nu}(T_r)$
Θ = dimensionless temperature, T/T_r
θ = polar angle between the normal to the solid and the direction of pencil of radiation within the solid
θ' = polar angle outside the solid
κ = absorption coefficient
κ_ν^* = dimensionless absorption coefficient $= \kappa_\nu/\kappa_r(T_r)$
λ = wavelength
μ = direction cosine, $\mu = \cos\theta$
ν = frequency
ξ = dimensionless depth, y/L
ρ = reflectivity
τ_ν = optical depth defined as $\int_0^y \kappa_\nu(y')dy'$
$\tau_{0\nu}$ = optical thickness defined as $\int_0^L \kappa(y)dy$
τ_{0r} = reference value for $\tau_{0\nu} = \kappa_r L$
σ = root-mean-square (rms) deviation
ϕ_ν = dimensionless intensity leaving the solid defined as $I_\nu^-(0,\mu')/\{[1 - \rho_{1\nu}(\mu)]I_{b\nu}(T_r)\}$
ψ_j = function defined in equation (8)

Subscripts

r = refers to reference value
0 = refers to surrounding medium
1 = refers to semitransparent solid or front surface
2 = refers to opaque material or back surface
λ = wavelength
ν = frequency

Superscripts

$+$ = forward (positive μ) direction
$-$ = backward (negative μ) direction

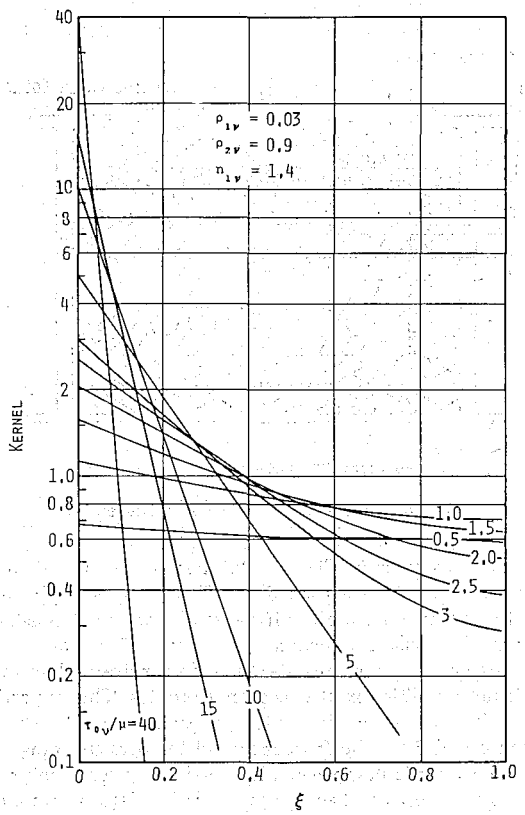

Fig. 2 Typical variation of the kernel in equation (7) with dimensionless depth (ξ) and optical thickness ($\tau_{0\nu}/\mu$)

diation incident on the material. The directional reflectivities $\rho_{1\nu}$ and $\rho_{2\nu}$ are for radiation incident on the interfaces from inside the solid and they vary with μ.

Equations (2) through (5) can be solved [5] to give the intensity incident on interface 1 from inside $I_\nu^-(0, \mu)$. An energy balance on this interface shows that the emerging intensity $I_\nu^-(0, \mu')$ is related to the intensity just inside the solid by

$$I_\nu^-(0,\mu') = [1 - \rho_{1\nu}(\mu)](n_{0\nu}^2/n_{1\nu}^2)I_\nu^-(0,\mu) \qquad (6)$$

Combining this equation with that for $I_\nu^-(0, \mu)$, ignoring any external radiation, and introducing dimensionless variables gives

$$\phi_\nu(\mu') = \beta_\nu(\tau_{0\nu}, -\mu)\{[1-\rho_{2\nu}(\mu)]\eta_\nu(1)e^{\tau_{0\nu}/\mu} - \tau_{0\nu}\int_0^1 \eta_\nu(\xi)[e^{\tau_\nu/\mu} + \rho_{2\nu}(\mu)e^{(2\tau_{0\nu}-\tau_\nu)/\mu}]\kappa_\nu^*(\xi)d\xi/\mu\},$$
$$-1 \le \mu < 0 \qquad (7)$$

The dimensionless absorption coefficient κ_ν^* varies with ξ since it is a function of both temperature and frequency. The direction cosines μ and μ' are related by Snell's law of refraction, $n_{1\nu}\sin\theta = n_{0\nu}\sin\theta'$.

Equation (7) is the primary equation considered in the inversion analysis. It is a nonlinear, inhomogeneous Fredholm integral equation of the first kind. Assuming that κ_ν^* and n_ν are known functions and ϕ_ν is known within experimental error, the problem is to recover the temperature distribution $\theta(\xi)$ between $\xi = 0$ and 1. Specifically, find $\theta(\xi)$ given N observations (within experimental error) of the emerging intensity ϕ_ν for N independent conditions (at frequencies $\nu_1, \nu_2, \ldots \nu_N$ and corresponding directions $\mu_1, \mu_2, \ldots, \mu_N$) assuming $\kappa_\nu^*(\theta)$ is known.

To show qualitatively how $\theta(\xi)$ is recovered from equation (7), the characteristics of the kernel in this equation should be understood. Fig. 2 shows a typical plot of the kernel versus ξ with $\tau_{0\nu}/\mu$ being a parameter. It reveals that the kernel drops sharply with increasing ξ for $\tau_{0\nu}/\mu > 1.5$, while being nearly constant for $\tau_{0\nu}/\mu < 0.5$, i.e., the solid acts as if it were optically thin. The kernel must vary differently with ξ for each emission data point for the measurements to be independent. Thus, only one data point is necessary for $\tau_{0\nu}/\mu < 0.5$. Also, only a few data points having large $\tau_{0\nu}/\mu$ are needed because the kernel decreases so rapidly with ξ that such data only affect the temperature profile near the front surface. Results will be presented later to indicate an optimum $\tau_{0\nu}/\mu$ range for which to sample emission data.

Method of Inversion. There are difficulties associated with inversion. For example, inversion of a Fredholm integral equation such as equation (7) encounters problems of instability, nonuniqueness, ill conditioning and finite measurements. Many investigators have pointed out that inversion methods are inherently unstable and that input errors tend to produce greatly amplified output errors [6–9]. The errors arising in inversion are primarily of four types: (1) imprecise measure of the emitted radiation, (2) imperfect models for the spectral absorption coefficient, (3) computational errors due to inversion, and (4) errors due to the limited set of measured values of $\phi_\nu(\mu')$. Inversion tends to amplify these errors and mathematical procedures such as linear [8], nonlinear [9], statistical [10], quasilinearization [11], relaxation [12], smoothing, [13], and others [14] have been developed to overcome these problems. A summary of these studies is given by Wang [1].

In an attempt to overcome some of the difficulties discussed, a nonlinear optimization procedure has been adopted. This is a general procedure of inversion where Planck's function is not linearized and *a priori* information about the temperature profile can be incorporated, if desired, to reduce the effect of data error. Use of optimization in inversion problems was first employed by Florence [15] and later by Barnett [16]. The procedure developed can be summarized as follows. In an attempt to recover the temperature distribution which best fits the spectral emission data, the integral equation (7) is solved repeatedly with trial (assumed) temperature distributions until the best least squares fit of the emission data is obtained. Two ways are considered for representing the temperature distribution: (1) a discrete set of points $T(\xi_j)$, and (2) a linear combination of given functions, preferably orthogonal, e.g., Legendre polynomials,

$$\theta = T/T_r = \sum_{j=1}^{m} C_j\psi_j(\xi), \quad 0 \le \xi \le 1 \qquad (8)$$

The particular optimization program employed in the analysis is described by Fletcher and Powell [17] and has been applied to many nonlinear problems. This routine can also include inequality constraints which the final solution must satisfy using the procedure developed by Allran and Johnsen [18]. Two possible inequality constraints are: the temperature must vary monotonically through the material or there can only be one extremum in the temperature distribution. Imposing constraints can decrease the calculation time by "guiding" the procedure to an acceptable solution and can improve the results if data error is significant. However, meaningful results can be obtained even if constraints are not imposed.

Both of the methods of representing the temperature distribution have been investigated. The discrete-point approach has the advantage that spacing of the points may be varied within the material to best represent the data, whereas, the linear combination of functions approach requires fewer coefficients because the temperature distribution is expected to be fairly smooth. Details concerning the inversion procedure are given elsewhere [4, 5].

The inversion procedure is programmed for computer solution. Typical runs require about one second per temperature profile on the IBM 370-165 computer.

Numerical Inversion Results

Inversion results were obtained using analytical spectral emission data to verify the inversion technique prior to performing an experiment. The data were generated by assuming a temperature

profile within the material and solving equation (7) by numerical integration for the emergent radiation intensity ϕ_ν in the spectral region of 2.5 to 4.1 μm. Temperature profiles were then recovered from sets of emission data. The technique was evaluated by comparing the recovered temperature profiles with the assumed ones. Results will be summarized in this paper to show how well the technique recover the temperature distribution with exact data, the effect of data error, and the effect of optical thickness range. A detailed discussion is given elsewhere [4, 5].

Exact Emission Data Results. Recovered temperature profile results were obtained using exact emission data for a variety of optical thickness ranges and profile shapes. Recovered discrete-point and polynomial profiles agreed well (within 0.1 percent) with the assumed profiles, thus, validating the technique.

Effect of Data Error. Realistically, there will be error in any experimental emission data considered. To model such data, random error was introduced into the exact analytical emission data. Each data case (containing N points) was perturbed five times, generating five data sets, in order to get representative results. The effect of error in the independent parameters ν and $\tau_{0\nu}/\mu$ was not considered.

Fig. 3 shows typical recovered results with random error (σ = 5 percent) in the emission data for one assumed linear temperature profile. Both discrete-point and polynomial results are given in this figure. The spectral emission data employed consisted of ten equally spaced wavelength points in the spectral region $2.5 \leq \lambda \leq 4.1$ μm. Five recovered profiles are plotted for each case in Fig. 3 corresponding to the five different sets of perturbed emission data. The discrete temperature points in this figure are spaced closer together near $\xi = 0$. This indicates that the resolution of the recovered profiles is better near the front surface which is a result of the way the kernel varies with ξ and $\tau_{0\nu}/\mu$, as shown in Fig. 2.

The errors listed in Fig. 3 are overall rms errors for the five profiles. The error for each profile is evaluated at the discrete points or at fourteen different locations for the polynomial profiles. The rms error is the lowest for the linear recovered profiles which are of the same order as the assumed one. The higher order profiles deviate more from the assumed one because they have more degrees of freedom to better fit the perturbed emission data. The

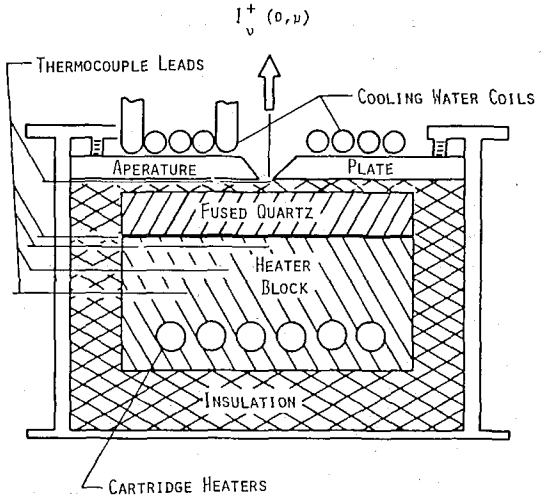

Fig. 4 Cross-sectional view of test assembly

maximum rms error in Fig. 3 is 2.5 percent compared to the 5 percent error in the emission data. This error would have been larger for higher order profiles if the results were not constrained. However, the constraint had no effect on profiles having two or three unknowns. These results then demonstrate that random error is not amplified in the recovered profiles. This is partly because ϕ_ν is a strong function of temperature ($\phi_\nu \sim T^\alpha$, where a is between 4 and 6 for the frequency and temperature range of interest) and error is dampened when evaluating temperature. The error is also dampened because ten emission data points are considered versus four unknowns. However, the rms error was increased only slightly when the number of data points was decreased to six [5].

Effect of Optical Thickness Range. The selection of optical thicknesses at which to measure emission data does affect the recovered results. The desired optical thickness range was discussed previously in relation to Fig. 2. To investigate the effect of optical thickness range, recovered profile results similar to those in Fig. 3

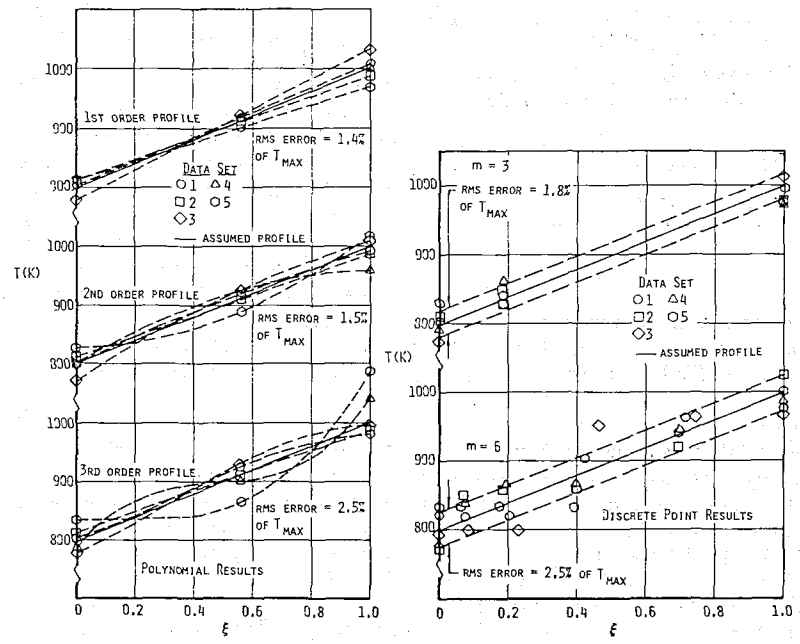

Fig. 3 Comparison of assumed and recovered temperature profiles with T_r = 1000 K, N = 10, $0.35 \leq \tau_{0\nu}/\mu \leq 13.5$, $n_1 = 1.5$, $n_0 = 1.0$ $\tilde{n}_2 = 0.8 + i\,18.9$, $\mu' = 1.0$, σ = 5 percent and results constrained

were obtained for various optical thickness ranges with the same linear temperature profile [5]. The optical thicknesses were equally spaced logarithmically within each range. The results indicate that the recovered profile error varies significantly with optical thickness range considered. The minimum error occurred for emission data which had the following optical thicknesses:

1 One value as low as 0.5,

2 A very large value to establish the front surface temperature, and

3 A number of values between 0.5 and 5.

Including many optical thicknesses larger than five is desirable only for nearly linear profiles where better defining the recovered profile near the front surface helps in determining the whole profile.

Experiment

An experiment was conducted to verify the inversion procedure. It was designed to determine feasibility of the procedure rather than accuracy. The experiment provided spectral emission data from a semitransparent solid whose temperature profile could be predicted. One-dimensional heat transfer was modeled using Corning Code 7940 fused quartz for the semitransparent solid. Fused quartz was selected because it has desirable thermophysical properties and its optical properties are reasonably well known. The sample was heated from the back side and spectral energy leaving the front surface was measured. The samples had a 15-cm dia and thicknesses as large as 2.54 cm. The diameter-to-thickness ratio was large enough so that one-dimensional heat transfer was modeled. A thin, opaque layer of gold was coated on the sample's back surface. This coating blocked radiation emitted by the heater from entering the sample. The sample's surfaces were very smooth so that the gold coating-sample interface was specular.

Fig. 4 shows a cross-sectional view of the test assembly. Thermocouples are embedded in the block to measure heat flux and heater surface temperature. The sample sits on top of the heater block with a 0.007-cm gap between the two to insure uniform heating. The temperature of the sample's back surface is calculated from the heater surface temperature and heat flux. The front-surface temperature of the sample was measured using 0.005-cm dia thermocouples which are soldered to the samples. These thermocouples are located near the center of the front surface. A water cooled aperature plate above the sample serves as a heat sink and an aperature for emerging radiation. There is also a gap between the sample and aperature plate to provide uniform thermal resistance and to model the boundary condition in Fig. 1. The sample and heater block are immersed in insulation to minimize heat losses.

Spectral radiation (2.0 to 5.5 μm) passing through the aperature of the test assembly is detected by a Perkin-Elmer Model 112 spectrometer. In this spectral range fused quartz changes from being nearly transparent to opaque, i.e., semitransparent. The spectrometer was calibrated using a black-body installed *in situ*. During calibration and testing the spectrometer and test assembly were purged with nitrogen to remove any gases having absorption bands in the spectral region of interest. A detailed discussion of the experiment is given elsewhere [5].

Experimental Results

The experiment yielded spectral emission data for fused quartz samples at various temperature levels. The temperature profile through the samples was predicted from a heat transfer analysis (described in the Appendix) using experimental temperature data to define the boundary conditions. Temperature profiles were recovered from the experimental spectral emission data and were compared with the predictions to evaluate the inversion technique.

The physical property data for the Corning Code 7940 glass samples were taken from published data. Spectral absorption coefficient values were calculated from transmission data for Corning 7940 glass from Wedding [19]. These data were supplemented by fused quartz data [20, 21] for lower κ values. Data from Wray and Neu [22] were employed for the index of refraction for Corning 7940 glass. Thermal conductivity data, needed for the heat transfer analysis, were taken from Lucks, et al. [23]. The index of refraction of the gold coating $\tilde{n}_2$ was assumed to be $1.31 + i10.7$. This value yields a reflectivity in the normal direction of 0.96 for the contiguous medium having an index of refraction of unity. This reflectivity agrees well with experimental data for electrolytic gold in the spectral region of interest [24]. The assumed value of $\tilde{n}_2$ gives a normal reflectivity of 0.94 for $n_1 = 1.4$ (an approximate value for fused quartz).

Typical recovered and predicted temperature profiles derived

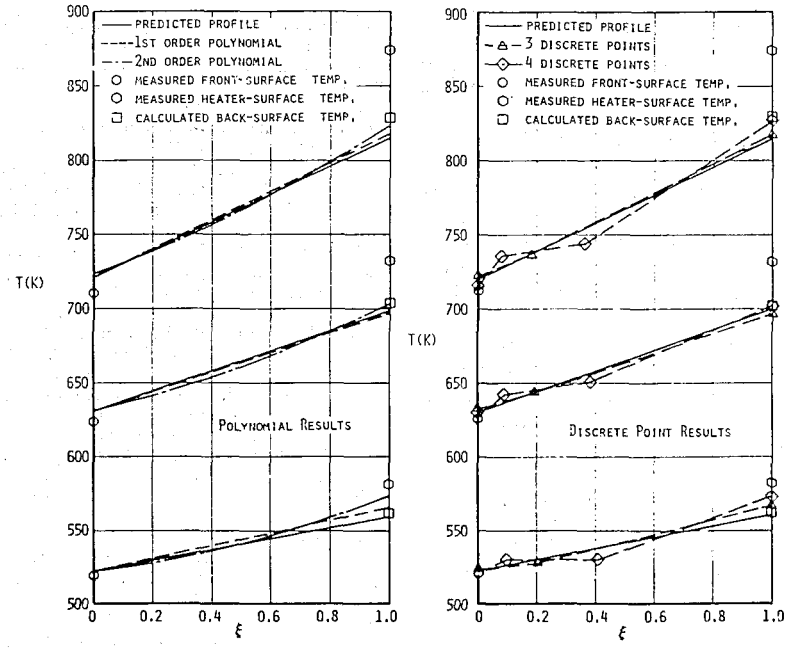

Fig. 5 Comparison of predicted and recovered temperature profiles with $L = 1.27$ cm, $\rho_2 = 0.94$, $N = 11$, $3.32 \leq \lambda \leq 4.75$ μm and $0.3 \leq \tau_{0\lambda} \leq 39$

from the experimental data are shown in Fig. 5. The recovered profiles are defined in terms of three and four discrete points, and first and second order polynomials. The measured front-surface temperature and heater-block surface temperature plus the calculated back-surface temperature are also shown in this figure. The optical thicknesses considered follow the recommendations from the numerical results with three values greater than 5.0 included.

The predicted profiles in Fig. 5 were derived from a five-band analysis with the back surface temperature and heat-transfer coefficient at the front surface defined. The profiles are nearly linear which show that conduction is dominant. This is due in part to a large fraction of the radiation emitted being in a spectral range where fused quartz is opaque. In establishing the predicted profile, the back surface temperature was adjusted until the predicted temperature at the front surface agreed with the recovered value. This approach was taken since neither surface temperature taken from the thermocouple data is very accurate. The measured front-surface temperature has been shown in subsequent testing to be low by about 10K [25]. The calculated back surface temperature is subject to error because of inaccuracies in gap height and heat flux. The choice of matching the predicted and recovered profiles at the front surface was made because any error in the recovered profile at this location is due to measurement error and not the inversion technique. In effect the boundary conditions employed in the heat transfer analysis were the temperature and heat-transfer coefficient at the front surface. This approach of predicting the temperature profile was justifiable in checking out rather than evaluating accuracy of the inversion technique. Accuracy is the subject of another investigation [26]. The thermocouple data, although not directly used, do qualitatively show that the predicted profiles are correct.

The discrete-point and polynomial approaches yield similar recovered profiles in Fig. 5. The profiles become lower in the middle and higher toward the back as the number of unknowns increases. Three discrete points and second order profiles have the same number of unknowns and the resulting profiles are nearly the same except near the back surface where the second order polynomials diverge. This indicates that variable spacing in the discrete-point approach has a favorable effect. Thus, the polynominal approach could be improved by transforming the space variable y, e.g., $y \rightarrow y^a$, where a is a constant [5]. The recovered results in Fig. 5 were obtained with the monotonic constraint enforced. However, enforcing the constraint only affected results for four discrete points. The resulting errors in fitting the measured emission data varied from 1 to 1.5 percent. As the number of unknowns defining the profile increases, the fit of the emission data becomes better, as expected.

The predicted and linear recovered profiles in Fig. 5 agree well especially for the two highest temperature cases. The slight deviations in slope could be caused by error in the thermal conductivity or optical properties employed for the samples or error in the measurements. Because of uncertainties in property data, it is concluded that the predicted and linear recovered profiles agree within the accuracy of the predictions. The consistent deviations of higher order recovered profiles from the linear ones are due to errors in the emission data, absorption coefficient data and/or back surface reflectivity. Random emission data error could not explain these deviations because the trends are consistent. Fixed emission data error could occur but this error would have to average 5 percent to explain the deviations observed, based on the numerical results. Any fixed emission data error would not be expected to be this large. Thus, at least part of the deviations are caused by error in the absorption coefficient data and/or back surface reflectivity. Sensitivity studies have shown that the back surface reflectivity could not have caused the deviations because a change in the back surface reflectivity has an opposite effect on the emitted radiation from the conductor than on the reflected radiation from the semitransparent solid [5].

Sensitivity studies were also performed to indicate the effect of absorption coefficient data error [5]. The deviations of higher order profiles were cut in half by adjusting the smaller $\kappa_{i\nu}$ values by less than ten percent. Thus, absorption coefficient data error caused much of the deviations observed. Larger $\kappa_{i\nu}$ values were not varied because transmission data [19] for a 1.0 mm thick sample should yield accurate absorption coefficient values for $\kappa_\nu > 1$ cm^{-1}. These findings show that available property data are sufficiently accurate to recover simple profiles but better data would be needed for more complex profiles.

Conclusions

The results presented in this paper demonstrate that the inversion procedure developed does properly recover the temperature distribution in a semitransparent solid from spectral emission data.

Analytical results show that error in the emission data is not amplified in the recovered profiles and that the emission data should include optical thicknesses as low as 0.5, a very large value, and a number of values between 1 and 5 to get optimum results. Including many optical thicknesses greater than five will be beneficial only for nearly linear profiles.

In the experimental results, the recovered linear profiles agreed with the predicted ones within the accuracy of the predictions. Higher order recovered profiles deviated from the linear ones due partly to error in the absorption coefficient data. Available property data are then sufficiently accurate to recover simple profiles, i.e., nearly linear, but better data are needed for more complex profiles.

Acknowledgments

The authors wish to acknowledge the assistance of Dr. D. A. Nealy and Messrs. H. E. Helms and W. C. Davis, Detroit Diesel Allison; and Drs. J. S. Toor and E. E. Anderson, and Messrs. P. J. Hommert and G. L. Groninger, Purdue University. Financial support was provided by the National Science Foundation under Grant No. 8K32373X and General Motors Corporation. Computer facilities were made available by Purdue University Computer Center and Detroit Diesel Allison.

References

1 Wang, J. Y., "Theory and Applications of Inversion Techniques: A Review," Purdue University, School of Aeronautics, Astronautics and Engineering Sciences, Report AA&ES 70-6, September 1970.

2 Van Laethen, R., Leger, L. G., Boffé, M., and Plumet, E., "Temperature Measurement of Glass by Radiation Analysis," *Journal of the American Ceramic Society*, Vol. 44, No. 7, July 1961, pp. 321–332.

3 Beattie, J. R., "Application of Radiation Pyrometry to Glass Temperature Measurement and Control," *Ceramic Age*, Vol. 81, No. 4, April 1965, pp. 70–78.

4 Chupp, R. E., and Viskanta, R., "Thermal Remote Sensing of Temperature Distribution in Semitransparent Solids: A Numerical Experiment," ASME Paper No. 72-HT-5, 1972.

5 Chupp, R. E., "Development and Experimental Evaluation of a Technique to Determine the Temperature Distribution in Semitransparent Solids from Remotely Sensed Spectral Emission Data," Ph.D. Thesis, Purdue University, August 1973.

6 King, J. I. F., "Infrared Radiative Transfer in the Terrestrial Atmosphere," *Journal of Quantitative Spectroscopy and Radiative Transfer*, Vol. 8, No. 1, January 1968, pp. 1–16.

7 Wark, D. Q., and Fleming, H. E., "Indirect Measurements of Atmospheric Temperature Profiles from Satellites: I. Introduction," *Monthly Weather Review*, Vol. 94, No. 6, June 1966, pp. 351–362.

8 Twomey, S., "Indirect Measurements of Atmospheric Temperature Profiles from Satellites: II. Mathematical Aspects of the Inversion Problem," *Monthly Weather Review*, Vol. 94, No. 6, June 1966, pp. 363–366.

9 King, J. I. F., "Inversion of Slabs of Varying Thickness," *Journal of Atmospheric Sciences*, Vol. 21, No. 3, May 1964, pp. 324–326.

10 Turchin, V. F., Malkevich, M. S., and Gorchakova, I. W., "The Use of Statistical Regularization in Determining the Vertical Atmospheric Temperature Profile," *Atmospheric and Oceanic Physics*, Vol. 5, No. 5, May 1969, pp. 252–256.

11 Kagiwada, H. H., and Belman, R. E., "Direct and Inverse Problems for Integral Equations via Initial Value Methods," Rand Corporation, Memorandum RM-5447, 1967.

12 Chahine, M. T., "Inverse Problems in Radiative Transfer: Determination of Atmospheric Parameters," *Journal of Atmospheric Sciences*, Vol. 27, No. 6, September 1970, pp. 960–967.

13 Twomey, S., "On the Numerical Solution of Fredholm Integral

Equations of the First Kind of the Inversion of Linear Systems Produced by Quadrature," *Journal of the Association for Computing Machinery,* Vol. 10. No. 1. January 1963, pp. 97–101.

14 Wang, J. Y., "Mathematical Analysis of Optical Remote Sensing of a Thermal System," Ph.D. Thesis, Purdue University, August 1971.

15 Florence, E. T., "Numerical Study of Nonlinear Inversion," in *Specialist Conference on Molecular Radiation* (R. Goulard, Editor), NASA TM X-53711, 1968, pp. 443–448.

16 Barnett, T. L., "Application of a Nonlinear Least-Squares Method to Atmospheric Temperature Sounding," *Journal of Atmospheric Sciences,* Vol. 26, No. 3, May 1969, pp. 456–461.

17 Fletcher, R., and Powell, M. J. D., "A Rapidly Convergent Descent Method for Minimization," *The Computer Journal,* Vol. 3, No. 6, July 1963, pp. 163–168.

18 Allran, R. R., and Johnsen, S. E. J., "An Algorithm for Solving Nonlinear Programming Problems Subject to Nonlinear Inequality Constraints," *The Computer Journal,* Vol. 13, No. 2, May 1970, pp. 171–177.

19 Wedding, B., "High-Temperature Infrared Transmittance of Some Optical Materials," Research and Development Laboratories, Corning Glass Works, Corning, New York, 1970.

20 Edwards, O. J., "Optical Transmittance of Fused Silica at Elevated Temperatures," *Journal of the Optical Society of America,* Vol. 56, No. 10, October 1966, pp. 1314–1319.

21 Goldsmith, A., Waterman, T. E., and Hirschhorn, H. J., *Handbook of Thermophysical Properties of Solid Materials,* Volume 3, Macmillan, New York, 1961, p. 897.

22 Wray, J. H., and Neu, J. T., "Refractive Index of Several Glasses as a Function of Wavelength and Temperature," *Journal of the Optical Society of America,* Vol. 59, No. 6, June 1969, pp. 774–776.

23 Lucks, C. F., Matolich, J., Deem, H. W., and Thompson, H. B., "The Experimental Measurement of Thermal Conductivities, Specific Heats, and Densities of Metallic, Transparent and Protective Materials," Part III, USAF Report No. AF TR 6145, 1954.

24 Gier, J. T., Dunkle, R. V., and Bevans, J. T., "Measurement of Absolute Spectral Reflectivity from 1.0 to 15 Microns," *Journal of the Optical Society of America,* Vol. 44, No. 7, July 1954, pp. 558–562.

25 Hommert, P. J., "Application of a Thermal Remote Sensing Method to Measurement of Temperature Distribution in Glass," MS Thesis, Purdue University, December 1973.

26 Groninger, G. L., "Experimental Verification of Thermal Remote Sensing for Measuring Temperature Distribution in Fused Silica," MS Thesis, Purdue University, August 1973.

APPENDIX

Heat Transfer Analysis

The temperature profile in the test samples was predicted from a one-dimensional combined conduction-radiation heat transfer analysis with the boundary conditions established from the thermocouple measurements. The heat transfer analysis is briefly described in this Appendix.

The conservation of energy equation for steady, one-dimensional heat transfer by conduction and radiation within the material may be written as

$$dq/dy = d[-k(dT/dy) + F]/dy = 0 \tag{9}$$

The spectral radiative flux F_ν is obtained from the definition

$$F_\nu(y) = 2\pi \int_0^1 I_\nu^+(\mu)\mu d\mu - 2\pi \int_0^{-1} I_\nu^-(\mu)\mu d\mu \tag{10}$$

Combining equations (2) through (5) and substituting into equation (10) yields an expression for the local radiative flux at any plane y [5],

$$\begin{aligned} F_\nu(y) = {} & 2\pi \int_0^L \kappa_\nu(t) I_{b\nu}(t) \operatorname{sign}(y-t) E_2(|\tau_\nu(y) - \tau_\nu(t)|)dt \\ & + 2\pi \int_0^L \kappa_\nu(t) I_{b\nu}(t) \{G_2[\rho_{1\nu}\rho_{2\nu}, [2\tau_{0\nu} + \tau_\nu(y) - \tau_\nu(t)]] \\ & - G_2[\rho_{1\nu}\rho_{2\nu}, [\tau_\nu(t) - \tau_\nu(y)]] + G_2[\rho_{1\nu}, [\tau_\nu(t) + \tau_\nu(y)]] \\ & - G_2[\rho_{2\nu}, [2\tau_{0\nu} - \tau_\nu(y) - \tau_\nu(t)]]\} dt \\ & + 2\pi \int_0^1 I_{0\nu}^+(\mu)\beta_\nu [e^{-\tau(y)/\mu} - \rho_{2\nu} e^{-[2\tau_{0\nu} - \tau(y)]/\mu}] \mu d\mu \\ & + 2\pi I_{b\nu}(T_2)\{G_3[(1-\rho_{2\nu})\rho_{1\nu}, [\tau_{0\nu} + \tau(y)]] \\ & - G_3[(1-\rho_{2\nu}), [\tau_{0\nu} - \tau(y)]]\} \end{aligned} \tag{11}$$

where

$$\operatorname{sign}(y-t) = \begin{cases} +1, & y > t \\ -1, & y < t \end{cases} \tag{12}$$

$$G_n(f,a) = \int_0^1 \beta_\nu f(\mu) \exp(-a/\mu)\mu^{n-2} d\mu \tag{13}$$

In equation (11), the first term represents emission from within the material, the second is the emission that has been reflected by one or both of the interfaces, the third represents energy incident on interface 1 from external sources which reaches y, and the fourth is energy emitted by the conductor which reaches y. The total radiative flux was calculated from F_ν using a band approximation where F_ν is assumed to be constant within each band. Five bands were employed in the analysis in order to model the spectral absorption coefficient variation [5].

The temperature distribution was calculated by integrating equation (9) twice with respect to y and numerically solving the resultant expression using a method of successive approximations [5]. The boundary conditions employed were the back surface temperature and, either the front surface temperature, total heat flux or conductive flux, at the front surface. All these conditions could be determined from the thermocouple measurements in the test.

C. A. Anderson

Visiting Lecturer,
University of Wales at Swansea,
Staff Member,
Los Alamos Scientific Laboratory,
Los Alamos, N. M.

O. C. Zienkiewicz

Professor and Head,
Department of Civil Engineering,
University of Wales at Swansea,
Wales, U. K.

Spontaneous Ignition: Finite Element Solutions for Steady and Transient Conditions

Steady-state and transient ignition problems are solved by the finite element method. Discretized equations for the reactive heat equation are set down using Galerkin's method. The steady-state discretized equations are solved by an incremental Newton-Raphson procedure using the Frank-Kamenetskii parameter as the incremented or "loading" variable. Critical values of the Frank-Kamenetskii parameter are given for both common and unusual shapes using isoparametric finite elements to describe the geometrical features of the bodies. The transient ignition problem is solved by using the finite element spatial description together with a midinterval time differencing scheme.

1 Introduction

The transient-heat-conduction equation for a reactive solid obeying zero order kinetics is

$$\rho c \frac{\partial T}{\partial t} = k \nabla^2 T + \rho Q z e^{-E/RT}, \tag{1}$$

where T is the absolute temperature measured in degrees Kelvin. The constants occurring in equation (1) are:

ρ, c, k = density, heat capacity, and thermal conductivity, respectively,
Q = heat of decomposition of the solid (J/kg),
z = frequency factor (sec^{-1}),
E = Arrhenius activation energy (J/mole), and
R = universal gas constant (J/mol − deg K).

This paper presents the calculation of approximate solutions to equation (1) for two and three-dimensional situations by means of the finite-element method.

The steady-state problem

$$\left(\frac{\partial T}{\partial t} = 0 \text{ in equation (1)} \right)$$

has been investigated for the three simple cases—the infinite slab, the infinite circular cylinder, and the sphere—in which temperature is a function of one coordinate only and where the boundary conditions are of Dirichlet type, in particular, a fixed value of the boundary temperature T_a. It has been shown that the existence of steady-state solutions for these situations depends wholly on a single dimensionless parameter δ, the Frank-Kamenetskii parameter, given by

$$\delta = r^2 \rho \frac{QzE}{kRT_a^2} \exp(-E/RT_a), \tag{2}$$

where r is the radius of the sphere and cylinder or the slab half-width.[1] The Frank-Kamenetskii approximation leads to a much simpler equation for steady-state situations

$$\nabla^2 \varphi + \delta e^{\varphi} = 0 \tag{3}$$

with the boundary condition, $\varphi = 0$. The behavior of solutions to equation (3) is such that there exists a critical value of δ, called δ_{crit}, above which no solutions of equation (3) should be expected, and below which ($\delta < \delta_{crit}$) multiplicity of solutions can occur. This nonuniqueness property of solutions to equation (3) is discussed in reference [2].[1] Analytical solutions previously have been obtained for the infinite slab[3] ($\delta_{crit} = 0.878$) and the infinite circular cylinder[4] ($\delta_{crit} = 2$, exactly).

For bonafide two- and three-dimensional steady-state situations equation (3) is a nonlinear partial differential equation and no general analytical solutions are known. In spite of this, approximate methods have been devised that lead to estimates of the critical value of the Frank-Kamenetskii parameter.[5,6] The method of reference [5] which builds on the Semenov approximation (a spatially uniform temperature field in the body exceeding the ambient temperature T_a with heat transfer occurring only at the boundary) leads to good bounds on the critical value but is restricted to bodies with a center of symmetry. In addition the methods of both references [5 and 6] require the body to be convex, and it is not clear how these approximate methods can be altered for improved accuracy. The finite element method described here does not possess these topological limitations, does allow for improved accuracy, and can accommodate quite general boundary conditions as well.

Contributed by the Heat Transfer Division for publication in the JOURNAL OF HEAT TRANSFER. Manuscript received by the Heat Transfer Division, July 16, 1973. Paper No. 74-HT-K.

[1] Numbers in brackets designate References at end of paper.

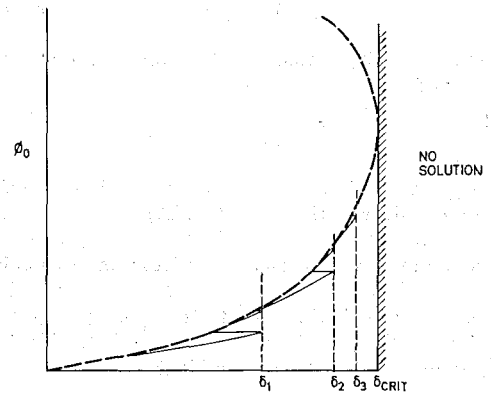

Fig. 1 Schematic of incremental Newton-Raphson procedure for determination of δ_{crit}

In Section 2 of this paper, the discretized finite-element equations for equation (1) and for the criticality problem described by equation (3) are derived using the Galerkin's method. The resulting set of nonlinear discretized equations for the criticality problem is solved in Section 2 by an incremental Newton-Raphson procedure where the incremented variable is δ itself. In Section 3, the critical value of δ is computed for both common and unusual two- and three-dimensional solids using isoparametric finite elements, and comparisons are made with known or previously computed results. The multiplicity of solutions to equation (3)[2] is demonstrated for the case of an infinitely long cylinder of elliptical cross section, and an example calculation involving a finite surface heat-transfer coefficient is given.

In Section 4 we treat the more difficult time-dependent problem of equation (1). Here we are mainly interested in the situation of a reactive solid initially at room temperature and immersed in a constant temperature bath, where the bath temperature T_a yields δ given by equation (2) greater than δ_{crit} for a body of the given size, shape, and thermo-kinetic properties. Under these conditions an equilibrium thermal state cannot be attained and spontaneous ignition will occur after a certain time interval called the induction time.[7] The discretized equations for equation (1) are employed together with an unconditionally stable time differencing scheme in Section 4 to predict induction times for reactive solids. The stability feature allows us to use a time-step adjustment method which, in turn, is very successful in following the thermal behavior of a reactive solid right up to its ignition time (or equilibration) with only modest demands on computing time. Again using isoparametric elements, two examples are given in Section 4 where the induction times are computed for a reactive sphere and for a composite geometry involving both a reactive and an inert solid.

2 The Finite Element Method

***A* Equations of the Discrete Model.** The finite-element method is now well known and accounts of the method are available.[8] Briefly, we suppose that the region of interest Ω is divided into a finite number of subregions—called finite elements (as shown, for example, in Fig. 4 of this paper). The subdivided region will not, in general, correspond to the region Ω because of disparities along the boundary; however, isoparametric elements allow an accurate description of curvilinear boundaries. At the interconnections (either along edges or at joints) of the assemblage of elements, nodal-point values of the dependent variables of the problem are defined (e.g., φ in equation (3)). Once nodal point values of φ are defined, the variation of φ is completely defined within an element by the shape functions

$$N_i(x,y),\ i = 1,2.\ldots L,$$
$$\varphi(x,y) = \sum_{i=1}^{L} N_i(x,y)\varphi_i, \tag{4}$$

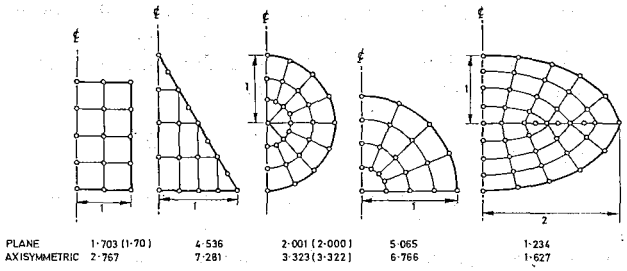

Fig. 2 Critical numbers for common shapes (exact results or previously published approximations in parenthesis)

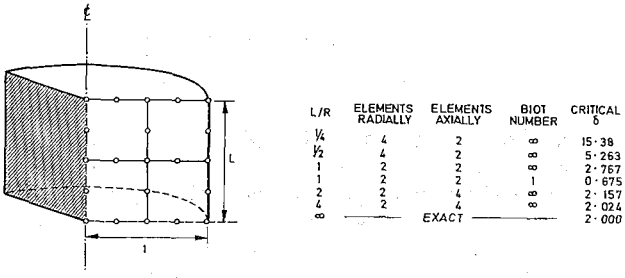

L/R	ELEMENTS RADIALLY	ELEMENTS AXIALLY	BIOT NUMBER	CRITICAL δ
¼	4	2	∞	15·38
½	4	2	∞	5·263
1	2	2	∞	2·767
1	2	2	1	0·675
2	2	4	∞	2·157
4	2	4	∞	2·024
∞	EXACT		∞	2·000

Fig. 3 Table of critical numbers for cylinders of finite length

where L is the number of element nodal points. For the problems treated in this paper the shape functions are chosen to preserve continuity of φ across the interface between two elements. Popular choices of these compatible shape functions for two-dimensional field problems of engineering and physics are the linear shape functions for the three-noded triangle and the shape functions for the linear, quadratic, and cubic isoparametric quadrilaterals. The isoparametric elements can be deformed into curvilinear quadrilaterals by using the shape functions themselves to effect the coordinate transformations. See reference [8] for details.

Once elemental shape functions are taken, all that remains is the determination of the nodal values of φ that satisfy the field equations and boundary conditions of the problem. To make matters explicit, we consider a slightly more general equation than equation (1),

$$\frac{\partial}{\partial x}\left(k\frac{\partial\varphi}{\partial x}\right) + \frac{\partial}{\partial y}\left(k\frac{\partial\varphi}{\partial y}\right) + \delta Q(\varphi) - c\frac{\partial\varphi}{\partial t} = 0 \text{ in } \Omega \tag{5}$$

with the boundary conditions

$$\varphi - \varphi_a = 0 \text{ on } \Gamma_1 \tag{6}$$

$$k\frac{\partial\varphi}{\partial n} + \lambda(\varphi - \varphi_a) = 0 \text{ on } \Gamma_2 \tag{7}$$

The field equation, equation (5), includes, as special cases, both equations (1) and (3) and we have, in addition, allowed for the situation in which the heat capacity and thermal conductivity depend on φ. The boundary condition, equation (6), corresponds to that of a specified temperature, whereas equation (7) typifies Newton cooling with surface heat transfer coefficient λ;

$$\frac{\partial}{\partial n}$$

denotes the normal derivative to Γ.

To obtain the discretized equations on the element level we use the Galerkin method and weight the residuals of equations (5) and (7) with the shape functions $N_i(x, y)$, $i = 1, \ldots L$ given in equation (4). Assuming that the right-hand sides of equations (5) and (7) are not zero, we let R_Ω be the residual of equation (5) in Ω, and R_Γ be the residual of equation (7) on Γ_2 (boundary condition, equation (6), involves zero residual), and set to zero the sum of the weighted residuals

$$\int_\Omega N_i R_\Omega\, d\Omega + \int_{\Gamma_2} N_i R_\Gamma\, ds = 0, i = 1,2\ldots L, \tag{8}$$

where the integrals in equation (8) are taken over each element of Ω.

Inserting equations (5) and (7) as residuals into equation (8) then gives contributions to nodal point residuals,

$$\int_{\Omega^e} N_i \{ \frac{\partial}{\partial x}(k\frac{\partial \varphi}{\partial x}) + \frac{\partial}{\partial y}(k\frac{\partial \varphi}{\partial y}) + \delta Q(\varphi) - c\frac{\partial \varphi}{\partial l} \} d\Omega$$

$$- \int_{\Gamma_2{}^e} N_i \{ k\frac{\partial \varphi}{\partial n} + \lambda(\varphi - \varphi_a) \} ds = R_i, \; i = 1,2 \ldots L. \quad (9)$$

Using Green's theorem on the first two terms of the first integral and multiplying through by -1 then yields

$$\int_{\Omega^e} \{ k[\frac{\partial N_i}{\partial x}\frac{\partial \varphi}{\partial x} + \frac{\partial N_i}{\partial y}\frac{\partial \varphi}{\partial y}] - \delta N_i Q(\varphi) + cN_i\frac{\partial \varphi}{\partial t} \} d\Omega$$

$$- \int_{\Gamma^e} kN_i \frac{\partial \varphi}{\partial n} ds + \int_{\Gamma_2{}^e} N_i \{ k\frac{\partial \varphi}{\partial n} + \lambda(\varphi - \varphi_a) \} ds = R_i, \quad (10)$$

$$i = 1,2 \ldots L.$$

Finally, the shape function representation for φ itself, equation (4), is substituted into equation (10) with the understanding that the nodal-point values φ_i now depend on time $\varphi_i = \varphi_i(t)$. Cancelling like-surface integrals over Γ_2 then gives

$$\int_{\Omega^e} k[\frac{\partial N_i}{\partial x}\sum_{j=1}^{L}\frac{\partial N_j}{\partial x}\varphi_j(t) + \frac{\partial N_i}{\partial y}\sum_{j=1}^{L}\frac{\partial N_j}{\partial y}\varphi_j(t)] d\Omega$$

$$- \delta \int_{\Omega^e} N_i Q(\varphi)\, d\Omega + \int_{\Gamma_2{}^e} cN_i \sum_{j=1}^{L} N_j \dot{\varphi}_j(t) d\Omega$$

$$+ \int_{\Gamma_2{}^e} \lambda N_i [\sum_{j=1}^{L} N_j \varphi_j(t) - \varphi_a] ds = R_i, i = 1,2 \ldots L, \quad (11)$$

which we write in formal matrix notation as

$$[H]^e\{\varphi\}^e + [C]^e\{\dot{\varphi}\}^e - \delta\{F\}^e = \{R\}^e. \quad (12)$$

In equation (12) $\{\varphi\}$ and $\{\dot{\varphi}\}$ are the element nodal point φ vector and its time derivative, $[H]^e$ and $[C]^e$ are matrices whose components are

$$h_{ij}{}^e = \int_{\Omega^e} k\{ \frac{\partial N_i}{\partial x}\frac{\partial N_j}{\partial x} + \frac{\partial N_i}{\partial y}\frac{\partial N_j}{\partial y} \} d\Omega + \int_{\Gamma_2{}^e} \lambda N_i N_j ds \quad (13)$$

and

$$c_{ij}{}^e = \int_{\Omega^e} cN_i N_j d\Omega, \quad (14)$$

and $\{F\}^e$ is a vector with components

$$f_i{}^e = \int_{\Omega^e} N_i Q d\Omega + \int_{\Gamma_2{}^e} \lambda N_i \varphi_a ds. \quad (15)$$

The second integrals in equations (13) and (15) contribute only if the element has an external boundary on which equation (7) is specified.

The process of obtaining nodal values of φ described in the foregoing applies on the element level. The elemental equations are then assembled to give the nonlinear set of equations for the M-dimensional nodal-point vector $\{\varphi\}$

$$[H]\{\varphi\} + [C]\{\dot{\varphi}\} - \delta\{F\} = \{0\}, \quad (16)$$

where

$$H_{ij} = \sum_e h_{ij}{}^e \; C_{ij} = \sum_e c_{ij}{}^e \; F_i = \sum_e f_i{}^e$$

and summation is taken over the elements. In the assembled set of equations the residual vector $\{R\}$ is annihilated. The set of equations, equation (16) is highly nonlinear with $[H]$, $[C]$, and $\{F\}$ depending on $\{\varphi\}$. However, for the steady-state criticality problem described by equation (3), the matrix $[H]$ in equation (16) depends on the shape functions alone and the second term is dropped, resulting in the equation

$$[H]\{\varphi\} - \delta\{F\} = \{0\} \quad (17)$$

with the nonlinearity confined to $\{F\}$ whose elemental components now take the form

$$f_i{}^e = \int_{\Omega^e} N_i e^{\varphi} d\Omega. \quad (18)$$

The remainder of this section is concerned with solving the finite-element criticality equations, equation (17).

***B* Solving the Discretized Criticality Equations.** Several methods are available to solve a nonlinear set of equations such as equation (17) and we have adopted an incremental Newton-Raphson procedure, beginning with the solution $\{\varphi\} = \{0\}$ for $\delta = 0$; this method also provides a value of δ_{crit}. In the Newton-Raphson procedure one again defines a residual vector $\{\psi\}$

$$\{\Psi(\varphi_1, \varphi_2, \ldots \varphi_M)\} = [H]\{\varphi\} - \delta\{F(\varphi_1, \ldots \varphi_M)\} \quad (19)$$

for the M unknown values of φ. Given a value of δ, and a starting value $\{\varphi\}^0$, succeeding estimates of the solution vector for the given δ are computed from the algorithms,

$$[\frac{\partial \Psi}{\partial \varphi}]_n \{\Delta\varphi\} = -\{\Psi\}^n, \; \{\varphi\}^{n+1} = \{\varphi\}^n + \{\Delta\varphi\}, \quad (20)$$

where

$$[\frac{\partial \Psi}{\partial \varphi}]_n$$

is a matrix with components

$$\frac{\partial \Psi_i}{\partial \varphi_j} = H_{ij} - \delta \sum_e \int_{\Omega^e} N_i N_j e^{\varphi} d\Omega. \quad (21)$$

In equation (21) H_{ij} are the components of $[H]$ in equation (17), and the summation again occurs over the elements making up Ω. It is apparent that the matrix

$$[\frac{\partial \Psi}{\partial \varphi}]_n$$

can be assembled element-wise just as $[H]$ was, and, furthermore, that the matrix is symmetric. This symmetry of

$$[\frac{\partial \Psi}{\partial \varphi}]_n$$

is not present if $[H]$ depends on $\{\varphi\}$. It is also apparent that

$$[\frac{\partial \Psi}{\partial \varphi}]_n$$

must be reassembled at each interation since it depends on $\{\varphi\}$.

The strongest case for use of the Newton-Raphson method to solve systems of nonlinear equations is its high rate of convergence, if convergence does indeed occur, and the fact that power-

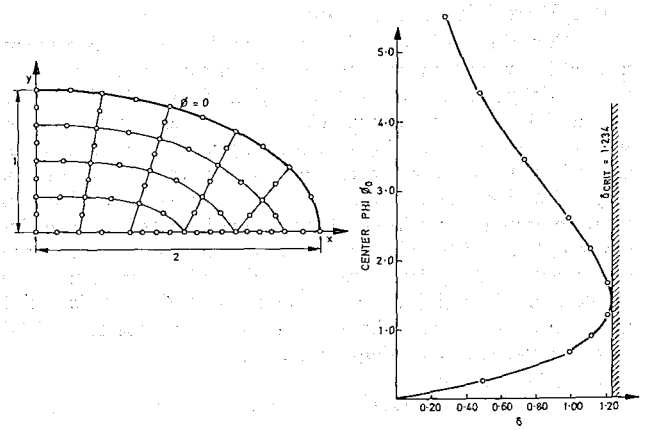

Fig. 4 Finite element mesh for ellipse and plot of φ_0 versus δ showing both solution branches

ful theorems exist concerning conditions for convergence and rate of convergence. These theorems for convergence of Newton's method, as applied to operator equations in Banach spaces, are due to Kantorovic and are discussed in reference [9] with a view toward the computational theory of nonlinear equations. In fact, a very high rate of convergence was observed in the Newton-Raphson procedure for solving equation (17)—usually three iterations, or at most five, would give residuals of less than 10^{-9} for all of the problems tested in Section 3.

The incremental Newton-Raphson process was carried out in the following fashion. Beginning with a set value of δ and the initial vector $\{\varphi\} = \{0\}$ an attempt was made to solve equation (17) using the algorithm of equations (19) and (20). If convergence occurred, δ was incremented and the procedure repeated using as the initial $\{\varphi\}$ the solution vector of the preceeding increment. If convergence did not occur, δ was taken at its half-increment value and this process was continued until convergence occurred. Where the change in δ required to produce convergence was less than 10^{-3}, the incremental process was terminated and the previous δ was taken to be the critical value. This incremental Newton-Raphson process is shown schematically in Fig. 1. Usually 10 increments served to determine δ_{crit}.

In Section 1 we indicated the existence of several solution vectors $\{\varphi\}$ for every value less than the critical value. As in the foregoing, the second solution branch can be determined by the incremental Newton-Raphson procedure, but here there is a difficulty in finding a suitable initial vector $\{\varphi\}^0$ to guarantee that the Newton-Raphson method will converge to a solution on the upper branch. The procedure used with success was to guess a trial vector $\{\varphi\}^0$ for the region; δ^0 was then computed using

$$\delta^0 = \frac{\{F\}^T[H]\{\varphi\}^0}{\{F\}^T\{F\}}, \tag{22}$$

which follows directly from equation (17). In equation (22) $\{F\}^T$ denotes the transpose of the vector $\{F\}$. The Newton-Raphson method was carried out using these values of δ^0 and $\{\varphi\}^0$ to obtain a starting solution on the upper branch, and the incremental procedure was then carried out as described for the lower branch.

In all cases the critical value of the Frank-Kamenetskii parameter obtained from above or below agreed within 10^{-3}.

3 Critical Parameters for Common Shapes Described by Isoparametric Elements

The processes of numerical analysis described in Section 2 have been incorporated into a two-dimensional finite-element analysis program. The program uses linear (4 nodes), quadratic (8 nodes), or cubic (12 nodes) isoparametric elements to describe the various regions and their curvilinear boundaries, and the integrations in equations (13), (14), (15), and (21) are carried out numerically as described in reference [8] using four and nine Gauss integration points for the linear and quadratic elements, respectively. Not more than 20 quadratic elements with a total of between 40 and 80 nodal points were used for most problems. This required about five minutes of computation time on an ICL 1905-E computer for the determination of one solution branch and the critical value of the Frank-Kamenetskii parameter. Symmetry conditions were used whenever possible.

The first test was to check a numerically computed solution against a known solution. For this test we chose the reactive slab of unit semi-width whose analytical solution is known (references [1 and 3]) and whose critical value of the Frank-Kamenetskii parameter is 0.878. A crude approximation, using only three nodal points across the half-width, was used with the outside mesh point values of φ set to zero, corresponding to the Frank-Kamenetskii boundary condition. Table 1 illustrates the results obtained using, as a description of the region, two linear elements, one parabolic element, or a three-point finite-difference approximation. (For this problem the use of linear or quadratic finite elements is equivalent to assumption of a linear or quadratic variation of φ within the element.) Again, for the finite-difference approximation, the resulting nonlinear equations were solved by the incremental Newton-Raphson procedure. The accuracy of the single quadratic element in predicting both the center value of φ, given δ, and the critical parameter was very reassuring and prompted the use of the quadratic isoparametric element in all of the criticality calculations presented in this section. This accuracy can be explained somewhat if one recalls that the slab-heat equation with constant internal heat generation has as its solution a quadratic function.

Table 1 Comparison of finite element and finite difference numerical solutions with the analytical solution for the slab reactive heat equation

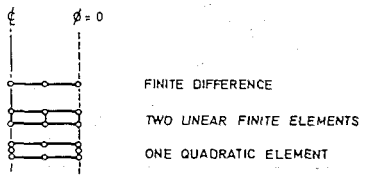

VALUE OF δ	ANALYTICAL SOLN (LOWER)	FINITE DIFFERENCE	LINEAR FINITE ELEMENT	PARABOLIC FINITE ELEMENT
0·500	0·3290	0·3348	0·3230	0·3287
0·800	0·7465	0·8051	0·6944	0·7407
0·878	1·188	NO SOLN	0·8996	1·075
CRITICAL	0·878	0·848	0·924	0·885

Fig. 2 illustrates the results of the calculation of the Frank-Kamenetskii critical parameter for some common geometric shapes—both plane and axisymmetric. Only quadratic isoparametrics were used (the mid-side nodes of the elements making up the five shapes of Fig. 2 are not shown). Our results are in excellent agreement with analytical, or previously computed, values of the critical parameter. For instance, the critical values for the infinite circular cylinder and the sphere are 2 (exactly) and 3.322, respectively, and the published value for the infinite square rod is 1.70.[5] For the last three shapes of Fig. 2 the reader should realize that approximation involves both inexact variations of φ within each element as well as an approximation of the shape of the boundary; the first two shapes involve no boundary approximation.

Fig. 3 lists the critical parameter for finite-length circular cylinders of unit radius and various L/R ratios, where $2L$ is the length of the cylinder. As can be seen in the table accompanying Fig. 3, the critical value of the finite-length cylinder with L/R equal to 4 is very close (within about one percent) to that of the infinite cylinder. This result contradicts a corresponding result in reference [5] which claims a six percent end correction for a cylindrical reactant mass with L/R equal to 4. On the other hand, for relatively thin circular disks the critical parameter is determined mainly by heat conduction axially. Fig. 3 gives a critical parameter of 15.38 for L/R equal to $\frac{1}{4}$. If this value is normalized to a unit half-thickness by dividing by 16 (see equation (2)), then the critical parameter is 0.961—still 10 percent greater than the critical parameter of the infinite slab of unit half-thickness. The result for the equicylinder ($L/R = 1$) agrees with the value 2.76 given in reference [5].

To demonstrate the versatility of the finite-element method, a criticality calculation was also carried out on the equicylinder with finite-surface heat-transfer coefficient. For this case, the boundary condition is that of equation (7) over the whole of Γ. In terms of φ, the boundary condition becomes

$$\frac{\partial \varphi}{\partial n} + \eta\varphi = 0 \text{ on } \Gamma,$$

where η is the ratio of the surface heat-transfer coefficient and the thermal conductivity of the reactant mass. The critical values of δ for the equicylinder were found to be 0.081, 0.675, and 2.143 for η equal to $\frac{1}{10}$, 1, and 10, respectively.

Fig. 4 illustrates a finite-element mesh for one quadrant of an infinitely long rod of a reactant mass, the cross section of the rod being elliptical with minor and major axes of lengths one and two, respectively. In this figure can also be seen the plot of the

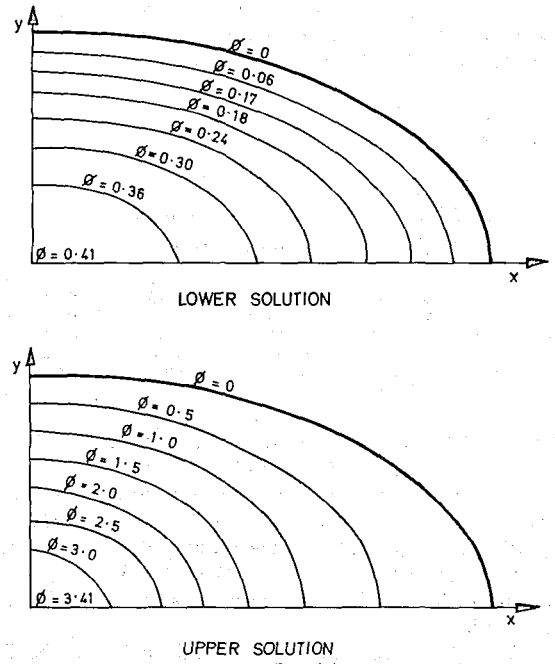

Fig. 5 Contour lines of φ for lower and upper solutions for an ellipse, $\delta = 0.75$

center value of φ versus δ up to the critical value 1.234, obtained from the incremental Newton-Raphson procedure. The upper branch of center φ versus δ is also shown in Fig. 4. This branch was obtained by using as an initial vector, $\{\varphi\}^0$, a set of nodal point values interpolated parabolically along the radius from the center through the point using a center value of 4, a zero center slope, and a zero value on the outer boundary of the ellipse. The initial δ computed from equation (22) was 0.314. For these trial values the Newton-Raphson process converged to the uppermost point shown in the upper solution branch. The complete upper solution branch was then generated, as for the lower branch, by the incremental Newton-Raphson procedure. Fig. 5 illustrates contour lines for φ for the two solutions when δ equals 0.75.

The last example in this section concerns a configuration that does not possess a center lying inside of the body of reactive material. Consequently, this configuration is not amenable to many approximate methods for determination of its critical parameter such as those described in references [5, 6]. The finite-element method is not restricted by such topological considerations. Fig. 6 illustrates a finite-element mesh for such a configuration—a doughnut of unit radius with inner radius R. Using the incremental Newton-Raphson procedure, the critical value of the Frank-Kamenetskii parameter was computed to be 1.843, 1.978, and 1.993 for R equal to 0, 1, and 2 units, respectively. Solutions for all positive R are bounded above by 2, the critical value for the infinitely long circular cylinder of unit radius.

4 Transient Solutions for Spontaneous Ignition

***A* Solution Method.** In this section we are concerned with solutions of the transient reactive heat equation (1). The discretized equations for equation (1) have been derived previously in Section 2, equation (16),

$$[H]\{\varphi\} + [C]\{\dot{\varphi}\} - \delta\{F\} = \{0\},$$

where the dot indicates time derivative. In addition initial conditions

$$\{\varphi\} = \{\varphi\}_0 \tag{23}$$

must be specified at $t = 0$ for a well-posed problem. The elemental components of $\{F\}$, in the absence of the Frank-Kamenetskii approximation, are

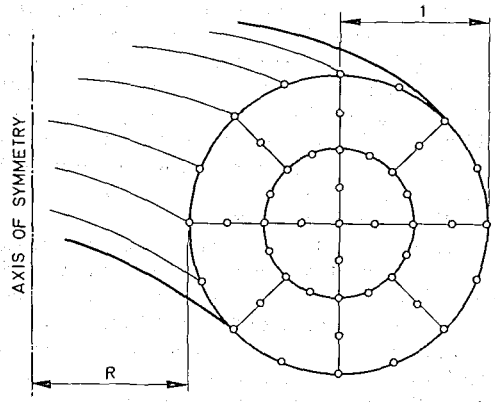

R	δ_{CRIT}
0	1·843
1·0	1·978
2·0	1·993

Fig. 6 Geometry and finite element mesh for the doughnut of unit radius

$$f_i^e = \delta \int_{\Omega^e} N_i e^{-E/R\varphi}\, d\Omega + \int_{\Gamma_2{}^e} \lambda N_i \varphi_a\, ds\,, \tag{24}$$

where now $\delta = \rho Q z$, φ is the absolute temperature itself, and φ_a is the ambient temperature to which the reactant mass is subjected.

To solve the transient equation equation (16) we proceed by discretizing time pointwise, i.e., we consider a sequence of points in time $t_0 = 0, t_1, t_2 \ldots . t_n, \ldots .$ At a time t_n, say, we can write a midinterval approximate for the vector $\{\varphi\}$,

$$\{\varphi\}_{n+1/2} = \frac{\{\varphi\}_{n+1} - \{\varphi\}_n}{\Delta t},$$

where $\Delta t = t_{n+1} - t_n$. If we evaluate the remaining terms in equation (16) at the mid-interval (for instance, $\{\varphi\}_{n+1/2} = \frac{1}{2}(\{\varphi\}_n + \{\varphi\}_{n+1})$ etc.,) we obtain the equation

$$1/2[H](\{\varphi\}_{n+1} + \{\varphi\}_n) + \frac{[C]}{\Delta t}(\{\varphi\}_{n+1} - \{\varphi\}_n) - \frac{\delta}{2}(\{F\}_n + \{F\}_{n+1}) = \{0\}\,. \tag{25}$$

We now make the further assumption that the conductivity and heat-capacity matrices $[H]$ and $[C]$ do not vary greatly with φ so that they can be regarded as constant with respect to the change in φ occurring in the time interval Δt. Equation (25) can then be rearranged, putting the components of $\{\varphi\}_{n+1}$ on one side, to give

$$([H] + \frac{2}{\Delta t}[C])\{\varphi\}_{n+1} - \delta\{F\}_{n+1} = -([H] - \frac{2}{\Delta t}[C])\{\varphi\}_n + \delta\{F\}_n \tag{26}$$

where the right-hand side is known since $\{\varphi\}_n$ is known at t_n. The nonlinear equation (26) is not unlike the discretized criticality equation (17).

Equation (26) provides the algorithm for advancing in time from the initial $\{\varphi\}_0$ in solving the transient equations (16). In contrast to explicit methods of solving equation (16) this algorithm is unconditionally stable for linear problems and corresponds to the Crank-Nicolson method[10] of time stepping for finite-difference equations. This stability feature is very important for the spontaneous-ignition problem, as will be shown later, since it allows the use of arbitrary size time steps Δt-large time steps being used in the induction period when the heat generated by reaction is trivial, and very small time steps being used to follow the temperature field of the reactive solid at times close to spontaneous ignition. In addition, the truncation error associated with the Crank-Nicolson procedure is on the order of $(\Delta t)^2$ contrasted

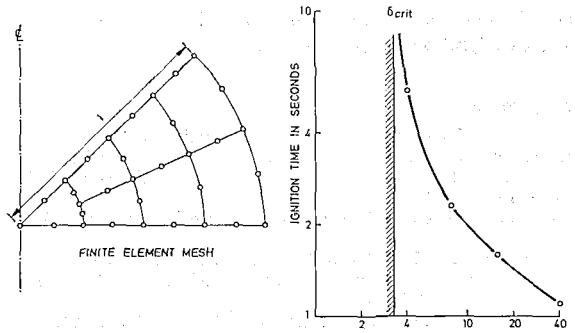

Fig. 7 Reactive sphere—induction time versus Frank-Kamenetskii parameter

with (Δt) for the usual explicit time-differencing method.

At each time step, then, the nonlinear set of equations, equation (26) must be solved. Again we found that the Newton-Raphson method, in spite of the greater amount of computation for each iteration, was more efficient for solving equation (26) than the method of successive approximations. The Newton-Raphson procedure for solving equation (26) is little different than that for handling equation (17) discussed previously—the only difference being a constant vector (the right-hand side) that must be included in the calculation of residuals, and in the form of $\{F\}$ (see equation (24)).

An automatic time-step-adjustment feature was incorporated into the transient program for studying spontaneous ignition. Two parameters, $\Delta\varphi_{\max}$ and $\Delta\varphi_{\min}$, were read into the program. Over any time interval of length Δt, equation (26) was solved using the right-hand side determined by $\{\varphi\}$; for problems where $[H]$ and $[C]$ depended on $\{\varphi\}$, these matrices were likewise evaluated. The norm of the difference $(\{\varphi\}_{n+1} - \{\varphi\}_n)$ was then computed excluding those points of Γ where $\{\varphi\}$ was specified. If the norm was less than $\Delta\varphi_{\min}$, Δt was doubled before going on to the next time step, whereas if the norm was greater then $\Delta\varphi_{\max}$, Δt was halved and the calculation for that time step repeated (this procedure was repeated until the norm was acceptable). Finally, if the norm lay between the two limits the calculation was advanced directly to the next time step. Over the spectrum of transient problems solved by this method, Δt varied over enormous ranges of values—from 10^{-4} sec, near spontaneous ignition, up to 10^4 sec, for slowly varying φ whenever an equilibrium situation was approached. This in itself is an indication of the saving in computer time compared with constant time-increment methods.

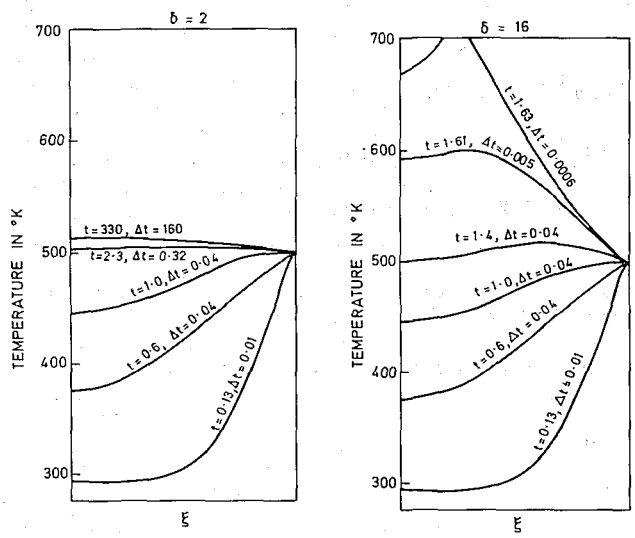

Fig. 8 Temperature profiles for ignition (δ = 16) and nonignition (δ = 2) transient behavior of a reactive sphere

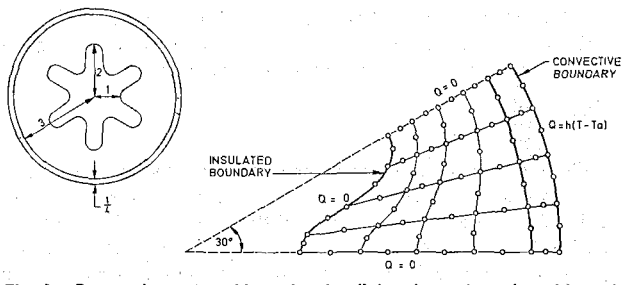

Fig. 9 Composite test problem showing finite element mesh and boundary conditions

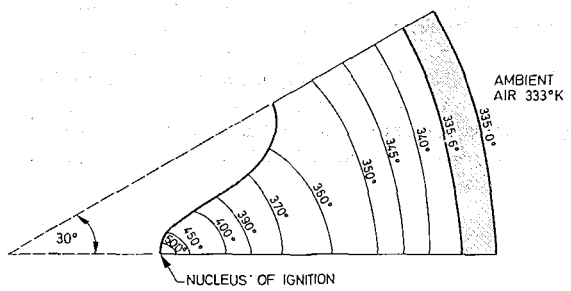

Fig. 10 Temperature profiles at ignition for inert—explosive composite

***B* Results.** The calculational procedure described in the foregoing was tested on the problem of a reactive sphere of unit cm radius, initially at room temperature, and subjected to an ambient temperature φ_a equal to 500 deg K. Again, this is a one-dimensional problem but is treated here as a two-dimensional axisymmetric problem using the seven quadratic isoparametric elements shown in Fig. 7. A constant thermal conductivity of 0.2 W/cm − °K and a unit heat capacity were assumed for the reactive solid, and the kinetic properties occurring in equation (1) were selected so that $E/R\varphi_a$ was 20. The heat of decomposition was then chosen to give values of the Frank-Kamenetskii parameter δ (equation (2)) equal to 2, 4, 8, 16, and 40, respectively, the first value being less than, and the succeeding values greater than, the critical value of the unit sphere 3.32.

The results of these calculations were as expected with spontaneous ignition of the sphere occurring for all but the case where δ = 2. Fig. 7 illustrates (roughly) the relationship in the induction time calculated as a function of δ—this relationship bearing close resemblence to that obtained by Zinn and Mader.[7] As also observed in references [7 and 11], our results showed the nucleus of ignition moving away from the center of the sphere toward the outer surface as δ became larger. Fig. 8 illustrates profiles of temperature through the sphere for various times up to equilibration for the case δ = 16. Also indicated on the temperature profile is the value of Δt being used by the computer program at that time. Each one of these problems ran in less than 10 min on the ICL-1905E computer using a starting value of Δt equal to 0.01 sec and using limits on the norm of the change in φ over any time interval between 5 and 25 deg K.

The last problem provided a test of the calculational method to handle a reactive solid of complex and composite geometry together with realistic boundary conditions. In Fig. 9 a schematic of the problem is shown; a cylinder of a reactive solid is contained within a circular cylindrical shell of inert material. We will assume that the length-to-diameter ratio of the cylinder is greater than 4, whereupon the heat flow is almost entirely within the plane of the cross section of the cylinder. The inner radius of the inert cylinder is 3m. No heat flows across the inner surface of the reactive solid and the surface-heat transfer coefficient of the inert material to the ambient air is 1.0 W/deg K − m². The composite is initially at room temperature and then immersed in ambient air whose temperature is 60 deg C (333 deg K). The thermal conductivity of the reactive mass was taken to be 1.0 W/deg K − m,

and that of the inert material to be ten times greater. Both materials have a heat capacity per unit volume of 2.0×10^6 J/deg K − m^3. The kinetic properties of the reactive material are:

$E/R = 10{,}000$ deg K
$\rho Q z = 1.0 \times 10^{14} W/m^3$.

Fig. 9 shows the finite-element mesh for a 30-deg sector of the cross section, made up of quadratic isoparametric elements. Using this finite-element mesh and the procedures for solving the criticality equations discussed in Section 2, the critical value of δ was computed and found to be 1.95 (based on a 1-m radius of the reactive material). Then using the thermal and kinetic properties of the reactive material, the Frank-Kamenetskii parameter δ (equation (2)) was computed to be 7.56, hence spontaneous ignition of the composite will occur.

A transient solution to the problem was then carried out using room temperature initial conditions and limits on the change in absolute temperature over a time increment of 2 and 10 deg K. Spontaneous ignition occurred after 2.1×10^3 hr along the inner surface of reactive material. Fig. 10 illustrates temperature profiles through the cross section at the time of ignition where the nucleus of ignition can also be seen.

References

1 Frank-Kamenetskii, D. A., *Diffusion and Heat Exchange in Chemical Kinetics*, Princeton University Press, Princeton, N. J., 1955.

2 Joseph, D. D., and Lundgren, T. S., *Arch. Rational Mech. Anal.*, Vol. 49, 1973, p. 241.

3 Frank-Kamenetskii, D. A., *Acta Physicochim.*, USSR, Vol. 10, 1939, p. 365.

4 Chambre, P. L., *J. Chem. Phys.*, Vol. 20, 1952, p. 1795.

5 Boddington, T., Gray, P., and Harvey, D. I., *Phil. Trans. Roy. Soc., London*, Vol. 270, 1971, p. 467.

6 Wake, G. C., *Combustion and Flame*, Vol. 17, 1971, p. 171.

7 Zinn, J., and Mader, C. L., *J. Appl. Phys.*, Vol. 31, 1960, p. 323.

8 Zienkiewicz, O. C., *The Finite Element Method*, McGraw-Hill, London, 1971.

9 Rall, L., *Computational Solution of Nonlinear Operator Equations*, Wiley, New York, 1969.

10 Crank, J., and Nicolson, P., *Proc. Cambridge Phil. Soc.*, Vol. 43, 1947, p. 50.

11 Merzhanov, A. G., Abramov, V. G., and Gontkovskaya, V. T., *Dokl. Akad. Nauk SSSR*, Vol. 148, 1963, p. 156.

ERRATA

An errata on S. A. Anderson, L. A. Hale, H. H. Hunt, and P. E. Pulley, "A Technique for Determining the Transient Heat Flux at a Solid Interface Using the Measured Transient Interfacial Temperature," published in the November, 1973, issue of the JOURNAL OF HEAT TRANSFER, pp. 492–497.

Equation (5), p. 493 should read

$$q(t) = \chi(0) \cdot \theta(t) + \int_0^t \left\{ -\frac{k_s}{2\sqrt{\pi \alpha_s}} (t - \tau)^{-3/2} \right\} \theta(\tau) \cdot d\tau;$$

Equation (6), p. 493 should read

$$q(t) = \frac{k_s}{\sqrt{\pi \alpha_s}} \left\{ \frac{\theta(t)}{\sqrt{t}} + \frac{1}{2} \int_0^t \frac{\theta(t) - \theta(\tau)}{(t - \tau)^{3/2}} d\tau \right\};$$

Equation (13), p. 494 should read

$$q_j(t) = \frac{k_s}{\sqrt{\pi \alpha_s}} \left(2S_{(1,1)} t^{1/2} + \frac{8}{3} S_{(1,3)} t^{3/2} + \frac{16}{5} S_{(1,3)} t^{5/2} \right.$$

$$\left. + \frac{16}{5} \sum_{i=2}^{i=j} \left[S_{(i,3)} - S_{(i-1,3)} \right] \left[t - t_i \right] \right), \; t_{j+1} \geq t \geq t_j, \; t_1 = 0,$$

$$j = 1, 2, \ldots, = n - 1.$$

L. A. Kennedy
Assoc. Professor.
Mem. ASME

C. Scaccia[1]
Instructor.

Faculty of Engineering and
Applied Sciences,
State University of New York at Buffalo,
Buffalo, N. Y.

Modeling of Combustion Chambers for Predicting Pollutant Concentrations

This investigation presents the results of numerically modeling the combustion processes with a combustor. This furnace model consists of a rectangular chamber with rear and forward facing steps. The fuel and oxidizer are injected from two separate inlets. The swirl produced by the oxidizer inlet vanes in the actual physical situation is also modeled. The governing elliptical equations are solved numerically using a modified Gauss-Siedel procedure. Upwind differences are employed in the nonlinear convective terms to insure stability for all the Reynolds numbers considered. A parametric study to show the influence of the inlet conditions on the interior recirculation flow was performed. The burning of methane was studied within the model combustor with particular attention focused on the formation of nitrogen oxide and carbon monoxide. Stream lines, temperature, and concentration profiles are obtained within the combustor. The effect of inlet conditions on center-line profiles is discussed.

Introduction

In continuous combustion devices, it is becoming increasingly important to have a knowledge of the velocity, temperature, and concentration distributions along with the degree of advancement of the reactions within the combustor. At the present time, most numerical studies dealing with combustors have employed stirred reactor techniques to consider combustor efficiency, mixedness, etc., and the influence of volume parameters on pollutant emissions. Recently Spalding [1][2] and his colleagues have developed numerical models for predicting velocity and temperature fields within combustors utilizing step reactions and they have applied these to a variety of flows. Subsequently, a number of studies using his technique with one step reactions (reactants to products) have been performed wherein the composition of the products is based upon equilibrium chemistry. A review of the various modeling techniques is summarized in reference [2]. However, in many applications the finite rate chemistry is important.

In this paper a numerical modeling approach is described which differs in a number of aspects from Spalding's method and in addition includes finite rate chemistry. The velocity, temperature and concentration distributions along with the degree of advancement of the reactions within the combustor may be obtained.

The model is applied to a combustor described as a rectangular chamber with rear and forward facing steps. The hydrocarbon fuel and the oxidant are injected at separated inlets with assigned values of vorticity. Subsequently, these chemically reacting jets interacts in this confined region.

While the problem of mixing of reacting jets in an unconfined region has been studied quite extensively, the corresponding flow in a confined region has not. The goal of the present modeling studies has been to obtain predictions of pollutant concentrations within a two-dimensional combustor and begin investigations of the influence of inlet conditions upon these profiles.

Governing Equations

The system of conservation equations governing this nonequilibrium flow is simplified through the use of the Shvab-Zeldovich approximations [3]. In addition, it is convenient to introduce the stream function Ψ and the vorticity Ω and place the equations into a nondimensional form. The resulting system of four nonlinear partial differential equations describe the global continuity equation and the conservation of species, momentum and energy. These may be written in vector form as

$$\text{div (grad } \Psi) = -\Omega \tag{1}$$

$$V \cdot \text{grad } \Omega = (\text{Re})^{-1} \text{ div (grad } \Omega) \tag{2}$$

$$V \cdot \text{grad } T^* + \frac{L \sum_i h_i \omega_i}{\rho C_p V_0 T_0} = (\text{RePr})^{-1} \text{ div (grad } T^*) \tag{3}$$

$$V \cdot \text{grad } Y_i + \frac{L \omega_i}{\rho V_0} = (\text{ReSc})^{-1} \text{ div (grad } Y_i) \tag{4}$$

Here Y_i is the mass fraction of species i, T^* is the dimensionless

[1] Presently Staff Engineer, Linde Division, Union Carbide Corp., Tonawanda, N. Y.

[2] Numbers in brackets designate References at end of paper.

Contributed by the Heat Transfer Division for publication in the JOURNAL OF HEAT TRANSFER. Manuscript received by the Heat Transfer Division, October 24, 1973. Paper No. 74-HT-NN.

temperature, ω_i is the rate of production of species i, h_i is the enthalpy of species i and Re, Sc, and Pr are, respectively, the Reynolds, Schmidt, and Prandtl numbers assumed to be constant. Then the only required transport property is the effective viscosity. The simple expression of Spalding [1] is used in the present work:

$$\mu_{\text{eff}} = CD^{2/3}L^{-1/3}\rho^{2/3}(\dot{m}_f V_f^2 + \dot{m}_{\text{ox}} V_{\text{ox}}^2)_{\text{inlet}}$$

The boundary conditions employed will consider the stream function Ψ to be known along any wall and the boundary surfaces adiabatic and noncatalytic. The vorticity may then be obtained using equation (1). Coupled to these equations are the kinetics for the oxidation of a hydrocarbon and nitric oxide formation. The specific rate constants are all expressed as functions of temperature in the form

$$k_i = A_i T^{\alpha_i} \exp(-E_i/RT) \tag{5}$$

where the parameters A_i, α_i, and E_i are obtained from empirical data. For the generalized chemical reaction

$$\sum_{i=1}^{N} \nu_{i,k}' M_i \rightleftarrows \sum_{i=1}^{N} \nu_{i,k}'' M_i$$

the rate of production of a given species is given by

$$\dot{Y}_i = W \sum_{k=1}^{M} (\nu_{i,k}'' - \nu_{i,k}') k_f \Big\{ \prod_{i=1}^{N} ((Y_i\rho)/W_i)^{\nu_{i,k}''} - \frac{1}{K_c} \prod_{i=1}^{N} ((Y_i\rho)/W_i)^{\nu_{i,k}'} \Big\} \tag{6}$$

where $k = 1 \ldots M$ (reactions) and $i = 1 \ldots N$ (species).

The complete kinetic model is a composite of two separate models for the basic reaction systems involved. These kinetic submodels are: *(a)* the C-H-O system which controls the energy release and the concentrations of carbon monoxide and unburnt hydrocarbons; and *(b)* the N-O system which controls the nitric oxide concentrations. A discussion of this approach is given in Scaccia [4].

For most practical fuels, the detailed kinetic mechanisms for the C-H-O reaction system are not available or in those simpler cases where the mechanisms are known, the rate constants are not. Therefore, there have been many attempts to model the hydrocarbon process with a quasi-global mechanism [5, 6, 7]. Such a mechanism can be utilized to study the coupling between nitric oxide kinetics and the combustion process without using the fuel's detailed reaction mechanisms for which either the mechanism themselves or their rates are often unknown.

One such approach takes the hydrocarbon reaction to be of the form

$$C_nH_m + (1/2n + 1/4a_1)O_2 = (n)CO + 1/2a_1H_2O + (1/2)(m - a_1)H_2 \tag{7}$$

Here reaction rate and the stoichiometric coefficient a_1 are empirically fitted so that this step represents the rate of fuel consumption and the temperature rise. Edelman, et al. [7] has used a finite rate for this reaction (equation (7)) and found good agreement for lean mixtures at high temperatures and pressure. Other global models which includes additional intermediate species have been examined. Their inclusion showed little sensitivity [8] and do not appear to alter the global predictions. Hence, the additional intermediate species have not been employed in this study.

The global model of Edelman (equation (7)) accounts for the partial oxidation of the hydrocarbon and the remaining kinetic processes are assumed to follow the CO oxidation mechanism. These latter mechanisms provide the kinetic link between the nitric oxide and the hydrocarbon combustion reactions through their influence on the concentration of hydroxyl radicals and monatomic species. The pertinent reactions and their rate data are listed in Table 1. The rates of the first four reactions are so fast that they can be considered to be in a state of partial equilibrium. This assumption then offers a set of algebraic equations which are used to reduce the number of kinetic rate equations that must be integrated to obtain the overall composition of the system.

The literature on the kinetics of nitric oxide formation is quite abundant and the important reactions for NO formation in the temperature-pressure ranges of interests are the last three reactions in Table 1. The principle reactions are the Zeldovich reactions given by the first two nitric oxide reactions. Since these nitric oxide mechanisms have been recently questioned in the literature [9, 10, 11] their validity will be discussed with the results.

Numerical Approach

The governing equations were put into a finite difference approximation. For the vorticity and stream function, upwind differencing was performed and Varga's point successive over-relaxation approach was employed to obtain these two variables [2]. However, in order to improve and speed up the convergence of the entire system of equations governing the reacting flow, an under-relaxation method was utilized to obtain the temperature T and the mass fraction Y_i.

In evaluating the energy and species equation, the more dominant source of instability is the rate of change of the mass fraction $\omega_i = \dot{Y}_i$ expressed by equation (6). This gives a system of "stiff" ordinary differential equations which are very unstable. Explosive divergence, characterized by a rapid unbounded divergence within two or three iterations is common.

To control this behavior, the variables T and Y_i may be under-relaxed after each iteration. However this usual approach would increase manyfold the number of iterations required for convergence. It is more appropriate to directly under-relax the source of divergence after each iteration i.e., Y_i. From equation (17) it is noted that any error induced will be amplified by the terms $(Y_i\rho/W)^{\nu'}$ and $(Y_i\rho/W)^{\nu''}$. In this paper the rate of change of the mass fraction is under-relaxed by replacing these terms with

$$\left(\frac{Y_i\rho}{W}\right)^{\nu'(r-(\Delta r)n)} \quad \text{and} \quad \left(\frac{Y_i\rho}{W}\right)^{\nu''(r(\Delta r)n)} \tag{22}$$

Here r is the relaxation parameter, Δr is an arbitrary incremental change in r and n is the interaction counter. After each iteration the relaxation parameter returns to one and all stoichiometric coefficients return to their initial values. For the methane-air reaction, r was selected to be 1.6 and Δr was set to 0.005. This

Nomenclature

A_i = rate parameter (see equation (5))
C_p = specific heat
D = diameter of combustor
E_i = activation energy
h_i = enthalpy of species i
K_c = equilibrium constant
k_i = specific rate constant
$\dot{m}$ = mass flow rate
L = length of combustor
Pr = Prandtl number
Re = Reynolds number
Sc = Schmidt number
T = temperature
V = velocity
W = molecular weight
Y_i = mass fraction of species i
α_i = rate parameter (see equation (5))
ν = stoichiometric coefficient
ρ = density
ψ = stream function
Ω = vorticity
ω_i = rate of production species i

Subscripts

f = fuel
i = number of species
k = number of reaction
o = reference condition
ox = oxidizer

Table 1 Rate parameters for kinetic model

$k_k = AT^b \exp(-E/RT)$ (cm³/mole sec)

Reaction	A	b	E/R	Reference
Hydrogen reactions				
$OH + H_2 = H_2O + H$	2.19×10^{13}	0	2590	17
$OH + OH = O + H_2O$	5.75×10^{12}	0	393	17
$O + H_2 = H + OH$	1.74×10^{13}	0	4750	17
$H + O_2 = O + OH$	2.24×10^{14}	0	8450	17
$O + H + M = OH + M$	1×10^{16}	0	0	18
$O + O + M = O_2 + M$	9.38×10^{14}	0	0	19
$H + H + M = H_2 + M$	5×10^{15}	0	0	18
$H + OH + M = H_2O + M$	1×10^{17}	0	0	17
Carbon monoxide reactions				
$CO + OH = H + CO_2$	5.6×10^{11}	0	543	17
$CO + O_2 = CO_2 + O$	3×10^{12}	0	25000	20
$CO + O + M = CO_2 + M$	1.8×10^{19}	−1	2000	21
Nitric oxide reactions				
$N + NO = N_2 + O$	4.2×10^{13}	0	0	22
$N + O_2 = NO + O$	1.2×10^{13}	0	7100	22
$N + OH = NO + H$	1.2×10^{13}	0	0	22

(Reverse reaction rate, k_r, is obtained from k_f and the equilibrium constant, K_c.)

choice of the relaxation factor is a trial and error procedure since it depends on the stiffness of the equations. The solution was assumed to have converged when the set of equations were satisfied to an order of 10^{-4} and when $\Sigma_{i=1}^{N} Y_i = 1$ at various selected grid locations. Both requirements are satisfied during the iteration procedure at the same rate of convergence so that either criteria is sufficient. The computational time per iteration is reduced considerably when the mass fraction is calculated only at preselected grid locations extrapolated. The rate of change was calculated for 90 equally spaced grid points and the values at intermediate locations were linearly interpolated from the known values. This resulted in a reduction of the computational time per iteration by a factor of four.

Using this "under-over relaxation" method, equations (1) to (4) and (6) were solved in the following manner. Initial values were assumed at each grid point. The boundary conditions and reaction rates were calculated at each node. The set of equations were solved by successive substitution with the field scanned row by row and the previous values replaced by the new values as soon as they were obtained. After each iteration a new set of variables was obtained along with updating the boundary conditions and the reaction rates and the process repeated. In this procedure, the vorticity and stream function were over-relaxed and the temperature and species mass fraction were under-relaxed as discussed earlier.

Discussion of Results

It should be noted that the development and understanding of two-dimensional models of combustors are a necessary prelude to obtaining a physically realistic three-dimensional model of a combustor. The work described in the foregoing is part of such an effort.

For the present two-dimensional case, sample results have been obtained for our rectangular combustion chamber. The gaseous fuel is injected along the center line and the air is injected with a given vorticity at an inlet separated from the fuel. Nitric oxide is formed in the post flame region and is then quenched due to mixing of cooler gases.

To simulate the swirl of an actual oxidizer injector, the effect of inlet vorticity on the recirculation patterns was examined for a nonreacting flow. Some results are shown in Fig. 1 to 3. For $\Omega = 0$, a recirculation zone is established off the entrance step and stretches downstream along the bottom wall with a concave curvature for the dividing streamline. For $\Omega = +5$, Fig. 2, this recirculation zone grows in size, stretching three times as far as the $\Omega = 0$ case and tends to deflect the oxidant jet upward due to the upward tendency of this jet. Also of interest is the appearance of a new small recirculation zone of opposite spin inside the main recirculation. Increasing the magnitude of the vorticity to $\Omega = +15$, Fig. 3, the large recirculation cell near the wall extends four times as far as the $\Omega = 0$ case and moves significantly into the main flow region. The secondary recirculation within this zone also grows in magnitude. In addition, there now appears an opposite spin recirculation region upstream of the forward facing step. Between the fuel and oxidant inlets, two recirculating flow cells are developed for all values of vorticity studied. The actual shape of this region is dependent upon magnitude of the vorticity. For

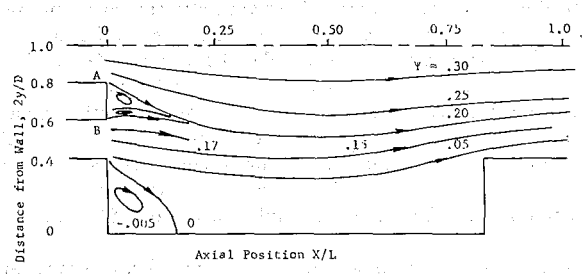

Fig. 1 Constant stream line contour $\omega = 0$

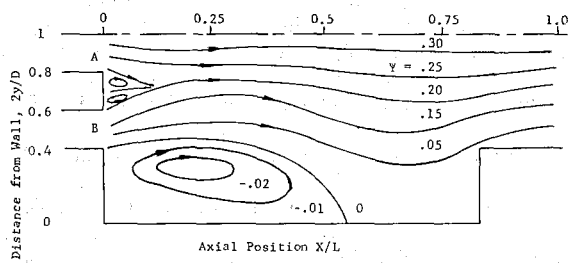

Fig. 2 Constant stream line contour $\omega = +5$

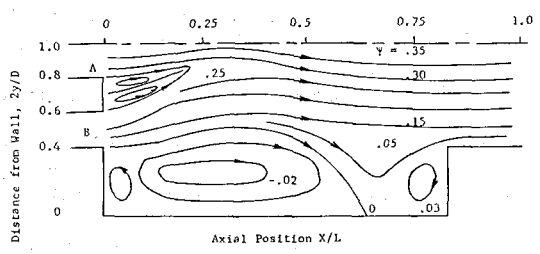

Fig. 3 Constant stream line contour $\omega = +15$

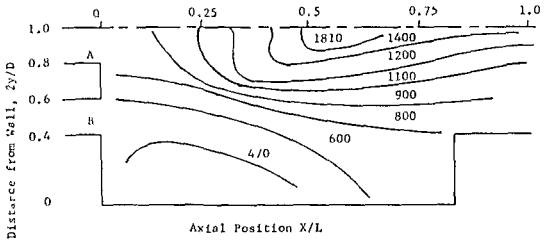

Fig. 4 Constant temperature contour, deg K

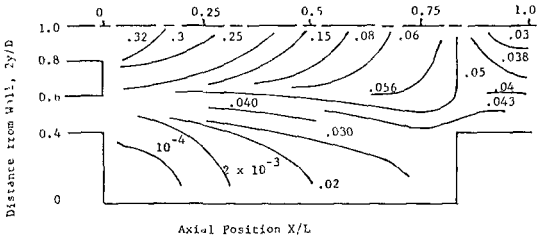

Fig. 5 CH_4 constant mass fraction contour

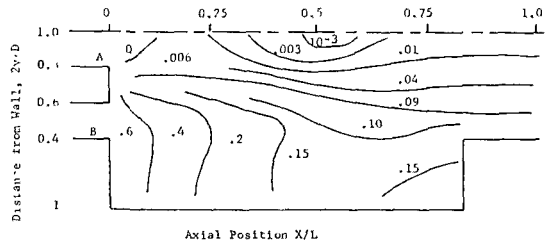

Fig. 6 O_2 constant mass fraction contour

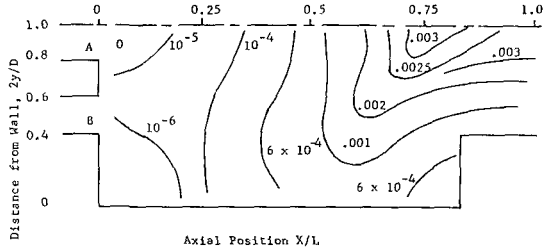

Fig. 7 NO constant mass fraction contour

large values of vorticity these cells are stretched almost one fourth of the combustor length.

The combustion of methane-air was studied with the goal of modeling two-dimensional combustors and obtaining information on the parameters influencing pollutant formation. Representative results of the computations on this combustion process are given in Fig. 4 for adiabatic wall conditions and inlet air vorticity equal to five, $\Omega = 5$. The fuel enters with an axial velocity of 120 m/sec at 300 deg K and the air is injected at 30 m/sec and 300 deg K. The overall equivalence ratio is 0.8. All calculations were performed at atmospheric pressure. The isotherms calculated (Fig. 4) are symmetrical about the axis and roughly oval in pattern. The predicted maximum temperature, 1810 deg K, agrees well with independent flame temperature calculations.

The distribution of the mass fractions of CH_4 and O_2 is shown in Fig. 5 and 6. As is physically expected, initially the methane tends to be contained near the axis of the furnace. As the combustion progresses, and the flow moves down the channel, the unburnt CH_4 mixes with the products and spreads away from the axis. Near the exit of the furnace the concentration of unburnt CH_4 is quite uniform about a mass fraction of 0.038 but does increase slightly as the wall of the combustor is approached. The oxidant shows a reciprocal pattern being mixed toward the furnaces center and reacting with the methane. The oxidation of the methane occurs continuously from the point of initial interaction of the fuel/air jets. The maximum oxygen consumption occurs in the vicinity of the maximum temperature region and gives rise to a local minimum concentration of oxygen.

The nitric oxide mass fraction profiles are seen to have a local maximum near the center line of the furnace downstream of the "flame" region (Fig. 7). This concentration level of NO decays very little between the location of this maximum and the exit. These computed results which show that once formed, NO levels are essentially fixed. The principle reactions used in the NO kinetics were those of the modified Zeldovich mechanism. Recently there has been discussions in the literature over the validity of the model. Other reaction sources for "prompt NO" have been proposed [8, 9, 10] while the Zeldovich mechanisms has been defended as consistent if the concentration of atomic oxygen in the vicinity of the flame is larger than equilibrium [12, 13, 14, 15]. To examine the influence of atomic oxygen, parallel runs were made with and without the NO_x reaction included. For the latter case, the atomic oxygen distribution resulting from the CO reaction mechanisms indicates a "super-equilibrium" concentration is present in the post flame region. This level of O is the required parameter to allow the Zeldovich mechanism to correctly predict nitric oxide concentrations. The existence of these large atomic oxygen concentrations in the post flame result in values of nitric oxide concentrations larger than that predicted by equilibrium chemistry. With the high O atom levels encountered in the model it will be necessary to include the oxidation of NO to NO_2 in future calculations.

The concentration profiles of carbon monoxide, carbon dioxide, water vapor, atomic hydrogen, atomic nitrogen, and the hydroxil radical also have been obtained. The carbon dioxide concentrations appearing in the post flame region are the same order of magnitude as calculated by equilibrium chemistry. The CO is rapidly oxidized as the flow proceeds downstream.

The center-line profiles of the principle species are summarized in Fig. 8. Initially O_2 increases as it mixes with the methane and subsequently decays to a minimum value near the maximum temperature region. During this period the methane continuously reacts with the O_2, and the temperature continuously increases. Downstream of this region the concentration of O_2 again increase due to additional oxygen being brought toward the center line of the furnace by the two-dimensional mixing. During this period the temperature decays due to dilution effects. The concentration of free hydrogen and atomic oxygen are seen to peak, respectively, in the maximum temperature region and slightly downstream of it. Since the production of these species are favored by temperature increases, these results are consistent with equilibrium predictions and von Hoff's equation. The concentration of the hydroxil radical continuously increases as the reaction and flow proceeds downstream; the same is observed for water vapor. Both decay as one moved from the center of the furnace toward the wall.

The effects of varying the inlet vorticity of the air was found to yield similar results in the mass fraction contours. The principle affect of the inlet air vorticity being to alter the relative positions of the maximum temperature and the maximum (minimum) concentrations. At large values of inlet vorticity, the maximum temperature appears to move towards the inlet jets and be somewhat reduced. This results in the calculated levels of NO also being slightly reduced. The movement of the maximum temperature location can be explained as due to the earlier stronger mixing of air and fuel. However the authors can only speculate that dilution effects cause the temperature drop. Nevertheless, it appears that by altering inlet conditions, the relative positions of maxima and minima can be altered hopefully to the benefit of reducing their levels.

To evaluate how realistic these models may be, one must ultimately compare their predictions with experiments. This has not

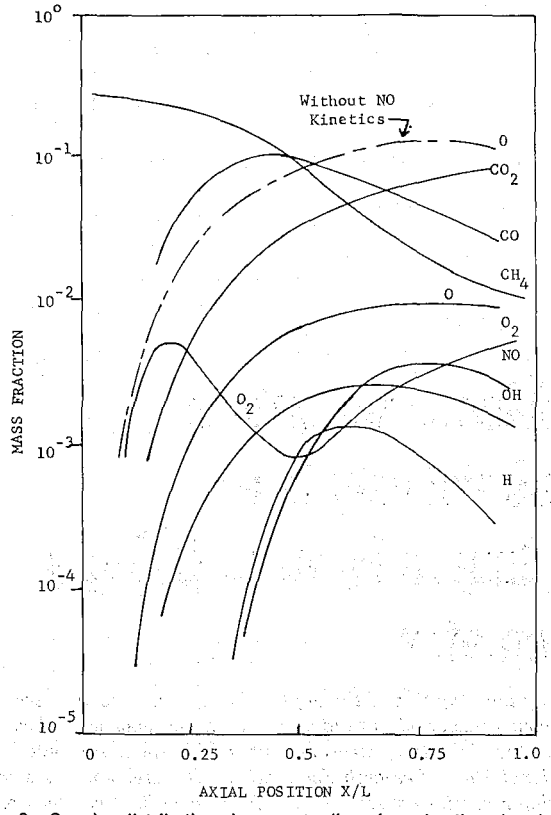

Fig. 8 Species distribution along center line of combustion chamber

been done for the present case. However, an analogous calculation was performed for a model turbine combustor and compared with measured data [23]. The temperature and concentration distribution patterns as well as the sequence of events agreed quite reasonably. The magnitude of the concentrations tended to be high (10 to 25 percent) and this was attributed to a neglect of certain chemical reactions such as the NO_2 reactions, which could reduce the large values of O atoms and hence the final NO concentrations. These comparisons reinforces our belief that the initial work described in this paper is a correct beginning for the future development of practical combustor models.

References

1 Gosman, A. D., Pun, W. M., Runchal, A. K., Spalding, D. B., and Wolfstein, M., *Heat and Mass Transfer in Recirculating Flows*, Academic Press, New York, 1969.

2 Caretto, L. S., "Modeling Pollutant Formation in Combustion Processes," presented at the Fourteenth Symposium (International) on Combustion, Pennsylvania State Univ., Aug. 1972.

3 Williams, F. A., *Combustion Theory*, Addison-Wesley, Reading, Mass., 1965.

4 Scaccia, C., "A Numerical Model for Predicting Pollutants Concentrations Within Furnaces and Turbine Combustors," PhD thesis, State University of New York at Buffalo, 1973.

5 Avery, W. H., and Hart, R. W., "Combustor Performance With Instantaneous Mixing," *Industrial and Engineering Chemistry*, Vol. 45, No. 8, Aug. 1953, pp. 1634–1637.

6 Chinitz, W., and Baurer, T., "An Analysis of Non-Equilibrium Hydrocarbon Air Combustion," Fall Meeting, Western States Section/The Combustion Institute, Paper No. 65-19, 1965.

7 Edelman, R., and Fortune, O., "A Quasi-Global Chemical Kinetic Model for the Finite Rate Combustion of Hydrocarbon Fuels," AIAA Seventh Aerospace Sciences Meeting, Paper No. 69-86, 1969.

8 Kollrack, R., and Aceto, L. D., "Nitric Oxide Formation in Gas Turbine Combustors," *AIAA Journal*, Vol. 11, No. 5, May 1973, pp. 664–669.

9 Fenimore, C. P., "Formation of Nitric Oxide in Premixed Hydrocarbon Flames," Thirteenth Symposium (International) on Combustion, The Combustion Institute, 1971, p. 373.

10 Livesey, J. B., Roberts, A. L., and Williams, A., "The Formation of Oxides of Nitrogen in Some Oxy-Propane Flames," *Combustion Science and Technology*, Vol. 4, No. 1, 1971, pp. 9–15.

11 Iverach, D., Basden, K. S., and Kirov, N. Y., "Formation of Nitric Oxide in Fuel-Lean and Fuel-Rich Flames," Paper presented at the Fourteenth Symposium (International) on Combustion, Pennsylvania State Univ., 1972.

12 Kennedy, L. A., and Scaccia, C., "Mixing of Coaxial Jets in a Confined Tube," *Proceedings of the 13th Midwestern Mechanics Conference*, University of Pittsburgh Press, Aug. 1973, pp. 95–111.

13 Bowman, C. T., "Investigation of Nitric Oxide Formation Kinetics in Combustion Processes: The Hydrogen-Oxygen-Nitrogen Reaction," *Combustion Science and Technology*, Vol. 3, No. 1, Apr. 1971, pp. 37–45.

14 Sarofim, A. F., and Phl, J. H., "Kinetics of Nitric Oxide Formation in Premixed Laminar Flames," Paper presented at the Fourteenth Symposium (International) on Combustion, Pennsylvania State University, 1972.

15 Thompson, D., Brown, T. D., and Beer, J. M., "The Oxides of Nitrogen in a Combustion System," University of Sheffield, U. K., Department of Chemical Engineering and Fuel Technology, Report, 1970.

16 Kennedy, L. A., and Scaccia C., "A Two-Dimensional Model of a Combustor," *Bulletin of the American Physical Society*, Vol. 17, No. 11, Nov. 1972, p. 1116.

17 Baulch, D. L., "Critical Evaluation of Rate Data for Homogeneous Gas Phase Reactions," The University, Leed, U. K., Report No. 1-5, 1968–1970.

18 Moretti, G., "A New Technique for Numerical Analysis of Nonequilibrium Flows," *American Institute of Aeronautics and Astronautics Journal*, Vol. 3, No. 2, Mar. 1965, pp. 223–229.

19 Amman, P. R., and Timmins, R. S., "Chemical Reactions During Rapid Quenching of Oxygen-Nitrogen Mixtures From Very High Temperatures," *American Institute of Chemical Engineering Journal*, Vol. 12, No. 5, Sept. 1966, pp. 956–963.

20 Brokaw, R. S., Eleventh Symposium (International) on Combustion, *The Combustion Institute*, 1967, p. 1063.

21 Carnicom, M. L., "Reaction Rates for High Temperature Air With Carbon and Sodium Impurities," Sandia Laboratory Report SC-R-68-1797, 1968.

22 Schofield, K., "An Evaluation of Kinetic Rate Data for Reactions of Neutrals of Atmospheric Interest," *Planet Space Sciences*, Vol. 15, 1967, pp. 643–670.

23 Starkman, E. S., Mizutani, Y., Sawyer, R. F., and Teixeira, D. P., "The Role of Chemistry in Gas Turbine Emissions," JOURNAL OF ENGINEERING FOR POWER, TRANS. ASME, Series A, Vol. 93, July 1971, pp. 333–348.

R. J. Baker
Research Fellow,
Imperial College of Science
and Technology,
London, England

P. Hutchinson
Principle Scientific Officer,
A. E. R. E.,
Harwell, England

J. H. Whitelaw
Reader in Convective Heat Transfer
Imperial College of Science
and Technology,
London, England

Preliminary Measurements of Instantaneous Velocity in a Two-Meter Square Furnace Using a Laser Anemometer

The results of an exploratory investigation of the application of laser anemometry to the measurement of instantaneous velocity within industrial flames is reported. A laser anemometer was used to assess the viability of measurements within the 2 m-sq experimental furnace of the International Flame Research Foundation. Measurements were carried out, in the forward scattering real fringe mode, in a hot furnace without combustion and in gas, oil, and coal flames. The particle concentration was observed for each flow configuration and, where possible, the mean velocity value obtained from the laser anemometer was compared with that from a water cooled pitot probe. On the basis of this investigation, the value of laser anemometry to the improvement of furnace design is discussed.

Introduction

The type of instrumentation presently in use to measure flow properties in industrial furnaces is described in reference [1].[1] The hostile nature of the environment within a furnace together with the relatively ad hoc procedures used in furnace design has caused this instrumentation to be concerned exclusively with mean-flow properties and subject to uncertainties which, in general, exceed 5 percent. Thus, although there is a considerable need to develop new design procedures which will increase furnace efficiency and, at the same time reduce the output of pollutants, the available instrumentation is unable to measure sufficient flow properties with adequate precision to further the development of these procedures and to test their accuracy.

The present paper is concerned with the measurement of velocity and turbulence intensity in a furnace environment using a laser Doppler anemometer. The purpose is to assess the difficulties and the likely benefits of using this technique.

The potential benefits of laser Doppler anemomety include good spatial resolution, a linear relationship between instantaneous velocity and the measured signal, sensitivity to one velocity vector at a time, a lack of dependence of the measured signal on thermodynamic properties and no need for calibration. These advantages were demonstrated in the measurements described in references [1–4]. Each of the flames considered in these papers was, however of small physical size, unconfined and involved gas velocities less than 30 m/s. In addition, these flames were located in a controlled laboratory environment and could readily be seeded with the particles to scatter light. In contrast, the present experiments were effected in a flame of dimensions approximately 2 m long and 0.5 m in diameter. The flame was confined by the furnace and the furnace-wall temperature was around 1000 deg C. The gas velocity exceeded 50 m/s and both swirl and recirculation were present. There was little possibility of seeding the flow and part of the present purpose was, therefore, to determine the availability of suitable particles to scatter light for the laser anemometer.

Measurements were recorded in natural gas, pulverized coal, and oil flames and showed that the particle concentration in the natural gas flame was too low and in the pulverized coal flame the particles were too large to allow precise measurements of velocity with the available instrumentation. Positive suggestions are made to permit future measurements in flames of this type. In the oil flames sufficient particles were available and permitted measurements of velocity—probability—density distributions from which the mean and rms components of the fluctuating velocity were obtained.

Among the practical problems encountered in the investigation were optical alignment, laser-beam divergence, fluctuating location of the laser beam, mechanical vibrations and measurements in the recirculation zone. The extent of these problems and the authors' present attempts to overcome these are described.

Experimental Arrangements

The Furnace. The internal dimensions of the furnace were 2 m wide, 2 m high, and 10 m long with approximately 0.5 m thick walls. The burner was located at one end of the furnace and an exhaust duct at the other, as shown in Fig. 1. The central jet was

[1] Numbers in brackets designate References at end of paper.

Contributed by the Heat Transfer Division of THE AMERICAN SOCIETY OF MECHANICAL ENGINEERS and presented at the ASME-AIChE Heat Transfer Conference, Atlanta, Ga., August 5–8, 1973. Revised Manuscript received by the Heat Transfer Division October 6, 1973. Paper No. 73-HT-34.

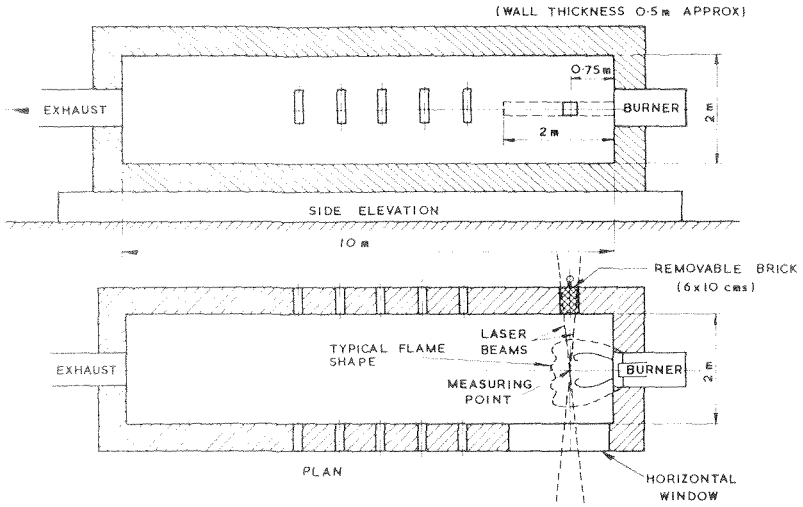

Fig. 1 Furnace geometry

interchangeable for different fuels and swirl of the air flow. In all cases the inlet air was preheated to 300 deg C.

Various combinations of air flow, fuel mixture, and swirl were investigated; the quantities shown in Table 1 refer to a total gas flow and rate of 166 kg/hr and air flow rate (5 percent above stoichiometric) of 2282 kg/hr; the swirl number indicates the ratio of angular to axial momentum. For convenience, the hot air jets are referred to as flames I and II.

Table 1

Flame No.	Fuel	Air	Swirl	Measured axial vel (m/s)
I	0	50%	0	20[a]
II	0	70%	0	30[a]
III	Gas 71%	31%	40%	
IV	Gas 89%	45%	40%	
V	Coal	Variable	Variable	
VI	Oil	47%	0	23[b], 24[a]
	(90 l hr)			
VII	(90 l hr)	47%	30%	12[b]
VIII	(90 l hr)	47%	50%	13[b]

[a] By Pitot-probe.
[b] By optical anemometry.

Optical Arrangement. Fig. 2 shows a cross section of the furnace with the optical components located in their correct positions. The argon-ion laser was operated multimode at 488 nm with an output power of 200 mW. A combined beam splitter and mirror arrangement to cross the beams at selected locations between 2 to 3 m range was specially constructed for the present tests. The unit provided a separation between the beams of 0.2 m, and hence an intersection half angle of about 2 deg. The optical arrangement provided equal path lengths of the laser beam and prevented phase coherence interference associated with operating the laser multimode. No focussing of the laser beam was incorporated in the transmitting optics as calculations indicated that, at 2-3 m focal length, the waist diameter of the laser beam (1.1 mm at $1/e^2$ points) would not be reduced unless the beam was previously expanded. This seemed unnecessary since the anticipated control volume dimensions of 1 mm dia × 10 mm long were already small in relation to the scale of the flame. The receiving optics consisted of a Galilean telescope with an adjustable focal length of between 0.5 and 2.0 m.

A schematic diagram of the complete light collecting system is shown in Fig. 3. Three separate optical benches supported the photomultiplier, receiving optics and optical unit. The laser and optical benches were mounted on tables which were isolated from the ground by anti-vibration pads which were designed particularly to prevent damage to the laser head. An EMI 9635 QB photomultiplier was used with a quantum efficiency in the blue of 17 percent. The receiving aperture incorporated a narrow band optical filter of bandwidth 2.3 nm which gave 35 percent transmission at 488 nm. Six apertures from 0.25 mm to 2.00 mm dia on a disk enabled the receiving aperture size to be varied without misaligning the photomultiplier.

Instrumentation. A block diagram of the signal processing instrumentation is shown in Fig. 4. Due to the anticipated intermittent nature of the signal, a signal processing procedure previously described in reference [4] was adopted. This involved sweeping the desired frequency range on the wave analyzer in discreet steps, squaring and integrating the output over preset times, and plotting the output as probability density distributions. It should be noted in this case, however, that a wide band (100 MHz) preamplifier was used before the wave analyzer, whereas a variable gain amplifier with high and low pass filters (to remove the low frequency components of the signal and unnecessary noise) was used before the oscilloscope. This ensured that the wave analyzer output noise band had an almost flat characteristic.

The derivation of the electrical signal from a single particle traversing a real fringe pattern formed by two equal intensity beams is shown diagrammatically in Fig. 3. It is assumed here that the particle is smaller than a half fringe spacing so that almost maximum intensity modulation of the scattered light is achieved. The electrical (Doppler) signal thus consists of a sine waveform within a Gaussian envelope, where the frequency is proportional to the velocity of the particle perpendicular to the fringes. If this frequency coincides with the center frequency of the narrow band filter of the Spectrum Analyzer, a squared output results which, if integrated over a sufficiently large number of particles is proportional to the velocity probability. By scanning the filter of the Spectrum Analyzer, the probability distribution may be obtained.

Alignment. To achieve a satisfactory alignment, it was found necessary to insert a quartz scattering plate into the furnace; successful alignment of the optical components was then confirmed by observation of the familiar Doppler signal bursts on the oscilloscope. The first alignment was maintained for a period of 26 hr, and was occasionally checked by inserting the quartz plate to ensure the beams intersected at the same position in the furnace.

During alignment of the optical components, it was observed that the unfocused laser beam, after having passed through the furnace, exhibited appreciable divergence and spatial fluctuation.

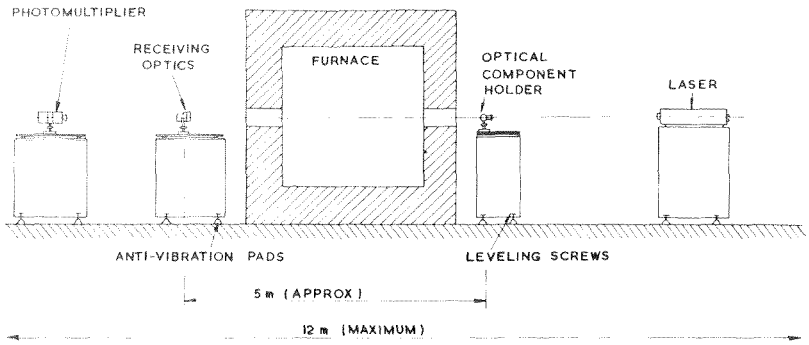

Fig. 2 Arrangement of optical components

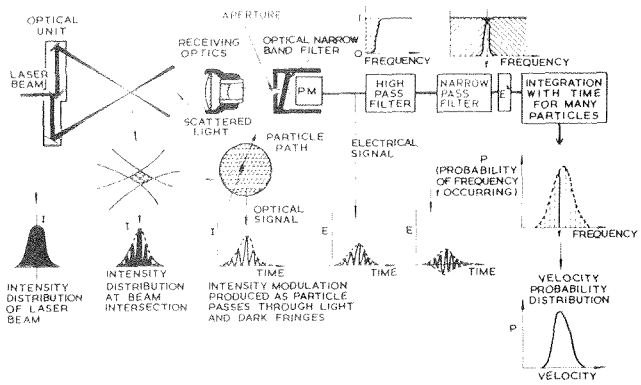

Fig. 3 Schematic of velocity determination

These effects were observed with and without the flames and with little difference from one flame to another. The unfocused beam expanded from 1.1 mm dia waist before the furnace, to an estimated 4 mm dia 2 m after the furnace and fluctuated approximately 2.5 mm about a mean position with a relatively low frequency. This indicated that the beam diameters at the intersection point were about 2 mm and crossed intermittently.[2]

Results

Observation of the signals from the hot air jets (flames I and II) and gas flames (III and IV) indicated a very low concentration of suitable scattering particles. Particle counts of approximately 10 particles/min were obtained in these flames equivalent to a signal presence about 0.001 percent of all time.

In the coal flames, however, the majority of the particles appeared too large to produce a suitable Doppler signal.[3] The signal noise level increased dramatically due to the large increase in scattering intensity from larger particles (not necessarily passing through the fringe pattern), and the "dc" component of the signal (as observed on the oscilloscope by removing the high pass filter) showed almost a 50 db gain.

Three oil flames were investigated since it was anticipated that these would contain particles of smaller mean diameter than those in the coal flames but with a concentration considerably greater than the naturally occurring particles in the gas flames. For flame VI a velocity probability distribution was recorded with about a 5 percent scatter in the points after 100 sec integration time. This spectrum is shown in Fig. 5(*a*) together with the relative measurement position in the flame. The data were accumulated in 20 sec integration periods, with a minimum of five periods per point, in order to obtain some estimation of the accuracy of the measured spectrum (numerical integration of the spectrum indicated that the mean velocity was within 5 percent and the turbulence intensity 6 percent). The lower set of points in Fig. 5(*a*) represents the time-averaged noise level measured by alternately blanking out each beam from the optical unit (i.e., measuring only time averaged unmodulated scattered light plus electronic noise). Before the flame conditions were changed, the mean velocity at the same location was checked by a single-hole water-cooled pitot probe (in this case a single hole probe was adequate as no swirl was present in the flame). A mean value of 24 m/s was obtained compared with 22.7 m/s from the measured spectrum and within the accuracy of the pitot probe and laser anemometer measurements. The turbulence intensity from this spectrum was 24.2 percent.

Swirl was then introduced to produce flames VII and VIII, and velocity spectra measured in a similar manner to that previously described, as shown in Figs. 5(*b*) and 5(*c*), respectively. The mean velocities were 11.9 m/s and 13.5 m/s, and turbulence intensities 42.0 percent and 57.6 percent, respectively.

Discussion

The present investigation has demonstrated that the laser—Doppler anemometer can be used to measure mean velocity and the rms value of the fluctuating velocity in oil-fired furnace flames. The precision of measurement is of the order of 5 percent

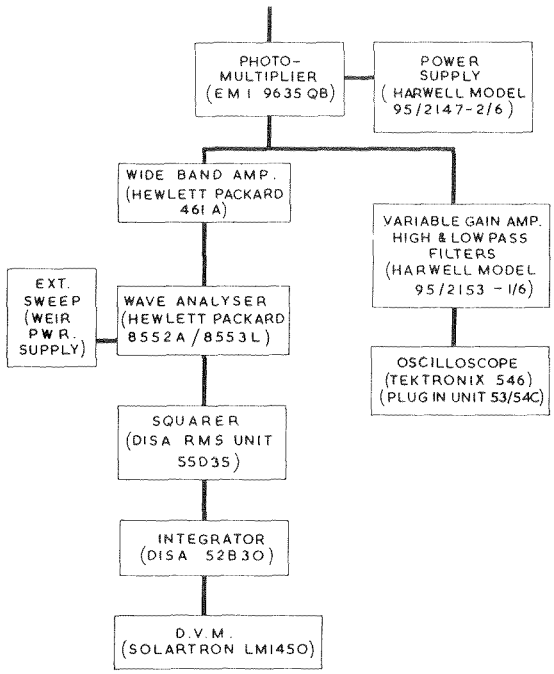

Fig. 4 Signal processing instrumentation

[2] Intermittency here refers to the percentage time the beams are *not* intersecting.

[3] In general the amplitude of the ac component (containing the velocity information) of the Doppler signal decreases with increasing particle size beyond the fringe spacing (5 μm)

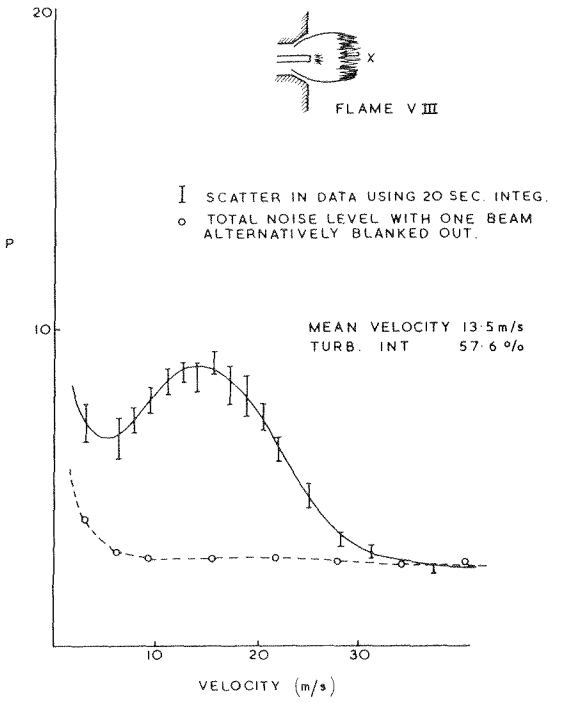

Fig. 5 (*a*) Velocity probability distribution in an oil flame with 0 percent swirl

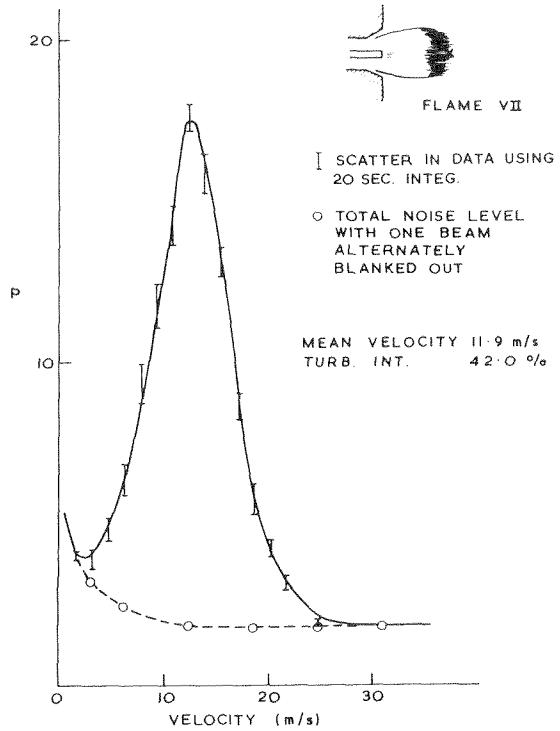

Fig. 5 (*b*) Velocity probability distribution in an oil flame with 30 percent swirl

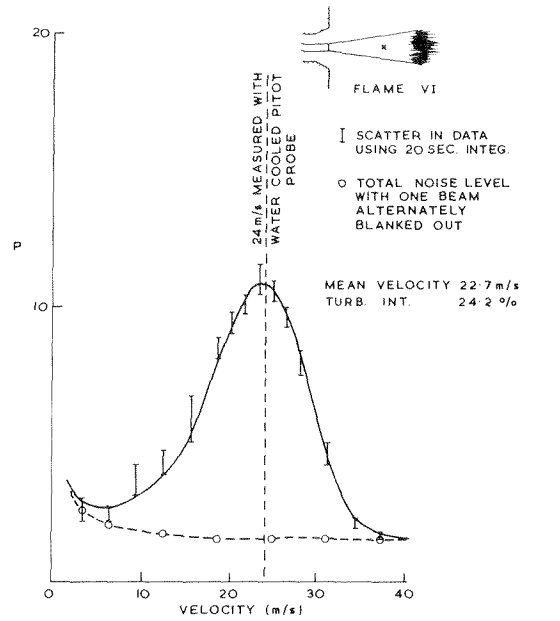

Fig. 5 (*c*) Velocity probability distribution in an oil flame with 50 percent swirl

and 6 percent for the mean and rms values respectively and the measuring time of the order of 20 min per probability distribution.[4] The following paragraphs consider the influence of the fluctuating location of the laser beams due to refractive index gradients on the dimensions of the control volume and on the speed and ease of measurement.

The frequency of mechanical vibrations is normally less than 60 Hz and makes no contribution to the optical signal, and the subsequent photomultiplier output signal, other than to cause the two beams to cross intermittently around the predetermined location and consequently cause slight variations in the intersection angle. In addition, these vibrations may also cause the light collecting system to focus only intermittently on the same predetermined location. In practice, the mechanical vibrations were effectively damped and therefore caused no problem.

As a result of the dependance of the refractive index on the local density, chemical composition, and temperature, turbulence in the presence of thermal gradients produces fluctuations in the local value of the refractive index, and its gradient with position. These fluctuations have a wavelength of similar order as the turbulent fluctuations, but much greater than that of the laser beam traversing the medium; it follows, therefore, that the path of the light beam can be described in terms of geometrical optics. Application of Fermats principle[5] shows that the equation for the path of the beam is given by:

$$\frac{d\hat{l}}{dl} = \frac{1}{n(r)}\left|\nabla n(r) - \hat{l}(\hat{l}\cdot\nabla n(r))\right| \qquad (1)$$

where l is the path length along the beam, $\hat{l}$ the unit vector in the direction of the beam, and $n(r)$ is the local value of the refractive index. It follows from the equation (1) that the effect of fluctuations in the local value of the refractive index will be to produce variations in the path of light beam around its mean position, and divergence of a beam of finite size.

Moreover the terms on the right-hand side of equation (1), show that the magnitude of such variations will be directly related to the magnitude of the variations in gradient of the density, concentration and temperature. (The direct effect of temperature will be small as it is only weakly coupled to the dielectric constant). The overall effect of the refractive index fluctuations is identical to that of mechanical vibrations, with the additional difficulty that they are not susceptible to damping. However, the frequency of variations in optical path is also small ($<10^4$ Hz) in comparison with frequencies produced by particles passing through the scattering volume (10^6 to 10^7 Hz) and thus the precision of velocity measurement is not significantly affected. Nevertheless, the increased signal intermittency and variation in the effective size of control volume are both of importance to measurements in furnace environments and further analytical work to es-

[4] Gradient and transit-time broadening are negligible: the fuel and air flows were sensibly constant.

[5] For particles of approximately 1 μm in size (reference [8]).

timate their magnitude is currently in progress. The effect of the refractive index gradients thus causes the volume in which velocity measurements are obtained to be larger than would be the case if these gradients were absent. The intermittancy necessitated an integration time of around 20 min for each probability distribution.

This measuring time may be reduced by a factor of approximately 20 if the spectrum analyzer is replaced by a bank of filters; an instrument of this type, incorporating 50 filters per decade, of band width $Q = 20$, and with a typical frequency range from 100 kHz to 10 MHz has been developed at Harwell for this purpose.

The dimensions of the measuring control volume may be reestimated, incorporating the movement of the laser beams passing through the furnace; this movement was measured outside the furnace, as previously noted, and together with the estimated beam diameter, suggests a control volume of the order of 4.5 mm dia by 90 mm long. The Gaussian distribution of the light intensity and random beam fluctuation implies that the signals which made up a probability-density distribution have a higher probability of stemming from the center of the control volume; thus, the effective control-volume dimensions will be less than those given in the foregoing. The control volume dimensions can be further reduced by the choice of a suitable discrimination level in the operation of the filter bank; the measuring time will, of course, increase. In terms of a 2 m furnace, a measuring control volume of this magnitude is acceptable for most purposes.

In future work, it will undoubtedly be preferable to use an integrated optical arrangement which operates in the back scatter mode, is prealigned and is pre-located with respect to the light-collecting system. It can be estimated that the use of back scatter will result in a scattered light intensity approximately 25 times less[5] than forward scatter: this, together with the use of a filter bank implies a time of approximately 5 min for measurements of mean and rms velocity at each location. The use of 2W of laser power will reduce this time by a factor of 3. Due to the statistical nature of the signal processing, the time required to obtain measurements of mean velocity alone is, of course, much less.

To obtain measurements in coal flames, it will undoubtedly be necessary to vary the fringe spacing. The particles observed in the course of the present investigations were significantly bigger than the 5 μm fringe spacing and are probably larger in some regions of the flow and smaller in others. If the particle diameter is greater than 10 μm it will not be possible to obtain precise turbulence information since the particles will not follow the flow: the possible precision of turbulence information obtained from such particles may be estimated with the help of reference [6].

The low particle concentrations observed in gas flames imply that measuring times will be longer than those estimated for oil flames. The authors have successfully used TiO_2 particles, dispersed in a fluidised bed, to seed laboratory flames and these can also be used in furnace situations.

In the regions of high turbulence level (>40 percent) and recirculation commonly encountered in industrial furnaces, it will be necessary to adopt frequency shifting techniques as previously outlined in references [7 and 9].

Conclusions

The following conclusions may be extracted from the present investigation:

1 Measurements of the mean and rms values of velocity have been obtained in a 2m sq furnace operating with oil fuel and various degress of swirl. The accuracy of the mean velocity measurement is of the order of 5 percent and of the rms measurements of the order of 6 percent. The time taken to obtain values of mean and rms velocity at one location was approximately 20 min. The control volume dimensions were less than 4.5 mm in diameter and 90 mm long.

2 The convenience and accuracy of making future measurements will be significantly increased by making use of a prealigned optical system, operating in backward scatter together with a laser power of the order of 2W: the authors favour the use of a filter bank rather than a spectrum analyser with a measuring time per location of the order of 2 min.

3 Measurements of rms velocity values in coal flames should be confined to regions of the flow where the particle diameters are significantly less than 10 μm. Mean velocity values can be obtained in regions of the flow where larger particles predominate but are likely to require an optical arrangement with variable fringe spacing.

4 Measurements in gas flames may require times which are unacceptably long. In such cases, local seeding with TiO_2 is recommended.

5 The prognosis for the use of laser anemometry in furnaces is very encouraging and the authors envisage its use for diagnostic purposes; in conjunction with predictive techniques, it should lead to significant improvements in the design of burners and furnace configurations.

Acknowledgments

The present work was carried out at the International Flame Research Foundation, Ijmuiden, Holland. The authors gratefully acknowledge Dr. T. Lowes for permission to use the IFRF facilities and for his considerable assistance with the organization of the experimental programme. We are also indebted to Dr. M. Heap and other members of the IFRF staff who operated the furnace and worked long hours to allow the completion of the work, and Dr. G. Hewitt of AERE, Harwell who provided valuable advice.

References

1 Baker, R. J., Bourke, P., and Whitelaw, J. H., "Measurements of Instantaneous Velocity in Lamminar and Turbulent Diffusion Flames Using an Optical Anemometer," *J. Institute of Fuel*, Dec. 1973.

2 Durst, F., Melling, A., and Whitelaw, J. H., "The Applications of Optical Anemometry to Measurements in Combustion Systems," *Comb. & Flame*, Vol. 18, 1972, p. 197.

3 Durao, D., Durst, F., and Whitelaw, J., "Optical Measurements in a Pulsating Flame," JOURNAL OF HEAT TRANSFER, TRANS. ASME, Series C, Vol. 95, 1973, p. 277.

4 Baker, R., "The Application of Laser Anemometry to the Measurement of Flow Properties in an Industrial-Burner Flame," AERE-R7137, 1972.

5 Landau, L. D., and Liftshitz, E. M., *Electrodynamics of Continuous Media*, Pergamon.

6 Melling, A., "Scattering Particles for Laser Anemometry in Air: Selection Criteria and Their Realization," Imperial College Rept ET/TN/B/7, 1971.

7 Baker, R. J., Bourke, P., and Whitelaw, J. H., "The Application of Laser Anemometry to the Measurement of Flow Properties in Industrial Burner Flames," *Proceedings of the 14th Combustion Symposium*, p. 699.

8 Meyers, J. F., "Investigation of Basic Parameters for the Application of Laser Doppler Velocimeter," AIAA Paper No. 71-288.

9 Baker, R. J., Hutchinson, P., and Whitelaw, J. H., "Detailed Measurements in the Recirculation Region of an Industrial Burner by Laser Anemometry," *Proceedings of the European Combustion Symposium*, Academic Press, 1973, p. 583.

T. E. Cooper
Assoc. Professor.
Assoc. Mem. ASME

W. K. Petrovic[1]
LCDR, USN.

Department of Mechanical Engineering,
Naval Postgraduate School,
Monterey, Calif.

An Experimental Investigation of the Temperature Field Produced by a Cryosurgical Cannula

Liquid crystals, a material that exhibits brilliant changes in color over narrow temperature bands, have been successfully used to study the temperature field that is produced by a cryosurgical cannula (cryoprobe). Cryoprobe tip temperatures ranging from −36 to −117 C were used to produce frozen regions in a clear gel. Experimental results compare within experimental uncertainty with results of a one-dimensional analytical solution for predicting ice growth rates.

Introduction

The use of low temperatures as a medical tool is not new. As early as 3500 B.C., the Egyptians used ice as a local anesthetic by applying it to wounds and other ailments. It was not until 1851, however, that extreme cold was used as a surgical procedure. Dr. James Arnott, a British physician, used a small container filled with a −24 C ice-brine mixture as a surgical instrument. The container was placed in direct contact with skin cancers and was found helpful in restricting the growth of the cancerous tissue [1].[2]

In 1961, with the development of the first cryosurgical cannula, or cryoprobe, for use in the treatment of Parkinson's Disease, "Cryosurgery" became an established surgical procedure. Dr. Irving Cooper of the Saint Barnabas Hospital in New York is acknowledged as the founder of the present-day cryosurgical technique [2-4]. Cooper developed a small diameter, vacuum-insulated, cylindrical probe with a hemispherical tip. The probe tip was cooled by circulating liquid nitrogen down through the thermally insulated stem to the uninsulated tip.

Contemporary cryosurgical units employ cryoprobes possessing outer diameters as small as 1.5 mm. Tip temperatures ranging from 37 C to −196 C may be selected. Tissue destruction is accomplished by locating the tip of the cryoprobe in the diseased region and dropping the temperature of this target tissue below its freezing point. The temperature of the probe stem remains near body temperature during the procedure due to a vacuum insulation system along the probe length. Cryosurgery has a variety of applications ranging from the treatment of Parkinsonism to the destruction of cancerous tumors. An extensive bibliography of papers describing the various cryosurgical procedures has been published by the Linde Division of the Union Carbide Corporation [5].

Cryosurgery, as presently practiced, is highly empirical [4]. Control of the "cryolesion" is an art that is gained from experience. Several analytical and numerical heat-transfer models have been developed to aid the surgeon in predicting the rate of growth and ultimate steady-state size of the frozen region produced by typical cryoprobes [6-8], but these models have yet to be verified experimentally. The objectives of our investigation were: *(a)* to experimentally determine the growth rate of the frozen region around a typical cryoprobe; *(b)* to compare the experimental results with an approximate, one-dimensional analytical solution of the same problem, and *(c)* to investigate the feasibility of using liquid crystals, a material that indicates temperature through a change in color, as a temperature sensor in the unfrozen region.

A prototype cryoprobe, 1.27 cm in diameter and 14.63 cm long, was designed and built. This probe produced ice regions that were approximately spherical in shape and were easily studied. A clear, 1.5 percent gelatin-98.5 percent water, test medium was used to simulate tissue. A range of probe tip temperatures varying from −36 C to −117 C were used to create the frozen regions. In all cases studied, experimental and analytical predictions of the ice growth rates compared within the estimated experimental uncertainty of 9 percent. The details of the magnitude and extent of the temperature field in the unfrozen region surrounding the probe tip were successfully obtained with the liquid crystal material. The liquid crystals exhibited brilliant color displays that were photographed through the clear gel and later correlated with temperature.

Cryoprobe Design

The cryoprobe used in the present investigation was designed and fabricated after a standard Linde cryoprobe [9]. The probe consists of three concentric stainless-steel tubes arranged as

[1] Present Address: Norfolk Naval Shipyard, Portsmouth, Va.

[2] Numbers in brackets designate References at end of paper.

Contributed by the Bioengineering Division of THE AMERICAN SOCIETY OF MECHANICAL ENGINEERS and presented at the Winter Annual Meeting, Detroit, Mich., November 11-15, 1973. Manuscript received at ASME Headquarters July 26, 1973; revised manuscript received August 22, 1973. Paper No. 73-WA/Bio-20.

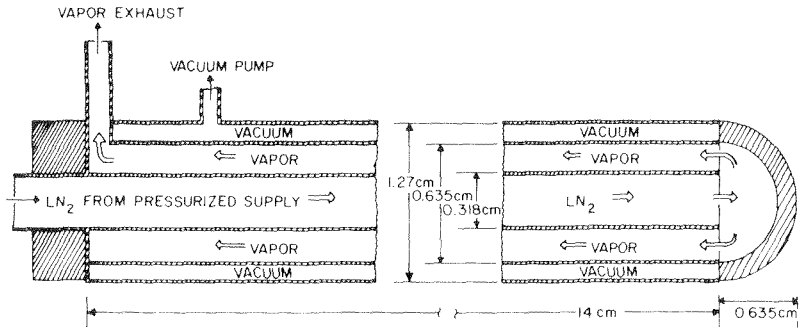

Fig. 1 Schematic of cryoprobe

shown in Fig. 1. Upon activation, liquid nitrogen flows from a pressurized supply through the inner tube, ultimately reaches the hemispherical tip, and is vaporized by the energy that has been absorbed from the surroundings. The annulus formed by the inner tube and its neighbor allows the vapor to escape to the room. The outermost annulus is evacuated, with the aid of a vacuum pump, thus providing a vacuum insulation along the probe stem. This insulation prevents the probe stem from acting as a lesion generating surface during the cryosurgical procedure.

The temperature of the probe tip is a function of the liquid nitrogen flow rate. In our experimental setup, a copper-constantan thermocouple was spot welded to the probe tip. The liquid nitrogen from the pressurized supply, Fig. 2, was manually adjusted to obtain the desired tip temperature. Barron [9] presents a discussion of the various cryosurgical units presently in use.

Liquid Crystals

Background. Fergason [10-12], in a series of articles, presents excellent discussions on the chemistry, varieties, properties, uses, and limitations of cholesteric liquid crystals. The most striking feature of the liquid crystal material is its ability to display brilliant changes in color over discrete temperature bands. This is due to circular dichroism. An incident beam of light, on striking the liquid crystals, is split into two components having electrical vectors rotated in opposite directions. One component is transmitted through the material while the other is reflected. The reflected light has a wavelength peak that is a strong function of the temperature of the liquid crystals. Temperature changes in the crystals result in a change in the molecular structure, thereby causing a shift in the peak wavelength of the reflected light. When the temperature of the liquid crystal material falls in an appropriate range, this peak wavelength shifts into the visible. The material then passes through the entire visible spectrum (red, yellow, green, blue, violet) as the temperature is increased through the band. This color change is stable and reappears whenever the liquid crystal material passes through the appropriate temperature band.

Through proper calibration, color can be correlated with temperature to within approximately ±0.1 C. By careful choice of the chemical formulation, liquid crystals can be made to respond over temperature bands as small as 1 C, starting at 0 C and running upward to several hundred deg Celsius.

Preparation and Calibration of Liquid Crystal Sheet. Clear mylar sheeting was chosen as the substrate for the liquid crystal material since it is thin (0.008 cm), pliable, and has a low thermal capacitance. The liquid crystals, which were of the encapsulated variety, were obtained in slurry form from the National Cash Register Co.

The mylar sheet was cut square, 20 cm on a side, with a notch, 10 × 1.27 cm, cut into one side to accommodate the probe. The liquid crystals were applied to the mylar sheet with an artist's airbrush. Before applying the crystals, the sheet was thoroughly cleaned with acetone to remove any residue. Three separate coats of crystals were applied. Approximately 1 hr was allowed between coats. After the crystals were applied, two coats of flat black paint were applied directly over the crystals. Since the crystals were of the encapsulated variety, no alteration in the crystal properties occurred. The black background is used to obtain optimum brilliance. All light that is transmitted through the crystal material is absorbed and, therefore, does not compete with the light reflected from the crystals themselves. To complete the composite, two coats of polyurethane were applied over the flat black to provide waterproofing.

Five different range liquid crystal formulations were applied to the mylar sheet as shown in Fig. 3. Calibration was accomplished with the aid of a Rosemount Constant Temperature Bath capable of establishing and maintaining temperatures to within ±0.01 C. Color was determined by eye. Although liquid crystals display all the colors in the visible spectrum, only the onset of red, green, and blue were used as calibration points. In a typical calibration run, the water-proofed liquid crystal sheet was placed directly into the constant temperature water bath. The temperature of the bath was then slowly raised until the event temperature of the liquid crystal under consideration had been reached. By carefully adjusting the bath temperature, an accurate measure of the event temperature corresponding first to red, then to green, and finally to blue was made. No attempt was made to determine shades of red, green, or blue. It is estimated that temperature was

Nomenclature

c = specific heat of unfrozen region, cal/gm-C
c_f = specific heat of frozen region, cal/gm-C
k = thermal conductivity of unfrozen region, cal/cm-C-s
k_f = thermal conductivity of frozen region, cal/cm-C-s
L = latent heat of fusion, cal/gm
r = radial location, cm
r_0 = cryoprobe radius, cm
R = ice ball radius, cm
t = time, s
T = temperature of unfrozen region, C
T_f = temperature of frozen region, C
T_0 = initial temperature, C
T_{pc} = phase change temperature, C
T_s = cryoprobe tip temperature, C
ρ = density, gm/cc

Nondimensional groups

$r^* = R/r_0$

$R = r/r_0$

$\tau = \dfrac{k(T_0 - T_{pc})t}{\rho L r_0^2}$

$\theta = \dfrac{(T - T_0)}{(T_s - T_0)}$

$\theta_f = \dfrac{(T_f - T_0)}{(T_s - T_0)}$

$\theta_{pc} = \dfrac{(T_{pc} - T_0)}{(T_s - T_0)}$

$\eta = \dfrac{k_f}{k}\dfrac{(\theta_{pc} - 1)}{(\theta_{pc})} - 1$

Fig. 2 Pressurized liquid nitrogen container

correlated with color to an accuracy of ±0.1 C. Calibration results are shown in Fig. 3.

Experimental Procedure

The experimental setup in our investigation was quite similar to the one employed by Cooper and Groff [13] in their study of a resistively heated surgical probe. The test medium used to simulate tissue was a clear gel composed of 1.5 percent gelatin-98.5 percent water. The gel was contained in a cubical plexiglass box, 20 cm on a side. Ten centimeters down from the top, on the inside of the box, was a small "lip" that supported the frame encased liquid crystal sheet. A 1.27-cm-dia hole in the side of the box and frame, together with the notch in the liquid crystal sheet, allowed the cryoprobe to be inserted such that its tip was in the geometric center of the box. The box, liquid crystal sheet and cryoprobe are shown in Fig. 4. The cryoprobe was connected to the pressurized liquid nitrogen supply with the aid of a neoprene insulated feeder line as shown in Fig. 5.

The gelatin offered two highly desirable features as a test medium. First, it was very clear and allowed excellent photos of the liquid crystal sheet to be taken through it. Second, when set, the gel behaved as a solid with thermal properties quite similar to water [14].

Before filling the box with the gel, the probe and liquid crystal sheet were carefully positioned so that the plane of the sheet uniformly intersected the long axis of the probe. This assured that

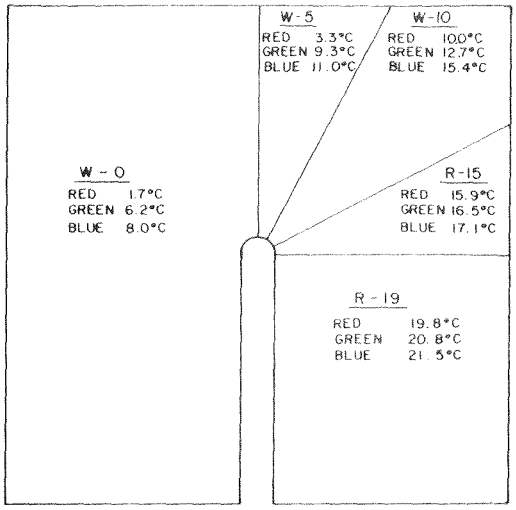

Fig. 3 Schematic of liquid crystal sheet indicating the arrangement of the various crystals together with the calibrated event temperatures

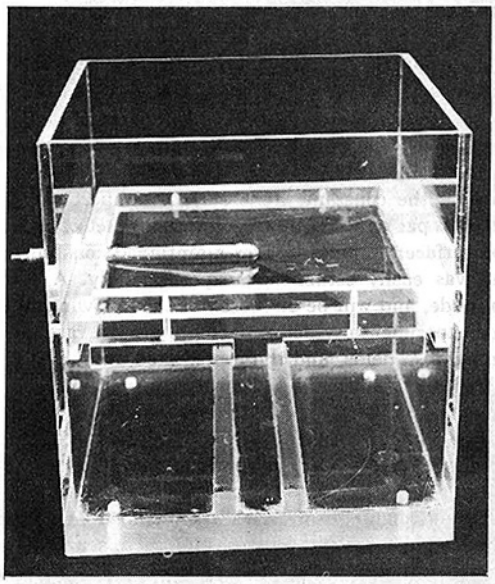

Fig. 4 Test cell with cryoprobe and liquid crystal sheet in place

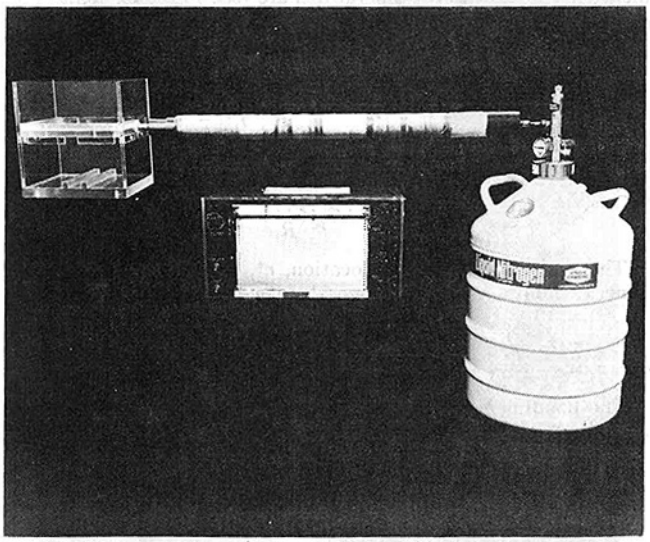

Fig. 5 Complete experimental setup. Shown are the test cell, cryoprobe, transfer line, pressurized liquid nitrogen container, and temperature recorder.

the liquid crystals gave an accurate, undistorted display of the temperature field surrounding the probe. Next, the gel, which was still in liquid form, was slowly poured into the box to within 1 cm of the top. The entire system was then allowed to sit for 24 hr in a room at 22 C to assure temperature uniformity throughout the gel. Two copper-constantan thermocouples, one on the probe tip and the other near one corner of the box, were used to check temperature uniformity.

In a typical experimental run, the liquid nitrogen was suddenly introduced into the cryoprobe. When the tip temperature of the probe reached a predetermined value, the regulator on the pressurized dewar was manually adjusted to maintain the tip temperature constant. Approximately 1 min was required to bring the probe temperature to its final value.

Photographs of the frozen region and the various isotherms displayed on the liquid crystal sheet surrounding the probe were taken at various time intervals using a Graflex 4 × 5 Press camera fitted with a Polaroid Land film holder. Polaroid 4 × 5 Land film, type 57, 3000 speed, was used. Photographs were normally taken at times of 0, 1, 3, 5, 10, 15, 30 min and every 15 min thereafter until the 21.5 C isotherm, displayed by liquid crystal R-19, moved to the edge of the test cell. At this point in time, the experiment was terminated. Six experimental runs were made with probe tip temperatures varying from −36 to −117 C.

Theoretical Analysis

Approximate theoretical analyses of the growth rate of the frozen region around a cryoprobe have previously been made by Barron [6] and Cooper and Trezek [8]. Barron's analysis assumed that the heat removed at the probe surface was constant. This is in contrast to the constant probe surface temperature case considered by Cooper and Trezek. In the present set of experiments, the probe surface temperature was maintained constant, a condition that was easily established experimentally. A comparison has been made, and will be discussed in the following section, between our experimentally determined ice growth rate, and attendant temperature fields, and those predicted analytically by Cooper and Trezek.

Briefly, the analytical model proposed by Cooper and Trezek assumes that heat capacity effects in both the frozen and unfrozen regions surrounding the probe are negligible compared to the latent heat of fusion effects resulting from the phase change. Blood flow and metabolism terms are included in the complete model, but will be neglected in the present discussion since the test medium was a gel. Neglecting heat capacity effects allows quasi-steady state temperatures to be determined in both frozen and unfrozen regions surrounding the spherical probe. In nondimensional form, these temperatures are (see Fig. 6 for nomenclature):

Frozen Region ($R < r^*$):

$$\theta = 1 + (\theta_{pc} - 1)\left(\frac{r^*}{R}\right)\left(\frac{R - 1}{r^* - 1}\right) \tag{1}$$

Unfrozen Region ($R > r^*$):

$$\theta = \theta_{pc}\left(\frac{r^*}{R}\right) \tag{2}$$

The normalized ice front location, r^*, is related to normalized time, τ, and probe surface temperature, η, by the relationship:

$$\tau = \eta(\eta + 1)\ln\left(\frac{\eta + 1}{\eta + r^*}\right) + \left(\frac{2\eta - 1}{2}\right)(r^* - 1) \tag{3}$$

The nondimensional quantities used in equations (1), (2), and (3) are defined as:

$$\theta_f = \frac{(T_f - T_0)}{(T_s - T_0)} = \text{normalized frozen phase temperature}$$

$$\theta = \frac{(T - T_0)}{(T_s - T_0)} = \text{normalized unfrozen phase temperature}$$

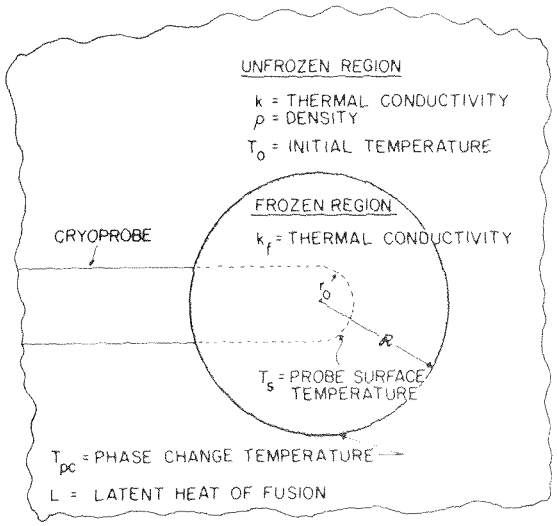

Fig. 6 Schematic of cryoprobe depicting the frozen and unfrozen regions. Nomenclature used in the theoretical analysis is indicated on the sketch.

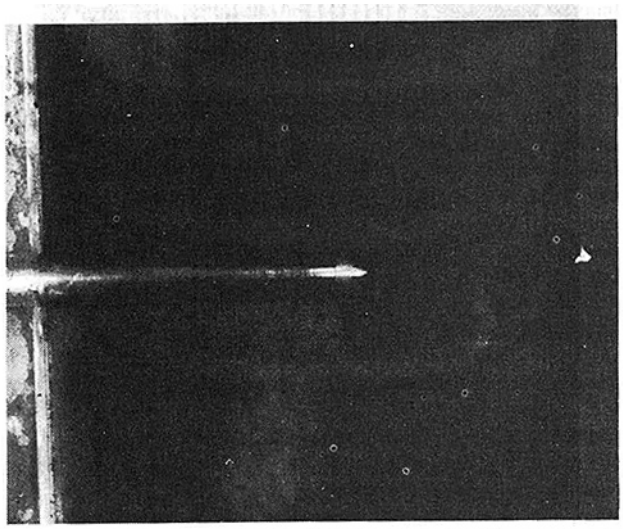

Fig. 7 Cryoprobe and liquid crystal sheet prior to lowering the tip temperature to −75 C. A clear gel surrounds the probe.

$$\theta_{pc} = \frac{(T_{pc} - T_0)}{(T_s - T_0)} = \text{normalized phase change temperature}$$

$$R = \frac{r}{r_0} = \text{normalized radial location}$$

$$r^* = \frac{R}{r_0} = \text{normalized ice front location}$$

$$\tau = \frac{k(T_0 - T_{pc})}{\rho L r_0^2} t = \text{normalized time}$$

$$\eta = \frac{(k_f)(T_{pc} - T_s)}{(k)(T_{pc} - T_0)} - 1 = \text{normalized probe surface temperature}$$

A computer code was written to solve equation (3) for values of r^* as a function of τ and η. These values of r^* were then substituted into equations (1) and (2) to generate values of θ_f and θ as functions of τ and η. Typical theoretical values are compared with our experimental results in the following section.

Results

Figs. 7 through 10 are black and white reproductions of colored photos taken of the frozen region and liquid crystal sheet at times of 0, 5, 30, and 60 min. Although the black and white reproductions do not clearly delineate the various isotherms corresponding

to each liquid crystal range, these isotherms are brilliantly displayed in red, green, and blue in the colored photos.

Agreement between experimentally determined values of the ice growth rate and those predicted theoretically using equation (3) was excellent. Experimental versus theoretical values of the normalized ice ball radius, r^*, versus normalized time, τ, are compared in Fig. 11. Each curve is parameterized by a normalized probe surface temperature, η. Under each value of η is shown the actual probe surface temperature used in the run. For all experimental runs, agreement between theory and experiment as well within the estimated experimental and theoretical uncertainties of ±9 percent. Uncertainty in the exact placement of the theoretical curves is due primarily to uncertainties in the values of the thermophysical properties assumed for gel. Property values were taken to be those of pure water. The primary uncertainty in the experimental points resulted from inaccuracies in locating the perimeter of the ice ball on the photos. As can be seen, however, the ice region was nearly spherical in shape. Diameters were measured from the probe center along a line perpendicular to the probe axis. Details of the uncertainty analysis can be found in reference [15].

Agreement between the experimentally determined transient temperature field in the unfrozen region and values predicted with equation (2) was not good, as is shown in Fig. 12. The results of this run were obtained using a probe tip temperature of −75 C and an initial gel temperature of 22 C. The discontinuity at −2 C, the gel phase change temperature, indicates the ice ball size at a particular time after initiating cooling. The actual temperature gradient in the unfrozen gel is much steeper than the theoretically predicted value. This is to be expected since the heat capacity influence of the gel is not taken into account in the theoretical model.

Although the theory does not satisfactorily predict the details of the transient temperature field in the unfrozen region, it does yield excellent predictions of the growth rate of the frozen region. This seems to be contradictory to what one would expect. However, for the water-like gel, the latent heat of fusion, L, is large compared to the thermal capacity, $c\,|T_0 - T_{pc}|$. For our experi-

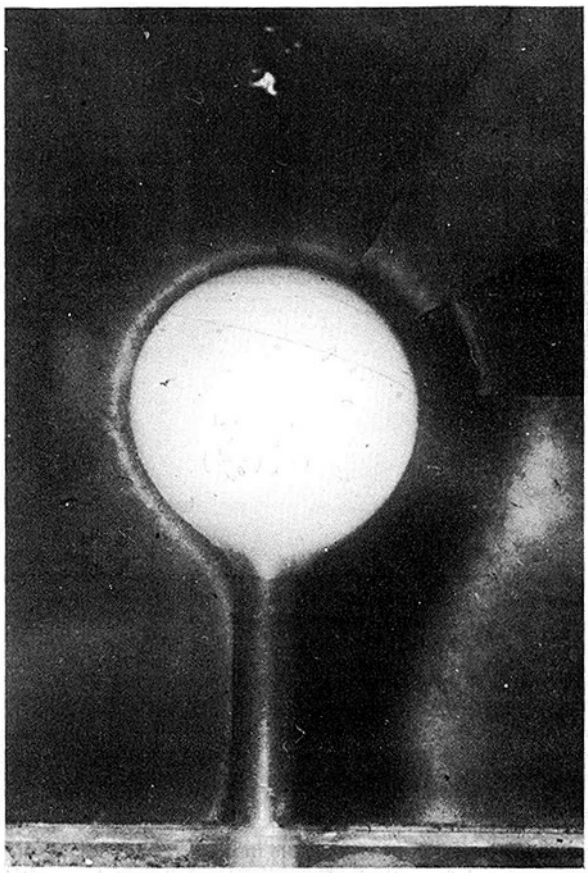

Fig. 9 Cryoprobe and liquid crystal sheet 30 min after initiating cooling

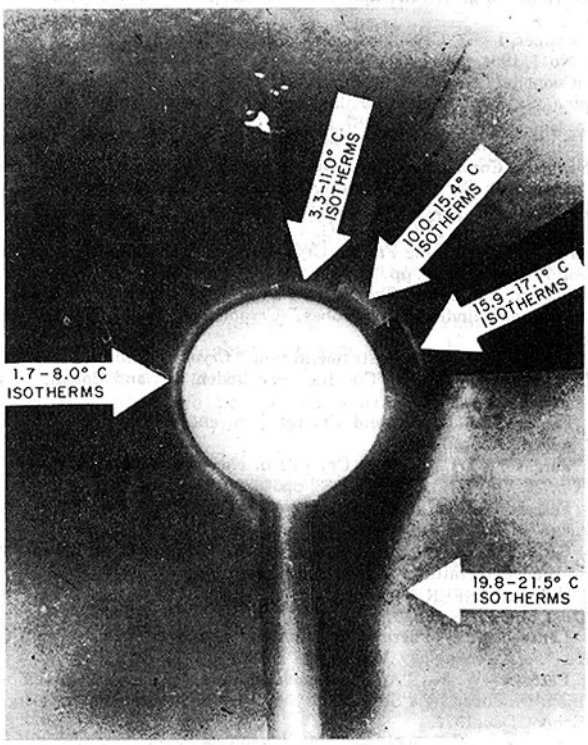

Fig. 8 Cryoprobe and liquid crystal sheet five min after initiating cooling. Various isotherms depicted by the arrows are clearly evident in colored photos.

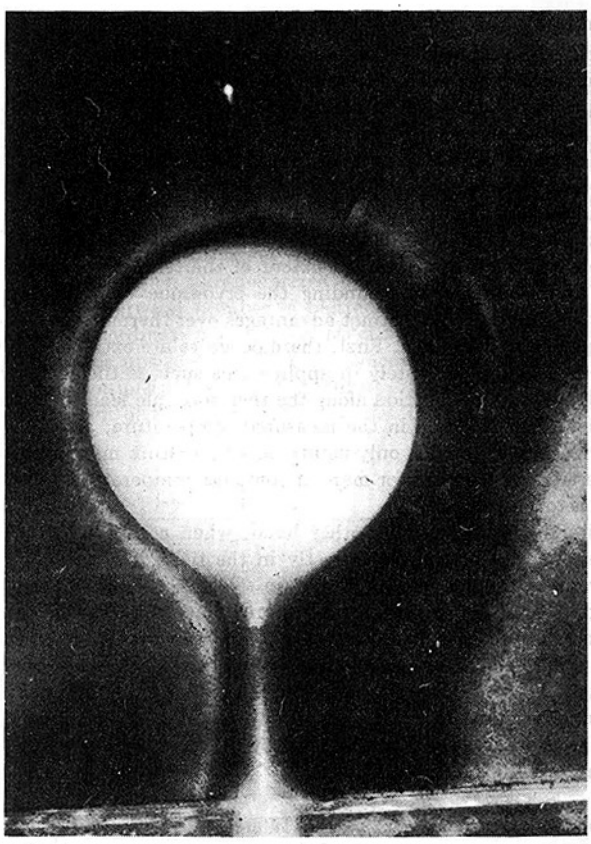

Fig. 10 Cryoprobe and liquid crystal sheet 60 min after initiating cooling

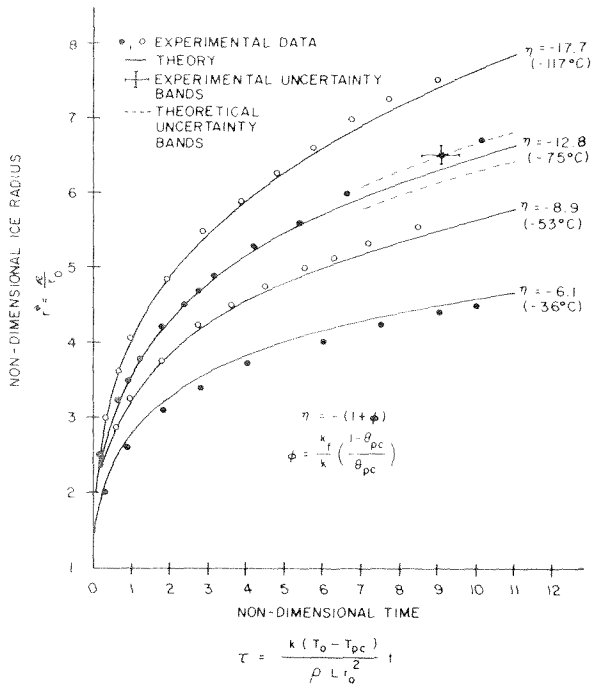

Fig. 11 Comparison of experimentally measured values of the ice growth rate with those predicted using equation (3). Each curve is parameterized with the normalized probe surface temperature, η. Actual probe tip temperatures are shown in parenthesis.

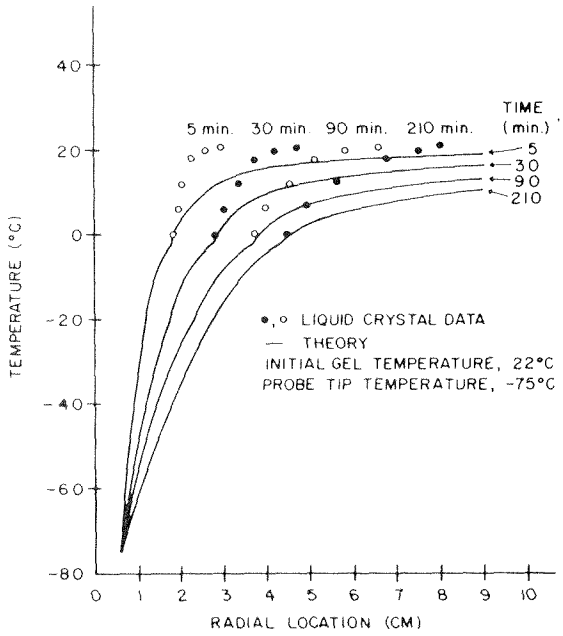

Fig. 12 Comparison of experimentally measured values of the temperature in the unfrozen region with the temperature field predicted using equation (2). The probe surface temperature for this particular run was −75 C.

ments, $c\,|T_0 - T_{pc}|/L = 0.25$. This indicates that the majority of energy removed from the unfrozen phase is latent heat and not sensible heat. Since latent heat is the controlling factor on the ice growth rate, and since the latent heat effect is treated correctly in the theoretical model, theoretical predictions of the ice growth rate are reasonable.

Summary

The rate of growth of the frozen region surrounding a 1.27-cm-dia cryoprobe has been determined experimentally by embedding the probe in a clear gel. Experimental values of the ice ball radius compare within ±9 percent of those predicted using a theoretical model which neglects the heat capacity of both the frozen and unfrozen phases.

Liquid crystals, a material that exhibits brilliant changes in color over known, well-defined temperature bands, were used to determine the magnitude and extent of the temperature field in the unfrozen region surrounding the cryoprobe tip. The liquid crystals offered three distinct advantages over thermocouples as a temperature transducer. First, thermocouples are extremely difficult to position accurately in applications such as the one under study; second, conduction along the thermocouple lead wires may introduce large errors in the measured temperature; and finally, thermocouples provide only pointwise temperature measurements necessitating the need for many if complete temperature information is to be obtained.

Liquid crystals, on the other hand, when coated on a mylar substrate and positioned correctly in the field, allow one to observe a continuous display of certain select isotherms. The mylar used in our investigation was approximately 0.008 cm thick. When sprayed with liquid crystals and coated with a waterproofing agent, the thickness of the overall composite was approximately 0.025 cm. Since the composite was formed of low thermal conductivity and thermal capacity materials, it is estimated that isotherm locations were influenced by no more than one-half the composite thickness, or 0.013 cm.

Acknowledgments

The authors gratefully acknowledge the assistance given by George Baxter in the design and construction of the cryoprobe. We would also like to acknowledge the support of the Naval Postgraduate School Research Foundation and Research Grant NS-08236-03 CVA.

References

1 Arnott, J. B., "On Treatment of Cancer by the Regulated Application of an Anaesthetic Temperature," *J. Churchill*, London, 1851.

2 Cooper, I. S., Grossman, F., and Johnston, P., "A Complete System for Cryogenic Surgery," *St. Barnabas Medical Bulletin*, Vol. 1, 1962, pp. 11-16.

3 Cooper, I. S., "Cryobiology as Viewed by the Surgeon," *Cryobiology*, Vol. 1, No. 1, 1964, pp. 44-49.

4 Cooper, I. S., "Cryogenic Surgery," *Engineering in the Practice of Medicine*, Segal, B. L., and Kilpatrick, D. G., eds., The Williams and Wilkins Co., Baltimore, Md., 1967, pp. 122-141.

5 *Bibliography of Cryogenic Procedures in Surgery*, 87-0039, F-2878-A Union Carbide Corporation, Linde Division, N. Y.

6 Barron, R. F., "Heat Transfer Problems in Cryosurgery," *Journal of Cryosurgery*, Vol. 1, No. 4, Dec. 1968, pp. 316-325.

7 Cooper, T. E., and Trezek, G. J., "Analytical Prediction of the Temperature Field Emanating From a Cryogenic Surgical Cannula," *Cryobiology*, Vol. 7, No. 2-3, 1970, pp. 79-93.

8 Cooper, T. E., and Trezek, G. J., "Rate of Lesion Growth Around Spherical and Cylindrical Cryoprobes," *Cryobiology*, Vol. 7, No. 4-6, 1971, pp. 183-190.

9 Barron, R. F., "Cryoinstrumentation," *Cryogenics in Surgery*, Medical Examination Publishing Co., Inc., von Leden, H., and Cohan, W. G., eds., June 1971, pp. 80-127.

10 Fergason, J. L., "Liquid Crystals," *Scientific American*, Vol. 211, No. 2, Aug. 1964, pp. 76-86.

11 Fergason, J. L., "Liquid Crystals in Non-Destructive Testing," *Applied Optics*, Vol. 7, No. 9, Sept. 1968, pp. 1729-1737.

12 Fergason, J. L., "Experiments With Cholesteric Liquid Crystals," *American Journal of Physics*, Vol. 38, no. 4, Apr. 1970, pp. 425-428.

13 Cooper, T. E., and Groff, J. P., "Thermal Mapping, via Liquid Crystals, of the Temperature Field Near a Heated Surgical Probe," JOURNAL OF HEAT TRANSFER, TRANS. ASME, Series C, Vol. 95, No. 2, May 1973, pp. 250-256.

14 Lentz, C. P., "Thermal Conductivity of Meats, Fats, Gelatin Gels and Ice," *Food Technology*, Vol. 15, No. 5, 1961, pp. 243-247.

15 Petrovic, W. K., "An Experimental Investigation of the Temperature Field Produced by a Surgical Cryoprobe," MS thesis, Naval Postgraduate School, Dec. 1972.

journal of heat transfer

technical briefs

This section consists of contributions of 1500 words or less (about 5 double-spaced typewritten pages, including figures). Technical briefs will be reviewed and approved by the specific division's reviewing committee prior to publication. After approval such contributions will be published as soon as possible, normally in the next issue of the journal.

Effect of Tube Relocation on the Transfer Capabilities of a Fin and Tube Heat Exchanger

F. E. M. Saboya[1] and E. M. Sparrow[1]

Introduction

Local and average transfer coefficients on the fins of a one-row plate fin and tube heat exchanger configuration have been determined in [1][2] by employing the analogy between heat and mass transfer. In the range of Reynolds numbers that is encountered in present-day air-conditioning machines, the local transfer coefficients were found to be very low on the portion of the fin that is washed by the wake downstream of the tube. Consequently, that portion of the fin contributes very little to the overall transfer capabilities of the exchanger.

In view of the aforementioned finding, it is natural to consider candidate approaches for eliminating the deleterious effect of the wake that is shed from the tube. One approach is to relocate the tube toward the rear of the fin, thereby placing the wake region outside (i.e., downstream of) the exchanger. Experiments that were performed to explore the effect of relocating the tube are reported here. As in [1], the naphthalene sublimation technique was employed to obtain local and average mass transfer coefficients.

Fig. 1 shows a plan view of the two heat exchanger configurations whose transfer characteristics are to be compared. The upper diagram depicts the standard arrangement studied in [1] in which the tubes are positioned centrally with respect to the streamwise length of the exchanger. For the configuration pictured in the lower diagram, the tubes are positioned on the rear portion of the fin. Aside from the rearward displacement of the tubes, the two configurations are geometrically identical. The figure also displays dimensional nomenclature and the surface coordinates x,y. The dimensions D, S, L, and h (spacing between fins) are the same as those of [1].

The fins of the heat exchanger were simulated by specially cast naphthalene plates. Local transfer coefficients were determined by measuring the local changes of surface elevation which resulted from sublimation of naphthalene during a data run. The average transfer coefficient was found both by integrating the local mass transfer rates and from direct measurement (by a precision balance) of the overall mass transferred. The experimental method and data reduction procedures have been described in detail in [1] and need not be repeated here.

A dimensionless representation of the mass transfer coefficients is made in terms of the Sherwood number, which is the mass transfer analogue of the Nusselt number. The Sherwood number results can be converted to Nusselt number results by employing equations (15) and (16) of [1].

Results and Discussion

The effect of tube relocation on the transfer characteristics has been investigated for Re $\cong$ 650. This Reynolds number was selected because it falls at about the midpoint of the range studied in [1] and because it corresponds to operating conditions encountered in present-day air conditioning machines.

The distribution of local transfer coefficients on the fin surface is presented in Fig. 2 for the case of rear-positioned tubes. The figure contains a succession of graphs, each corresponding to a given axial station parameterized by x/L. At each such station, the local Sherwood number is plotted against the dimensionless spanwise coordinate $y/(S/2)$. Values of $x/L < 0.538$ correspond to fin locations upstream of the tube, whereas $0.538 < x/L < 1$ denote fin locations at the side of the tube.

Inspection of the figure indicates that the transfer coefficients

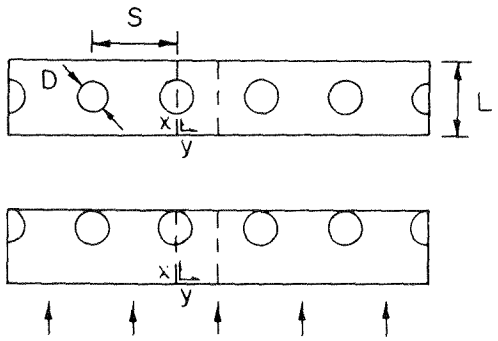

Fig. 1 Plan view of central-tube and rear-tube heat exchanger configurations

[1] Department of Mechanical Engineering, University of Minnesota, Minneapolis, Minn.

[2] Numbers in brackets designate References at end of technical brief.

Contributed by the Heat Transfer Division of THE AMERICAN SOCIETY OF MECHANICAL ENGINEERS. Manuscript received by the Heat Transfer Division, January 30, 1974.

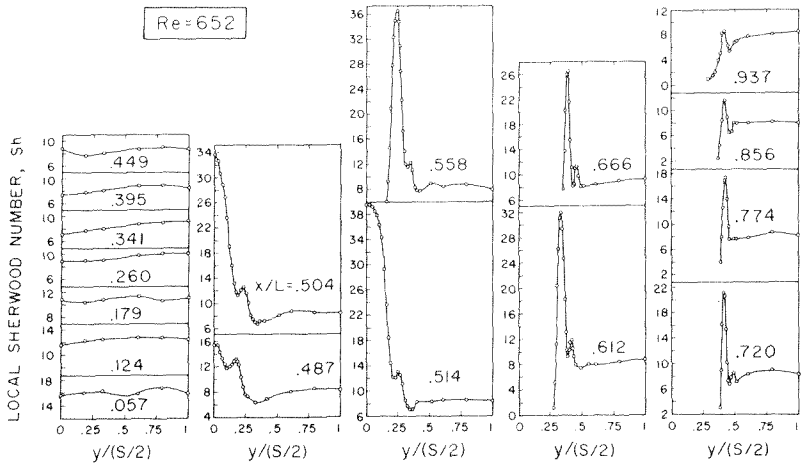

Fig. 2 Distribution of local Sherwood number on the fin surface for rear-positioned tubes. Re = 652 and Schmidt number = 2.5.

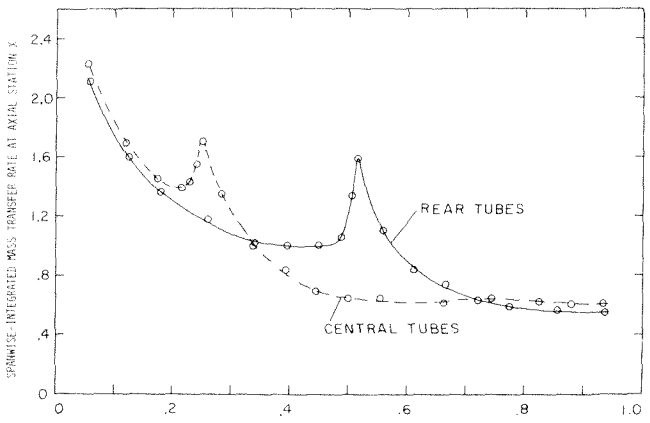

Fig. 3 Spanwise-integrated mass transfer rate as a function of axial position

on the forward part of the fin display trends typical of those for a channel flow, with a thermal entrance region at smaller x/L which gives way to a thermally developed state at about $x/L \sim 0.4$. Thereafter, owing to the influence of a vortex system which develops in front of the tube and is swept around the side, a peak appears in the transfer coefficient distributions. The peak diminishes at larger x/L as the vortex is dissipated. The curves for $x/L > 0.538$ do not extend all the way to $y = 0$ owing to the fact that a part of the fin is blocked out by the tube.

Local results comparable to those of Fig. 2 are presented in Fig. 4 of [1] for the case of centrally positioned tubes. A comparison between the two figures reveals a number of differences. First of all, as expected, the first appearance of the peaks in the distribution curves is shifted to larger x/L when the tubes are relocated at the rear. Also, with the tubes at the rear, the blockage of the channel by the tubes is not felt at forward locations on the fin. Since the forward part of the fin is influenced to a lesser degree by the vortex pattern and by the upstream effect of blockage when the tubes are relocated, thermal development of the channel flow can take place.

The effect of tube relocation on the overall transfer capabilities of the system will be discussed in terms of additional information to be presented shortly. However, on the basis of Fig. 2 and Fig. 4 [1], it appears that there is greater transfer from the forward part of the fin with centrally placed tubes, greater transfer from the middle region of the fin with rear-positioned tubes, and a near parity on the rearward part of the fin.

One assessment of the relative transfer capabilities of the two configurations may be made by comparing the mass transfer rates at various axial stations. To this end, at any axial station, one can evaluate

$$\int_{y=0}^{s/2} \dot{m}(x,y)dy \tag{1}$$

where $\dot{m}(x,y)$ is the local rate of mass transfer per unit area. In carrying out the integration, $\dot{m}(x,y)$ was set equal to zero at fin locations x,y that are blocked out by the tube. Equation (1) gives the spanwise-integrated mass transfer rate at x.

The mass transfer rates evaluated from equation (1) are plotted in Fig. 3, with solid and dashed lines, respectively, used to connect data points for the rear-tube and central-tube configurations. The data have been scaled to correspond to identical operating conditions for the two cases. Inasmuch as the figure is concerned only with relative rates of transfer, the ordinate scale is in arbitrary units.

The figure shows that relative to the standard central tube arrangement, the use of rear-positioned tubes yields higher transfer rates in the mid-region of the fin and lower transfer rates in the forward portion and, to a lesser extent, in the rear portion. The overall transfer rates for the two fin configurations are represented by the areas under the respective curves. The outcome of a comparison of areas is that the overall transfer rate is about five percent greater when the tubes are positioned at the rear of the fin.

A related comparison can be made in terms of the average transfer coefficient defined using the overall mass transfer rate[3] and the log mean (wall-to-bulk) concentration difference. The average transfer coefficient can be represented in dimensionless form by the average Sherwood number $\overline{Sh}$. The values of $\overline{Sh}$ for the rear-tube and central-tube configurations were found to be 10.2 and 9.7, respectively, (both at Re $\sim$ 650), which amounts to a difference of about five percent.

Although the overall transfer capability of the system is increased by the rearward relocation of the tubes, the extent of the improvement is quite small. Since such a relocation might well necessitate an investment to alter the fabrication and assembly of the heat exchanger, it does not appear to be a viable approach in view of the modest gains in transfer capability.

Reference

1 Saboya, F. E. M., and Sparrow, E. M., "Local and Average Transfer Coefficients for One-Row Fin and Tube Heat Exchanger Configurations," to be published in the JOURNAL OF HEAT TRANSFER, TRANS. ASME, Series C, Vol. 96, No. 3, Aug. 1974, pp. 265–272.

[3] For both data runs, the overall mass transfer rate determined by integration of the local values agreed to within 0.15 percent of that determined by direct weighing with a precision balance.

Power-Law Solutions for Evaporation From a Finned Surface

D. K. Edwards,[1] A. Balakrishnan,[1] and Ivan Catton[1]

Introduction

Gregorig [1][2] numerically calculated the capillary flow on a fluted condenser surface and showed that high condensation coefficients could be obtained near the tips of the flutes. Surface-tension-induced pressures drive the liquid condensate off the tip of each flute, thinning the liquid film and thus reducing its thermal resistance. Navabian and Bromley [2] using 16 Gregorig-type flutes per in. were able to attain a value of $U = 14000$ Btu/hr ft^2 F for the surface transfer coefficient on a horizontal cylinder.

It is the purpose of this work to develop an analytical solution for the capillary flow on a finned surface for the case of *evaporation*. The work here thus augments that work presented earlier [3] in which the "valley flow" region between fins or flutes was analyzed numerically and recommendations for the number of fins per inch were made. The present work accounts for the variation in the meniscus radius of curvature near the fin tips, the previous work [3] having taken the curvature to be constant.

Analysis

The Model. Evaporation of a pure liquid from a finned surface is modeled under the following set of assumptions: *(a)* The meniscus is attached to the tip of the fin. *(b)* Resistance to transverse heat flow in the fin is negligible to that in the liquid film. *(c)* Longitudinal heat flow in the liquid is negligible compared to that in the fin. *(d)* Flow in the film toward the fin tip is quasi-established laminar film flow accompanying a pressure gradient and an associated meniscus curvature gradient. The model is thus what Potash and Wayner [4] term an "intrinsic meniscus." It neglects the effect of chemical adsorption causing what they describe as a "thin film . . . (if present)" extending above the intrinsic meniscus. *(e)* The interfacial mass transfer resistance is negligible. Fig. 1 illustrates the situation envisioned. A fin of length L having thickness $\delta(x)$ available for longitudinal heat flow has a film with thickness $y(x)$ on the wetted flat face, where x is measured along the face. Both $\delta(x)$ and $y(x)$ are imagined to go to zero as x goes to zero at the tip. Although the figure is drawn for a linear $\delta(x)$, the functional dependency of δ on x is not yet fixed. The back of the fin is a no-flux surface.

Consistent with this model the temperature distribution along the wetted face of the fin is governed by the well-known fin equation, e.g., [5]. The heat loss from the fin represented by the right-hand side of equation (1) is accompanied by evaporation $d\Gamma/dx$

$$\frac{d}{dx}\left(\delta(x)k\frac{dT}{dx}\right) = \frac{k_l T(x)}{y(x)} \tag{1}$$

$$\frac{d\Gamma}{dx} = \frac{k_l T(x)}{\hat{h}_{fg} y(x)} \tag{2}$$

where T is the temperature excess over the saturation temperature, k is fin conductivity, k_l is liquid conductivity, and $\hat{h}_{fg}$ is latent heat. The mass flow rate per unit width of meniscus $\Gamma(x)$ is related to the pressure gradient and meniscus curvature by assuming quasi-established film flow

$$\frac{dP}{dx} = -\frac{3\mu_l \Gamma(x)}{\rho_l y^3(x)} \tag{3}$$

$$P = \frac{\sigma}{R} \tag{4}$$

where P is the vapor-liquid pressure difference, σ surface tension, R the meniscus radius of curvature, μ_l liquid viscosity, and ρ_l liquid density. The radius of curvature in turn is related to $y(x)$, so that

$$\frac{1}{R} = \frac{d^2y/dx^2}{[1 + (dy/dx)^2]^{3/2}} \tag{5}$$

$$\frac{d^2y}{dx^2} = \frac{P(x)}{\sigma} \tag{6}$$

The approximation, suitable only for small x, that dy/dx is small has been introduced in passing to equation (6).

Equations (1), (2), (3), and (6) are four simultaneous ordinary differential equations in four unknown dependent variables, T, Γ, P, and y. They are subject to boundary conditions

$$x = 0:\ y = 0,\ \frac{dy}{dx} = 0,\ \Gamma = 0 \tag{7}$$

$$x = L:\ T = T_0,\ P = \sigma/R_0 \tag{8}$$

Power-Law Solutions. We seek power-law solutions for the purpose of gaining insight into the action of surface enhancements without introducing distracting mathematical complexity. We imagine that, at the tip of the fin where the meniscus attaches, the pressure is singular, due to the effect of the $1/y^3$ term in equation (3) as x and y go to zero. Hence we choose

$$P = (\sigma/R_0)(x/L)^{-n} \tag{9}$$

$$y = y_0(x/L)^{2-n} \tag{10}$$

Equations (9) and (10) satisfy equation (6) when

$$y_0 = \frac{1}{(1-n)(2-n)}\frac{L^2}{R_0} \tag{11}$$

With $P(x)$ having been prescribed we must regard $\delta(x)$ as an unknown dependent variable. A condition upon δ must replace the lost boundary condition on P at $x = L$. Equations (3), (9), and (10) and the condition $\Gamma(0) = 0$ yield

$$\Gamma = \Gamma_0(x/L)^{5-4n} \tag{12}$$

$$\Gamma_0 = \frac{n}{(1-n)^3(2-n)^3}\frac{\sigma\rho_l}{3\mu_l}\frac{L^5}{R_0^4} \tag{13}$$

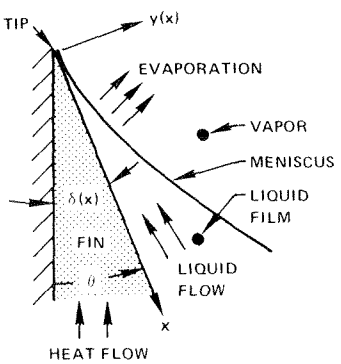

Fig. 1 Fin-meniscus geometry

[1] University of California, Los Angeles, Calif.

[2] Numbers in brackets designate References at end of technical brief.

Contributed by the Heat Transfer Division of THE AMERICAN SOCIETY OF MECHANICAL ENGINEERS. Manuscript received by the Heat Transfer Division, January 16, 1974.

Table 1 Properties of interest

Fluid	b	k/k_ℓ				
	Eq. (21) [ft/F]	Copper k=204	Red Brass k=92	Bronze k=40	Cupro-Nickel k=26	Titanium k=11.8
Water at 220°F	7.32×10^{-12}	517	233	101	66	30
Freon 12 at 160°F	4.20×10^{-11}	6755	3046	1325	861	391
Freon 22 at 160°F	5.26×10^{-11}	5500	2480	1080	700	318
Ammonia at 120°F	3.29×10^{-11}	829	374	163	106	48

Table 2 Calculated heat transfer coefficient per pair of fin faces per inch; $n = 0.973$

Fluid	hW Btu-inch/hr ft^2 F		
	T_0/L = 500°F/ft	T_0/L = 1000°F/ft	T_0/L = 2000°F/ft
Water at 220°F	206.4	179.7	156.4
Freon 12 at 160°F	11.1	9.7	8.4
Freon 22 at 160°F	13.1	11.4	9.9
Ammonia at 120°F	95.2	82.9	72.1

Equations (2), (10), and (12) dictate that

$$T = T_0(x/L)^{6-5n} \tag{14}$$

$$T_0 = \frac{n(5-4n)}{(1-n)^4(2-n)^4}\,\frac{\sigma\rho_l\hat{h}_{fg}}{3\mu_l k_l}\,\frac{L^6}{R_0^5} \tag{15}$$

Finally equation (1) prescribes

$$\delta = \delta_0(x/L)^n \tag{16}$$

$$\delta_0 = \frac{(1-n)(2-n)}{(5-4n)(6-5n)}\,\frac{k_l}{k}\,R_0 \tag{17}$$

Constraints: Equation (15) is not merely a definition of the quantity T_0. Reference to equation (8) indicates that it represents an imposed boundary condition. That this boundary condition can always be met by suitable choice of n is evident from the fact that the right-hand side varies from zero at $n = 0$ to infinity at $n = 1$ for any property values and geometrical lengths L and R_0.

The resulting value of n impacts upon the thickness of the fin which can be accommodated by the power law solutions, according to equation (17). Let the ratio of δ_0/L be denoted by $\tan\theta$, and substitute into equation (17)

$$\tan\theta = \frac{\delta_0}{L} \tag{18}$$

$$\tan\theta = \frac{(1-n)(2-n)}{(5-4n)(6-5n)}\,\frac{k_l}{k}\,\frac{R_0}{L} \tag{19}$$

Since k_l/k is small for a dielectric liquid and a metal wall, the quantity R_0/L must be large in order to avoid a small $\tan\theta$. But equation (15) is a constraint. Eliminating R_0 from equation (15) by virtue of equation (19) and rearranging yields

$$\left(\frac{bT_0}{L}\right)^{1/5}\frac{k}{k_l}\tan\theta = \frac{n^{1/5}(1-n)^{1/5}(2-n)^{1/5}}{(5-4n)^{4/5}(6-5n)} \leq 0.394 \tag{20}$$

$$b = \frac{3\mu_l k_l}{\sigma\rho_l\hat{h}_{fg}} \tag{21}$$

The right-hand side of equation (20) is seen to possess a maximum of 0.394 at $n = 0.973$. Hence a large value of T_0 can be accommodated by our power-law solution only by accepting a small value of $\tan\theta$, and vice versa.

The dimensional fluid-property grouping and the ratio k/k_l are shown in Table 1. For a value of $T_0/L = 1000$ F/ft, equation (20) indicates for water-copper, according to Table 1,

$$\tan\theta \leq 0.032 \qquad \theta \leq 1.85°$$

and for water-titanium, again using values from Table 1,

$$\tan\theta \leq 0.51 \qquad \theta \leq 29.2°$$

The constraints on the power-law solutions appear to limit application of the results to relatively poor conductors such as titanium or cupro-nickel in association with good conductors such as water or ammonia, if it is desired to treat triangular fins with angles of $\theta = 30$ deg or so. Of course, one would expect that the heat transfer indicated for a small value of θ would be a lower limit to that pertaining to a larger value of θ.

Heat Transfer Coefficient. Per unit width of fin, say in the circumferential direction for a circumferential groove, the total mass flow Γ_0 at $x = L$ is evaporated. Let the distance which includes two wet fin faces be W. For a given W, a heat transfer coefficient may be defined as

$$h \equiv \frac{2\Gamma_0\hat{h}_{fg}}{WT_0} \tag{22}$$

$$W \geq 2L\sin\theta \tag{23}$$

With equations (13) and (15), equation (22) can be written

$$h = \frac{n^{1/5}(1-n)^{1/5}(2-n)^{1/5}}{(5-4n)^{4/5}}\,\frac{2k_l}{b^{*1/5}W} \tag{24}$$

$$b^* = bT_0/L \tag{25}$$

Table 2 gives values of hW for $n = 0.973$ for a few values of T_0/L and the four fluids listed in Table 1. With $n = 0.973$, $T_0/L = 1000$ F/ft, $1/W = 18$ double-sided fins per in., and k_l and b corresponding to water, one obtains $h = (179.7)(36) = 3234$ [Btu/hr ft^2 F]. The value $T_0/L = 1000$ F/ft corresponds to a temperature difference of approximately 3.5 deg F, if $L = 0.0035$ ft. For such a value equation (23) states that one can have no more than 18 fins per in. for titanium, but many more would be permitted for copper, the number restricted by the need for flow areas as explained in reference [3].

Wayner and Coccio [6] measured $hW \doteq 20$ Btu/hr ft F = 240 Btu-in./hr ft^2 F with $T_0/L \doteq 500$ F/ft for water on a 0.112 in. uniformly thick 304 stainless steel fin heated from the dry end. The 240 value is somewhat above the value 206.4 in Table 2 for the tapered fin. This comparison, which is approximate in that the experiment did not match exactly the situation under analysis here, is interesting for the excellent order of magnitude agreement.

In summary, it has been demonstrated that a power-law solution exists for the capillary flow supplying liquid to the tip of an evaporator fin. The solution indicates a maximum heat transfer coefficient *limited by the fluid properties only* but requiring a fin with a certain $k\cdot\tan\theta$ value. The fluid properties enter predominantly as thermal conductivity k_l and secondarily as a grouping b involving viscosity, conductivity, surface tension, density and latent heat. The power-law solutions indicate that heat transfer coefficients on the order of 3230 Btu/hr ft^2 F should be obtainable with water on 18 titanium fins or grooves per in.

References

1 Gregorig, Romano, "Hautkondensation an feingewellten Oberflächen bei Berücksichtigung der Oberflächenspannungen," *Zeitschrift fur Angewandte Mathematik und Physik*, Vol. V, 1954, pp. 36–49.

2 Navabian, K., and Bromley, L. A., "Condensation Coefficient of Water," *Chemical Engineering Science*, Vol. 18, 1963, pp. 651–660.
3 Edwards, D. K., Gier, K. D., Ayyaswamy, P. S., and Catton, I., "Evaporation and Condensation in Circumferential Grooves on Horizontal Tubes," ASME Paper No. 73-HT-25.
4 Potash, Jr., M., and Wayner, Jr., P. C., "Evaporation From a Two-Dimensional Extended Meniscus," *International Journal of Heat and Mass Transfer*, Vol. 15, 1972, pp. 1851–1863.
5 Gardner, K. A., "Efficiency of Extended Surface," TRANS. ASME, Vol. 67, 1945, pp. 621–631.
6 Wayner, Jr., P. C., and Coccio, C. L., "Heat and Mass Transfer in the Vicinity of the Triple Interline of a Meniscus," *AIChE Journal*, Vol. 17, 1971, pp. 569–574.

Transient Flow Heat Transfer Measurements Using The Thin-Skin Method

C. S. Landram[1]

Introduction

In determining steady, convective heat transfer coefficients using the thin-skinned method, the instrumented body has typically been shuttled into a heated fluid flowing at a constant rate [1, 2].[2] The distributed conductance often impressed parallel temperature gradients within the skin that were usually more severe than those normal to the skin's surface [1].

Recently a somewhat different application for the thin-skin was used to measure wall heat transfer during combustion [3]. In this application *(a)* the thermal conductance varied temporally owing to a transient flow field, and *(b)* thermal gradients parallel to the skin were not as important as those normal to its surface. The temperature gradient across the skin thickness was assessed to be a result of its thermal capacitance, as opposed to the possible normal gradients caused by heat leakage to the substrate insulation of the skin [4] or to temperature gradients caused by the thermocouple lead wire on the insulated surface of the skin [5]. This present note was motivated by the necessity to correct the measured data in reference [3] for the temperature variation through the thickness of the skin.

Analysis

The skin is taken to be a one-dimensional slab of material perfectly insulated at $x = 0$ where the temperature $T_1 = T(0,t)$ is measured. The initial temperature of the slab T_0 is uniform. In terms of the mean slab temperature T_M the heat flux to the slab q_w is given by

$$-q_w = -k \frac{\partial T}{\partial x}(\ell, t) = -\rho C \ell \frac{dT_M}{dt} \tag{1}$$

The last equality of equation (1) was derived by spatially integrating the equation of heat conduction across the thickness ℓ. If equation (1) is to be evaluated for q_w, then the measured temperature T_1, must be related to T_M. Also, the value of the instantaneous heat transfer coefficient h is defined by

$$h = \frac{q_w}{T_f - T_2}, \quad T_2 = T(\ell, t) \tag{2}$$

where T_f is the (known) fluid temperature. Hence, both T_M and T_2 must be related to the measured temperature T_1.

In the solution for the slab temperature field $T(x,t)$, the boundary value problem cannot accommodate both of the prescriptions of zero heat flux and specified (measured) temperature at $x = 0$. The procedure here is to use the zero heat flux condition at $x = 0$ and determine the temperature field $T(x,t)$[6], including T_1 and T_M, for a particular history $T_2 = T(\ell,t)$. The purpose of this procedure is to show that there exist certain limiting relationships for $T_M - T_1$ and $T_2 - T_1$ that are independent of the history T_2 and therefore useful in evaluating equations (1) and (2). Table 1 summarizes the quasi-steady results when the skin is "thin" enough to assure that

$$\frac{\pi^2}{4\ell^2} \alpha t >> 1 \tag{3}$$

in which it is implied that times scales associated with the changing flow are large compared to diffusional time scales into the skin.

In addition to the requirement given by condition (3), the results of Table 1 show the design criterion for the practical use of the skin to measure transient flows:

$$\frac{\beta \ell^2}{\alpha} \text{ or } \frac{\omega \ell^2}{2\alpha} << 1 \tag{4}$$

where $1/\beta$ or $1/\omega$ is indicative of the time constant or period, respectively, of the flow field. From Table 1, when conditions (3) and (4) are met, equations (1) and (2) can, independently of β or ω, be evaluated for T_M and T_2 from the known, measured temperature T_1 through[3]

$$T_M = T_1 + \frac{1}{6} \frac{dT_1}{d(\frac{\alpha t}{\ell^2})} \tag{5}$$

and

$$T_2 = T_1 + \frac{1}{2} \frac{dT_1}{d(\frac{\alpha t}{\ell^2})} \quad . \tag{6}$$

Even if condition (4) is only weakly satisfied, the second order terms shown in Table 1 are very small. In fact, for the ramp they are identically zero; for the exponential functions, they are $\pm 1/20\ \beta l^2/\alpha$ and $\pm 1/12\ \beta l^2/\alpha$ for equations (5) and (6), respectively.

Application

The foregoing results were applied to the measured temperature response obtained from the insulated thin hemispherical constantan skin (membrane) shown in Fig. 1. The skin assembly was mounted flush within the inner wall of a simulated spherical combustion chamber into which a gas was injected through an orifice from a smaller upstream chamber. The cold gas (i.e., combustion absent) wall thermal conductance in the spherical chamber was then determined through equation (2) by the gas temperature rise provided by compression heating. Thermocouple recordings at four preselected skin locations (as in Fig. 1) disclosed only minor spatial variations when compared to the overall temporal response of the membrane.

Among the many cases tested [3], only one is herein considered for demonstrating the use of equations (5) and (6). Helium was allowed to flow from an upstream chamber to the spherical downstream chamber with an initial, respective pressure ratio of 1.99/1. Under adiabatic conditions this flow was calculated to cease in 0.019 sec, producing an adiabatic gas temperature rise of 59.9F deg in the spherical chamber.

The calculated curves for T_M and T_2 shown in Fig. 2 were determined from equations (5) and (6) by differentiating the following curve fit to the measured recording of T_1:

---

[1] Member of Technical Staff, Sandia Laboratories, Livermore, Calif. Mem. ASME.

[2] Numbers in brackets designate References at end of technical brief.

Contributed by the Heat Transfer Division of THE AMERICAN SOCIETY OF MECHANICAL ENGINEERS. Manuscript received by the Heat Transfer Division, December 14, 1973.

[3] Equations (5) and (6) can also be derived using the inverse solution given by Burggraf [7].

2 Navabian, K., and Bromley, L. A., "Condensation Coefficient of Water," *Chemical Engineering Science*, Vol. 18, 1963, pp. 651–660.
3 Edwards, D. K., Gier, K. D., Ayyaswamy, P. S., and Catton, I., "Evaporation and Condensation in Circumferential Grooves on Horizontal Tubes," ASME Paper No. 73-HT-25.
4 Potash, Jr., M., and Wayner, Jr., P. C., "Evaporation From a Two-Dimensional Extended Meniscus," *International Journal of Heat and Mass Transfer*, Vol. 15, 1972, pp. 1851–1863.
5 Gardner, K. A., "Efficiency of Extended Surface," TRANS. ASME, Vol. 67, 1945, pp. 621–631.
6 Wayner, Jr., P. C., and Coccio, C. L., "Heat and Mass Transfer in the Vicinity of the Triple Interline of a Meniscus," *AIChE Journal*, Vol. 17, 1971, pp. 569–574.

Transient Flow Heat Transfer Measurements Using The Thin-Skin Method

C. S. Landram[1]

Introduction

In determining steady, convective heat transfer coefficients using the thin-skinned method, the instrumented body has typically been shuttled into a heated fluid flowing at a constant rate [1, 2].[2] The distributed conductance often impressed parallel temperature gradients within the skin that were usually more severe than those normal to the skin's surface [1].

Recently a somewhat different application for the thin-skin was used to measure wall heat transfer during combustion [3]. In this application *(a)* the thermal conductance varied temporally owing to a transient flow field, and *(b)* thermal gradients parallel to the skin were not as important as those normal to its surface. The temperature gradient across the skin thickness was assessed to be a result of its thermal capacitance, as opposed to the possible normal gradients caused by heat leakage to the substrate insulation of the skin [4] or to temperature gradients caused by the thermocouple lead wire on the insulated surface of the skin [5]. This present note was motivated by the necessity to correct the measured data in reference [3] for the temperature variation through the thickness of the skin.

Analysis

The skin is taken to be a one-dimensional slab of material perfectly insulated at $x = 0$ where the temperature $T_1 = T(0,t)$ is measured. The initial temperature of the slab T_0 is uniform. In terms of the mean slab temperature T_M the heat flux to the slab q_w is given by

$$-q_w = -k\frac{\partial T}{\partial x}(\ell,\ t) = -\rho C\ell\frac{dT_M}{dt} \tag{1}$$

The last equality of equation (1) was derived by spatially integrating the equation of heat conduction across the thickness l. If equation (1) is to be evaluated for q_w, then the measured temperature T_1, must be related to T_M. Also, the value of the instantaneous heat transfer coefficient h is defined by

$$h = \frac{q_w}{T_f - T_2},\quad T_2 = T(\ell, t) \tag{2}$$

where T_f is the (known) fluid temperature. Hence, both T_M and T_2 must be related to the measured temperature T_1.

In the solution for the slab temperature field $T(x,t)$, the boundary value problem cannot accommodate both of the prescriptions of zero heat flux and specified (measured) temperature at $x = 0$. The procedure here is to use the zero heat flux condition at $x = 0$ and determine the temperature field $T(x,t)$[6], including T_1 and T_M, for a particular history $T_2 = T(l,t)$. The purpose of this procedure is to show that there exist certain limiting relationships for $T_M - T_1$ and $T_2 - T_1$ that are independent of the history T_2 and therefore useful in evaluating equations (1) and (2). Table 1 summarizes the quasi-steady results when the skin is "thin" enough to assure that

$$\frac{\pi^2}{4\ell^2}\alpha t >> 1 \tag{3}$$

in which it is implied that times scales associated with the changing flow are large compared to diffusional time scales into the skin.

In addition to the requirement given by condition (3), the results of Table 1 show the design criterion for the practical use of the skin to measure transient flows:

$$\frac{\beta\ell^2}{\alpha}\ \text{or}\ \frac{\omega\ell^2}{2\alpha} << 1 \tag{4}$$

where $1/\beta$ or $1/\omega$ is indicative of the time constant or period, respectively, of the flow field. From Table 1, when conditions (3) and (4) are met, equations (1) and (2) can, independently of β or ω, be evaluated for T_M and T_2 from the known, measured temperature T_1 through[3]

$$T_M = T_1 + \frac{1}{6}\frac{dT_1}{d(\frac{\alpha t}{\ell^2})} \tag{5}$$

and

$$T_2 = T_1 + \frac{1}{2}\frac{dT_1}{d(\frac{\alpha t}{\ell^2})}\ . \tag{6}$$

Even if condition (4) is only weakly satisfied, the second order terms shown in Table 1 are very small. In fact, for the ramp they are identically zero; for the exponential functions, they are $\pm 1/20\ \beta l^2/\alpha$ and $\pm 1/12\ \beta l^2/\alpha$ for equations (5) and (6), respectively.

Application

The foregoing results were applied to the measured temperature response obtained from the insulated thin hemispherical constantan skin (membrane) shown in Fig. 1. The skin assembly was mounted flush within the inner wall of a simulated spherical combustion chamber into which a gas was injected through an orifice from a smaller upstream chamber. The cold gas (i.e., combustion absent) wall thermal conductance in the spherical chamber was then determined through equation (2) by the gas temperature rise provided by compression heating. Thermocouple recordings at four preselected skin locations (as in Fig. 1) disclosed only minor spatial variations when compared to the overall temporal response of the membrane.

Among the many cases tested [3], only one is herein considered for demonstrating the use of equations (5) and (6). Helium was allowed to flow from an upstream chamber to the spherical downstream chamber with an initial, respective pressure ratio of 1.99/1. Under adiabatic conditions this flow was calculated to cease in 0.019 sec, producing an adiabatic gas temperature rise of 59.9F deg in the spherical chamber.

The calculated curves for T_M and T_2 shown in Fig. 2 were determined from equations (5) and (6) by differentiating the following curve fit to the measured recording of T_1:

[1] Member of Technical Staff, Sandia Laboratories, Livermore, Calif. Mem. ASME.
[2] Numbers in brackets designate References at end of technical brief.
Contributed by the Heat Transfer Division of THE AMERICAN SOCIETY OF MECHANICAL ENGINEERS. Manuscript received by the Heat Transfer Division, December 14, 1973.

[3] Equations (5) and (6) can also be derived using the inverse solution given by Burggraf [7].

Table 1 Results of quasi-steady calculations for several choices of the temperature of the exposed surface of the slab

Assumed Surface Temperature at $x = \ell$, $(T_2 - T_0)/V$	Calculated Quasi-Steady Temperature at $x = 0$, $(T_1 - T_0)/V$	Calculated Mean Slab Temperature $(T_M - T_0)/V$	Series Expression for Difference $T_2 - T_1$	Series Expression for Difference $T_M - T_1$
$1 - e^{-\beta t}$	$1 - \dfrac{e^{-\beta t}}{\cos\left(\sqrt{\dfrac{\beta \ell^2}{\alpha}}\right)}$	$1 - \dfrac{e^{-\beta t}\tan\sqrt{\dfrac{\beta \ell^2}{\alpha}}}{\sqrt{\dfrac{\beta \ell^2}{\alpha}}}$	$\frac{1}{2}\left[1 - \frac{1}{12}\left(\frac{\beta \ell^2}{\alpha}\right) + \ldots\right]\frac{dT_1}{d\left(\frac{\alpha t}{\ell^2}\right)}$	$\frac{1}{6}\left[1 - \frac{1}{20}\left(\frac{\beta \ell^2}{\alpha}\right) + \ldots\right]\frac{dT_1}{d\left(\frac{\alpha t}{\ell^2}\right)}$
βt	$\beta\left(t - \dfrac{\ell^2}{2\alpha}\right)$	$\beta\left(t - \dfrac{\ell^2}{3\alpha}\right)$	$\frac{1}{2}\dfrac{dT_1}{d\left(\frac{\alpha t}{\ell^2}\right)}$	$\frac{1}{6}\dfrac{dT_1}{d\left(\frac{\alpha t}{\ell^2}\right)}$
$e^{\beta t}$	$\dfrac{e^{\beta t}}{\cosh\sqrt{\dfrac{\beta \ell^2}{\alpha}}}$	$\dfrac{e^{\beta t}\tanh\sqrt{\dfrac{\beta \ell^2}{\alpha}}}{\sqrt{\dfrac{\beta \ell^2}{\alpha}}}$	$\frac{1}{2}\left[1 + \frac{1}{12}\left(\frac{\beta \ell^2}{\alpha}\right) + \ldots\right]\frac{dT_1}{d\left(\frac{\alpha t}{\ell^2}\right)}$	$\frac{1}{6}\left[1 + \frac{1}{20}\left(\frac{\beta \ell^2}{\alpha}\right) + \ldots\right]\frac{dT_1}{d\left(\frac{\alpha t}{\ell^2}\right)}$
$\sin(\omega t + \epsilon)$	$A(o)\sin[\omega t + \epsilon + \theta(o)]$	$\int_0^1 A(x)\sin[\omega t + \epsilon + \theta(x)]dx/\ell$	$\left(-\frac{Z^2}{6} + \ldots\right)T_1 + \frac{1}{2}\left(1 + \frac{2}{3}Z^2 + \ldots\right)\frac{dT_1}{d\left(\frac{\alpha t}{\ell^2}\right)}$	$\left(-\frac{Z^2}{10} + \ldots\right)T_1 + \frac{1}{6}\left(1 + \frac{2}{3}Z^2 + \ldots\right)\frac{dT_1}{d\left(\frac{\alpha t}{\ell^2}\right)}$
			where $Z = \frac{\omega \ell^2}{2\alpha} \ll 1$	$A(x) = 1 - \frac{Z^2}{3}\left[1 - \left(\frac{x}{\ell}\right)^4\right] + \ldots$ $\theta(x) = -Z\left[1 - \left(\frac{x}{\ell}\right)^2\right] + \ldots$

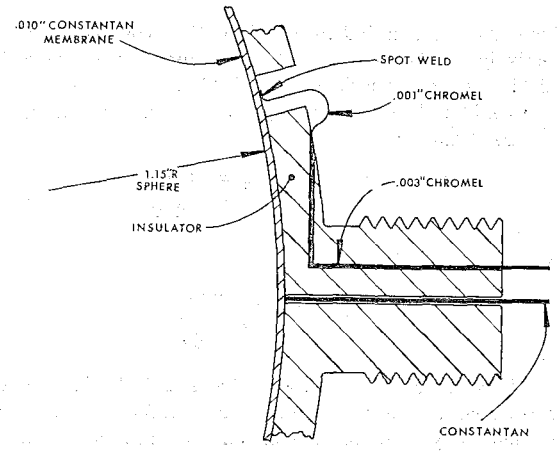

Fig. 1 Intrinsic heat flux sensor and skin assembly. Only one of four thermocouple attachments is shown.

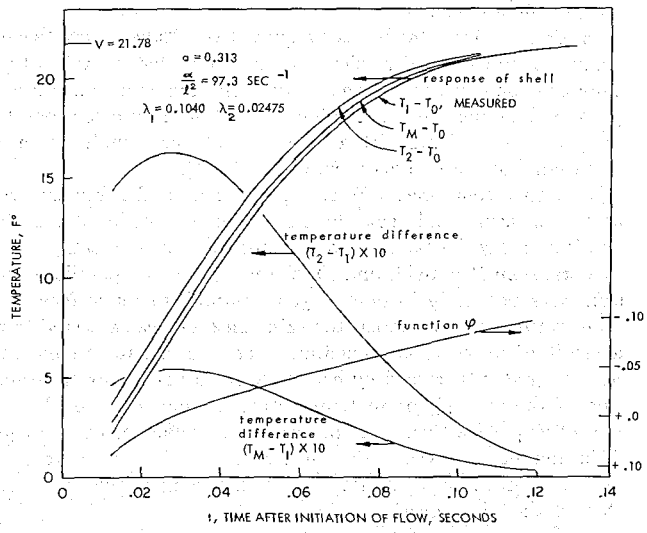

Fig. 2 Results of particular application. Ordinates to the left, depicting T_M and T_2, are evaluated from equations (5) and (6). The ordinate to the right is the fractional first order error in the heat flux made by equating T_1 and T_M.

$$\frac{T_1 - T_0}{V} = 1 - \exp\left[-\lambda_1\left(\frac{\alpha t}{\ell^2} - a\right) - \lambda_2\left(\frac{\alpha t}{\ell^2} - a\right)^2\right] \qquad (7)$$

where the numerical constants λ_1, λ_2, a, and V for the case considered here are as shown in Fig. 2. Equation (7) was written for time scales greater than about 0.0125 sec, thus satisfying condition (3), and only those times are shown plotted in Fig. 2.

For the case considered in Fig. 2, the gas-wall temperature difference is large (varying from about 40 to 60F deg) compared to the difference $T_2 - T_1$ (as much as about 1.6F deg). Therefore, the denominator of equation (2) is not too sensitive to the necessary inclusion of $T_2 - T_1$ to the measured temperature T_1 in determining $T_f - T_2$. However, because of the indicated differentiation of T_M for determining the heat flux in equation (1), the numerator of equation (2) must be carefully evaluated when making the necessary addition of the small difference $T_M - T_1$ to the measurements of T_1. In fact, the first order fractional error φ in q_ω, which would result using T_1 in equation (1) rather than T_M, is shown in Fig. 2.

For the case of equation (7), the ratios of second to first order terms in the expressions for $T_2 - T_1$ and $T_M - T_1$ are given by 3φ and $9\varphi/5$, respectively. These ratios are negligibly small for times when the first order terms are appreciable; and in other times, the magnitudes of these ratios are unimportant.

References

1 George, A. R., and Reinecke, W. G., "Conduction in Thin-Skinned Heat Transfer and Recovery Temperature Models," *AIAA Journal*, Vol. 1, No. 8, Aug. 1963, pp. 1956–1958.

2 Manos, W. P., and Taylor, D. E., "Analysis of Interpretation of Data on Thin-Skinned Heat Transfer Models," JOURNAL OF HEAT TRANSFER, TRANS. ASME, Series C, Vol. 84, No. 3, May 1962, pp. 191–192.

3 Landram, C. S., and Hartley, D. L., "Transient Forced Convection During Dual Chamber Combustion," Sandia Laboratories Report SLL-73-0074, Jan. 1974; and presented at ASME/CSME Joint Fluids Engineering Conference (Combustion Symposium), Montreal, Canada, May 1974.

4 Cooper, M., and Mayo, E. E., "Normal Conduction Effects on Heat-Transfer Data During Transient Heating of Thin-Skin Models," *Journal Aeronaut. Sci.*, Vol. 24, 1957, pp. 461–462.

5 Hennecke, D. K., and Sparrow, E. M., "Local Heat Sink on a Convectively Cooled Surface—Application to Temperature Measurement Error," *International Journal of Heat and Mass Transfer*, Vol. 13, 1970, pp. 287–304.

6 Carslaw, H. S., and Jaeger, J. C., *Conduction of Heat in Solids*, Second Ed., Oxford University Press, 1959, pp. 104–105.

7 Burggraf, O. R., "An Exact Solution of the Inverse Problem in Heat Conduction Theory and Applications," JOURNAL OF HEAT TRANSFER, TRANS. ASME, Series C, Vol. 86, No. 3, Aug. 1964, pp. 373–382.

Temperature Distribution Around a Moving Cylindrical Source

R. Trivedi[1] and S. R. Srinivasan[2]

Introduction

Temperature distributions around moving point and line sources have been obtained by Rosenthal [1],[3] and the importance of such an analysis in understanding many practical problems in welding and solidification is well established in literature [2–4]. Many important problems, however, involve moving sources or sinks which are finite in size. In this communication, therefore, the Rosenthal treatment is extended to obtain temperature distribution around a moving source whose shape corresponds to a circular cylinder of infinite height and radius R.

Analysis

The heat flow equation which governs the temperature distribution around the moving source is

$$\frac{\partial T_i}{\partial t} = a_i \nabla^2 T_i \quad (i = 1,2), \tag{1}$$

where $i = 1,2$ represents the temperature fields outside and inside of boundary of the moving source and a_i is thermal diffusivity. We now consider the case in which the source is moving at a constant velocity, $\vec{V}$, in a direction normal to the axis of cylinder. As postulated by Rosenthal [1], such problems can be simplified by assuming a quasi-stationary state in a coordinate system attached to the moving source. The steady-state heat flow equation, in a moving coordinate system, is obtained as [2]

$$a_i \nabla^2 T_i + \vec{V} \cdot \nabla T_i = 0 \tag{2}$$

We now define dimensionless Cartesian coordinates by dividing the dimensional coordinates by R. This gives for equation (2),

$$\nabla^2 T_i + 2p_i \frac{\partial T_i}{\partial x} = 0 \tag{3}$$

where the source is moving in the x direction and $p_i = VR/2a_i$ is the thermal Peclet number.

We shall now obtain the solution of equation (3) under the boundary conditions that $T = T_\infty$ as $x \to \infty$ and that along the boundary, the temperature profile is arbitrary but known. Such a solution for a cylindrical source is easy to obtain if dimensionless cylindrical coordinates (r,θ) are used. In this coordinate system, the temperature distribution is obtained as [2]

$$T_i - T' = e^{-p_i r \cos\theta} \psi(r,\theta) \tag{4}$$

where T' is a constant temperature T_∞ for outside field and zero for inside field. The direction $\theta = 0$ corresponds to the direction of the source motion. The function $\psi(r,\theta)$ is governed by the differential equation

$$\nabla^2 \psi - p^2 \psi = 0 \tag{5}$$

The solution of equation (5) is obtained by the separation of variables method and the temperature field, T_1, outside the cylinder and the temperature field, T_2, inside the cylinder are obtained as

$$T_1 - T_\infty = e^{-p_1 r \cdot \cos\theta} \sum_{n=0}^{\infty} A_n \frac{K_n(p_1 r)}{K_n(p_1)} \cos n\theta \tag{6a}$$

and

$$T_2 = e^{-p_2 r \cdot \cos\theta} \sum_{n=0}^{\infty} B_n \frac{I_n(p_2 r)}{I_n(p_2)} \cos n\theta \tag{6b}$$

where I_n and K_n are modified Bessel functions of first and second kind, respectively. The values of coefficients A_n and B_n are obtained from the boundary condition along the moving cylindrical surface.

We now consider a boundary condition such that the temperature profile can be analyzed into Fourier components. The temperature profile is symmetric with respect to the Z axis, the direction of motion of the source. Thus, along the boundary $r = 1$,

$$T_1 = T_2 = \sum_{\nu=0}^{\infty} a_\nu \cdot \cos \nu\theta \tag{7}$$

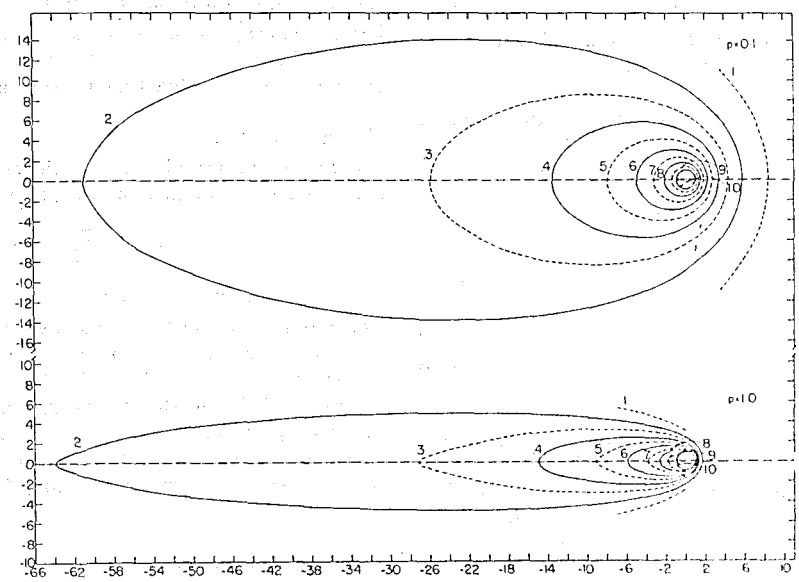

Fig. 1 Temperature distribution around a moving cylindrical source for *(a)* $p = 0.1$, and *(b)* $p = 1.0$. The lines represent constant value of $(T - T_\infty)/(T_0 - T_\infty)$. The coordinate axes represent distances in the units of R, the radius of the moving cylinder.

[1] Assoc. Professor, Department of Metallurgy and Metallurgist, Ames Laboratory of USAEC, Iowa State University, Ames, Iowa.

[2] Graduate Research Assistant, Ames Laboratory of USAEC, Ames, Iowa. Now at Max Planck Institute, Düsseldorf, West Germany.

[3] Numbers in brackets designate References at end of technical brief.

Contributed by the Heat Transfer Division of THE AMERICAN SOCIETY OF MECHANICAL ENGINEERS.

Manuscript received by the Heat Transfer Division, December 26, 1973.

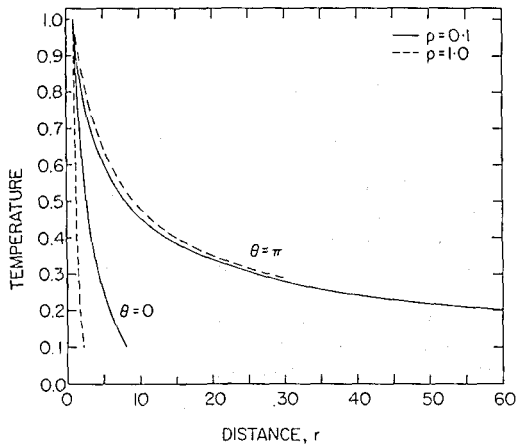

Fig. 2 Temperature profiles along $\theta = 0$ and $\theta = \pi$ for a moving source with $p = 0.1$ and 1.0

where a_ν, the Fourier coefficients of the boundary value, are known. Comparing equation (7) with equation (6*a*) at $r = 1$, we get

$$\sum_{n=0}^{\infty} A_n \cdot \cos n\theta = -T_\infty \cdot e^{p_1 \cos\theta} + e^{p_1 \cos\theta} \sum_{\nu=0}^{\infty} a_\nu \cdot \cos \nu\theta$$

The value of coefficient A_n is then obtained as

$$A_n = -T_\infty \frac{\epsilon_n}{\pi} \int_0^\pi e^{p_1 \cos\theta} \cos n\theta \cdot d\theta + \frac{\epsilon_n}{\pi} \int_0^\pi e^{p_1 \cos\theta} \sum_{\nu=0}^{\infty} a_\nu \cos \nu\theta \cos n\theta \cdot d\theta$$

or

$$A_n = -T_\infty \cdot \epsilon_n \cdot I_n(p_1) + \frac{\epsilon_n}{2} \cdot \sum_{\nu=0}^{\infty} a_\nu [I_{\nu+n}(p_1) + I_{\nu-n}(p_1)] \quad (8a)$$

$$\text{where } \epsilon_n = \begin{cases} 1, & n = 0 \\ 2, & n \geq 1 \end{cases}$$

Similarly, comparing equation (7) with equation (6*b*), we get

$$B_n = \frac{\epsilon_n}{2} \sum_{\nu=0}^{\infty} a_\nu [I_{\nu+n}(p_2) + I_{\nu-n}(p_2)] \quad (8b)$$

The temperature distribution outside the inside moving cylinder is then given by equations (6*a*) and (6*b*) in which the coefficients A_n and B_n are obtained from equations (8*a*) and (8*b*), respectively.

If the moving cylinder is isothermal with temperature T_0 on its surface, the coefficients A_n and B_n have simple values given by the expressions

$$A_n = (T_0 - T_\infty)\epsilon_n I_n(p_1)$$

$$B_n = T_0 \epsilon_n I_n(p_2)$$

Discussion

For an isothermal cylindrical surface, the inside temperature will be constant and equal to T_0. The temperature distribution in the outside region of the cylinder will depend on the velocity, or more precisely on the Peclet number p_1. Fig. 1 shows isotherms around a moving cylinder for two growth conditions, viz. $p = 0.1$ and 1.0. Note that for a stationary cylinder, the isotherms will be symmetrical around the source. However, as velocity is increased, the isotherms tend to bunch closer together in front and tend to spread apart in the rear of the source. As velocity is further increased, the temperature profile in front of a moving cylinder becomes quite steep. The temperature profiles at $\theta = 0$ and $\theta = \pi$ directions are shown in Fig. 2.

The present results can be profitably applied to the arc welding case in which a molten pool of liquid is present surrounding the source. Here the thermal diffusivity will be in liquid, a_1^L, and the extent of liquid pool will be given by the isotherm which corresponds to the melting point of the solid. The temperature distribution in solid can be calculated by using the thermal diffusivity in solid, a_1^S, and by considering temperature continuity at the solid-liquid interface.

References

1 Rosenthal, D., "The Theory of Moving Sources of Heat and Its Application to Metal Treatments," TRANS. ASME, Vol. 68, 1946, pp. 849–866.

2 Carslaw, H. S., and Jaeger, J. C., *Conduction of Heat in Solids*, Second ed., Oxford, London, 1959.

3 Trivedi, R., "Growth of Dendritic Needles From a Supercooled Melt," *Acta Met.*, Vol. 18, 1970, pp. 287–296.

4 Crank, J., *The Mathematics of Diffusion*, Oxford, London, 1956.

Solution of Anisotropic Heat Conduction Problems by Monte Carlo Procedures

J. Padovan[1]

Introduction

Under certain circumstances, an engineering designer is sometimes faced with requiring the temperature at only a few isolated points of a given design configuration. In this context, since the general purpose finite element [1],[2] as well as the classical finite difference techniques [2], must treat the global thermal problem, the Monte Carlo procedure [3], which handles the problem from an individual point basis, may be used as an alternate solution procedure. With this in mind, this note is concerned with extending the Monte Carlo [3] procedure to the solution of anisotropic heat conduction problems. For simplicity, using the floating random walk technique of Haji-Sheikh and Sparrow [3], only the steady-state Dirichlet problem will be considered herein. Based on this development, direct extensions are also possible for the mixed Dirichlet, Neumann and Cauchy problems for the steady-state and transient problems, using both the fixed and floating random walk procedures. As will be seen from the results given herein, contrary to the isotropic treatment [3], as might be expected, thermal material anisotropy induces a directional preferentiality for both the fixed and floating random walk procedures.

Development

For homogeneous fully anisotropic media, the governing steady-state conduction equation takes the form [2]

$$\kappa_{ij} \frac{\partial^2 T}{\partial x_i \partial x_j} + Q = 0 \quad (1)$$

Following Haji-Sheikh and Sparrow [3], the basis of the anisotropic form of the floating random walk may be deduced in terms of a Poisson integral type solution. For the given problem, due to the noncanonical form of equation (1) [4–6], such a solution is not directly available in the (x_1, x_2, x_3) space. Rather, the required integral representation must be obtained in a transformed space which reduces equation (1) to a canonical form. For the present note, this is achieved by transforming (x_1, x_2, x_3) to the principal

[1] Assoc. Professor, University of Akron, Akron, Ohio, Assoc. Mem. ASME.

[2] Numbers in brackets designate References at end of technical brief.

Contributed by the Heat Transfer Division of THE AMERICAN SOCIETY OF MECHANICAL ENGINEERS. Manuscript received by the Heat Transfer Division, January 14, 1974.

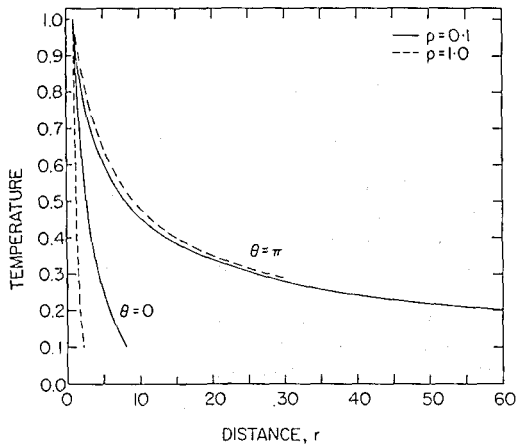

Fig. 2 Temperature profiles along $\theta = 0$ and $\theta = \pi$ for a moving source with $p = 0.1$ and 1.0

where a_ν, the Fourier coefficients of the boundary value, are known. Comparing equation (7) with equation (6a) at $r = 1$, we get

$$\sum_{n=0}^{\infty} A_n \cdot \cos n\theta = -T_\infty \cdot e^{p_1 \cos\theta} + e^{p_1 \cos\theta} \sum_{\nu=0}^{\infty} a_\nu \cdot \cos \nu\theta$$

The value of coefficient A_n is then obtained as

$$A_n = -T_\infty \frac{\epsilon_n}{\pi} \int_0^\pi e^{p_1 \cos\theta} \cos n\theta \cdot d\theta + \frac{\epsilon_n}{\pi} \int_0^\pi e^{p_1 \cos\theta} \sum_{\nu=0}^{\infty} a_\nu \cos \nu\theta \cos n\theta \cdot d\theta$$

or

$$A_n = -T_\infty \cdot \epsilon_n \cdot I_n(p_1) + \frac{\epsilon_n}{2} \cdot \sum_{\nu=0}^{\infty} a_\nu [I_{\nu+n}(p_1) + I_{\nu-n}(p_1)] \quad (8a)$$

$$\text{where } \epsilon_n = \begin{cases} 1, & n = 0 \\ 2, & n \geq 1 \end{cases}$$

Similarly, comparing equation (7) with equation (6b), we get

$$B_n = \frac{\epsilon_n}{2} \sum_{\nu=0}^{\infty} a_\nu [I_{\nu+n}(p_2) + I_{\nu-n}(p_2)] \quad (8b)$$

The temperature distribution outside the inside moving cylinder is then given by equations (6a) and (6b) in which the coefficients A_n and B_n are obtained from equations (8a) and (8b), respectively.

If the moving cylinder is isothermal with temperature T_0 on its surface, the coefficients A_n and B_n have simple values given by the expressions

$$A_n = (T_0 - T_\infty)\epsilon_n I_n(p_1)$$

$$B_n = T_0 \epsilon_n I_n(p_2)$$

Discussion

For an isothermal cylindrical surface, the inside temperature will be constant and equal to T_0. The temperature distribution in the outside region of the cylinder will depend on the velocity, or more precisely on the Peclet number p_1. Fig. 1 shows isotherms around a moving cylinder for two growth conditions, viz. $p = 0.1$ and 1.0. Note that for a stationary cylinder, the isotherms will be symmetrical around the source. However, as velocity is increased, the isotherms tend to bunch closer together in front and tend to spread apart in the rear of the source. As velocity is further increased, the temperature profile in front of a moving cylinder becomes quite steep. The temperature profiles at $\theta = 0$ and $\theta = \pi$ directions are shown in Fig. 2.

The present results can be profitably applied to the arc welding case in which a molten pool of liquid is present surrounding the source. Here the thermal diffusivity will be in liquid, a_1^L, and the extent of liquid pool will be given by the isotherm which corresponds to the melting point of the solid. The temperature distribution in solid can be calculated by using the thermal diffusivity in solid, a_1^S, and by considering temperature continuity at the solid-liquid interface.

References

1 Rosenthal, D., "The Theory of Moving Sources of Heat and Its Application to Metal Treatments," TRANS. ASME, Vol. 68, 1946, pp. 849–866.
2 Carslaw, H. S., and Jaeger, J. C., *Conduction of Heat in Solids*, Second ed., Oxford, London, 1959.
3 Trivedi, R., "Growth of Dendritic Needles From a Supercooled Melt," *Acta Met.*, Vol. 18, 1970, pp. 287–296.
4 Crank, J., *The Mathematics of Diffusion*, Oxford, London, 1956.

Solution of Anisotropic Heat Conduction Problems by Monte Carlo Procedures

J. Padovan[1]

Introduction

Under certain circumstances, an engineering designer is sometimes faced with requiring the temperature at only a few isolated points of a given design configuration. In this context, since the general purpose finite element [1],[2] as well as the classical finite difference techniques [2], must treat the global thermal problem, the Monte Carlo procedure [3], which handles the problem from an individual point basis, may be used as an alternate solution procedure. With this in mind, this note is concerned with extending the Monte Carlo [3] procedure to the solution of anisotropic heat conduction problems. For simplicity, using the floating random walk technique of Haji-Sheikh and Sparrow [3], only the steady-state Dirichlet problem will be considered herein. Based on this development, direct extensions are also possible for the mixed Dirichlet, Neumann and Cauchy problems for the steady-state and transient problems, using both the fixed and floating random walk procedures. As will be seen from the results given herein, contrary to the isotropic treatment [3], as might be expected, thermal material anisotropy induces a directional preferentiality for both the fixed and floating random walk procedures.

Development

For homogeneous fully anisotropic media, the governing steady-state conduction equation takes the form [2]

$$\kappa_{ij} \frac{\partial^2 T}{\partial x_i \partial x_j} + Q = 0 \quad (1)$$

Following Haji-Sheikh and Sparrow [3], the basis of the anisotropic form of the floating random walk may be deduced in terms of a Poisson integral type solution. For the given problem, due to the noncanonical form of equation (1) [4–6], such a solution is not directly available in the (x_1, x_2, x_3) space. Rather, the required integral representation must be obtained in a transformed space which reduces equation (1) to a canonical form. For the present note, this is achieved by transforming (x_1, x_2, x_3) to the principal

[1] Assoc. Professor, University of Akron, Akron, Ohio, Assoc. Mem. ASME.
[2] Numbers in brackets designate References at end of technical brief.
Contributed by the Heat Transfer Division of THE AMERICAN SOCIETY OF MECHANICAL ENGINEERS. Manuscript received by the Heat Transfer Division, January 14, 1974.

coordinates and subsequently introducing the appropriate coordinate stretches.

Since κ_{ij} is a second order tensor, following the usual treatment [2], the principal coordinates are defined by

$$y_i = n_{ji} x_j \tag{2}$$

such that the direction cosines n_{ij} satisfy the eigenvalue problem

$$[\kappa_{ij} - \kappa_l \delta_{ij}] n_{jl} = 0 \tag{3}$$

Using equation (2) in conjunction with the coordinate stretch

$$z_i = \sqrt{(\kappa_1/\kappa_i)}\, y_i \tag{4}$$

equation (1) reduces to the usual isotropic form in (z_1, z_2, z_3) space. For the Dirichlet problem of homogeneous two and three-dimensional regions with radius R and centers (z_{10}, z_{20}) and (z_{10}, z_{20}, z_{30}), respectively, the aforementioned steady-state Poisson integrals take the forms [3]

$$2\text{-D}; \quad T(z_{10}, z_{20}) = \int_0^1 \left[T(R,\theta) + \frac{QR^2}{4\kappa_1} \right] dF(\theta) \tag{5}$$

$$3\text{-D}; \quad T(z_{10}, z_{20}, z_{30}) = \int_0^1 \int_0^1 \left[T(R,\theta,\phi) + \frac{QR^2}{6\kappa_1} \right] dU(\phi) dF(\theta) \tag{6}$$

In terms of equations (5) and (6), the probability distribution functions for the two and three-dimensional developments are given by

$$2\text{-D}, F(\theta) = \theta/2\pi; \quad 3\text{-D}, F(\theta) = \theta/2\pi, \quad U(\phi) = (1/2)(1 - \cos\phi) \tag{7}$$

These equations describe the probability distribution of the random walking "particles" instantaneously situated at the centers of the circular (2-D) and spherical (3-D) regions preparing for their next step in z space. Referring to Fig. 1, transformed to x space, the circle and sphere map to

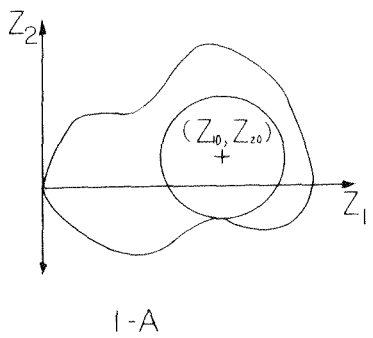

I-A

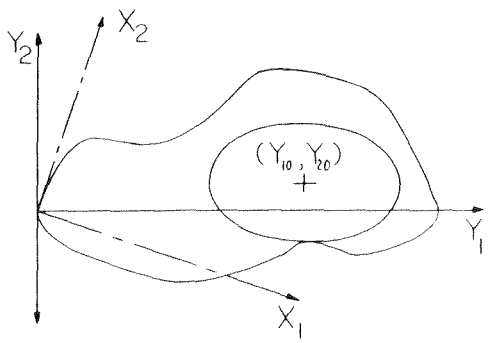

I-B

Fig. 1 Floating random walk for 2-D region

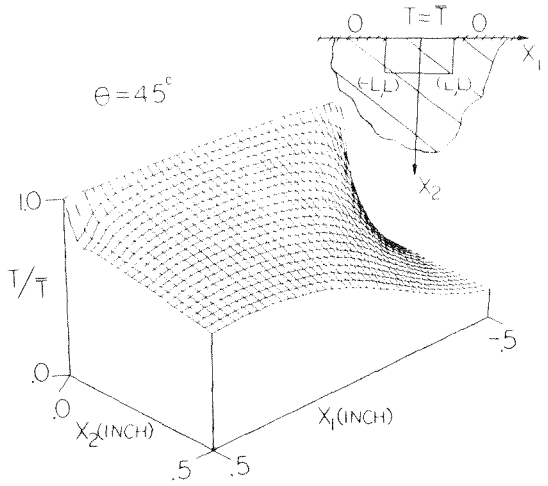

Fig. 2 Effects of principal orientation on temperature field

$$R^2 = (\kappa_1/\kappa_i)(n_{1i}x_1 - y_{i0})(n_{1i}x_1 - y_{i0}) \begin{cases} 2\text{-D}; & i,l = 1,2 \\ 3\text{-D}; & i,l = 1,2,3 \end{cases} \tag{8}$$

Considering the two-dimensional case, the probabilistic interpretation of equations (7) indicates that a random walking particle instantaneously at (z_{10}, z_{20}) will step to a new position on the circumference of the surrounding circle, Fig. 1(*a*), in accordance with the probability F. In (x_1, x_2) space, the random walking particle steps to the elliptic curve, Fig. 1(*b*), defined by equation (8). As can be seen from the foregoing figures, the main effect of material anisotropy is to induce a directional preferentiality on the random walking particle in x space. From the form of the elliptic curves described by equations (8) it follows that the greatest preference is in the coordinate direction associated with the maximum principal conductivity. Since every random walking particle has such a directional preference, the final temperature distribution in the 2-D x space will be distorted in the direction of maximum principal conductivity. Similar preferential distortions will occur for the three-dimensional problem as evidenced by the ellipsoidal surface, equation (8), surrounding the random walking particles in x space. Apart from the aforementioned distortions, the traditional floating random walk concept applies with no revision necessary for the Dirichlet problem.[3]

Discussion

To illustrate the distortion to the temperature field induced by thermal material anisotropy, as well as the potential accuracy of the modified floating random walk type Monte Carlo procedure described herein, the following two-dimensional steady-state problem is considered. Recently, Padovan [5] developed a solution for the transient thermal response of an anisotropic half space subject to arbitrary surface conditions. For the purposes of the present discussion, the floating random walk procedure was used to evaluate the steady-state temperature distribution of the portion of the half space described in Fig. 2. The boundary conditions used for the procedure were given by the exact [5] steady-state half space temperatures along the boundary edges described in Fig. 2. This figure also illustrates the temperature profile of the said region for the principal conductivity orientation defined by θ = 45 deg with respect to the half space surface. As can be seen, anisotropy causes significant asymmetries in the temperature profile. For all the calculations performed, the agreement between the floating random walk prediction and the exact solution was quite good. In general from 1500 to 4500 random walks were re-

[3] The boundary representations developed by Haji-Sheikh and Sparrow [3] are used herein.

quired to insure adequate accuracy.

Similar numerical results have also been obtained using a modified version of the fixed random walk procedure. In that case, due to the anisotropy of the conductivity tensor, the finite difference representation of the conduction equation yielded directionally dependent nodal probabilities akin to those of the modified floating random walk procedure described in the foregoing.

References

1 Zienkiewicz, O. C., *The Finite Element Method in Engineering Science*, McGraw-Hill, London, 1971.

2 Ozisik, M. N., *Boundary Value Problems of Heat Conduction*, International Textbook Company, Scranton, Pa., 1968.

3 Haji-Sheikh, A., and Sparrow, E. M., "The Solution of Heat Conduction Problems by Probability Methods," JOURNAL OF HEAT TRANSFER, TRANS. ASME, Series C, Vol. 89, No. 2, May 1967, pp. 121.

4 Padovan, J., "Temperature Distributions in Anisotropic Shells of Revolution," *AIAA Jr.*, Vol. 10, No. 1, Jan. 1972, p. 60.

5 Padovan, J., "Transient Temperature Distributions of an Anisotropic Half Space," *AIAA Jr.*, Vol. 11, No. 4, Apr. 1973, p. 565.

6 Padovan, J., "Quasi-Analytical Finite Element Procedure for Conduction in Anisotropic Axisymmetric Solids," *International Journal for Numerical Methods in Engineering*, Vol. 8, No. 2, 1974, pp. 295–310.

Turbulent Heat Transfer for Pipe Flow With Prescribed Wall Heat Fluxes and Uniform Heat Sources in the Stream

B. T. F. Chung[1] and L. C. Thomas[1]

Introduction

Turbulent heat transfer from fluid with internal heat generation has recently received considerable attention. This area of study is significant in the design of fluid-fueled nuclear reactors, electromagnetic pumps, flow meters, and some chemical process equipment. The problem of turbulent generating flow was first investigated by Poppendiek [1][2] and further studied by others [2–5]. All of the earlier theoretical analyses in this field have been based on the classical eddy diffusivity model. However, this approach leads to exact solutions for the heat transfer coefficient or wall temperature that are too involved for engineering computations. In the present work, the same problem will be attacked by a different approach which makes use of the principle of surface renewal [6, 7]; emphasis will be placed on moderate Prandtl numbers.

Mathematical Model

Let us consider fully developed turbulent tube flow of a Newtonian fluid in which a uniform heat per unit volume, Q is generated, with the tube walls subjected to a constant heat flux, q_0. Employing the simple surface renewal and penetration model and assuming constant fluid properties, we may express the temperature field for an individual eddy in the vicinity of the wall as

$$\frac{1}{\alpha}\frac{\partial t}{\partial \theta} = \frac{\partial^2 t}{\partial y^2} + \frac{Q}{k} \qquad 0 \le y < \infty \tag{1}$$

$$t = T_b \text{ at } \theta = 0 \tag{2}$$

$$k\frac{\partial T}{\partial y} = q_0 \text{ at } y = 0 \tag{3}$$

$$t = T_b \text{ as } y \to \infty \tag{4}$$

where θ is the instantaneous contact time and T_b is the bulk stream temperature. q_0 is assumed to be positive for heat transfer from the fluid to the wall. The solution to the foregoing system of equations gives rise to an expression for the instantaneous temperature profile of the eddy of the form

$$t - T_b = -\frac{q_0}{\sqrt{\rho c k}}\left[2\sqrt{\theta/\pi}\cdot\exp\left(-y^2/4\alpha\theta\right) - \frac{y}{\sqrt{\alpha}}\operatorname{erfc}\left(y/\sqrt{4\alpha\theta}\right)\right] + \frac{\alpha Q}{k\pi}\int_0^{\theta}\int_0^{\infty}\frac{1}{\sqrt{\alpha(\theta-\theta')}}\exp\left[-\frac{y'^2}{4\alpha(\theta-\theta')}\right]dy'd\theta' \tag{5}$$

The local mean wall temperature, T_0, may be obtained by use of the random contact time distribution of Danckwerts [6] as

$$T_0 - T_b = \frac{1}{\tau}\int_0^{\infty}(t_0 - T_b)\exp\left(-\frac{\theta}{\tau}\right)d\theta \tag{6}$$

where t_0 is the instantaneous temperature at the wall and τ is the mean residence time of the eddies in contact with the wall. Combining equations (5) and (6) yields a simple expression for the dimensionless mean wall temperature of the form

$$\frac{T_0 - T_b}{2q_0R/k} = \frac{\eta}{G} - \frac{\sqrt{\eta}}{2} \tag{7}$$

where $G = 2q_0/QR$, $\eta = \alpha\tau/R^2$ and R is the radius of the pipe.

The mean residence time can be determined from the adaptation of the surface renewal and penetration model to momentum transfer and is given by [7]

$$\tau = \frac{2\nu}{fu^{*2}} \tag{8}$$

for $\mathrm{Re} \gtrsim 10^4$; u^* is the friction velocity and f is the Fanning friction factor [9]. With the aid of this expression, equation (7) can be rewritten as

$$\frac{T_0 - T_b}{2q_0R/k} = \frac{16}{G\mathrm{Re}^2 f^2 \mathrm{Pr}} - \frac{2}{\mathrm{Re}f\sqrt{\mathrm{Pr}}} \tag{9}$$

Only the first term is retained if $q_0 = 0$, and only the second term is retained if $Q = 0$.

Discussion

The numerical results of the present model are shown in Fig. 1 with G arbitrarily set equal to 0.5. No experimental data exist on heat transfer for fluid subjected to simultaneous heat flux and internal heat generation. However, analytical solutions based on the eddy diffusivity model are available [2, 3]. Due to the complexity of the exact solutions, Michiyoshi and Nakajima [3] also proposed an empirical formula which has been reported to agree well with their exact solution. This empirical equation is shown by dashed lines on Fig. 1. Agreement between two models appears to be fairly good.

For the case of zero wall flux, i.e., $G = 0$, equation (9) yields a simple expression for the adiabatic wall to bulk temperature difference of a generating flow. To the authors' knowledge, only two papers have been published which deal with the experimental study of heat transfer in the presence of heat sources in a fluid with moderate Prandtl number. The experiments by Poppendiek [1] and Kinney and Sparrow [5] were carried out with sulphuric acid solutions and salt water, respectively. Both papers presented experimental data for fully developed adiabatic wall-to-bulk temperature differences. Parenthetically, the predictions of reference [4] agree well with the experimental data of reference [5]. Fig. 2 compares the present model with data of Kinney and Sparrow. Their analytical solutions, which are based on an earlier analysis [2] are also included. Although data scatter is a problem, the eddy diffusivity model appears to best correlate the data at high Reynolds numbers, while the surface renewal model is preferred at low Reynolds numbers. Clearly, more heat transfer data are needed before any positive conclusions can be drawn.

[1] Department of Mechanical Engineering, The University of Akron, Akron, Ohio.

[2] Numbers in brackets designate References at end of technical brief.

Contributed by the Heat Transfer Division of THE AMERICAN SOCIETY OF MECHANICAL ENGINEERS. Manuscript received by the Heat Transfer Division, October 25, 1973.

quired to insure adequate accuracy.

Similar numerical results have also been obtained using a modified version of the fixed random walk procedure. In that case, due to the anisotropy of the conductivity tensor, the finite difference representation of the conduction equation yielded directionally dependent nodal probabilities akin to those of the modified floating random walk procedure described in the foregoing.

References

1 Zienkiewicz, O. C., *The Finite Element Method in Engineering Science*, McGraw-Hill, London, 1971.

2 Ozisik, M. N., *Boundary Value Problems of Heat Conduction*, International Textbook Company, Scranton, Pa., 1968.

3 Haji-Sheikh, A., and Sparrow, E. M., "The Solution of Heat Conduction Problems by Probability Methods," JOURNAL OF HEAT TRANSFER, TRANS. ASME, Series C, Vol. 89, No. 2, May 1967, pp. 121.

4 Padovan, J., "Temperature Distributions in Anisotropic Shells of Revolution," *AIAA Jr.*, Vol. 10, No. 1, Jan. 1972, p. 60.

5 Padovan, J., "Transient Temperature Distributions of an Anisotropic Half Space," *AIAA Jr.*, Vol. 11, No. 4, Apr. 1973, p. 565.

6 Padovan, J., "Quasi-Analytical Finite Element Procedure for Conduction in Anisotropic Axisymmetric Solids," *International Journal for Numerical Methods in Engineering*, Vol. 8, No. 2, 1974, pp. 295–310.

Turbulent Heat Transfer for Pipe Flow With Prescribed Wall Heat Fluxes and Uniform Heat Sources in the Stream

B. T. F. Chung[1] and L. C. Thomas[1]

Introduction

Turbulent heat transfer from fluid with internal heat generation has recently received considerable attention. This area of study is significant in the design of fluid-fueled nuclear reactors, electromagnetic pumps, flow meters, and some chemical process equipment. The problem of turbulent generating flow was first investigated by Poppendiek [1][2] and further studied by others [2–5]. All of the earlier theoretical analyses in this field have been based on the classical eddy diffusivity model. However, this approach leads to exact solutions for the heat transfer coefficient or wall temperature that are too involved for engineering computations. In the present work, the same problem will be attacked by a different approach which makes use of the principle of surface renewal [6, 7]; emphasis will be placed on moderate Prandtl numbers.

Mathematical Model

Let us consider fully developed turbulent tube flow of a Newtonian fluid in which a uniform heat per unit volume, Q is generated, with the tube walls subjected to a constant heat flux, q_0. Employing the simple surface renewal and penetration model and assuming constant fluid properties, we may express the temperature field for an individual eddy in the vicinity of the wall as

$$\frac{1}{\alpha}\frac{\partial t}{\partial \theta} = \frac{\partial^2 t}{\partial y^2} + \frac{Q}{k} \qquad 0 \le y < \infty \tag{1}$$

$$t = T_b \text{ at } \theta = 0 \tag{2}$$

$$k\frac{\partial T}{\partial y} = q_0 \text{ at } y = 0 \tag{3}$$

$$t = T_b \text{ as } y \to \infty \tag{4}$$

where θ is the instantaneous contact time and T_b is the bulk stream temperature. q_0 is assumed to be positive for heat transfer from the fluid to the wall. The solution to the foregoing system of equations gives rise to an expression for the instantaneous temperature profile of the eddy of the form

$$t - T_b = -\frac{q_0}{\sqrt{\rho c k}}\left[2\sqrt{\theta/\pi}\cdot\exp\left(-y^2/4\alpha\theta\right) - \frac{y}{\sqrt{\alpha}}\operatorname{erfc}\left(y/\sqrt{4\alpha\theta}\right)\right] + \frac{\alpha Q}{k\pi}\int_0^{\theta}\int_0^{\infty}\frac{1}{\sqrt{\alpha(\theta-\theta')}}\exp\left[-\frac{y'^2}{4\alpha(\theta-\theta')}\right]dy'd\theta' \tag{5}$$

The local mean wall temperature, T_0, may be obtained by use of the random contact time distribution of Danckwerts [6] as

$$T_0 - T_b = \frac{1}{\tau}\int_0^{\infty}(t_0 - T_b)\exp\left(-\frac{\theta}{\tau}\right)d\theta \tag{6}$$

where t_0 is the instantaneous temperature at the wall and τ is the mean residence time of the eddies in contact with the wall. Combining equations (5) and (6) yields a simple expression for the dimensionless mean wall temperature of the form

$$\frac{T_0 - T_b}{2q_0R/k} = \frac{\eta}{G} - \frac{\sqrt{\eta}}{2} \tag{7}$$

where $G = 2q_0/QR$, $\eta = \alpha\tau/R^2$ and R is the radius of the pipe.

The mean residence time can be determined from the adaptation of the surface renewal and penetration model to momentum transfer and is given by [7]

$$\tau = \frac{2\nu}{fu^{*2}} \tag{8}$$

for $\mathrm{Re} \gtrsim 10^4$; u^* is the friction velocity and f is the Fanning friction factor [9]. With the aid of this expression, equation (7) can be rewritten as

$$\frac{T_0 - T_b}{2q_0R/k} = \frac{16}{G\mathrm{Re}^2 f^2 \mathrm{Pr}} - \frac{2}{\mathrm{Re}f\sqrt{\mathrm{Pr}}} \tag{9}$$

Only the first term is retained if $q_0 = 0$, and only the second term is retained if $Q = 0$.

Discussion

The numerical results of the present model are shown in Fig. 1 with G arbitrarily set equal to 0.5. No experimental data exist on heat transfer for fluid subjected to simultaneous heat flux and internal heat generation. However, analytical solutions based on the eddy diffusivity model are available [2, 3]. Due to the complexity of the exact solutions, Michiyoshi and Nakajima [3] also proposed an empirical formula which has been reported to agree well with their exact solution. This empirical equation is shown by dashed lines on Fig. 1. Agreement between two models appears to be fairly good.

For the case of zero wall flux, i.e., $G = 0$, equation (9) yields a simple expression for the adiabatic wall to bulk temperature difference of a generating flow. To the authors' knowledge, only two papers have been published which deal with the experimental study of heat transfer in the presence of heat sources in a fluid with moderate Prandtl number. The experiments by Poppendiek [1] and Kinney and Sparrow [5] were carried out with sulphuric acid solutions and salt water, respectively. Both papers presented experimental data for fully developed adiabatic wall-to-bulk temperature differences. Parenthetically, the predictions of reference [4] agree well with the experimental data of reference [5]. Fig. 2 compares the present model with data of Kinney and Sparrow. Their analytical solutions, which are based on an earlier analysis [2] are also included. Although data scatter is a problem, the eddy diffusivity model appears to best correlate the data at high Reynolds numbers, while the surface renewal model is preferred at low Reynolds numbers. Clearly, more heat transfer data are needed before any positive conclusions can be drawn.

[1] Department of Mechanical Engineering, The University of Akron, Akron, Ohio.

[2] Numbers in brackets designate References at end of technical brief.

Contributed by the Heat Transfer Division of THE AMERICAN SOCIETY OF MECHANICAL ENGINEERS. Manuscript received by the Heat Transfer Division, October 25, 1973.

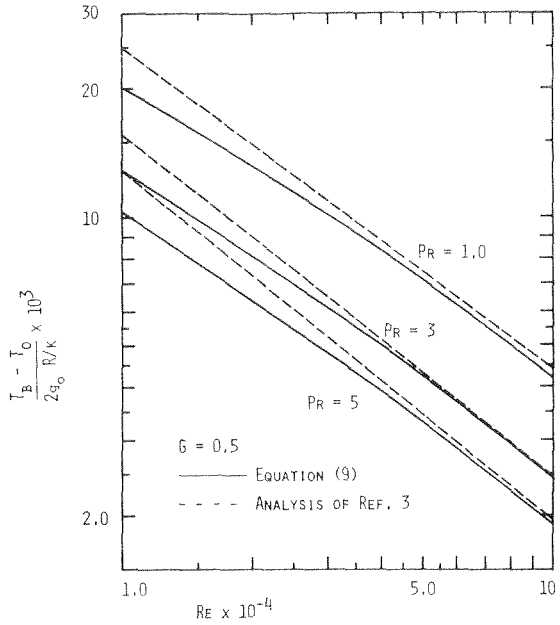

Fig. 1 Dimensionless bulk-to-wall temperature differences of a heat generating pipe flow

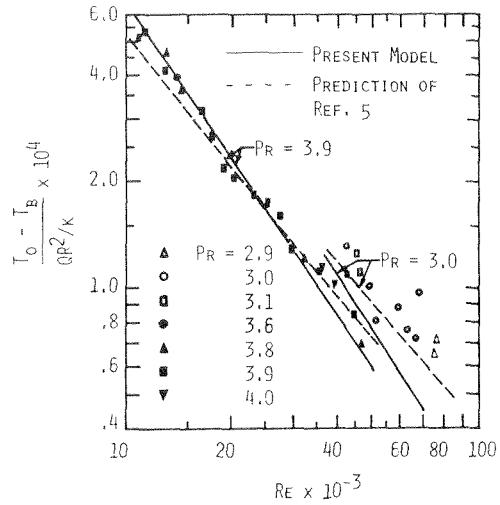

Fig. 2 Comparison between the experimental data [5] and the predicted dimensionless adiabatic wall-to-bulk temperature differences

In the case of no internal heat generation, i.e., $G \to \infty$, equation (9) correlates fairly well with the experimental data for air [8] for wall-to-bulk temperature difference. The present predictions are parallel to the data, but slightly lower. This is due to the assumption made in the analysis that the eddy temperature at the first instant of renewal t_i, is set equal to the bulk stream temperature, T_b.

Since equations (7) and (9) are derived on the basis of the assumption that eddies move into direct contact with the wall and $t_i = T_b$, the application of the present analysis is restricted to moderate Prandtl numbers. It should be pointed out that the assumption that eddies can be considered as semi-infinite in extent further restricts the present analysis to the evaluation of wall temperature (not temperature profile) for cases in which internal heat generation is involved.

Conclusion

An analysis has been presented to estimate heat transfer characteristics for turbulent fully developed flow with constant heat generation in the fluid and uniform heat flux at the tube wall. The present model appears to be much simpler than the earlier eddy diffusivity models. The expression of dimensionless wall to bulk temperature difference derived on the basis of the present analysis is easy to use while the results are in reasonable agreement with the available data. Although the predictions for adiabatic wall-to-bulk temperature difference based on the surface renewal and eddy diffusivity models are not in complete agreement throughout the entire range of Reynolds numbers, the trends and the orders of magnitude are consistent.

Acknowledgment

This study was supported in part by the National Science Foundation under grant GK-35883.

References

1 Poppendiek, H. F., "Forced Convection Heat Transfer in Pipes With Heat Sources Within the Fluid," *Chem. Engrg. Progress Symposium Series 50*, 1954, p. 93.

2 Siegel, R., and Sparrow, E. M., "Turbulent Flow in a Circular Tube With Arbitrary Internal Heat Sources and Wall Heat Transfer," JOURNAL OF HEAT TRANSFER, TRANS. ASME, Series C, Vol. 81, 1959, p. 280.

3 Michiyoshi, I., and Nakajima, T., "Heat Transfer in Turbulent Flow With Internal Heat Generation in Concentric Annulus Fully Developed Thermal Situation," *J. of Nuclear Sci. and Tech.*, Japan, Vol. 5, 1968, p. 476.

4 Petukhov, B. S., and Genin, L. G., "Heat Transfer in Tubes With Internal Heat Sources in the Fluid Stream," *International Chem. Eng'g.*, Vol. 3, 1963, p. 483.

5 Kinney, R. B., and Sparrow, E. M., "Turbulent Pipe Flow of an Internally Heat Generating Fluid," JOURNAL OF TRANSFER, TRANS. ASME, Series C, Vol. 88, 1966, p. 314.

6 Danckwerts, P. V., "Significance of Liquid-Film Coefficients in Gas Absorption," *I&EC*, Vol. 43, 1951, p. 1460.

7 Thomas, L. C., "Temperature Profile for Liquid Metals and Moderate Prandtl Number Fluids," JOURNAL OF HEAT TRANSFER, TRANS. ASME, Series C, Vol. 92, 1970, p. 565.

8 Presler, A. E., and Leoffler, A. L., Jr., Personal communication (cited from reference [2]).

9 Kays, W. M., *Convective Heat and Mass Transfer*, McGraw-Hill, New York, 1966, p. 73.